Exploring the low-temperature regime of doped Hubbard models

Theoretical insights leveraging quantum simulation

Henning Schlömer

München 2025

Exploring the low-temperature regime of doped Hubbard models

Theoretical insights leveraging quantum simulation

Henning Schlömer

Dissertation
der Fakultät für Physik
der Ludwig-Maximilians-Universität
München

vorgelegt von
Henning Schlömer
aus Solingen

München, den 10.02.2025

Erstgutachter: Prof. Dr. Fabian Grusdt
Zweitgutachter: Prof. Dr. Kaden Hazzard
Tag der mündlichen Prüfung: 24.03.2025

Contents

Abstract

Studying the low-temperature phases of doped Hubbard models, including the emergence of collective order and exotic normal phases, is at the heart of strongly correlated physics. This thesis offers new theoretical insights into the low-energy physics of doped Hubbard models, with a particular emphasis on leveraging quantum simulation as a powerful investigative tool. We explore the emergence of collective order driven by many-body interactions, by predicting and observing stripe-like structures in quantum gas microscopes of engineered Hamiltonians. These fluctuating stripe patterns are developed into a theoretical framework for the pseudogap—a highly enigmatic phase in hole-doped cuprates—where we show how fluctuating domain walls yield effective toric code descriptions. Ultracold atoms in optical lattices provide a unique platform for directly probing and testing this theory. We further investigate unconventional bilayer nickelate superconductors, predicting an exceptionally stable superfluid state in a single-band Hubbard model at experimentally accessible temperatures. By proposing schemes to observe coherent pair-pair correlations, this advances the long-standing goal of realizing and observing long-range superconducting order in ultracold atomic systems in optical lattices. On non-bipartite lattices, we examine kinetic magnetism in Hubbard models and moiré heterostructures. Additionally, the low-temperature regime of doped Hubbard models with enhanced symmetries is analyzed, revealing exotic phenomena such as sub-dimensional polaronic particles. We develop machine learning techniques to extract key physical insights from many-body snapshots, offering a new avenue for understanding intricate quantum phases. Finally, we go beyond the Fermi-Hubbard paradigm and show how non-local strongly correlated models can be leveraged to address classical optimization problems through quantum annealing.

Zusammenfassung

Das Studium der Tieftemperaturphasen dotierter Hubbard-Modelle, einschließlich des Auftretens kollektiver Ordnung und exotischer Normalphasen, steht im Zentrum der stark korrelierten Physik. Diese Dissertation liefert neue theoretische Einblicke in die Niedrigenergiephysik dotierter Hubbard-Modelle, mit besonderem Schwerpunkt auf der Nutzung der Quantensimulation als leistungsstarkes Untersuchungswerkzeug. Wir untersuchen die Entstehung kollektiver Ordnung, die durch Vielteilchenwechselwirkungen angetrieben wird, indem wir stripe-artige Strukturen in Quantengas-Mikroskopen für konstruierte Hamiltonoperatoren vorhersagen und beobachten. Diese fluktuierenden Muster werden zu einem theoretischen Rahmen für die Pseudogap entwickelt—einer äußerst rätselhaften Phase in lochdotierten Cupraten—, in dem wir zeigen, wie die fluktuierenden Domänenwände effektiver Toric-Code-Beschreibungen unterliegen. Ultrakalte Atome in optischen Gittern bieten eine einzigartige Plattform, um diese Theorie direkt zu untersuchen und zu testen. Darüber hinaus analysieren wir bilagige Nickelat-Supraleiter und sagen einen außergewöhnlich stabilen Superfluidzustand in einem Einband-Hubbard-Modell bei experimentell zugänglichen Temperaturen voraus. Mit vorgeschlagenen Methoden zur Beobachtung kohärenter Paar-Paar-Korrelationen wird ein langjähriges Ziel vorangetrieben: die Realisierung und Beobachtung von langreichweitiger supraleitender Ordnung in ultrakalten atomaren Systemen in optischen Gittern. Auf nicht-bipartiten Gittern untersuchen wir kinetischen Magnetismus in Hubbard-Modellen und Moiré-Heterostrukturen. Darüber hinaus analysieren wir das Tieftemperaturregime dotierter Hubbard-Modelle mit erweiterten Symmetrien, das exotische Phänomene wie sub-dimensionale polaronische Teilchen offenbart. Mithilfe von maschinellen Lerntechniken entwickeln wir Ansätze, um aus Vielteilchen-Schnappschüssen zentrale physikalische Erkenntnisse zu gewinnen und so neue Wege zur Erforschung komplexer Quantenzustände zu eröffnen. Abschließend geben wir einen Ausblick darauf, wie nicht-lokale Systeme genutzt werden können, um klassische Optimierungsprobleme durch Quanten-Annealing zu lösen.

List of publications

This thesis is based on the publications listed below; these publications include large parts of the material presented in this thesis, often with textual overlap. These works are the result of collaborations involving various authors, all of whom contributed to the research and the preparation of the manuscripts. The author of this thesis has made significant and substantial contributions to the publications presented in this thesis, including the conceptual development, literature review, theoretical calculations, creation and implementation of computational algorithms, examination of data, interpretation of findings, and writing of the manuscripts. The following order is given by the chronological appearance of the publications in this thesis.

- [1] **HS**, U. Schollwöck, A. Bohrdt, and F. Grusdt. **Robust stripes in the mixed-dimensional t-J model**, Phys. Rev. Research 5 L022027 (2023)
  Tags: Numerical simulations, Experimental proposals

- [2] D. Bourgund, T. Chalopin, P. Bojović, **HS**, S. Wang, T. Franz, S. Hirthe, A. Bohrdt, F. Grusdt, I. Bloch, and T. A. Hilker. **Formation of stripes in a mixed-dimensional cold-atom Fermi-Hubbard system**, Nature 637, 57–62 (2025)
  Tags: Quantum Simulation, Phenomenological Theories, Numerical Simulations

- [3] **HS**, T. Hilker, I. Bloch, U. Schollwöck, F. Grusdt, and A. Bohrdt. **Quantifying hole-motion-induced frustration in doped antiferromagnets by Hamiltonian reconstruction**, Commuications Materials 4, 64 (2023)
  Tags: Numerical Simulations, Phenomenological Theories

- [4] **HS**, A. Bohrdt, and F. Grusdt **Geometric fractionalized Fermi liquids: Hidden antiferromagnetism and pseudogap from fluctuating stripes**, arXiv 2411.03419 (2024)
  Tags: Phenomenological Theories

- [5] **HS**, U. Schollwöck, F. Grusdt, and A. Bohrdt. **Superconductivity in the pressurized nickelate $La_3Ni_2O_7$ in the vicinity of a BEC-BCS crossover**, Communications Physics 7, 366 (2024)
  Tags: Numerical Simulations

- [6] **HS**, H. Lange, T. Franz, T. Chalopin, P. Bojović, S. Wang, I. Bloch, T. A. Hilker, F. Grusdt, and A. Bohrdt. **Local control and mixed dimensions: Exploring high-temperature superconductivity in optical lattices**, PRX Quantum 5, 040341 (2024)
  Tags: Experimental Proposals

- [7] **HS**, U. Schollwöck, A. Bohrdt, and F. Grusdt. **Kinetic-to-magnetic frustration crossover and linear confinement in the doped triangular t-J model**, Phys. Rev. B 110, L041117 (2024),
  Tags: Numerical Simulations, Phenomenological Theories

- [8] Borislav Polovnikov*, Johannes Scherzer*, Subhradeep Misra*, **Henning Schlömer**, Julian Trapp, Xin Huang, Christian Mohl, Zhijie Li, Jonas Göser, Jonathan Förste, Ismail Bilgin, Kenji Watanabe, Takashi Taniguchi, Annabelle Bohrdt, Fabian Grusdt, Anvar S. Baimuratov, and Alexander Högele, **Implementation of the bilayer Hubbard model in a moiré heterostructure**, arXiv 2404.05494
  Tags: Quantum Simulation, Phenemenological Theories

- [9] **HS**, F. Grusdt, U. Schollwöck, K. R. A. Hazzard, and A. Bohrdt. **Sub-dimensional magnetic polarons in the one-hole doped SU(3) t-J model**, Phys. Rev. B 110, 125134 (2024)
  Tags: Numerical Simulations, Phenomenological Theories

- [10] **HS** and A. Bohrdt. **Fluctuation based interpretable analysis scheme for quantum many-body snapshots**, SciPost Phys. 15, 099 (2023)
  Tags: Data analysis

- [11] **HS** and S. Sachdev **Quantum Annealing with chaotic driver Hamiltonians**, arXiv 2409.20538 (2024)
  Tags: Numerical Simulations

Other contributions by the author, which are not part of this thesis, include:

- [12] A. Suresh, **HS**, B. Hashemi, and A. Bohrdt. **Interpretable correlator Transformer for image-like quantum matter data**, arXiv 2407.21502 (2024)

- [13] A. Böhler, **HS**, U. Schollwöck, A. Bohrdt, and F. Grusdt. **Probing a Modified Luttinger Sum Rule in the Strongly Interacting 1D Fermi-Hubbard Model**, Phys. Rev. B 111 (045107) (2025)

- [14] **HS**, C. Tan, S. Haas, and H. Saleur. **Parity effects and universal terms of $\mathcal{O}(1)$ in the entanglement near a boundary**, SciPost Phys. 13, 110 (2022)

- [15] G. Rai, **HS**, C. Matsumura, S. Haas, and A. Jagannathan. **Bulk topological signatures of a quasicrystal**, Phys. Rev. B 104, 184202 (2021)

1

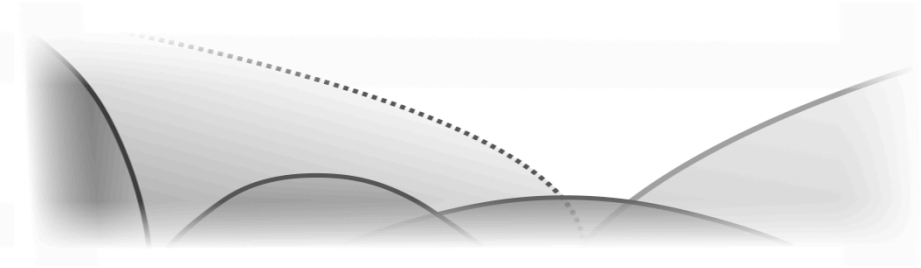

Introduction

The theory and understanding of weakly interacting quantum particles have led to fundamental insights that shape modern society. For example, the study of band structures in periodically modulated potentials (e.g., when weakly interacting electrons move through an ionic lattice) has directly contributed to the development of the transistor, a cornerstone of the digitized world. During what is now referred to as the first quantum revolution, the wave nature of particles play a crucial role in their quantum mechanical description, leading to the physics of band insulators, conductors, and semiconductors. The emergent behavior of many-body systems in this regime is well understood, with the most famous theory being that of a Fermi liquid. Fermi liquids can be characterized by a small number of parameters and provide a robust quasiparticle picture where excitations behave like weakly interacting fermions. This drastically simplifies the numerical complexity required to describe their entanglement structures, and methods such as density functional theory (DFT), mean-field approximations (e.g., Hartree-Fock), and perturbative approaches (e.g., the random phase approximation) yield remarkably accurate results in many cases.

However, when interaction effects are so strong that they dominate the physics, corresponding wavefunctions involve highly entangled superpositions of many-body states that cannot be well approximated by Slater determinants or weak perturbations around them[1]. In the past decades, this has revealed a broad plethora of emergent phenomena in many-body quantum systems, shaping the field of modern quantum physics. Prominent examples of the breakdown of the quasiparticle picture and emergence of collective behavior include high-temperature superconductivity, fractionalized excitations, non-Fermi liquid behavior, topological order, and quantum criticality [16].

Historically, the first experimental signatures of strongly correlated effects in condensed matter systems were observed in dilute magnetic impurity systems, where an anomalous behavior of

[1] Fermi liquids can be described with $\mathcal{O}(N)$ states (with N the number of particles), whereas strongly correlated systems generally scale exponentially with N.

resistivity as a function of temperature was detected—this phenomenon is known as the Kondo effect[2] [17]. With the development of theoretical approaches to describe the formation of local moments, the range of materials exhibiting strong correlation effects rapidly expanded. These include heavy fermion metals [18] and superconductors [19], (topological) Kondo insulators [20], non-Fermi liquid systems [21], fractional quantum Hall systems [22], and high-temperature superconductors [23, 24].

In particular with regard to the latter, the two-dimensional (2D) Fermi-Hubbard (FH) model—consisting of only two terms, the kinetic energy and short-range interactions between particles—has emerged as a paradigmatic model that captures the bare essentials of strongly correlated physics. While its study has led to significant insights into many features of strong correlations over the past decades, numerous phases of matter and their microscopic origins remain enigmatic. Understanding, classifying, and predicting these emergent, collective phenomena driven by correlation effects remains a central goal of modern quantum physics.

The failure of perturbative methods to account for strong correlation effects necessitated the development of alternative theoretical tools. For instance, the discovery of the Kondo effect resulted in renormalization group calculations [25], parton constructions [16], and the Bethe ansatz [26]. Furthermore, a variety of numerical algorithms have been developed to handle systems featuring strong correlations. Among the most notable examples are quantum Monte Carlo methods [27], variational tensor network methods (including the density matrix renormalization group [28–30], which will be extensively used in this thesis), dynamical mean field theory (DMFT) [31], and neural network quantum states [32]. While these approaches are capable of taming and capturing the strongly correlated nature of certain systems to a significant extent (surpassing the limitations of exact diagonalization), they come with inherent constraints. For example, quantum Monte Carlo methods suffer from the sign problem, severely limiting their applicability to fermionic and frustrated systems. Similarly, while DMRG excels in one dimension, its effectiveness diminishes in higher-dimensional systems. Thus, studying 2D doped quantum magnets, both in the ground state and at finite temperature, in most cases remains intractable with current numerical techniques.

To overcome these challenges, the vision of simulating quantum systems using real-world quantum particles has emerged [33]. For a long time, this remained a conceptual dream of physicists. However, a series of breakthroughs in cooling, trapping, controlling, and manipulating atoms over the past decades has transformed this vision into a practical reality, giving rise to quantum simulation as a tangible tool. Quantum simulation platforms that enable the study of strongly correlated systems in the laboratory include a diverse range of systems, from neutral atoms [34, 35] and ions [36] in optical and quadrupole traps, respectively, to superconducting qubit devices [37] and solid-state materials such as moiré heterostructures [38]. The development of these quantum hardware devices is commonly viewed as the second step in the quantum revolution, where, in addition to exploiting the wave-like nature of particles, the entanglement of quantum systems is harnessed[3].

[2] In particular, the resistivity features a minimum at low temperatures, below which a logarithmic increase is observed; the resistivity converges to a constant when $T \to 0$.

[3] From a different perspective, digital quantum computing devices aim to perform universal computations by

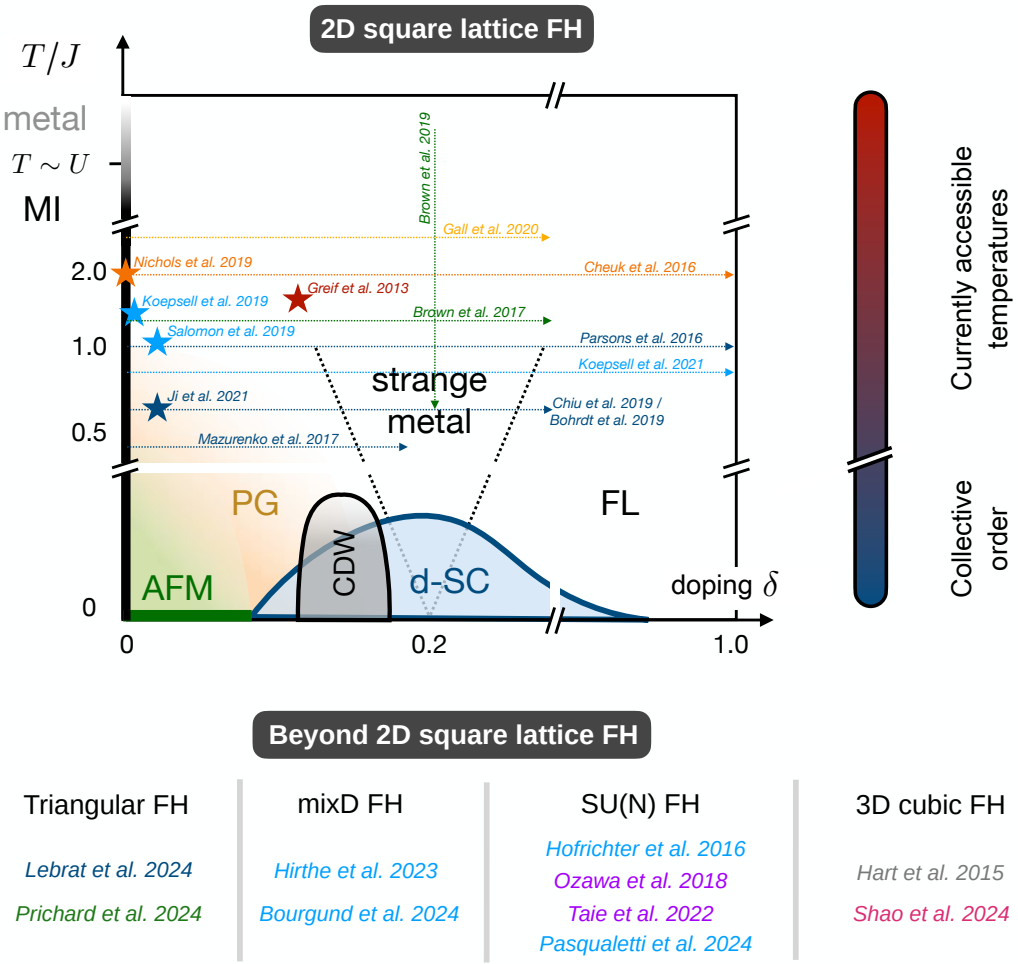

Figure 1.1: **Overview of ultracold atom experiments.** Many experiments have explored the 2D FH model on the square lattice. Notable experiments from various groups (marked by color) are highlighted in the upper part of the figure in the (conjectured) phase diagram of the FH model; Figure taken and adapted from Ref. [40]. Harvard group (dark blue): Mazurenko et al 2015. [41], Chiu et al 2019. [42], Bohrdt et al. 2019 [43], Ji et al. 2021 [44], Parsons et al. 2016 [45]. Munich group (light blue): Koepsell et al. 2019 [46], Salomon et al. 2019 [47], Koepsell et al. 2021 [48]. Princeton group (green): Brown et al. 2019 [49], Brown et al. 2017 [50]. ETH Zurich group (red): Greif et al. 2013 [51]. MIT group (orange): Cheuk et al. 2016 [52], Nichols et al. 2019 [53]. Bonn group (yellow): Gall et al. 2020 [54]. While a broad range of interesting physics around individual dopants has been unraveled in these experiments, the temperatures achieved to date remain too high to observe collective ordering behavior, such as charge- and spin-density waves or superconductivity. Experiments of systems that go beyond the plain-vanilla 2D square lattice FH model paradigm are highlighted in the lower part of the figure. These include experiments on the triangular lattice (Lebrat et al. 2024 [55], Prichard et al. 2024 [56]), mixed-dimensional FH models (Hirthe et al. 2023 [57], Bourgund et al. 2025 [2]), SU(N) symmetric FH models (Hofrichter et al. 2016 [58], Ozawa et al. 2018 [59], Taie et al. 2022 [60], Pasqualetti et al. 2023 [61]), and the 3D cubic FH model (Hart et al. 2015 [62], Shao et al. 2024 [63]). Works from the Kyoto, Rice and Hefei groups are shown in purple, grey, and pink, respectively.

leveraging entanglement as a resource [39]. In this thesis, we will, however, mainly focus on devices that perform quantum simulation in an analog manner.

1.1 Quantum gas microscopes: Milestones and Roadmap

What has been achieved with ultracold atoms in optical lattices so far? As will be discussed in more detail in Chap. 4, the remarkable technological progress in quantum simulation platforms now enables the controlled realization of a broad variety of quantum states. Specifically regarding the physics of the FH model, (a subset of) notable experiments are presented in Fig. 1.1.

One of the first major breakthroughs has been the preparation and observation of Mott insulating states with antiferromagnetic order [41, 51, 64–66], reaching up to ~ 8 sites at the coldest temperatures [41]. As the energy scale for magnetic ordering is set by the superexchange $J = 4t^2/U$ (with t the hopping amplitude and U the on-site interaction strength), spin ordering emerges for $T/J \lesssim 1$, which corresponds to temperatures achievable in state-of-the-art ultracold atom experiments. Upon doping these spin-ordered Mott insulators, quantum gas microscopes have provided significant insights into the formation and evolution of magnetic polarons—mobile holes dressed with spin excitations [41–54] at intermediate temperatures, as illustrated in Fig. 1.1 and reviewed in detail in Ref. [40].

What are the open problems and milestones yet to be achieved? Current studies of the doped Fermi-Hubbard model using ultracold atom experiments focus on the intermediate temperature regime (see Fig. 1.1), where individual mobile dopants and their dressing can be studied in detail. However, state-of-the-art temperatures (reached by the end of 2024) are not low enough to access the collective orders dominating the low-energy physics of the FH model, such as charge- and spin-density waves and superconductivity. This is because these phases emerge from the intricate competition between kinetic and interaction energies, resulting in much lower critical temperatures compared to observing spin order at one particle per site, where the superexchange is the only dominant energy scale. Hence, realizing these states remains a decade-old dream, with the potential to uncover the microscopic origin of strongly correlated phases of matter and to gain a unified theory of doped Mott insulators. Beyond studying symmetry-breaking order, reaching these regimes also promises microscopic insights into exotic normal phases, such as the pseudogap phase in the Hubbard model (prominent in particular in hole-doped cuprates), from which symmetry-breaking orders emerge.

However, the technological challenges involved in lowering effective temperatures T/J to an extend that allows for the observation of collective order renders these milestones extremely challenging to achieve. Can we make progress nevertheless and gain insights into the formation of collective order in doped quantum magnets with current state-of-the-art simulators? One possible path, which will be central throughout this thesis, involves implementing closely related, adjusted models to realize "parent Hamiltonians" of symmetry-broken ordered states in strongly interacting fermionic systems. These models can be (i) theoretically motivated or (ii) directly inspired by certain classes of strongly correlated materials.

Enhanced energy scales for collective behavior in these systems then facilitate their quantum simulation, allowing for microscopic insights into their formation, properties, and potentially their relation to other collective orders. In this thesis, we will present how this enables the realization and observation of states exhibiting stripe and superconducting order, two of the most

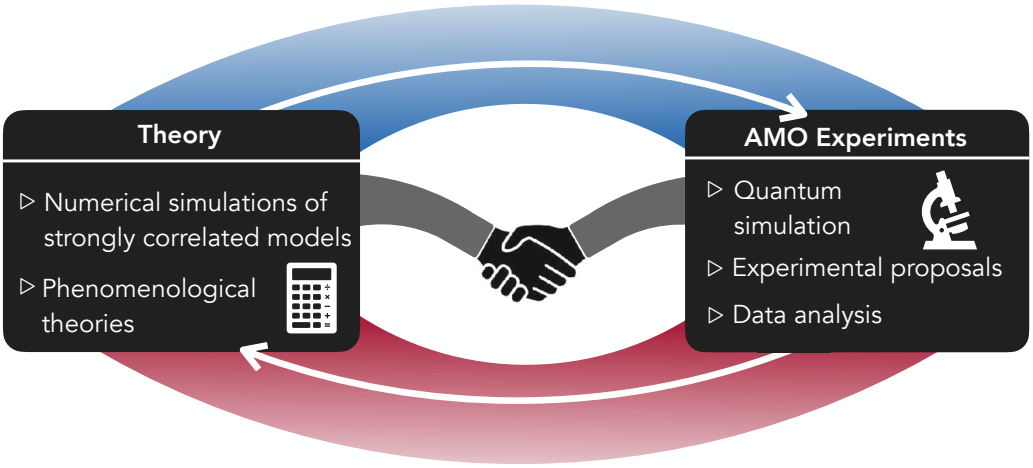

Figure 1.2: **Handshake of theory and experiment.** Theoretical predictions based on numerical calculations or phenomenological considerations inspire experimental realizations of model Hamiltonians, often necessitating the development of novel experimental techniques or sequences. Conversely, observations of many-body phases in quantum simulation experiments—particularly in regimes that are inaccessible numerically—drive the development of theoretical models, leading to a deeper understanding of strongly correlated phases of matter.

prominent phases of matter in hole-doped cuprates and the Hubbard model. In particular, we will see how typical associated energy scales of these ordered states directly fall within the reach of optical lattice experiments.

Directions of interest beyond the 2D square lattice Fermi-Hubbard paradigm include the study of frustration in doped quantum magnets on non-bipartite lattices, such as the triangular lattice. In these systems, kinetic effects can give rise to exotic magnetic behaviors. While these phenomena have been theoretically extensively studied over the past decades, the realization of ultracold atom experiments using triangular optical lattices, see also Fig. 1.1, has brought renewed attention and interest to the field in recent years [55, 56, 67].

Another promising direction in the field of ultracold atoms in optical lattices is the study of fermionic Hubbard models with higher symmetries, where theoretically predicted intricate magnetic structures in Mott insulating states suggest the emergence of exotic physics upon doping. This avenue is particularly motivated by the pristine realization of SU(N) symmetric Hubbard models using alkaline-earth atoms (AEAs) in optical lattices [58–61], see also Fig. 1.1; such advancements pave the way for exploring a plethora of exotic phenomena in doped SU(N) quantum magnets, and may help to gain a unified understanding of doped Mott insulators.

The above insights illustrate how the modern field of strongly correlated electronic systems is characterized by an intricate interplay between theoretical considerations and practical experimental implementations, as illustrated in Fig. 1.2. While the theoretical exploration of many-body phases of matter motivates their extensive study in quantum simulators in the laboratory, the results of these experiments, in turn, inspire novel theoretical developments to explain the observed phenomena. This dynamic creates a close "handshake" between theory and experiment, where each influences and drives the other forward. This thesis closely follows this philosophy, and in the following, we briefly outline its scope, goal, and structure.

1.2 Outline and goal of this thesis

We begin by introducing strongly correlated solid-state systems and their minimal model Hamiltonians in Chap. 2. In Chap. 3, we review numerical approaches used to calculate or approximate the properties of these Hamiltonians, focusing on matrix product state methods, in particular the density matrix renormalization group (DMRG). In Chap. 4, we describe how quantum gas microscope experiments with ultracold atoms in optical lattices (and, furthermore, moiré materials) offer pristine platforms for studying these systems in the laboratory.

Then follows the main part of this thesis. In many chapters, we perform large-scale numerical simulations of strongly correlated systems, complemented by phenomenological theories that provide physical intuition. Beyond gaining insights from these numerical and phenomenological (mostly semi-analytical) approaches, our considerations and physical settings maintain a strong emphasis on ultracold atom experiments. Ultimately, the aim is to gain a deeper understanding of the low-temperature phases of doped Hubbard models, while motivating and leveraging new experiments that push the boundaries of quantum simulation platforms.

First, we shall address the question of simulating collective order in optical lattice experiments with ultracold, repulsively interacting fermions. In Chap. 5, we study the Fermi-Hubbard model in the strongly interacting regime (i.e., the t-J model) while suppressing hopping of mobile holes in one spatial direction. As we demonstrate numerically, this leads to a stable stripe phase (i.e. a coupled charge- and spin-density wave) at temperatures directly accessible with current quantum gas microscopes. This part of the chapter is based on publication Ref. [1]. Afterwards, we analyze experimental results from the Lithium experiment at the Max Planck Institute of Quantum Optics (MPQ), which realizes this setting through optical superlattice engineering. We study the interplay of charge and spin degrees of freedom, as well as the formation of individual stripes at intermediate temperatures, making a significant step toward experimentally realizing long-range, collective spin- and charge-order in Fermi-Hubbard systems. This part of the chapter is based on the publication Ref. [2].

To understand the interplay of spin and charge degrees of freedom at low temperatures, it is useful to first quantitatively study this interplay at elevated temperatures, away from any collectively ordered state. In Chap. 6, we reconstruct effective spin Hamiltonians by effectively removing the hole degrees of freedom. Using numerical gradient descent methods, we find that the resulting system is accurately described by a Heisenberg model on the square lattice with longer-range interactions, introducing strong frustration in the spin background. In a similar spirit, through these Hamiltonian reconstruction schemes, we further observe how the spin background mediates an effective attractive interaction between hole dopants, which can give insights into the microscopic nature of pairing in doped Hubbard models. Chap. 6 is based on the publication Ref. [3].

Motivated by these theoretical and experimental insights, in Chap. 7, we construct a phenomenological theory for the pseudogap phase in hole-doped cuprates, based on the intuition of fluctuating domain walls when melting away stripes. In the scenario discussed in Chap. 7, fluctuating stripes efficiently hide the magnetic order and lead to the formation of a $\mathbb{Z}_2$ quantum

spin liquid. This, in turn, results in fractionalization and the emergence of a small Fermi surface. Notably, this theory—characterized by the hallmark of hidden order—can be directly tested using large-scale snapshots from ultracold atom experiments, provided these experiments reach temperatures deep within the pseudogap phase. Chap. 7 is based on the preprint Ref. [4].

Certainly, one of the major goals of analog quantum simulation is the realization of a superconducting state in Fermi-Hubbard-type model Hamiltonians—a vision that has been shaped more than two decades ago [68]. As with other collective orders such as stripes, however, the critical temperatures below which seizable coherent pairing correlations exist in the plain Hubbard model are far below the current capabilities of ultracold atom experiments. In this context, certain bilayer Fermi-Hubbard models have been proposed [69], and real-space pairing has indeed been observed in tailored ladder geometries [57]. Shortly thereafter, a new class of high-temperature superconductivity was discovered in bilayer nickelate compounds [70], which have been argued to be described by precisely these minimal models previously proposed in Ref. [69].

In Chap. 8, we study these bilayer systems numerically. By analyzing limiting cases of strong inter-layer interactions, we find that these models exhibit extraordinarily high critical temperatures to form a coherent superfluid state, peaking at a crossover from a BEC-to-BCS state. The numerical results presented in Chap. 8 are based on the publication Ref. [5]. As a striking consequence of the high critical temperatures, preparing states with long-range pairing order in ultracold atom experiments is in direct reach.

However, observing this type of order requires measuring operators that are non-diagonal in the Fock basis. In Chap. 9, we address this challenge and provide a detailed proposal for measuring coherent pair-pair correlations through a partial particle-hole transformation. Furthermore, we demonstrate that applying gate sequences in optical lattice setups enables the measurement of pairing correlations in the plain-vanilla Fermi-Hubbard model. This positions hybrid digital-analog approaches as a highly promising direction for extending the scope of optical lattice experiments, and facilitates the observation of both s- and d-wave superconducting order in Fermi-Hubbard bilayers and single layers, respectively. Chap. 9 is based on the publication Ref. [6].

Going beyond the square lattice paradigm, introducing geometric frustration into the competition between kinetic and magnetic energy (e.g., the Fermi-Hubbard model on non-bipartite lattices such as the triangular lattice) is a central theme that can lead to exotic physics. In the first part of Chap. 10, we study a single dopant introduced into the triangular lattice t-J model. As the model lacks particle-hole symmetry, the resulting physics strongly depends on whether a hole or an electron is doped into the system. In the case of electron doping, magnetic interactions (which favor an antiferromagnetic alignment of spins) compete with kinetic frustration (which favors ferromagnetic spin alignment), leading to a non-trivial dependence of magnetic correlations on temperature. This part of Chap. 10 is based on the publication [7].

Beyond ultracold atoms in optical lattices, moiré materials offer a promising platform to simulate effective Fermi-Hubbard physics on the triangular lattice. In the second part of Chap. 10, we explore stacked $MoSe_2/WS_2$ and discuss how their unique charging behavior effectively simulates a bilayer Fermi-Hubbard model. To gain a qualitative understanding of the underly-

ing physics, we employ two-particle self-consistent theory, classical Monte Carlo methods, and DMRG simulations. This second part of Chap. 10 is based on the preprint Ref. [8].

Studying model Hamiltonians that extend beyond the Fermi-Hubbard model with spin-1/2 degrees of freedom is yet another promising direction for gaining deeper insights into the competition between kinetic and interaction energies. Motivated by the properties of ultracold alkaline-earth atoms, the SU(N) symmetric Fermi-Hubbard model has become a popular framework. In this model, fermions hopping on a lattice possess N colors and interact symmetrically. At one particle per site, it has been established that exotic magnetic structures emerge, stabilized by quantum fluctuations. However, the behavior of these systems upon doping remains largely unexplored.

In Chap. 11, we take a first step in this direction by studying a single hole doped into the SU(3) t-J model. By comparing our results with phenomenological theories, we demonstrate that magnetic polarons that form upon doping are constrained to move along a single effective dimension. This finding suggests the potential for exotic physics in doped SU(N) symmetric models and strongly motivates quantum gas experiments as powerful tools to systematically explore these systems on a microscopic level. Chap. 11 is based on the publication Ref. [9].

The natural output of quantum gas simulators consists of many-body snapshots in the measurement (Fock) basis. These snapshots contain an enormous amount of information, as any (local and non-local) observable can, in principle, be evaluated within the measurement basis. In particular, for phases characterized by non-trivial, non-local observables, it is crucial to develop analysis schemes that can extract and highlight the physical features encoded in these snapshots for a given quantum phase of matter.

With their immense success in fields such as image classification, natural language processing, and many others, neural networks have become indispensable tools in numerous areas of research. Consequently, their application to the analysis of many-body snapshots holds significant promise. In Chap. 12, we use a specific neural network architecture coupled with a tailored training procedure to develop a robust toolkit for unsupervised analysis of quantum phases of matter. We further look at transformer and autoencoding architectures, setting the stage to analyze intricate many-body phases using machine assisted schemes. Chap. 12 is based on the publication Ref. [10].

What are interesting models of strongly interacting fermions that lie fully beyond the Fermi-Hubbard paradigm? One particularly prominent example is the Sachdev-Ye-Kitaev (SYK) model, which has emerged as a paradigmatic framework for studying non-Fermi liquid behavior. The SYK model features highly entangled low-energy states and is characterized by fast scrambling of quantum information, saturating certain theoretical bounds. These properties make it not only relevant to condensed matter physics but also to the field of quantum gravity, as connections between the quantum description of black holes and the SYK model have been established. Consequently, the quantum simulation of the SYK model is highly anticipated.

In Chap. 13, we take a look at the SYK model from a different angle and investigate their efficiency in quantum annealing settings. Quantum annealing aims to find the ground state of a classical optimization problem through adiabatic state preparation. We demonstrate that

incorporating non-local terms of the SYK model as part of the driver Hamiltonian significantly improves the ability to solve hard optimization problems. Finally, we explore potential digital quantum simulation approaches for the SYK model. Chap. 13 is based on the preprint Ref. [11].

In Chap. 14, we briefly summarize and conclude the findings and progress made in this thesis, and discuss possible future directions.

Part I

Theory and Methods

2

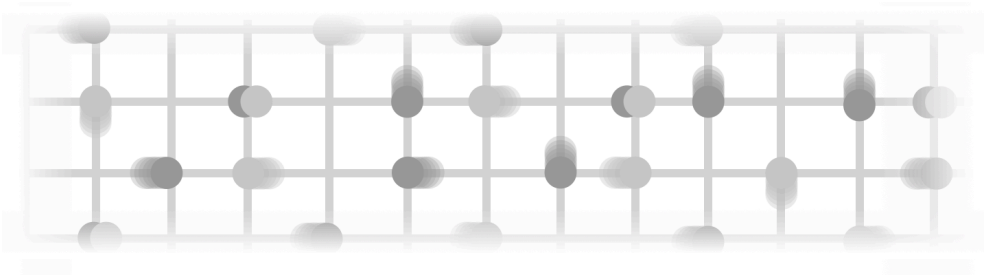

Strongly correlated systems

Summary. This chapter provides a brief overview of strongly correlated systems, with a particular focus on cuprate and nickelate high-temperature superconductors. We examine their electronic structure and summarize the phases of matter observed in these materials. Effective descriptions based on Fermi-Hubbard models are motivated, and we introduce relevant descendants of these models, such as the t-J model and the SU(N)-symmetric Fermi-Hubbard model, which are central to this thesis.

Central to the emergence of strong correlation effects is the electronic structure in solid-state systems, where, under certain conditions, many-body interaction energies dominate over kinetic energies—leading to significant changes in the macroscopic properties of the material. Before introducing the electronic structure of high-temperature superconductors in more detail, let us build some intuition about when correlation effects are expected to play a significant role.

Strong electronic interactions are anticipated when orbitals are localized: small overlaps of orbitals localized around a nucleus with their nearest neighbors result in narrow electronic bands, while local interactions between electrons within the same and neighboring orbitals remain strong. Many classes of strongly correlated materials exhibit partially filled d- and f-orbitals. Two trends can be observed when considering the degree of orbital localization as a function of the principal and angular quantum numbers of electronic orbitals. First, orbitals with a higher principal quantum number n contain more radial nodes, making them less localized[1]. Second, as the d-shell fills and transitions into f-orbitals, the increasing nuclear charge pulls the electrons closer to the nucleus, effectively squeezing the orbitals and making them more localized. Thus, quite generally, the degree of localization increases in the following sequence [71]:

$$5d < 4d < 3d < 5f < 4f. \tag{2.1}$$

[1] An analogy are the states in an harmonic oscillator, which feature a spread $\sigma_{\hat{\mathbf{x}}}^2 = \langle \hat{\mathbf{x}}^2 \rangle = \frac{\hbar}{2m\omega}(2n+1)$.

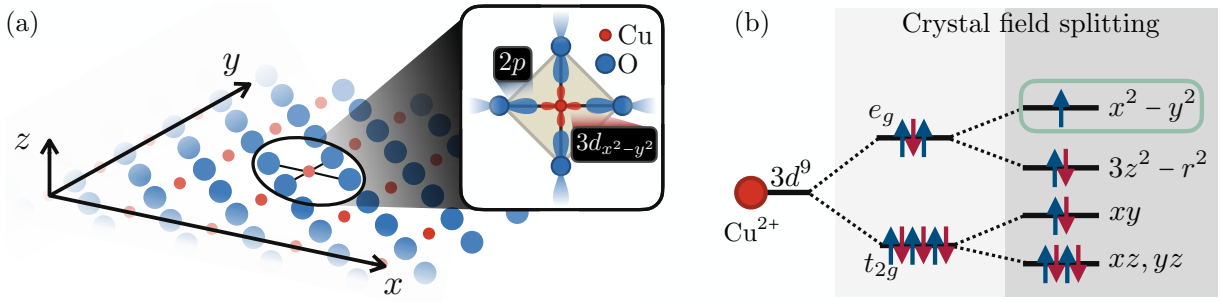

Figure 2.1: **Copper oxide planes and active orbitals.** (a) A single copper-oxide plane, which in cuprates are layered and separated by spacer layers that can act as charge reservoirs. (b) Due to crystal field splitting caused by the oxygen octahedra around Cu^{2+} sites (light grey) and the Jahn-Teller effect (dark grey), the active orbital is the half-filled $3d_{x^2-y^2}$ orbital. As the orbitals are strongly localized, interaction effects dominate, and in the undoped parent compound, the $3d_{x^2-y^2}$ electrons form an antiferromagnetic Mott insulator. Through atomic substitution, holes can be doped into the $2p$ orbitals. These holes form Zhang-Rice singlets centered at the copper sites (see ocher diamond in the inset of (a)), leading to an effective single-band description of hopping electrons in the $3d_{x^2-y^2}$ orbitals with a filling that deviates from one particle-per-site.

In actinide and rare-earth compounds, the $5f$ and $4f$ shells are partially filled, respectively, resulting in strong localization and correlation effects. Consequently, these systems often form Mott insulating antiferromagnets, where insulating states with spin order emerge, even though their non-interacting band structure would suggest metallic behavior [71].

At the crossover between heavily localized orbitals and itinerant bands, as seen in materials dominated by electrons in $5d$ orbitals, other classes of intriguing many-body phases arise, such as heavy-fermion metals and iron-based superconductors. In heavy-fermion metals, localized moments interact with itinerant electrons, giving rise to fermionic quasiparticles with effective masses that exceed the bare electron mass by factors of up to 1000. In iron-based superconductors, multiple active $3d$ bands and moderate interaction strengths lead to unconventional superconductivity and magnetic ordering tendencies [71].

2.1 Cuprates

Next to the above-mentioned examples, doped copper oxide compounds (cuprates) are arguably one of the most famous classes of strongly correlated materials, discovered by Bednorz and Müller in 1986[2] [23]. The cuprates' fame primarily stems from their extraordinarily high critical temperatures for superconductivity, which in some compounds surpass the boiling point of liquid nitrogen. However, next to superconductivity, they host a plethora of intriguing correlated states that, from their discovery to the present day, fuel intense theoretical debates and research. In the following, we will first introduce the atomic structure of cuprates and their single-band Fermi-Hubbard description, before briefly traversing the phase diagram to summarize the most important features of this class of materials.

Cuprates are layered materials characterized by copper oxide planes forming a Lieb lattice,

[2]For their discovery, Bednorz and Müller were awarded the Nobel prize in physics already one year later, in 1987.

where copper atoms reside on a square lattice and oxygen atoms occupy the links of the square lattice, see Fig. 2.1 (a). Although copper in isolation has an electronic configuration where the $3d$ shell is completely filled ($[\mathrm{Ar}]4s^1 3d^{10}$), in the crystal structure, two electrons from the copper atom are donated when binding with oxygen, leaving an effective Cu^{2+} atom with a $[\mathrm{Ar}]3d^9$ configuration. The crystal field further lifts the degeneracy of the $2L+1 = 5$ d-orbitals due to geometrical distortions of the ionic lattice[3], see Fig. 2.1 (b). As a result, the five orbitals are split into d_{xz}, d_{yz}, d_{xy}, $d_{3z^2-r^2}$, and $d_{x^2-y^2}$, with increasing energy. Filling these orbitals with nine electrons results in all orbitals being fully occupied except for the $3d_{x^2-y^2}$ orbital, which hosts one electron per site (see Fig. 2.1 (b)). Through hybridization of the $3d_{x^2-y^2}$ orbitals of copper with the in-plane $2p$ orbitals of oxygen, the d-shell electrons can hop across the square lattice. While a non-interacting system would result in conducting properties, the localized nature of the $3d$ orbitals instead leads to the formation of local moments, where interaction energies dominate over kinetic energies, forming a Mott insulator.

By substituting atoms in the spacer layers between the CuO_2 planes, electrons can effectively be added to or removed from the CuO_2 planes. A typical cuprate compound is the lanthanum-based La_2CuO_4, where the spacer layers are composed of lanthanum and oxygen atoms. Replacing La with Sr to a certain extent introduces hole doping, as Sr^{2+} replaces La^{3+}, absorbing an electron from the CuO_2 planes. Similarly, the copper-oxide planes can be electron doped when replacing La by Ce atoms.

2.1.1 Phase diagram

In the undoped parent compound, cuprates exhibit long-range antiferromagnetic (AFM) correlations driven by superexchange interactions among localized electrons in the $3d_{x^2-y^2}$ orbitals, a characteristic shared by many strongly correlated Mott insulators. The wide variety of many-body phases hosted by cuprates upon doping the system is summarized in the schematic phase diagram shown in Fig. 2.2, and it is widely accepted that strong correlations play a pivotal role in these phases [72,73]. In the following, we briefly summarize the various observed phases in both electron- and hole-doped cuprates. While the electron-doped side is generally considered relatively well understood, many open questions persist on the hole-doped side. Therefore, we begin by reviewing the physics of electron-doped cuprates before summarizing the hole-doped side of the phase diagram.

This section provides only a brief description of the qualitative physics and experimental signatures of the various phases. In particular, the prominent pseudogap phase appearing in hole-doped cuprates will be discussed in much more depth in Chap. 7, where we also take a close look at Luttinger's theorem, which is a fundamental result in Fermi liquids that relates the Fermi surface to the particle density.

[3]The crystal field splitting occurs in two steps: First, the presence of oxygen octahedra around the copper sites splits the $3d$ orbitals into e_g and t_{2g} orbitals. Then, the Jahn-Teller effect lifts the degeneracy of these orbitals due to geometrical distortions in the lattice.

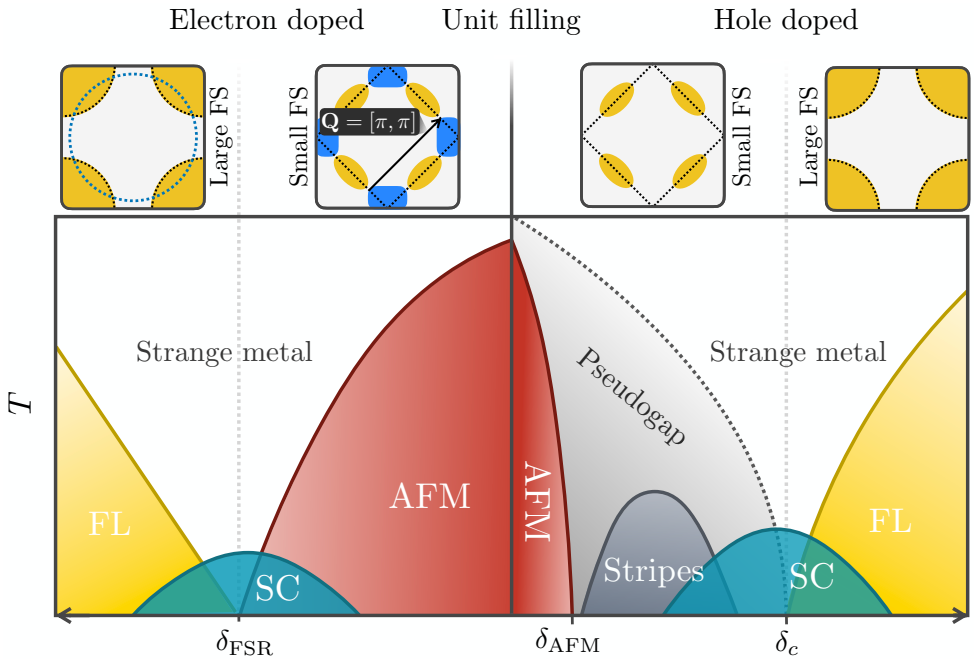

Figure 2.2: **Schematic phase diagram of cuprates.** Phases in electron-doped (left) and hole-doped (right) cuprates. **Electron-doped side:** A broad AFM metallic region with commensurate order leads to a metallic phase with a small Fermi surface (top row). Superconducting order (d-wave symmetry) peaks where AFM fluctuations vanish at zero temperature, transitioning into a Fermi liquid with a conventional, large Fermi surface. Experimentally, the doping level at which Fermi surface reconstruction occurs can be measured through Hall conductivity measurements, yielding $\delta_{\text{FSR}} \approx 15\%$. Above the superconducting phase, an extended region of strange metallicity is observed, characterized by non-Fermi liquid metallic behavior. One proposed scenario is that AFM fluctuations act as the glue for superconductivity, peaking at a quantum critical point. This quantum criticality, in turn, leads to an extended region of non-Fermi liquid behavior around the critical doping. **Hole-doped side:** The AFM phase rapidly vanishes upon doping, persisting only up to a few percent doping, $\delta_{\text{AFM}} \approx 2\%$. In many cases, superconducting and AFM phases do not overlap, forming disjoint phases. In numerous compounds (particularly La-based cuprates), prominent stripe phases emerge between the AFM and SC phases, featuring coupled charge- and spin-density waves. Most notably, hole-doped cuprates exhibit an extended pseudogap region, encompassing a wide range of enigmatic observations. In this phase, no clear symmetry breaking is observed, yet signatures of a small Fermi surface are detected (top row).

Electron-doped side

Fermi liquid. Starting in heavily electron-doped cuprates, the system exhibits metallic behavior and adheres to Fermi-liquid theory across all observables. In particular, these materials display clear signatures of standard (large) Fermi surfaces (FS), consistent with Luttinger's theorem for metals with no broken symmetry. This is illustrated in the upper part of Fig. 2.2.

AFM Phase. At low to intermediate levels of electron doping, extensive antiferromagnetic (AFM) correlations persist away from one particle per site, although the critical temperature for achieving long-range correlations decreases with increasing doping. In a broad doping range, these AFM correlations remain commensurate at $\mathbf{Q} = [\pi, \pi]$ and are not qualitatively affected by

electron doping. The presence of local moment order introduces the concept of Fermi surface reconstruction (FSR). Here, electrons scatter off the potential background induced by the AFM order, coupling momenta $\mathbf{q}$ with $\mathbf{q} + \mathbf{Q}$. This is illustrated in Fig. 2.2, where the dashed blue line in the large Fermi surface picture corresponds to a FS shifted by $\mathbf{Q}$. This coupling results in points in the Brillouin zone (BZ) where the two bands cross, gapping out the spectrum at these hotspots. Consequently, small hole pockets (from the lower band in the symmetry-broken metal) and electron pockets (from the upper band) form. Notably, the size of the Fermi surface reduces during this process and is now determined by the doping level δ rather than $1 + \delta$ (where the latter represents the full electronic density). This reduction complies with Luttinger's theorem, which permits a small Fermi surface when the metal's translational symmetry is broken, as discussed in more detail in Chap. 7. In electron doped cuprates, this change of carrier density can be detected e.g. in Hall measurements, where the Hall resistivity as a function of doping gives direct access to the active carrier density, which shows a jump at δ_{FSR} [73].

Superconductivity. At intermediate doping values, around $\delta \sim 15\%$, superconductivity emerges with critical temperatures of approximately $T_c \approx 30$ K. One of the most remarkable features of cuprates is that this superconducting state emerges from an insulating state at lower doping, in stark contrast to standard BCS-type superconductors, which arise from Fermi-liquid metallic states. While early experiments suggested s-wave symmetry for the superconducting order parameter in electron-doped cuprates, higher-quality samples and techniques such as angle-resolved photoemission spectroscopy (ARPES) have revealed a d-wave character [74].

The disappearance of AFM order[4] at optimal doping, where superconductivity reaches its maximum T_c, suggests a close connection between AFM fluctuations and the origin of superconductivity in electron-doped cuprates. In this view, electron interactions mediated by AFM spin fluctuations give rise to d-wave superconductivity. This perspective further implies that, upon suppressing superconductivity, a quantum critical point (QCP) exists on the doping axis where long-range AFM correlations vanish. This QCP suggests the presence of a quantum critical fan, where non-Fermi liquid behavior dominates at zero temperatures. Indeed, a broad region of strange metallicity is observed in electron-doped cuprates, consistent with this scenario, as explained next (see also Fig. 2.2).

Strange Metal. The hallmark of strange metals is the absence of well-defined quasiparticles, unlike in regular metals. This is particularly evident in transport properties, where strange metals exhibit a linear temperature dependence of electrical resistivity, $\rho \propto T$, in contrast to the $\rho \propto T^2$ dependence of Fermi liquids. This behavior extends over a wide temperature range, even surpassing the Mott-Ioffe-Regel (MIR) limit, which sets an upper bound on resistivity in conventional metals when the mean-free path becomes comparable to the atomic lattice spacing. In particular, in conventional metals, resistivity saturates beyond the T^2 scaling at higher temperatures. In contrast, in the strange metal phase of doped cuprates, resistivity significantly exceeds the MIR limit, a clear hallmark of non-Fermi liquid behavior.

The above findings suggest that non-Fermi liquid behavior emerges near the quantum critical

[4] Regions of true long-range order and regions of strong AFM fluctuations are often distinguished [73]. For simplicity, we mark the region of strong AFM fluctuations as the AFM phase.

point (masked by the superconducting phase without external magnetic fields). However, alternative scenarios for the strange metal phase have also been proposed, including marginal Fermi liquids and Planckian dissipation. We will not go into more detail of these possibilities here, but instead turn to the phases observed in hole-doped cuprates. For comprehensive reviews of electron-doped cuprates, we refer the reader to Refs. [73, 75].

Hole-doped side

While the phase diagram of hole-doped cuprates shares some similarities with the electron-doped side, there are also profound differences that clearly set apart hole- from electron-doping. While a phase with long-range AFM order exists at very low doping, it vanishes extraordinarily quickly at only a few percent of hole doping. This stands in striking contrast to the electron-doped side, where AFM order persists up to $\approx 15\%$ doping.

Stripes. Instead of AFM order, charge order emerges at low temperatures and finite doping in a broad range of cuprate families, often[5] in the form of stripes: a simultaneous charge- and spin-density wave, where AFM order experiences a domain wall at regions of enhanced hole density [76–78]. This results in a transformation from commensurate to incommensurate magnetic order, as the domain walls shift the magnetic structure factor away from $\mathbf{Q} = [\pi, \pi]$. Stripes have been shown to be particularly prominent around $\delta = 1/8$ doping [79–81]. More subtle stripe-like signatures, predominantly in the charge sector, have further been shown to exist in Bismuth [82–84] and Yttrium-based [85] cuprate families through scanning-tunneling-microscope (STM) and nuclear magnetic resonance (NMR) measurements. In particular, by applying magnetic fields that suppress superconductivity, stripe order can be induced in samples where static order without additional fields is absent [85, 86]. We again emphasize the stark contrast to electron-doping, where no charge order is observed. In Chap. 7, we interpret the appearance of charge order in hole-doped cuprates as a symptom of *hidden* AFM correlations at higher temperatures.

Pseudogap. As a result of the rapid disappearance of the AFM phase at low doping, the superconducting and AFM domes do not overlap on the hole-doped side in most compounds, forming two disjoint phases. Instead, these phases are sandwiched by the pseudogap phase, widely regarded as one of the most puzzling and enigmatic phases of cuprate materials. Sec. 7.3 discusses the most prominent features of the pseudogap phase in much more detail. Here, we will restrict its introduction to brief overview of experimental findings and theoretical descriptions. The following overview is based on the introduction given in Ref. [4], partially with textual overlap.

The pseodugap phase is characterized by a partial depletion of low-energy excitations, most prominent in spectroscopic observables, resulting in notorious "Fermi arcs" [87–90]. While photoemission experiments suggest the absence of coherent fermionic quasiparticles, quantum oscillations advocate the opposite, i.e., the existence of Fermi-liquid-like fermionic quasiparticles moving on closed semiclassical orbits around small Fermi pockets [91–94]. This is corroborated by Hall [95–97], optical conductivity [98] and magnetoresistence [99] measurements, showing

[5] Specifically, in lanthanum based cuprates.

Fermi liquid behavior consistent with a small Fermi surface, i.e., with carrier density δ (where δ is the hole doping away from the Mott insulating state), and not $1 + \delta$ as expected from Luttinger's theorem [100].

While antiferromagnetic (AFM) order that breaks the lattice translational symmetry constitutes a simple possible explanation for several characteristics of the pseudogap phase [16,101], it is inconsistent with experimental data across broad families of cuprates, where only short-range AFM correlations that span a few lattice sites are observed beyond $\sim 5\%$ doping [24,102]. Nevertheless, spin-wave like excitations (paramagnons) with dispersions and spectroscopic characteristics similar to those of magnons in antiferromagnetic (AFM) Mott insulators exist in the entire pseudogap phase [103–105]. The question of how doping concentrations of a few percent can diminish long-range AFM order in such an efficient way while preserving spin-wave-like excitations remains an unsolved problem. Furthermore, a significant open question in the field is how to unify the various phases in the underdoped[6] region of the phase diagram.

Recent theoretical attention has thus shifted towards understanding the pseudogap's role as the normal phase out of which superconductivity arises, in contrast to electron-doped cuprates, where the normal state is a relatively well understood AFM metal. In particular, the observation of stripes in broad classes of copper oxides has motivated studies of the relation between the pseudogap phase and symmetry breaking order [106]. This is supported by NMR measurements on various La-based compounds, which indicate that intertwined spin- and charge stripes are inherently present up to a critical doping δ_c, beyond which stripe order as well as signatures of the pseudogap phase vanish [107–109].

On the one hand, it has been put forward that the nature of quantum oscillations in the pseudogap at low temperature is linked to translational symmetry breaking, whereby density-wave order reconstructs the (large) conventional Fermi surface into small electron pockets [110–113]. It has been argued, however, that the disruption of a large Fermi surface by conventional (thermally fluctuating) order unlikely explains universal Fermi liquid-like observations with carrier density δ in the pseudogap phase [101,114]. One particular objection is that the transition into the pseudogap at temperature T^* does not seem to be captured by a thermodynamic phase transition, though Berezinskii–Kosterlitz–Thouless-type transitions with weak thermodynamic signatures can not be ruled out [106].

On the other hand, the pseudogap has been described as a precursor of superconductivity, whereby the formation of incoherent, preformed Cooper pairs leads to a partial depletion of fermionic spectral weight. While support of this idea has been reported in a variety of experiments [115–118], temperatures where evidence of preformed pairs has been found are significantly below the pseudogap temperature T^*. Furthermore, recent measurements of iridates revealed that the pseudogap can exist in broad parameter regimes without the appearance of superconductivity at lower temperatures, which supports a disparate nature of the the two phases [119,120].

This has led to a third class of proposed scenarios, where the symmetry-breaking orders

[6] All doping below the optimal doping, where superconductivity peaks, is referred to as underdoped. In contrast, the Fermi-liquid side of the phase diagram is called overdoped.

found at low temperatures are interpreted as instabilities of a distinct "pseudogap" phase of matter [101, 114, 121]. A prominent scenario is the formation of a fractionalized Fermi liquid (FL*) [122], which features well-defined fermionic quasiparticles in the absence of symmetry-breaking order while violating Luttinger's theorem. In the single-band Hubbard model, this scenario can be realized when assuming that local moments form an odd spin liquid with topological excitations (visons) [123,124], into which mobile hole carriers are doped [125–130]. While dopants in a spin liquid can decay into fractionalized spin and charge constituents [131], assuming bound states of the latter leads to a metal with a small Fermi surface [114]. On technical grounds, this apparent violation of Luttinger's theorem is caused by topological excitations of the spin liquid, which can absorb momentum in Oshikawa's flux insertion protocol (discussed in detail in Sec. 7.2) that corresponds exactly to unit density (leading to a Fermi surface of volume $\propto \delta$ instead of $\propto 1+\delta$).

In Chap. 7, we will discuss the above theoretical scenarios in detail and propose as a possible description for the pseudogap phase the formation of a *geometric fractionalized Fermi liquid*. The essential idea is that long-range order in the pseudogap phase is not entirely absent but is instead *hidden* by fluctuations of domain walls in the AFM background. As we will demonstrate, this allows for a possible unification of the AFM, stripe, and pseudogap phases: in all cases, the symmetry of the spin background is spontaneously broken, albeit manifesting in different ways. We will show that the formation of percolating string nets of AFM domain walls naturally leads to the emergence of an odd $\mathbb{Z}_2$ quantum spin liquid at low temperatures, enabling the formation of a small Fermi surface composed of magnetic polarons that exist in the (ordered) background.

Strange metal. As in the electron-doped case, hole-doped cuprates also exhibit an extended strange metal region around optimal doping [132,133], which may suggest the existence of quantum criticality. With regard to scenarios where symmetry breaking order takes the main role, the existence of a quantum critical point as a function of doping has been proposed to explain the anomalous transport properties found in the high-temperature region of the pseudogap regime. Here, the corresponding critical doping corresponds to the point where the critical temperature of a putative symmetry-breaking order that competes with superconductivity vanishes. Extending these arguments, in Chap. 7 we propose that the strange metal regime is driven by the loss of hidden order, suggesting the existence of a *hidden quantum critical point*. As we will discuss in detail in Chap. 7, this may provide a unifying framework for understanding various phases in the cuprate phase diagram and may even hint at a deeper connection between the hole- and electron-doped sides.

2.2 The Fermi-Hubbard model

Considering the electronic and orbital structure, a three-band model involving the $3d_{x^2-y^2}$ and $2p_x$, $2p_y$ orbitals emerges as a natural candidate to capture the low-energy description of the copper-oxide planes. In particular, when the system is hole-doped, electrons are typically removed from the oxygen $2p$ orbitals, further supporting the three-band model. However, the formation of Zhang-Rice singlets (singlets formed between a hole in a $2p$ orbital and the localized

electron in the $3d$ orbital) has been argued to reduce this description to an effective single-band model.

Originally introduced by John Hubbard in 1963 [134] and later proposed to capture the essential physics of high-temperature superconductors by Anderson [135], this single-band, SU(2)-symmetric Fermi-Hubbard model (FH) has become a paradigmatic framework for strongly correlated electronic systems. The Hamiltonian is given by

$$\hat{\mathcal{H}} = -t \sum_{\langle \mathbf{i},\mathbf{j}\rangle,\sigma} \left(\hat{c}^{\dagger}_{\mathbf{i},\sigma} \hat{c}_{\mathbf{j},\sigma} + \text{H.c.} \right) + U \sum_{\mathbf{i}} \hat{n}_{\mathbf{i},\uparrow} \hat{n}_{\mathbf{i},\downarrow}. \tag{2.2}$$

Here, $\hat{c}^{(\dagger)}_{\mathbf{i},\sigma}$ are fermionic creation and annihilation operators acting at site $\mathbf{i}$ with spin $\sigma = \uparrow, \downarrow$. The particle densities are given by $\hat{n}_{\mathbf{i},\sigma} = \hat{c}^{\dagger}_{\mathbf{i},\sigma} \hat{c}_{\mathbf{i},\sigma}$, and particles on the same site experience an on-site repulsion U. In the undoped parent compound with one particle per site, the superexchange mechanism leads to long-range antiferromagnetic correlations between the $3d_{x^2-y^2}$ copper electrons[7].

What do we know about the solution of the FH model? Despite its conceptual simplicity, the long-standing goal of understanding the ground- and low-temperature physics of the model within a universal framework remains an unsolved task. Nevertheless, tremendous numerical progress has been made over the past decades. In the strongly interacting limit $U \gg t$, all state-of-the-art numerical methods broadly agree on the emergence of stripes in the ground state, where charges accumulate around AFM domain walls, forming a charge density wave [136–143]. However, very small energy differences between stripe states with different ordering wavelengths are observed, making their study challenging numerically [144]. Large-scale simulations have further revealed that, in the plain-vanilla square lattice FH model as described in Eq. (2.2), superconducting order is absent, and stripe order is dominant [145]. However, this balance can be altered through the introduction of next-nearest neighbor (NNN) terms, enabling the co-existence of d-wave superconductivity and stripes [146, 147]. At elevated temperatures, the FH model displays a pseudogap characterized by short-range AFM correlations [148–154] and a reconstructed Fermi surface [155]. Interestingly, the doping and interaction regimes where pseudogap and stripe phases emerge at high and low temperatures, respectively, align precisely [154,156]. This suggests an intricate connection between the stripe and pseudogap phases, a relationship that we will explore in detail in Chap. 7.

2.2.1 The t-J model

In most strongly correlated materials, the interaction energy U is much larger than t (typically, $t/U \sim 10$). In this limit, sites are rarely doubly occupied, and primarily only virtual doublon-hole pairs exist, which then recombine into two singly occupied sites. This virtual exchange of particles leads to an effective antiferromagnetic interaction, as adjacent particles with the same

[7] In truly two-dimensional systems, the Mermin-Wagner theorem prohibits long-range order at finite temperatures for systems with continuous symmetries. However, since cuprates are layered materials, the coupling between layers—although negligible for essential physics—plays a role in stabilizing order due to the three-dimensional structure.

spin cannot participate in virtual exchange due to the Pauli exclusion principle. By fully projecting out states with double occupancy, perturbation theory up to order t^2/U via a Schrieffer-Wolff transformation yields the following Hamiltonian in the strongly interacting limit,

$$\hat{\mathcal{H}} = -t \sum_{\sigma,\langle \mathbf{i},\mathbf{j}\rangle} \hat{\mathcal{P}}_{GW} \left(\hat{c}^\dagger_{\mathbf{i},\sigma}\hat{c}_{\mathbf{j},\sigma} + \text{h.c.}\right)\hat{\mathcal{P}}_{GW} + J \sum_{\langle \mathbf{i},\mathbf{j}\rangle} \left(\hat{\mathbf{S}}_\mathbf{i}\cdot\hat{\mathbf{S}}_\mathbf{j} - \frac{\hat{n}_\mathbf{i}\hat{n}_\mathbf{j}}{4}\right) - \frac{J}{8}\hat{T}_{\text{corr. hop}}. \tag{2.3}$$

Here, $\hat{\mathbf{S}}_\mathbf{i} = \frac{1}{2}\sum_{\sigma,\sigma'} \hat{c}^\dagger_{\mathbf{i},\sigma}\boldsymbol{\sigma}_{\sigma,\sigma'}\hat{c}_{\mathbf{i},\sigma'}$ are spin operators on site $\mathbf{i}$, and $\hat{\mathcal{P}}_{GW}$ is the Gutzwiller operator that projects out states with double occupancy. The term $\hat{T}_{\text{corr. hop}}$ is a correlated hopping term involving a sum over a series of nearest neighbors $\langle \mathbf{i},\mathbf{j},\mathbf{k}\rangle$.

Although $\hat{T}_{\text{corr. hop}}$ is part of the perturbation theory up to order t^2/U, it is often neglected in practice. The primary purpose of the t-J model is to describe the competition between kinetic energy (hopping) and spin exchange (superexchange), which the additional three-site term does not qualitatively change. Though it becomes more relevant at higher doping levels, where three-site processes are more probable, in the low-to-moderate doping regime (relevant for many cuprate studies), its contribution is minor. In particular, neglecting the three-site term simplifies the t-J model, making it more tractable for analytical and numerical studies without significantly affecting the qualitative accuracy of most physical predictions.

Note that at one particle per site, this model reduces to the standard SU(2) symmetric Heisenberg Hamiltonian that describes an antiferromagnet,

$$\hat{\mathcal{H}} = J \sum_{\langle \mathbf{i},\mathbf{j}\rangle} \hat{\mathbf{S}}_\mathbf{i}\cdot\hat{\mathbf{S}}_\mathbf{j}. \tag{2.4}$$

2.2.2 The SU(N) symmetric Fermi-Hubbard model

The Fermi-Hubbard model in Eq. (2.2) is symmetric under SU(2) rotations of the spin degree of freedom, i.e.,

$$\hat{\mathcal{H}} = \hat{U}\hat{\mathcal{H}}\hat{U}^\dagger, \quad \hat{U}\left|\sigma\right\rangle_\mathbf{i} = \sum_{\sigma'=\uparrow,\downarrow} U_{\sigma,\sigma'}\left|\sigma'\right\rangle_\mathbf{i}. \tag{2.5}$$

This symmetry arises directly from the unitarity of $\hat{U}$, leaving all bilinears composed of creation and annihilation operators invariant. Technically, this symmetry can easily be generalized to an SU(N) symmetry by considering fermions of N colors (indexed by α) instead of just the two spin states. The corresponding Hamiltonian reads

$$\hat{\mathcal{H}} = -t \sum_{\langle \mathbf{i},\mathbf{j}\rangle,\alpha} \left(\hat{c}^\dagger_{\mathbf{i},\alpha}\hat{c}_{\mathbf{j},\alpha} + \text{H.c.}\right) + \frac{U}{2}\sum_\mathbf{i}\sum_{\alpha\neq\beta} \hat{n}_{\mathbf{i},\alpha}\hat{n}_{\mathbf{i},\beta}. \tag{2.6}$$

Here, the interaction term penalizes configurations where multiple particles of different colors occupy the same site, with the factor of $1/2$ introduced to remove double-counting. Similar to the SU(2) case, the Hamiltonian in Eq. (2.6) is symmetric under SU(N) rotations in the color subspace,

$$\hat{\mathcal{H}} = \hat{U}\hat{\mathcal{H}}\hat{U}^\dagger, \quad \hat{U}\left|\alpha\right\rangle_\mathbf{i} = \sum_{\beta=1}^{N} U_{\alpha,\beta}\left|\beta\right\rangle_\mathbf{i}. \tag{2.7}$$

It is worth noting that this non-abelian SU(N) symmetry is global rather than a gauge symmetry, as encountered in the standard model of particle physics.

Why is the SU(N) symmetric FH model interesting to study? After all, electrons in real materials exhibit an effective SU(2) symmetry. The goal of understanding the phases of the SU(2) symmetric FH model is to gain insight into the competition between kinetic and strong interaction energies. However, the SU(2) model is also a pathological case with special band structure effects unlikely to play a role in real materials. This already becomes evident when considering weak interactions: in the random phase approximation, the interacting spin susceptibility χ_{sp} reads [157]

$$\chi_{\mathrm{sp}}(i\omega, \mathbf{q}) = \frac{\chi_0(i\omega, \mathbf{q})}{1 - \frac{1}{2}U\chi_0(i\omega, \mathbf{q})}, \tag{2.8}$$

where $\chi_0(i\omega, \mathbf{q})$ is the non-interacting susceptibility,

$$\chi_0(i\omega, \mathbf{q}) = -2\frac{T}{N_{\mathbf{k}}} \sum_{i\omega_n, \mathbf{q}} \frac{n_F(\epsilon_{\mathbf{k}} - \mu) - n_F(\epsilon_{\mathbf{k}+\mathbf{q}} - \mu)}{i\omega_n + \epsilon_{\mathbf{k}} - \epsilon_{\mathbf{k}+\mathbf{q}}}. \tag{2.9}$$

Here, $\epsilon_{\mathbf{k}}$ is the non-interacting energy dispersion, and $n_F(x) = 1/(1 + e^{x/T})$ is the Fermi function at temperature T with k_B set to unity. At $\mathbf{q} = \mathbf{Q} = (\pi, \pi)$, the static susceptibility $\chi_0(i\omega = 0, \mathbf{q} = \mathbf{Q})$ thus scales as

$$\chi_0(i\omega = 0, \mathbf{q} = \mathbf{Q}) \propto \int d\epsilon \frac{n_F(-\epsilon) - n_F(\epsilon)}{\epsilon} \propto |\log T|. \tag{2.10}$$

The logarithmic divergence of the susceptibility results in a Mott insulating instability with antiferromagnetic (AFM) order for any arbitrarily small $U > 0$. This is due to the perfect nesting property of non-interacting fermions on the square lattice, where $\epsilon(\mathbf{q}) \propto \sum_{\mu=x,y} \cos(k_\mu a) = -\epsilon(\mathbf{q} + \mathbf{Q})$. In SU($N$) systems with $N > 2$, perfect nesting is not fulfilled at one particle per site, requiring a finite on-site interaction U to drive a metal-to-Mott-insulator transition [158]; this allows for tuning strong correlation effects independently from single-particle physics.

Apart from this, understanding Fermi-Hubbard type models with higher symmetries is intrinsically interesting in its own right. If exotic physics emerges in simple SU(2) FH models, even more exotic phenomena can be expected in systems with higher symmetries. This simply arises from particle statistics: particles of the same color prefer to be far apart, maximizing delocalization and lowering energy[8].

Moreover, against possible naive expectations, large N FH systems do not become classical, as in SU(2) systems with large spin. This distinction is illustrated in Fig. 2.3. In SU(2) systems, quantum fluctuations $\propto \hat{S}_{\mathbf{i}}^{+} S_{\mathbf{j}}^{-}$ are negligible for large spins, as the number of states is much larger compared to the amount of states coupled through quantum fluctuations. In contrast, the symmetric interactions of the SU(N) FH model lead to an exchange mechanism where all particle colors interact equally. The superexchange mechanism works identically to the SU(2) counterpart, resulting in the following magnetic Heisenberg Hamiltonian in the strongly inter-

[8] Consider three particles of the same color. The outer particles create a box potential for the central particle. Greater separation allows greater delocalization, lowering the energy.

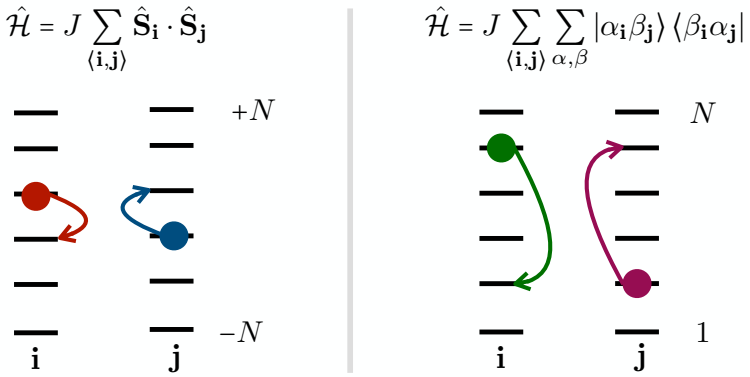

Figure 2.3: **Large spin vs. large N.** In the SU(2) FH model with large spin, the effective magnetic model at one particle per site raises and lowers angular momentum states by ± 1. For large spin, quantum fluctuations are negligible, and the system is well described by a classical spin model. In contrast, in the SU(N) symmetric Heisenberg or FH model, symmetric interactions lead to exchange interactions among all colors. Quantum fluctuations remain significant at all N, stabilizing exotic magnetic structures.

acting limit,

$$\hat{\mathcal{H}} = J \sum_{\langle \mathbf{i},\mathbf{j} \rangle} \sum_{\alpha,\beta} |\alpha_\mathbf{i} \beta_\mathbf{j}\rangle \langle \beta_\mathbf{i} \alpha_\mathbf{j}| \,. \tag{2.11}$$

In particular, the symmetric exchange stabilizes quantum fluctuations even at large N, see Fig. 2.3. At one particle per site, numerical and semi-analytical techniques such as infinite projected entangled-pair states (iPEPS), exact diagonalization, and flavor-wave theory have been employed to study magnetic ordering in SU(N) FH models [159–161]. This has revealed a broad variety of magnetic order, illustrated in Fig. 2.4. In the case of the SU(3) symmetric FH model, the strongly interacting limit replaces the usual Néel pattern seen in the SU(2) case with a spin-stripe pattern, where the three colors align diagonally [159]. For finite U, away from the Heisenberg limit, constrained path quantum Monte Carlo simulations revealed that the system exhibits even richer behavior, with various ordering patterns emerging as a function of U/t [162]. In SU(4) and SU(5) symmetric systems, further intriguing ground states are realized [160, 161], such as valence bond solid-like states in the SU(4) case [160].

While the intricate magnetic structures of SU(N) Heisenberg magnets have garnered increasing interest [159–165], the physics of doped SU(N) Mott insulators remains largely unexplored. This is primarily due to the immense computational complexity associated with the exponential growth of the Hilbert space, which scales as $\mathcal{D} \sim N^L$, where L represents the number of lattice sites. Nevertheless, overcoming these challenges could be very rewarding; in particular, gaining a deeper understanding of doped SU(N) Mott insulators may shed further light on the competition between spin and motional degrees of freedom and contribute to a unified understanding of doped Mott insulators in general.

This motivation to study the doped SU(N) FH model is further supported by advances in ultracold atom experiments. When trapping and cooling alkaline-earth-like atoms (AEAs), the absence of electronic hyperfine structure allows for the implementation of the SU(N) FH model with extraordinary precision; we refer to Sec. 4.1.3, where this will be discussed in more detail.

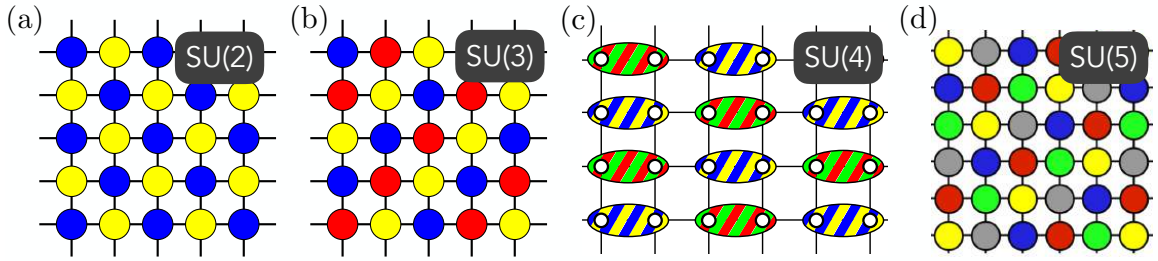

Figure 2.4: **Magnetic order in SU(N) systems.** Magnetic structures in the SU(N) FH model at one particle per site in the strongly interacting limit. (a) Checkerboard pattern in the SU(2) model, corresponding to a Néel state, taken from Ref. [159]. (b) Spin stripes in the SU(3) FH model for $U/t \gg 1$, taken from Ref. [159]. (c) The SU(4) model realizes a state reminiscent of a valence bond solid; taken from Ref. [160]. (d) Exotic magnetic order in the SU(5) model, taken from Ref. [161].

For now, we highlight these advancements as further motivation, showcasing the potential for analog quantum simulation platforms to provide a significant quantum advantage.

In Chap. 11, we take a first step toward exploring the physics of doped SU(N) FH systems by examining the behavior of a single hole in the symmetry-broken background of the SU(3) Heisenberg model. As we will demonstrate, doping a hole into the spin stripes results in the formation of exotic magnetic polarons, which are strongly constrained to move only along one effective dimension. This suggests the emergence of exotic physics at finite doping, where we propose the existence of a Luttinger liquid state of magnetic polarons propagating along the ordered diagonals.

2.2.3 Mixed-dimensional systems

Coming back to the study of the doped SU(2) FH model, its analysis is particularly challenging due to the property that different orderings, such as superconductivity and stripes with various orientations and fillings, are very close in energy. This motivates the study of slightly modified Hamiltonians, which bias certain orders over others, allowing for valuable insights into strongly correlated phases of matter while circumventing the difficulty posed by tiny energy gaps between different symmetry-breaking orders.

In Chap. 5, we propose the mixed-dimensional t-J model as a parent system that realizes stable stripe phases. In this model, tunneling is turned off along one direction, while superexchange interactions remain intact in 2D. The resulting Hamiltonian reads

$$\hat{\mathcal{H}} = -t \sum_{\sigma,\langle \mathbf{i},\mathbf{j}\rangle_x} \hat{\mathcal{P}}_{GW}\left(\hat{c}^\dagger_{\mathbf{i},\sigma}\hat{c}_{\mathbf{j},\sigma} + \text{h.c.}\right)\hat{\mathcal{P}}_{GW} + J \sum_{\langle \mathbf{i},\mathbf{j}\rangle} \left(\hat{\mathbf{S}}_\mathbf{i} \cdot \hat{\mathbf{S}}_\mathbf{j} - \frac{\hat{n}_\mathbf{i}\hat{n}_\mathbf{j}}{4}\right), \tag{2.12}$$

where $\langle \mathbf{i},\mathbf{j}\rangle_x$ denotes nearest neighbor (NN) sites along the x-direction only. Intuitively, eliminating hopping along one direction reduces the Pauli repulsion of holes along this axis, favoring the formation of correlated, extended structures of holes. As we show in Sec. 5.2, our numerical simulations predict high critical temperatures for the stripe phase, approximately $T_c \sim J/2$,

which are realistic for ultracold atom experiments. Indeed, in Sec. 5.3, in an experimental collaboration we report the observation of individual, fluctuating stripes in this mixed-dimensional setting.

From another perspective, a mixed-dimensional model that promotes the formation and condensation of spin-singlet pairs can be constructed. Originally proposed theoretically in Ref. [69], this model consists of two coupled 2D layers, where inter-layer hopping is prohibited. The Hamiltonian reads

$$\begin{aligned}\hat{\mathcal{H}}_{\mathrm{BL}} = -t_{\parallel} \sum_{\langle \mathbf{i},\mathbf{j}\rangle,\sigma,\alpha} \hat{\mathcal{P}} \left(\hat{c}^{\dagger}_{\mathbf{i},\sigma,\alpha} \hat{c}_{\mathbf{j},\sigma,\alpha} + \mathrm{h.c.}\right) \hat{\mathcal{P}} + J_{\parallel} \sum_{\langle \mathbf{i},\mathbf{j}\rangle,\alpha} \left(\hat{\mathbf{S}}_{\mathbf{i},\alpha} \cdot \hat{\mathbf{S}}_{\mathbf{j},\alpha} - \frac{\hat{n}_{\mathbf{i},\alpha} \hat{n}_{\mathbf{j},\alpha}}{4} \right) \\ + J_{\perp} \sum_{\mathbf{i}} \left(\hat{\mathbf{S}}_{\mathbf{i},1} \cdot \hat{\mathbf{S}}_{\mathbf{i},2} - \frac{\hat{n}_{\mathbf{i},1} \hat{n}_{\mathbf{i},2}}{4} \right),\end{aligned} \tag{2.13}$$

where $\alpha = 1, 2$ is the layer index. Using potential energy offsets, mixD ladders have been realized in ultracold atom experiments, where real-space pairing has been observed [57].

Apart from applications in ultracold atom settings, the above mixed-dimensional model has also gained attention in the solid state community. Indeed, as introduced in the following section, the mixD bilayer model Eq. (2.13) arises naturally in minimal descriptions of certain classes of nickelate materials.

2.3 Nickelates

With extraordinarily high critical temperatures in copper oxide compounds, the question arises whether similar physics can be observed in other materials characterized by partially filled $3d$ orbitals. Nickel, being adjacent to copper in the periodic table, has the same $3d^9$ configuration for Ni^+ as Cu^{2+}, and has long been considered a candidate for high-temperature superconductivity. In recent years, a variety of layered nickelate materials have been synthesized and studied. These materials are typically characterized by an integer m, corresponding to the number of nickel-oxide planes separated by insulating spacer (usually rock-salt) layers. For example, Fig. 2.5 (a) illustrates the atomic configuration of a bilayer nickelate compound ($m = 2$) [70], where two nickel oxide layers are strongly coupled through vertical, apical oxygen atoms, and these bilayers are separated by spacer layers (here, lanthanum).

Infinite-layer nickelates correspond to an electron count of Ni^+, and are thus comparable in their electronic structure as parent compounds of copper oxides. Remarkably, when doping these systems, superconductivity emerges [167]. Moving away from the infinite-layer case has a similar effect to hole doping: the spacer layers absorb some electrons from the nickel oxide layers, leading to hole-doped coupled m-layer systems. Simple electron counting of the nickel atoms for varying m reveals that the doping levels of $m = 5, 6$ nickelates correspond to the electron count of optimally doped cuprates. Indeed, these materials exhibit superconductivity, albeit at much lower critical temperatures compared to optimally doped cuprates [168].

In bilayer systems, such as $La_3Ni_2O_7$ (LNO), the formal electron count is $Ni^{7.5}$, meaning that each unit cell containing two nickel atoms has, on average, 15 electrons. When comparing this

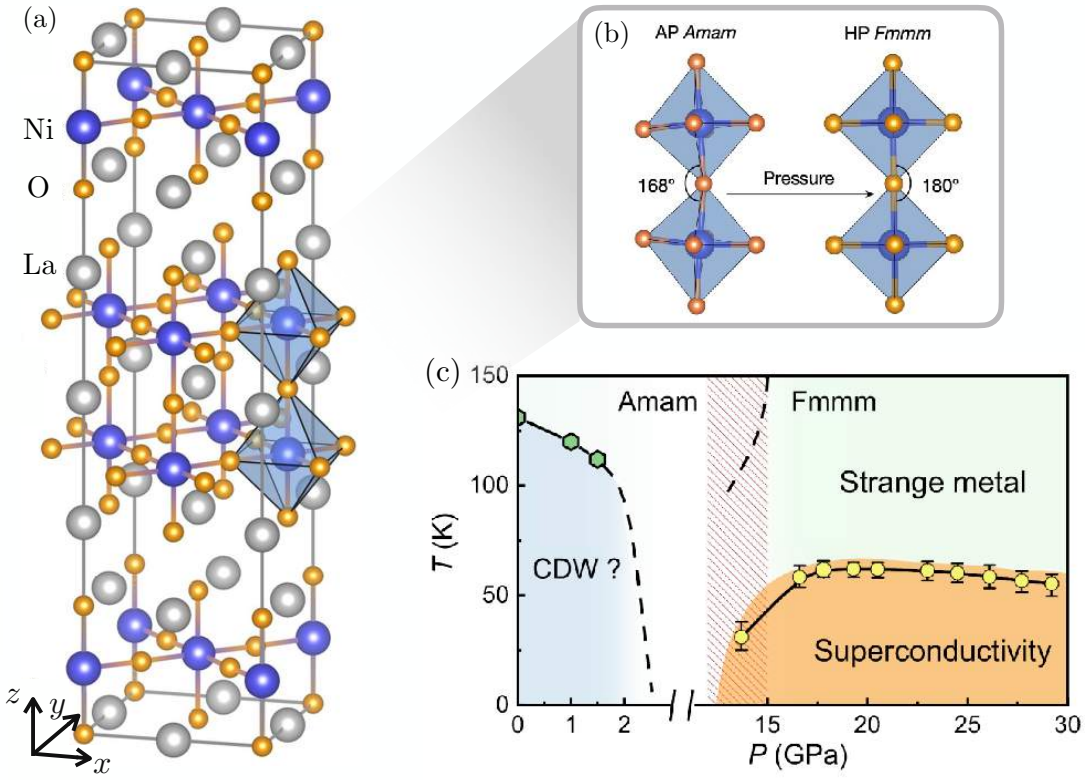

Figure 2.5: **Bilayer nickelates.** (a) Atomic structure of LNO. Nickel oxide layers form bilayer systems separated by rock-salt layers. Figure taken and adapted from Ref. [70]. (b) At ambient pressure, the two vertically stacked octahedra with Ni atoms in their center and O atoms at their edges are not fully aligned. At high pressures, a structural transition to an Fmmm point group takes place, aligning the orbitals vertically. Figure taken and adapted from Ref. [70]. (c) Experimentally measured phase diagram of LNO. In the high pressure phase (i.e. beyond the structural transition point), high-temperature superconductivity emerges. At temperatures beyond T_c, a large extended region of linear in T resistivity appears, i.e., the system features strange metallicity. Figure taken from Ref. [166].

electronic structure to cuprates, it corresponds to heavily overdoped systems, at $\delta = 50\%$, where a standard Fermi liquid metal is expected. Consistent with this expectation, the system does not exhibit superconductivity at ambient pressure. However, under externally applied pressure, the point group symmetry of the underlying atomic lattice transitions from an Amam structure to an Fmmm structure, as illustrated in Fig. 2.5 (b). The critical change involves the alignment of orbitals along the vertical direction, forming an angle of 180° in the high-pressure phase, compared to 168° at ambient pressure.

This structural transition has profound consequences for the observed physics. In the high-pressure phase, superconductivity emerges with remarkably high critical temperatures, reaching an onset temperature of $T_c = 80$ K. The measured phase diagram of LNO is shown in Fig. 2.5 (c). Moreover, above the superconducting phase, an extended regime of linear-in-T resistivity is observed. As we shall propose in Chap. 8, this strange metallic behavior likely does not originate from quantum criticality but may instead result from the emergent hard-core bosonic transport of inter-layer singlets.

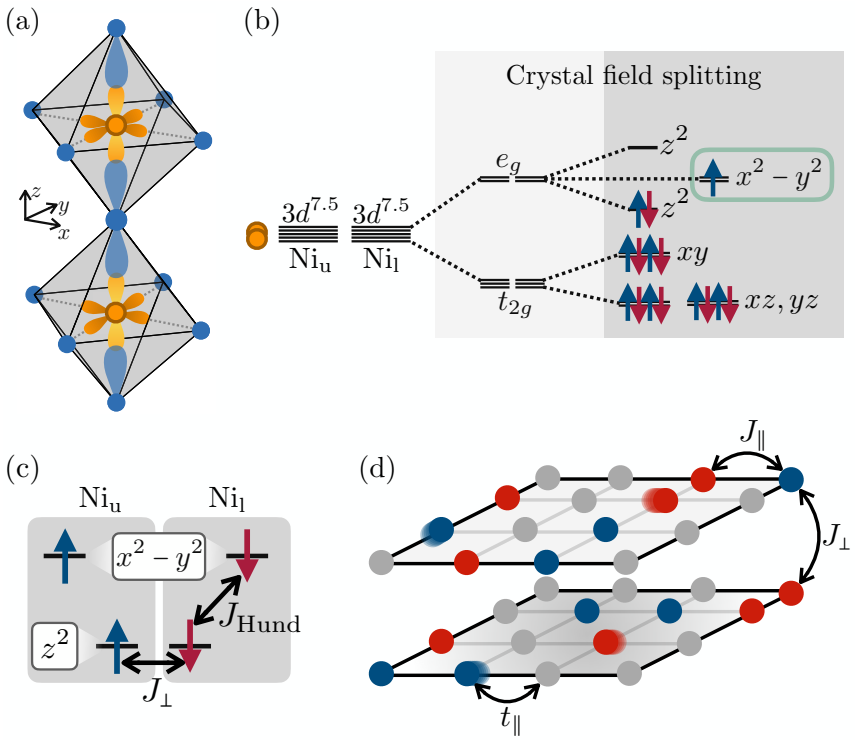

Figure 2.6: **Bilayer Nickelates.** (a) Atomic structure of a unit cell in the high-pressure phase of the bilayer nickelate LNO. Nickel atoms with active $3d_{z^2}$ and $3d_{x^2-y^2}$ orbitals are shown in yellow and orange, respectively. Oxygen atoms with their $2p$ orbitals are depicted in blue. (b) Crystal field splitting and electronic structure of the upper and lower nickel atoms, where each atom is, on average, in a $3d^{7.5}$ configuration. (c) When the electrons in the $3d_{z^2}$ orbitals (singly occupied per site) form a rung singlet Mott insulator, atomic Hund's coupling elevates AFM interactions to the $3d_{x^2-y^2}$ orbitals. (d) To a first approximation, integrating out the $3d_{z^2}$ orbitals results in an effective single-band, mixed-dimensional t-J model at 50% hole doping in each layer, Eq. (2.13). Inter-layer hopping is suppressed ($t_\perp = 0$), whereas $t_\parallel$, $J_\parallel$, and $J_\perp$ are positive.

2.3.1 Bilayer t-J model

The strong dependence of the observed physics on the vertical alignment of the nickel and apical oxygen atoms suggests that inter-layer couplings in the bilayer play a crucial role in the low-energy physics. To construct effective models, let us analyze the electronic configuration of the upper and lower nickel atoms within a unit cell in the crystal field. Similar to cuprates, the oxygen octahedra surrounding the nickel atoms lift degeneracies at the first level, followed by Jahn-Teller splitting (see Fig. 2.6 (a) and (b)). The number of vertically stacked lines in Fig. 2.6 (b) represents the number of d orbitals, each of which can be occupied by up to two electrons.

When filling electrons into the $3d$ orbitals, two active orbitals take the main role: the $3d_{z^2}$ and $3d_{x^2-y^2}$ orbitals. While the z^2 orbital is singly occupied at each site, the $3d_{x^2-y^2}$ orbital is quarter-filled, corresponding to one electron per unit cell of two nickel atoms. Due to the strong localization and correlations of the d orbitals, the z^2 orbitals are expected to form a Mott insulating state with antiferromagnetic (AFM) correlations driven by superexchange $J_\perp$ along the vertical direction, leading to a rung singlet insulator.

Electrons in the $3d_{x^2-y^2}$ orbitals can hop in-plane through hybridization with the apical oxygen atoms, but inter-layer hopping is heavily suppressed. Due to strong on-site repulsion, these electrons experience in-plane AFM interactions $J_\parallel$. Furthermore, it has been proposed that via the AFM interaction of the $3d_{z^2}$ orbitals, the $3d_{x^2-y^2}$ electrons acquire a vertical interaction $J_\perp$ through Hund's coupling (see Fig. 2.6 (c)). When two electrons occupy the upper and lower nickel $3d_{x^2-y^2}$ orbitals, their spins tend to align with the respective $3d_{z^2}$ orbital spin [169–171]. Importantly, Hund's coupling operates at atomic energy scales (on the order of $\sim$ eV), effectively transferring the vertical AFM alignment to the $3d_{x^2-y^2}$ electrons. Therefore, this suggest a minimal, single-band description of bilayer nickelates in mixed dimensions.

In this thesis, we will numerically study the mixD bilayer t-J model Hamiltonian Eq. (2.13), illustrated in Fig. 2.6 (d). While both inter- and intralayer superexchange terms are present, the orbital structure of the material suppresses hopping between different layers. To describe LNO, the quarter filled $d_{x^2-y^2}$ band corresponds to a doping level of $\delta = 0.5$ in the mixD $t_\parallel$-$J_\perp$-$J_\parallel$ model compared to the half-filled state with one particle per site.

In Chap. 8, we analyze this model numerically in detail and predict extraordinarily high critical temperatures of $T_c \sim J_\perp/2$. This, in turn, strongly suggests the preparation and observation of a superconducting state with currently achievable temperatures in ultracold atom experiments, which we propose in detail in Chap. 9.

3

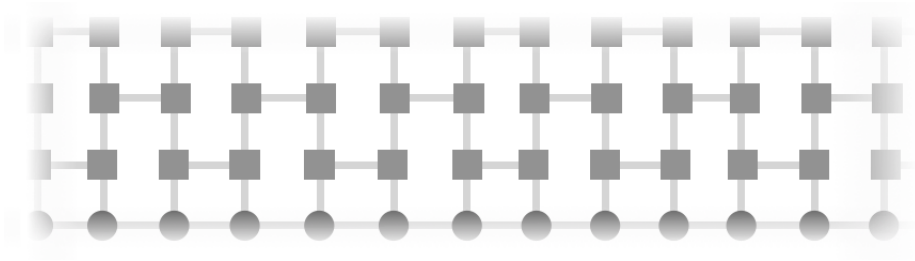

Numerical techniques

Summary. This chapter provides a brief overview of the numerical techniques used in this thesis to study strongly correlated electronic systems. Following a general introduction, we discuss matrix product states and the density matrix renormalization group (DMRG) algorithm, one of the central methods employed throughout this thesis. Additionally, we describe time evolution methods, which enable the simulation of dynamics and finite temperatures through purification. Finally, we introduce the two-particle self-consistent theory, a perturbative approach with certain vertex corrections that has been shown to perform remarkably well across broad parameter regimes of the Fermi-Hubbard model.

Due to the complexity of strongly correlated systems, which feature intricate, highly entangled superpositions of many-body wavefunctions, exact diagonalization of the exponentially growing Hilbert space becomes intractable even for systems with just tens of sites. As Carlton M. Caves famously remarked, *Hilbert space is a big place*. Along similar lines, in his 1999 Nobel lecture, Walter Kohn stated, *In general the many-electron wavefunction for a system of N electrons is not a legitimate scientific concept* [172].

What mitigates this catastrophe of dimensionality, at least to some extent, is that the full complexity of the Hilbert space is often an illusion: While in general quantum mechanics permits superpositions of vastly different microscopic states (such as Schrödinger's cat), such states rarely arise naturally in physical systems. This dramatically restricts the portion of the Hilbert space relevant to real-world observations.

Formally, this can be attributed to the concept of locality—reasonable physical systems do not exhibit true long-range interactions. It can be rigorously shown that, in (local) one-dimensional (1D) gapped systems, the entanglement entropy of two subsystems follows an area law, meaning the entanglement entropy of a region is proportional to the area of its boundary [173]. In 1D, this area corresponds to a constant (or logarithmic) scaling in gapped (or gapless) systems. For low-

energy states in higher-dimensional systems, the area law is similarly applicable[1], significantly narrowing the portion of Hilbert space relevant to physical systems.

Intuitively, the area law arises from the concept of local entanglement. Consider a d-dimensional spin system forming an antiferromagnet. The system's energy can be minimized locally through the formation of singlets, due to its local interactions. The contribution to the entanglement entropy is then determined by the number of singlet bonds crossing the boundary of a subsystem, which is proportional to the area of the hypersurface in the d-dimensional system.

Thus, numerical tools should be developed that inherently capture the area law to efficiently address ground states of local Hamiltonians. Tensor networks achieve this goal by representing quantum states as products of tensors, providing an efficient way to represent and compress the quantum states of interest. Among the various tensor network methods, we will focus on matrix product states (MPS) in this discussion. Further tensor network architectures, such as PEPS (projected entangled pair states) [174], MERA (multiscale entanglement renormalization ansatz) [175], tree tensor networks [176], and others, have distinct applications in various settings, depending on the dimensionality, structure, or type of quantum system being studied.

Using MPS, a wide range of optimized algorithms have been developed in the past decades for finding ground states, thermal states, and performing time evolution. In the following, we will provide a brief overview of MPS and the algorithms utilized throughout this thesis. However, as the focus of this work lies on the physical interpretation of numerical simulations, we will not dive deeply into technical details but rather emphasize intuitive concepts that facilitate a qualitative understanding of the numerical tools relevant to this thesis. For additional details, we refer to the excellent reviews Refs. [29, 177]. Throughout this thesis, we will utilize the `SyTen` toolkit [178, 179] for simulations based on MPS.

3.1 Matrix product states

Consider a general quantum state of N particles, each with D internal degrees of freedom labeled by $\sigma = 1, \ldots, D$,

$$|\Psi\rangle = \sum_{\sigma_1,\ldots,\sigma_N} \Psi^{\sigma_1,\ldots,\sigma_N} |\sigma_1, \ldots, \sigma_N\rangle \,. \tag{3.1}$$

Here, $|\sigma_1, \ldots, \sigma_N\rangle$ corresponds to the tensor product basis states of N particles, and $\Psi^{\sigma_1,\ldots,\sigma_N}$ is a tensor with N indices, each having D states, that describes the superposition of the many-body state. As a concrete example, consider two spins with internal degrees of freedom $|\uparrow\rangle_j, |\downarrow\rangle_j$ on sites $j = 1, 2$. For a separable state,

$$|\Psi\rangle = (A^{\uparrow_1} |\uparrow\rangle_1 + A^{\downarrow_1} |\downarrow\rangle_1) \otimes (A^{\uparrow_2} |\uparrow\rangle_2 + A^{\downarrow_2} |\downarrow\rangle_2), \tag{3.2}$$

[1] Exceptions include models like the Sachdev-Ye-Kitaev model, which features all-to-all connectivity and exhibits volume-law entanglement scaling.

the corresponding tensor Ψ^{σ_1,σ_2} can be written as

$$\Psi^{\sigma_1,\sigma_2} = A^{\sigma_1} A^{\sigma_2}, \tag{3.3}$$

i.e., the wavefunction coefficients are simply the product of the coefficients of the local states. This represents a mean-field-like wavefunction with no entanglement. In contrast, consider the state (neglecting normalization)

$$|\Psi\rangle = |\uparrow,\uparrow\rangle + |\downarrow,\downarrow\rangle\,. \tag{3.4}$$

For this state, the tensor Ψ^{σ_1,σ_2} can be expressed as

$$\Psi^{\sigma_1,\sigma_2} = \sum_{i=1,2} A_i^{\sigma_1} A_i^{\sigma_2} = \mathbf{A}^{\sigma_1} \cdot \mathbf{A}^{\sigma_2}, \tag{3.5}$$

where the tensor is written as a product of two vectors with internal indices i,

$$\mathbf{A}^{\uparrow_1} = \mathbf{A}^{\uparrow_2} = \begin{pmatrix} 1 \\ 0 \end{pmatrix}, \quad \mathbf{A}^{\downarrow_1} = \mathbf{A}^{\downarrow_2} = \begin{pmatrix} 0 \\ 1 \end{pmatrix}. \tag{3.6}$$

Importantly, in Eq. (3.5), the summation over multiple values of the index i indicates that the state is non-separable and hence entangled.

In general, it can be shown that the coefficients $\Psi^{\sigma_1,\ldots,\sigma_N}$ can always be rewritten as [29]

$$\Psi^{\sigma_1,\ldots,\sigma_N} = \sum_{i_1,\ldots i_N} A_{i_1}^{\sigma_1} A_{i_1,i_2}^{\sigma_2} \cdots A_{i_{N-1}}^{\sigma_N}, \tag{3.7}$$

or equivalently,

$$\Psi^{\sigma_1,\ldots,\sigma_N} = \mathbf{A}^{\sigma_1} \cdot \mathbf{A}^{\sigma_2} \ldots \mathbf{A}^{\sigma_N}. \tag{3.8}$$

In the above representation, we assume open boundary conditions, where the first and last $\mathbf{A}$ are vectors, while all others are matrices (i.e., they carry two external indices). What is particularly appealing about this form is its ability to naturally and efficiently compress information in a quantum state, as will be discussed later; this compression is especially effective for states that satisfy the area law for entanglement entropy.

To illustrate how to manipulate MPS and to apply algorithms, graphical representations of tensor networks are very useful. The MPS from Eq. (3.8) can be graphically represented by the following network

$\Psi^{\sigma_1,\ldots,\sigma_N} = \mathbf{A}^{\sigma_1} \cdot \mathbf{A}^{\sigma_2} \ldots \mathbf{A}^{\sigma_N} =$ 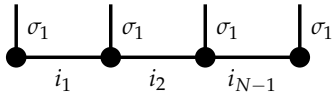

. (3.9)

Here, the nodes correspond to the site index. Vertical open lines are the physical indices, $\sigma_1,\ldots,\sigma_N$, and the horizonal connected lines between nodes are the internal indices. Connections between the nodes indicates summation over the corresponding internal indices.

Operators act as maps between many-body basis states and, similar to quantum states, can

be expressed as

$$\hat{O} = \sum_{\substack{\sigma_1,\ldots,\sigma_N \\ \sigma_1',\cdots,\sigma_N'}} O^{\sigma_1,\ldots,\sigma_N}_{\sigma_1',\ldots,\sigma_N'} \left|\sigma_1,\ldots,\sigma_N\right\rangle \left\langle\sigma_1',\ldots,\sigma_N'\right| . \tag{3.10}$$

Here, the corresponding tensor $O^{\sigma_1,\ldots,\sigma_N}_{\sigma_1',\ldots,\sigma_N'}$ has two physical indices for each site: σ for the ket and σ' for the bra. This tensor can, in general, be rewritten as

$$O^{\sigma_1,\ldots,\sigma_N}_{\sigma_1',\ldots,\sigma_N'} = \sum_{i_1,\ldots,i_{N-1}} W^{\sigma_1\sigma_1'}_{i_1} W^{\sigma_2\sigma_2'}_{i_1 i_2} \cdots W^{\sigma_N\sigma_N'}_{i_{N-1}} =$$

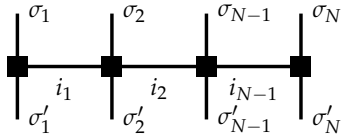

. (3.11)

In analogy to Eq. (3.7), this is the general form of a matrix product operator (MPO). In the last step of Eq. (3.11), the corresponding graphical representation is shown, where the tensors $W^{\sigma_k\sigma_k'}_{i_k}$ are connected through their virtual indices i_k, representing the internal structure of the MPO. MPOs, like matrix product states (MPS), provide an efficient representation of operators that act on quantum many-body systems, especially those that satisfy locality.

The graphical representation of matrix product states (MPS) and matrix product operators (MPO) provides an intuitive way to visualize their applications and inner products. For instance,

$\langle\Psi|\Phi\rangle =$

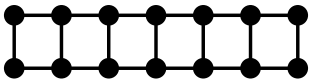

,

$\hat{O}\,|\Psi\rangle =$

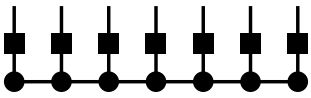

,

$\langle\Psi|\hat{O}|\Phi\rangle =$

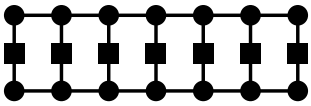

. (3.12)

As previously, the circles (squared) represent tensors for the MPS (MPO), with physical indices extending vertically and virtual indices connecting horizontally. Lines connecting the tensors correspond to contracted indices, while unconnected lines represent open indices.

Up to now, we have only formally rewritten quantum states and operators in matrix product form. How is this done in practice? The answer lies in performing a series of singular value decompositions (SVDs), a cornerstone of linear algebra and one of the most powerful tools for data compression. By breaking down the large tensor $\Psi^{\sigma_1,\ldots,\sigma_N}$ into smaller tensors through SVDs, we can efficiently represent the quantum state in terms of its most significant components, which allows for an efficient truncation of less relevant contributions. In essence, MPS representations naturally isolate the relevant states in the Hilbert space, compressing information while retaining the essential physics of the system.

For a general two-component tensor, the singular value decomposition reads

$$\Psi^{\sigma_1',\sigma_2'} = \sum_i L_i^{\sigma_1'} s_i R_i^{\sigma_2'} = (\mathbf{L}\cdot\mathbf{s}\cdot\mathbf{R})_{\sigma_1',\sigma_2'} , \tag{3.13}$$

where **s** is a diagonal matrix containing the singular values s_i; **L** and **R** are orthogonal matrices satisfying

$$\sum_{\sigma}(L_i^{\sigma})^{\dagger}L_j^{\sigma} = \sum_{\sigma} R_i^{\sigma}(R_j^{\sigma})^{\dagger} = \delta_{ij}, \tag{3.14}$$

with δ_{ij} the Kronecker delta. We can now start at one end of the MPS and interpret the indices in Eq. (3.13) as $\sigma_1' = \sigma_1$ and $\sigma_2' = \{\sigma_2, \ldots, \sigma_N\}$. Proceeding sequentially and moving all the way to the other side of the chain yields (graphically)

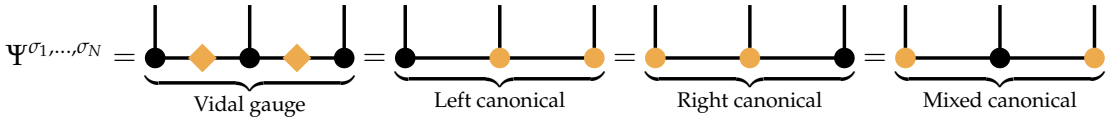

(3.15)

In the above, the orange diamonds represent the diagonal singular value matrices s_i. When summing over a contracted index i, the singular values s_i are multiplied. There is a gauge degree of freedom of MPS that we very briefly mention: Leaving the singular value matrices explicitly in the MPS corresponds to the Vidal gauge. Absorbing the singular values into the left (**L**) or right (**R**) matrices results in the right canonical or left canonical gauges, respectively. In Eq. (3.15), this results in updated nodes shown in orange. Lastly, choosing a reference site and applying the left and right canonical gauges on either side yields the mixed canonical gauge. The mixed canonical gauge simplifies variational optimization algorithms significantly, as it allows efficient calculations of physical quantities and facilitates algorithms like density matrix renormalization group (DMRG). This heavily reduces the computational complexity of MPS-based methods, which we will discuss in the following sections.

3.1.1 Variational compression

Before explaining concrete algorithms for ground state search and unitary time evolution, let us first understand how a quantum state $|\Psi\rangle$ can be systematically compressed into a truncated state $|\tilde{\Psi}\rangle$. One straightforward approach is to locally retain only the χ largest singular values of the state after performing the sequence of SVDs, while discarding all others. This constitutes a simple local update rule, which minimizes the truncation error at the given link by discarding contributions with small singular values. However, one might already anticipate that truncating the singular values on the first link may affect the optimal compression process for subsequent links.

To address this, variational compression algorithms are employed, where the compression of each link considers the full environment of the state. This approach allows for a global optimization of the truncated state and ensures that errors introduced at one link are accounted for when compressing the others; it is therefore usually referred to as a full environment algorithm. The power of variational compression becomes apparent when we consider its application to practical algorithms. For instance, the celebrated density matrix renormalization group (DMRG) algorithm can be viewed as a natural extension of variational compression.

To optimize compression, we would like to adapt the MPS parameters of $|\tilde{\Psi}\rangle$ (which has some fixed maximal dimension of its matrices, referred to as the bond dimension χ) to minimize

the norm of the difference between the two wave functions,

$$\min_{|\tilde{\Psi}\rangle}\big(\langle\Psi| - \langle\tilde{\Psi}|\big)\big(|\Psi\rangle - |\tilde{\Psi}\rangle\big) = \min_{|\tilde{\Psi}\rangle}\big[-2\langle\tilde{\Psi}|\Psi\rangle + \langle\tilde{\Psi}|\tilde{\Psi}\rangle\big], \tag{3.16}$$

where we have assumed real overlaps $\langle\tilde{\Psi}|\Psi\rangle = \langle\Psi|\tilde{\Psi}\rangle$ for simplicity. Graphically, the objective function which has to be minimized corresponds to

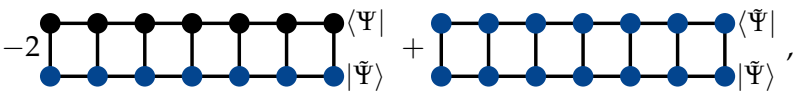

(3.17)

where the goal is to optimize over all entries of the blue matrices. However, this represents a highly multi-linear problem with a complex optimization landscape, making direct minimization computationally expensive and unreliable. To address this, we instead perform a variational minimization with respect to a single matrix in the MPS representation. Let us evaluate the gradient of the objective function with respect to the vectorized representation $\mathbf{a}$ of the matrix at site m, where the entries of $\mathbf{a}$ are given by $a_{\sigma_m,i,j} = A^{\sigma_m}_{i,j}$. Setting the gradient to zero reduces the problem to a linear algebra problem by identifying parts of the tensor network as matrices and vectors,

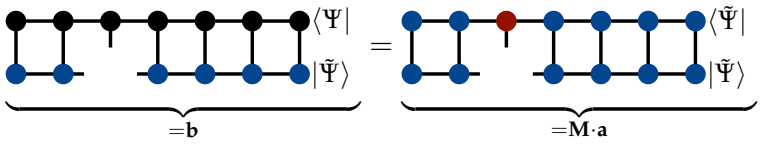

(3.18)

Here, the red tensor corresponds to the one over which we optimize; note that the second term of Eq. (3.17) is quadratic in $\mathbf{a}$, leading to an additional factor of two that cancels out in the gradient equations. When using the mixed canonical MPS form for optimizing the tensor $A^{\sigma_m}_{ij}$, the above linear algebra problem is trivially solved as the matrix $\mathbf{M}$ reduces to the unit matrix $M_{ij} = \delta_{ij}$. Therefore, the update rule reduces to a simple assignment,

$$\mathbf{a} \to \mathbf{b}. \tag{3.19}$$

After optimizing the tensor $\mathbf{a}$ at site m, a SVD decomposition is applied to bring the MPS back into the mixed canonical form with respect to the next site, $m+1$. Repeating this process across the entire chain—referred to as sweeping—updates one tensor at a time locally. After multiple sweeps, the MPS is likely to converge toward the optimal compressed representation of the wavefunction $|\Psi\rangle$[2]. Variational compression is particularly efficient for MPS. However, in other tensor network architectures, such as PEPS, full environment algorithms are computationally much more intensive, and often local updates must be employed.

Lastly, we note that efficient compression is a necessary step in any MPS algorithm involving manipulations of MPS, such as the application of operators or the addition of MPS. To illustrate with two key examples: when applying an MPO with bond dimension χ_O to an MPS with bond dimension χ_S, the resulting state has a bond dimension of $\chi = \chi_O\chi_S$. Similarly, when adding two matrix product states with bond dimensions $\chi^{(1)}_M$ and $\chi^{(2)}_M$, the resulting bond dimension

[2]This assumes the algorithm avoids becoming trapped in local minima, a challenge we briefly comment on later.

becomes $\chi = \chi_M^{(1)} + \chi_M^{(2)}$. Consequently, after manipulating matrix product states, the aforementioned compression is routinely performed to restore the MPS to the desired maximal bond dimension χ.

3.1.2 Density matrix renormalization group

We would now like to use similar strategies to minimize the energy of a variational state $|\Psi\rangle$ given a Hamiltonian $\hat{\mathcal{H}}$, i.e., we aim to find the MPS $|\Psi\rangle$ for a given bond dimension χ that minimizes the variational energy

$$\min_{|\Psi\rangle} \frac{\langle\Psi|\hat{\mathcal{H}}|\Psi\rangle}{\langle\Psi|\Psi\rangle} \geq E_0, \tag{3.20}$$

where the last inequality corresponds to the variational principle of quantum mechanics, stating that any variational energy is greater than or equal to the true ground state energy E_0 [180]. Eq. (3.20) is equivalent to minimizing the following objective function

$$\min_{|\Psi\rangle} \left(\langle\Psi|\hat{\mathcal{H}}|\Psi\rangle - \lambda \langle\Psi|\Psi\rangle \right), \tag{3.21}$$

where λ is a Lagrange multiplier that ensures the normalization of the optimized wave function. Writing the optimization problem as in Eq. (3.21), we observe a bilinear form similar to that in variational compression. Following the same strategy, we can again sweep through the system tensor by tensor and update the matrix entries accordingly. Evaluating the gradient of the tensor at site m and setting it to zero yields graphically:

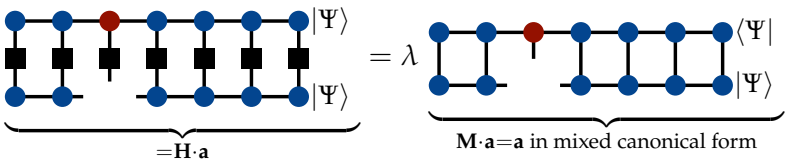

(3.22)

In mixed canonical form, we see that updating the red tensor at site m corresponds to finding the lowest eigenvalue eigenstate of the superblock Hamiltonian $\mathbf{H}$. This can be efficiently achieved using Lanczos methods [181], with tensors iteratively updated by sweeping through the system. Since the Hamiltonian MPO alters the bond dimension of the MPS, after each optimization, the state is compressed back to bond dimension χ, and a sequential SVD is performed to restore the MPS to the desired mixed canonical form.

The above corresponds to single-site update DMRG, which is presented here for its conceptual simplicity. However, strict single-site DMRG is susceptible to getting stuck in local minima. More robust numerical optimization methods include two-site updates or the addition of weak perturbations to the optimized MPS in a strictly single-site algorithm. In this thesis, we adopt the latter approach (referred to as DMRG3S), see Ref. [182] for details.

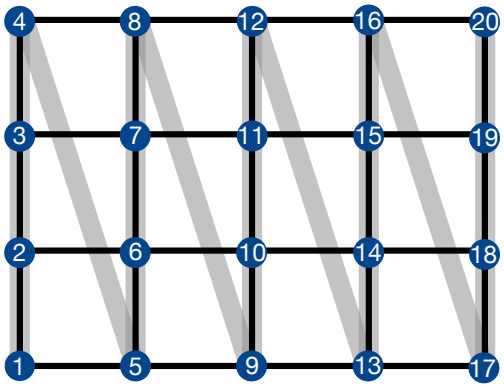

Figure 3.1: **2D MPS mapping.** Mapping of a 2D square lattice to a 1D MPS. To keep long-range interactions at a minimum, a Z-like mapping of often employed, illustrated by the grey line and site numbering. For width L_y and NN interactions on the square lattice, this introduces couplings of sites with distance L_y in the mapped system.

Higher dimensional systems

The MPS formulation as introduced above is particularly suited for local 1D Hamiltonians, as MPS naturally capture the entanglement properties of those systems. However, in many cases, simulating higher-dimensional systems, like the 2D Fermi-Hubbard model, is desired. To this end, the same MPS formulation as in 1D can be used by mapping the target system to a 1D MPS chain. Note that this necessarily introduces longer-range couplings in the Hamiltonian, and hence larger bond dimensions are needed to capture the entanglement structure of higher dimensional systems. In most applications, a Z-like mapping is employed, which minimizes the number of long-range bonds in the system, illustrated in Fig. 3.1.

How do we need to choose the maximum bond dimension χ to capture the entanglement of the system? To see this, note that the maximum entanglement an MPS can capture is given by

$$S \leq \log_2 \chi. \tag{3.23}$$

In particular, this results in the following scalings of the bond dimensions as a function of system size L:

- ▷ 1D: In gapped systems, $S = \text{const.} \rightarrow \chi > 2^{\text{const.}}$. In critical systems, there are logarithmic corrections to the entanglement entropy $S = \text{const.} \times \log_2(L)$, resulting in a power law $S \sim L^{\text{const.}}$.
- ▷ 2D: Here, the area law reads $S \sim L$, resulting in an exponential scaling of the bond dimension with system size, $\chi > 2^L$.
- ▷ Generally, in d dimensions, $\chi > 2^{L^{d-1}}$.

Therefore, DMRG works exceptionally well in a single dimension, where it has a clear scaling advantage over exact diagonalization. However, in higher dimensions, DMRG (unfortunately) faces again an exponential scaling with system size. Hence, to study 2D systems, we are restricted to shallow systems, and usually simulate cylindrical lattices of size $L_x \times L_y$ with $L_y \ll L_x$.

3.1.3 Symmetries

Symmetries play a crucial role in accelerating numerical calculations by effectively reducing the dimensionality of the diagonalization problem encountered in the DMRG algorithm. For $\mathrm{U}(1)$ symmetries, which are primarily used in this thesis, their implementation at the MPS level is as follows, see Refs. [179, 183]: The MPS tensors are adapted to include quantum number labels for both physical and bond indices. The full tensor then becomes a direct sum of all block tensors within a given symmetry sector q,

$$\mathbf{A} = \bigoplus \mathbf{A}_q. \tag{3.24}$$

Intuitively, the quantum numbers of the bond indices (which themselves carry no physical meaning) can be understood as representing how quantum numbers are transferred between neighboring sites. Specifically, for quantum numbers $q_{i_{m-1}}$ and q_{i_m} associated with the bond indices i_{m-1} and i_m, and the quantum number q_{σ_m} associated with the physical index σ_m, the quantum conservation rule reads

$$q_{\sigma_m} + q_{i_{m-1}} = q_{i_m}. \tag{3.25}$$

This rule must be satisfied for the matrix element to be nonzero. If a ground state in a specific symmetry sector is searched for, only the block corresponding to that sector needs to be diagonalized in the DMRG routine. Similarly, MPOs can be adapted to explicitly incorporate a block-diagonal structure.

In the following chapters, we will specifically consider scenarios where the system possesses multiple $\mathrm{U}(1)$ symmetries. By specifying the quantum numbers for each symmetry, the computational efficiency is significantly improved, as the additional constraints further reduce the effective dimensions of the tensors and operators involved in the calculations.

3.1.4 Time evolution

In addition to finding ground states of Hamiltonians, MPS techniques can also be employed to perform time evolutions of quantum states. This can be achieved in both the real and imaginary time domains: While the former describes the unitary time evolution of a quantum state under a Hamiltonian, imaginary-time evolution can be used to simulate finite-temperature properties of quantum systems. In the following, we provide a brief overview of commonly used MPS techniques for time evolution, followed by an introduction to finite-temperature simulations through purification. Again, we will only focus on the bare essentials of the algorithms. For a full technical overview, benchmarks and comparisons between various methods, we refer to the excellent review in Ref. [177].

Trotterization (Time-Evolving Block Decimation)

The solution of the time-dependent Schrödinger equation (for time-independent Hamiltonians) can formally be expressed as the task of applying the unitary time-evolution operator $\hat{U}(t)$ to an

initial quantum state $|\Psi(t=0)\rangle$,

$$|\Psi(t)\rangle = \hat{U}(t)\,|\Psi(t=0)\rangle = e^{-it\hat{\mathcal{H}}}\,|\Psi(0)\rangle\,. \tag{3.26}$$

There are various strategies to numerically approximate Eq. (3.26). One of the most straightforward methods, widely used in many contexts including time evolution in digital quantum simulations, is trotterization. In this approach, the goal is to approximate the time-evolution operator $\hat{U}(t)$ directly.

As an illustration of the method, consider a one-dimensional, local model with nearest-neighbor interactions, which can be decomposed into terms $\hat{h}_{i,i+1}$ including operators of sites i and $i+1$,

$$\hat{\mathcal{H}} = J\sum_i \hat{h}_{i,i+1}. \tag{3.27}$$

To evaluate the time-evolution operator, Trotterization divides the time evolution from $t=0$ to T into N small time steps $\delta, 2\delta, \ldots, N\delta = T$. Since the terms in the Hamiltonian do not generally commute, this introduces errors. In numerical implementations of Trotterization, the property of the Hamiltonian that it can be decomposed into clusters of commuting operators (i.e., all operators within a cluster commute with each other), is used. For local Hamiltonians, a straightforward decomposition involves separating even and odd bonds,

$$\hat{\mathcal{H}} = \hat{\mathcal{H}}_{\text{even}} + \hat{\mathcal{H}}_{\text{odd}}. \tag{3.28}$$

The time evolution for a short time slice δ can then be approximated as

$$\hat{U}(\delta) = e^{-i\delta\hat{\mathcal{H}}_{\text{even}}}e^{-i\delta\hat{\mathcal{H}}_{\text{odd}}}e^{-i\delta^2[\hat{\mathcal{H}}_{\text{even}},\hat{\mathcal{H}}_{\text{odd}}]} \approx e^{-iT\hat{\mathcal{H}}_{\text{even}}}e^{-iT\hat{\mathcal{H}}_{\text{odd}}}, \tag{3.29}$$

where in the first step the Baker-Campbell-Hausdorff formula is applied. As all terms within $\hat{\mathcal{H}}_{\text{even}}$ and $\hat{\mathcal{H}}_{\text{odd}}$ commute, the exponentials of the even and odd parts of the Hamiltonian are easy to evaluate,

$$e^{-i\delta\hat{\mathcal{H}}_{\text{even}}} = \prod_{i\in\text{even}} e^{-i\delta\hat{h}_{i,i+1}}. \tag{3.30}$$

The error per time step is thus proportional to $\epsilon \propto \delta^2$. After $N = T/\delta$ steps, the accumulated error scales as $\mathcal{O}(\delta)$.

Using the above decomposition in the MPS and MPO language, each trotter step can be implemented through applying the two series of local time evolutions in the following way,

$|\Psi(\delta)\rangle \approx$ 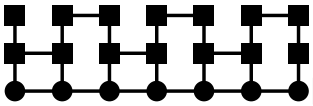 $|\Psi(t=0)\rangle$. (3.31)

After each application of an MPO to MPS, the state is truncated, before proceeding with the next operator application. Note that higher-order algorithms can be constructed to reduce the error rate, for which we refer to more detailed review articles such as Ref. [177].

Global Krylov Subspace Expansion

Instead of directly approximating the time-evolution operator $\hat{U}(t)$ as done in the Trotterization approach, one can approximate the action of $\hat{U}(t)$ on a given quantum state without explicitly evaluating or approximating the operator itself. Krylov subspace methods are well-known techniques in linear algebra and have been adapted for time-evolution problems. For the case considered here, the method closely follows the Lanczos time-evolution method used in exact diagonalization [184].

The general idea is to construct a Krylov subspace starting with the initial state $|K_0\rangle = |\Psi(0)\rangle$, and iteratively generate orthonormalized vectors by successively applying the Hamiltonian $\hat{\mathcal{H}}$ to $|K_{i-1}\rangle$. For N such states $\{|K_0\rangle, \ldots, |K_N\rangle\}$, the action of the time-evolution operator can be approximated as [177]

$$|\Psi(\delta)\rangle \approx \hat{K}_N^\dagger e^{-i\delta\hat{T}_N}\hat{K}_N |\Psi(0)\rangle , \tag{3.32}$$

where $\hat{K}_N^\dagger$ is the column matrix of the Krylov vectors $\{|K_1\rangle, \ldots, |K_N\rangle\}$, and $\hat{T}_N$ is the representation of the Hamiltonian in the N-element Krylov subspace with elements $(\hat{T}_N)_{i,j} = \langle K_i|\hat{\mathcal{H}}|K_j\rangle$.

In most cases, the error of the Krylov subspace expansion scales as $\mathcal{O}(\delta^N)$. Thus, as with Trotterization, smaller timesteps result in smaller errors. Additionally, errors can be reduced by increasing the dimension of the Krylov subspace.

Time dependent variational principle

As seen in the previous sections, MPS algorithms based on variational approaches provide powerful tools to study equilibrium properties of quantum systems. In a similar spirit, the time-dependent Schrödinger equation can be reformulated into a variational form, known as the Dirac-Frenkel time-dependent variational principle (TDVP). Here, the idea is that when using a variational ansatz for the wave function, such as MPS, the time evolution of the true state is best approximated by projecting the Schrödinger equation onto the tangent space of the variational manifold (with projection operator $\hat{P}_T$),

$$\hat{P}_T\left(\frac{\partial}{\partial t}|\Psi(t)\rangle + i\hat{\mathcal{H}}|\Psi(t)\rangle\right) = 0. \tag{3.33}$$

The tangent space of a variational state $|\Psi\rangle$ is defined through infinitesimal variations of the matrices $\mathbf{A}_i$, i.e.,

$$|\delta\Psi\rangle = \sum_i \frac{\partial|\Psi\rangle}{\partial\mathbf{A}_i}\delta\mathbf{A}_i. \tag{3.34}$$

By definition, the term $\partial_t|\Psi(t)\rangle$ belongs to the tangent space of $|\Psi(t)\rangle$. However, the action of the Hamiltonian typically rotates $|\Psi(t)\rangle$ out of the tangent space, introducing projection errors when computing $\hat{P}_T\hat{\mathcal{H}}|\Psi(t)\rangle$[3].

We can now formally solve the equations of motion for the variational parameters of the

[3]The projection can be interpreted as a necessary step to ensure variational consistency. The action of the Hamiltonian moves the state outside the variational tangent space, requiring projection back onto the tangent space to find the best variational state that describes the system's time evolution.

MPS[4]. This can be done either for one tensor at a time (1-TDVP) or for multiple adjacent sites simultaneously (in most practical implementations, two sites are chosen, corresponding to 2-TDVP). In 1-TDVP algorithms, the bond dimension remains constant as the time evolution progresses, while in 2-TDVP, the bond dimension can increase due to the tangent space projection. For technical details on how the projection operators are implemented using MPS, we refer to Ref. [177].

Note that the projection error incurred during time evolution with TDVP strongly depends on the bond dimension of the MPS. For small bond dimensions, the tangent space forms a low-dimensional subspace of the full Hilbert space, capturing only low-entanglement states. Applying the Hamiltonian to these states typically increases the entanglement significantly, which cannot be captured with a low bond dimension, resulting in large projection errors. Conversely, when time-evolving states with significant entanglement and correspondingly large bond dimensions, projection errors are much more controlled (i.e., the tangent space better approximates the Hilbert space).

Due to these considerations, special care must be taken when starting the time evolution with states that have low entanglement, such as product states. In such cases, global methods (e.g., the Krylov subspace expansion) are often employed initially until the bond dimension reaches a threshold where TDVP becomes reliable. Alternatively, enhanced TDVP algorithms with enriched basis states by averaging over Krylov vectors (called the "global subspace expansion", GSE) can be used [185]. In this thesis, we will primarily use the Krylov method followed by the 2-TDVP approach.

3.1.5 Purification

While time evolution in the real domain enables the study of unitary dynamics, applying imaginary time evolution can simulate finite-temperature properties of quantum states. Various methods based on imaginary time evolution exist; however, in this thesis, we will focus on the purification scheme, which is outlined below[5].

To implement purification, the Hilbert space is augmented with an auxiliary (often referred to as ancilla) site for each physical site. This allows mixed states in the physical subset of the Hilbert space to be represented as pure states in the enlarged Hilbert space. The algorithm begins with a purified infinite-temperature state $|\Psi(\beta = 0)\rangle$ of the system, which consists of a product of maximally entangled states between the physical and corresponding ancilla sites. This initialization depends on the Hilbert space and symmetry sector of the quantum system under consideration. Whenever purification is utilized in this thesis, the corresponding infinite-temperature state and its matrix product state (MPS) representation are explicitly stated[6].

Using time evolution methods (as e.g. given above), the state can then be evolved in imagi-

[4]Typically, this is achieved by decomposing the projection operators in a manner similar to a Trotterization procedure, enabling efficient implementation through a sequence of small time evolution steps.

[5]In addition to purification, another prominent method utilizes a class of states known as minimally entangled typical thermal states (METTS), as proposed in Ref. [186].

[6]We will mostly use ground state searches of tailored entangler Hamiltonians to find the maximally entangled states, which allows to target a given symmetry sector [187].

nary time, resulting in

$$|\Psi(\beta)\rangle = e^{-\beta\hat{H}/2}\,|\Psi(\beta=0)\rangle\,, \tag{3.35}$$

where $\tau = \beta/2$ corresponds to the imaginary time, and β is the inverse temperature.

Thermal expectation values at temperature β^{-1} can then be represented as quantum averages over the time evolved pure state,

$$\langle\hat{O}\rangle_\beta = \frac{\langle\Psi(\beta)|\hat{O}|\Psi(\beta)\rangle}{\langle\Psi(\beta)|\Psi(\beta)\rangle}. \tag{3.36}$$

Here, $\mathcal{O}$ is an operator acting on the physical sites only (i.e., all auxiliary degrees of freedom are traced out in the evaluation of the expectation value). Note that this is indeed an exact formulation of the usual form $\langle\hat{\mathcal{O}}\rangle = \frac{1}{Z}\mathrm{Tr}(\rho\hat{O})$, where $Z = \dim(\mathcal{H})\,\langle\psi(\beta)|\psi(\beta)\rangle$ with $\dim(\mathcal{H})$ the dimension of the Hilbert space. Thus, the problem boils down to an imaginary time evolution from the infinite temperature, maximally entangled state $|\Psi(\beta=0)\rangle$.

3.2 Two-particle self-consistent theory

While (quasi-)exact numerical methods are indispensable for studying strongly correlated systems, perturbative methods often provide valuable insights into the essential physics. One such example is the two-particle self-consistent theory (TPSC), which extends the random phase approximation by incorporating specific vertex contributions for improved accuracy. In the following, we skech the main ideas behind the TPSC method. In Sec. 10.4 and Sec. 11.4, we will apply TPSC to analyze a bilayer triangular SU(2) FH model and the SU(N) FH model, respectively. For a more rigorous derivation of the TPSC equations, we refer to Appendix A and Refs. [188, 189], where general arguments based on Luttinger-Ward functionals and Bethe-Salpeter equations are outlined.

Let us start by a brief recap of the random-phase approximation (RPA), a standard perturbative technique to account for interactions in weakly interacting systems. Within the RPA framework, the spin and charge susceptibilities for the Fermi-Hubbard model in momentum and Matsubara space are given by [157]

$$\begin{aligned}\chi_{\mathrm{sp}}(\mathbf{q}, i\omega_n) &= \frac{\chi_0(\mathbf{q}, i\omega_n)}{1 - \frac{1}{2}U\chi_0(\mathbf{q}, i\omega_n)},\\ \chi_{\mathrm{ch}}(\mathbf{q}, i\omega_n) &= \frac{\chi_0(\mathbf{q}, i\omega_n)}{1 + \frac{1}{2}U\chi_0(\mathbf{q}, i\omega_n)}.\end{aligned} \tag{3.37}$$

Here, $\chi_0(\mathbf{q}, i\omega_n)$ is the non-interacting susceptibility, i.e., the bubble diagram (see also Eq. (2.9)),

$$\chi_0(\mathbf{q}, i\omega_n) = -2\frac{T}{N_\mathbf{k}}\sum_\mathbf{k}\frac{n_F(\epsilon_\mathbf{k} - \mu) - n_F(\epsilon_{\mathbf{k}+\mathbf{q}} - \mu)}{i\omega_n + \epsilon_\mathbf{k} - \epsilon_{\mathbf{k}+\mathbf{q}}}. \tag{3.38}$$

$N_\mathbf{k}$ is the number $\mathbf{k}$-points in the BZ (i.e., the number of lattice sites), $n_F(x) = (1 + e^{x/T})^{-1}$ is the

Fermi-Dirac distribution, and μ is chosen such that the particle density per spin n_σ is given by

$$n_\sigma = \frac{1}{N_\mathbf{k}} \sum_\mathbf{k} n_F(\epsilon_\mathbf{k} - \mu). \tag{3.39}$$

The non-interacting susceptibility is thus determined by T, $\epsilon_\mathbf{k}$ and n_σ.

While RPA in weakly interacting systems and at large electronic density (such as graphene) is a fantastic approximation, it has several drawbacks that severely reduce its predictive power. For one, being a mean-field theory, it heavily overestimates the appearance of long-range order. For instance, in the 2D FH model, a finite transition temperature to an antiferromagnetic Mott insulating phase is predicted, violating the Mermin-Wagner theorem. Furthermore, it does not conform with Pauli's principle, which is a bit more subtle to see and will be outlined in the following.

Pauli's principle generally states that, for fermions, $\langle \hat{n}_\sigma \hat{n}_\sigma \rangle = \langle \hat{n}_\sigma \rangle$. This can be used to derive certain sum rules that the interacting susceptibilities must fulfil (see Appendix A),

$$\begin{aligned} \frac{T}{N_\mathbf{q}} \sum_{\mathbf{q}, i\omega_n} \chi_{\mathrm{sp}}(\mathbf{q}, i\omega_n) &= n - 2 \langle \hat{n}_\uparrow \hat{n}_\downarrow \rangle , \\ \frac{T}{N_\mathbf{q}} \sum_{\mathbf{q}, i\omega_n} \chi_{\mathrm{ch}}(\mathbf{q}, i\omega_n) &= n - n^2 + 2 \langle \hat{n}_\uparrow \hat{n}_\downarrow \rangle . \end{aligned} \tag{3.40}$$

Summing both equations in Eq. (3.40) and using the RPA results Eq. (3.37) leads to

$$\frac{T}{N_\mathbf{q}} \sum_{\mathbf{q}, i\omega_n} \frac{\chi_0(\mathbf{q}, i\omega_n)}{1 - \frac{1}{2} U \chi_0(\mathbf{q}, i\omega_n)} + \frac{\chi_0(\mathbf{q}, i\omega_n)}{1 + \frac{1}{2} U \chi_0(\mathbf{q}, i\omega_n)} = 2n - n^2. \tag{3.41}$$

As $\chi_0(\mathbf{q}, i\omega_n)$ is the non-interacting susceptibility, it by itself fulfills the sum-rule

$$\frac{T}{N_\mathbf{q}} \sum_{\mathbf{q}, i\omega_n} \chi_0(\mathbf{q}, i\omega_n) = 2n - n^2. \tag{3.42}$$

By expanding the denominators in Eq. (3.41), we see that for a general U, Eq. (3.41) is not guaranteed to be fulfilled.

This above stated problem can be mitigated through a simple trick, which will lead us to the TPSC equations. The core idea is that in the RPA, appropriate vertex corrections U_{sp} and U_{ch} can always be chosen to fulfill the sum rule (and hence Pauli's principle) *by construction*. Hence, we make the ansatz

$$\begin{aligned} \chi_{\mathrm{sp}}(\mathbf{q}, i\omega_n) &= \frac{\chi_0(\mathbf{q}, i\omega_n)}{1 - \frac{1}{2} U_{\mathrm{sp}} \chi_0(\mathbf{q}, i\omega_n)} \\ \chi_{\mathrm{ch}}(\mathbf{q}, i\omega_n) &= \frac{\chi_0(\mathbf{q}, i\omega_n)}{1 + \frac{1}{2} U_{\mathrm{ch}} \chi_0(\mathbf{q}, i\omega_n)}, \end{aligned} \tag{3.43}$$

which, together with the sum rule Eq. (3.40), defines the TPSC equations. If the correlator $\langle \hat{n}_\uparrow \hat{n}_\downarrow \rangle$ is known for a given system, we can self-consistently solve Eq. (3.40) for the irreducible spin and charge vertices, $U_{\mathrm{sp}}, U_{\mathrm{ch}}$. However, in most practical situations the number of on-site pairs,

$\langle \hat{n}_\uparrow \hat{n}_\downarrow \rangle$, is unknown.

In order to arrive at a fully solvable, self-consistent theory for the Hubbard model, Vilk and Tremblay introduced the following relation between $\langle \hat{n}_\uparrow \hat{n}_\downarrow \rangle$ and U_{sp} via the bare Hubbard-U,

$$\frac{U_{\mathrm{sp}}}{U} = \frac{\langle \hat{n}_\uparrow \hat{n}_\downarrow \rangle}{n_\sigma^2}. \tag{3.44}$$

As was demonstrated in a variety of settings, this ansatz works astoundingly well for the SU(2) case away from half-filling [188–191]. On a fundamental level, it can be motivated by the equations of motion of the Green's function, which include highly local four-point correlators. By doing a Hartree-Fock type factoring in a way such that it becomes exact when the correlators are truly local, the ansatz Eq. (3.44) is retrieved.

For details on the numerical implementation, including the consideration of symmetries, we refer to Appendix A.

4

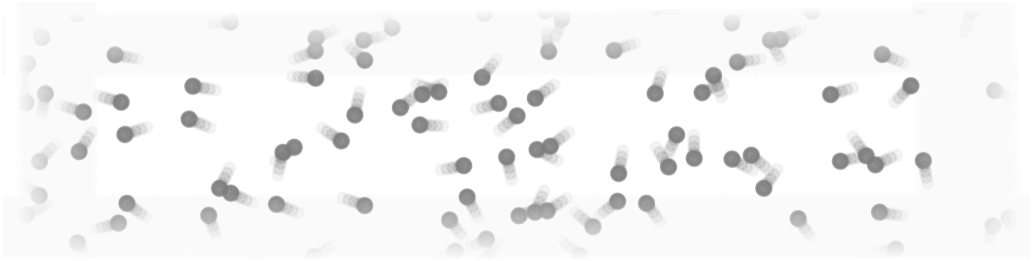

Quantum simulation

Summary. Quantum simulation refers to the process of studying a quantum system of interest by implementing a controlled quantum system in the laboratory. For instance, in exploring the physics of the Fermi-Hubbard model, the goal is to create a controlled physical system in the laboratory that closely replicates the behavior of the target system. In this chapter, we provide a brief overview of the working principles behind quantum simulation using ultracold atoms in optical lattices. This includes the processes of cooling, trapping, state preparation, and imaging of atomic clouds. Additionally, we discuss how moiré materials offer a tabletop experimental platform to study Hubbard physics on triangular lattices.

4.1 Ultracold atoms in optical lattices

The unique capabilities of studying inherently fermionic, strongly interacting atoms in optical lattice experiments have positioned them as a primary tool for studying strongly correlated systems in an analog setting[1]. In this chapter, we provide a basic overview of the working principles behind analog quantum simulation of the fermionic Hubbard model. The following discussion is not intended to comprehensively describe the sophisticated experimental apparatus used in quantum simulation but rather to serve as an introduction and overview from a theorist's perspective, highlighting concepts that will be relevant in later chapters. For a more in-depth discussion of the physical principles discussed here, we refer the reader to the excellent review articles

[1]Note that implementing a system that is described by a certain Hamiltonian is typically called analog quantum simulation. In contrast, using gate-based quantum computing to simulate the physics governed by an arbitrary Hamiltonian is referred to as digital quantum simulation. These terms are borrowed from classical analog computers, where a specific machine is designed to perform tailored computational tasks, while digital computers modify classical bits using a gate-based scheme.

Refs. [192–194] and theses [195, 196]. For the particular experimental sequence of the Lithium quantum gas microscope at the Max Planck Institute of Quantum Optics (MPQ), we refer to the PhD thesis by Joannis Koepsell [197].

4.1.1 Basics

The working principle of optical lattice experiments is based on trapping atoms in counter-propagating lasers creating a standing wave that generates a crystal-like structure of varying light field intensity. This spatially modulated lattice of light serves as a direct analog to the (attractive) ionic potential experienced by electrons due to Coulomb interactions with localized ions. For neutral atoms, the corresponding force that traps atoms in a lattice arises from dipolar interactions. Although neutral atoms lack a permanent dipole moment, exposure to an external field polarizes the atom, inducing a dipole moment proportional to the (generally time-dependent) applied electric field,

$$\mathbf{p}(t) = \alpha \mathbf{E}(t). \tag{4.1}$$

Here, α represents the polarizability of the atom. The induced dipole interacts with the applied field itself, leading to an interaction energy given by

$$U_{\text{dip}}(t) \propto -\mathbf{p}(t) \cdot \mathbf{E}(t) = -\alpha |\mathbf{E}(t)|^2 \propto -\alpha I(t), \tag{4.2}$$

where $I(t)$ is the intensity of the light field. This relationship implies that the interaction generates an attractive (repulsive) potential for $\alpha > 0$ ($\alpha < 0$).

The magnitude and sign of the polarizability, and thus the direction of the induced dipole moment relative to the external field, depend on the frequency of the applied field. A simple classical picture provides useful intuition: consider an electron in a two-level system modeled as a classical oscillator with eigenfrequency ω_0, corresponding to the energy difference between the atom's two levels. When the oscillator is driven by an external electric field with frequency ω, the response differs based on the detuning. For $\omega < \omega_0$ (red-detuned), the electron motion is in phase with the external field, resulting in $\alpha > 0$. In contrast, for $\omega > \omega_0$ (blue-detuned), the oscillator experiences a π-phase shift relative to the external field, oscillating out of phase and yielding $\alpha < 0$. Consequently, the potential is attractive in the former case and repulsive in the latter. Thus, in a red-detuned setting, atoms are trapped at the intensity maxima, whereas in a blue-detuned scenario, atoms are confined to the local intensity minima (i.e. the nodes of the standing wave).

This driven harmonic oscillator model also provides insight into the damping rate Γ, which corresponds to the imaginary part of the polarizability and accounts for the radiation loss of the oscillating electrons. Quantum mechanically, this loss is determined by the dipole matrix element between the ground ($|0\rangle$) and first excited ($|1\rangle$) states,

$$\Gamma \propto |\, \langle 0|\hat{\mathbf{d}}|1\rangle \,|^2, \tag{4.3}$$

where $\hat{\mathbf{d}} = -e\hat{\mathbf{x}}$ is the dipole operator. This damping rate corresponds to the spontaneous decay

rate of the first excited state into the ground state. In this semi-classical framework, by transitioning into the "rotating frame" of the laser light, we can find an explicit expression for the polarizability and hence the dipolar interaction from Eq. (4.2),

$$U_{\text{dip}}(\mathbf{r}) = \frac{3\pi c^2}{2\omega_0^3}\frac{\Gamma}{\Delta} I(\mathbf{r}), \tag{4.4}$$

where c is the speed of light, $\Delta = \omega - \omega_0$ is the detuning, and the spatial dependence of the intensity is given by the lattice modulations of the standing laser light wave.

Another important property of atoms in an optical lattice potential is the off-resonant scattering rate of photons from the laser beams by the atoms,

$$\Gamma_{\text{sc}} = \frac{\langle \mathbf{E} \cdot \partial_t \mathbf{p} \rangle}{\hbar\omega} = \frac{3\pi c^2}{2\hbar\omega_0^3}\left(\frac{\Gamma}{\Delta}\right)^2 I(\mathbf{r}). \tag{4.5}$$

This quantity characterizes the rate at which atoms trapped in the optical lattice heat up due to the laser source, and is one of the main sources of decoherence. Notably, while the dipole potential scales as $\propto I/\Delta$, the scattering rate scales as $\propto I/\Delta^2$. Therefore, a balance must be found between using strong fields and large detunings to create a sufficiently deep lattice potential while minimizing heating effects caused by scattering. In particular, it is preferable to limit the experiment to time scales $< 1/\Gamma_{\text{sc}}$. In far-detuned lattices, this time scale is typically of the order of seconds [196].

By adjusting the angles of multiple laser sources, one can engineer a wide variety of lattice potentials through Fourier synthesis. For instance, two aligned but counter-propagating laser waves along the x-axis with wavelength λ create a lattice potential described by

$$V(\mathbf{x}) = V_0 \cos^2\left(\frac{\pi \mathbf{x}}{a}\right), \tag{4.6}$$

where a is the lattice constant of the light-induced lattice, which in this case equals $\lambda/2$[2].

Notably, in optical lattice experiments, lattice constants (when using optical frequencies) are on the order of $\mathcal{O}(1\,\mu\text{m})$, which is approximately four orders of magnitude larger than the ionic lattice spacings in solid-state systems, typically of the order of Å (i.e., 10^{-10} m). This is illustrated in Fig. 4.1. This significant difference in length scales leads to drastically different time scales for the microscopic constituents: while electrons in solids typically hop with frequencies on the order of THz, the natural time scale for atoms in optical lattices is in the kHz range; this extended time scale enables the modeling and study of phenomena such as quench dynamics in electronic systems, which is completely out of range with solid state materials.

However, this substantial increase in length scales—and consequently, a density of atoms many orders of magnitude lower than air—raises the question of whether quantum effects remain significant. To reach the quantum degenerate regime, the (thermal) de Broglie wavelength λ_{dB} of the microscopic particles and their average spacing a must be comparable. Since $\lambda_{\text{dB}} \propto T^{-1/2}$, achieving this regime requires much lower temperatures in optical lattice experi-

[2] In general, when two beams interfere at a relative angle β, the lattice spacing is given by $a = \lambda/[2\sin(\beta/2)]$.

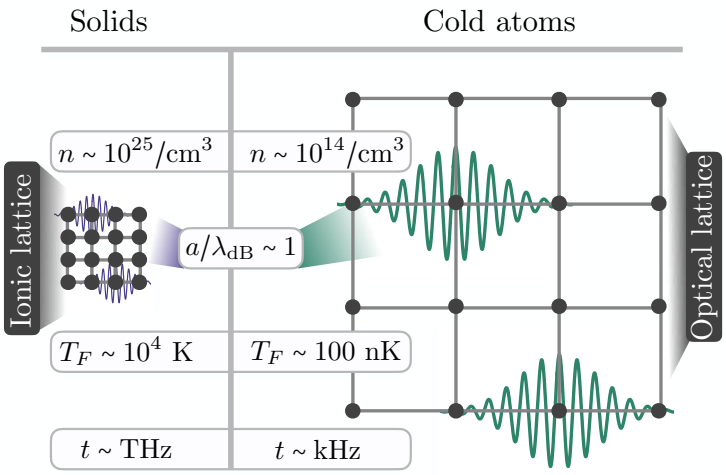

Figure 4.1: **Solids and cold atoms in optical lattices.** A comparison of scales in solids and ultracold atoms in optical lattices. Due to the significant difference in lattice spacing and corresponding densities, much lower temperatures are required to reach the quantum degenerate regime, where the thermal de-Broglie wavelength becomes comparable to the lattice spacing, $a/\lambda_{\mathrm{dB}} \sim 1$. This drastic change in spatial and temporal scales enables the microscopic study of strongly correlated phases of matter both in and out of equilibrium.

ments. The Fermi temperature in solid-state materials is on the order of $T_F = \mathcal{O}(10,000\,\mathrm{K})$. In ultracold atomic systems, by contrast, $T_F = \mathcal{O}(100\,\mathrm{nK})$, see Fig. 4.1.

Hence, while the enhanced spatial and temporal scales offer entirely new ways of studying *in situ* quantum systems, they come at the cost of requiring temperatures extremely close to absolute zero. Addressing this challenge—cooling atomic clouds to such extreme extents—has been a central focus of past and ongoing experimental efforts.

To simulate fermionic systems with both charge and spin degrees of freedom, the spin degree of freedom is typically encoded in the hyperfine structure of alkali atoms, such as Lithium and Potassium[3]. In optical lattices, these atoms interact via two-body van der Waals interactions. At the ultralow temperatures considered here, only scattering in states with the lowest angular momentum (in the relative motion) are possible[4]. For spinless fermions, for instance, only p-wave scattering is allowed due to Pauli's principle, realizing a non-interacting fermionic gas at low temperatures. For bosons and spinful fermions, on the other hand, s-wave scattering will lead to an interacting gas. These interactions between atoms i and j at positions $\mathbf{x}_i$ and $\mathbf{x}_j$ can be modeled as a contact potential with a scattering length a_{sc},

$$\hat{\mathcal{H}}^{\mathrm{int}}_{i,j} = \frac{4\pi\hbar^2 a_{\mathrm{sc}}}{m}\delta(\mathbf{x}_i - \mathbf{x}_j). \tag{4.7}$$

Due to Pauli's exclusion principle, this contact interaction allows only atoms in different hyperfine states (i.e., with different spins) to interact.

[3] In particular, fermionic isotopes ^{6}Li and ^{40}K are used.

[4] Pictorially, for low temperatures the wave packet of an atom extends beyond the spatial extent of the atom itself, meaning the detailed shape of the van der Waals potential is negligible, and only s-wave scattering plays a significant role

At this point, it is useful to introduce a typical energy scale in optical lattices, the recoil energy,

$$E_R = \frac{\hbar^2 \mathbf{k}^2}{2m}. \tag{4.8}$$

It equals the momentum an atom of mass m gains when absorbing a photon from the lattice potential with momentum $\hbar\mathbf{k}$. If the potential depth V_0 is sufficiently large ($V_0 \gtrsim 5E_R$), the system can be described using maximally localized Wannier orbitals centered at the minima of the optical lattice potential. For a finite potential depth, the band structure of the imposed lattice potential becomes gapped, allowing the system to be described—at sufficiently low temperatures and with at most two particles per site—by the single-band, SU(2)-symmetric Fermi-Hubbard model, Eq. (2.2). The scalings of the Fermi-Hubbard parameters in terms of the optical lattice are given by

$$\frac{t}{E_R} \propto \left(\frac{V_0}{E_R}\right)^{3/4} e^{-2\sqrt{V_0/E_R}}, \qquad \frac{U}{E_R} \propto \frac{a_{\mathrm{sc}}}{a}\left(\frac{V_0}{E_R}\right)^{3/4}. \tag{4.9}$$

The on-site interaction strength U can be tuned in two primary ways. First, increasing the lattice depth V_0 directly increases U. Second, manipulating the scattering length a_{sc} of the contact interaction provides an additional tuning mechanism. It is worth noting that for Lithium, the background scattering length is typically only a few nanometers, whereas $a \sim 0.1 - 1\,\mu$m. This large disparity heavily suppresses the interaction strength, resulting in only weakly interacting fermionic gases. To reach the strongly correlated regime in dilute quantum gases, it is necessary to enhance the scattering length relative to the average inter-particle distance.

This can be achieved through so-called Feshbach resonances. Such a resonance occurs in a two-particle collision when a bound state in a closed channel is coupled resonantly with the scattering continuum of an open channel. For instance, the two channels can represent different spin configurations of the atoms. By applying an external magnetic field near a Feshbach resonance, the interactions can be highly tunable. For example, the two commonly used hyperfine states of Lithium exhibit a broad Feshbach resonance, making Lithium a promising candidate for fermionic quantum simulations[5]. This potential is further corroborated by Lithium's small atomic mass, which leads to fast thermalization times and thus lower heating rates[6].

We highlight once again that the above approach allows for the direct simulation of *fermionic* models, such as the Fermi-Hubbard system, using *fermionic* atoms. This capability is a unique feature of cold atoms in optical lattices and sets it apart from other platforms, such as Rydberg atoms in tweezer arrays, ions in Paul traps, or superconducting qubits. In these systems, the intrinsic degrees of freedom are of bosonic nature, and the particles are distinguishable. In contrast, optical lattice experiments involve fermionic atoms whose wave function centers of mass significantly overlap. This overlap naturally enforces fermionic statistics without requiring any additional overhead, making it a very powerful platform for simulating fermionic systems. Though control over this external degree of freedom is theoretically possible using

[5] Other alkali atoms with Feshbach resonances used in quantum gas experiments include fermionic and bosonic Potassium (K) as well as bosonic Rubidium (Rb).

[6] As a comparison, for identical lattice geometries, the dynamics of ^{6}Li is 7 times faster compared to ^{40}K. Studying the FH model with ^{40}K is thus significantly more influenced by heating effects [198].

tweezer arrays, where coherent tunneling between adjacent tweezers can be engineered, it remains a challenging task. However, if achieved, this control could be utilized to realize universal, error-corrected fermionic quantum computing [199–201].

4.1.2 Experimental sequence

In each cycle, the experimental sequence consists of three main steps: cooling and trapping, quantum simulation, and obtaining many-body snapshots through imaging. As the final step collapses the quantum state, the entire sequence must be repeated for each obtained snapshot. In the following, we will trace the path of a Lithium atom from its source to its eventual disposal after imaging, providing a brief overview of the various steps involved in simulating the Fermi-Hubbard model. The experimental sequence to obtain a single spin and charge resolved many-body snapshot is summarized in Fig. 4.2. While other fermionic atoms can also be used for quantum simulation, we focus here on ^{6}Li and, in particular, the experimental setup at MPQ in Garching. For more details, we refer the reader to the PhD Thesis by Joannis Koepsell [197]. Note that most of the following concepts and sequences are widely used in quantum gas microscopy, though specific details (especially regarding cooling strategies and imaging) may vary.

Cooling and trapping

In the first step, hot Lithium atoms are directed into a magneto-optical trap (MOT), which consists of an inhomogeneous magnetic field (vanishing at the center and increasing away from it) and pairs of counter-propagating lasers in all three spatial dimensions, which are slightly red-detuned from an atomic resonance. The combination of magnetic field gradients and red-detuned lasers achieves two main effects:

1. **Zeeman trapping.** The Zeeman effect shifts atomic energy levels depending on the atom's position in the magnetic field. This shift causes atoms at different spatial locations to preferentially absorb photons from laser beams that push them toward the trap center, providing the restoring force needed for trapping. Note that this restoring force is velocity-independent. While it confines atoms near the MOT's central region, it does not reduce their kinetic energy and therefore does not directly cool the atoms.

2. **Doppler cooling.** Doppler cooling, in contrast, leverages the velocity-dependent Doppler shift of atoms. Counter-propagating laser beams, slightly red-detuned from an atomic resonance, interact with the atoms. In Lithium, cooling typically involves the D1 or D2 lines, corresponding to transitions near $\lambda \sim 671\,\text{nm}$, a wavelength range where lasers are commercially available.[7] The Doppler effect slightly alters the resonance frequency of these transitions. An atom moving toward one of the lasers preferentially absorbs photons from the opposing beam, reducing its momentum by an amount corresponding to one recoil energy of the cooling laser. After spontaneous emission, the atom regains momentum in a random direction, resulting in net heating when averaged over many cycles.

[7] This is yet another reason why Lithium is a popular atom for quantum simulation.

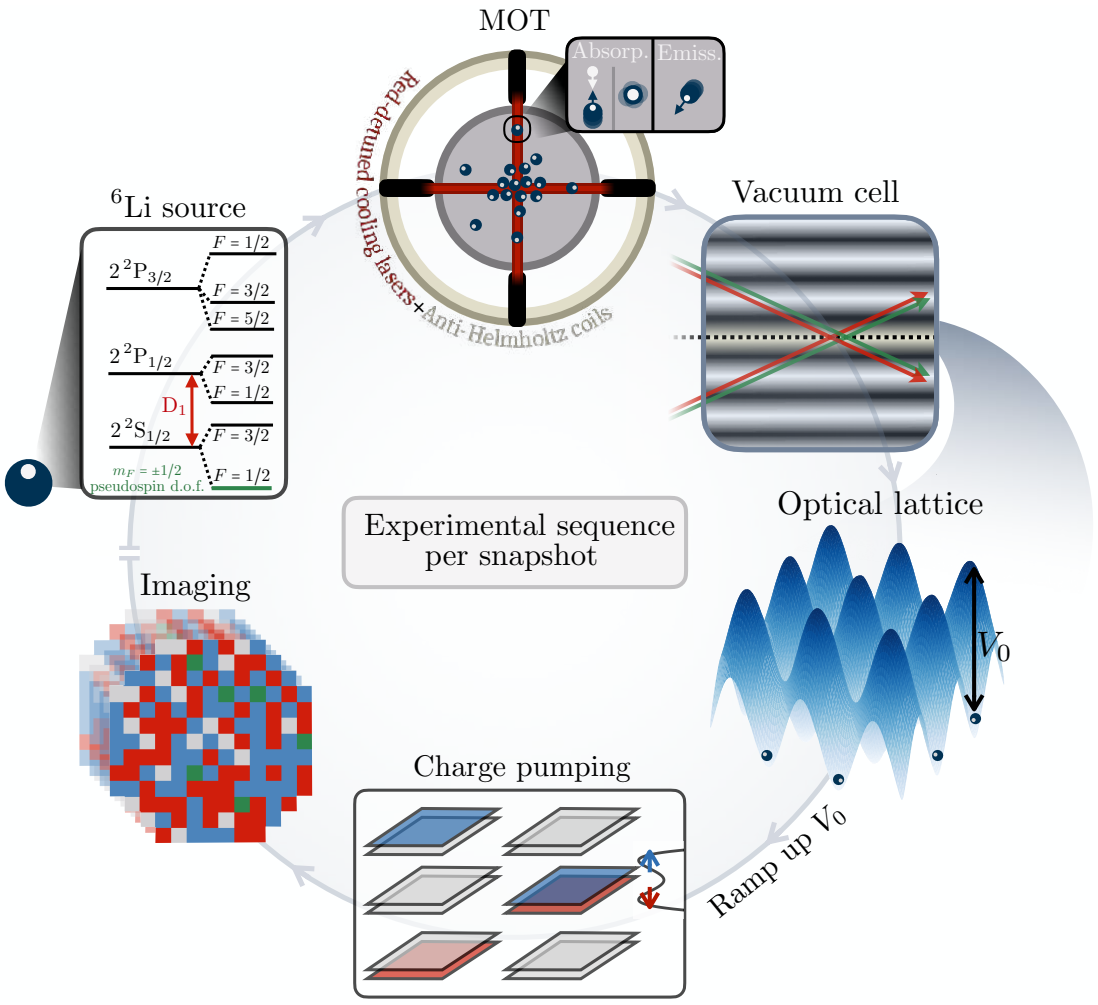

Figure 4.2: **Experimental sequence.** Overview of the experimental sequence used to obtain a single (spin- and charge-resolved) quantum many-body snapshot of the FH model in ultracold atom experiments. The sequence begins by loading hot Lithium atoms from a source into a magneto-optical trap (MOT), where Doppler laser cooling (typically on the D_1 or D_2 transition) reduces the atomic temperature. A magnetic field gradient generated by anti-Helmholtz coils traps the atoms at the center of the MOT. The atoms are then transferred to a dipole trap, which transports them to a vacuum cell, where they are loaded into a single sheet of an optical lattice formed by crossed dipole traps. After final evaporative cooling, the lattice depth is ramped up non-adiabatically, projecting the wavefunction onto one of its Fock states. Using optical superlattices along the vertical direction, each sheet is split into a double-well bilayer. Strong magnetic field gradients are applied to physically separate the $|F = 1/2, m_F = \pm 1/2\rangle$ spin states into the upper and lower layers. Charge pumping further separates the two layers, which can then be imaged independently. During the imaging process, active laser cooling (Raman sideband cooling) is employed to reduce vibrational quanta, ensuring that atoms remain in the optical lattice despite scattering many imaging photons. Finally, images captured by a CCD camera are used to reconstruct the full (spin- and charge-resolved) many-body snapshot of the system. The sequence is repeated many times, and resulting snapshots are used to estimate correlation functions of the underlying wavefunction.

The rate at which laser photons are absorbed and re-emitted is characterized by the linewidth Γ of the relevant atomic transition:

$$T_D = \frac{\hbar\Gamma}{2k_B}. \tag{4.10}$$

At equilibrium, the heating effect from spontaneous emission balances the cooling effect of the laser, preventing further cooling. This fundamental limit, known as the Doppler cooling limit, sets a lower bound on the temperature achievable in a MOT. For instance, laser cooling on Lithium's D2 transition can cool atoms down to $T_D \sim 300\,\mu$K, corresponding to $\Gamma \sim 2\pi \cdot 5.87\,$MHz[8].

Through the combination of Zeeman trapping and Doppler cooling, a cold atomic cloud is created, reaching temperatures within the quantum degenerate regime. Hyperfine states of ^{6}Li are used as a pseudospin degree of freedom; in most experimental settings, the two spin-projections of the $2S_{1/2}$ hyperfine states with $F = 1/2$ are used, $|F = 1/2, m_F = \pm 1/2\rangle$ (see Fig. 4.2). Repumping after laser cooling ensures a spin-balanced mixture of $m_F = \pm 1/2$ atoms for the next step.

Simulation

The quantum simulation of the Fermi-Hubbard model takes place in a high-fidelity vacuum glass cell. From the MOT, the spin-balanced atomic cloud is trapped in a focused laser beam (dipole trap) and physically transported into the glass cell. A crossed dipole trap is then ramped up to confine the atoms in the glass cell, providing strong confinement within the xy-plane with a Gaussian waist of approximately one micron. After this step, the Lithium atoms form a cold quasi-2D degenerate Fermi gas.

Final cooling is usually achieved through evaporative cooling. Several strategies can be employed here; one common approach involves using strong magnetic field gradients to tilt the potential experienced by the atoms, allowing the hottest particles to escape the trap[9]. After losing the hottest atoms, the system re-thermalizes through collisions. This highlights a fundamental difference between cooling fermions and bosons: for bosons, the absence of Pauli's exclusion principle allows for s-wave scattering even at very low temperatures, while higher angular momentum states are frozen out. For fermions, however, scattering and hence thermalization can only occur between different spin states, making evaporative cooling slower and more challenging. Further reducing the temperature of fermionic gases is a key focus for next-generation quantum gas microscopy. Techniques such as sympathetic cooling [202], entropy redistribution schemes [41], and Sisyphus cooling [203] are among the promising approaches.

The 2D Fermi gas is now ready to be loaded into the optical lattice. For lattice loading, sheets of 2D optical lattices are created, with a large lattice spacing along the z-direction. By aligning one of these sheets with the 2D Lithium gas, the atoms populate only this specific layer. The

[8] Through additional Doppler cooling in an ultraviolet MOT using the 2S-3P transition, temperatures as low as $T_D \sim 60\,\mu$K can be achieved due to the long lifetime of the 3P state.

[9] By tuning the magnetic field to specific regimes, the nuclear spin can be decoupled from the angular momentum of the valence electrons. This ensures that both hyperfine states experience the same force, preserving spin balance.

optical lattice depth is typically ramped up quasi-adiabatically[10] to $V_0/E_R \sim 7$. At this depth, the system reaches the tight-binding limit in the lowest band, effectively realizing the single-band Fermi-Hubbard model. Typical simulation parameters are $U/t = 8$ and $t/J = 2$. For simulating the lowest possible temperatures, imaging occurs immediately. However, holding the atoms in the lattice for some time before imaging allows systematic tuning of the simulation temperature[11].

On top of the optical lattice potential, the ^{6}Li atoms experience an overall radial harmonic confinement force due to the Gaussian beam profile of the laser beams used. This results in a radially inhomogeneous particle density across the lattice, as the harmonic potential is minimized at the center of the lattice. To mitigate this effect, digital mirror devices (DMDs) can be employed. DMDs allow for the application of a site-resolved repulsive potential imprinted on the optical lattice, which counteracts the harmonic confinement and creates a flat potential landscape. In addition to flattening the energy potential, DMDs can also be used to engineer arbitrary potential landscapes, such as ladder geometries [57].

Detection and imaging

How can the prepared many-body quantum state be observed? One significant advantage of the enhanced length scales in cold atoms in optical lattices compared to solid-state systems is that the inter-particle distances, on the order of $\sim 1\,\mu$m, can be readily resolved using cameras placed below the glass cell. To image the system, the lattice depth is non-adiabatically ramped up to maximum intensity (typically on the order of 50 E_R in less than a hopping time $1/t \sim 1$ ms). This process freezes the degrees of freedom and projects the many-body quantum state onto one of its Fock basis states. The atoms in this state are then imaged using resonant light. The atoms absorb the imaging light, and their fluorescence is captured by the camera. However, imaging presents a challenge: detecting the atoms requires them to absorb and emit many photons, often exceeding the lattice depth in units of the recoil energy. Therefore, to prevent atoms from leaving the lattice during imaging, active cooling techniques must be employed.

Raman sideband cooling is a widely used method to remove energy from the atoms through interactions with light fields via two-photon Raman transitions, routinely used in ion traps [204], optical lattices [198, 205], and optical tweezers [206]. After ramping up the lattice depths for imaging, the atoms are approximately harmonically confined to their lattice sites. Excited states in this configuration correspond to motional excitations of the Lithium atoms in the deep trap, referred to as sidebands.

A two-photon Raman transition is employed to transfer the atoms from the $F = 1/2$ to $F = 3/2$ hyperfine state. The lasers are carefully tuned such that the final state after the transition has one quantum less vibrational excitation. Following the removal of one vibrational quantum, the atoms are optically pumped to an excited state. If the system is in the Lamb-Dicke regime, the vibrational excitation remains conserved during the optical pumping sequence. When the

[10] In a many-body system, gap closures may hinder full adiabaticity. Typically, ramp times on the order of a tenth of a second are used.

[11] Mechanisms such as photon absorption, three-body losses, collisions with background particles in the glass cell, and other effects contribute to a constant heating rate.

atoms de-excite through spontaneous emission, they return to the $F = 1/2$ hyperfine state (in a lower vibrational state compared to the beginning of the sequence). The light emitted during this scattering process is then collected with a CCD camera. By repeating this cooling and imaging process over many cycles, a large number of fluorescence photons (on the order of 1000) can be collected, enabling imaging of the atomic distribution.

Bilayer techniques. Traditional quantum gas microscopes lack the ability to distinguish between (i) doublons and holes, and (ii) the two $|F = 1/2, m_F = \pm 1/2\rangle$ states. The former limitation arises from parity projections: during imaging, atom pairs on a single lattice site are lost due to light-induced collisions, resulting in measurements of the particle number modulo two on each site. The latter limitation stems from the insensitivity of fluorescence light to the angular momentum projection $m_F = \pm 1/2$. A common workaround for measuring spin-spin correlations is to prepare a Mott insulating state with one particle per site and then selectively remove one spin species. This is achieved by driving cycling optical transitions for either spin state using a spin-removal beam, causing one of the spin species to appear as holes [45, 52]. However, in a doped setting, this method significantly restricts the range of accessible observables in single-shot measurements; eliminating parity projections and enabling spin-resolved measurements are therefore highly desirable improvements for quantum gas microscopes.

Bilayer imaging techniques can be employed to achieve full spin- and charge resolution. To this end, a second optical lattice along the vertical direction, with half the lattice spacing of the original lattice and a tunable and stable phase shift, is adiabatically ramped up to high intensities after the dynamics in the xy-plane have been frozen out. This second lattice in the z-direction creates an optical superlattice, effectively splitting each 2D sheet into two coupled sheets. This structure can be visualized as a double well, as illustrated in Fig. 4.2. By applying strong magnetic field gradients, one spin species is directed into one of the double wells, while the other species occupies the other well. The phase shift of the two lattices and their intensities provide tuning knobs for the energy difference between the two sites in the double well. Time-dependent modulation of these superlattice parameters is then used to spatially separate the "up" and "down" sheets, dynamically transporting them to layers with a larger separation. Once sufficiently separated, both layers can be imaged individually. By imaging the same configuration twice in a row, the imaging fidelity of around 98% can be estimated [57].

In addition to enabling spin resolution, this method inherently resolves the issue of parity projections. Below the band-insulating limit of the lowest band, there will be at most one spin species per lattice site. Therefore, after Zeeman separating the species and transferring them into separate xy sheets of the optical lattice, each lattice site contains either zero or one particle. This allows for full resolution of holes, doublons, and both singlon states.

4.1.3 SU(N) symmetry in alkaline-earth atoms

Most of the above analog quantum simulation schemes have been optimized for alkali atoms, which feature a single valence electron and exhibit broad Feshbach resonances, enabling advanced quantum control techniques. Moving one step beyond alkali atoms in the periodic table,

we encounter alkaline-earth atoms (AEAs)[12], characterized by two valence electrons occupying an s-orbital. In the following, we briefly summarize the special physical features of AEAs, and refer to the review article Ref. [207] as well as Ref. [208] for details.

Due to their completely filled s-shells, these atoms possess a unique electronic structure, where the ground state forms a spin singlet with total angular momentum $\mathbf{J} = \mathbf{S} + \mathbf{L} = 0$ (i.e., the ground state is the ${}^1S_0$ state). Many AEAs also have stable excited states with $\mathbf{J} = 0$ and extremely narrow linewidths, such as the ${}^3P_0$ state in ^{173}Yb. For instance, the ${}^1S_0 \leftrightarrow {}^3P_0$ transition has a linewidth of $\Gamma \sim 2\pi \cdot 10$ mHz [207]. In contrast, the D_1 line in ^{6}Li has a lifetime of $\Gamma \sim 2\pi \cdot 1$ MHz [209], which is eight orders of magnitude larger. This makes AEAs promising candidates for atomic clocks [210][13] and quantum memories [211].

One of the most striking consequences of a vanishing $\mathbf{J}$ in the ground state of AEAs is the absence of hyperfine structure, which typically arises from the multipole coupling between the electron cloud and the nucleus. As a result, the scattering length a is identical for all total spin states $\mathbf{F}$ (whose contribution comes solely from the nucleus), and the interaction potential simplifies to:

$$V(\mathbf{r}) = \frac{4\pi\hbar^2}{m} a\delta(\mathbf{r}). \tag{4.11}$$

This leads to an effective SU(N) symmetry of the interactions, which is realized in AEAs with remarkable precision. The symmetry is directly given by the nuclear spin, with the relation $N = 2I + 1$. For example, in the ground state of ^{173}Yb, $I = 5/2$, leading to $N = 6$. However, using optical pump techniques, all values $N < 2I + 1$ can be accessed, by depleting certain nuclear projection states through optical pulses [61][14]. Notably, the deviation from perfect SU(N) symmetry is only of the order $\delta a/a \sim 10^{-9}$. While certain materials, such as graphene, can exhibit approximate SU(N) symmetries (e.g. due to spin- and valley degeneracies), the precision achieved in ultracold AEAs is unparalleled.

The unique properties of AEAs, including their electronic structure and highly symmetric interactions, position them as powerful platforms for exploring complex quantum phenomena and for use in analog quantum simulations. In terms of the experimental setup, quantum simulation experiments operate very similarly to what was described in the previous section. Using fermionic isotopes of ^{87}Sr and ^{173}Yb, recent ultracold atom experiments have successfully observed Mott insulating states [58, 213, 214], nearest-neighbor (NN) antiferromagnetic correlations [59, 60], and have measured the equation of state in the SU(6) Fermi-Hubbard (FH)

[12] AEAs include Be, Mg, Ca, Sr, Ba, and Ra, as well as the rare-earth element Yb. Yb has the electronic configuration [Xe]$4f^{14}6s^2$.

[13] Here, a laser is carefully tuned and locked to the frequency of the atomic ${}^1S_0 \rightarrow {}^3P_0$ transition. Since this is an electronic dipole-forbidden transition, it exhibits extremely narrow linewidths (long lifetimes). To ensure the laser is locked to the unperturbed atomic transition, atoms are cooled to minimize Doppler shifts and are trapped at magic wavelengths, where the two relevant states experience no relative AC Stark shift due to the laser light. Once calibrated with the atom, the laser is sent for interference into a photodetector with a frequency comb. This allows optical frequencies to be bridged to radio frequencies; standard techniques then enable precise measurement of the locked laser frequency, which can subsequently be used for timekeeping.

[14] For instance, to realize an SU(4) symmetric system, the two states $m_F = \pm 1/2$ are depleted. For SU(3), an additional pulse depletes the $m_F = -3/2$ state. The spin distribution can then be tested using optical Stern-Gerlach techniques, where a spin-dependent Gaussian potential leads to different forces acting on the different spin states. By applying the potential and performing (e.g. absorption) imaging after a given time, the atomic clouds have separated [212].

model [61].

Most cooling, trapping, and imaging techniques used in state-of-the-art quantum gas simulators are tailored for alkali atoms. Achieving single-site resolution for cold AEA gases in optical lattices remains an active field of research; in particular the narrower transitions in AEA atoms and their more complex electronic structure pose significant challenges for imaging. However, techniques such as singlet-triplet oscillations enable the study of magnetic structures of SU(N) magnets even in the absence of single-site resolution. In these experiments, a spin-dependent field gradient that is adiabatically turned on induces coherent oscillations between spin-singlet and spin-triplet states on neighboring sites. By recombining the two atoms into a single potential minimum using optical superlattice techniques, spin-singlets form doubly occupied sites due to the symmetry of the wave function, whereas spin-triplets occupy the ground and first excited bands. Photoassociation pulses can then transform doubly occupied sites into molecules, which leave the trap. This process allows the detection of the imbalance between singlets and triplets, providing insights into the short-range magnetic tendencies of the system [59, 60, 212]. In recent years, significant progress has been made in realizing quantum gas microscopy with AEA atoms. For example, single-site resolution has been demonstrated for bosonic isotopes of Strontium [215] and Ytterbium [216], paving the way toward fermionic microscopy.

Notably, for a fixed entropy per site of the cold atomic gas (comparable to, for example, cold Lithium gases), the entropy distributes among a greater number of spin projections. This results in significantly lower temperatures T/t achievable in SU(N) Fermi-Hubbard simulations, with temperatures as low as $T \sim 1$nK, corresponding to $T/t \lesssim 0.1$, being attainable[15]. This enables the simulation and study of FH physics at very low temperatures, which, together with the exotic physics to be expected (see Sec. 2.2.2 and Chap. 11), makes AEAs a highly promising platform for exploring quantum magnetism and doped Mott insulators with analog quantum simulation.

Apart from AEAs, polar molecules have been proposed as promising candidates for simulating SU(N) symmetric Hubbard models with possible $N > 30$ [217]. While AEAs are restricted to fermionic systems, for which $I > 0$ is needed, ultracold molecules can realize both fermionic and bosonic models. Furthermore, polar molecules offer the advantage of controllable interactions, whereas in AEAs, the background scattering lengths are positive, resulting in interactions that are always repulsive.

4.2 Moiré materials

Another direction for controlling, simulating, and studying strongly correlated physics is the use of stacked van der Waals materials [38]. These materials feature weak coupling along one spatial dimension, which allows for the synthesis of genuine 2D materials, i.e., single atomic 2D layers. When isolating and stacking layers composed of different atomic compositions, a lattice mismatch causes interference between the constituent lattices, leading to enlarged superlattices with a periodicity $\tilde{a}$, which differs significantly from the atomic lattice spacing a. This lattice interference pattern, which arises when stacking two 2D material layers, gives these systems the

[15] This effect is often referred to as the Pomeranchuk cooling effect.

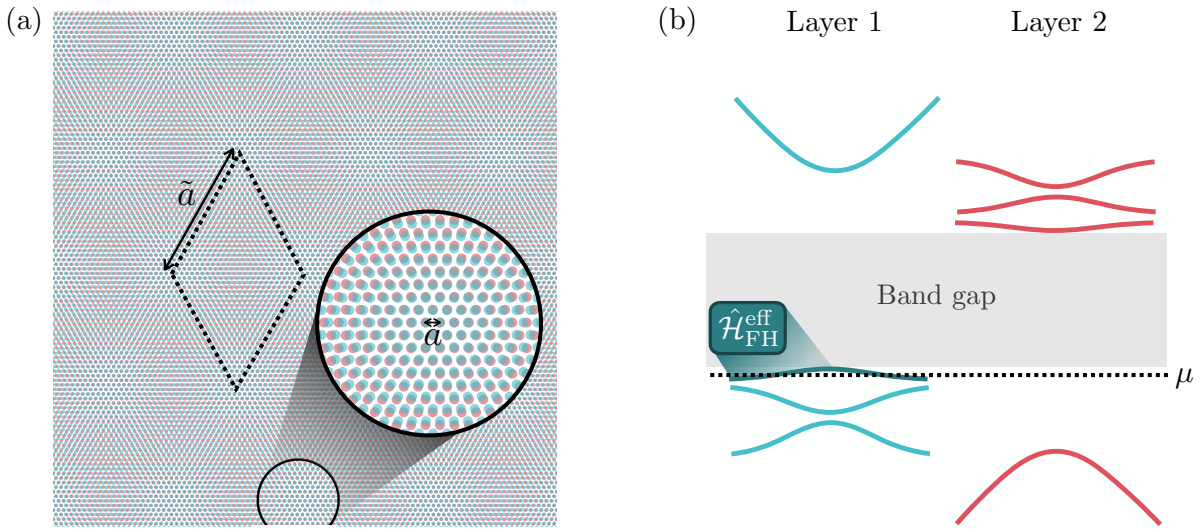

Figure 4.3: **TMD moiré materials.** (a) Geometric interference pattern arising when stacking two lattices with the same hexagonal lattice structure but a mismatch of lattice constants (here chosen to be 4%, a typical value in moiré materials). Bright spots that appear periodically (where atoms align) correspond to a triangular lattice with lattice constant $\tilde{a} \gg a$; the resulting unit cell is underlined with the black dashed line. (b) Typical band structure with type-II band alignment of TMD heterostructures. The left and right bands correspond to the two layers. When doping the system into the (blue) valence or (red) conduction band, the effective model reduces to a single-band FH model, whose parameters are determined by the moiré scale $\tilde{a}$ and Wannier orbital localization a_W. Valley degeneracies of the bands lead to an effective pseudospin degree of freedom, in turn realizing an SU(2) symmetric effective model.

name "moiré materials"[16]. Fig. 4.3 (a) shows the geometric interference effect for two aligned hexagonal lattices with a lattice mismatch of 4%. The resulting moiré lattice (see the bright spots in Fig. 4.3 (a)) encloses many atomic sites, and forms a triangular lattice. Similarly, a moiré superlattice can be created by stacking two layers with a relative twist angle [218]. Next to twisted bilayer graphene, typical moiré materials are composed of transition metal dichalcogenide (TMD) heterobilayers (HBL), e.g., WSe_2/WS_2.

As seen in Fig. 4.3 (a), the resulting superlattice constant $\tilde{a} \sim 10$ nm can be hundreds of times larger than the atomic lattice spacing $a \sim 1$ Å. It is determined by the lattice mismatch d and the relative rotation angle Θ between the two layers, with $\tilde{a} \approx \frac{a}{\sqrt{d^2+\Theta^2}}$ [218]. This stark difference in length scales allows for a separation of low-energy, long-wavelength physics on the scale $\tilde{a}$ from high-energy physics on the scale a. Electrons can be described as moving in a smooth lattice potential defined by $\tilde{a}$, while short-wavelength modulations at the scale of a can be neglected at low energies. Correspondingly, the moiré density $\propto \tilde{a}^{-2}$ is many orders of magnitude smaller than real atomic densities $\propto a^{-2}$ [218].

As length scales are enhanced, the Brillouin zone (BZ) is folded down into a mini-BZ, giving rise to a multitude of bands. Interlayer hybridization then leads to a splitting of these mini-bands, resulting in the formation of nearly dispersion-less flat bands [38, 218]. TMDs often fea-

[16]The term "moiré" originates from the French textile industry, where two layers of textile are pressed together when wet. Imperfect spacing of threads creates geometric interference patterns.

ture a type-II band alignment, as illustrated in Fig. 4.3 (b). When hole (electron) doping the system into the nearest valence (conduction) band, the quenched dispersion drastically reduces the effective kinetic energy scales, pushing the system into interaction-dominated regimes. Notably, in TMD bilayers, degeneracies from the spin and layer degrees of freedom are lifted by strong spin-orbit coupling and layer displacement, respectively, leaving only the valley degree of freedom degenerate. This results in an effective single-band Fermi-Hubbard (FH) model on the moiré lattice, describing a single isolated flat band whose dispersion is governed by the smoothly varying moiré potential. Here, the pseudospin exhibits SU(2) symmetry and acts as the spin [219].

The hopping term of the Fermi-Hubbard model is determined by the bandwidth W of the flat mini-band, which in turn depends on the moiré scale, $t \propto W \propto \tilde{a}^{-2} \sim 1 - 5$ meV [218, 219]. In contrast, the on-site interaction U is related to the width a_W of maximally localized Wannier orbitals of the electronic wave functions in the moiré lattice potential, such that $U \propto a_W^{-1} \sim 100 - 200$ meV (with typical $a_W \sim 2$ nm). The doping level δ (holes per moiré unit cell) can be tuned using electrostatic gating, which allows control over the filling of individual mini-bands and hence the doping level of the effective FH model that describes the low-energy physics.

Note the conceptual similarity between the enhanced length scales in moiré materials and ultracold atoms. Similar to the latter, enhanced scales in moiré materials enable the direct use of optical spectroscopic methods to probe local properties of these systems [38]. While van der Waals materials are less isolated than ultracold atom systems, their broad tunability and the ability to achieve temperatures significantly lower than the effective hopping energy[17] allow for the exploration of a wide variety of phases of matter in strongly correlated model Hamiltonians, both in and out of equilibrium. Furthermore, interactions in these systems can be flexibly tuned, including long-range and screened Coulomb interactions [38]. External electric and magnetic fields, which are readily accessible experimentally, provide additional tunability.

A straightforward method for probing the properties of moiré materials is electrical transport. For example, the quantum Hall effect has been observed in graphene stacked on hBN, evidenced by the appearance of Hofstadter butterflies [220]. Correlated Mott insulating [221] and unconventional superconducting [222] phases have also been discovered in moiré twisted bilayer graphene near certain (so-called magic) angles, where flat band emerge[18]. More recently, correlated physics have been explored in stacked TMD materials, which are effectively described by a single-band FH model (see the discussion above). To name one concrete example, in stacked and aligned WSe_2/WS_2 layers, a moiré pattern due to a lattice mismatch forms. Hole doping the lowest valence band of WSe_2 revealed that at unit filling of the valence band, resistivity peaks sharply, indicating an interaction-driven Mott insulator [223]. Interestingly, these resistivity peaks are accompanied by peaks in the reflection contrast [223]. The latter measures the energy-resolved reflectivity of a sample compared to a reference, and signals the existence of excitons with enhanced oscillator strengths. It has been argued that in the Mott insulating state, screening

[17] With $J = 4t^2/U \approx 0.02 - 1$ meV, temperatures as low as $T/J \leq 1/10$ can be reached.

[18] In twisted bilayer graphene, flat bands only emerge at very specific angles. In contrast, in TMD materials, flat bands appear much more generically, often also for aligned stacking due to lattice mismatches and inherent energy gaps in transition metals.

of electron-hole interactions is reduced, leading to a partial regain of oscillator strength, which is suppressed when free carriers screen interactions [223].

Probing excitons in a magnetic field can further illuminate the magnetic structure of local moments at half-filling. A magnetic field B breaks the valley degeneracy (acting similarly to a Zeeman splitting on pseudospins). As each handedness of circularly polarized light couples exclusively to one valley degree of freedom, measuring the energy difference Δ_Z between left- and right-handed light as a function of B yields the exciton valley g-factor, where $g \propto \lim_{B\to 0} \Delta_Z / B$. Furthermore, excitons serve as sensors for the magnetic environment of localized holes: the overall exciton Zeeman splitting reflects both the applied magnetic field and the magnetization of local moments. This allows for direct measurement of magnetization and magnetic susceptibility $\chi = \lim_{B\to 0} M/B$, which can be extracted from the measured g-factors [223],

$$\chi \propto g + \text{const.} \tag{4.12}$$

The resulting susceptibility can be fitted to the Curie-Weiss law,

$$\chi \propto \frac{1}{T - \Theta}. \tag{4.13}$$

A negative Weiss constant $\Theta < 0$ signals antiferromagnetic correlations between localized moments, which can be described by a valley pseudospin Heisenberg model with antiferromagnetic exchange couplings $J \propto 4t^2/U$. Indeed, negative Curie temperatures have been experimentally confirmed in TMD moiré materials [223]. However, note that due to the Mermin-Wagner theorem, true long-range order is only achieved in the ground state at absolute zero temperature.

Excitons can also serve as delicate sensors for their dielectric environment. They can be modeled as 2D hydrogen-like atoms, where the hole and electron interact through an attractive Coulomb potential. The ground state exciton corresponds to the 1s state, with excited states given by the 2s, 3s, and higher states. Notably, excited states with $n \geq 2$ possess Bohr radii much larger than the thickness of a monolayer. Conceptually, this is akin to the large radius of Rydberg atoms. This property makes excitons highly sensitive to the dielectric environment of, for instance, a TMD heterobilayer when a monolayer is brought into close proximity to the probe. By measuring the resonance frequency and oscillator strength of the sensing monolayer, insights into the nature of correlations—such as charge order—in the probe material can be obtained. This approach avoids complications arising from large contact resistance effects that may occur when directly probing moiré bilayers. In WSe_2/WS_2, this method has uncovered a rich variety of insulating states, which are attributed to charge-ordered Wigner crystals at numerous commensurate filling factors [224].

Quantum simulation of the triangular lattice FH model has garnered significant interest in recent years. Here, in addition to the competition between hole motion and magnetic order, geometric frustration exists even in the undoped Mott insulating state. As discussed above, cold atom and condensed-matter quantum simulators can provide valuable insights into the resulting physics: For instance, in TMDs, the effective moiré potential forms a flat-band triangular lattice, making them promising candidates for studying the effects of geometric (and kinetic)

frustration in strongly correlated systems [38]. In Chap. 10, we will explore a single hole doped into a triangular lattice t-J model, focusing on cold atom implementations in triangular optical lattices. Furthermore, we will develop a theoretical framework for interpreting measurements in moiré heterostructures, where a combination of induced RKKY-type interactions and kinetic frustration effects may play a crucial role.

Part II

Applications

5

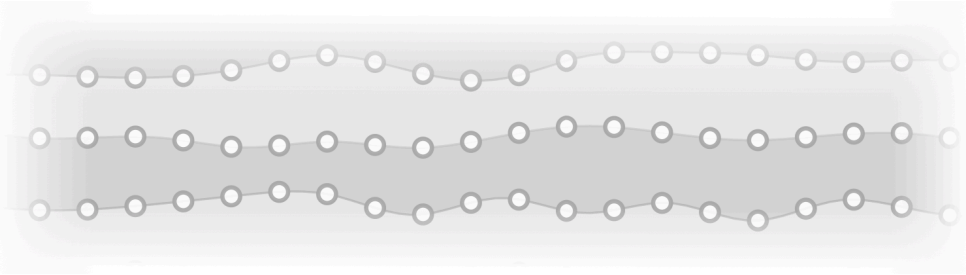

Stripes in mixed dimensions

Summary. The stripe phase is one of the key collective phases in strongly correlated systems. Emerging from the intricate competition between spin and motional degrees of freedom, the critical temperatures required to observe stripes in quantum gas microscope experiments of the plain-vanilla Hubbard model, however, remain beyond reach with current techniques. In the first part of this chapter, we propose the doped mixed-dimensional (mixD) variant of the t-J model as a parent Hamiltonian for the stripe phase. In this system, charge carriers are restricted to move in only one direction, while magnetic $\mathrm{SU}(2)$ interactions remain two-dimensional. We demonstrate the existence of a stable vertical stripe phase across a broad range of doping levels, with high critical temperatures on the order of the magnetic coupling. This renders the stripe phase directly observable with quantum simulation platforms. In the second part of this chapter, we microscopically investigate the formation of extended stripe-like charge structures in a mixed-dimensional Lithium Fermi-Hubbard simulator, comparing the experimental results to MPS and mean-field calculations.

5.1 Introduction

Correlated phases of matter featuring charge-density waves are a prominent characteristic of hole-doped cuprates, which, as introduced in Sec. 2.1, distinguishes them from their electron-doped counterparts. Particularly in Lanthanum-based copper-oxides, charge- and spin-density waves appear simultaneously, forming a stripe phase that is most prominent around doping $\delta = 1/8$, see Refs. [79–81] and Sec. 2.1.

A simplified illustration of the stripe phase is shown in Fig. 5.1. Charges organize into a density wave along one direction, explicitly breaking the C_4 symmetry of the underlying square lattice. Simultaneously, the spins align antiferromagnetically. To maintain AFM alignment even

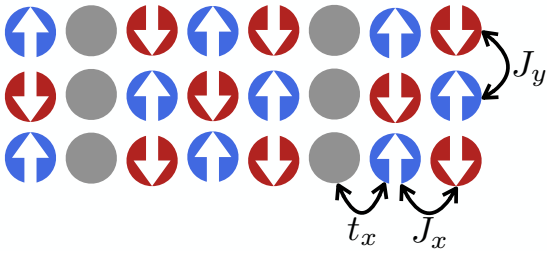

Figure 5.1: **Stripes and the mixed-dimensional t-J model.** Illustration of the stripe phase on the square lattice. Holes form a density wave along the x-direction, while the AFM spin background features domain walls across lines of holes. In this chapter, we focus on a mixD setting: while superexchange interactions are present in both the x- and y-directions, the tunneling of dopants is restricted to the x-direction. This corresponds to the standard 2D t-J model with $t_y = 0$.

as holes fluctuate, magnetic domain walls form along the lines of charges. As a result, the system exhibits both a charge-density wave and incommensurate long-range magnetic order. The latter is characterized by an ordering vector shifted away from $\mathbf{Q} = (\pi, \pi)$, a consequence of the finite density of domain walls within the system.

Though the specific characteristics of stripe phases are well understood, their relationship to superconducting order and the pseudogap phase at higher temperatures remains an open question. For instance, it is yet to be clarified whether stripes and superconductivity are competing phases or if they represent different manifestations of a common origin [145, 225–227]. Furthermore, both experimental [107–109] and numerical [154, 156] results suggest a profound relationship between the pseudogap and the stripe phase, a topic we will discuss and explore in detail in Chap. 7.

As introduced in Sec. 4.1, quantum gas microscopes provide a unique platform to simulate Fermi-Hubbard physics in a scalable and controllable manner. Coupled with the capability to take spin- and charge-resolved many-body snapshots, these simulators offer a promising avenue to address the above questions, specifically to gain a microscopic understanding of the formation of stripes and their relation to other phases of matter. However, accessing states that exhibit collective spin- and charge order remains beyond the reach of current analog quantum simulators due to temperature limitations.

This challenge highlights the need to propose, implement, and analyze modified but closely related Fermi-Hubbard models that push the energy scales for certain phases of matter, making their quantum simulation feasible. In this chapter, we will study stripe formation in the t-J model in mixed dimensions (mixD), illustrated in Fig. 5.1. The model describes mobile fermions whose motion is restricted to be along one dimension, while their spin is coupled through 2D SU(2) invariant superexchange interactions. The Hamiltonian reads (see also Sec. 2.2.3)

$$\hat{\mathcal{H}} = -t \sum_{\sigma,\langle \mathbf{i},\mathbf{j}\rangle_x} \hat{\mathcal{P}}_{GW}\left(\hat{c}^\dagger_{\mathbf{i},\sigma}\hat{c}_{\mathbf{j},\sigma} + \text{h.c.}\right)\hat{\mathcal{P}}_{GW} + J \sum_{\langle \mathbf{i},\mathbf{j}\rangle} \left(\hat{\mathbf{S}}_\mathbf{i} \cdot \hat{\mathbf{S}}_\mathbf{j} - \frac{\hat{n}_\mathbf{i}\hat{n}_\mathbf{j}}{4}\right), \tag{5.1}$$

where $\hat{c}^{(\dagger)}_{\mathbf{i},\sigma}$, $\hat{n}_\mathbf{i}$ and $\hat{\mathbf{S}}_\mathbf{i}$ are fermionic annihilation (creation), particle density, and spin operators on site $\mathbf{i}$, respectively; $\langle \mathbf{i},\mathbf{j}\rangle_{(x)}$ denotes nearest neighbor (NN) sites on the 2D square lattice (with

subscript x indicating NN sites along the x-direction only), and $\hat{\mathcal{P}}_{GW}$ is the Gutzwiller operator projecting out states with double occupancy.

In Sec. 5.2, we focus on the general physical aspects of stripe order in the mixD setting. Specifically, we analyze the order for various hole densities and map out the phase diagram. Using finite-temperature MPS methods via symmetry-conserving purification schemes, we predict the thermal properties of the system with high accuracy. Our results indicate high critical temperatures for stripe formation, where incommensurate order becomes visible on finite-size geometries. This part of the chapter, including the above introduction, is based on and closely follows the following publication, partially with textual overlap:

> [1] **HS**, U. Schollwöck, A. Bohrdt, and F. Grusdt. **Robust stripes in the mixed-dimensional t-J model**, Phys. Rev. Research 5 L022027 (2023)

The results presented in Sec. 5.2 render the stripe phase readily observable in ultracold atom experiments using optical lattices, where the mixD setting can be realized experimentally through the application of potential gradients or superlattice engineering. In Sec. 5.3, we discuss and analyze experimental results in a collaboration with the Lithium experiment at MPQ. Special acknowledgements go to Dominik Bourgund, Immanuel Bloch, and Timon A. Hilker, who led the experimental realization. The author of this thesis further acknowledgements Titus Franz, Thomas Chalopin, Petar Bojović, Si Wang, and Sarah Hirthe for the collaboration. The experimental results of the ^{6}Li experiment demonstrate how the quantum simulator accesses regimes where individual stripes begin to form, paving the way toward the observation of long-range charge- and spin-density wave order at lower temperatures. After introducing the experimental setup, Sec. 5.3 focuses on comparing these experimental findings with predictions from both MPS and mean-field descriptions, to which the author of this thesis has significantly contributed. Sec. 5.3 is based on the following publication, partially with textual overlap in the theory discussions:

> [2] D. Bourgund, T. Chalopin, P. Bojović, **HS**, S. Wang, T. Franz, S. Hirthe, A. Bohrdt, F. Grusdt, I. Bloch, and T. A. Hilker. **Formation of stripes in a mixed-dimensional cold-atom Fermi-Hubbard system**, Nature 637, 57–62 (2025)

5.2 Robust stripes in the mixed-dimensional t-J model

In this section, we will numerically analyze the mixD t-J model, Eq. (5.1), to gain insights into its ground state and finite-temperature properties. We find that the ground state is characterized by fully filled stripes, i.e., L_y holes form a single stripe in a system of width L_y. In particular, we demonstrate how the resulting charge-density wave fundamentally differs from Friedel oscillations at open boundaries, showing that it is stabilized by the (incommensurate) spin-spin correlations.

At finite temperatures, we uncover a crossover from a chargon gas, where no order is present, to the stripe phase, where spin- and charge correlations extend across the entire system. Notably, the temperatures required to observe the emergence of extended stripe correlations are extraordinarily high, on the order of the coupling $J/2$. This stands in stark contrast to the FH model at

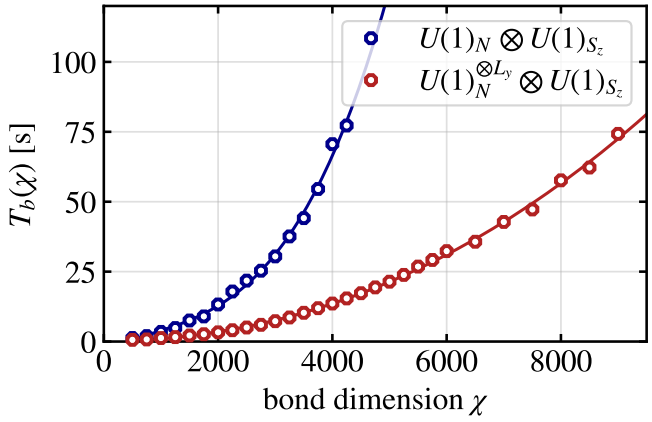

Figure 5.2: **Computational resources for different implemented symmetries.** CPU time per DMRG step as a function of bond dimension χ when using a global U(1) charge conservation symmetry (blue circles) and when including the $\mathrm{U}(1)^{\otimes L_y}$ symmetry in the ground state search (red circles). For $\chi = 5,000$, we gain a speedup of a factor ~ 6, for $\chi \gtrsim 10,000$, speedup factors are > 10. Enforcing particle conservation makes large scale computations significantly more efficient, allowing to study the ground state of arbitrary hole configurations with high precision.

strong coupling, where tiny energy differences between various stripe filling factors and other symmetry-breaking orders, such as pairing, result in very low critical temperatures of the order $T/J \lesssim 0.1$ [228].

When analyzing many-body snapshots of the ground state and thermal MPS, commensurate spin correlations are revealed upon removing the holes from the quantum many-body snapshots. We argue that these hidden spin correlations contribute to the predicted resilience of the stripe phase against quantum and thermal fluctuations.

5.2.1 Ground state properties

Using DMRG and the `SyTen` toolkit, we calculate the ground state of the doped mixD t-J model Eq. (5.1) on cylinder geometries with dimensions $L_x \times L_y$, where L_x (L_y) is the number of sites in the x- (y-) direction. Due to the additional constraint of hole motion in purely one dimension, the mixD model features an enhanced $\left(\bigotimes_l \mathrm{U}(1)_{N_\ell}\right) \otimes \mathrm{U}(1)_{S_z^{\mathrm{tot}}}$ symmetry. Therefore, denoting the number of particles in each leg ℓ by N_ℓ, and the total spin of the system by S_z^{tot}, the conserved quantum numbers are $[N_1, N_2, \ldots, N_{L_y}, S_z^{\mathrm{tot}}]$.

By targeting a smaller subspace in the Hilbert space fulfilling the constraints imposed by the quantum numbers, DMRG sweeps can be done more efficiently during the ground state search, see also Sec. 3.1. This is exemplified in Fig. 5.2, where the average time per sweep as a function of maximum MPS bond dimension χ is shown with and without using the extended symmetries. The computational cost for each DMRG sweep generally scales as $\mathcal{O}(\chi^3)$; however, implementing additional symmetries can reduce the matrix sizes by a substantial constant factor, leading to slower growth of computational resources as a function with χ. Comparison of a global U(1) charge conservation symmetry with the $\mathrm{U}(1)^{\otimes L_y}$ symmetry in the ground state search indeed leads to a substantial reduction of computational costs—for instance, the DMRG ground state

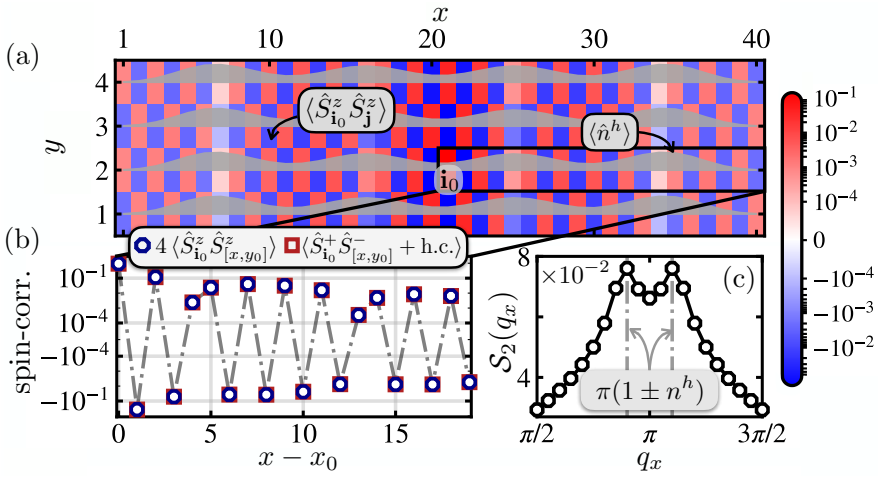

Figure 5.3: **Ground state properties.** (a) Spin-spin correlations $\langle \hat{S}^z_{\mathbf{i}_0} \hat{S}^z_{\mathbf{j}} \rangle$ with reference site $\mathbf{i}_0 = [x_0 = 21, y_0 = 2]$ for a 40×4 system with $n^h = 0.1$. Boundaries are open (closed) in x- (y-) direction. Correlations are color coded using a symmetric logarithmic scale, with linear scaling between $-10^{-4} \ldots 10^{-4}$. Average hole densities $\langle \hat{n}^h_{\mathbf{i}} \rangle$ are shown in grey. (b) correlation functions $4\,\langle \hat{S}^z_{\mathbf{i}_0} \hat{S}^z_{[x,y_0]} \rangle$, $\langle \hat{S}^+_{\mathbf{i}_0} \hat{S}^-_{[x,y_0]} + \text{h.c.} \rangle$, which are indistinguishable on the scale of the plot. Dash-dotted grey lines connecting the data points underline the incommensurate peak structure of spin-correlations. (c) static spin structure factor along $y = 2$, Eq. (5.2), with peaks located at $q_x = \pi(1 \pm n^h)$.

search is around six times faster for a bond dimension of χ =5,000, and around ten times faster for χ =10,000. The solid lines in Fig. 5.2 correspond to a fit to a third order polynomial, giving good agreement in both cases. In order to guarantee sufficient convergence for ladders of large width, the bond dimension must be increased exponentially in L_y, see the discussion in Sec. 3.1.

For the following ground state calculations, we choose bond dimensions $\chi = 10,000$, which become accessible through the additional symmetries. This allows for a high level of convergence of our results, e.g. the ground state of the $L_x \times L_y = 40 \times 4$ system studied below features expectation values $\langle \hat{S}^z_{\mathbf{i}} \rangle \sim \mathcal{O}(10^{-7})$ and $4\,\langle \hat{S}^z_{\mathbf{i}} \hat{S}^z_{\mathbf{j}} \rangle - \langle \hat{S}^+_{\mathbf{i}} \hat{S}^-_{\mathbf{j}} + \text{h.c.} \rangle \sim \mathcal{O}(10^{-5})$, which are both expected to vanish for SU(2) symmetric states. In fact, we note that explicit implementation of the separate U(1) symmetries is essential to guarantee convergence in the correct symmetry sector; when only conserving the total particle number conservation, tunnel events during the DMRG sweeps may nevertheless couple states with varying quantum numbers $\{N_\ell\}$. Thus, explicitly implementing the full mixD symmetry allows us to study the mixD system with arbitrary hole configurations with high precision.

From now on, we use an equal number of holes in each leg, i.e., $N_\ell = N^h$ for all $\ell = 1 \ldots L_y$, and choose $t/J = 3$. The color coded background in Fig. 5.3 (a) shows spin-spin correlations $\langle \hat{S}^z_{\mathbf{i}_0} \hat{S}^z_{\mathbf{j}} \rangle$ with fixed reference site $\mathbf{i}_0$ in the center of the second leg for a system of size $L_x \times L_y = 40 \times 4$ with open (periodic) boundaries along x (y). Grey filled lines depict local hole densities $\langle \hat{n}^h_{\mathbf{i}} \rangle$ in each leg. In the ground state, we see clear indications for the formation of fully filled stripes, by observing (i) a periodic modulation of hole densities, and (ii) the appearance of AFM domain walls at positions of maximum hole density.

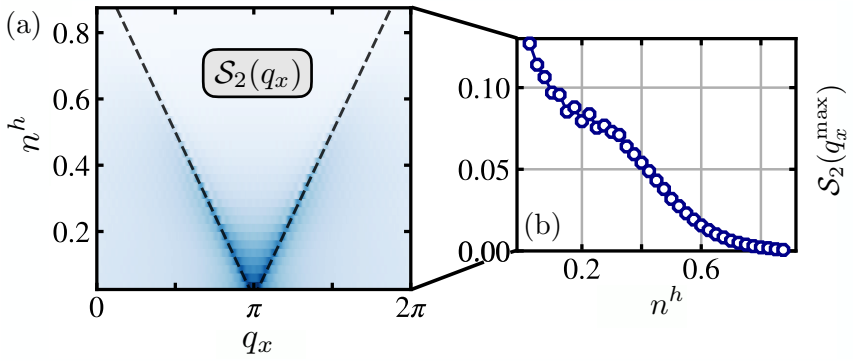

Figure 5.4: **Incommensurate order.** (a) Spin structure factor of the central leg as a function of doping n^h for a 40×3 system. A narrower system size is chosen to keep numerical costs reasonable. Open boundaries are taken to avoid magnetic frustration of the ladder. (b) Peak height $\mathcal{S}_2(q_x^{\max})$ at $q_x^{\max} = (1 - n^h)\pi$ as a function of doping n^h.

The latter is further underlined in Fig. 5.3 (b), where the spin-spin correlations are shown for the central $y = 2$ region. Correlations are observed to be incommensurate with the lattice, i.e., the total number of peaks in the spin-correlation function in each ladder leg—given by $N_p = 18$ in Fig. 5.3 (a)—is incommensurate with the length of the system, $L_x = 40$. This corresponds to a modulation of spin-correlations with wavelength $\lambda = (1 - n^h)^{-1}$, where $n^h = N^h / L_x$. Emerging incommensurate antiferromagnetic order is further revealed in the static spin structure factor along leg y,

$$\mathcal{S}_y(q_x) = \frac{1}{L_x} \sum_{x_1, x_2} \langle \hat{S}^z_{[x_1,y]} \hat{S}^z_{[x_2,y]} \rangle \exp\big[i q_x (x_1 - x_2) \big], \tag{5.2}$$

which features a double-peak structure at points $q_x^{\max} = \pi(1 \pm n^h)$, depicted in Fig. 5.3 (c). When increasing the doping level, incommensurate magnetic order and stripes persist, as shown in Fig. 5.4 (a), where the peak of the structure factor, $q_x^{\max}$ appears consistently at $(1 - n^h)\pi$ (black dashed lines). However, the overall magnetic order decreases due to the enhanced disturbance by the holes, as shown in Fig. 5.4 (b). Beyond $n^h \gtrsim 0.5$, no clear signs of stripe formation are visible anymore.

As we consider quasi-1D systems in our finite-size numerics, the question arises whether the charge-density wave-like correlations capture features of a genuine phase in the thermodynamic limit, or if they arise due to the imposed open boundaries. After all, charge-density wave-like correlations are also expected in purely 1D systems with open boundaries. The oscillation amplitudes of such Friedel oscillations away from the edges decay as r^{-K}, with K the Luttinger exponent [229]. Note that in the 1D t-J model, charge alternations correspond to $2k_F$ oscillations of free chargons—which is why we use the term "Friedel oscillations" also in the context of the mixD system. In order to clarify the difference between 1D and mixD, consider Fig. 5.5, where the hole density in the ground state is shown for (i) a 100×1 t-J model and (ii) a 100×3 mixD t-J system, each with $n^h = 0.2$, i.e., 20 holes (per leg).

In the purely 1D system, Friedel oscillations are expected with density modulations decaying like x^{-K} far away from the boundary, with K the Luttinger parameter of the system. Focusing

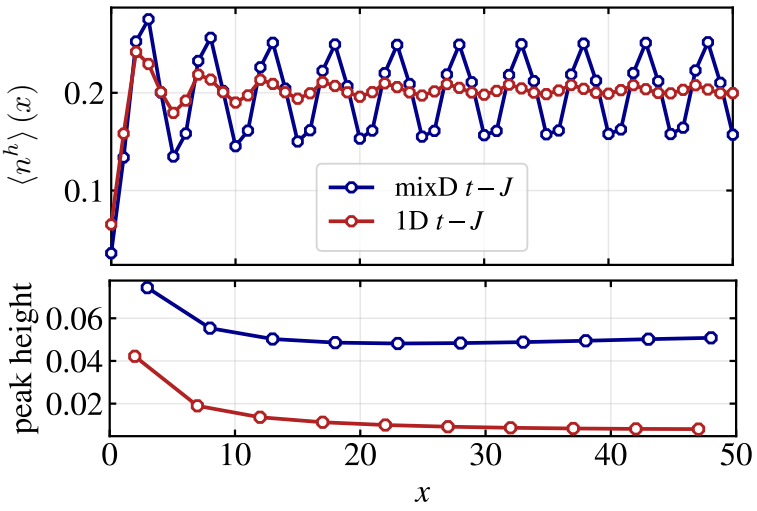

Figure 5.5: **Charge density oscillations in 1D and mixD systems.** The hole density distribution as a function of position x for both a purely 1D t-J system of length 100 (red connected dots) as well as a 100×3 mixD t-J system (blue connected dots). In the mixD system, the mean hole density $\langle \hat{n}^h_{[x,y=2]} \rangle$ of the central leg is shown. Lower panel: charge density oscillation amplitude as a function of peak position x. In the 1D case, the oscillations decay with increasing distance from the boundary, whereas constant amplitudes signal stable charge density order in the mixD setting.

first on the red curve in the upper panel of Fig. 5.5, we observe this typical decay of charge density wave amplitude with increasing distance from the boundary. This is underlined by the lower panel of Fig. 5.5, where we explicitly show the peak height as a function of its position. The decay of charge density wave order in 1D is in stark contrast to the oscillations observed in the stripe phase in the mixD system, where the oscillations are seen to quickly converge towards a finite plateau, see the blue curve in Fig. 5.5. This underlines that, though pinning the charge density order, the boundaries are not responsible for the formation of charge density waves. Instead, the magnetic background and arising linear string potential [230] ultimately lead to the formation of stripes.

To corroborate the stability of the vertical stripes, we now show that in the mixD setting, intraleg hole pairing is heavily suppressed, while stripe formation is in turn strongly favored. We illustrate this by calculating the binding energy of two holes doped into the central leg of $L_y = 4$ cylinders. If $E(N^h)$ corresponds to the ground state energy of the mixD t-J model with N^h holes in the central ladder leg, the binding energy of a hole pair is given by

$$E_b = [E(2) - E(0)] - 2[E(1) - E(0)]. \tag{5.3}$$

Hence, for negative binding energies $E_b < 0$, a bound state is formed between the two holes. By computing the ground state energies $E(0), E(1), E(2)$, we evaluate the binding energy for a 20×4 mixD t-J system with PBC (OBC) in y- (x-) direction, which we find to be $E_b/t \sim -\mathcal{O}(10^{-3})$. In the thermodynamic limit, in fact, we expect the binding energy to exactly vanish, ultimately supporting the absence of pairing in the mixD t-J model.

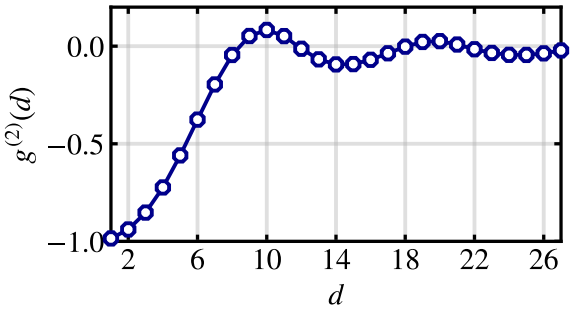

Figure 5.6: **Charge-charge correlations.** The $g_2^{(2)}$ function of holes along a single ladder leg $y = 2$, cf. Eq. (5.4), for the 40×4 system studied in Fig. 5.3 in the main text. Values close to -1 at short short distances $d \gtrsim 1$ signal the strong tendency of holes to repel each other, and instead arrange themselves in stripes – signaled by the peak at $d = 1/n^h = 10$ and the following modulation of $g_2^{(2)}$.

To further underline the suppression of hole pairing, we study the $g_y^{(2)}$ function of the holes along ladder leg y, given by

$$g_y^{(2)}(d) = \left[\frac{1}{L_x - d} \sum_{i=1}^{L_x - d} \frac{\langle \hat{n}_{i+d}^h \hat{n}_i^h \rangle}{\langle \hat{n}_{i+d}^h \rangle \langle \hat{n}_i^h \rangle} \right] - 1. \tag{5.4}$$

Given a hole at position $[i, y]$, the summand evaluates how likely the existence of a hole at site $[i + d, y]$ is. Thus, if $g_y^{(2)}(d)$ is negative, it is less likely to find holes at positions separated by distance d, whereas a positive correlator signals a larger likelihood. Fig. 5.6 shows $g_2^h(d)$ of a 40×4 system. Strong negative values close to the lower bound of $g_y^{(2)}(d)$, i.e., -1, underlines the tendency of holes avoiding each other. Upon increasing the distance, the connected correlator $g_2^{(2)}(d)$ increases, until reaching a maximum at the mean stripe-stripe distance $d = 1/n^h = 10$. Visible modulations for further growing distance d signal the presence of a charge-density wave in the ground state, in accordance to the results presented in Fig. 5.3.

5.2.2 Finite temperature crossover

In order to estimate critical temperatures for stripe formation, we use mixed state purification and imaginary time evolution schemes while conserving the system's symmetries, see Sec. 3.1.5. In order to target our desired subspace also for finite temperature calculations, we need to incorporate the symmetries in the enlarged Hilbert space, i.e. we would like to perform a calculation in the canonical ensemble while conserving the number of charges in each ladder leg.

In particular, during the time evolution we conserve the particle number in each physical leg $N_\ell, \ell = 1..L_y$, as well as the total spin $S^{z,\text{tot}}_{\text{phys.+aux.}}$ (the latter allowing for finite total magnetizations of the physical system at finite temperate). Note that we do not conserve the particle number in each ancilla ladder leg individually[1], but instead conserve only the total particle number in the auxiliary system $N^{\text{tot}}_{\text{aux.}}$. Thus, conserved quantum numbers are

[1] This is, in fact, redundant and merely increases computational costs when sorting the density matrix.

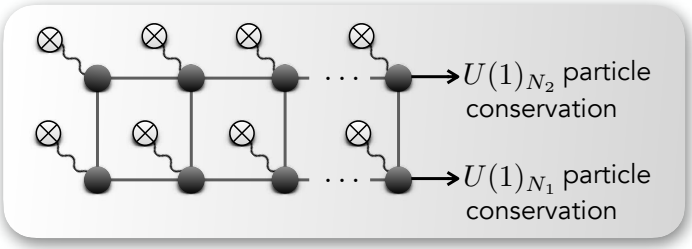

Figure 5.7: **Purification in mixD.** Cartoon of the physical and ancilla system to emulate a thermal bath for finite temperature calculations. Physical sites and bonds are illustrated by grey filled circles and black lines, auxiliary sites and their artificial connection to the physical system are shown by crosses and wavy lines. There exists no physical connection between the two Hilbert spaces, nevertheless ancilla sites can act on physical sites implicitly through their entanglement.

$[N_1, N_2, \ldots, N_{L_y}, N^{\text{tot}}_{\text{aux.}}, S^{z,\text{tot}}_{\text{phys.+aux.}}]$, resulting in $L_y + 2$ conserved quantities. The structure of the system employed in our calculations is depicted in Fig. 5.7.

In the subset of the Hilbert space that fulfils the particle number constraints, the maximally entangled state at infinite temperature reads

$$|\Psi(\beta = 0)\rangle = \prod_{\ell} \hat{\mathcal{P}}_{N_\ell} \bigotimes_{i=0}^{L-1} \left(|0,0\rangle + \sum_{\sigma=\uparrow,\downarrow} |\sigma, \bar{\sigma}\rangle \right). \tag{5.5}$$

Here, ℓ is the physical chain index, $L = L_x L_y$ the total number of physical sites in the ladder system, $\{|0\rangle, |\uparrow\rangle, |\downarrow\rangle\}$ is the single particle basis of the t-J model with $\bar{\uparrow} = \downarrow$, $\bar{\downarrow} = \uparrow$, and $\hat{\mathcal{P}}_{N_\ell}$ is the projector to the subspace with N_ℓ dopants in the ℓ^{th} physical chain; the first and second entries in the kets correspond to physical and auxiliary sites, respectively.

To get the MPS representation of the maximally entangled state, we perform a ground state search of a specifically tailored entangler Hamiltonian, given by

$$\hat{\mathcal{H}}^{\text{ent.}} = -\sum_{y} \sum_{\substack{x<x' \\ x\neq x'}} \Delta^\dagger_{[x,y]} \Delta_{[x',y]} + \text{h.c.}, \tag{5.6}$$

where $\Delta^\dagger_{\mathbf{x}} = \frac{1}{\sqrt{2}} \left(c^\dagger_{\mathbf{x},\uparrow} c^\dagger_{a(\mathbf{x}),\downarrow} - c^\dagger_{\mathbf{x},\downarrow} c^\dagger_{a(\mathbf{x}),\uparrow} \right)$ creates a singlet on site $\mathbf{x} = [x, y]$ paired with its corresponding ancilla site $a(\mathbf{x})$. It is instructive to think of Eq. (5.6) as a tight-binding Hamiltonian of hopping singlets on enlarged sites including both the physical and its auxiliary site, from which it can be proven that the ground state of Hamiltonian Eq. (5.6) is given by Eq. (5.5) (see e.g. [187] for a discussion of the 1D t-J model).

A technical remark: since the entangler Hamiltonian Eq. (5.6) blocks into parts where the physical and ancilla sites are correctly or incorrectly paired in the sense of the maximally entangled ground state, it is important to choose an initial DMRG MPS state that fulfills the pairing for the ground state search of Eq. (5.6) (for example, a site in the state $|0, \uparrow\rangle$ is not paired correctly). A DMRG run will then yield Eq. (5.5) as the ground state, with eigenvalue $-(L_x - N^h)N^h$. For our system sizes and hole dopings, we notice good DMRG convergence, whereby the variational

ground state search results in representations of Eq. (5.5) with typical maximal bond dimensions $\chi_{\max} \sim 100$. We can now employ imaginary time evolution techniques to evolve the state away from $\beta = 0$ towards finite temperatures.

Since the projected product states are of rather low bond dimension, local approximations of the Hamiltonian (and subsequent exponentiation) will suffer from large projection errors and are of low quality, see the discussion in Sec. 3.1.4. Hence, we start by employing global methods to cool the system to moderate temperatures, after which the entanglement in the system (and the bond dimension of the thermal MPS) has sufficiently increased to switch to local methods.

In particular, we start with the global Krylov scheme, where we let the bond dimension expand until $\chi_{\max} = 1024$, after which we switch to the local two-site TDVP method. For the imaginary time evolution, we choose time steps of $\Delta\tau = 0.05$. We fix weight and truncation cutoffs to 10^{-7} and 10^{-8}, respectively, and use an overall maximum bond dimension of $\chi = 10,000$. When reaching $\tau = 2$, we switch to time steps $\Delta\tau = 0.1$. Around the transition into the stripe phase, we choose $\Delta\tau = 0.02$. Using the scheme outlined above, we cool the system down to $\tau = 4$, which lets us evaluate convergence to the ground state—a crucial step to assess the quality of the moderate temperature states where the transition from chargon gas to stripes happens.

Low temperature convergence is illustrated exemplary for a 40×2 system and $N^h = 6$, i.e. $n^h = 0.15$, in Fig. 5.8. Upon cooling the system from the $\beta = 0$ state, the energy $\langle \hat{\mathcal{H}} \rangle_T$ approaches the energy of a ground state DMRG calculation for $\beta \to \infty$, see Fig. 5.8 (a). In Fig. 5.8 (b), the charge density profile $\langle \hat{n}^h_{[x,1]} \rangle_T$ is shown for the lowest temperature $T/J = 1/8$ compared to the ground state results. Good convergence is observed between the $\tau = 4$ and ground state. The same holds for spin-spin correlations, where we show $\langle \hat{S}^z_{[1,1]} \hat{S}^z_{[x,1]} \rangle$ for $T/J = 1/8$ and $T/J = 0$. Again, convergence of ground state and low-temperature purification results is observed. When comparing the density profiles along the two ladder legs, we find that hole densities are indistinguishable for $y = 1, 2$, cf. Fig. 5.8 (d). This underlines good convergence of the two-leg systems.

Upon cooling the ladder, the entanglement of the system grows rapidly, which results in large bond dimensions of the thermal MPS. With weight and truncation cutoffs as introduced above, we reach the maximal value of $\chi = 10,000$ at around $T/J = 1$. From these magnitude of bond dimensions, it is evident that using the $\mathrm{U}(1)$ symmetries in each ladder leg renders an accurate evaluation of the transition from a disordered to a stripe phase significantly more feasible. Furthermore, we note that purification approaches for systems with $L_y > 2$ with the same accuracy is a challenging task. In these cases, using maximally entangled typical thermal states (METTS) might be more advantageous, as demonstrated e.g. in [228]. We note, however, that when aiming to reach temperatures of the order $T/J \sim 1$, the number of needed sampled METTS is expected to drastically increase (i.e., long auto-correlation times are expected), making the intermediate temperature regime particularly challenging.

Before analyzing the finite-temperature transition towards the ordered ground state in more detail, let us look at wider systems. We implement a 30×3 lattice with open boundaries and run the cooling process identically to the ladders, with maximal bond dimension $\chi = 15,000$. We then analyze the density distribution in the low-temperature regime. Fig. 5.8 (e) shows finite

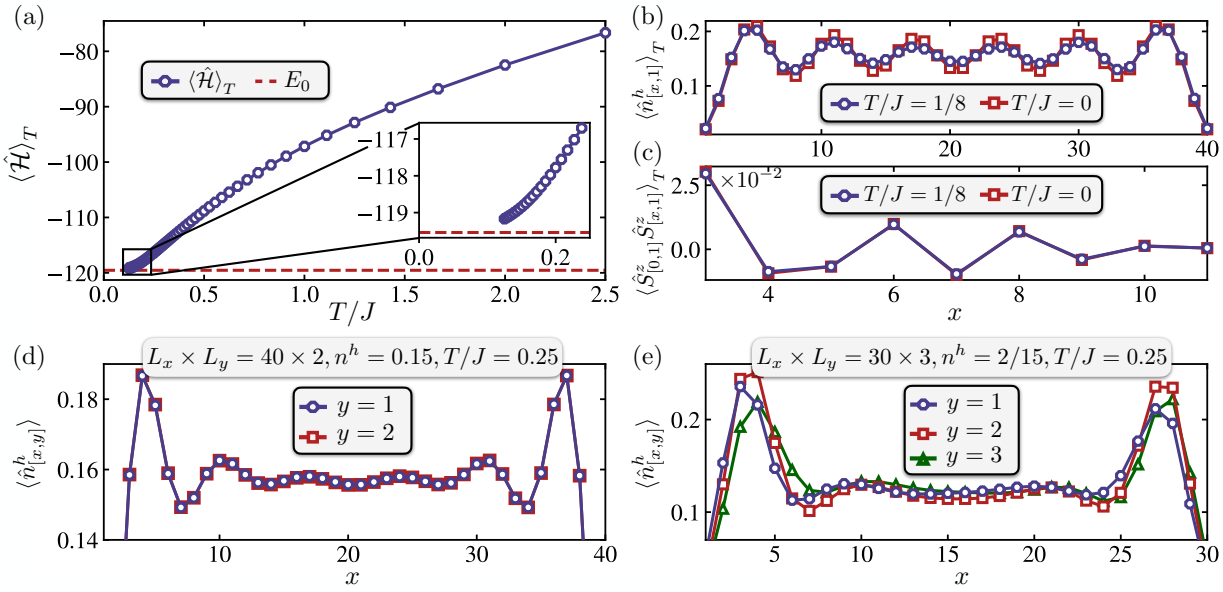

Figure 5.8: **Convergence of finite temperature calculations.** (a) Energy $\langle\hat{\mathcal{H}}\rangle_T$ as a function of temperature T/J for a 40×2 system at hole doping $n^h = 0.15$. $\langle\hat{\mathcal{H}}\rangle_T$ approaches the energy E_0 from a DMRG ground state search (red line) when $T/J \to 0$ for a system with identical parameters. (b) Particle density along the lower leg, i.e., $\langle\hat{n}^h_{[x,1]}\rangle_T$ for temperatures $T/J = 1/8$ (blue dots) and in the ground state $T/J = 0$ (red squares). The density profile converges towards the ground state result for temperatures approaching zero. (c) Spin-spin correlations $\langle\hat{S}^z_{[1,1]}\hat{S}^z_{[x,1]}\rangle$, again for $T/J = 1/8$ (blue dots) and $T/J = 0$ (red squares). Correlations are seen to converge towards the ground state result. (d)&(e) Mean hole density profile $\langle\hat{n}^h_{[x,y]}\rangle_T$ along each ladder leg for a two-leg (d) and three-leg (e) ladder at temperature $T/J = 0.25$. Specifically, the system sizes are $L_x \times L_y = 40 \times 2$ for (d) and $L_x \times L_y = 30 \times 3$ for (e), with hole doping $n^h = 0.15$ and $n^h = 2/15$, respectively. In both cases, boundaries are open (OBC). In the two-leg ladder, results along both $y = 1$ and $y = 2$ are indistinguishable. For the three-leg ladder, charge-density wave patterns are visible, but density distributions are asymmetric. Maximum bond dimensions are 10,000 and 15,000 for (d) and (e), respectively.

temperature expectation values $\langle\hat{n}^h_{[x,y]}\rangle_T$ at hole doping $n^h = 2/15$, i.e., $N^h = 4$, along each ladder leg $y = 1, 2, 3$ at temperature $T/J = 0.25$. Though showing clear signs of charge-density wave features, the resulting hole distributions are not fully converged—leading to asymmetric densities as in Fig. 5.8 (e). In particular, density profiles for $y = 1, 3$ are expected to be identical, but show visible deviations. We have checked that the spin structure factor shows a split peak with maxima at $q_x = (1 - n^h)\pi$ in the three-leg ladder in the stripe regime, but refrain from showing this here.

As we will show in Sec. 5.3, it is possible to reach convergence of wider systems at low doping. For instance, we analyze the formation of a single stripe in a $L_x \times L_y = 8 \times 4$ system in Sec. 5.3. However, when attempting to study the onset of incommensurate order for a variety of doping values, we restrict our considerations in the following to 2-leg ladders.

Detailed results for a 40×2 physical system with open boundary conditions (OBC) are shown in Fig. 5.9. Starting from high temperatures, we measure the static spin structure factor, localize its peak position $\pm q_x^{\max}$ and calculate the peak split parameter defined by $\Delta_T = \mathcal{S}_y(q_x^{\max}) -$

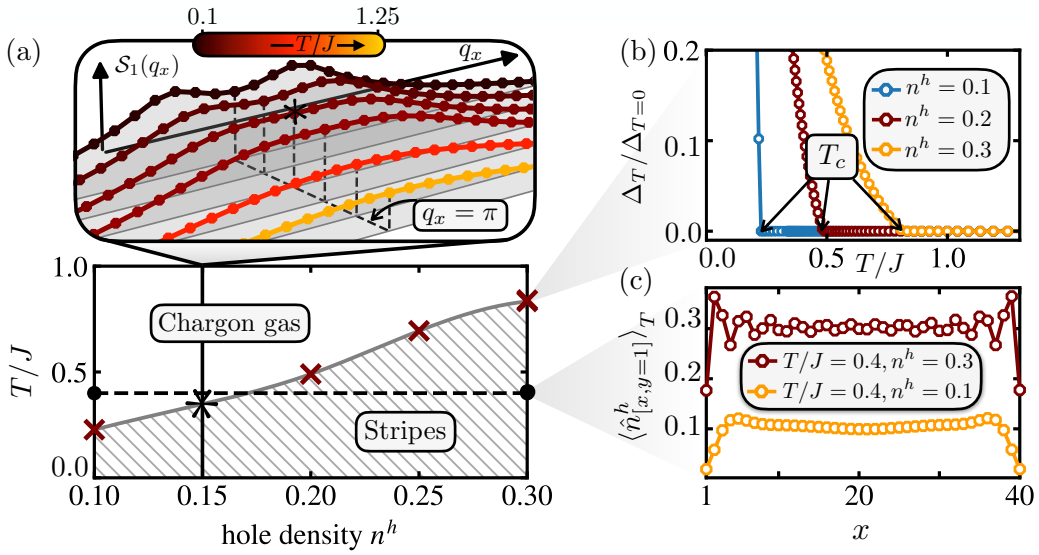

Figure 5.9: **Finite temperature properties.** (a) Lower panel: Phase diagram of the mixD t-J model for a 40×2 system (OBC). In the stripe phase, charge- and spin-density waves are present, whereas in the chargon gas phase holes can move freely and AFM spin correlations are short-range. We define the critical temperature $T_c(n^h)$ as the point where the double peak of the spin structure factor washes out into a single broad peak, illustrated for $n^h = 0.15$ in the upper panel of (a) and marked by an asterisk. Temperatures $T/J = 1.25, 0.83, 0.4, 0.35, 0.25, 0.1$ are shown, ranging from yellow to dark red upon lowering the temperature. (b) Peak split $\Delta_T/\Delta_{T=0}$, with $\Delta_T = S(q_x^{\max}) - S(\pi)$, as a function of temperature. (c) Hole density profiles $\langle \hat{n}^h_{[x,y=1]} \rangle_T$ for $n^h = 0.1, 0.3$ at constant temperature $T/J = 0.4$ (solid dots connected by dashed line in (a)). In the stripe phase, clear charge oscillation signals in the hole density profile are visible, whereas in the chargon gas the profile is flat.

$\mathcal{S}_y(\pi)$. The upper panel of Fig. 5.9 (a) shows the structure factor for various temperatures. At high temperatures, correlations are short-range and in particular commensurate with the lattice, i.e., the structure factor is characterized by a broad peak around $q_x = \pi$ and $\Delta_{T>T_c}$ is strictly zero. Upon lowering the temperature to the critical value T_c, a finite split in the structure factor is observed, i.e., incommensurate magnetic features emerge. The transition point is marked by an asterisk in the upper panel of Fig. 5.9 (a).

Fig. 5.9 (b) underlines the definition of the critical temperature, where the peak split becomes finite, i.e., $\Delta_{T<T_c} > 0$. The corresponding critical temperatures as a function of hole doping are plotted in the lower panel of Fig. 5.9 (a), for hole densities ranging from $n^h = 0.1...0.3$. Note how critical temperatures are of the order of magnitude $\sim J/2$, rendering the stripe phase significantly more robust against thermal fluctuations in the mixD setting compared to its analog in 2D [144, 228].

We illustrate the emergence of stripes further by showing the average hole density profile for two different doping levels while keeping the temperature constant, Fig. 5.9 (c). For $T/J = 0.4$ and $n^h = 0.1$, the hole density forms a flat plateau, i.e. there is no charge order and holes are in a deconfined chargon gas phase (i.e. holes are not confined within stripes and move freely through the magnetic background) [230]. In contrast, clear charge oscillations are visible for

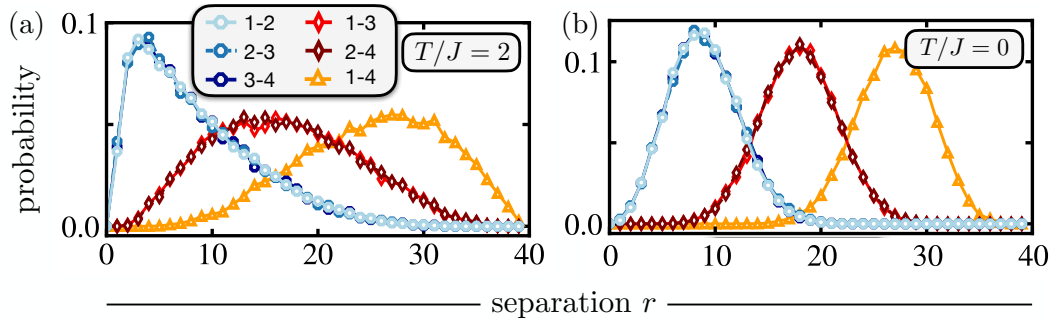

Figure 5.10: **Full counting statistics.** (a) Full counting statistics of hole distances along a single ladder leg for $n^h = 0.1$ and $T/J = 2$ and $T/J = 0$. The notation i-j corresponds to the distance r between hole i and hole j along x. In the stripe phase (b), the probability distributions are symmetric, whereas in the chargon gas (a), hole-hole distance probability distributions acquire long tails. We use 20,000 snapshots of the (thermal) MPS.

$n^h = 0.3$, underlining how in the stripe phase both charge and spin density waves are present. By computing the charge structure factor, we have checked that charge order is present over the whole range of temperatures $T < T_c(n^h)$, in fact setting in at slightly higher temperatures than incommensurate magnetic order. This is characteristic for a crossover driven by the charges [231, 232], as is the case for the chargon gas to stripe transition observed here.

Note that the Néel temperature of the SU(2) symmetric 2D Heisenberg model is strictly zero, however with a magnetic correlation length scaling as $\sim e^{T_0/T}$. Akin to the cold atom antiferromagnet realized in [41], we argue that stripe features—that is, the emergence of charge- and spin-density wave patterns—become visible on the length scale of the system size for temperatures below T_c. For sufficiently strong magnetic correlations, we expect that true long-range charge order (breaking the discrete translational symmetry of the system) is stabilized at finite temperatures also in the thermodynamic limit $L_x, L_y \to \infty$.

5.2.3 Snapshots and hidden correlations

In quantum gas microscopy experiments, projective measurements are taken in the Fock basis of the many-body state. These snapshots contain a plethora of information about the system beyond averages and local observables, allowing for further insights into the quantum many-body wave function. Using (thermal) matrix product states, we sample independent snapshots via the perfect sampling approach [233, 234].

First, let us analyze the stripe-chargon gas crossover by full counting statistics of hole-hole distances within a single ladder leg. In particular, for each snapshot, we start from one side of the system and count the distance from the i'th to the j'th hole. We then collect these distances for many snapshots and approximate corresponding probability distributions, presented in Fig. 5.10. In the stripe phase, probability distributions for hole-hole distances are symmetrically peaked around a maximal distance probability, Fig. 5.10 (b). On the other hand, in the chargon gas phase, Fig. 5.10 (a), the discrete probability distributions develop long tails, i.e., mean and maximum are far separated from another. These kind of rare event distributions of-

ten govern the physics of the system [235], here indicating a phase of freely moving, deconfined holes through the magnetic background.

As a direct consequence of the restricted charge motion to 1D, spins can be relabeled by the new positions they have after moving all holes to the right in each chain—resulting in a distinct definition of squeezed space, a concept originally formulated in 1D settings [236, 237]. This is illustrated explicitly in Fig. 5.11 (a). After removing the holes from snapshots, spins are shuffled around, and can be relabeled as spins living in squeezed space. As this concept will repeatedly appear throughout this thesis, we will in the following define it more formally in the mixD setting, see also Refs. [230, 238].

Squeezed space in mixD

Consider a Fock state

$$\bigotimes_y |\sigma_{[1,y]}, \sigma_{[2,y]}, \ldots, \sigma_{[L_x,y]}\rangle ,$$

where $\sigma_{x,y} \in \{0, \uparrow, \downarrow\}$ is the single particle basis of the t-J model. These local spin charge configurations are relabeled upon squeezing, whereby each Fock state is now given by

$$\bigotimes_y |\tilde{\sigma}_{[\tilde{1},y]}, \sigma_{[\tilde{2},y]}, \ldots, \sigma_{[\tilde{L}_x,y]}\rangle \otimes \hat{h}^\dagger_{[x_1,y]} \ldots \hat{h}^\dagger_{[x_{N_y},y]} |0\rangle .$$

Here, $\tilde{\sigma}_{[\tilde{x},y]} = \uparrow, \downarrow$ (but note that $\tilde{\sigma}_{[\tilde{x},y]} \neq 0$) denotes spins on the squeezed lattice $\tilde{x} = 1, \ldots, L_x - N_y$, where N_y is the number of holes in rung y, and $\hat{h}_{[x,y]}$ creates a hard core fermionic chargon at site $\mathbf{i} = [x, y]$. By squeezing the spins out, spins on the squeezed and real space lattice relate as

$$\tilde{\sigma}(\tilde{x}, y) = \sigma(\tilde{x} + \sum_{j<\tilde{x}} n^h_{[j,y]}, y),$$

where $n^h_{[x,y]}$ refers to the number of chargons at real space lattice site $[x, y]$. The process is illustrated in Fig. 5.11 (a). Spatially separating occupied and unoccupied sites by squeezing allows to analyze the interplay between hole motion and magnetism in more detail, explicitly utilizing non-local information contained in snapshots of the many-body wave function.

Fig. 5.11 (b) shows the spin structure factor along $y = 1$ of a 40×2 mixD t-J model in the ground state (i.e., in the stripe phase) in real (black circles) and squeezed (red squares) space after removing holes from the snapshots. When transforming ground state snapshots to squeezed space, hidden AFM correlations are revealed, i.e., the double peak structure turns into a sharp peak around $q_x = \pi$. Indeed, when comparing to the pure Heisenberg model[2] with $J = 1$, both structure factors agree on a quantitative level, showing how the holes confined within the stripes

[2] We compare the magnetic mixD system in squeezed space with the Heisenberg model, given by the Hamiltonian

$$\hat{\mathcal{H}} = J \sum_{\langle \mathbf{i},\mathbf{j} \rangle} \hat{\mathbf{S}}_\mathbf{i} \cdot \hat{\mathbf{S}}_\mathbf{j},$$

where J is the magnetic coupling constant and $\langle \mathbf{i}, \mathbf{j} \rangle$ denotes nearest-neighbour pairs on a square lattice.

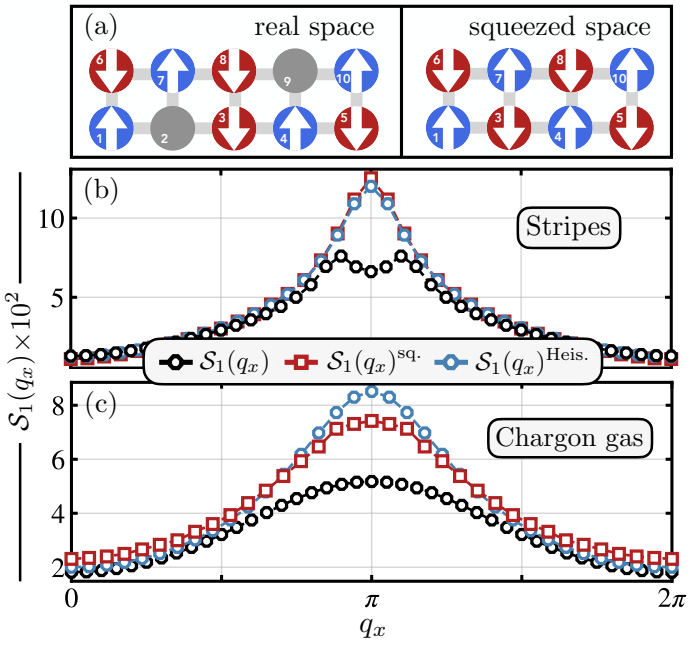

Figure 5.11: **Correlations in real and squeezed space.** (a) Illustration of squeezed space. Left panel: Snapshot of holes moving through a Néel background. Right panel: Upon squeezing out the holes, Néel order is restored in the magnetic background. (b) Spin structure factor $\mathcal{S}_1(q_x)$ for a mixD t-J system in the striped ground state with $n^h = 0.1$, featuring a double peak structure in real space (black circles). Squeezing snapshots reveals hidden AFM correlations (red squares), being in quantitative agreement with the $J = 1$ Heisenberg ground state (blue circles). (c) The same for the chargon gas phase at $T/J = 5/7 \approx 0.71$, $n^h = 0.15$. Upon squeezing, the peak around $q_x = \pi$ becomes considerably sharper. Compared to the pure Heisenberg model with $J = 1$ and $T/J = 5/7 \approx 0.71$ (light blue circles), the spin structure in the chargon gas phase has a shifted weight towards FM correlations. For both cases above, the mixD system is of size 40×2.

leave the underlying magnetic state in squeezed space almost undisturbed.

In the chargon gas phase, on the other hand, the movement of the holes distorts the magnetic background in a more notable manner. Black circles in Fig. 5.11 (c) show $\mathcal{S}_1(q_x)$ evaluated via the thermal MPS at $T/J = 5/7 \approx 0.71$. When transforming snapshots to squeezed space, the initially broad peak around $q_x = \pi$ again becomes significantly sharper, showing how AFM correlations are reduced due to the holes' motion through the Mott insulator. Compared to the Heisenberg model with $J = 1$ at $T/J = 5/7 \approx 0.71$ (blue circles in Fig. 5.11 (c)), the squeezed mixD system has shifted weight from AFM ($q_x = \pi$) to more FM ($q_x = 0, 2\pi$) correlations. Enhanced FM signals in squeezed space emerge due to the frustrating effect of hole motion on spins in squeezed space, whereby the hole motion induces effective longer-range couplings between spins in squeezed space. We will not go into more depth of hole-motion-induced frustration at this point, and point to Chap. 6, where it will be analyzed in detail using Hamiltonian reconstruction schemes. Now, we will proceed to discuss and analyze experimental results from a Fermi-Hubbard quantum simulator, which implements the mixD setting at intermediate temperatures where individual stripes can be seen to form.

5.3 Stripe formation in cold atom simulators

Our insights from Sec. 5.2 strongly motivate the exploration of stripe phases in ultracold atom experiments. Here, the mixD setup can be realized by simulating the Fermi-Hubbard model in the large U/t limit with a y-directed on-site potential tilt Δ, i.e., $V_{\text{tilt}}(y) = \Delta y$.

The potential gradient Δ here effectively suppresses resonant tunneling along y, which results in freezing the projected density on the y-axis. On the other hand, virtual particle exchanges (and hence spin superexchange) remain intact—hence realizing the mixD t-J setting. In particular, if $\tilde{t}_x$, $\tilde{t}_y$ denote parallel (along x) and perpendicular (along y) hopping parameters in the simulated FH model, standard perturbation theory in the limit $\tilde{t}_x, \tilde{t}_y \ll U$ yields effective spin couplings (see also Refs. [239–241]),

$$J_y = \sum_{\pm} \frac{2\tilde{t}_y^2}{U \pm \Delta}, \quad J_x = \frac{4\tilde{t}_x^2}{U}. \tag{5.7}$$

Pictorially, this becomes clear when considering a single double well, as illustrated in Fig. 5.12 (a) and (c). Note that this tunability can even result in ferromagnetic couplings for $\Delta > U$, and diverges when $|U| = |\Delta|$. Using Eq. (5.7), the ratio J_y/J_x reads

$$\frac{J_y}{J_x} = \left(\frac{\tilde{t}_y}{\tilde{t}_x}\right)^2 \frac{U^2}{U^2 - \Delta^2}. \tag{5.8}$$

For $\tilde{t}_y < \Delta < U$, tunneling along the perpendicular direction in the effective t-J model is suppressed, $t_y = 0$, while parallel hopping remains approximately unchanged, i.e., $t_x = t = \tilde{t}_x$.

Let us illustrate the above arguments through a 1D example, Fig. 5.12. We simulate the time dynamics of a 1D Fermi-Hubbard model using exact diagonalization with a single hole and half-filled sites elsewhere, in the strong repulsive regime, and with varying potential tilts. Specifically, we initialize a system with eight sites in the product state $|\uparrow\downarrow\uparrow\downarrow \circ \uparrow\downarrow\uparrow\rangle$ and focus on the time evolution of the particle occupation $\sum_\sigma \langle \hat{n}^\sigma_\circ \rangle (t)$ of the initially empty site. As the potential gradient Δ increases, the density profile rapidly freezes to the initial configuration, whereas in the $\Delta = 0$ limit, the hole delocalizes on very short time scales. This demonstrates that applying tilts suppresses resonant tunneling in the y-direction on intermediate to large time scales, thereby stabilizing the mixD setup in this meta-stable state.

In this section, we discuss experimental results obtained in collaboration with the Lithium team at MPQ, lead by Dominik Bourgund, Immanuel Bloch, and Timon A. Hilker. We begin by describing the experimental setup, where the engineering of superlattices results in an effective suppression of vertical hopping events, realizing the mixD setting. We then describe how the effective temperature of the experiment is estimated by comparing spin correlations to MPS calculations, followed by a discussion of various observables that indicate the formation of individual, fluctuating stripes in the system. One of the major advantages of quantum simulators is their ability to access a vast array of observables that are entirely inaccessible in solid-state experiments. To this end, we analyze stripe length distributions from many-body snapshots and compare these results to mean-field theories of single, fluctuating stripes.

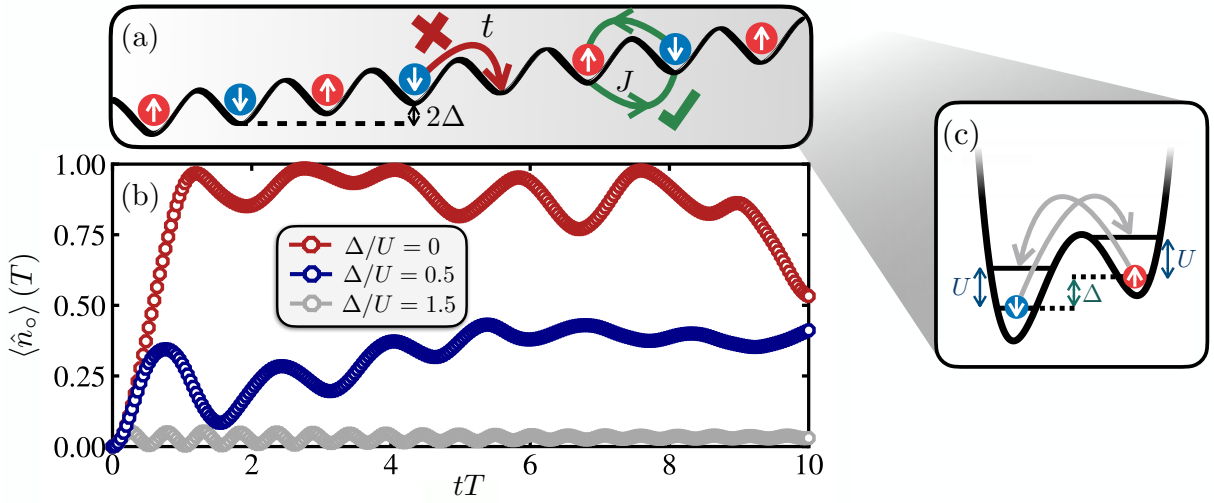

Figure 5.12: **Realizing the mixD setting through potential gradients.** (a) Schematic of the space directed tilt procedure (indicated by the slope and gradient background), here shown for a 1D Fermi-Hubbard model in the Mott insulating regime $U/t \gg 1$. While virtual spin exchanges still take place, hopping of spins/holes is suppressed. (b) Time evolution after initializing an eight-site system as shown in (a). Here, $U/t = 8$, and Δ/U (Δ/t) is varied to values $0, 0.5, 1.5$ $(0, 4, 12)$. For strong tilts, e.g. $\Delta/U = 1.5$, the density profile is locked in space for exponentially long times, whereas quick delocalization of the hole takes place for both $\Delta/U = 0, 0.5$. (c) While hopping along the field gradient is suppressed, the super-exchange mechanism is intact. In particular, perturbation theory yields the expressions in Eq. (5.7).

5.3.1 Experimental setup

One way to experimentally implement the spin-independent energy tilt Δ is by imprinting it on the system through DMDs, as demonstrated for ladder systems in Ref. [57]. In the following realization of a (single layer) 2D mixD system at MPQ as described by Eq. (5.1), instead of implementing an overall energy shift, a superlattice is utilized instead. This is depicted in Fig. 5.13. While the lattice in the y-direction is uniform in the 2D setup (Fig. 5.13 (a)), utilizing a second laser in the y-direction and carefully calibrating its phase[3] creates the configuration shown in Fig. 5.13 (b). In this configuration, neighboring sites always have an energy difference of $\pm\Delta$, realizing the mixD setup on intermediate time scales. In the following, we will work with $\Delta/U = 0.65(5)$ in the experiment.

While nearest-neighbor (NN) hopping is suppressed ($t_y \approx 0$), next-nearest-neighbor (NNN) hopping $t_y^{(2)}$ along y remains resonant and finite. The bare NNN tunneling $\tilde{t}_y^{(2)} \approx 0$ in the optical lattice can be neglected, so the NNN contribution from resonant tunneling is given by the second-order process,

$$t_y^{(2)} = \frac{\tilde{t}_y^2}{\Delta} \approx 1.54 \frac{\tilde{t}_y^2}{U}. \tag{5.9}$$

This NNN term introduces a Pauli-repulsion between NNN legs, which may destabilize fully

[3] This is achieved by loading atoms into decoupled double wells along the y-direction. By varying the phase between the lattice and the superlattice and measuring the imbalance of atoms on the two sides of the double well, precise offset calibration can be performed [197].

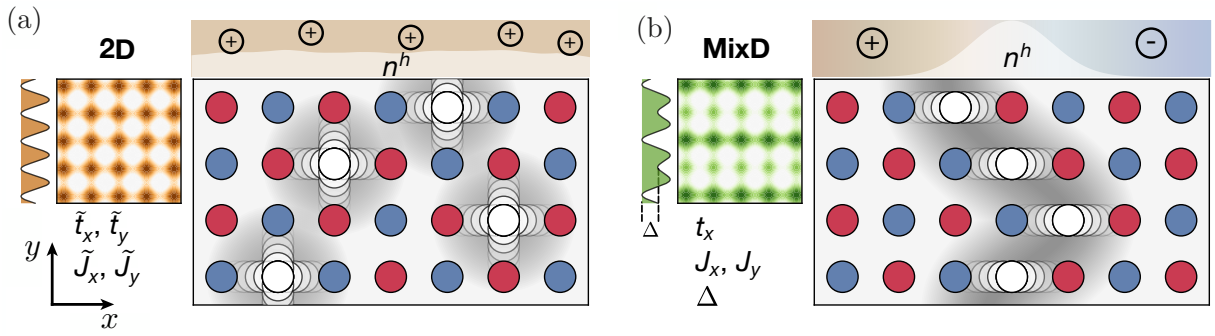

Figure 5.13: **Implementing the mixD FH model with ultracold atoms.** (a) Schematic illustration of the isotropic 2D Fermi-Hubbard model. Holes delocalize and disturb the surrounding spin background, forming magnetic polarons at intermediate temperatures. The overall hole density remains uniform, and holes repel each other due to their fermionic statistics at experimentally accessible temperatures of $T \lesssim J$. At very low temperatures, however, stripe order becomes energetically favored. (b) By increasing the potential on every other lattice site along the y-direction by Δ, nearest-neighbor tunneling along this direction is suppressed while preserving the superexchange coupling J_y. In this configuration, holes form stripe structures at significantly higher temperatures, as indicated by the enhanced hole density at specific positions and the alternating antiferromagnetic parity across the stripe ($\oplus$ and $\ominus$ symbols). Figure adapted from Ref. [2].

filled stripes and favor other filling fractions. In the experiment, however, $J_y \approx 6.9\tilde{t}_y^2/U$, so

$$J_y/t_y^{(2)} \approx 4.5. \tag{5.10}$$

Thus, the effect of $t_y^{(2)}$ is negligible compared to the effect of J_y, which provides the binding glue for stripe structures. In the limit of strong interactions, the ultracold atom setup in the optical superlattice hence realizes the Hamiltonian

$$\begin{aligned}\hat{\mathcal{H}} = -t_x \sum_{\sigma,\langle \mathbf{i},\mathbf{j}\rangle_x} \hat{\mathcal{P}}_{GW}\left(\hat{c}^\dagger_{\mathbf{i},\sigma}\hat{c}_{\mathbf{j},\sigma} + \text{h.c.}\right)\hat{\mathcal{P}}_{GW} + J_x \sum_{\langle \mathbf{i},\mathbf{j}\rangle_x}\left(\hat{\mathbf{S}}_\mathbf{i}\cdot\hat{\mathbf{S}}_\mathbf{j} - \frac{\hat{n}_\mathbf{i}\hat{n}_\mathbf{j}}{4}\right) \\ + J_y \sum_{\langle \mathbf{i},\mathbf{j}\rangle_y}\left(\hat{\mathbf{S}}_\mathbf{i}\cdot\hat{\mathbf{S}}_\mathbf{j} - \frac{\hat{n}_\mathbf{i}\hat{n}_\mathbf{j}}{4}\right).\end{aligned} \tag{5.11}$$

Through a DMD, a flat-energy landscape is imprinted on the optical lattice, which is surrounded by a low-density reservoir at higher energies. The resulting physical system has ≈ 110 sites, illustrated in Fig. 5.14. For imaging, charge pumping methods are used to Zeeman split the two hyperfine $m_F = \pm 1/2$ states and image them separately, as discussed in Sec. 4.1. The parameters of Eq. (5.11) in the experiment read

$$\frac{U}{t_x} = 27(2), \quad \frac{J_y}{t_x} = 0.6(2), \quad \frac{J_x}{t_x} = 0.15(3). \tag{5.12}$$

For comparisons with numerical data, we simulate the system Eq. (5.11) with parameters Eq. (5.12) at finite temperature using imaginary time evolution as described in Sec. 5.2.2. For

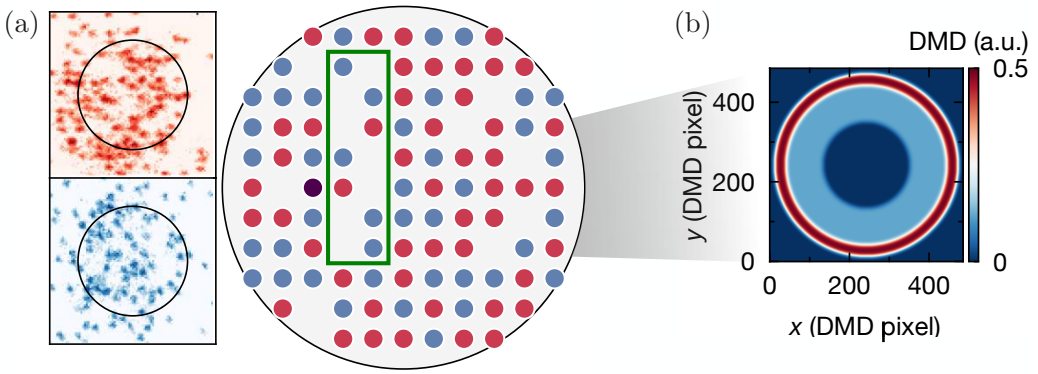

Figure 5.14: **Experimental system and snapshot.** (a) Spin-resolved sample snapshot of the mixD system in the ^{6}Li experiment at MPQ. The left-hand side are images directly from the CCD camera for both layers, the right is the corresponding reconstruction (the purple site corresponds to a doubly occupied site). (b) The potential imprinted by the DMD, generating a flat potential landscape in the center inside a box potential. Outside the box potential, a low-density particle reservoir exists. Figure adapted from Ref. [2].

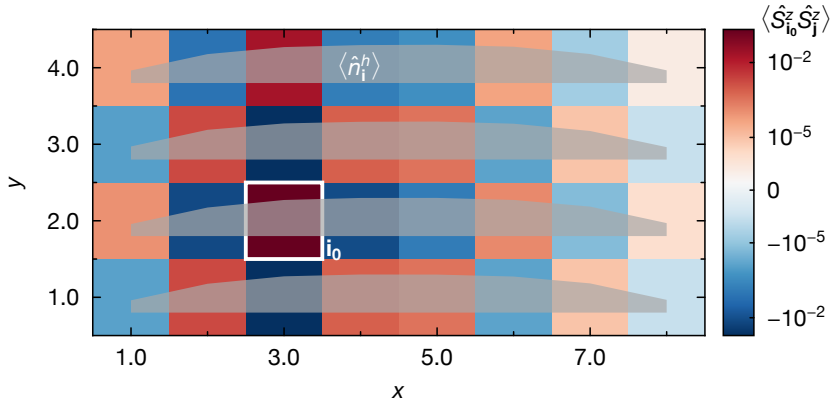

Figure 5.15: **Finite temperature numerics.** DMRG calculations for a $L_x \times L_y = 8 \times 4$ system with periodic boundaries along the short direction, temperature $T/t_x \sim 0.4$, and Hamiltonian parameters as in the experimental setup. Shown are the on-site hole density distributions in each leg, $\langle \hat{n}^h_{\mathbf{i}} \rangle$ (grey lines), as well as spin-spin correlations $\langle \hat{S}^z_{\mathbf{i}_0} \hat{S}^z_{\mathbf{j}} \rangle$ (colour coded) for reference site $\mathbf{i}_0 = [x = 3, y = 2]$ (white frame). At the maximum hole density distribution in the center of the chain, a domain wall of the AFM background forms, i.e., a single stripe is observed.

doping scans, we limit the system size to $L_x \times L_y = 8 \times 3$ with open boundaries, and hole configurations $N_\ell = 1, 2, 3$ for each $\ell = 1, 2, 3$. For a single hole per chain, we simulate systems up to $L_y = 4$. We here stress again that, as this mixD model suffers from the Fermion sign problem, these limited system sizes at finite temperature are state-of-the-art for numerical calculations; they thus mostly allow for general qualitative comparison to the much larger experimental system.

We follow the same purification scheme in our mixD setting as in Sec. 5.2.2. In particular, we start by evolving the infinite-temperature state $|\Psi(\beta = 0)\rangle$ using global Krylov schemes by a single step $t_x \Delta\tau = 0.01$. Weight cutoffs are set to 10^{-10}, expanding the bond dimension to $\chi(\tau = \Delta\tau) \sim \mathcal{O}(1000)$. From here on, we switch to the local two-site TDVP method, with

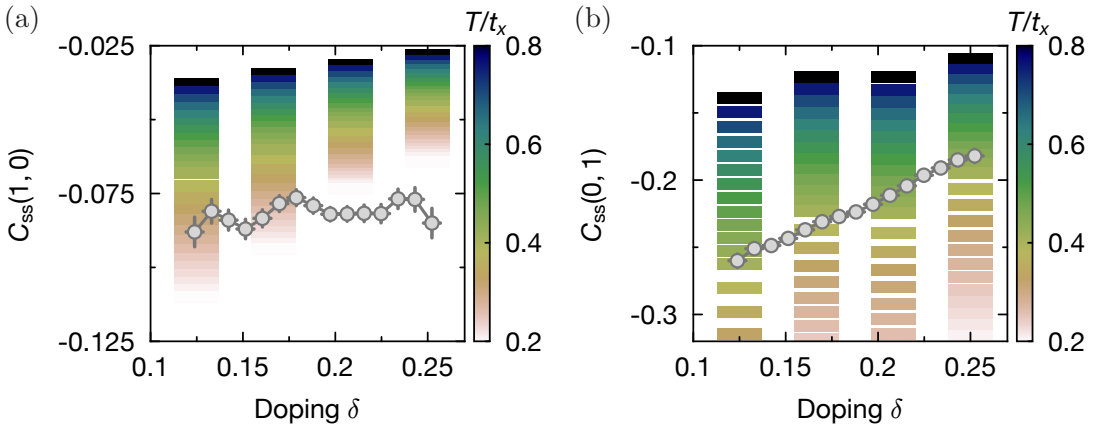

Figure 5.16: **Thermometry.** Nearest-neighbor spin correlations along x (a) and y (b) for different doping levels. The experimental data (grey markers) are compared to numerical data for $C_{ss}(1,0)$ and $C_{ss}(0,1)$ at various temperatures obtained from simulations on $L_x, L_y = 8, 3$ (colorbar). This provides an estimate for the effective temperature of the experiment. Figure adapted from Ref. [2].

time steps of $t_x \Delta\tau = 0.03$, weight and truncation cutoffs of 10^{-10} and 10^{-12}, respectively, and cutting edge maximum bond dimensions of $\chi_{\text{TDVP}} = 30000$. We evolve the system to $\tau t_x = 2.0$, corresponding to a temperature of $T/t_x = 0.25$.

As an example, we show spin-spin correlations as well as hole distributions in each leg in Fig. 5.15, for $T/t_x \sim 0.4$ and for a system of size $L_x \times L_y = 8 \times 4$ with periodic boundaries along the short direction and $N_\ell = 1$ for all $\ell = 1 \ldots 4$. At the center of the chains, where the hole density peaks, an AFM domain wall forms, signalling the formation of a single, fully filled stripe at experimentally accessible temperatures.

Thermometry

Before discussing experimental and theoretical results in detail, let us first focus how the effective temperature of the experiment is estimated. To this end, we compare spin-spin correlations obtained from DMRG calculations at varying temperatures and doping levels, down to $T/t_x = 0.25$. Since we aim to resolve correlations as a function of doping, we use the $L_y = 3$ data. However, we have verified for $\delta = 0.125$ that the temperature estimations below are not significantly influenced by the finite-size effects of the DMRG calculations.

We estimate the system's temperature using the connected spin correlations,

$$C_{ss}(\mathbf{d}) = \frac{1}{\mathcal{N}_\mathbf{d}} \sum_\mathbf{i} \frac{\langle \hat{S}^z_\mathbf{i} \hat{S}^z_{\mathbf{i}+\mathbf{d}} \rangle - \langle \hat{S}^z_\mathbf{i} \rangle \langle \hat{S}^z_{\mathbf{i}+\mathbf{d}} \rangle}{\sigma(\hat{S}^z_\mathbf{i}) \sigma(\hat{S}^z_{\mathbf{i}+\mathbf{d}})}, \tag{5.13}$$

where $\mathcal{N}_\mathbf{d}$ is a proper normalization, i.e., the number of bonds with distance $\mathbf{d}$ in the system, and $\sigma(\hat{S}^z_\mathbf{i})$ is the standard deviation of the spin projection at site $\mathbf{i}$. We evaluate $C_{ss}(\mathbf{d})$ as a function of doping, and compare this to matrix product state (MPS) calculations in Fig. 5.16. We fit the experimental data for individual doping bins to the numerical data to extract the corresponding temperatures. To this end, we simulate systems with varying number of holes per leg, such that

we can access a finer doping grid. Since the short y-direction may exhibit finite-size effects in the DMRG calculations, we independently determine the temperatures along x and y. By extracting temperatures per doping level, we estimate an effective temperature of $T/t_x \approx 0.3(1)$ along x and $T/t_x \approx 0.4(1)$ along y.

5.3.2 Formation of stripes

To test and study microscopically the formation of extended stripe-like structures, we will look at both charge and spin sectors. This in particular includes charge-charge correlations for the former and spin-charge correlations for the latter. We will see that extended hole like structures can be identified, which as we will see can be captured in mean-field-like descriptions of holes bound to an individual stripe.

Charge sector

We analyze tendencies for charge ordering by evaluating the connected, normalized two-point hole-hole correlator, defined as

$$g^{(2)}_{\mathrm{hh}}(\mathbf{d}) - 1 = \frac{1}{\mathcal{N}_{\mathbf{d}}} \sum_{\mathbf{i}} \left(\frac{\langle \hat{n}^h_{\mathbf{i}} \hat{n}^h_{\mathbf{i}+\mathbf{d}} \rangle}{\langle \hat{n}^h_{\mathbf{i}} \rangle \langle \hat{n}^h_{\mathbf{i}+\mathbf{d}} \rangle} - 1 \right), \tag{5.14}$$

where $\hat{n}^h_{\mathbf{i}}$ is the hole density operator at position $\mathbf{i}$, and the normalization factor $\mathcal{N}_{\mathbf{d}}$ corresponds to the number of bonds with distance $\mathbf{d}$. In the experiment, a global, doping-dependent offset is corrected in Eq. (5.14), as discussed in more detail in Ref. [2].

The hole correlation map for doping $\delta = 0.18$ is shown in Fig. 5.17 (a). Following the directions $(d_x, 0)$ and $(0, d_y)$, we observe clear positive signals along y, while along x anti-bunching is visible due to Pauli repulsion. This observation is corroborated in Fig. 5.18, where correlations along the two cuts $(d_x, 0)$ and $(0, d_y)$ are explicitly shown. Notably, correlations along y remain positive for extended regions well beyond $d_y = 1$, suggesting the formation of vertically aligned hole structures. In contrast, in the 2D system (which was implemented with similar parameters as in the mixD setting for comparison in the experiment), both directions show clear negative signals due to Pauli anti-bunching. The positive correlations in the mixD setting indeed appear to form vertical fans in Fig. 5.17 (a), which we interpret as signs of charge fluctuations along x in weakly bound stripes. Additionally, the positive signals observed at $d_x = \pm 5$ may indicate the formation of a second, vertically aligned stripe-like hole structure.

We compare this correlation map to DMRG theory calculations for a system of size $L_x \times L_y = 8 \times 3$, with a single hole doped into each leg. When comparing the absolute values of hole-hole correlations to simulations, care must be taken due to differences in doping, fluctuations, and boundary conditions. For $L_y = 3$, all calculations are performed with open boundary conditions along x and y to avoid frustrating spin couplings on a cylinder. In contrast, the finite width of the potential at the experimental edges causes charge features to fluctuate and wash out. Consequently, in the experiment we observe signals in $g^{(2)}_{\mathrm{hh}}(\mathbf{d})$ but not in the density, unlike in theory where stripes appear prominently as density features. Using connected correlators on theoreti-

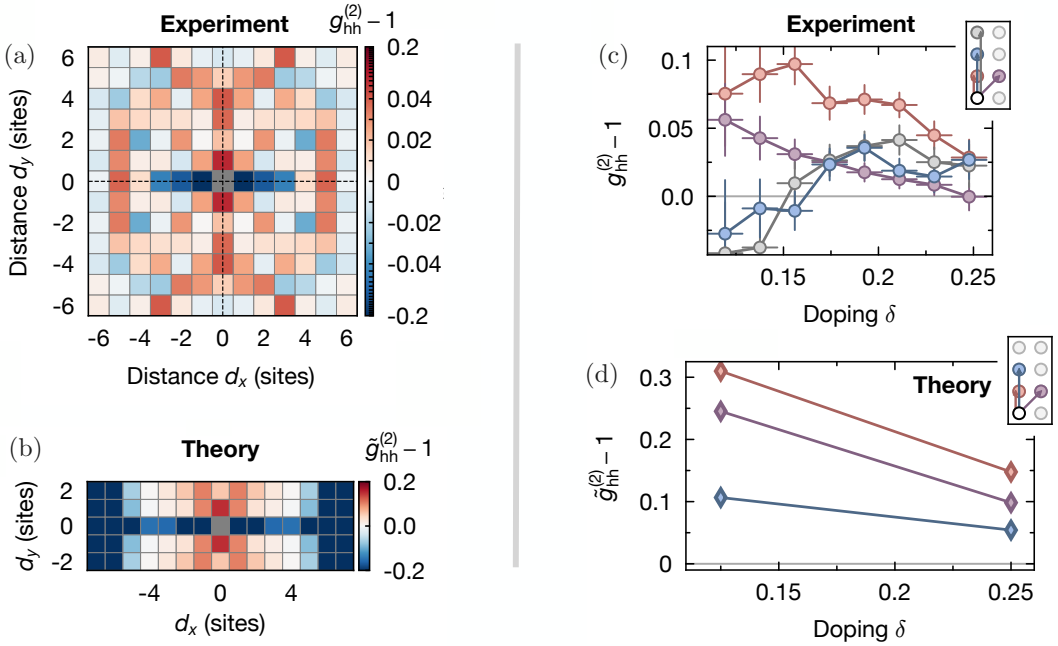

Figure 5.17: **Charge correlations.** (a) Hole-hole correlation map $g^{(2)}_{\mathrm{hh}}(\mathbf{d})$ as a function of $\mathbf{d}$ in the experiment, post selected on dopings $\delta = 0.18$. Clear anti-bunching is visible in the x-direction, whereas positive signals are observed in a vertical fan centered around $(0, d_y)$. The latter indicates the formation of extended hole structures, forming a fluctuating stripe. Correlation maps are symmetrized around the $(d_x, 0)$ and $(0, d_y)$ cuts, indicated by the black dashed lines. (b) Hole-hole correlations obtained from MPS calculations, in a $L_x \times L_y = 8 \times 3$ system with a single hole per leg, i.e., $\delta = 0.125$. Signatures are very similar to the experiment, with negative signals along x and an extended positive vertical region. Boundary effects lead to negative signals for $|d_y| > 6$. (c) Doping dependence of $g^{(2)}_{\mathrm{hh}}$ for several $\mathbf{d}$, see the inset. In a doping region $\delta \gtrsim 0.15$, all vertically aligned correlations are positive. The reduction of NN correlations is compatible with a reduction of spin-spin correlations with increasing doping, which is responsible for hole bunching. (d) Theory calculations show consistent behavior, though the observed sign change of $(0, 2)$ is not captured. The two data points per correlator correspond to $N_\ell = 1, 2$, i.e., one and two holes per leg in the 8×3 system. Figure adapted from Ref. [2].

cal data reduces the correlations accordingly.

To analyze numerical results, we thus employ a slightly modified correlator $\tilde{g}^{(2)}_{\mathrm{hh}}(\mathbf{d})$, defined as

$$\tilde{g}^{(2)}_{\mathrm{hh}}(\mathbf{d}) - 1 = \frac{1}{\mathcal{N}_{\mathbf{d}}} \sum_{\mathbf{i}} \left(\frac{\langle \hat{n}^h_{\mathbf{i}} \hat{n}^h_{\mathbf{i}+\mathbf{d}} \rangle}{n^h n^h} - 1 \right), \tag{5.15}$$

where, compared to Eq. (5.14), the normalization uses the *global* doping level n^h instead of the *local* densities. This approach assumes a homogeneous density distribution across the system, facilitating a more direct comparison with the experimental results. The resulting correlation map is shown in Fig. 5.17 (b). The experimental observations qualitatively match the theoretical hole-hole correlations well, though the theory calculations are heavily limited by their small width. Strong negative signals for $|d_y| \geq 6$ arise from the open boundaries.

By binning the experimental snapshots according to their hole-doping, we can further study

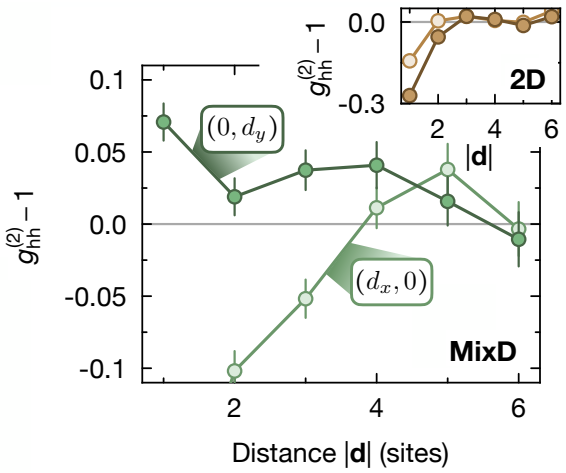

Figure 5.18: **Charge correlations along x and y.** Hole-hole correlations $g^{(2)}_{\mathrm{hh}}(\mathbf{d})$ along $\mathbf{d} = (d_x, 0)$ and $\mathbf{d} = (0, d_y)$ for the mixD setting (main panel, green) and the 2D setting with $\Delta = 0$ but otherwise unchanged parameters (inset, ocher). While in 2D both directions show clear anti-bunching tendencies, in the mixD case vertically aligned correlations are positive. In both cases, snapshots binned to doping $\delta = 0.18$ are used, cf. Fig. 5.17 (a). Figure adapted from Ref. [2].

the doping dependence of charge-charge correlations. The results, shown in Fig. 5.17 (c), indicate that both the nearest-neighbor and diagonal correlations remain positive across the entire doping range, though their magnitude decreases with increasing doping. This behavior is consistent with the decrease in spin-spin correlations with doping, cf. Fig. 5.16, which act as the binding glue for holes forming stripes. Additionally, a non-trivial dependence is observed for the $\mathbf{d} = (2, 0)$ and $(3, 0)$ correlations: around $\delta \approx 0.15$, these correlations transition from negative to positive. This may suggest a shift in the system from individual pairs to extended stripe-like structures.

While DMRG captures the main qualitative features of the NN and diagonal correlations, it does not account for the sign change in more distant hole-hole correlators, as shown in Fig. 5.17 (d). This discrepancy may stem from subtle effects, such as next-nearest-neighbor hopping events and a statistical distribution of holes in each ladder leg, which we do not consider in our idealized numerical model.

Besides the hole-hole correlators studied above, higher-order correlations such as two-point pair-hole and pair-pair as well as three-point hole-hole-hole correlations all show a consistent behavior, i.e., they are in line with the formation of fluctuating, stripe-like charge structures. Details analysis of these fully and partially connected correlators of the experimental data can be found in Ref. [2], but shall not be of further focus here.

Signals of extended charge structures beyond hole pairing motivates to analyze fluctuating charge structures in more detail. For this, we define a vertical stripe as a consecutive cluster of holes where each hole has at most a distance of $d_x = 1$ to its neighboring holes in y-direction. By counting the occurences of these structures, we would like to compare the experiment to effective, mean-field descriptions of fluctuating holes. In the following, we first describe two theories of fluctuating stripes, before analyzing snapshots generated from these theories to the

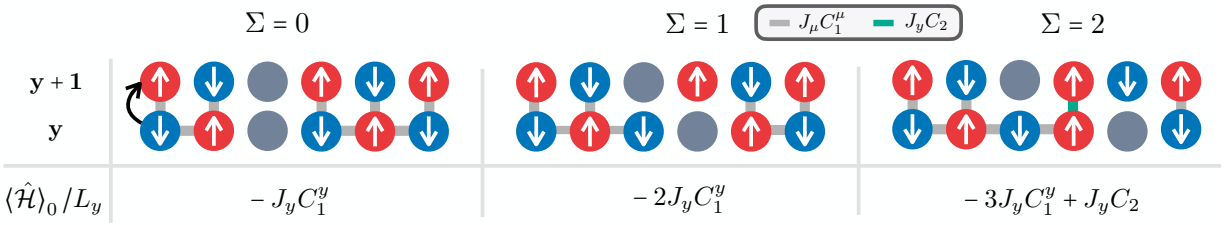

Figure 5.19: **String potential.** Illustration of the effective potential between chain y with its neighbouring chain $y+1$. Grey lines illustrate energy contributions $\sim J_\mu C_1^\mu$, $\mu = x, y$; green lines denote diagonal correlations with energy $\sim J_y C_2$ starting at $|\Sigma| \geq 2$. Intra-chain energy corrections from the Néel state $\sim J_x C_1^x$ are constant and not written down explicitly in the potential.

experiment.

Mean field theory

We start by setting up a mean field theory for the stripe phase in the mixD t-J model. We focus on describing an individual stripe in y-direction with exactly one hole per chain, bound by the magnetically mediated confining potentials. In particular, we neglect the interaction between multiple stripes at positions $\mathbf{i}_1$ and $\mathbf{i}_2$, i.e., we focus on the low doping regime. To illustrate the concept, we first consider a mean field description of the ground state, before generalizing to finite temperature.

For $t \gg J_x, J_y$, quantum correlations between strongly fluctuating holes and spins in squeezed space can be neglected. Hence, we make the ansatz

$$|\psi\rangle = |\psi\rangle_{\text{sq}} \otimes |\psi\rangle_{\text{c}}\,, \tag{5.16}$$

where $|\psi\rangle_{\text{sq}}$ is the spin state of the undoped Heisenberg model in squeezed space, and $|\psi\rangle_{\text{c}}$ is the chargon wave function. Our starting point for the description of the single-stripe phase is the variational Gutzwiller wave function, given by

$$|\psi\rangle_{\text{c}} = \bigotimes_{y=-\infty}^{\infty} |\phi^{(0)}\rangle_y\,, \tag{5.17}$$

i.e., we describe the charge sector by the product of identical single-leg wave functions $|\phi^{(0)}\rangle_y$ in chain y. Assuming that the stripe is centered around $x = 0$, we express $|\phi^{(0)}\rangle_y$ within the string basis,

$$|\phi^{(0)}\rangle_y = \sum_{\Sigma=-\infty}^{\infty} \phi_\Sigma^{(0)} |y, \Sigma\rangle\,, \tag{5.18}$$

where Σ can be understood as the length of the string measured relative to the center of the stripe.

Within this variational ansatz, coefficients $\phi_\Sigma^{(0)}$ can be found by minimizing the trial state's

energy, $\langle\hat{\mathcal{H}}\rangle_0 = \langle\psi|\hat{\mathcal{H}}|\psi\rangle = \Big(\langle\psi|_{\mathrm{sq}} \otimes \langle\psi|_{\mathrm{c}}\Big)\,\hat{\mathcal{H}}\,\Big(|\psi\rangle_{\mathrm{sq}} \otimes |\psi\rangle_{\mathrm{c}}\Big)$,

$$\frac{\langle\hat{\mathcal{H}}\rangle_0}{L_y} = \frac{E_0}{L_y} - t\sum_{\Sigma}\Big(\phi^{(0)*}_{\Sigma+1}\phi^{(0)}_{\Sigma} + \text{c.c.}\Big) + \sum_{\Sigma,\Sigma'}|\phi^{(0)}_{\Sigma}|^2|\phi^{(0)}_{\Sigma'}|^2 V_{\mathrm{pot}}(\Sigma-\Sigma'). \tag{5.19}$$

Here, $V_{\mathrm{pot}}(\Sigma)$ is the inter-chain potential defined by the potential energy of two holes in neighboring chains separated by the string Σ,

$$V_{\mathrm{pot}}(\Sigma) = J_y\Big[\big(|\Sigma|-1+\delta_{\Sigma,0}\big)C_2 - \big(|\Sigma|+1\big)C_1^y\Big], \tag{5.20}$$

where $C_1^\mu = \langle\psi_{\mathrm{s}}|\hat{\mathbf{S}}_{\mathbf{i}}\cdot\hat{\mathbf{S}}_{\mathbf{i}+\mathbf{e}_\mu}|\psi_{\mathrm{s}}\rangle$, $\mu = x,y$, are nearest neighbor, and $C_2 = \langle\psi_{\mathrm{s}}|\hat{\mathbf{S}}_{\mathbf{i}}\cdot\hat{\mathbf{S}}_{\mathbf{i}+\mathbf{e}_x+\mathbf{e}_y}|\psi_{\mathrm{s}}\rangle$ diagonal spin-spin correlations in the undoped Heisenberg model in the ground state. Note that there are also intra-chain contributions, which, however, are constant and only lead to a trivial energy shift on top of the Heisenberg ground state energy E_0, cf. Fig. 5.19.

By averaging over the upper and lower chain for a given leg, we can reformulate the variational problem, Eq. (5.19), as a self-consistent ground state search of the mean field Hamiltonian per chain,

$$\hat{\mathcal{H}}_{\mathrm{MF}} = \frac{E_0}{L_y} - t\sum_{\Sigma,\Sigma'}\Big[\hat{h}^\dagger_{\Sigma'}\hat{h}_{\Sigma} + \text{h.c.}\Big] + \sum_{\Sigma}\hat{h}^\dagger_{\Sigma}\hat{h}_{\Sigma}V_{\mathrm{eff}}(\Sigma), \tag{5.21}$$

where $\hat{h}^\dagger_\Sigma\,|y,0\rangle = |y,\Sigma\rangle$ and

$$V_{\mathrm{eff}}(\Sigma) = 2\sum_{\Sigma'}|\phi^{(0)}_{\Sigma'}|^2 V_{\mathrm{pot}}(\Sigma'-\Sigma). \tag{5.22}$$

Note the factor of 2 in the potential energy, arising from energy contributions between chains $y\pm1$ with chain y. When considering the total energy of the variational wave function, Eq. (5.19), however, there is no additional factor to not double count inter-chain energy contributions.

In practice, we set a maximal cutoff for the string length, here chosen as $|\Sigma_{\max}| = 15$. By exact diagonalization and self-consistently solving for Eq. (5.21), the string length distribution $|\phi^{(0)}_\Sigma|^2$ within the mean field picture can be calculated.
At finite temperature, we generalize the ansatz to a product of density matrices,

$$\hat{\rho} = \hat{\rho}_{\mathrm{sq}} \otimes \left(\bigotimes_{y=-\infty}^{\infty}\hat{\rho}^{(0)}_{\mathrm{MF}}\right), \tag{5.23}$$

where

$$\hat{\rho}^{(0)}_{\mathrm{MF}} = \frac{1}{Z}e^{-\beta\hat{\mathcal{H}}_{\mathrm{MF}}(\hat{\rho}^{(0)}_{\mathrm{MF}},T)} \tag{5.24}$$

defines the self-consistency equation via

$$\begin{aligned}\frac{\hat{\mathcal{H}}_{\mathrm{MF}}(\hat{\rho}^{(0)}_{\mathrm{MF}})}{L_y} &= \frac{E_0}{L_y} - t\sum_{\Sigma,\Sigma'}\Big[\hat{h}^\dagger_{\Sigma'}\hat{h}_{\Sigma} + \text{h.c.}\Big] + \sum_{\Sigma}\hat{h}^\dagger_{\Sigma}\hat{h}_{\Sigma}V_{\mathrm{eff}}(\Sigma;\hat{\rho}^{(0)}_{\mathrm{MF}},T)\\ V_{\mathrm{eff}}(\Sigma;\hat{\rho}^{(0)}_{\mathrm{MF}},T) &= 2\sum_{\Sigma'}\langle\Sigma|\hat{\rho}^{(0)}_{\mathrm{MF}}|\Sigma\rangle\; V_{\mathrm{pot}}(\Sigma'-\Sigma;T).\end{aligned} \tag{5.25}$$

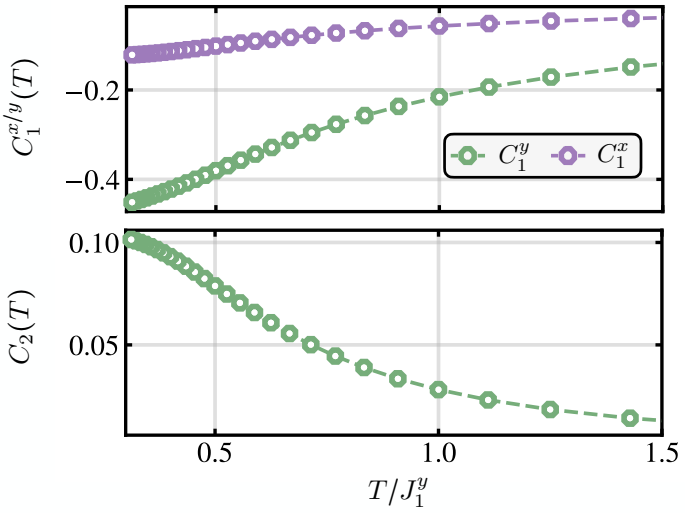

Figure 5.20: **Two-point correlators of the squeezed background.** Thermally averaged two-point correlations of the undoped Heisenberg model $C_1^\mu(T) = \langle \hat{\mathbf{S}}_\mathbf{i} \cdot \hat{\mathbf{S}}_{\mathbf{i}+\mathbf{e}_\mu} \rangle_T$, $\mu = x$ (grey), y (red) and $C_2(T) = \langle \hat{\mathbf{S}}_\mathbf{i} \cdot \hat{\mathbf{S}}_{\mathbf{i}+\mathbf{e}_x+\mathbf{e}_y} \rangle_T$ (blue) calculated from DMRG calculations for $J_x/J_y = 0.3$ on a 12×4 lattice with PBC applied along the short (y-) direction.

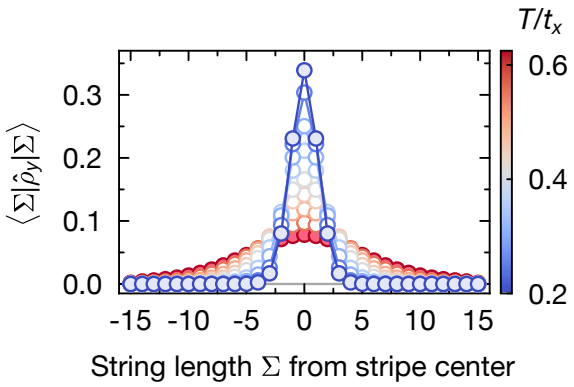

Figure 5.21: **String length distribution.** Thermally averaged string length distribution $\langle \Sigma | \hat{\rho}^{(0)}_{\mathrm{MF}} | \Sigma \rangle$ for temperatures $T/t_x = 0.2 \ldots 0.625$, and $t_x/J_y = 2$ using the thermal correlations in the Heisenberg model in Fig. 5.20.

Here, $C_1^\mu(T) = \langle \hat{\mathbf{S}}_\mathbf{i} \cdot \hat{\mathbf{S}}_{\mathbf{i}+\mathbf{e}_\mu} \rangle_T$, $\mu = x, y$ and $C_2(T) = \langle \hat{\mathbf{S}}_\mathbf{i} \cdot \hat{\mathbf{S}}_{\mathbf{i}+\mathbf{e}_x+\mathbf{e}_y} \rangle_T$ entering V_{pot} in Eq. (5.20) are thermally averaged two-point correlators of the 2D Heisenberg model. Given the self-consistent solution of $\hat{\rho}^{(0)}_{\mathrm{MF}}$, the mean field string length distribution is determined by the diagonal elements of $\hat{\rho}^{(0)}_{\mathrm{MF}}$, i.e., $p_\Sigma = \langle \Sigma | \hat{\rho}^{(0)}_{\mathrm{MF}} | \Sigma \rangle$.

We use finite temperature DMRG methods to calculate thermally averaged nearest-neighbour and diagonal correlations of the undoped Heisenberg model with $J_x/J_y = 0.3$ on a $L_x \times L_y = 12 \times 4$ lattice with periodic boundaries along y, see Fig. 5.20. Results for the corresponding mean field estimates of the string length distributions in the stripe phase are shown in Fig. 5.21 for $t_x/J_y = 2$ and temperatures $T/t_x = [0.2, 0.625]$.

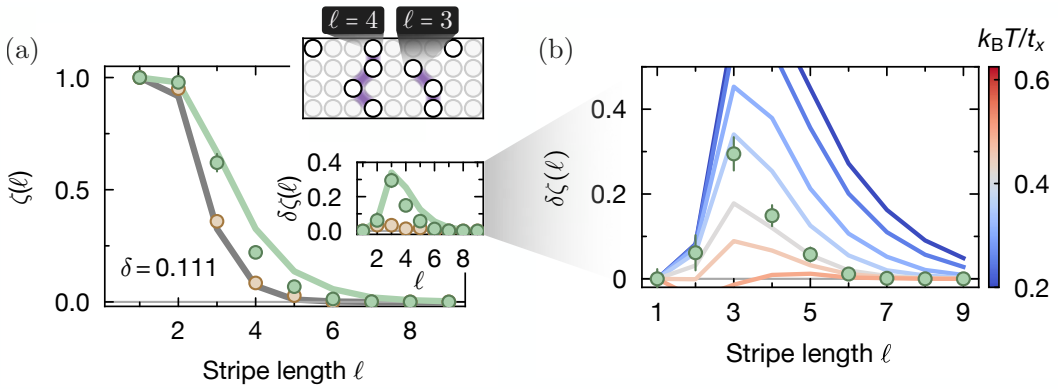

Figure 5.22: **Counting stripes.** (a) Normalized histogram of the stripe length distribution $\zeta(\ell)$ for mixD (green points) and 2D (ocher points). Snapshots are counted as containing a structure of length ℓ if they feature at least one continuous "stripe" where ℓ holes on neighboring legs in the y-direction differ by at most 1 site along x. The result of randomly placing holes (while accounting for anti-correlations due to Pauli repulsion, see text), is shown in grey. Results from mean field calculations at $T/t_x \approx 0.35$ are shown in solid green. Panel (b) provides a detailed illustration of $\zeta(\ell)$ for varying temperatures in the MFT. For $T/t_x \approx 0.35$, there is the best agreement between the MFT and mixD snapshots. Figure adapted from Ref. [2].

Counting charge stripes

The MFT described above enables sampling of charge snapshots according to the self-consistently determined stripe length distribution, which we compare to the hole-channel of experimentally obtained snapshots. To this end, we define a fully filled "stripe" as a connected line of holes along y, where the pairwise distance along x between holes in neighboring chains is at most 1. The length ℓ of this structure is defined by the number of holes involved. This is depicted in the inset of Fig. 5.22 (a) for $\ell = 3, 4$.

The fraction $\zeta(\ell)$ of (theoretical or experimental) snapshots containing such a stripe structure of at least length ℓ is then evaluated. We highlight at this point again that these types of observables are entirely inaccessible to solid-state experiments, emphasizing quantum simulation as a unique tool for studying the microscopic properties of strongly correlated phases of matter.

In Fig. 5.22 (a), we compare the mixD (green) case with the 2D system (ocher) at a doping level of $\delta = 0.111$, analyzed on a subsystem of 9×9 sites. This doping level corresponds to snapshots containing 9 holes, which, for fully filled stripes, represents a single stripe. This configuration can then be directly compared to our MFT calculations. For further comparison, we calculate the stripe length distribution for randomly placed holes. Rather than using fully random placement, we incorporate experimentally observed anti-correlations along x, accounting for the effects of Pauli repulsion. This approach provides a more genuine comparison of the charges' tendency to form stripe-like structures.

From Fig. 5.22 (a), it is evident that the 2D data closely follows the random distribution with Pauli anti-correlations, indicating no significant formation of extended structures in 2D at the simulated temperature. In contrast, mixD shows significantly higher probabilities of forming extended charge structures along the y-direction. This is corroborated in the lower inset of

Fig. 5.22 (a), where the difference $\delta\zeta(\ell)$ between the random distribution and the mixD and 2D data is displayed. Particularly for structures containing 3-5 holes, mixD exhibits substantially higher signals.

We now compare stripe length distributions with snapshots obtained from mean field theory, shown in Fig. 5.22 (b) (see also the solid line in the lower inset of Fig. 5.22 (a)). The resulting stripe length distributions for various temperatures in the MFT are color-coded in Fig. 5.22 (b). At $T/t_x \approx 0.35$, there is a strong match between MFT predictions and experimental snapshots. Notably, this temperature aligns with the thermometry derived from pure spin correlations, which estimated $T/t_x \approx 0.3$.

Müller-Hartmann-Zittartz estimate

In the MFT, stripes, although fluctuating, are pinned to the center of the system. This means that all holes follow the same string length distribution around a fixed position of the single stripe. We now aim to describe stripes in a way that more naturally captures situations where these structures are not pinned to a specific position $\mathbf{x}_0$, as illustrated in the inset of Fig. 5.23 (a).

To this end, we reduce the mixD system to a 1D, purely classical model of fluctuating holes bound together by the effective potential V, Eq. (5.20). Denoting with x_ℓ the x-position of the doped hole in leg ℓ (we again consider one hole per chain, i.e. a single fluctuating domain wall), the effective Hamiltonian (excluding quantum fluctuations from the hopping of the holes) for a system of size $(L_x+1)\times(L_y+1)$ reads

$$\hat{\mathcal{H}}_{\mathrm{MHZ}} = \sum_{\ell=1}^{L_y} V_{\mathrm{pot}}(|x_\ell - x_{\ell+1}|; T), \tag{5.26}$$

where again the temperature dependent correlators $C_1^\mu(T) = \langle \hat{\mathbf{S}}_{\mathbf{i}} \cdot \hat{\mathbf{S}}_{\mathbf{i}+\mathbf{e}_\mu} \rangle_T$, $\mu = x, y$ and $C_2(T) = \langle \hat{\mathbf{S}}_{\mathbf{i}} \cdot \hat{\mathbf{S}}_{\mathbf{i}+\mathbf{e}_x+\mathbf{e}_y} \rangle_T$ enter the effective potential $V_{\mathrm{pot}}(|x_\ell - x_{\ell+1}|; T)$ in Eq. (5.20).

The partition function, Z, decouples when being expressed solely by distances $d_\ell = x_\ell - x_{\ell+1}$,

$$\begin{aligned} Z &= \sum_{\{x_\ell\}} \prod_{\ell=1}^{L_y} \exp\left[-\beta V_{\mathrm{pot}}(|x_\ell - x_{\ell+1}|; T)\right] \\ &= \sum_{d_1=-L_x}^{L_x} \cdots \sum_{d_{L_y}=-L_x}^{L_x} \prod_{\ell=1}^{L_y} \exp\left[-\beta V_{\mathrm{pot}}(|d_\ell|; T)\right] \\ &= \left[\sum_{d=-L_x}^{L_x} \exp\left[-\beta V_{\mathrm{pot}}(|d|; T)\right]\right]^{L_y} = [Z_1]^{L_y}. \end{aligned} \tag{5.27}$$

The probability of finding two adjacent holes at a distance of d in chains $\ell, \ell+1$ is hence given by

$$p(d) = \exp\left[-\beta V_{\mathrm{pot}}(|d|; T)\right] / Z_1, \tag{5.28}$$

shown for various temperatures T/J_y in Fig. 5.23 (a).

Fixing the first hole at the center and sampling distances according to Eq. (5.28), we generate snapshots of the hole configurations. The results are compared to experimental data in

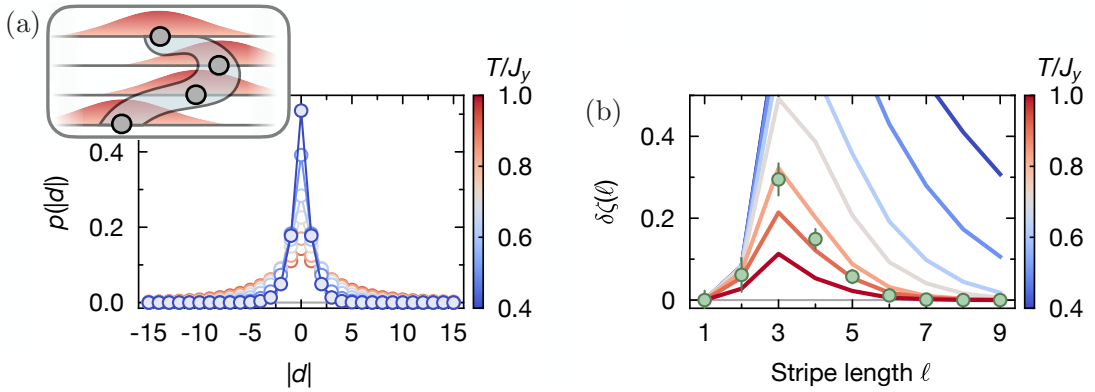

Figure 5.23: **MHZ estimate.** (a) Hole distance distributions, Eq. (5.28), for various temperatures T/J_y. Inset: When sampling snapshots according to the distance distributions, fluctuating stripes that are not pinned to the center are captured. Hole positions are sampled according to the red probability distributions, whereby the distribution for position $x_{\ell+1}$ is centered around x_ℓ. (b) Stripe length histograms using the classical MHZ estimate for temperatures of $T/J_y \in [0.4, 1]$, showing qualitatively similar results to the MFT and capturing the experimental data well for $T/J_y \approx 0.8$. Figure adapted from Ref. [2].

Fig. 5.23 (b). For $T/J_y \approx 0.8$, we observe matching behavior between the classical theory, the experiment, and the MFT results at $T/t_x \approx 0.35$.

Spin sector

Apart from the charge structures appearing as stripes, the stripe phase also exhibits specific properties in the spin sector. Across regions of enhanced hole density, the underlying AFM forms domain walls. While measuring long-range incommensurate order is not currently feasible due to temperature limitations, the experiment's microscopic resolution in both spin and charge sectors allows us to evaluate real-space spin observables around holes. In particular, short-range AFM correlations across extended charge structures can be revealed through nonlocal and higher-order spin-charge correlators.

We begin by evaluating a string correlator, which measures spin-spin correlations along the x-direction while explicitly accounting for sign changes introduced by holes between two spins [236, 242]. This reveals domain walls in the short-range AFM order caused by the charge structures. The string correlator is defined as

$$C_{\mathrm{str}}(d) = \frac{1}{\mathcal{N}_d} \sum_i \frac{\left\langle \hat{S}^z_i \left(\prod_{j=1}^{d-1} \hat{R}_{i+j} \right) \hat{S}^z_{i+d} \right\rangle - \langle \hat{S}^z_i \rangle \langle \hat{S}^z_{i+d} \rangle}{\sigma(\hat{S}^z_i)\sigma(\hat{S}^z_{i+d})}, \tag{5.29}$$

where $\hat{R}_i = e^{i\pi \hat{n}^h_i}$, and we normalize by the spin standard deviation $\sigma(\hat{S}^z)$. If $\hat{R}_i = 1$, the usual spin-spin correlator is recovered, which we compare to the case $\hat{R}_i = e^{i\pi \hat{n}^h_i}$ in Fig. 5.24 (a).

Evaluating NNN spin-spin correlations directly in real space reveals positive signals at low doping, transitioning to weakly negative signals for $\delta \gtrsim 0.15$. At low doping, AFM correlations remain largely undisturbed, producing positive signals across NNN. Across holes, however, the

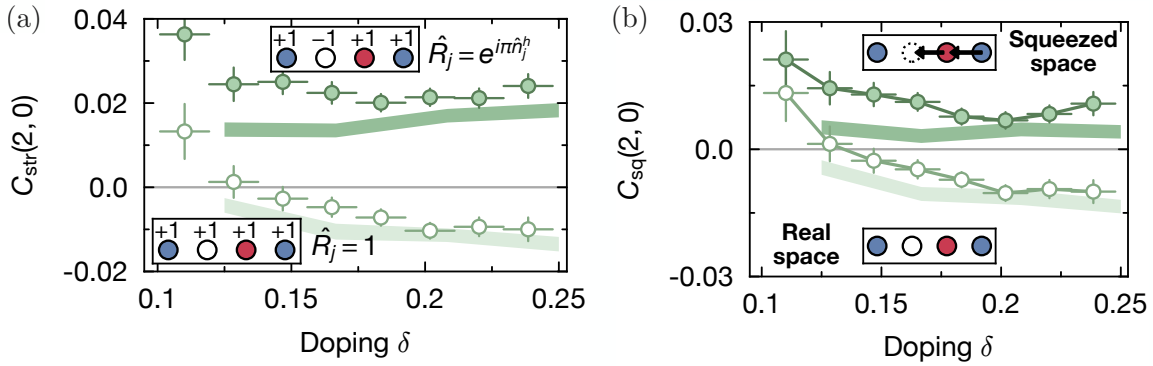

Figure 5.24: **String correlator and squeezed space.** (a) Standard two-point spin correlations (light green points) and the spin-string correlator, Eq. (5.29) (dark green points), for distance $\mathbf{d} = (2,0)$. A sign change consistent with domain walls in short-range AFM correlations across holes is observed. Experimental results are compared to MPS calculations for a $L_x \times L_y = 8 \times 3$ system at $T/t_x = 0.3$, showing consistent behavior. (b) Spin-spin correlations in squeezed space, showing qualitatively identical behavior to the spin-string correlator. Figure adapted from Ref. [2].

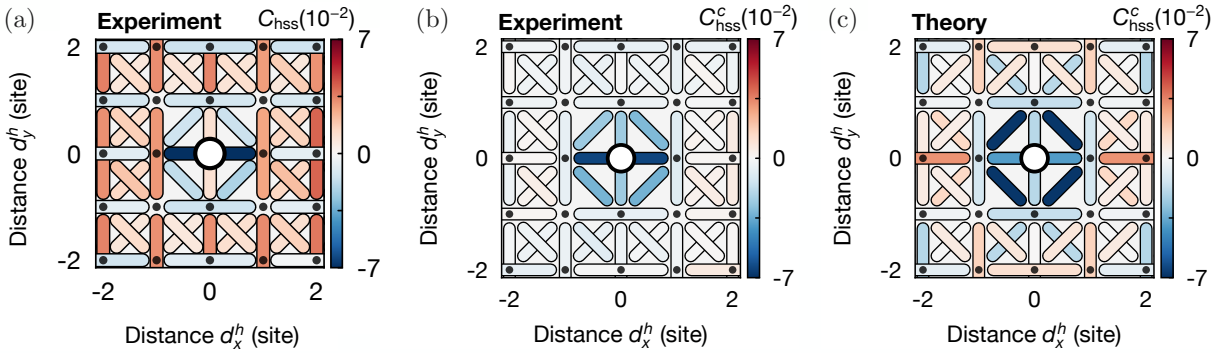

Figure 5.25: **Hole-spin-spin correlations.** (a) Bare hole-spin-spin correlations, Eq. (5.30). Genuine three-point hole-spin-spin correlations induce a sign change in the vicinity of the hole, where NNN correlations across the hole are negative. (b) Fully connected hole-spin-spin correlations, Eq. (5.31). By subtracting contributions from the AFM-ordered background, the primary effect of the hole becomes evident: strong negative signals at the diagonals and horizontal bonds around the hole. (c) MPS theory snapshots of the $L_x \times L_y = 8 \times 4$ system at $\delta = 0.125$ reveal similar structures. Slight asymmetries stem from a finite size data set. Figure adapted from Ref. [2].

AFM parity changes, leading to negative signals. These domain walls wash out real-space correlations, especially at higher doping. The spin-string correlator accounts for these domain walls, showing consistently strong positive signals across all doping levels. MPS calculations for a $L_x \times L_y = 8 \times 3$ system at $T/t_x = 0.3$ corroborate these findings (solid lines in Fig. 5.24 (a)), with a qualitative (and, to some extend, quantitative) match between theory and experiment.

Similarly, we can directly transform the snapshots into squeezed space by removing holes and relabeling the spins, as described in Sec. 5.2.3. The NNN correlations in squeezed space are shown in Fig. 5.24 (b), exhibiting qualitatively identical behavior to the spin-string correlator defined in Eq. (5.29).

Lastly, we analyze 3-point hole-spin-spin correlators, beginning with the normalized, bare correlator,

$$C_{\text{hss}}(\mathbf{d}^s, \mathbf{d}^h) = \frac{1}{\mathcal{N}_{\mathbf{d}^s,\mathbf{d}^h}} \sum_{\substack{\mathbf{i} \\ \mathbf{j}=\mathbf{i}+\mathbf{d}^h-\mathbf{d}^s/2}} \frac{\langle \hat{n}^h_{\mathbf{i}} \hat{S}^z_{\mathbf{j}} \hat{S}^z_{\mathbf{j}+\mathbf{d}^s} \rangle}{\langle \hat{n}^h_{\mathbf{i}} \rangle \sigma(\hat{S}^z_{\mathbf{j}}) \sigma(\hat{S}^z_{\mathbf{j}+\mathbf{d}^s})}, \tag{5.30}$$

where $\mathbf{d}^s$ is the spin bond vector, $\mathbf{d}^h$ is the distance of the bond from the dopant, and normalization is performed using the hole density $\langle \hat{n}^h \rangle$ and the spin standard deviation $\sigma(\hat{S}^z)$. The corresponding correlation map of the experimental mixD data in Fig. 5.25 can be interpreted as follows: For a hole located at some position $\mathbf{i}$, diagonal ($\mathbf{d}^s = (\pm 1, \pm 1)$) and NNN ($\mathbf{d}^s = (2,0), (0,2)$) spin-spin correlations around the hole are plotted. Previous studies in 2D have shown that a single hole is surrounded by a dressing cloud of spin excitations, leading to reduced correlations [46, 48, 243]. These magnetic polarons have been analyzed across a broad doping range, revealing a transition from a collection of magnetic polarons at low doping to a Fermi liquid state at high doping [48].

In the mixD setting, we observe strong negative signals across the hole (Fig. 5.25 (a)), consistent with the presence of an AFM domain wall across the charge structures. Similarly, diagonal correlators near the hole are negative. NNN correlations along y remain largely unaffected by the presence of a hole and exhibit positive signals, as expected in a system with AFM order along y.

To further assess the effect of mobile dopants on the spin background, we analyze the connected hole-spin-spin correlator, which subtracts all lower-order contributions. This allows to disentangle signals arising from genuine higher-order correlations versus those stemming from lower-order contributions. For instance, if a hole is located at position $\mathbf{i}$, local AFM correlations may exist far from the hole; these correlations, however, are independent of the hole and do not reflect genuine 3-point hole-spin-spin correlations. Since 2-point correlations are significant in our system, we analyze the fully connected 3-point hole-spin-spin correlator,

$$\begin{aligned} C^c_{\text{hss}}(\mathbf{d}^s, \mathbf{d}^h) = \frac{1}{\mathcal{N}_{\mathbf{d}^s,\mathbf{d}^h}} \sum_{\substack{\mathbf{i} \\ \mathbf{k}-\mathbf{j}=\mathbf{d}^s, \\ (\mathbf{k}+\mathbf{j})/2-\mathbf{i}=\mathbf{d}^h}} \frac{1}{\langle \hat{n}^h_{\mathbf{i}} \rangle \sigma(\hat{S}^z_{\mathbf{j}}) \sigma(\hat{S}^z_{\mathbf{k}})} \Big(\langle \hat{n}^h_{\mathbf{i}} \hat{S}^z_{\mathbf{j}} \hat{S}^z_{\mathbf{k}} \rangle - \langle \hat{n}^h_{\mathbf{i}} \rangle \langle \hat{S}^z_{\mathbf{j}} \hat{S}^z_{\mathbf{k}} \rangle - \langle \hat{n}^h_{\mathbf{i}} \hat{S}^z_{\mathbf{j}} \rangle \langle \hat{S}^z_{\mathbf{k}} \rangle \\ - \langle \hat{n}^h_{\mathbf{i}} \hat{S}^z_{\mathbf{k}} \rangle \langle \hat{S}^z_{\mathbf{j}} \rangle + 2 \langle \hat{n}^h_{\mathbf{i}} \rangle \langle \hat{S}^z_{\mathbf{j}} \rangle \langle \hat{S}^z_{\mathbf{k}} \rangle \Big) . \end{aligned} \tag{5.31}$$

Results for the experimental data are shown in Fig. 5.25 (b), and for $L_x \times L_y = 8 \times 4$ MPS calculations at $\delta = 0.125$ in Fig. 5.25 (c). Prominent negative signals across the hole are evident, dominating over the AFM background. This dominance results in a full sign change of the correlator, even in the bare correlator (Fig. 5.25 (a)). Signals farther from the hole in the connected correlator are negligible, indicating that the contributions observed in the bare correlator are primarily due to the AFM background, rather than the presence of a hole. MPS calculations exhibit the same key features, with strong negative correlations across the hole's vicinity. Note that the correlations from MPS simulations are evaluated using thermal snapshots; the finite data size leads to slight asymmetries in hole-spin-spin correlations in regions where correlations are weak, as seen in Fig. 5.25 (c).

5.4 Outlook

In this chapter, we presented numerical DMRG results that demonstrate the formation of stable stripes in the t-J model of mixed dimensionality. Above critical temperatures T_c on the order of J, we find commensurate, short-range antiferromagnetic correlations together with deconfined holes. Below the critical temperature, incommensurate order as well as charge density waves emerge on long length scales of the numerically accessible system size, i.e., stripes form in the system.

By implementing the model in an ultracold atom quantum simulator, in an experimental collaboration with the ^{6}Li team at MPQ we presented first evidence of the formation of extended, stripe-like structures at intermediate temperatures. This regime allows for the microscopic exploration of the formation of collectively ordered states, paving the way to gain a detailed understanding of the physics underlying low-temperature phases in strongly correlated systems. In particular, our results set the stage for more detailed studies of stripes, including the extraction of their precise periodicity, fluctuations, and filling. Moreover, gaining a microscopic understanding of how stripes form and melt can give insights into exotic phases of matter such as the pseudogap phase, a prospect we discuss in detail in Chap. 7.

Observations of strong AFM correlations in three dimensional (3D) realizations of the FH model [62] further motivate the existence of resilient sheets of stripes in a possible generalization of the mixD t-J model to 3D, where—in contrast to 2D—true long-range magnetic order appears also at finite temperature.

Previously, the mixD t-J_z model including solely Ising-type interactions has been analyzed [230]. There, an exact mapping revealed an emergent $\mathbb{Z}_2$ lattice gauge structure, which allowed to draw analogies with gauge theories and distinguish phases by emergent properties. The mixD t-J_z model has been shown to exhibit a rich phase diagram when restricted to a single gauge sector (i.e. a fixed AFM Néel background), including stripes, a deconfined chargon gas as well as a meson gas, where in the latter holes form pairs at low hole concentrations and temperatures slightly above T_c. It remains to be analyzed whether a confined phase of mesonic character exists also in the mixD t-J model (including spin fluctuations as well as gauge mixing in comparison to [230]), and if any conclusive connections can be drawn in the context of $\mathbb{Z}_2$ lattice gauge theories.

6

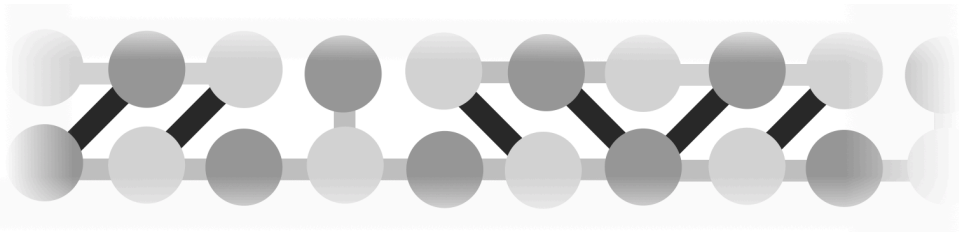

Effective models: Hamiltonian reconstruction

Summary. When holes move through an antiferromagnetic spin background, they displace the positions of spins, which induces effective frustration in the magnetic environment. In this chapter, we present a Hamiltonian reconstruction scheme that allows for a precise quantification of this effect. We access non-local correlation functions through projective measurements of the many-body state, from which effective spin-Hamiltonians can be recovered after detaching the magnetic background from dominant charge fluctuations. The scheme is applied to systems of mixed dimensions, where we demonstrate that hole-motion drives the spin background into a highly frustrated regime, which can quantitatively be described by an effective J_1-J_2-type spin model. Similarly, we use Hamiltonian reconstruction to quantify the net attraction of hole dopants mediated by the spin background. Lastly, we exemplify the applicability of the reconstruction scheme to ultracold atom experiments by recovering effective spin-Hamiltonians of experimentally obtained 1D Fermi-Hubbard snapshots.

6.1 Introduction

In the last chapter, we identified a crossover between a chargon gas (a phase without charge and spin order) and a stripe phase, which was corroborated by experimental evidence of the formation of extended stripe-like structures at temperatures at the edge of the onset of charge and incommensurate spin order.

As already demonstrated in Sec. 5.2.3, holes displace spins along their way when hopping through an insulating spin environment, which effectively frustrates the magnetic background. In particular, we saw that in the chargon gas phase, while AFM correlations can be restored when removing the holes, spin-spin correlations have a shifted weight from AFM to FM correlations,

cf. Fig. 5.11 in Sec. 5.2.3. It is this arising competition of kinetic energy gain via delocalization and associated magnetic energy cost that is believed to be at the heart of the formation of strongly interacting many-body phases [24, 72].

In this chapter, we demonstrate that this effect can be precisely quantified using tailored machine learning routines. We show that the analysis of many-body snapshots, which contain a huge amount of information, can be utilized to disentangle spin and charge sectors through non-local correlation functions, which allow us to recover emergent effective spin-Hamiltonians for parts of the system. In particular, we present a snapshot-based Hamiltonian reconstruction scheme for the spin channel alone, which removes dominant charge fluctuations [236, 242] from individual snapshots. This allows us to quantify the effective spin-Hamiltonian, which includes the back-action of mobile dopants on the spin environment. We exemplify the proposed method by considering mixD t-J model introduced in the previous chapter. In Sec. 6.3, we find that hole hopping drives and stabilizes the spins in a highly frustrated regime, which we show to be accurately described by a J_1-J_2-type spin-Hamiltonian. Similarly, in Sec. 6.4, we demonstrate that when reconstructing effective Hamiltonians for the charge sector alone, attractive interactions arising from the spin background can be quantified precisely.

The Hamiltonian reconstruction method is directly applicable to experimental data obtained from ultracold quantum gas microscopes. In Sec. 6.5, we showcase this by reconstructing effective Hamiltonians from 1D measurements of the FH model [242], where spin-charge separation governs the physics of the chains. Furthermore, our insights could be used to effectively simulate the highly frustrated J_1-J_2 model in ultracold atom experiments by implementing the mixD setting and post-processing the measurements.

The content presented in this chapter including the above introduction is based on the following publication, and contains textual overlap:

> [3] **HS**, T. Hilker, I. Bloch, U. Schollwöck, F. Grusdt, and A. Bohrdt. **Quantifying hole-motion-induced frustration in doped antiferromagnets by Hamiltonian reconstruction**, Commuications Materials 4, 64 (2023)

6.2 Hamiltonian reconstruction

Our aim will be to reconstruct effective Hamiltonians of doped Mott insulators in the spin- or charge sector, for which we will use Hamiltonian reconstruction schemes. Before applying the latter to data from the mixD t-J model, let us introduce how a system's underlying Hamiltonian can be reconstructed from many-body snapshots in the Fock basis. As a specific example relevant for our application later on in this chapter, we consider the J_1^x-J_1^y-J_2 Heisenberg Hamiltonian [244],

$$\hat{\mathcal{H}}_{\{K_H\}} = \sum_{\mu=x,y} K_1^\mu \sum_{\langle \mathbf{i},\mathbf{j}\rangle_\mu} \hat{\mathbf{S}}_\mathbf{i} \cdot \hat{\mathbf{S}}_\mathbf{j} + K_2 \sum_{\langle\langle \mathbf{i},\mathbf{j}\rangle\rangle_{\text{diag}}} \hat{\mathbf{S}}_\mathbf{i} \cdot \hat{\mathbf{S}}_\mathbf{j}. \tag{6.1}$$

Here, $\hat{\mathbf{S}}_\mathbf{i}$ is a spin-1/2 operator at site $\mathbf{i}$, and $\{K_H\} = \{K_1^x, K_1^y, K_2\}$ are the coupling strengths of neighboring spins in x- and y-direction, and diagonal spins on a 2D square lattice, respectively.

Given a set of measurements sampled from the equilibrium Gibbs state at finite temperature

at fixed (target) couplings $\{K_H\}$, we now aim to reconstruct the coupling values of the underlying Hamiltonian. This can be achieved by following the procedure introduced in [245]. To this end, we write down an objective function $\mathcal{G}$, which depends on (now variable) coupling strengths $\{J_H\} = \{J_1^x, J_1^y, J_2\}$ and takes the following form,

$$\mathcal{G} = \ln Z(\beta, \{J_H\}) + 3\beta \left(J_1^\mu \mathcal{M}_1 + J_2 \mathcal{M}_2\right). \tag{6.2}$$

Here, $Z = \mathrm{Tr}[e^{-\beta \hat{\mathcal{H}}_{\{J_H\}}}]$ is the partition function of Hamiltonian Eq. (6.1) with couplings $\{J_H\} = \{J_1^x, J_1^y, J_2\}$, and

$$\mathcal{M}_1^\mu = \sum_{\langle \mathbf{i},\mathbf{j}\rangle_\mu} \langle \hat{S}_\mathbf{i}^z \hat{S}_\mathbf{j}^z \rangle_K, \quad \mathcal{M}_2 = \sum_{\langle\langle \mathbf{i},\mathbf{j}\rangle\rangle_{\mathrm{diag}}} \langle \hat{S}_\mathbf{i}^z \hat{S}_\mathbf{j}^z \rangle_K \tag{6.3}$$

are the summed correlations along nearest- and diagonal neighbors of Hamiltonian Eq. (6.1) with couplings $\{K_H\} = \{K_1^x, K_1^y, K_2\}$ (here underlined by the subscript K). The objection function, Eq. (6.2), is then minimized over all possible values of $\{J_H\}$. Intuitively, this procedure corresponds to minimizing the differences of expectation values of the various terms appearing in the Hamiltonian. For instance,

$$\frac{\partial \mathcal{G}}{\partial J_1^\mu} = 3\beta \sum_{\langle \mathbf{i},\mathbf{j}\rangle_\mu} \langle \hat{S}_\mathbf{i}^z \hat{S}_\mathbf{j}^z \rangle_K - \beta \underbrace{\sum_{\langle \mathbf{i},\mathbf{j}\rangle_\mu} \langle \hat{\mathbf{S}}_\mathbf{i} \hat{\mathbf{S}}_\mathbf{j} \rangle_J}_{3 \sum_{\langle \mathbf{i},\mathbf{j}\rangle_\mu} \langle \hat{S}_\mathbf{i}^z \hat{S}_\mathbf{j}^z \rangle_J}. \tag{6.4}$$

When setting $\partial \mathcal{G} / \partial J_1^\mu = 0$, we thus see that minimization of $\mathcal{G}$ leads to the reconstructed Hamiltonian to match correlations from the original measurements. Due to the model Hamiltonian's SU(2) symmetry, which ensures equal $\langle \hat{S}_\mathbf{i}^\mu \hat{S}_\mathbf{j}^\mu \rangle$ for all $\mu = x, y, z$, measurements in the z-basis are sufficient to fully reconstruct the Hamiltonian.

We note that, as quantum states are generally non-Markovian in nature, it is *a priori* unclear whether measured correlations are sufficient to learn the quantum interactions of the underlying Hamiltonian [246]. However, it has been shown that the strongly convex property of the free energy with respect to the interaction parameters renders the Hamiltonian learning problem feasible [245]. We will, however, not go into more detail at this point, but will rather demonstrate the Hamiltonian reconstruction scheme in practice.

From MPS purification simulations, we take snapshots of the thermal state of the J_1^x-J_1^y-J_2 Heisenberg model Eq. (6.1). We choose $J_1^y / J_1^x = 0.7$, $J_2 / J_1^x = 0.3$, and for now focus on a fixed temperature $T / J_1^x = 5/3$. In a first step, we sample snapshots of the thermal state, which we utilize to estimate spin-spin correlations. To get a feeling for how many snapshots are needed to accurately approximate the relevant correlations, we show corresponding estimates of $\mathcal{M}_1^{x,y}, \mathcal{M}_2$ as a function of sampling size in Fig. 6.1. Measurement outcomes using snapshots (solid lines) are seen to converge towards the exact MPS result of the simulated system (dashed lines) after an order of $\mathcal{O}(1000)$ measurements; nevertheless, already a few hundred snapshots seem to be sufficient to get access to good approximations of the relevant (local) correlations.

Having estimated correlations of our target system, we reconstruct the underlying coupling parameters. The minimization process of the objective function, Eq. (6.2), is done using standard

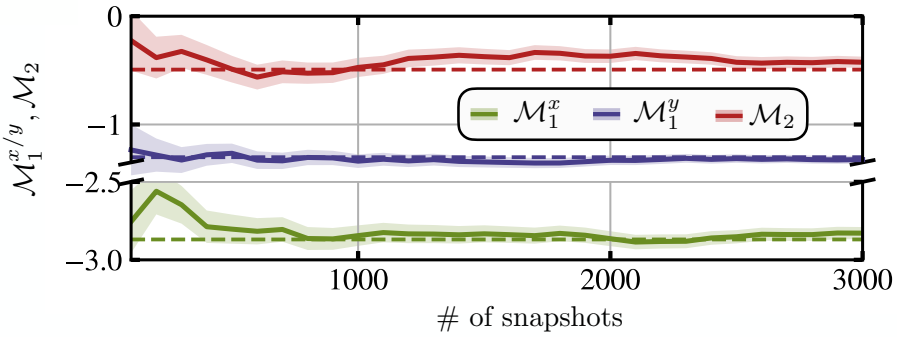

Figure 6.1: **Estimating correlations.** Approximation of correlations $\mathcal{M}_1^{x,y}, \mathcal{M}_2$ with randomly sampled snapshots (solid lines) together with an exact evaluation using the underlying thermalized MPS (dashed lines). Errors to the mean are indicated by the colored background. The J_1^x-J_1^y-J_2 system is of size $L_x \times L_y = 20 \times 4$, with $J_1^y/J_1^x = 0.7$, $J_2/J_1^x = 0.3$, and $T/J_1^x = 5/3$.

gradient descent (GD) methods, where in each iteration the parameters are updated according to the gradient $\nabla\mathcal{G}$ (where $\nabla = [\partial/\partial J_1^x, \partial/\partial J_1^y, \partial/\partial J_2]$). We sample 3000 snapshots, estimate correlations $\mathcal{M}_1^{x,y}, \mathcal{M}_2$, and initialize the GD with randomly chosen couplings. In each GD step, the partition function and relevant correlations are computed directly from the MPS. Due to the resulting numerical complexity, we do not consider advanced GD methods with varying step size e.g. given by the Amijo rule, but stick to a straightforward optimization using a fixed descent step. In particular, we choose the update step $\mathbf{d}$ to be 20 % of the objective gradient, i.e. $\mathbf{d} = 0.2\nabla\mathcal{G}$. When the norm of the gradient reaches a certain threshold, here chosen as $|\nabla\mathcal{G}| < 10^{-6}$, we stop the descent and assume converged results. The above procedure is repeated seven times, each time sampling new snapshots of the underlying state, to estimate errors resulting from sampling inaccuracies of $\mathcal{M}_1^{x,y}, \mathcal{M}_2$.

Fig. 6.2 (a) shows GD trajectories of the absolute value of the three parameters, $|J_H| = \sqrt{(J_1^x)^2 + (J_1^y)^2 + (J_2)^2}$ for all seven repetitions. We observe how each trajectory rapidly flows into the region of the correct (absolute value) of interaction parameters, i.e. $|K_H|$, illustrated by the red solid line in Fig. 6.2 (a). By averaging the final parameters of all trajectories after seven GD steps, the estimated couplings are seen to all lie within one standard deviation to the correct interaction strengths, cf. the inset in Fig. 6.2 (a). Note that we have verified that the descent converges to identical values independent of the initially chosen parameters—including initial points lying very far away from the true values.

As mentioned and analyzed in the original proposal of reconstructing Hamiltonians from many-body measurements [245], the algorithm's accuracy depends on the system's temperature. We repeat the process for several different temperatures $\beta K_1^x = 0.2, 0.4, 0.6, 0.8$ and measure the ℓ_2 norm between the true $\{K_H\}$ and learned $\{J_H\}$ interaction strengths, $\epsilon = [\sum_{\mu=x,y}(J_1^\mu - K_1^\mu)^2 + (J_2 - K_2)^2]^{1/2}$, again for multiple repetitions and after achieving GD convergence. The resulting ℓ_2 error as a function of inverse temperature is shown in Fig. 6.2 (b). We observe that reconstructions work best around intermediate temperatures $\beta J_1^x \sim 0.6$.

This can be intuitively understood by considering a simple ferromagnetic (FM) Ising model, which features a FM ground state for any non-zero interaction strength. Therefore, at low tem-

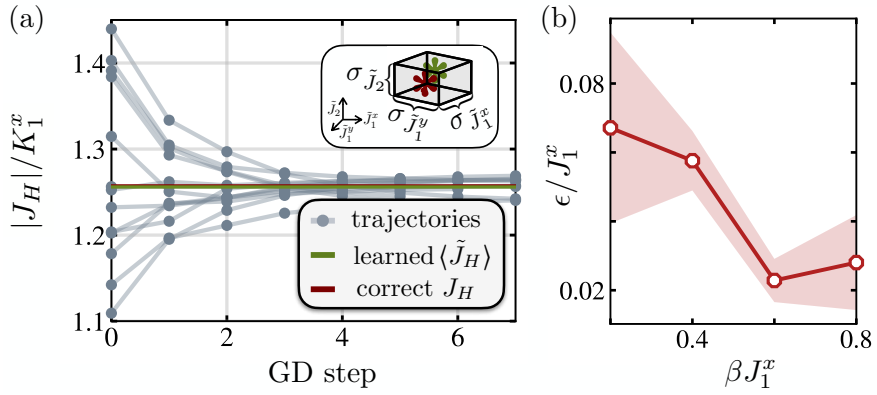

Figure 6.2: **Hamiltonian reconstruction.** (a) Learning the Hamiltonian's coupling parameters using GD. We start the GD from randomized positions in coupling space and plot the resulting paths of $|J_H| = \sqrt{(J_1^x)^2 + (J_1^y)^2 + (J_2)^2}$ during the GD. For each run, correlations are approximated using 3000 measurements. The actual Hamiltonian's parameters are marked by the red solid line. The green line results from averaging $|J_H|$ after 7 GD steps. The inset shows in more detail the resulting averages of $\{J_H\}$ (green asterisk), with their corresponding errors (black box). For all three parameters, the actual parameters (red asterisk) match the predicted ones. (c) ℓ_2 error of the learned and actual parameters for a 12×2 system after reaching convergence for varying temperature $\beta K_1^x \sim 0.2 \ldots 0.8$. Errors to the mean are indicated by the colored background. Intermediate temperatures are found to work best for a reconstruction.

peratures close to the ground state, the energy landscape $\mathcal{G}$ is nearly flat, resulting in bad reconstructions. Similarly, for $T/J \gg 1$ measured correlations only weakly depend on the underlying coupling parameters (e.g. the infinite temperature state is identical for all interaction strengths), which hinder precise reconstructions.

This illustrates that, when attempting to reconstruct the Hamiltonian from ground state measurements, the above method is not applicable. For such cases, tailored ground state schemes have been developed, where solving an eigenstate problem of a correlation matrix enables the reconstruction of the underlying Hamiltonian using only local measurements [247]. However, here we will primarily be interested in reconstructing effective Hamiltonians in the mixD t-J model at elevated temperatures, where the charges do not bind into stripes, and hence the above gradient descent methods can be applied.

Lastly, we note here that, in different contexts, the problem of reconstructing a Hamiltonian from measured correlations via machine learning schemes [248–251] has attracted considerable interest in recent years, including certifying quantum simulation devices [247].

6.3 Spin Hamiltonian reconstruction

In Chapter 5, we analyzed the mixD t-J in detail. For completeness, we reprint the model's Hamiltonian,

$$\hat{\mathcal{H}} = -t \sum_{\langle \mathbf{i},\mathbf{j} \rangle_x, \sigma} \hat{\mathcal{P}}_{GW} (\hat{c}^\dagger_{\mathbf{i},\sigma} \hat{c}_{\mathbf{j},\sigma} + \text{h.c.}) \hat{\mathcal{P}}_{GW} + J \sum_{\langle \mathbf{i},\mathbf{j} \rangle} \left(\hat{\mathbf{S}}_\mathbf{i} \cdot \hat{\mathbf{S}}_\mathbf{j} - \frac{\hat{n}_\mathbf{i} \hat{n}_\mathbf{j}}{4} \right), \tag{6.5}$$

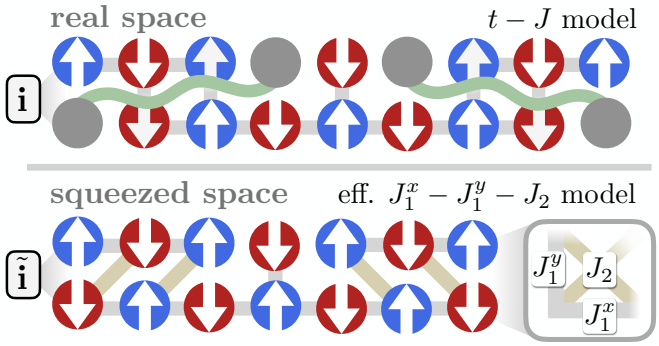

Figure 6.3: **Hole-motion-induced frustration**. Schematic of how hole hopping induces frustration in the spin background. Upper panel: Snapshot of holes moving through a Néel background. Spatial separation of holes on neighboring legs lead to the formation of geometric strings (green wiggly lines) costing magnetic energy. Lower panel: Upon transforming the snapshot to squeezed space, originally vertical bonds J_1^y in between two holes on neighboring legs become effective diagonal couplings J_2. The resulting energy penalty of aligned diagonal spins leads to frustration in the magnetic background.

where hopping only takes places along the x-direction, but spin-exchange is two-dimensional. In particular, we have demonstrated in Chapter 5 how hidden AFM correlations in the mixD t-J model result in the formation of a remarkably resilient stripe phase (i.e. a coupled charge- and spin-density wave), with critical temperatures on the order of the magnetic coupling $J/2$. Above these critical temperatures of charge- and spin-density wave formation, holes were found to form a deconfined chargon gas, i.e., a phase without order.

In the following, we focus on the latter regime, and study in detail how hole motion distorts the spins in the background. The effect is qualitatively depicted in Fig. 6.3. The upper panel shows an (idealized) real space snapshot of holes moving through an AFM Néel background. Bonds correspond to AFM interactions in the instantaneous charge configuration, illustrated by gray lines. In between holes on neighboring legs, spins are aligned, leading to a linearly increasing magnetic energy penalty via the formation of geometric strings (depicted by green wiggly lines). When squeezing out the holes, Fig. 6.3, the initial Néel order is restored in the isolated spin background. However, interactions on diagonal bonds emerge (ocher lines), which cause geometric frustration of the spins in squeezed space. From now on, we refer to lattice sites in real and squeezed space by $\mathbf{i}$ and $\tilde{\mathbf{i}}$, respectively, as also indicated in Fig. 6.3.

6.3.1 Quantifying frustration

In order to quantify the arising frustration on the squeezed lattice, we simulate the mixD t-J model, Eq. (6.5), at finite temperature and fixed doping using imaginary time evolution schemes (purification) via matrix product states, see also Chapter 5. For faster, more controllable numerics and to prevent post-selection of snapshots, we again implement the system's full U(1) symmetries in each ladder leg, i.e., we work in an ensemble where we allow for thermal spin fluctuations but keep the number of holes in each ladder leg constant. In particular, we simulate the mixD t-J model at intermediate temperature $T/J = 5/3$ ($\beta J = 0.6$), which lies inside the

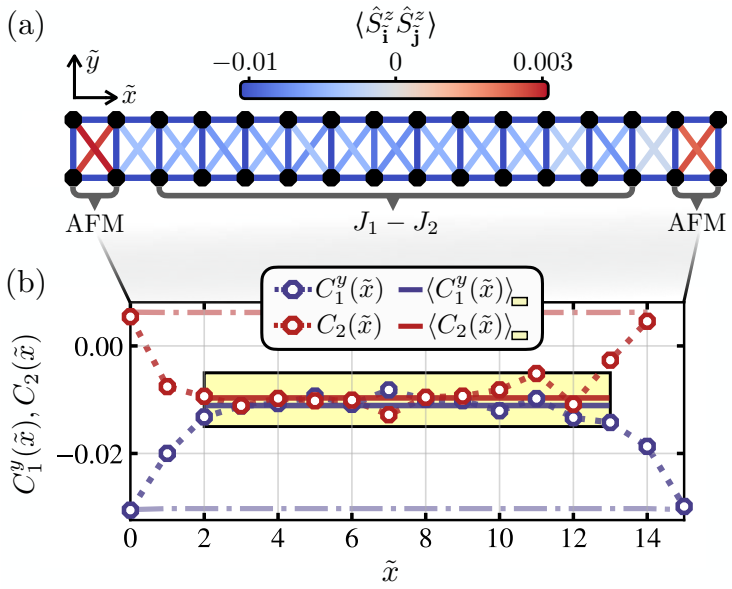

Figure 6.4: **Correlations in squeezed space.** (a) Spin-spin correlations $\langle \hat{S}^z_{\tilde{\mathbf{i}}} \hat{S}^z_{\tilde{\mathbf{j}}} \rangle$ on the squeezed lattice of an initially 20×2 mixD t-J ladder, with $n^h = 0.2$, $T/J = 5/3 \sim 1.67$, and using 20000 snapshots. In the bulk of squeezed space, hole motion distorts the spin background, leading to negative correlations across diagonals. In this region, effective J_1-J_2 physics is expected, as captured by the Hamiltonian Eq. (6.6). As holes are rarely located at the open boundaries of the system, correlations are left almost undisturbed and are of AFM type. Correlations along nearest neighbors in x go beyond the cutoff of the colorbar. (b) Rung $C_1^y(\tilde{x}) = \langle \hat{S}^z_{[\tilde{x},\tilde{0}]} \hat{S}^z_{[\tilde{x},\tilde{1}]} \rangle$ and diagonal $C_2(\tilde{x}) = \langle \hat{S}^z_{[\tilde{x},\tilde{0}]} \hat{S}^z_{[\tilde{x}+1,\tilde{1}]} \rangle + \langle \hat{S}^z_{[\tilde{x}+1,\tilde{0}]} \hat{S}^z_{[\tilde{x},\tilde{1}]} \rangle$ correlations. In the central bulk region of the ladder, correlations are approximately constant, the average being used as the input for J_1^x-J_1^y-J_2 Hamiltonian reconstructions. In particular, we discard the two outer sites in squeezed space, as illustrated by the yellow box. Dashed-dotted lines correspond to rung and diagonal correlations for a nearest-neighbor Heisenberg model with $\beta J_1^x = \beta J_1^y \sim 0.44$, which captures the physics at the edges, but fails to describe the correlations in the bulk of squeezed space. The introduction of diagonal (frustrating) bonds is hence an essential step to describe the spin system on the squeezed lattice

chargon gas phase (i.e. no charge- and spin-density waves form) and, furthermore, is within the operating temperature regime of quantum gas microscopes. Additionally, as discussed in Sec. 6.2, intermediate temperature regimes yield best reconstruction results from projective measurements.

From the thermal MPS at inverse temperature β, we sample uncorrelated snapshots of the corresponding Gibbs state. After post-processing the individual measurements by squeezing out the holes, spin-spin correlations $\langle \hat{S}^z_{\tilde{\mathbf{i}}} \hat{S}^z_{\tilde{\mathbf{j}}} \rangle$ can directly be evaluated in squeezed space. In Fig. 6.4 (a), nearest-neighbor as well as diagonal spin-spin correlations are shown on the squeezed lattice. In the bulk of the squeezed ladder, both nearest neighbor as well as diagonal correlators are negative and comparable in magnitude, signaling strong frustration in the spin background induced by the motion of the holes. In contrast, at both edges of the ladder, low average hole concentrations lead to only marginal perturbations of the spin background—resulting in AFM type correlations that are negative (positive) along nearest (diagonal) neighbors.

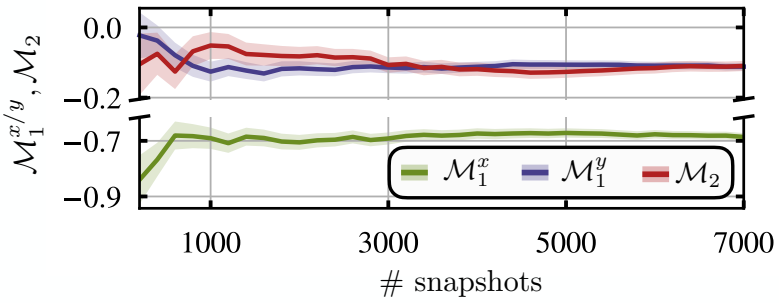

Figure 6.5: **Correlations from snapshots.** Summed correlations in the boxed bulk in Fig. 6.4 along rungs, legs and diagonals for varying snapshot set sizes. Light regions correspond to the standard error to the mean. After a few thousand measurements, convergence of the correlator proxies is reached. For the Hamiltonian reconstruction of the effective spin model in squeezed space, we use 7000 snapshots.

Fig. 6.4 (b) shows nearest-neighbor rung (blue) and diagonal (red) correlators in more detail. Dashed-dotted lines correspond to rung and diagonal correlations for a Heisenberg ladder with solely nearest-neighbor couplings (where $\beta J_1^x = \beta J_1^y = 0.44$), which describe the physics at the edges qualitatively well, but fail to reproduce the measured correlations in the bulk. Due to the frustrating effect of the hopping holes, diagonal couplings need to be taken into account to accurately capture the physics of the squeezed background. To this end, we introduce an effective J_1^x-J_1^y-J_2 Heisenberg model on the squeezed lattice

$$\hat{\mathcal{H}}_{\{J_H\}} = \sum_{\mu=x,y} J_1^\mu \sum_{\langle \tilde{\mathbf{i}},\tilde{\mathbf{j}}\rangle_\mu} \hat{\mathbf{S}}_{\tilde{\mathbf{i}}} \cdot \hat{\mathbf{S}}_{\tilde{\mathbf{j}}} + J_2 \sum_{\langle\langle \tilde{\mathbf{i}},\tilde{\mathbf{j}}\rangle\rangle_{\text{diag}}} \hat{\mathbf{S}}_{\tilde{\mathbf{i}}} \cdot \hat{\mathbf{S}}_{\tilde{\mathbf{j}}}. \tag{6.6}$$

As in Eq. (6.1), the Hamiltonian is defined through (variable) parameters $\{J_H\} = \{J_1^x, J_1^y, J_2\}$, corresponding to coupling strengths of neighbouring spins in x, y and diagonal direction on the squeezed lattice (underlined by the indices $\tilde{\mathbf{i}}$ in Eq. (6.6)).

To quantitatively pin down the strength of the arising frustration, we perform a Hamiltonian reconstruction with input Hamiltonian $\hat{\mathcal{H}}_{\{J_H\}}$, Eq. (6.6), together with the measured spin-spin correlations in squeezed space. Couplings in $\hat{\mathcal{H}}_{\{J_H\}}$ are chosen to be homogeneous throughout the bulk of squeezed space, justified by the approximately constant behavior of correlations in the bulk region of Fig. 6.4 (b)—solid lines are averages of the correlations over the marked box. Akin to the discussion in Sec. 6.2, many-body snapshots along a single spin axis—here chosen along z—are sufficient to reconstruct the full effective Hamiltonian, which is a consequence of the underlying SU(2) symmetry of the mixD t-J model.

We follow the procedure introduced in Sec. 6.2, and minimize the objective function $\mathcal{G}$ over all possible coupling parameters $\{J_H\}$, see Eq. (6.2). In this case, $\mathcal{M}_1^\mu = \sum'_{\langle \tilde{\mathbf{i}},\tilde{\mathbf{j}}\rangle_\mu} \langle \hat{S}^z_{\tilde{\mathbf{i}}} \hat{S}^z_{\tilde{\mathbf{j}}} \rangle$, $\mathcal{M}_2 = \sum'_{\langle\langle \tilde{\mathbf{i}},\tilde{\mathbf{j}}\rangle\rangle_{\text{diag}}} \langle \hat{S}^z_{\tilde{\mathbf{i}}} \hat{S}^z_{\tilde{\mathbf{j}}} \rangle$ are the summed correlations along nearest- and diagonal neighbors within the considered window in the bulk of squeezed space, underlined by the yellow box in Fig. 6.4. Fig. 6.5 shows how approximations for $\mathcal{M}_1^{x,y}, \mathcal{M}_2$ quickly saturate with the number of used snapshots, suggesting a qualitatively satisfactory proxy for the spin-spin correlators after a few thou-

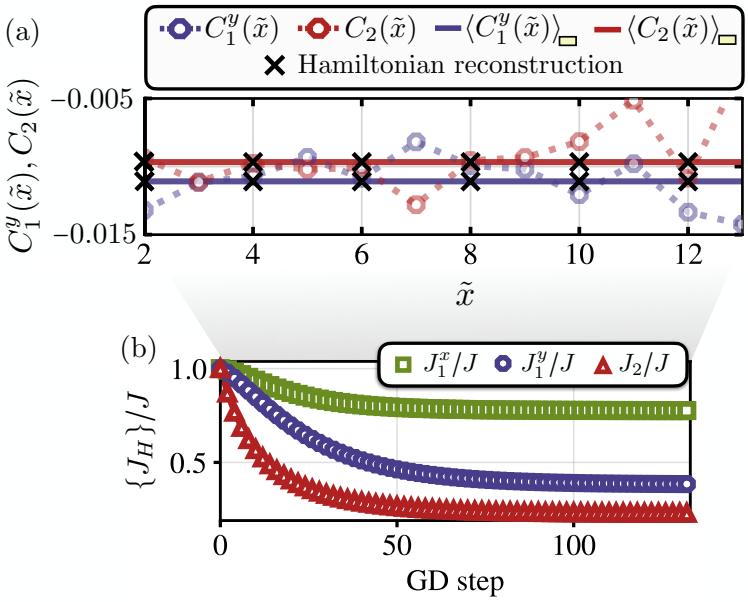

Figure 6.6: **Hamiltonian reconstruction.** (a) A single Hamiltonian reconstruction run of the effective spin Hamiltonian in squeezed space of an originally 20×2 mixD t-J ladder, with $n^h = 0.2$ and at $T/J = 5/3 \sim 1.67$. Results show perfect agreement between the correlations emerging from a reconstructed effective J_1^x-J_1^y-J_2 Heisenberg model (black crosses) and bulk averaged correlations of the doped mixD model in squeezed space (solid lines). The shown data corresponds to the boxed region in Fig. 6.4 (b). (b) The corresponding GD path for couplings $J_1^x/J, J_1^y/J, J_2/J$. The GD is initialized with parameters $J_1^x/J = J_1^y/J = J_2/J = 1$. Only every second data point is shown for illustrative purposes. Convergence is reached after ∼100 GD steps.

sand projective measurements. For the rest of the analysis, we use sample sizes of 7,000 snapshots for each approximation of the correlations.

Given a size $L_x \times L_y$ of the mixD system, the dimensions of the reconstructed J_1^x-J_1^y-J_2 Heisenberg ladder on the squeezed lattice is given by $\tilde{L}_x \times \tilde{L}_y = (1 - n^h)L_x \times L_y$. The temperature β^{-1} of the J_1^x-J_1^y-J_2 Heisenberg Hamiltonian is chosen identically to the underlying simulations of the mixD t-J system during the GD. Note that this choice might not reflect the actual effective temperature of the spin background. However, the relevant ratios J_1^y/J_1^x, J_2/J_1^x that quantify the frustration in the system are independent of the true temperature of the squeezed magnetic environment.

Hamiltonian reconstruction results for a single run are presented in Fig. 6.6 (a). Evaluated correlations of the best fitting J_1^x-J_1^y-J_2 model are seen to perfectly match the measured mean correlations in the bulk of squeezed space, hence strongly supporting that the physics of the magnetic background in the mixD t-J model is well captured by J_1^x-J_1^y-J_2 Heisenberg interactions on a square lattice. We have explicitly checked that independent of the initially chosen parameter values for the GD, $\{J_H\}$ always converge to identical points in parameter space, underlining the robustness of the GD scheme. One example where initial parameters are set to equal values (i.p. $J_1^x/J = J_1^y/J = J_2/J = 1$) is shown in Fig. 6.6 (b). Converge is observed after $\sim$ 100 GD steps.

To characterize and classify the reconstructed spin states in squeezed space as a function of doping, we perform ground state calculations of the J_1^x-J_1^y-J_2 Heisenberg model and evaluate the

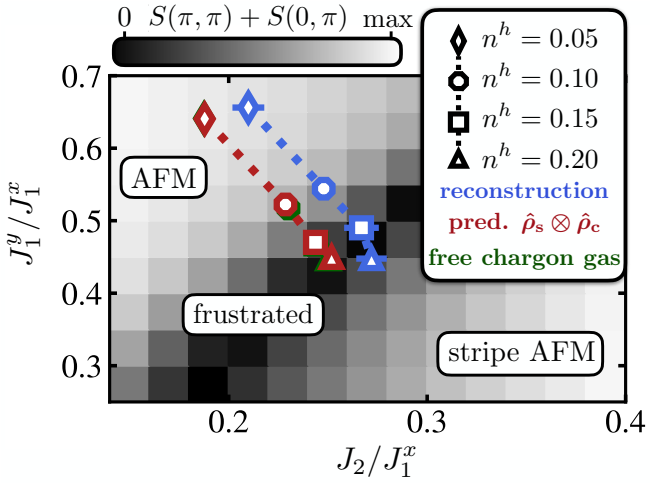

Figure 6.7: **Hole-motion-induced spin frustration**. Hamiltonian reconstruction results (blue) for hole dopings $n^h = 0.05 \ldots 0.2$ of a mixD t-J ladder with $t/J = 3$, $L_x \times L_y = 20 \times 2$ and $T/J = 5/3 \sim 1.67$. Reconstructions of squeezed space according to the input J_1^x-J_1^y-J_2 Heisenberg Hamiltonian, Eq. (6.6), are presented in a J_1^y/J_1^x, J_2/J_1^x diagram. Light regions in the background signal the presence of either AFM or stripe AFM order in the purely magnetic J_1^x-J_1^y-J_2 model in the ground state by plotting the sum of the spin structure factors $S(\pi,\pi) + S(0,\pi)$. Dark regions correspond to a highly frustrated regime without apparent order. Upon doping the system, the background spins are driven into a strongly frustrated state. Error bars correspond to the standard error to the mean when averaging over ten reconstruction runs. Red connected symbols show theoretical expectations assuming no spin-hole correlations in the mixD t-J model, i.e., $\hat{\rho} = \hat{\rho}_s \otimes \hat{\rho}_c$, evaluated via Eq. (6.8) and (6.9). Green data points show evaluation of Eq. (6.8) and (6.9) for a free chargon gas (non-interacting spinless fermions).

static spin structure factor (SSSF) given by

$$S(q_x, q_y) = \frac{1}{L_x^2 L_y^2} \sum_{\mathbf{i},\mathbf{j}} e^{i\mathbf{q}\cdot(\mathbf{i}-\mathbf{j})} \langle \hat{\mathbf{S}}_\mathbf{i} \cdot \hat{\mathbf{S}}_\mathbf{j} \rangle \,. \tag{6.7}$$

For $J_1^x = J_1^y = J_1$, it has been demonstrated that a highly frustrated magnetic regime exists for $0.4 \lesssim J_2/J_1 \lesssim 0.6$ that is sandwiched by a Néel and stripe AFM phase [252–257]. Though the exact nature of the non-magnetic ground state in the frustrated regime is still controversial, it remains a promising candidate for the realization of a quantum spin liquid phase possibly described by Anderson's resonating valence bond (RVB) paradigm [131, 135, 258–263].

We evaluate the hybrid order parameter $S(\pi,\pi) + S(0,\pi)$ in the $J_1^y/J_1^x - J_2/J_1^x$ parameter space, signaling whether AFM or stripe AFM order exists in the system. Dark regions in the background of Fig. 6.7 (b) correspond to no apparent spin ordering, and hence signal the existence of a strongly frustrated spin state akin to the observations in the homogeneous J_1-J_2 model.

The reconstruction process, consisting of (i) approximating correlations in squeezed space using snapshots and (ii) performing the GD, is repeated a total number of ten times. Averaging over the converged results of all runs leads to the main result of this chapter, presented in Fig. 6.7 by blue connected symbols. We observe how the spin state in squeezed space rapidly approaches the highly frustrated regime upon increasing the doping level, until seemingly sat-

urating within it to a certain configuration $\{J_H^*\}$. We note that at the considered system sizes, boundary effects become especially pronounced at low hole concentrations $n^h = 0.05, 0.1$. This leads to a slow saturation of the correlations in the bulk of squeezed space, which in turn shifts effective couplings averaged within the fixed window to smaller (larger) values of J_2/J_1^x (J_1^y/J_1^x). In the thermodynamic limit, we in fact expect any finite hole doping in the chargon gas phase to drive the squeezed spin system into a highly frustrated state. We will, however, not go into more detail here, and refer to the Sec. 6.7.1 for a more quantitative discussion and an analysis of longer ladders of size 40×2.

The reconstruction scheme as introduced above takes into account spin-spin correlations directly measured in squeezed space, hence providing an unbiased platform for the analysis of the spin background by explicitly including the back-action of hole motion on the spins. Motivated by the separation of energy scales in the mixD t-J model with $t/J \gg 1$, we make the ansatz of a fully decoupled thermal density matrix given by separate spin (s) and charge (c) sectors, $\hat{\rho} = \hat{\rho}_\mathrm{s} \otimes \hat{\rho}_\mathrm{c}$, and aim to test the resulting predictions against the unbiased reconstruction output.

Within the separation ansatz, interaction strengths in squeezed space are obtained by conditioned probabilities in real space [242]. Two nearest neighbors along x in squeezed space interact only if the corresponding sites are nearest neighbors along x in real space, leading to an effective coupling strength (assuming homogeneous hole density $\langle n_\mathbf{i}^h \rangle = n^h$)—see also the supplementary materials of Ref. [242],

$$J_1^x/J \propto \langle (1-\hat{n}_\mathbf{i}^h)(1-\hat{n}_{\mathbf{i}+\mathbf{e}_x}^h)\rangle = 1 - 2n^h + g_x^{(2)}. \tag{6.8}$$

Here, $g_\mu^{(2)} = \langle \hat{n}_\mathbf{i}^h \hat{n}_{\mathbf{i}+\mathbf{e}_\mu}^h \rangle$ with $\mathbf{e}_\mu$ the unit vector in direction $\mu = x, y$. Vertical and diagonal bonds are obtained similarly by conditioning the correlators by the total number of holes to the left of site $\mathbf{i}$, $\nu_{\mathbf{i}=[x,y]}^h = \sum_{x'<x} N_{[x',y]}^h$, with $N_\mathbf{i}^h$ the number of holes on site $\mathbf{i}$. Diagonal coupling strengths J_n spanning a distance of $\Delta x = n-1$ (vertical bonds J_1^y correspond to J_1 in this notation) are then given by

$$J_n/J \propto \langle (1-\hat{n}_\mathbf{i}^h)(1-\hat{n}_{\mathbf{i}+\mathbf{e}_y}^h)\rangle_{|\nu_\mathbf{i}^h - \nu_{\mathbf{i}+\mathbf{e}_y}^h| = n-1}. \tag{6.9}$$

We evaluate the estimated effective couplings, Eqs. (6.8) and (6.9), using the mixD t-J snapshots. Results are shown by red connected symbols in Fig. 6.7. We observe that the theoretically predicted expectations for J_1^x, J_1^y, J_2 within the separation ansatz agree remarkably well with the full reconstruction. Deviations from the above description, in particular the consistent underestimation of relative diagonal coupling strengths J_2/J_1^x, are likely caused by non-trivial spin-hole correlations in the mixD t-J model, which are implicitly included in the reconstruction analysis but discarded in the separation ansatz.

We note that the conditioned correlators Eqs. (6.8) and (6.9) calculated from mixD t-J snapshots are numerically almost identical to calculations of free spinless fermions (free chargon gas). We take snapshots of free fermions hopping on a lattice, and evaluate the same hole-hole correlators as above. This yields numerically almost indistinguishable results from the mixD snapshots, as illustrated in Fig. 6.7, where effective parameters J_1^x, J_1^y, J_2 are estimated both from

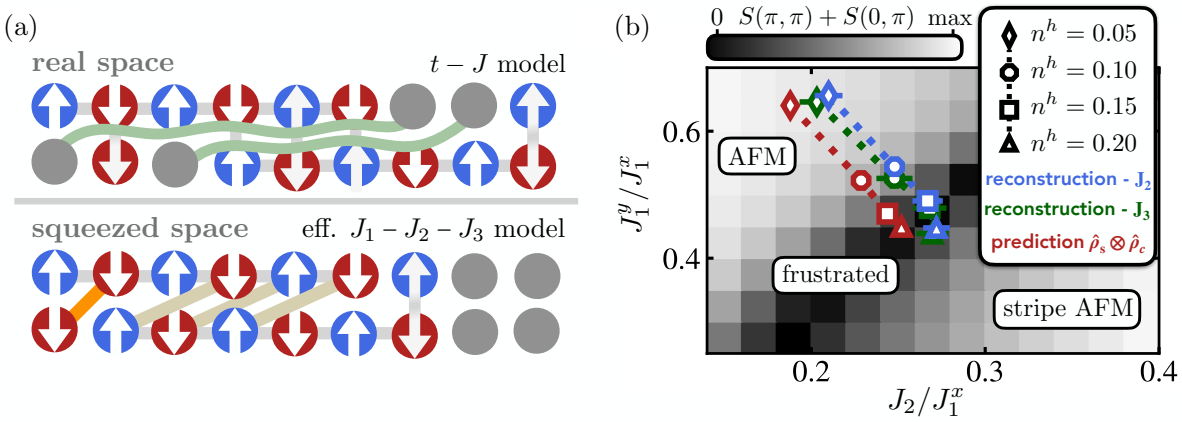

Figure 6.8: **Hamiltonian reconstruction including longer-range couplings.** (a), Schematic illustration of how longer-range bonds appear in the effective magnetic system in squeezed space. (b), Reconstruction results when including terms up to J_2 (blue connected symbols) and J_3 (green connected symbols). Though small corrections are visible, qualitative results in comparison to the separation ansatz (red connected symbols) remain unchanged.

mixD (red) as well as free chargon (green) snapshots. This lets us conclude that holes, while behaving like free fermions in the chargon gas phase of the mixD t-J model, nevertheless correlate non-trivially with the spin background.

6.3.2 Longer-range interactions

So far, our approach has been to restrict the effective Hamiltonian Eq. (6.6) to first order diagonal couplings J_2. We now aim to assess the systematic error related to this approximation. Fig. 6.8 (a) qualitatively depicts how longer-range diagonal couplings J_3 enter the effective description in squeezed space. When two holes on each ladder leg are separated by some real space distance, geometric strings overlap in a given region. Original vertical bonds that are cut by two (in general n) geometric strings lead to effective couplings spanning a distance of $\Delta x = 2$ ($\Delta x = n$), corresponding to bonds J_3 (J_n). This is formalized by the conditioned correlators in real space, which take into account that a non-zero difference between holes on neighboring legs lead to multiple geometric strings cutting vertical bonds, cf. Eq. (6.9).

We now reconstruct the effective spin-Hamiltonian from measurements in squeezed space, here by explicitly including bonds up to J_3 on the squeezed lattice. The corresponding J_1-J_2-J_3 type Hamiltonian that we reconstruct reads

$$\hat{\mathcal{H}}_{J_1^x,J_1^y,J_2,J_3} = \sum_{\mu=x,y} J_1^\mu \sum_{\langle \tilde{\mathbf{i}},\tilde{\mathbf{j}}\rangle_\mu} \hat{\mathbf{S}}_{\tilde{\mathbf{i}}} \cdot \hat{\mathbf{S}}_{\tilde{\mathbf{j}}} + J_2 \sum_{\langle\langle \tilde{\mathbf{i}},\tilde{\mathbf{j}}\rangle\rangle_{\text{diag}_2}} \hat{\mathbf{S}}_{\tilde{\mathbf{i}}} \cdot \hat{\mathbf{S}}_{\tilde{\mathbf{j}}} + J_3 \sum_{\langle\langle \tilde{\mathbf{i}},\tilde{\mathbf{j}}\rangle\rangle_{\text{diag}_3}} \hat{\mathbf{S}}_{\tilde{\mathbf{i}}} \cdot \hat{\mathbf{S}}_{\tilde{\mathbf{j}}}. \tag{6.10}$$

Reconstruction results are presented in Fig. 6.8 (b). We observe that corrections of the reconstructed parameter values when considering terms up to J_3 are very minor—underlining how the physics in squeezed space is well captured by nearest-neighbor and diagonal frustrating couplings, i.e., J_1^x, J_1^y, J_2.

To corroborate the above, we estimate the magnitude of longer-range couplings J_n by eval-

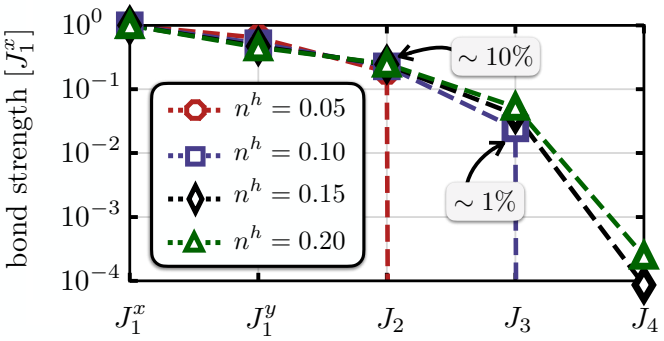

Figure 6.9: **Significance of longer ranged couplings.** By evaluating the conditioned correlators, Eqs. (6.8) and (6.9), we estimate the strengths of longer ranged couplings up to J_4. In units of the strongest interaction J_1^x, first order diagonal bonds J_2 are of the order of $\sim$ 10%, whereas couplings J_3 reach relative magnitudes of a few percent. Due to the finite system size, J_3 (J_4) and higher order couplings drop to zero for $n^h = 0.05$ ($n^h = 0.1$), as the corresponding conditioned probabilities Eq. (6.9) vanish for a single (two) hole(s) per leg.

uating the conditioned correlators Eq. (6.9) for $n \geq 3$. Relative strengths of couplings up to J_4 are depicted in Fig. 6.9, where a rapid decrease with real space distance is observed. The relative strength of J_2 in units of J_1^x is of order $\sim$ 10%, cf. Fig 6.7. J_3, on the other hand, reaches only a few percent in terms of J_1^x, suggesting that $n \geq 3$ couplings are negligible for the effective description.

6.4 Charge Hamiltonian reconstruction

The previous section has focused on Hamiltonian reconstruction schemes to learn about the effective spin physics in the background. Conversely, we can ask what effective interactions the spin background imposes on the charges. In particular, this approach may provide insights into the nature of pairing in Fermi-Hubbard-type models by reconstructing the pairwise attraction between dopants.

To this end, we use finite-temperature simulations of mixed-dimensional (mixD) ladders of size $L_x \times L_y = 12 \times 2$, focusing on a single doping level with $N_\ell^h = 2$ holes on each ladder leg. We compute charge-charge correlations of the dopants by evaluating the $g^{(2)}$ function between the two legs ($\Delta_y = 1$) for varying Δx, given by

$$g^{(2)}(\Delta x) = \sum_x \sum_\pm \left(\frac{\langle \hat{n}^h_{[x,0]} \hat{n}^h_{[x\pm\Delta x,1]} \rangle}{\langle \hat{n}^h_{[x,0]} \rangle \langle \hat{n}^h_{[x\pm\Delta x,1]} \rangle} - 1 \right). \tag{6.11}$$

The goal is to describe the holes as interacting spinless particles and reconstruct the interactions such that the resulting $g^{(2)}$ function of the spinless fermions matches that of the mixD system. To achieve this, we define the following ansatz Hamiltonian with spinless fermionic

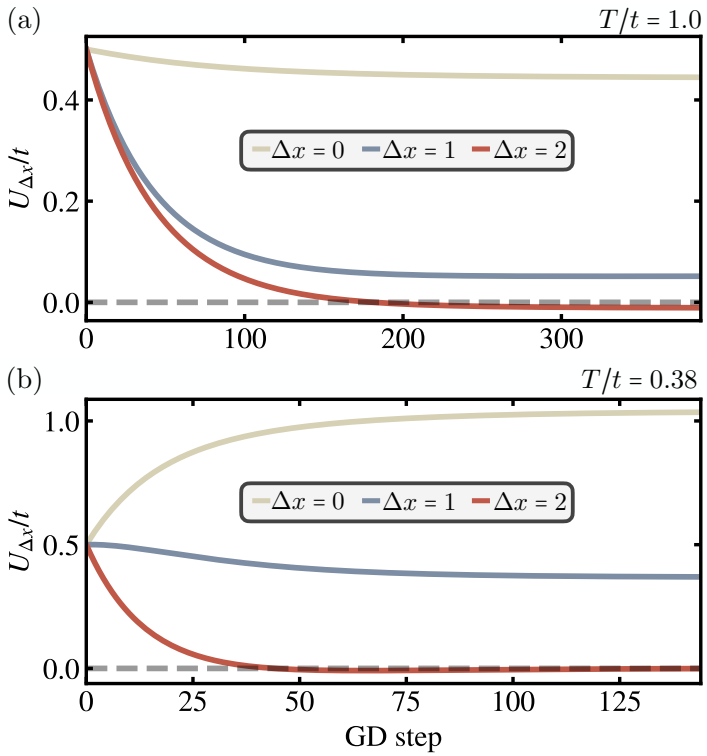

Figure 6.10: **Charge Hamiltonian reconstruction.** Effective attractions reconstructed from the mixD t-J model as a function of gradient descent steps for temperatures $T/t = 1.0$ and $T/t = 0.38$. In both cases, the system size is $L_x \times L_y = 12 \times 2$, and $t/J = 3$.

operators $\hat{c}_\mathbf{i}$ and densities $\hat{n}_\mathbf{i}$,

$$\hat{\mathcal{H}}_{\text{slf}} = -t \sum_{\langle \mathbf{i},\mathbf{j} \rangle_x} \left(\hat{c}_\mathbf{i} \hat{c}_\mathbf{j}^\dagger + \text{H.c.} \right) - \sum_x \sum_{\Delta x} U_{\Delta x} \sum_{\pm} \hat{n}_{[x,0]} \hat{n}_{[x \pm \Delta x, 1]}. \tag{6.12}$$

Here, the sign convention of the interaction terms is chosen such that positive $U_{\Delta x}$ corresponds to attractive interactions. Additionally, we neglect interactions between holes along each leg, focusing instead on interactions between holes in neighboring legs. Since hopping is suppressed in this direction, any finite interaction must arise from the spin background.

The results of the gradient descent procedure are presented in Fig. 6.10. Starting with an initial value of $U_{\Delta x} = 0.5$ and reconstructing interactions up to $\Delta x = 2$, we observe that after convergence, effective attractions between particles on neighboring rungs emerge at both temperatures. While U_2 remains consistent with zero, U_0 and U_1 attain finite values, with their magnitude increasing as the temperature decreases. This observation is corroborated in Fig. 6.11, which shows the converged values of $U_{\Delta x}$ across a range of temperatures.

Short-range spin correlations appear to induce an attractive potential between holes even for $T/J > 1$. Below $T/J < 1$ (or equivalently $T/t \lesssim 0.33$), this induced attraction grows significantly. These results highlight how, in the mixD ladder, spin-spin interactions facilitate the formation of strongly bound hole pairs along the y-direction. This mechanism ultimately provides the glue for the formation of stable stripe phases at lower temperatures, $T/J \lesssim 0.5$, in

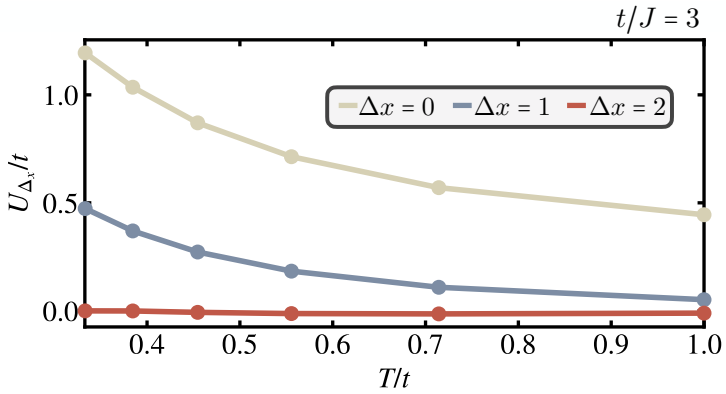

Figure 6.11: **Charge Hamiltonian reconstruction.** Effective attractions reconstructed from the mixD t-J model as a function of temperature. The system size is $L_x \times L_y = 12 \times 2$, and $t/J = 3$. While U_2 remains negligible across all temperatures, significant NN and NNN attractions across the rungs are observed.

wider systems.

The outlined scheme for extracting effective interactions between dopants presents a promising route to deepen our understanding of hole pairing mechanisms in the 2D Fermi-Hubbard model. Preliminary results based on experimental data from the MPQ Lithium quantum gas simulator similarly suggest an effective attraction between dopants compared to free fermions. However, the presence of significant doublon-hole pairs in the system complicates the analysis, as these unphysical dopants influence hole-hole correlations. A refined approach is required for quantitative accuracy, and we leave this as an outlook for future work, refraining from a more detailed discussion in this thesis.

6.5 Spin-charge separation in 1D

Lastly, we apply the above concepts to experimental snapshots from an ultracold atom experiment. In particular, we shall apply our squeezed space Hamiltonian reconstruction scheme and recover the effective spin-Hamiltonian of the doped 1D FH model using experimentally obtained snapshots in the Lithium ultracold Fermi gas at MPQ [242]. The author of this thesis particularly acknowledges Timon A. Hilker and Immanuel Bloch for providing the data.

In the 1D FH model, the ground state wave function is known to factorize into fully separated spin and charge channels in the strongly interacting limit, leading to the celebrated phenomenon of spin-charge separation (i.e., the exact absence of spin-hole correlations) [237]. In 1D, is has been demonstrated that hidden spin correlations—distorted in real space by the motion of holes—can be revealed by transformation to squeezed space, effectively described by a 1D Heisenberg Hamiltonian with nearest neighbor interaction $J_1^x(n^h)$ on the squeezed lattice [242, 264], cf. Fig. 6.12 (a),

$$\hat{\mathcal{H}}_{J_1^x} = J_1^x \sum_{\langle \tilde{i},\tilde{j} \rangle} \hat{\mathbf{S}}_{\tilde{i}} \cdot \hat{\mathbf{S}}_{\tilde{j}}. \tag{6.13}$$

Results are shown in Fig. 6.12 (b) by blue data points, where a consistent decrease of effec-

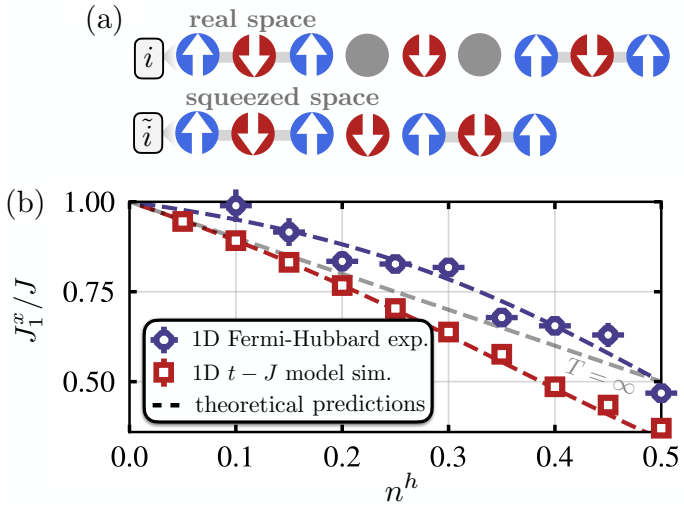

Figure 6.12: **Reconstructing 1D systems from experiments.** (a) Illustration of snapshots of the 1D FH model in real (top) and squeezed (bottom) space. (b) Evaluation of 1D FH snapshots of a cold atom experiment [242]. Reconstructions of the effective spin-Hamiltonian Eq. (6.13) in squeezed space for varying hole densities are shown by blue data points. Red data points correspond to reconstructions of the 1D t-J model, which we simulate using MPS for parameters as estimated in [242], i.e., $t/J = 1.82$ and $T/J = 0.87$. Results are compared to theoretical predictions (dashed lines) assuming spin-charge separation, Eqs. (6.14), (6.15), showing a good match with the reconstructed data. In particular, higher order hopping processes lead to the FH measurement reconstructions of J_1^x/J to consistently lie above predictions for the t-J model. Error bars are too small to be visible for the t-J reconstructions on the scale of the plot. The $T = \infty$ limit is shown by the grey dashed line, where a linear decrease $J_1^x = 1 - n^h$ is expected for both the FH and t-J model.

tive coupling strength $J_1^x(n^h)$ is observed upon increasing the hole doping—as expected from Eq. (6.8). For comparison, we further simulate the 1D t-J model with identical parameters as estimated in the experiment ($t/J = 1.82$, $T/J = 0.87$) and use sampled thermal snapshots in squeezed space for reconstructions, shown by red squares in Fig. 6.12 (b).

Effective interactions J_1^x/J reconstructed for an underlying 1D t-J model are seen to consistently lie below recovered coupling strengths of the 1D FH model. This discrepancy can be explained by higher order virtual processes in the FH model, which we illustrate by comparing the reconstructions to theoretical predictions within a separation ansatz. In the 1D t-J model, effective spin interactions in squeezed space can be calculated via Eq. (6.8), yielding

$$J_1^x/J = 1 - n^h - \frac{1}{1-n^h}\,[G(1)]^2\,. \tag{6.14}$$

Here, $G(d) = \frac{1}{\pi}\int_0^\pi dk \cos(kd) n_F(n^h, T)$ with $n_F(n^h, T)$ the Fermi-Dirac distribution of free chargons hopping on a 1D lattice at temperature T. When generalizing the t-J model to include next-nearest neighbor hole hopping processes mediated by doubly occupied virtual states as possible in the FH model, the effective coupling reads [242]

$$J_1^x/J = 1 - n^h + G(2), \tag{6.15}$$

with $J = 4t^2/U$ and U the Hubbard interaction.

Reconstructed values of J_1^x/J are observed to match the theoretical predictions for spin-charge separated systems well, depicted by red and blue dashed lines corresponding to Eqs. (6.14) and (6.15), respectively. This illustrates the (approximate) presence of spin-charge separation in the 1D FH and t-J model away from the $T = 0$ and strongly interacting limit, ultimately being mediated by their separation of energy scales.

6.6 Discussion

Using Hamiltonian reconstruction schemes, we have proposed a method to quantify hole-motion-induced frustration in a doped antiferromagnet by exploiting the full information stored in many-body snapshots. An advantage of the reconstruction process as introduced above is that the effective Hamiltonian—defined on the squeezed lattice—describes a reduced number of degrees of freedom, i.e., its local Hilbert space dimension is smaller than the one of the original system. In particular, the effective spin-Hamiltonian in squeezed space is of local dimension $d = 2$, rendering reconstructions for a given set of snapshots feasible even for larger system sizes. Experimental data of 2D systems that are inaccessible with classical simulations but within reach of current experiments could be used as input for a computational reconstruction of the spin background.

By analyzing a setting in mixed-dimensions, we have firmly established a quantitative connection between the doped mixD t-J model and the paradigmatic frustrated J_1-J_2 model. In particular, we demonstrated how hole motion drives the spin background into a highly frustrated state, whereby effective diagonal, frustrating magnetic bonds are induced on the squeezed lattice formed by the spins alone. Our results match theoretical predictions based on spin-charge separation reasonably well, differences being likely caused by weak remaining spin-hole correlations that deserve further investigation in the future. We note that due to the formation of stripes below temperatures $T \sim J/2$ in the mixD t-J model (see Sec. 5.2), its ground state is not directly related to a quantum spin liquid phase. Nevertheless, the ordered stripe phase at lower temperature may be merely covering a disordered quantum phase that dominates the physics of the model once the stripe order is melted away above the stripe critical temperature. As we will discuss in detail in the following chapter, this may lead to the appearance of peculiar hidden quantum critical points, where spin order in the squeezed background vanishes, and the pseudogap phase transitions into a regular Fermi liquid phase.

The reconstruction scheme can be generalized and applied to a variety of many-body phases. In the stripe phase, for instance, fluctuating holes bound into stripes are expected to lead to spatial modulations of the couplings between spins which can be reconstructed using the scheme we described. Furthermore, we have demonstrated that by reconstructing the charge sector, valuable insights into the effective interactions between dopants can be obtained. In particular, we have demonstrated that in the mixD setting, spin correlations lead to an effective attraction between hole dopants, ultimately providing the glue to form tightly bound pairs in ladders or

stripes in wider systems.

The presented method can be extended from mixD to fully 2D settings with homogeneous charge motion, where e.g. a weak easy-axis anisotropy of the Heisenberg interactions can enable string retracing [265] to remove dominant charge fluctuations and define a squeezed lattice. Applying the presented scheme to such snapshots could provide a microscopic perspective on the doped FH model and its relation to putative topological order in his enigmatic model. Making explicit use of all accessible correlation functions in squeezed space to further enhance the accuracy of the reconstructions is a promising direction for future research, for instance by directly comparing the distributions of measured and reconstructed snapshots.

Utilizing snapshots of a cold atom experiment simulating the 1D FH model, we already demonstrated the direct applicability of the reconstruction method to existing experimental data. From a converse experimental point of view, the above insights could further be utilized to effectively simulate the highly frustrated J_1-J_2 model by implementing the mixD setting and post-processing the measurements.

6.7 Additional data

We here present additional data to supplement the discussion in this section. First, we examine finite size effects in our numerical simulations, followed by a more detailed discussion of the finite-temperature numerics.

6.7.1 Finite size effects

We have argued in Sec. 6.3 that the observed flow into the highly frustrated regime when increasing the doping level (cf. Fig. 6.7) results from the finite size of the simulated ladders, and that in the thermodynamic limit we in fact expect any hole doping $n^h > 0$ to drive the spin background into a frustrated state. Fig. 6.13 shows correlations in squeezed space for all considered hole dopings $n^h = 0.05, 0.1, 0.15, 0.2$ in analogy to Fig. 6.7.

Solid lines illustrate averaged correlations in the fixed bulk window in squeezed space by discarding the outer two sites. For low hole concentrations, $n^h = 0.05, 0.1$, boundary effects are particularly noticeable. Correlations in squeezed space only slowly saturate, which in turn shifts effective couplings averaged within the fixed bulk window in squeezed space to smaller (larger) values of J_2/J_1^x (J_1^y/J_1^x). This effect ultimately results in the observed flow into the highly frustrated region when increasing hole doping as discussed in the main text.

To underline the former arguments, we simulate a long ladder of size 40×2, with $t/J = 3$ and at $T/J = 5/3$. Correlations in squeezed space are shown in Fig. 6.14 (a) for $n^h = 0.05$. When averaging the correlations in the bulk of squeezed space, we discard the outer eight sites, as illustrated by the yellow box. The larger system size leads to saturated correlations in the considered bulk window also for low hole concentrations.

After reconstructing effective J_1^x-J_1^y-J_2 Hamiltonians for the long ladder, we observe that even for small hole doping, $n^h = 0.05$, the spin system is reconstructed to lie inside the frustrated regime, as illustrated by blue symbols in Fig. 6.14 (b). We again observe that a separation ansatz

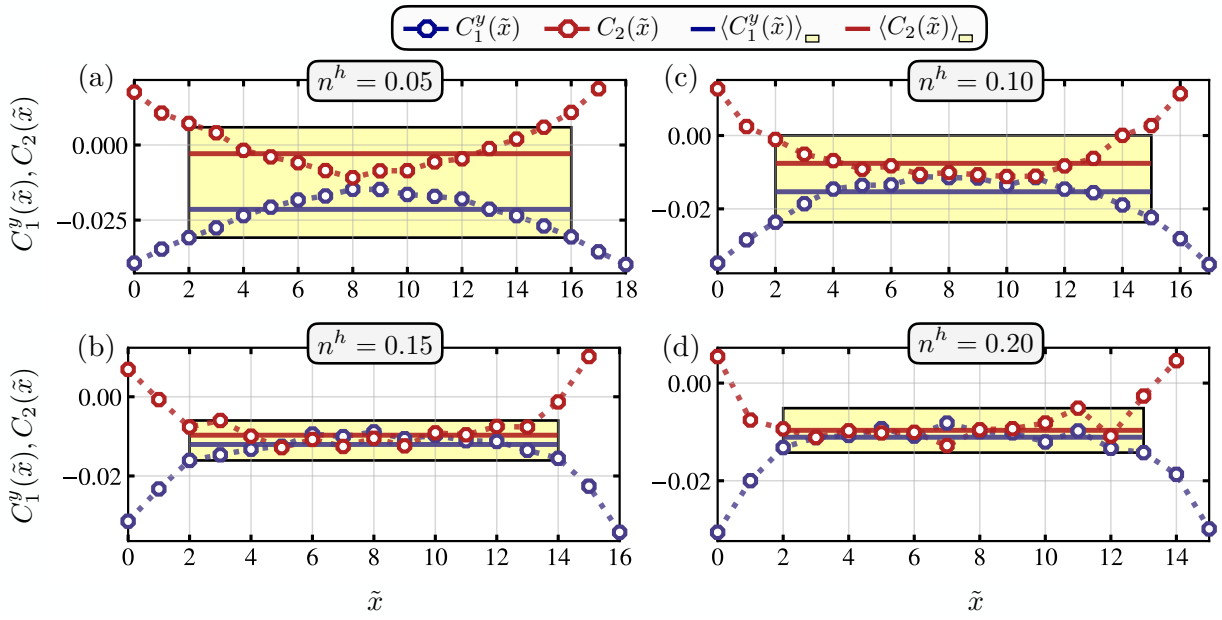

Figure 6.13: **Spin-spin correlations in squeezed space.** Correlations $C_1^y(\tilde{x}) = \langle \hat{S}^z_{[\tilde{x},\tilde{0}]} \hat{S}^z_{[\tilde{x},\tilde{1}]} \rangle$ and $C_2(\tilde{x}) = \langle \hat{S}^z_{[\tilde{x},\tilde{0}]} \hat{S}^z_{[\tilde{x}+1,\tilde{1}]} \rangle + \langle \hat{S}^z_{[\tilde{x}+1,\tilde{0}]} \hat{S}^z_{[\tilde{x},\tilde{1}]} \rangle$ for $n^h = 0.05, 0.1, 0.15, 0.2$. Parameters are chosen identically to Fig. 1 in the main text. Solid lines show averaged values over the window when discarding the outermost two sites. Correlations $C_1^y(\tilde{x})$ ($C_2(\tilde{x})$) are seen to strengthen (weaken) by averaging over non-saturated configurations.

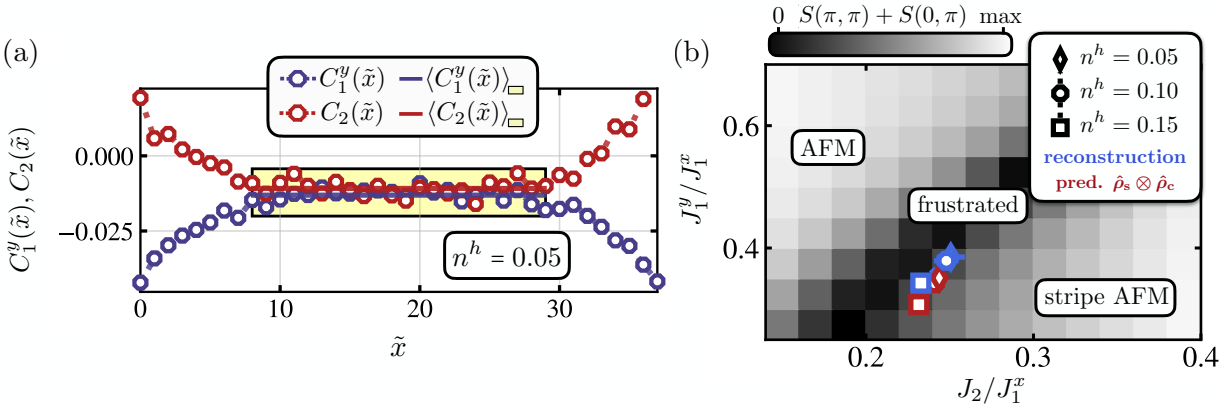

Figure 6.14: **Reconstruction of long ladders.** (a), Correlations $C_1^y(\tilde{x}) = \langle \hat{S}^z_{[\tilde{x},\tilde{0}]} \hat{S}^z_{[\tilde{x},\tilde{1}]} \rangle$ and $C_2(\tilde{x}) = \langle \hat{S}^z_{[\tilde{x},\tilde{0}]} \hat{S}^z_{[\tilde{x}+1,\tilde{1}]} \rangle + \langle \hat{S}^z_{[\tilde{x}+1,\tilde{0}]} \hat{S}^z_{[\tilde{x},\tilde{1}]} \rangle$ in squeezed space for a 40×2 mixD t-J ladder, with $t/J = 3$, $n^h = 0.05$ at $T/J = 5/3$ and using 20,000 snapshots. In the bulk of squeezed space, saturation of the correlators is observed for all considered hole dopings, as illustrated by the solid lines corresponding to averages within the boxed region. (b), Hamiltonian reconstruction results reveal that for all hole concentrations, hole motion drives the spins into a highly frustrated state (blue symbols). We discard the outer eight sites in squeezed space when reconstructing the effective Hamiltonians, as illustrated by the yellow box in (a). The separation ansatz yields similar results as the full reconstruction, illustrated by red symbols.

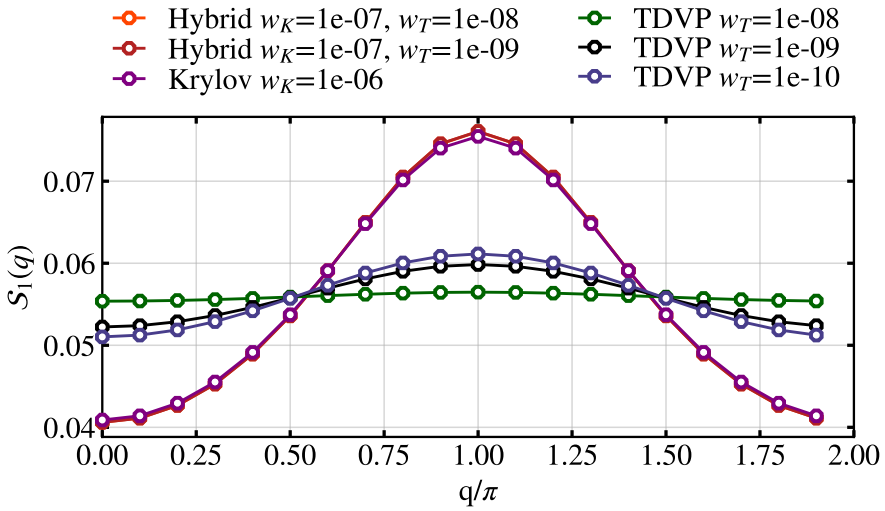

Figure 6.15: **Finite temperature convergence.** Convergence properties of finite-T simulations of a $L_x \times L_y = 40 \times 4$ J_1^x-J_1^y-J_2 Heisenberg model. To evaluate convergence of spin-spin correlations, we compute the static spin-structure factor (SSSF) along a single ladder leg y, given by $\mathcal{S}_y(q) = \frac{1}{\sqrt{L_x}} \sum_{x_i,x_j} e^{-iq(x_i-x_j)} \langle \hat{S}^z_{[x_i,y]} \hat{S}^z_{[x_j,y]} \rangle$. Purely local TDVP evolution schemes starting from the maximally entangled state, Eq. (6.16), perform poorly compared to global evolution methods (Krylov). A single global step with $\Delta\tau = 0.1$ followed by TDVP imaginary time evolution (denoted by "Hybrid") is observed to be sufficient to reach convergence towards to the fully global result.

$\hat{\rho} = \hat{\rho}_c \otimes \hat{\rho}_s$ yields similar qualitative results as the full reconstruction, cf. the red symbols in Fig. 6.14 (b).

6.7.2 Finite temperature simulations

We use purification schemes within the MPS framework to simulate both mixD t-J and J_1^x-J_1^y-J_2 Heisenberg models at finite temperature. In the spin sector, we employ a grand-canonical ensemble, allowing for thermal spin magnetizations. In the mixD model, we conserve its additional symmetries in the charge sector, namely the separate $U(1)$ charge conservation symmetries in each ladder leg (i.e. in the charge sector, calculations are canonical in each leg separately).

The maximally entangled state, which is the initial state of the imaginary time evolution under the purification scheme, for the Heisenberg model at infinite temperature and in the grand-canonical ensemble reads

$$|\Psi(\beta = 0)\rangle = \bigotimes_{i=0}^{L-1} \left(\sum_{\sigma=\uparrow,\downarrow} |\sigma, \bar{\sigma}\rangle \right). \tag{6.16}$$

Here, $\{|\uparrow\rangle, |\downarrow\rangle\}$ is the single particle basis of the Heisenberg model with $\bar{\uparrow} = \downarrow$, $\bar{\downarrow} = \uparrow$. On the other hand, in the mixD system, whose local Hilbert space dimension is larger by one degree, the maximally entangled state in the "leg-canonical" ensemble in the charge sector and the grand-canonical ensemble in the spin sector is given by Eq. (5.5).

After retrieving the maximally entangled state, we employ imaginary time evolution tech-

niques to evolve the state away from $\beta = 0$ towards finite temperatures. As done repeatedly throughout this thesis, we employ global methods for a single step in imaginary time, after which the entanglement in the system (and the bond dimension of the thermal MPS) has sufficiently increased to switch to local methods for computational speed. Convergence of the spin-structure factor in a 40×4 Heisenberg model for various evolution schemes and cutoff parameters is shown in Fig. 6.15. Starting solely via TDVP from the maximally entangled state shows poor convergence towards the global Krylov result (purple curve), even for low weight cutoffs of $w_T = 10^{-10}$ (blue curve). A single Krylov step followed by TDVP steps (denoted here the hybrid scheme) is seen to be sufficient to converge towards the purely global evolution.

For our mixD calculations, we fix weight cutoffs to $w_K = 10^{-7}$ and $w_T = 10^{-10}$ for the Krylov and TDVP imaginary time evolution, respectively, where convergence is observed. Reconstructions of the spin-Hamiltonian in squeezed space using the J_1^x-J_1^y-J_2 Heisenberg model are done with identical truncation parameters. For the J_1^x-J_1^y-J_2 Heisenberg model of size 20×4, we choose $w_K = 10^{-6}$ and $w_T = 10^{-9}$ for both the initial simulation as well as the reconstruction.

7

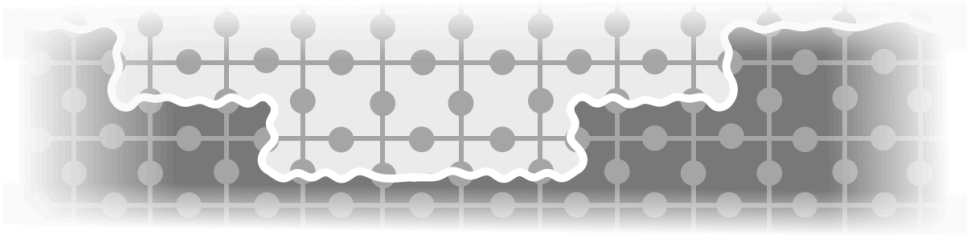

Geometric fractionalized Fermi liquid: A theory for the pseudogap

Summary. One of the central mysteries of hole-doped cuprates is the pseudogap phase, whose unusual properties are believed to be essential for understanding high-temperature superconductivity. While a broad variety of theoretical proposals have been put forward in the past decades (some of which are reviewed in this chapter), a unified view connecting the pseudogap to other observed phases, like AFM and stripe phases, has remained elusive. In this chapter, we propose a scenario in which these phases all have a common origin: The spins in the material form an ordered AFM background, on top of which fluctuating domain walls exist that can disrupt and obscure long-range order. We suggest that these fluctuating domain walls are at the heart of the pseudogap phase. They break down magnetic order in real space, leaving only short-range AFM correlations detectable in experiments. Additionally, we propose that these domain wall fluctuations lead to a topological phase (an odd $\mathbb{Z}_2$ spin liquid), which supports the formation of a small Fermi surface, aligning with experimental observations. At a critical point, the hidden AFM order fully dissolves, restoring spin symmetry without a divergent correlation length.

7.1 Introduction

As introduced in Sec. 2.1, one of the key features of hole-doped cuprates is the presence of an extended pseudogap phase, whose microscopic origin has been the subject of intense investigation since its discovery. Various explanations have been proposed for the pseudogap, including links to symmetry-breaking orders such as stripes or pairing, and the emergence of novel fractionalized Fermi liquid (FL*) phases. The topological nature of the FL* phase has been identified as a scenario compatible with a small Fermi surface without symmetry breaking, as suggested

experimentally. In the following, we will introduce Luttinger's theorem—a result central to the discussion of the pseudogap— in Sec. 7.2. We then give a brief overview of key experimental results in Sec. 7.3, and review some of the main theoretical scenarios that shape our current understanding of the pseudogap phase in Sec. 7.4.

With recent experimental and numerical studies supporting an intricate relationship between stripe order and the pseudogap phase, we then propose an alternative FL* scenario in Sec. 7.5: a fractionalized Fermi liquid with a geometric origin (GFL*) driven by fluctuating domain walls. The essential mechanism behind our proposal is hidden order, where the proliferation of domain walls stabilized by charge fluctuations obscures the underlying long-range antiferromagnetic order in real-space, but order is preserved in the reference frame of the background spins. As a result, well-defined fermionic quasiparticles in the form of magnetic polarons exist, which couple to $\mathbb{Z}_2$ topological excitations of the domain wall string-net condensate in the ground state and constitute a small Fermi surface. At a critical doping value, we argue that hole motion frustrates the spin background (see also Chap. 6) to an extend where hidden order is lost, driving a transition to a regular Fermi liquid at a hidden quantum critical point (hQCP) featuring quantum critical transport properties. By relating our theory to the experimental observations introduced in Sec. 7.3, we conclude this chapter in Sec. 7.6.

This chapter, in particular Sec. 7.5, is based on the following preprint, with partial textual overlap:

> [4] **HS**, A. Bohrdt, and F. Grusdt **Geometric fractionalized Fermi liquids: Hidden antiferromagnetism and pseudogap from fluctuating stripes**, arXiv 2411.03419 (2024)

7.2 Luttinger's Theorem

To begin our discussion on the pseudogap phase, we first examine Luttinger's theorem, which connects the volume of the Fermi surface in an interacting Fermi liquid to the particle density of the system. Initially, Luttinger's theorem was established using perturbative methods, applicable when interactions are weak enough to allow expansions around non-interacting fermions [100]. Later, it was generalized to strongly correlated systems by defining the Fermi surface via the zeros of the Green's function [266].

In 2001, M. Oshikawa proposed an elegant topological approach based on a flux insertion protocol for systems wrapped on a torus. Here, we will focus on this method and briefly rederive Oshikawa's proof, based on Ref. [130]. Following this, we will explore how the Luttinger count can be modified when a Fermi liquid couples to certain quantum spin liquids, leading to the fractionalization of the Fermi surface. This forms the foundation for our discussion of the geometric fractionalized Fermi liquid in the main part of this chapter. The following derivation is based on Refs. [16, 130], which we refer to for a detailed introduction into fractionalized Fermi liquids.

Consider a many-body system described by the Hamiltonian $\hat{\mathcal{H}}$ on a lattice, which we wrap on a torus with dimensions $L_x \times L_y$ (and unit lattice spacing), see Fig. 7.1 (a). The first assumption of Oshikawa's topological proof is that the system features translational invariance; in particular,

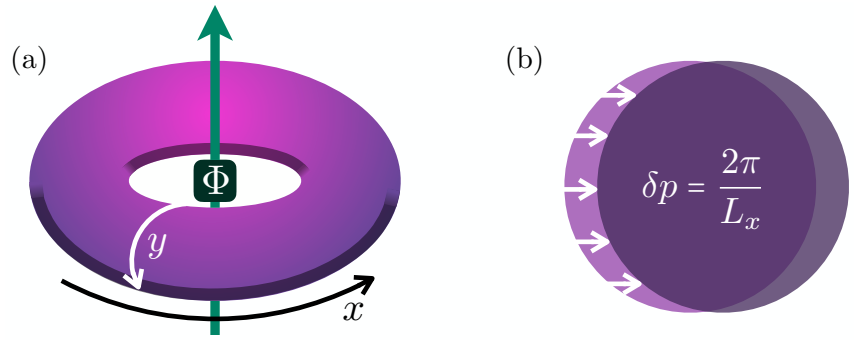

Figure 7.1: **Luttinger's theorem.** (a) Flux insertion protocol when gauging a global U(1) symmetry for a (lattice) system on a torus. Assuming translational invariance results in the very general expression Eq. (7.2) for the change of the total momentum of the gauged wave function. (b) When assuming that all low-energy excitations are given by fermionic quasiparticles forming a Fermi surface, their absorbed momentum can be calculated through a surface integral over the Fermi surface. This again leads to an expression for the change of momentum (by adding up all contributions from the Fermi surface), leading to Eq. (7.5). These two assumptions ultimately lead to Luttinger's theorem, Eq. (7.7).

this means that interactions preserve the total momentum of the state, which will be crucial for what follows. Furthermore, let us assume that the many-body system features a set of U(1) symmetries, e.g. charge and/or spin conservation.

Consider the ground state of the Hamiltonian, $|\Psi_0\rangle$, which is, accordingly, invariant under lattice translations. This implies that

$$\hat{T}_x |\Psi_0\rangle = e^{iP_x} |\Psi_0\rangle , \tag{7.1}$$

where $\hat{T}_x$ is the operator for translations along the x-direction, and P_x is the momentum of the state modulo 2π. Furthermore, $|\Psi_0\rangle$ has a well-defined total U(1) charge, which we label by the integer N.

What happens when we gauge this global U(1) symmetry? To probe this, we adiabatically introduce a flux Φ through one cycle of the torus, as illustrated in Fig. 7.1 (a). The resulting Hamiltonian is modified to $\hat{\mathcal{H}} \to \hat{\mathcal{H}}(\Phi)$. For each Φ, the instantaneous ground state is given by $|\Psi_0(\Phi)\rangle$, with energy $\epsilon_0(\Phi)$. Specifically, when inserting a 2π flux, the resulting state $|\Psi_0'\rangle = |\Psi_0(2\pi)\rangle$ is gauge equivalent to the state without inserted flux, $|\Psi_0\rangle$, i.e., there exists a gauge transformation $\hat{U}$ that maps $|\Psi_0'\rangle = \hat{U} |\Psi_0\rangle$. Nonetheless, $|\Psi_0'\rangle$ generally differs from $|\Psi_0\rangle$; specifically, the flux insertion shifts the momentum P_x by an amount ΔP_x, given by

$$\Delta P_x = \frac{2\pi}{L_x} N \,(\mathrm{mod}\, 2\pi). \tag{7.2}$$

We can easily see that the above is the case for non-interacting particles. Consider, for instance, free electrons on a periodic 1D lattice with L_x sites, such that energy levels are given by $\epsilon(k_x) = -2t\cos(k_x)$; allowed momenta are $k_x = \frac{2\pi}{L_x} M$, with $M = 0, \ldots L-1$. Inserting a 2π flux through the 1D ring modifies the energy levels to $\epsilon(k_x) = -2t\cos(k_x - 2\pi/L_x)$. Hence, the

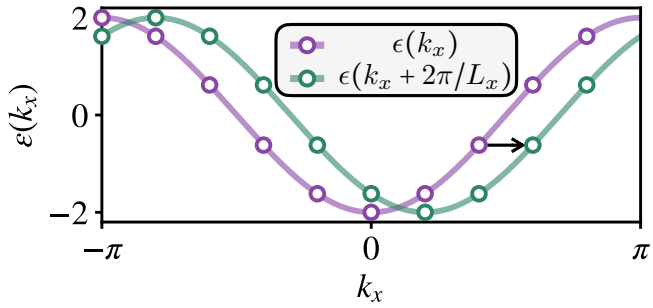

Figure 7.2: **Momentum shift upon flux insertion.** Change of energy levels upon threading a periodic 1D tight-binding hopping chain with a 2π flux. Though each single-particle state is shifted in its momentum by $2\pi/L_x$, the set of eigenstates stays invariant, i.e., $\hat{\mathcal{H}}(0)$ and $\hat{\mathcal{H}}(2\pi)$ are gauge-equivalent.

set of energy levels of $\hat{\mathcal{H}}$ and $\hat{\mathcal{H}}(2\pi)$ are equivalent, but the momentum of each single-particle state has been shifted by $2\pi/L_x$, see Fig. 7.2. Therefore, for a many-body wave function with N particles, the momentum shift is given by Eq. (7.2). As translationally invariant interactions preserve the systems's total momentum modulo 2π, the result remains valid even for interacting systems and is thus very general.

This reasoning so far only assumes translational invariance and global U(1) symmetry, without specifying further details about the system. Let us now assume that the ground state is that of a Fermi liquid, where low-energy excitations are fermionic quasiparticles near the Fermi surface. Including the spin degree of freedom ($\sigma = \uparrow, \downarrow$) introduces two global U(1) symmetries: one for total particle number and another for S_z. Each symmetry independently satisfies Luttinger's theorem. The quasiparticles, represented by operators $\hat{f}_{\mathbf{k},\sigma}$ (with $\sigma = \pm$ corresponding to spin-up and spin-down), are described by the following effective action,

$$\mathcal{S}_{FL} = \int d\tau \int \frac{d\mathbf{k}}{(2\pi)^2} \sum_{\sigma=\pm} \hat{f}^{\dagger}_{\mathbf{k},\sigma} \left(\partial_\tau - \frac{i}{2}\sigma A^s_\tau - iA^e_\tau + \varepsilon(\mathbf{k} - \sigma\mathbf{A}^s/2 - \mathbf{A}^e) \right) \hat{f}_{\mathbf{k},\sigma}. \tag{7.3}$$

Here, τ represents imaginary time, $\varepsilon(\mathbf{k})$ is the quasiparticle dispersion, and the gauge fields $A^e_\mu = (A^e_\tau, \mathbf{A}^e)$ and $A^s_\mu = (A^s_\tau, \mathbf{A}^s)$ couple to the two conserved U(1) charges: particle number and S_z, respectively. We now consider the system under a specific flux insertion, where a 2π flux couples to only the up-spin electrons. This corresponds to choosing $A^s_\mu = 2A^e_\mu \equiv A_\mu$. The momentum shift for this configuration from Eq. (7.2) is

$$\Delta P_x = \frac{2\pi}{L_x} N_\uparrow \,(\mathrm{mod}\, 2\pi) = \frac{2\pi}{L_x}\frac{N}{2} \,(\mathrm{mod}\, 2\pi), \tag{7.4}$$

assuming an equal number of spin-up and spin-down electrons ($N_\uparrow = N_\downarrow = N/2$). Now let us calculate ΔP_x of the spin-up quasiparticles using the Fermi liquid description. Each quasiparticle near the Fermi surface acquires a momentum shift of $\delta p_x = 2\pi/L_x$ due to the flux insertion, see Fig. 7.1 (b). To compute the total momentum shift, we sum over all quasiparticles near the Fermi surface. Using the divergence theorem, this surface integral is equivalent to integrating over the

volume enclosed by the Fermi surface, and we find

$$\Delta P_x = \frac{2\pi}{L_x}\left(L_x L_y \frac{V_{FS}}{(2\pi)^2}\right) \pmod{2\pi}, \tag{7.5}$$

where V_{FS} represents the momentum space area enclosed by the Fermi surface. Note that while the calculation extends to the entire momentum space for mathematical convenience, the physical contributions arise solely from the region near the Fermi surface where quasiparticles are well-defined. Naively equating Eq (7.4) and Eq. (7.5) yields Luttinger's theorem[1]:

$$\frac{V_{FS}}{2\pi^2} = \frac{N}{L_x L_y} \pmod{2}. \tag{7.6}$$

Finally, for hole-doped cuprates, where the hole density from the fully occupied band is $1+\delta$, this result implies for the hole-like Fermi surface

$$\frac{V_{FS}}{2\pi^2} = (1+\delta) \pmod{2}. \tag{7.7}$$

As we will introduce in the following section, while experiments are consistent with this picture in the overdoped FL region of cuprates, Luttinger's theorem seems to be violated in the pseudogap phase: Here, the volume of the Fermi surface is consistent with a density of δ, and not $1+\delta$ as in Eq. (7.7), which is one of the central mysteries surrounding the pseudogap phase in hole-doped cuprates.

7.3 A brief experimental survey of the pseodogap phase

Ever since its discovery, there has been an overwhelmingly vast number of experiments in the pseudogap phase. In this section, we shall focus on some key results to build up an understanding of the enigma of the pseudogap phase in hole-doped cuprates. Therefore, the following is by no means a comprehensive study of experimental findings, but should rather be interpreted as a brief survey of experimental evidence for various properties of the pseudogap which by now are well established. For recent reviews, we refer to Refs. [101, 267]

Magnetic correlations

Early experiments in the pseudogap regime heavily focused on its magnetic properties, primarily due to its proximity in the phase diagram to long-range antiferromagnetic (AFM) order. To probe magnetic properties, inelastic neutron scattering (INS) experiments have been instrumental [24]. This technique measures the spin structure factor with full momentum and energy resolution, providing a direct window into magnetic correlations and fluctuations. By analyzing the position and width of intensity peaks in momentum space, one can gain insights into magnetic order and fluctuations within the pseudogap regime.

[1] For the complete argument, one has to carefully handle $\pmod{2\pi}$ terms, which includes to choose L_x and L_y to be mutual prime numbers.

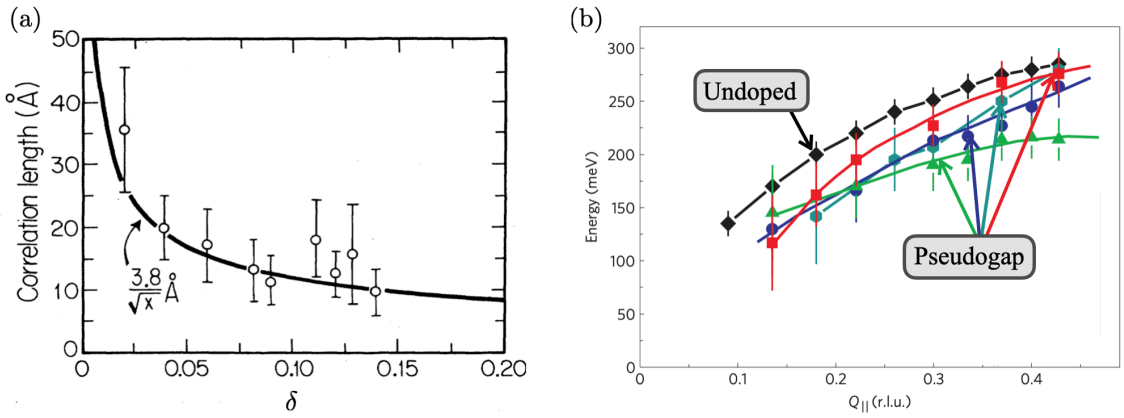

Figure 7.3: **Magnetic properties in the pseudogap phase.** (a) Antiferromagnetic correlation length as a function of hole-doping δ in a Lanthanum-based cuprate using neutron scattering. Figure taken and adapted from Ref. [268]. (b) Paramagnon dispersions from X-Ray scattering of an undoped parent compound (black) and in several underdoped systems (colorful). Figure taken and adapted from Ref. [103].

Fig. 7.3 (a) shows the AFM correlation length as a function of hole-doping δ in $La_{2-x}Sr_xCuO_4$, taken from Ref. [268]. One of the most striking characteristics when entering the pseudogap from the AFM phase is the sharp drop in AFM correlations: Beyond a few percent doping, the correlation length falls below approximately 15 Å, corresponding to just 2-3 lattice sites. The efficiency with which magnetic order is disrupted in this doping range remains one of the central puzzles of the pseudogap phase [24].

Paramagnons

INS experiments have mostly detected spin excitations in a narrow energy range and momentum region of the Brillouin zone, with limited spectral weight. The limitations of INS, including weak magnetic scattering signals and the need for large single-crystal samples, have hindered the exploration of high-energy and broad momentum-range spin excitations [103]. To this end, high-resolution resonant inelastic X-ray scattering (RIXS) have enabled a more detailed study of magnetic excitations across various doping levels in hole-doped cuprates. These experiments reveal dispersive spin-wave-like excitations (paramagnons) with energies up to 300 meV and spectral weights comparable to those of undoped parent compounds, suggesting that significant magnetic spectral weight persists even in doped systems. A a result, it has been established that spin-wave-like excitations are well defined even within the pseodogap regime; a RIXS study showing the paramagnon dispersions of various doped compounds in comparison to a prototypical undoped material is shown in Fig. 7.3 (b), taken from Ref. [103]. For further resonant X-ray scattering experiments underlining the existence of paramagnons, see e.g. Refs. [104, 105].

Partial suppression of spectral weight

One of the most well-known features of the pseudogap is the partial suppression of spectral weight observed in angle-resolved photoemission spectroscopy (ARPES) measurements [87–90].

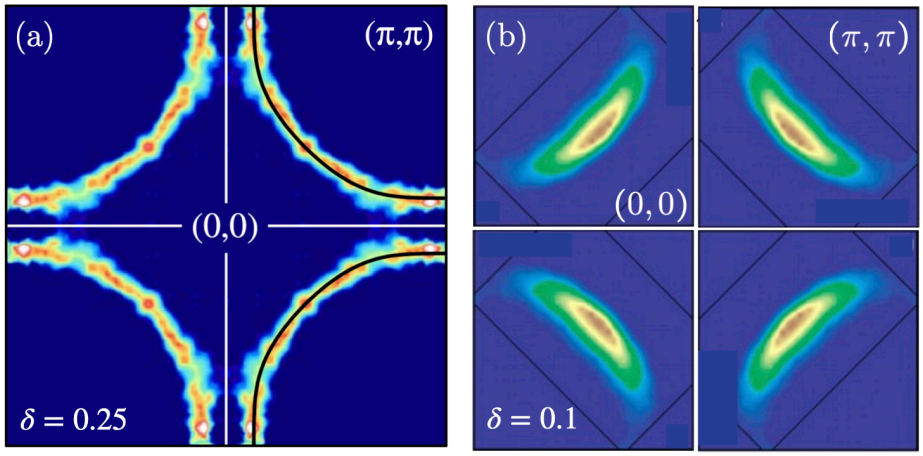

Figure 7.4: **ARPES in hole-doped cuprates.** (a) ARPES spectrum in overdoped $Tl_2Ba_2CuO_{6+\delta}$ at $\delta = 0.25$, revealing a closed, large hole-like Fermi surface. Image taken from [269]. (b) ARPES spectrum of underdoped $Ca_{2-\delta}Na_\delta CuO_2Cl_2$ at $\delta = 0.1$. A closed Fermi surface is replaced by Fermi arcs around the node; spectral weight at other parts of the BZ is heavily suppressed. Image taken and adapted from Ref. [87].

In these experiments, photons are directed at the material, causing the ejection of electrons. By analyzing the in-plane momentum (determined by the ejection angle) and the energy of the emitted electrons, ARPES provides a direct probe of low-energy fermionic excitations.

In a conventional Fermi liquid, regions of high intensity in ARPES spectra correspond to the Fermi surface of the underlying electrons. This behavior is observed in overdoped cuprates deep within the Fermi liquid regime. For example, in the overdoped $Tl_2Ba_2CuO_{6+\delta}$ (see Fig. 7.4 (a), adapted from Ref. [269]), ARPES reveals a large hole-like Fermi surface centered around $\mathbf{Q} = (\pi, \pi)$, consistent with the band structure of free carriers hopping on a 2D lattice.

In stark contrast, the underdoped regime exhibits a markedly different behavior. Here, spectral weight is predominantly observed near the nodal regions[2], resulting in the characteristic "Fermi arcs"—broad arc-like features around $(\pi/2, \pi/2)$, as shown for $Ca_{2-\delta}Na_\delta CuO_2Cl_2$ at $\delta = 0.1$ in Fig. 7.4 (b) (adapted from Ref. [87]). Around the antinodal regions[3], the spectrum is partially gapped, and no clear closed Fermi surface is observed, giving rise to the term "pseudogap". The emergence of Fermi arcs without evidence of a closed Fermi surface is one of the most intriguing and unresolved aspects of the pseudogap phase in hole-doped cuprates.

Quantum oscillations

The partial suppression of spectral weight in specific regions of the Brillouin zone raises a critical question: do coherent, fermionic quasiparticles exist in the pseudogap phase? Specifically, is the suppression caused by (i) a partial gap in the spectrum, or (ii) evidence of anomalously small Fermi pockets, with parts of the ARPES signal being suppressed on their back sides? To address this, quantum oscillation experiments have provided valuable insights into the pseudo-

[2]The nodal region corresponds to momenta close to $(\pi/2, \pi/2)$.
[3]The antinodal region corresponds to momenta close to $(0, \pi)$ and $(\pi, 0)$.

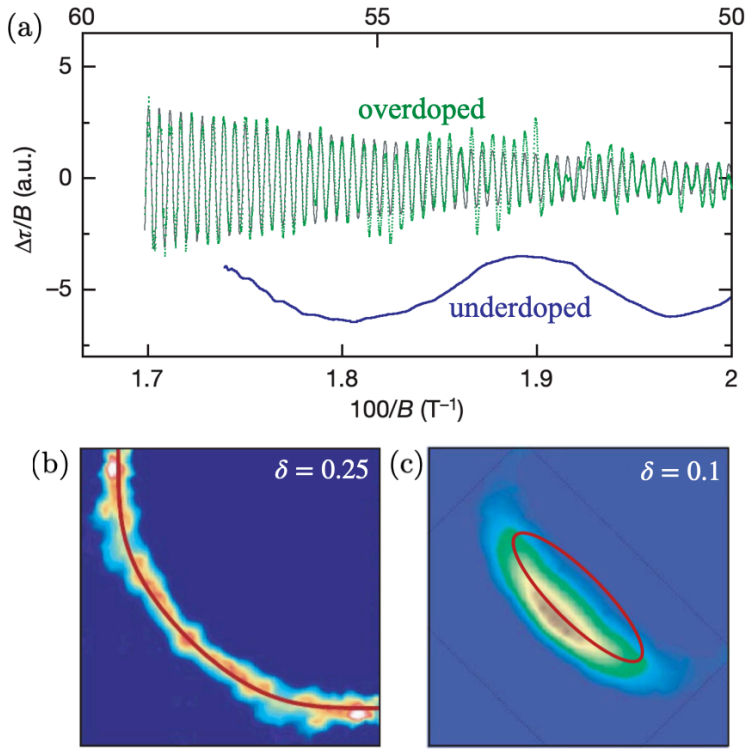

Figure 7.5: **Quantum oscillation experiments and Fermi surface volumes.** (a) Comparison of quantum oscillations in the overdoped regime of $Tl_2Ba_2CuO_{6+\delta}$ and the underdoped regime of $YBa_2Cu_4O_8$. Image taken and adapted from Ref. [92] (b) Fermi surface fit to ARPES data in the overdoped region of $Tl_2Ba_2CuO_{6+\delta}$ under the constraint of fixing V_{FS} to the value as given by quantum oscillations. Image taken from Ref. [91], see also Ref. [269]. (c) The same as in (b) for the underdoped region of $Ca_{2-\delta}Na_\delta CuO_2Cl_2$. Quantum oscillations are consistent with small Fermi surface pockets, enclosing a volume $\propto \delta$. Image taken from Ref. [91], see also Ref. [87].

gap phase.

In these experiments, strong magnetic fields quantize electronic states into Landau levels. The passage of Landau levels through the Fermi surface causes oscillations in observables coupled to the density of states as a function of the inverse magnetic field strength. These oscillations offer direct evidence of coherent quasiparticles and, if fermionic, reveal information about the Fermi surface, including its volume and geometry [91–94].

Fig. 7.5 (a) shows quantum oscillation measurements of magnetic torque for overdoped $Tl_2Ba_2CuO_{6+\delta}$ and underdoped $YBa_2Cu_4O_8$ (YBCO). In the overdoped compound, high-frequency oscillations are observed, consistent with a large Fermi surface. The frequency ν of these oscillations corresponds to the extremal cross-sectional area A of the Fermi surface, given by the Onsager relation [92]

$$A = 2\pi \frac{e\nu}{\hbar}, \tag{7.8}$$

where e is the elementary electronic charge. The Fermi surface area derived from these oscillations matches the surface inferred from ARPES measurements in the overdoped regime, as shown in Fig. 7.5 (b).

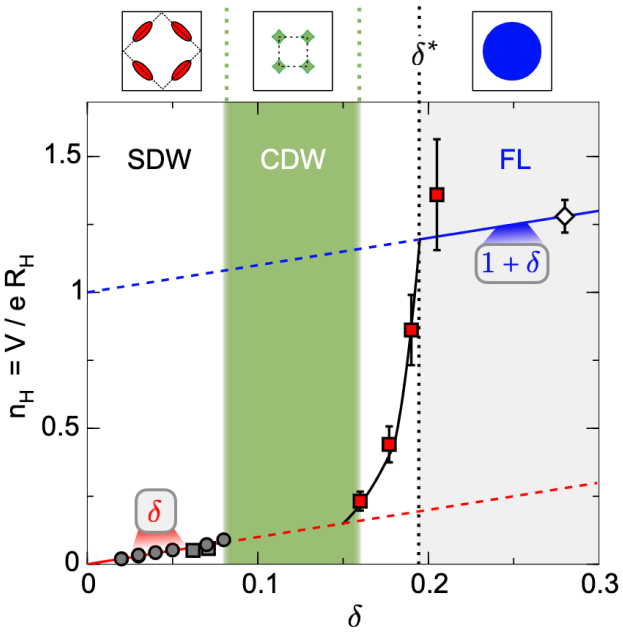

Figure 7.6: **Hall coefficient measurements.** The doping dependence of the Hall number, $n_H = V/eR_H$, which directly reflects the carrier density in hole-doped cuprates. Figure taken from Ref. [96]. Shown are data for $La_{2-x}Sr_xCuO_4$ (circles, Ref. [95]) and YBCO with $\delta < 0.08$ (gray squares, Ref. [270]), and $\delta > 0.15$ (red squares, Ref. [96]). The red and blue lines show $n_H = \delta$ and $n_H = 1 + \delta$, respectively. The green shaded region highlights the range of doping in YBCO where Fermi surface reconstruction due to CDW order occurs, where the Fermi surface is electron-like (i.e., $R_H < 0$). As doping decreases from the overdoped regime, the carrier density transitions sharply from $1 + \delta$ to δ at the critical doping $\delta^* \approx 0.19$ (black dashed line), which precisely corresponds to the onset of the pseudogap phase in YBCO. Above the plot, schematic representations of the Fermi surface illustrate the changes across doping regions: small nodal hole pockets (red) for $\delta < 0.08$ under magnetic order (SDW); small electron pockets (green) for $0.08 < \delta < 0.16$ associated with charge order (CDW); and a single large hole surface (blue) for $\delta > \delta^*$, corresponding to a Fermi-liquid state (gray region). Between $0.16 < \delta < 0.19$, the carrier density is consistent with a small Fermi surface, albeit no broken symmetries. This may facilitate a region where a fractionalized Fermi liquid is realized, see Sec. 7.4.

In the underdoped regime, quantum oscillations are also observed, though with a much lower frequency. Indeed, the observed frequencies are consistent with the the presence of coherent fermionic quasiparticles enclosing a small Fermi surface $\propto \delta$ instead of $\propto 1 + \delta$. Fig. 7.5 (c) illustrates how the small Fermi pocket inferred from quantum oscillation experiments can be fit to the ARPES data, where the observed spectral weight may be interpreted as the front side of a hole pocket. The overlays are taken from Ref. [91] (see also Refs. [87, 269]).

Hall measurements

The picture of fermionic quasiparticles forming a small Fermi surface is further supported by carrier density measurements, such as Hall effect experiments [95–97]. Fig. 7.6 illustrates the Hall carrier density n_H as a function of doping δ in (mainly) YBCO across a wide doping range, taken from Ref. [96].

At small doping values, spin- and charge-density wave order reconstruct the Fermi surface, leading to a modified Luttinger count and hence a small Fermi surface, as discussed in Sec. 7.4.1. For large doping levels ($\delta > 0.2$), Hall coefficient measurements align with the presence of a large Fermi surface, consistent with Luttinger's theorem of a metal without symmetry breaking, where $n_H \propto 1 + \delta$. As the system enters the pseudogap regime from the overdoped FL phase at $\delta < 0.19$, Hall measurements suggest the presence of small Fermi pockets, with $n_H \propto \delta$, although *no broken symmetries* are apparent. This transition in Hall response provides further compelling evidence for a reconstruction of the Fermi surface in the pseudogap phase, evident in Fig. 7.6 between $0.16 < \delta < 0.19$. As we will discuss in Sec. 7.4.3, this suggests the existence of a non-trivial topological structure of the metal, which can modify Luttinger's count without any broken symmetry.

The above results are corroborated by optical conductivity [98] and magnetoresistence [99] measurements, which all show strikingly accurate vanilla Fermi liquid behavior consistent with a small Fermi surface.

Summary

To conclude, we summarize the key experimental observations discussed above. While this list is somewhat subjective and not exhaustive, any comprehensive theory of the pseudogap phase should account for the following features:

- ☐ Short-range antiferromagnetic (AFM) correlations are present, but there is no evidence of long-range AFM order.
- ☐ Well-defined paramagnons, or spin-wave-like excitations, are observed.
- ☐ A partial suppression of the single-particle spectral function occurs, manifesting as the emergence of Fermi arcs.
- ☐ Coherent fermionic quasiparticles are evident.
- ☐ The system exhibits plain Fermi liquid behavior with a small Fermi surface area scaling as $V_{\mathrm{FS}} \propto \delta$.
- ☐ No local order parameter has been identified that drives a thermal or quantum phase transition into or out of the pseudogap phase.

7.4 Theoretical scenarios for the pseudogap phase

Over the past decades, numerous theories have been proposed to explain the pseudogap phenomenon, each shaped by the evolving body of experimental data. A particularly intriguing conceptual challenge emerged with the observation of coherent quantum oscillations: how to reconcile the existence of a small Fermi surface with the absence of symmetry breaking. In what follows, we provide a brief overview of the key ideas that have influenced theoretical investiga-

tions of the pseudogap phase. Again, note that this is not intended to be an exhaustive list, but rather a summary of foundational concepts that are relevant for our discussion in Sec. 7.5.

7.4.1 Symmetry broken metal

One of the most straightforward explanations for several characteristics of the pseudogap phase arises from a scenario that *does* involve long-range antiferromagnetic (AFM) order that breaks lattice translational symmetry in a metallic state [16, 101]. To this end, we will treat the Fermi-Hubbard model using a mean-field approximation. In its particle-hole symmetric formulation, the FH Hamiltonian reads

$$\hat{\mathcal{H}}_{\mathrm{FH}} = -t \sum_{\langle \mathbf{i},\mathbf{j}\rangle} \sum_{\sigma=\uparrow,\downarrow} \hat{c}^{\dagger}_{\mathbf{i},\sigma} \hat{c}_{\mathbf{j},\sigma} + \mathrm{h.c.} + U \sum_{\mathbf{i}} \left(\hat{n}_{\mathbf{i},\uparrow} - \frac{1}{2}\right)\left(\hat{n}_{\mathbf{i},\downarrow} - \frac{1}{2}\right). \tag{7.9}$$

Anticipating a metallic state close to an AFM instability at half filling, the system can be decoupled in the particle-hole channel by introducing the bosonic collective mode $\mathbf{\Phi}$ (Hubbard-Stratonovich field), often referred to as the "paramagnon field" [16]. The (exact) partition function then reads

$$\mathcal{Z} = \int \prod_{\mathbf{i},\sigma} \mathcal{D}c_{\mathbf{i}\sigma}(\tau) \prod_{\mathbf{i}} \mathcal{D}\mathbf{\Phi}_{\mathbf{i}}(\tau) \exp\Bigg(- \int d\tau \Bigg\{ \sum_{\mathbf{k},\sigma} \bar{c}_{\mathbf{k},\sigma} \Big[\frac{\partial}{\partial\tau} + \epsilon_{\mathbf{k}}\Big] c_{\mathbf{k},\sigma} + \sum_{\mathbf{i}} \left[\frac{3}{8U}\mathbf{\Phi}^2_{\mathbf{i}} - \mathbf{\Phi}_{\mathbf{i}} \cdot \mathbf{S}_{\mathbf{i}}\right] \Bigg\} \Bigg), \tag{7.10}$$

where we have used the local identity $U\left(\hat{n}_{\mathbf{i},\uparrow} - \frac{1}{2}\right)\left(\hat{n}_{\mathbf{i},\downarrow} - \frac{1}{2}\right) = -\frac{2U}{3}\mathbf{S}^2_{\mathbf{i}} + \frac{U}{4}$ with the spin defined as $\mathbf{S}_{\mathbf{i}} = \frac{1}{2}\sum_{\alpha,\beta} \bar{c}_{\mathbf{i},\alpha} \boldsymbol{\sigma}_{\alpha,\beta} c_{\mathbf{i},\beta}$.

Condensation of paramagnons leads to a spin-density wave instability with wave vector $\mathbf{Q} = [\pi, \pi]$ on the square lattice, resulting in a metallic state with spontaneous spin polarization that has opposite orientation $\mathbf{\Phi}_{\mathbf{i}\in A}/|\mathbf{\Phi}_{\mathbf{i}\in A}| = -\mathbf{\Phi}_{\mathbf{i}\in B}/|\mathbf{\Phi}_{\mathbf{i}\in B}|$ on A and B sublattices, i.e.,

$$\mathbf{\Phi}_{\mathbf{i}} = \mathbf{\Omega}_{\mathbf{i}} \exp(i\mathbf{Q}\cdot\mathbf{i}), \tag{7.11}$$

with $\langle \mathbf{\Omega}_{\mathbf{i}} \rangle \neq 0$ and $\mathbf{\Omega}_{\mathbf{i}}$ the alignment of the Néel field. Explicitly plugging Eq. (7.11) into Eq. (7.10) and describing the AFM symmetry breaking in a standard $\mathbf{\Omega}^4$ theory yields the following long-wavelength field theory (the "spin-fermion" model, see also Ref. [101]),

$$\mathcal{Z} = \int \prod_{\mathbf{i},\sigma} \mathcal{D}c_{\mathbf{i}\sigma}(\tau) \prod_{\mathbf{i}} \mathcal{D}\mathbf{\Omega}_{\mathbf{i}}(\tau) \exp\Bigg(- \int d\tau \Bigg\{ \sum_{\mathbf{k},\sigma} \bar{c}_{\mathbf{k},\sigma} \Big[\frac{\partial}{\partial\tau} + \epsilon_{\mathbf{k}}\Big] c_{\mathbf{k},\sigma} - \lambda \sum_{\mathbf{i},\alpha,\beta} \bar{c}_{\mathbf{i},\alpha} \mathbf{\Omega}_{\mathbf{i}} \cdot \boldsymbol{\sigma}_{\alpha,\beta} c_{\mathbf{i},\beta} e^{i\mathbf{Q}\cdot\mathbf{i}} + \int d\mathbf{r} \left[\frac{v^2}{2}(\nabla_{\mathbf{r}}\mathbf{\Omega})^2 + \frac{1}{2}(\partial\tau\mathbf{\Omega})^2 + \frac{s}{2}\mathbf{\Omega}^2 + \frac{u}{4}\mathbf{\Omega}^4\right] \Bigg\} \Bigg). \tag{7.12}$$

Here, the part proportional to λ is the spin-fluctuation induced scattering of fermions from one side of the Fermi surface to the other.

When AFM order establishes below $s < s_c$, the Fermi surface is reconstructed due to the

coupling of momenta $\mathbf{k}$ with $\mathbf{k}+\mathbf{Q}$. In particular, hole pockets are formed close to hot-spots where the spin-density wave gaps out the electronic spectrum [16, 101]. This realizes the well-understood scenario where the pseudogap emerges from a spontaneously broken translational symmetry.

We can see this concretely when analyzing the FH Hamiltonian within Hartree-Fock theory, where the Hamiltonian with long-range AFM order [i.e., for $s < s_c$ in Eq. (7.12)] can be expressed in a Nambu-like basis [271],

$$\hat{\mathcal{H}}_{\mathrm{MF}} = \sum_{\mathbf{k}} \begin{pmatrix} \hat{c}^\dagger_{\mathbf{k},\uparrow}, \hat{c}^\dagger_{\mathbf{k}+\mathbf{Q},\downarrow} \end{pmatrix} \begin{pmatrix} \epsilon_{\mathbf{k}} & \Delta \\ \Delta & \epsilon_{\mathbf{k}+\mathbf{Q}} \end{pmatrix} \begin{pmatrix} \hat{c}_{\mathbf{k},\uparrow} \\ \hat{c}_{\mathbf{k}+\mathbf{Q},\downarrow} \end{pmatrix}. \tag{7.13}$$

Here, $\epsilon_{\mathbf{k}} = -2t[\cos(k_x) + \cos(k_y)] - 4t' \cos(k_x)\cos(k_y)$ is the single-particle dispersion for electrons on a 2D lattice with nearest-neighbor (t) and diagonal (t') hopping terms. The mean-field gap Δ is determined self-consistently in the half-filled case, while in the doped case, Δ generally depends on doping. For simplicity, we focus on the properties of the mean-field Hamiltonian Eq. (7.13) for varying Δ and chemical potential μ, rather than a full self-consistent determination of Δ.

To compute the spectral function, we first evaluate the Green's function,

$$G_{ij}(\omega, \mathbf{k}) = \left[(\omega + i\eta) - \begin{pmatrix} \epsilon_{\mathbf{k}} & \Delta \\ \Delta & \epsilon_{\mathbf{k}+\mathbf{Q}} \end{pmatrix} \right]^{-1}_{ij}, \tag{7.14}$$

where η is an artificial broadening, and $i, j = 0, 1$ label the matrix elements of G. For $\Delta = 0$, the single-particle spectral function reads $A(\omega, \mathbf{k}) = -2\mathrm{Im}\left[G(\omega, \mathbf{k})\right] = -2\mathrm{Im}\left[(\omega + i\eta - \epsilon_{\mathbf{k}})^{-1}\right]$. Hence, for finite Δ, we evaluate $A(\omega, \mathbf{k}) = -2\mathrm{Im}\left[G(\omega, \mathbf{k})_{i=0,j=0}\right]$ to obtain the single-particle spectral function of the AFM metal.

Following Ref. [271], we fix the dispersion parameters as $t = 1$, $t' = -0.35$, and $\eta = 0.05$, and compute $A(\omega = 0, \mathbf{k})$ for varying μ and Δ, shown in Figure 7.7. The white lines indicate where $\epsilon_{\mathbf{k}} - \mu = 0$ and $\epsilon_{\mathbf{k}+\mathbf{Q}} - \mu = 0$. For slight hole doping ($\mu = -0.6$), hole pockets appear around $\mathbf{q} = (\pi/2, \pi/2)$, along with electron pockets originating from the upper band after band folding, Fig. 7.7 (a). As hole doping increases, the electron pockets vanish, leaving only hole pockets, Fig. 7.7 (b). Notably, the spectral weight on the backsides of these pockets, arising from the $\epsilon_{\mathbf{k}+\mathbf{Q}}$ band, is suppressed.

This suppression can also be understood by directly diagonalizing Eq. (7.13). Further following Ref. [271], this gives

$$\hat{U}^\dagger \hat{\mathcal{H}}_{\mathrm{MF}} \hat{U} = \sum_{\mathbf{k}} \sum_{s=\mp} E_{\mathbf{k},s} \hat{a}^\dagger_{\mathbf{k},s} \hat{a}_{\mathbf{k},s}, \tag{7.15}$$

where $E_{\mathbf{k},\mp}$ are the quasiparticle energies, given by

$$E_{\mathbf{k},\mp} = \frac{\epsilon_{\mathbf{k}} + \epsilon_{\mathbf{k}+\mathbf{Q}}}{2} \mp \sqrt{\frac{1}{4}\left(\epsilon_{\mathbf{k}} - \epsilon_{\mathbf{k}+\mathbf{Q}}\right)^2 + \Delta^2}. \tag{7.16}$$

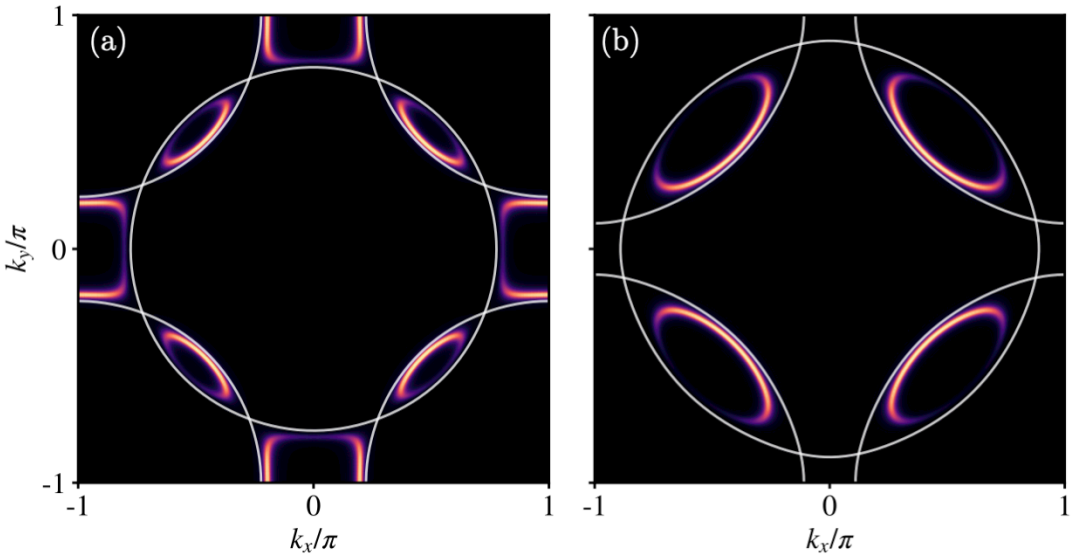

Figure 7.7: **AFM metal: Single-particle spectral weight.** (a) At slight hole doping, hole and electron pockets emerge from the hybridization of the $\epsilon_{\mathbf{k}}$ and $\epsilon_{\mathbf{k}+\mathbf{Q}}$ band. Parameters are chosen as $t = 1$, $t' = -0.35$, $\Delta = 0.4$, $\mu = -0.6$, and $\eta = 0.05$. (b) At higher hole doping levels, only hole pockets remain, located around $(0, \pm\pi)$ and $(\pm\pi, 0)$. Parameters: $t = 1$, $t' = -0.35$, $\Delta = 0.63$, $\mu = -1.2$, and $\eta = 0.05$. White lines indicate where $\epsilon_{\mathbf{k}} - \mu = 0$ (open lines) and $\epsilon_{\mathbf{k}+\mathbf{Q}} - \mu = 0$ (closed, centered lines).

The transformation to the diagonal basis is achieved through the matrix $\hat{U}$, such that

$$\begin{pmatrix} \hat{c}_{\mathbf{k},\uparrow} \\ \hat{c}_{\mathbf{k}+\mathbf{Q},\downarrow} \end{pmatrix} = \underbrace{\begin{pmatrix} \frac{\Delta}{\sqrt{\Delta^2+(\epsilon_{\mathbf{k}}-E_{\mathbf{k},-})^2}} & \frac{\Delta}{\sqrt{\Delta^2+(\epsilon_{\mathbf{k}}-E_{\mathbf{k},+})^2}} \\ \frac{-\Delta}{\sqrt{\Delta^2+(\epsilon_{\mathbf{k}}-E_{\mathbf{k},+})^2}} & \frac{\Delta}{\sqrt{\Delta^2+(\epsilon_{\mathbf{k}}-E_{\mathbf{k},-})^2}} \end{pmatrix}}_{=\hat{U}} \begin{pmatrix} \hat{a}_{\mathbf{k},-} \\ \hat{a}_{\mathbf{k},+} \end{pmatrix}. \tag{7.17}$$

Using this diagonalization, the spectral function is given by

$$A(\omega, \mathbf{k}) = \frac{\Delta^2}{\Delta^2 + (\epsilon_{\mathbf{k}} - E_{\mathbf{k},-})^2}\delta(\omega - E_{\mathbf{k},-}) + \frac{\Delta^2}{\Delta^2 + (\epsilon_{\mathbf{k}} - E_{\mathbf{k},+})^2}\delta(\omega - E_{\mathbf{k},+}). \tag{7.18}$$

For $A(\omega = 0, \mathbf{k})$ under hole doping, only the first term in Eq. (7.18) contributes, with a prefactor

$$\frac{\Delta^2}{\Delta^2 + \epsilon_{\mathbf{k}}^2}, \quad \text{for } E_{\mathbf{k},-} = 0. \tag{7.19}$$

This reveals that the spectral weight is anisotropic: it is maximized where $\epsilon_{\mathbf{k}} = 0$ and suppressed elsewhere. This explains the regions of high spectral weight in Fig. 7.7 (b) near the open white lines (corresponding to $\epsilon_{\mathbf{k}} = 0$) and the suppressed weight near regions where $\epsilon_{\mathbf{k}+\mathbf{Q}} = 0$.

How is the formation of a small Fermi surface in the AFM metal consistent with Luttinger's theorem? Looking back at Sec. 7.2, we see that the proof crucially builds on translational symmetry. When this invariance is broken, e.g. if the system forms an antiferromagnetic metal, the

size of the unit cell and hence the size of the BZ changes, wich we need to account for[4]. After going through similar arguments as presented in Sec. 7.2, Luttinger's theorem in the presence of an AFM ordered background reads

$$\frac{V_{FS}}{2\pi^2} = \delta \,(\mathrm{mod}\, 2). \tag{7.20}$$

This indeed corresponds to a small Fermi surface with the volume proportional to the doping level δ. Therefore, a small Fermi surface naturally arises ("legally" under Luttinger's theorem) when the system features symmetry breaking.

In this symmetry breaking scenario, the existence of a quantum critical point as a function of doping has been proposed to explain the anomalous transport properties found in the high-temperature region of the pseudogap regime, i.e. linear-in temperature resistivity [132, 133]. Here, the corresponding critical doping corresponds to the point where the critical temperature of the putative symmetry-breaking order that competes with superconductivity vanishes. It has been argued, however, that the disruption of a large Fermi surface by conventional (thermally fluctuating) order unlikely explains universal Fermi liquid-like observations with carrier density δ in the pseudogap phase [101,114]. One particular objection is that the transition into the pseudogap at temperature T^* does not seem to be captured by a thermodynamic phase transition, though Berezinskii–Kosterlitz–Thouless-type transitions with weak thermodynamic signatures can not be ruled out [106].

Building on the above discussion, one can also consider electrons coupling to and scattering off a different potential, such as one imposed by stripe order, see e.g. Ref. [106]. In this case, the unit cell becomes larger than two lattice sites, resulting in an $N \times N$ mean-field Hamiltonian, where N depends on the specific type of stripe order. Similar arguments apply, leading to Fermi surface reconstruction and, in certain cases, the emergence of small hole pockets. However, the size of these hole pockets is highly sensitive to the microscopic details of the theory, including doping level, stripe periodicity, and gap size. This sensitivity complicates efforts to explain the universal features of the pseudogap phase observed in hole-doped cuprates.

The preceding discussion focused on electrons on a 2D lattice, starting from the band structure of free particles coupled to and scattered by the potential of a long-range ordered background. This approach begins with non-interacting particles and introduces an instability towards long-range order, leading to Fermi surface reconstruction. Alternatively, one can adopt a strong-coupling perspective, beginning with an AFM Mott insulator at zero doping and developing a theory for doped holes in this state. When doped holes delocalize, they disrupt the background spin order, frustrating the AFM alignment. This process gives rise to magnetic polarons—heavy fermionic quasiparticles that gain kinetic energy through superexchange processes. The resulting theory describes magnetic (or spin-) polarons, with hole pockets forming around $\mathbf{q} = [\pi/2, \pi/2]$, consistent with low-energy charge excitations at low doping [265, 272–279].

In the above scenarios we must, however, address the elephant in the room: the assumption

[4] In particular, the unit cell is enlarged in each dimension by a factor of $a = \sqrt{2}$, such that we need to modify $L_\mu \to aL_\mu$ for $\mu = x, y$.

of a symmetry-broken metal with long-range AFM order fundamentally contradicts experimental observations across a wide range of cuprate families. Beyond approximately 5% doping, only short-range AFM correlations—spanning a few lattice sites—are observed, as discussed in Sec. 7.3. Thus, while the symmetry-broken metal captures some key features of the pseudogap phase, such as the formation of a Fermi liquid with a small Fermi surface, it fails to account for the lack of long-range order evident in the pseudogap phase.

7.4.2 Preformed pairing

The partial suppression of single-particle spectral weight in ARPES experiments around the nodal point has motivated the interpretation that the pseodogap can is a precursor of superconductivity. In this scenario, the formation of incoherent, preformed Cooper pairs in a subset of the BZ leads to a partial depletion of fermionic spectral weight around the anti-nodes, whereas the nodal region remains gapless. While support of this idea has been reported in a variety of experiments [115–118], temperatures where evidence of preformed pairs has been found are significantly below the pseudogap temperature T^*. Furthermore, recent measurements of iridates revealed that the pseudogap can exist in broad parameter regimes without the appearance of superconductivity at lower temperatures, which supports a disparate nature of the the two phases [119, 120].

7.4.3 Fractionalized Fermi liquid

Neither the picture based on symmetry breaking, nor the preformed pairing scenario can give a satisfactory explanation for the experimental observations that suggest the formation of a small Fermi surface without any observable long-range order. This has led to a third class of proposed scenarios, where the symmetry-breaking orders found at low temperatures are interpreted as instabilities of a distinct "pseudogap" phase of matter [101, 114, 121]. A prominent scenario is the formation of a fractionalized Fermi liquid (FL*) [122], which features well-defined fermionic quasiparticles in the absence of symmetry-breaking order while violating Luttinger's theorem. In the single-band Hubbard model, this scenario can be realized when assuming that local moments form an odd spin liquid with topological excitations [123, 124], into which mobile hole carriers are doped [125–130]. While dopants in a spin liquid can decay into fractionalized spin and charge constituents [131], assuming bound states of the latter leads to a metal with a small Fermi surface [114]. As we will show below, this apparent violation of Luttinger's theorem is caused by topological excitations of the spin liquid, which can absorb momentum in Oshikawa's flux insertion protocol [280] that corresponds exactly to unit density (leading to a Fermi surface of volume $\propto \delta$ instead of $\propto 1 + \delta$).

Toric code

Before exploring how a quantum spin liquid coupled to fermionic degrees of freedom can fractionalize the Fermi surface, we first review the foundational concepts of a paradigmatic $\mathbb{Z}_2$ quantum spin liquid (QSL): the toric code. This exactly solvable model, introduced by A. Kitaev as a

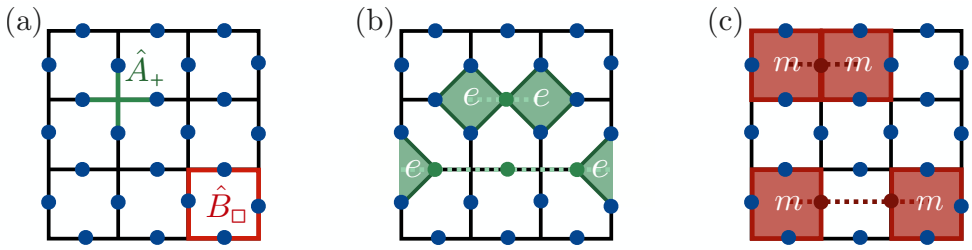

Figure 7.8: **Toric code.** (a) Illustration of the toric code Hamiltonian in Eq. (7.21). Qubits are placed on the links of a square lattice. The Hamiltonian includes products of $\hat{\tau}^x$ and $\hat{\tau}^z$ operators, represented by the green cross and red square, respectively. (b) Applying $\hat{\tau}^z_\ell$ locally (green dots) creates pairs of e-particles, where the star term violates the condition $\prod_{\ell\in+}\hat{\tau}^x = \eta_+$, highlighted by the green regions. (c) Similarly, applying $\hat{\tau}^x_\ell$ locally (dark red dots) creates pairs of m-particles, where the plaquette term violates the condition $\prod_{\ell\in\square}\hat{\tau}^z = \eta_\square$, indicated by the red regions. The e-particles reside on the original lattice (green dashed lines in (b)), while m-particles reside on the dual lattice, i.e., at the centers of the plaquettes (red dashed lines in (c)).

framework for topologically protected quantum computing [281], has significantly advanced our understanding of quantum spin liquids and topological phases of matter, and offers an intuitive understanding on how topological ground state degeneracies can alter the Luttinger count.

Consider a square lattice with $\mathbb{Z}_2$ degrees of freedom (qubits $\hat{\tau}$) placed on the links ℓ of the lattice, as shown in Fig. 7.8 (a). The toric code Hamiltonian consists of two terms: first, a product of spin-flip operators on the "star" terms around a lattice site, $\prod_{\ell\in+}\hat{\tau}^x_\ell$, represented by the green cross in Fig. 7.8 (a). Second, a product of operators on the plaquettes of the lattice, $\prod_{\ell\in\square}\hat{\tau}^z_\ell$, represented by the red square in Fig. 7.8 (a). The Hamiltonian is given by

$$\hat{\mathcal{H}}_{\mathrm{TC}} = -\eta_+ K_+ \sum_+ \underbrace{\prod_{\ell\in+}\hat{\tau}^x_\ell}_{:=\hat{A}_+} - \eta_\square K_\square \sum_\square \underbrace{\prod_{\ell\in\square}\hat{\tau}^z_\ell}_{:=\hat{B}_\square}. \tag{7.21}$$

Here, $\eta_+, \eta_\square = \pm 1$ are the signs of the two terms. Notably, the two terms in the Hamiltonian commute, $[\hat{A}_+, \hat{B}_\square] = 0$. For $K_+, K_\square > 0$ in Eq. (7.21), the ground state $|\Psi_0\rangle$ satisfies

$$\hat{A}_+|\Psi_0\rangle = \left(\prod_{\ell\in+}\hat{\tau}^x_\ell\right)|\Psi_0\rangle = \eta_+|\Psi_0\rangle\,, \quad \hat{B}_\square|\Psi_0\rangle = \left(\prod_{\ell\in\square}\hat{\tau}^z_\ell\right)|\Psi_0\rangle = \eta_\square|\Psi_0\rangle\,, \tag{7.22}$$

for all plaquette and star terms on the lattice. While individual spins fluctuate, as $[\hat{\mathcal{H}}_{\mathrm{TC}}, \hat{\tau}^\mu_\ell] \neq 0$, the products $\hat{A}_+$ and $\hat{B}_\square$ are fixed to ± 1 in the ground state.

Excited states then correspond to locally violating the conditions in Eq. (7.22). On the one hand, we can locally apply $\hat{\tau}^z_\ell$ operators, as illustrated in Fig. 7.8 (b). In the x-basis, these operations flip the corresponding qubits, resulting in a pair of star terms violating $\hat{A}_+ = \eta_+$. This operation always generates a pair of star term violations, denoted as e-particles[5]. Fig. 7.8 (b) depicts two scenarios involving e-particles: in the first, a single $\hat{\tau}^z_\ell$ operator is applied, while in

[5]The toric code is essentially a $\mathbb{Z}_2$ gauge theory; the e-particle represents an electric particle/excitation, while the m-particle corresponds to a magnetic excitation.

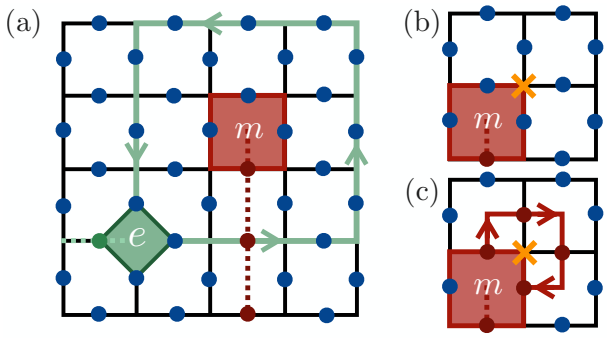

Figure 7.9: **Berry phases and braiding statistics.** (a) Depiction of braiding an e-particle around an m-particle. Both particles are created in pairs and are connected by lines of flipped $\hat{\tau}^z$ or $\hat{\tau}^x$ operators, represented by the dashed lines. During this process, when the e-particle crosses the line connecting the m-particle pair, it acquires a Berry phase of π, indicating that spinons and visons are mutual semions. (b) Moving an m-particle around a lattice site (indicated by the orange cross) corresponds to applying the star operator at that site, resulting in the ground state acquiring a Berry phase of η_+.

the second, a line of three operators is used, increasing the separation between the e-particles. Note that e-particles are always located on the vertices of the square lattice, as indicated by the light green dashed lines in Fig. 7.8 (b).

Similarly, we can locally apply $\hat{\tau}^x_\ell$ operators, which flip the spins in the z-basis. This action locally violates the constraint for $\hat{B}_\square$, resulting in the creation of a pair of m-particles (or visons), as shown in Fig. 7.8 (c). Visons reside on the dual lattice of the square lattice (i.e., at the centers of the plaquettes), as illustrated by the red dashed lines.

These e- and m-particles exhibit intriguing fractionalized statistics. Consider the case of moving a spinon (e-particle) around a vison (m-particle), as shown in Fig. 7.9 (a). When a spinon crosses the $\hat{\tau}^x$ string of a vison pair, it acquires a minus sign (as the vison string flips the spins in the z-basis). After completing a full loop around the vison, the final state is identical to the initial state, except for the π Berry phase acquired during braiding; this shows that spinons and visons are mutual semions, behaving as particles with statistics intermediate between fermions and bosons. Specifically, a full rotation of one particle around another produces a Berry phase of π (in contrast to indistinguishable fermions, where a single exchange suffices to introduce a minus sign).

Another property of visons, relevant to later discussions, is their braiding statistics when encircling a single lattice site, as shown in Fig. 7.9 (b) and (c). Moving a vison around the orange cross corresponds to applying the star term, $\prod_{\ell\in+}\hat{\tau}^x_\ell$, at the corresponding lattice site. This operation results in a state (Fig. 7.9 (c)) equivalent to the original state (Fig. 7.9 (b)), up to a sign of η_+. For $\eta_+ = -1$, this implies a π Berry phase, signifying an odd $\mathbb{Z}_2$ quantum spin liquid (QSL) ground state. The "odd" designation refers to the presence of a unit $\mathbb{Z}_2$ background charge in the gauge theory, causing magnetic visons to acquire a minus sign when encircling this charge. As we will discuss later, this property allows an odd QSL to absorb flux corresponding to unit density in the flux insertion protocol from Sec. 7.2, modifying the Luttinger count.

Finishing our discussion of braiding statistics, consider bound states of e- and m-particles.

The exchange statistics of these bound states are fermionic, meaning a minus sign is acquired when their positions are swapped (a process often called *e*&*m* fusion). This is a striking result: although the original Hamiltonian does not include fermionic degrees of freedom, the fused excitations exhibit fermionic statistics, showcasing a classic example of fractionalized statistics.

Before proceeding to the discussion on fractionalized Fermi liquids, let us study the ground state properties of the toric code Hamiltonian in more detail. We shall here fix $\eta_\square = 1$, but keep η_+ variable. To find a valid ground state, we need to find a state that satisfies Eq. (7.22). An obvious choice that satisfies the plaquette constraint is given by the all-up state,

$$|\Uparrow\rangle = \bigotimes_{\ell=1}^{L_x \times L_y} |\uparrow\rangle_\ell \,. \tag{7.23}$$

However, this state does not satisfy the gauge constraint, $\hat{A}_+ |\Uparrow\rangle \neq \eta_+ |\Uparrow\rangle$. We can fix this by introducing a superposition of closed loops (where a loop corresponds to a connected line of flipped spins) through application of the $\hat{A}_+$ term,

$$|\Psi_0\rangle = \prod_\ell (1 + \eta_+ \hat{A}_{+_\ell}) |\Uparrow\rangle \,. \tag{7.24}$$

It can be easily shown that the above state Eq. (7.24) satisfies the gauge constraint imposed by the star term,

$$\begin{aligned} \hat{A}_{+_\mathbf{m}} \prod_\ell (1 + \eta_+ \hat{A}_{+_\ell}) |\Uparrow\rangle &= \hat{A}_{+_\mathbf{m}} (1 + \eta_+ \hat{A}_{+_1}) \dots (1 + \eta_+ \hat{A}_{+_\mathbf{m}}) \dots (1 + \eta_+ \hat{A}_{+_{L_x \times L_y}}) |\Uparrow\rangle \\ &= (1 + \eta_+ \hat{A}_{+_1}) \dots (\hat{A}_{+_\mathbf{m}} + \eta_+) \dots (1 + \eta_+ \hat{A}_{+_{L_x \times L_y}}) |\Uparrow\rangle \\ &= \eta_+ |\Uparrow\rangle \,, \end{aligned}$$

where in the last step $\eta_+ = \eta_+^{-1}$ was used.

The ground state Eq. (7.24) corresponds to the equal superposition of all closed loops, with a prefactor of $\eta_+^{N_p}$ where N_p is the total number of plaquettes enclosed within the loops. Note that the condition $\hat{B}_\square = 1$ is still ensured, as on each plaquette the number of flipped spins is even for closed loops. Two interesting side notes: First, one can show that the toric code ground state is stable under arbitrary local perturbations, even those which break all symmetries. This is because the topological order of the toric code is encoded in its entanglement structure, which is fundamentally different from the symmetry breaking paradigm. Only closing the gap of *e*- and *m*-particles can break and "unwind" the topological structure [16]. Second, the toric code ground state can be exactly mapped to Anderson's resonating valence bond picture: when interpreting closed loops in the toric code as transition graphs from one dimer packing to another dimer packing on the dual lattice (i.e. one assigns each line of the loop with one out of two colors), the resulting state is equivalent to a superposition of dimer coverings as in the RVB state [16].

To see the topological nature of the model and its associated ground state degeneracy, consider wrapping the lattice in Fig. 7.8 (a) on a torus. We can now define Wilson loop operators

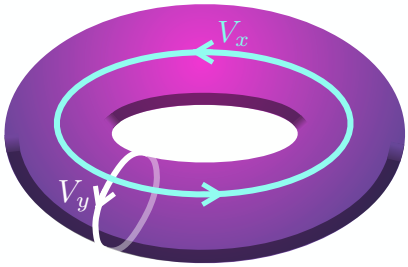

Figure 7.10: **Wilson loop operators.** Illustration of topological Wilson loop operators acting on closed loops through one of the cycles of the torus. For instance, one can define $\hat{V}_x = \prod_{\ell \in \mathcal{C}_x} \hat{\tau}^x_\ell$, $\hat{V}_y = \prod_{\ell \in \mathcal{C}_y} \hat{\tau}^x_\ell$.

that wrap around the two cycles of the torus along paths $\mathcal{C}_x$ and $\mathcal{C}_y$, as depicted in Fig. 7.10,

$$\hat{V}_x = \prod_{\ell \in \mathcal{C}_x} \hat{\tau}^x_\ell \,, \qquad \hat{V}_y = \prod_{\ell \in \mathcal{C}_y} \hat{\tau}^x_\ell . \tag{7.25}$$

Notably, these operators commute with the Hamiltonian (and can't be written just in terms of the $\hat{A}_+$ operators); their action hence transforms one ground state to another topologically distinct, but energetically degenerate ground state. As $\hat{V}_x^2 = \hat{V}_y^2 = 1$, this results in a four-fold degeneracy of the ground state,

$$\{ |\Psi_0\rangle \,, \hat{V}_x |\Psi_0\rangle \,, \hat{V}_y |\Psi_0\rangle \,, \hat{V}_x \hat{V}_y |\Psi_0\rangle \}. \tag{7.26}$$

Note that, in analogy, operators $\hat{W}_\mu = \prod_{\ell \in \mathcal{C}_\mu} \hat{\tau}^z_\ell$ commute with the Hamiltonian[6]. However, these do not lead to any additional ground state degeneracy, as the $\hat{V}$ and $\hat{W}$ operators do not commute,

$$\begin{aligned} \hat{W}_x \hat{V}_y &= -\hat{V}_y \hat{W}_x \\ \hat{W}_y \hat{V}_x &= -\hat{V}_x \hat{W}_y . \end{aligned} \tag{7.27}$$

This property will be a crucial ingredient at a later stage when we repeat Oshikawa's flux insertion argument for a $\mathbb{Z}_2$ spin liquid: The application of $\hat{V}_y$ will insert a π flux through the torus.

Luttinger's theorem revisited

The major assumption in Oshikawa's flux insertion protocol to proof Luttinger's theorem is that all low-energy excitations are given by fermionic quasiparticles close to the Fermi surface. If, however, we consider a system that has a topological ground state degeneracy, we must carefully consider how these low-energy states play into the flux insertion protocol.

We can do so by describing the $\mathbb{Z}_2$ QSL with a Chern-Simons field theory, by carefully ensuring that the ground state degeneracy, operator algebra of Wilson loop operators, and the braiding statistics of visons and spinons are fulfilled. An important point for the following result is that the e-particles of a QSL within an RVB description are fractionalized excitations (spinons) that

[6] These Wilson loop operators, $\hat{V}$ and $\hat{W}$, are the only non-trivial gauge-invariant observables of the toric code Hamiltonian.

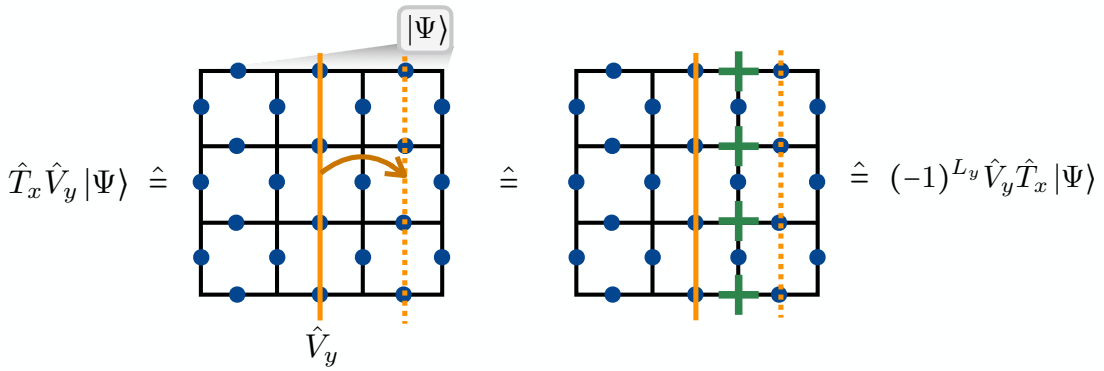

Figure 7.11: **Translation of a QSL.** Odd QSLs give rise to exotic commutation relations between Wilson loop operators and translation. Consider translation along x by one lattice site of the state $\hat{V}_y|\Psi_0\rangle$, which moves the Wilson loop from the solid to the dashed orange line. This can be achieved by applying star operators A_+ on all vertices next to the original position of the Wilson loop, see the green crosses. Due to the gauge constraint, during this process a sign of $\eta_+^{L_y}$ is picked up.

carry spin $S_z = 1/2$[7].

Introducing probe gauge fields that couple to, say, only spin-up particles, one can show that adiabatically inserting a 2π flux through the x-cycle of the torus (denoted by $\hat{U}_x$) corresponds to inserting a Wilson loop operator to the ground state [130],

$$\hat{U}_x|\Psi_0\rangle = \hat{V}_y|\Psi_0\rangle\,. \tag{7.28}$$

The intuition here is as follows: As spinon excitations carry a fractionalized U(1) charge $S_z = 1/2$, piercing a 2π flux through the torus will lead to the spinons seeing a π flux. When transforming the Hamiltonian back to the original gauge where the vector potential is zero, one has to account for this by adding a Wilson loop through the y-cycle of the Torus, i.e., $\hat{V}_y$.

If flux insertion leads to the application of a Wilson loop operator (i.e. it transfers one ground state to another, topologically distinct ground state), we need to test what happens under translation. In particular, this will tell us how the total momentum of the wave function will change when inserting the flux—a crucial ingredient to Luttinger's theorem. The process is shown in Fig. 7.11: We start from the state $\hat{V}_y|\Psi_0\rangle$, depicted by the orange line on the left-hand side of Fig. 7.11. When acting with the translational operator on this state, we must move the Wilson loop line by one lattice site along the x-direction. This can be achieved through the application of $\hat{A}_+$ on all vertices immediately to the right of the Wilson loop. In the case of an odd QSL with $\eta_+ = -1$, this leads to a non-trivial commutation relation between $\hat{V}_y$ and $\hat{T}_x$, namely

$$\hat{T}_x\hat{V}_y - \eta_+^{L_y}\hat{V}_y\hat{T}_x = 0. \tag{7.29}$$

[7] Microscopically, this can be argued as follows: When spin-1/2 particles form an RVB-type QSL, spinon excitations correspond to unbound spins. These can be described by Schwinger-bosons, and correspond to fractionalized spin-1/2 excitations. The resulting Hamiltonian can nevertheless be described by an Ising gauge theory as done above, but with the additional property that the e-particles carry a spin-1/2 degree of freedom.

Finally, we can analyze the momentum of the state after flux insertion, i.e., $|\Psi_0'\rangle = \hat{V}_y |\Psi_0\rangle$. With the momentum of the original state, $\hat{T}_x |\Psi_0\rangle = e^{iP_x} |\Psi_0\rangle$, and setting $\eta_+ = -1$ now, we get

$$\hat{T}_x |\Psi_0'\rangle = \hat{T}_x \hat{V}_y |\Psi_0\rangle = (-1)^{L_y} \hat{V}_y e^{iP_x} |\Psi_0\rangle = e^{i(\pi L_y + P_x)} |\Psi_0'\rangle . \tag{7.30}$$

The contribution to the momentum change from the spin liquid is thus

$$\Delta P_x = \pi L_y \,(\mathrm{mod}\, 2\pi) = \frac{2\pi}{L_x} \left(\frac{L_x L_y}{2} \right) \,(\mathrm{mod}\, 2\pi). \tag{7.31}$$

The same can be done for spin-down particles; we now see that the QSL can absorb flux that, expressed in the language of a Fermi liquid, corresponds to exactly unit density.

In particular, consider a system composed of a Fermi liquid and the Chern-Simons field theory of an odd quantum spin liquid, described by the action $\mathcal{S} = \mathcal{S}_{\mathrm{FL}} + \mathcal{S}_{\mathrm{oQSL}}$. The momentum balance consequently involves a sum of both the Fermi liquid and QSL, where according to the above arguments the latter absorbs flux that corresponds to exactly unit density. Hence, the sum of the Fermi liquid contribution Eq. (7.5) and the QSL contribution Eq. (7.31) must add up to the general result Eq. (7.2), i.e., $\Delta P_x = \frac{2\pi}{L_x} N_\uparrow \,(\mathrm{mod}\, 2\pi)$. Doing so and naively solving for V_{FS}, we find that Luttinger's count is modified from Eq. (7.7) to

$$\frac{V_{\mathrm{FS}}}{2\pi^2} = \delta \,(\mathrm{mod}\, 2). \tag{7.32}$$

Therefore, the presence of an odd $\mathbb{Z}_2$ QSL allows for the formation of a small Fermi surface without symmetry breaking!

The FL*

The above was first pointed out in Ref. [122], which led to a whole plethora of scenarios where the presence of a spin liquid fractionalizes the Fermi surface and forms a fractionalized Fermi liquid (FL*). Here, to gain an intuitive understanding how such an FL* can be realized in a one-band model, we shall focus on a toy description based on doping a quantum dimer model [114].

Imagine a situation where doping the AFM Mott insulator quickly leads to a destruction of magnetic order, and the local moments in the background form resonating singlet pairs. The dopants in such a scenario corresponds to "holons", which carry charge but no spin. Furthermore, spinon excitations exist in the quantum spin liquid formed by the local moments. Now, assume that there is an attractive potential between a holon and a spinon (which is larger than the energy needed to break apart a spin singlet to form two spinons), leading to a bound state. One indeed expects such an attractive potential from microscopic arguments: When a holon sits right next to a spinon, the spinon can gain kinetic energy by delocalizing over the two sites i.e. by forming a bonding orbital, $\frac{1}{\sqrt{2}}(|\uparrow, 0\rangle + |0, \uparrow\rangle)$. This composite particle now features the quantum numbers of a fermion, i.e., charge e from the holon and spin-1/2 from the spinon.

We now have a mixture of two types of dimers in the system: spin singlets and fermionic bound states of a holon and a spinon, illustrated in Fig. 7.12. These states will resonate with each other, such that the fermionic dimers can delocalize and form a metallic state. However, the

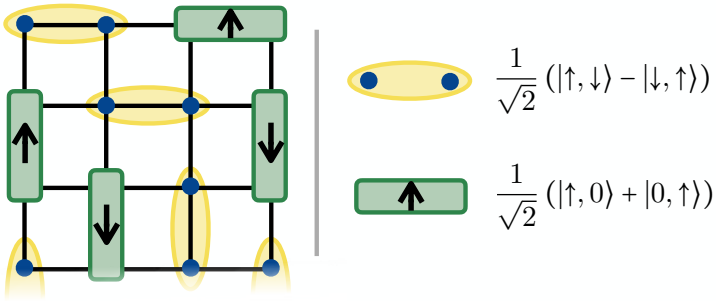

Figure 7.12: **Doped quantum dimer model.** Pictorial illustration of a doped quantum dimer model, leading to a fractionalized Fermi liquid (FL*), see i.p. Ref. [114]. The toy model is composed of two species of dimers: spin-singlets and bound states of holons and spinons, the latter forming a particle that carries the quantum numbers of a fermion. Through resonating, these fermionic dimers can gain kinetic energy, leading to a metallic state. Resonance of the spin-singlets in the background lead to a low-energy topological sector, which in turn allows for the formation of a small Fermi surface of the fermionic dimers.

presence of fermionic dimers will not disrupt the resonances of spin-singlet in the background, which can be analytically formulated through emergent gauge fields. The fermions in the system now are themselves dimers, they must be neutral under the gauge field, leading to a non-minimal coupling. Due to this coupling and the low-energy topological excitations of the resonating spin-singlets, the fermions form a small Fermi surface with volume $\propto \delta$.

Much work has been done in the literature to understand the FL* phase from a field-theoretic perspective, from which the structure of the Fermi surface as well as low-temperature instabilities of the pseudogap phase can be analyzed. One approach is to again start with the Hubbard-Stranonovich decoupled spin-fermion model, Eq. (7.12). The key to end up in an FL* phase is to "quantum disrupt" spin-density wave order, e.g. by restricting the AFM fluctuations to pure phase fluctuations [101],

$$\mathbf{\Omega} \to \hat{\mathbf{n}}\,, \quad |\hat{\mathbf{n}}| = 1. \tag{7.33}$$

It can be shown that by replacing $\mathbf{\Omega}$ by $\hat{\mathbf{n}}$ in Eq. (7.12) leads to an intermediate phase between a Fermi liquid with and without symmetry breaking, where nevertheless the volume of the Fermi surface is small—this is the FL* phase [101].

7.5 The geometric FL*

We now pick up upon the theoretical ideas underlying Fermi surface fractionalization and discuss a scenario where, instead of the microscopic spins themselves, a string net of fluctuating domain walls give rise to a $\mathbb{Z}_2$ quantum spin liquid. As we will discuss in the following, this will allow for a compelling unification of correlated phases of matter in hole-doped cuprates, including the AFM, stripe, and pseudogap phase.

Our description of the pseudogap phase builds upon the idea that domain walls of the underlying AFM—i.e. individual stripes—can be held together by strong spin-charge correlations, even in a regime where interactions between neighboring stripes can be overcome by thermal

or quantum fluctuations. This prevents the formation of charge-density wave order and results in a low-energy theory of string-like fluctuating stripes that leads us to propose an alternative scenario for an FL* phase: A string-net condensate of stripes introduces topological order which lends an emergent gauge charge to the magnetic polaron excitations of the underlying AFM. This fractionalizes their Fermi surface and geometrically suppresses long-range AFM correlations, in a state with an underlying spontaneously broken SU(2) symmetry. In particular, our proposed scenario consists of the following, summarized in Fig. 7.13:

1. The mechanism behind the efficient disruption of the AFM phase close to half-filling is *hidden order*, caused by fluctuating domain walls of the spin-background linked to charge fluctuations. Specifically we propose that, while the SU(2) symmetry of the AFM background is broken, the order is hidden through fluctuations of closed loops that enclose areas where the AFM order switches its sublattice. The transition between visible and hidden order is governed by an Ising* criticality characterized by highly non-local observables.

2. Hidden order allows for the existence of well-defined fermionic quasiparticles, i.e., magnetic (or spin-) polarons, as well as bosonic Goldstone modes (paramagnons). The latter live in the space of the ordered spin background, which is the 2D generalization of squeezed space.

3. At low temperatures, interactions between fluctuating domain walls drive a transition to the stripe phase, where individual stripes align that break the C_4 lattice symmetry. In this case, magnetic order reappears in the lab frame through long-range incommensurate spin correlations.

4. At zero temperature and enhanced doping (and strong magnetic fields), where neither stripes nor superconductivity appear in the ground state, the pseudogap phase is the realization of a loop gas of fluctuating domain walls. String-net condensation leads to hidden order and the formation of an odd $\mathbb{Z}_2$ spin liquid.

5. Magnetic polarons couple to the geometric spin liquid formed by the fluctuating domain walls, acquire an emergent gauge charge, and form a small Fermi surface. The broken SU(2) symmetry together with sublattice fluctuations define what we call a geometric fractionalized Fermi liquid (GFL*), which features topologial excitations that absorb momentum in Oshikawa's flux insertion protocol.

6. At a hidden quantum critical point (hQCP) on the doping axis, hidden order disappears and the SU(2) symmetry is fully restored as spin-interactions in squeezed space become frustrated. Signatures of this transition are detectable only through highly non-local observables or quantum critical transport properties. We conjecture these to underlie the bad metallicity observed in cuprates.

The picture of hidden order allows to naturally unite the AFM and stripe phases with the pseudogap: In all cases, the SU(2) symmetry of the spin background is spontaneously broken—it is merely hidden in the experimentalist's frame of reference within the pseudogap phase. We

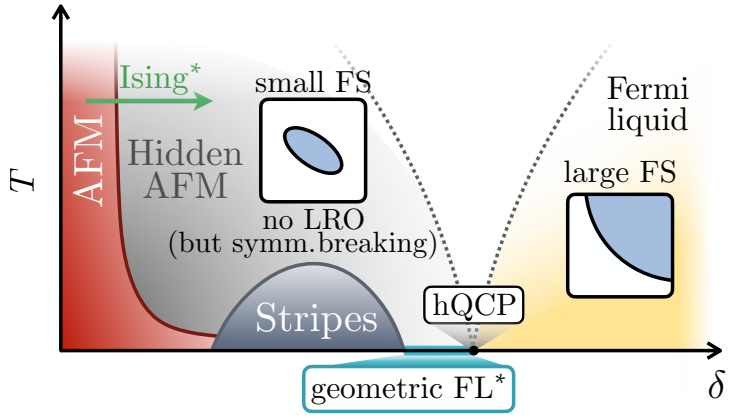

Figure 7.13: **Proposed phase diagram of hole-doped cuprates.** Interpretation of the phase diagram of hole-doped cuprates at strong magnetic fields, where superconductivity is suppressed. Around half-filling, long-range AFM order exists. Upon doping, the string tension h of domain wall loops decreases, driving an Ising* transition to a hidden ordered state (green arrow). At zero temperature, we propose that cuprates realize a geometric FL* (GFL*), whereby topological excitations of the fluctuating domain walls lead to the formation of a small Fermi surface constituted by magnetic (or spin-) polarons. At a critical doping, hidden order vanishes through a frustration mechanism governed by fluctuations of microscopic holes, resulting in a hidden quantum critical point (hQCP) that drives a topological transition from a GFL* (with a small Fermi surface) to a Fermi liquid (with a large Fermi surface).

argue that by postulating hidden order in the system, a geometric fractionalized Fermi liquid constituted by magnetic polarons naturally emerges. It further directly suggests the presence of spin-wave-like excitations, i.e. paramagnons (see Sec. 7.3), which, in contrast, should be absent when the physical spins in the system form the spin liquid [114].

Due to the inherent real-space nature of relevant observables, hidden order can be directly probed with ultracold atom experiments. In particular, by looking for signs of hidden order in spin-resolved snapshots of analog quantum simulation platforms, our scenario can be explored with existing experimental setups. This further stresses the potential of analog simulation of the FH model at finite temperatures, which may help to differentiate between various theoretical proposals of the pseudogap phase and pin down its microscopic nature.

In the following, we motivate the origin of hidden antiferromagnetism and the geometric fractionalized Fermi liquid starting from the microscopic two-dimensional (2D) FH model and the Hubbard-Stratonovic-decoupled partition function Eq. (7.10). As discussed in Sec. 7.4, condensation of paramagnons leads to Fermi surface reconstruction due to translational symmetry breaking. In the FL* scenario, see also Sec. 7.4, it has been argued that a fractionalized Fermi liquid (FL*) can be realized by restricting fluctuations of $\mathbf{\Phi}$ only to its angle [126, 127]. The spin-density wave can then become "quantum disordered" [101], stabilizing an exotic state of small hole pockets but without AFM order, i.e. $\langle \mathbf{\Omega_i} \rangle = 0$. Nevertheless, the local magnitude of AFM order is finite, which can be formalized by a Higgs field in an SU(2) gauge theory after transformation of the underlying electrons to a rotating frame [101, 130, 282–286]. Similarly, an FL* phase can be realized when the background spins form a quantum spin liquid e.g. through res-

onances of spin-singlet dimers (analytically represented by emergent gauge fields) [101]. This is in particular motivated by exploring possible ground states of the undoped parent Hamiltonian (e.g. a $\mathbb{Z}_2$ spin liquid), which is then doped to form a fractionalized Fermi liquid under certain assumptions, see the discussion in Sec. 7.4.3.

In the following, we take an alternative approach and include stripe-like AFM domain wall defects in an effective description of the FH model. These correspond to spatially well-localized sign-changes (π-phase slips, $\mathbf{\Omega} \to -\mathbf{\Omega}$) across line-like defects corresponding to individual (fluctuating) stripes [287], see Fig. 7.14. Fluctuations of these defects will then lead us to the geometric fractionalized Fermi liquid (GFL*) scenario. Before discussing the latter, we describe how fluctuating domain wall structures efficiently hide AFM correlations in real-space, which is the essential mechanism behind the GFL* at low temperatures and explains the quick demise of AFM at temperatures above the stripe ordering transition.

7.5.1 Hidden order from fluctuating stripes

We consider low-energy contributions to Eq. (7.10) that are directly motivated by the low-temperature phases of the FH model at finite doping: In the strongly interacting limit $U \gg t$, all state-of-the-art numerical methods broadly agree on the appearance of stripes in the ground state, where charges accumulate around AFM domain walls and form a charge density wave [138–145,147]. This results in long-range charge and incommensurate long-range magnetic order, in accordance with broad experimental evidence in cuprate materials [79–81]. Though quantum fluctuations of the microscopic holes lead to deformations of the lines of stripes, they are locked in place, i.e., individual stripes align and explicitly break the C_4 symmetry of the underlying square lattice. This scenario is schematically illustrated in Fig. 7.14 (a), showing a representative low-energy configuration in the stripe phase. Here, the indicated arrows represent the direction of $\mathbf{\Omega}$, i.e., they specify the sublattice parity [288] of the underlying AFM state.

Upon raising the temperature, stripes melt, and the FH model displays a pseudogap with only short-range AFM correlations present [148–154] and a reconstructed Fermi surface [155]. We particularly highlight Ref. [154], where the fate of the pseudogap in the FH model when tuning the temperature towards the ground state has been analyzed through a "handshake" of wave-function and finite temperature based methods. Quoting Ref. [154]: *The range of density and coupling strength where a pseudogap is found precisely coincides with that in which ground-state studies find a stripe phase with long-range spin and charge order.* This further aligns with experimental findings of various La-based cuprates with different balances between superconductivity and stripe order, where *the overarching conclusion is that the pseudogap and stripe phases are closely linked* [109]. This suggests an intricate interplay between the stripe and pseudogap phase in the FH model, with a possible common microscopic origin—it is this scenario that we work out in depth in the remainder of this chapter.

Specifically, we now propose a set of microscopic configurations that may be relevant for an effective description of the doped FH model at elevated temperatures. To this end, we note that the formation of stripes can be associated with two energy scales: (i) The energy gain for binding a doped hole into an (undirected) $(d-1)$-dimensional AFM domain wall structure,

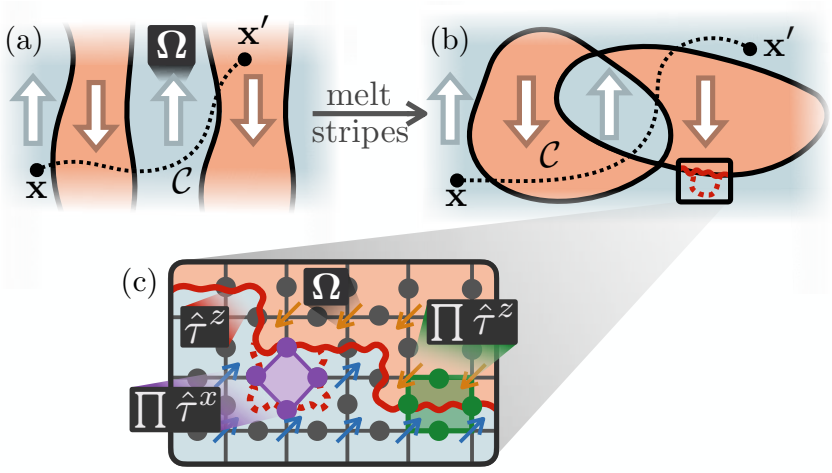

Figure 7.14: **Fluctuating stripes.** (a) Schematic illustration of ordered stripes, breaking the discrete C_4 lattice symmetry. Along lines of enhanced hole density, π-phase slips of the AFM order parameter $\mathbf{\Omega}$ appear, illustrated by the arrows. (b) Upon melting stripes, we propose a scenario where domain walls form closed loops and fluctuate. While magnetic order is obscured in real space, hidden order survives, which can be revealed through non-local spin-string-spin correlations by explicitly considering the domain walls that occur along a path $\mathcal{C}$ (dashed lines in (a) and (b)), cf. Eq. (7.38). (c) We describe fluctuating domain walls by introducing strings (red wiggly line) $\hat{\tau}^z$ that live on the links (grey dots) of the lattice. The classical Hamiltonian Eq. (7.35) describes thermal fluctuations of domain wall loops and includes plaquette terms $\propto \prod \hat{\tau}^z$ of the $\hat{\tau}^z$-field (green square). Adding quantum fluctuations $\propto \prod \hat{\tau}^x$ (purple diamond) to the Hamiltonian leads to an effective description of fluctuating domain walls through a perturbed toric code, Eq. (7.40).

i.e., sub-dimensional regions of accumulated charge density across which the AFM develops π-phase slips, and (ii) the interaction strength between such individual stripes, resulting in the formation of charge-density waves where individual stripes lock into place in the ground state. Generally, it is conceivable that either of the two energy scales is larger, which then governs the important contributions to Eq. (7.10) at intermediate temperatures.

We shall here focus on the scenario where the first energy scale is larger, i.e., breaking up stripe-like domain wall structures is associated with a higher energy cost compared to them locking into place. This is generally expected at low doping where the typical distance between individual stripes is large, and is supported by the cold-atom experiment discussed in Sec. 5.3, which suggest the formation of fluctuating, stripe-like structures at elevated temperatures, on the order of J, in (mixed-dimensional) FH systems.

We specifically focus on closed loops that enclose regions where the AFM order parameter is flipped, which we argue constitute a minimal scenario to describe the low-energy physics of domain wall fluctuations at temperatures above the stripe ordering transition. An exemplary configuration is shown in Fig. 7.14 (b); any closed loop encloses a region where the AFM order parameter $\mathbf{\Omega}$ is sign-flipped.

We note that in the ground state, it has been established that kinetic effects lead to directed stripes being energetically favorable over undirected configurations [138,289]. However, at finite

temperatures a scenario where the charge-density wave stiffness vanishes and loop defects proliferate is conceivable, as proposed in Ref. [290]. From a microscopic point of view, we propose that mobile holes in the form of magnetic polarons form a Fermi sea, and local spin-charge correlations arising from microscopic interactions stabilize closed-loop domain wall configurations of the AFM background.

Our starting point is hence a state with broken SU(2) symmetry, where $\mathbf{\Omega}$ points in a particular direction; thermal fluctuations of the AFM background are described through a non-linear σ model (NLSM) [291]. On top of this we allow for closed loop domain wall excitations where the AFM order parameter is flipped, i.e., $\mathbf{\Omega} \to -\mathbf{\Omega}$. Our aim is to simplify the full description of the field $\mathbf{\Omega}(\mathbf{x})$ to string configurations $\hat{\tau}(\mathbf{x})$ that describe the π-phase slips of $\mathbf{\Omega}$. To this end, we introduce operators $\hat{\tau}^z_\ell$ that live on the links of the lattice, where $\ell = \langle \mathbf{i}, \mathbf{j} \rangle$ is the link that connects sites $\mathbf{i}$ and $\mathbf{j}$. For sharp domain walls of width $\lesssim a$ (with a the lattice constant), we define

$$\hat{\tau}^z_{\ell=\langle \mathbf{i},\mathbf{j}\rangle} = \mathrm{sgn}(\mathbf{\Omega}_\mathbf{i} \cdot \mathbf{\Omega}_\mathbf{j}). \tag{7.34}$$

These local $\mathbb{Z}_2$ degrees of freedom then capture the structure of domain walls on the two-dimensional square lattice, illustrated in Fig. 7.14 (c).

Focusing on classical (thermal) fluctuations for now, this motivates the following Hamiltonian to describe the thermodynamic properties of closed line domain walls at elevated temperatures,

$$\hat{\mathcal{H}}_{\mathrm{cl}} = -K_\square \sum_\square \prod_{\ell \in \square} \hat{\tau}^z_\ell - h \sum_\ell \hat{\tau}^z_\ell, \tag{7.35}$$

where the sum runs over all plaquettes on the square lattice and $\hat{\tau}^z_\ell |q\rangle_\ell = \pm |q\rangle_\ell$ with $q = 0, 1$ a $\mathbb{Z}_2$ degree of freedom defined on links ℓ. The $K_\square > 0$ term energetically favors an even number of strings per plaquette, which suppresses open string configurations and favors closed loop structures (cf. the green plaquette in Fig. 7.14 (c)). h takes the role of a chemical potential, i.e. it relates to the density of strings, and corresponds to a linear string tension of the loops (with energy $2h|\Sigma|$ where $|\Sigma|$ is the length of the loop). Assuming that hole dopants provide the glue that stabilize AFM domain walls, i.e.

$$1 - \langle \hat{\tau}^z_\ell \rangle \propto \delta, \tag{7.36}$$

we can expect h to decrease with increasing doping δ.

We now analyze thermal fluctuations of the classical model in Eq. (7.35); the effect of quantum fluctuations and emergence of a small Fermi surface is addressed further below. In the subspace of closed loops (i.e. in the pure gauge scenario $K_\square \to \infty$), the Hamiltonian Eq. (7.35) is dual to the 2D Ising model [292, 293],

$$\hat{\mathcal{H}}_{\mathrm{Ising}} = -h \sum_{\langle \mathbf{i},\mathbf{j}\rangle} \hat{\sigma}^z_\mathbf{i} \hat{\sigma}^z_\mathbf{j} + \mathrm{const.}, \tag{7.37}$$

where $\hat{\sigma}^z_\mathbf{i}$ are qubit operators that live on sites $\mathbf{i}$ of the lattice. By construction of the duality mapping, $\hat{\sigma}^z_\mathbf{i} = \mathrm{sgn}(\mathbf{\Omega}_\mathbf{i} \cdot \mathbf{\Omega}_0)$, where $\mathbf{\Omega}_0$ denotes the Néel order parameter at an arbitrary reference site. We thus see that line-defects of π-phase slips in an AFM with spontaneously broken SU(2)

symmetry lead to an effective Ising description of the Néel order parameter.

The dual Ising Hamiltonian $\hat{\mathcal{H}}_{\text{Ising}}$ has a phase transition at the critical temperature $T_c/h \approx 2.27$, which separates a ferromagnetic from a paramagnetic phase. In terms of the Hamiltonian Eq. (7.35), for $T < T_c$ domain wall loops are confined and non-percolating. In the high-temperature phase, $T > T_c$, strings deconfine, i.e., loops span the whole system and percolate [294]. The Ising ferromagnetic (paramagnetic) phase of the dual model can hence be identified with a long-range (short-range) ordered $\mathbf{\Omega}$ field in the doped Mott insulator. Though no local order parameter can be defined in terms $\hat{\tau}^z_\ell$ that characterizes the confined-deconfined phase transition of Eq. (7.35), it is governed by an Ising criticality through the dual mapping (and is hence denoted by Ising*) [293].

The high-temperature deconfined phase defines the concept of *hidden order* in our scenario: While real space correlations of $\mathbf{\Omega}$ become short range for $T > T_c$, the order is merely hidden efficiently through the existence of a percolating string net. In other words, for a given snapshot of the physical system, one can reconstruct the loop configuration by tracking the sublattice parity of each spin. This is akin to our discussion of hidden order and squeezed space in 1D and mixed-dimensional systems, where the latter captures the non-local structure of correlations, cf. Chapter 6.

In Ref. [288], squeezed space has been generalized to uni-directed stripes in two dimensions. Sublattice parity order has been identified as the stripes' defining characteristic, which is defined by long-range properties of the non-local, topological correlation function (here written in the continuum limit and using our link variable $\hat{\tau}^z_\ell$ introduced above),

$$\mathcal{O}_{\text{top}}(\mathbf{x}-\mathbf{x}',\mathcal{C}) = \langle\Psi|\mathbf{\Omega}(\mathbf{x})e^{i\pi\int_{\mathcal{C}} d\mathbf{y}[1-\hat{\tau}^z_{\langle \mathbf{y},\mathbf{y}+d\mathbf{y}\rangle}]}\mathbf{\Omega}(\mathbf{x}')|\Psi\rangle\,, \tag{7.38}$$

where $\mathcal{C}$ is a path connecting points $\mathbf{x}$ and $\mathbf{x}'$. The contour integral ensures that domain walls are captured in the magnetic correlations, see Fig. 7.14 (a), and it becomes independent on the choice of $\mathcal{C}$ (i.e. topological in nature) when $\hat{\tau}^z$'s from closed loops. When all dopants are bound into stripes, $\hat{\tau}^z$ in Eq. (7.38) can be expressed in terms of the electron density operator $\hat{n}(\mathbf{y})$, with different relations for fully and partially filled stripes [288].

The notion of hidden order through fluctuating, closed domain wall loops is a natural extension of this concept: By identifying loops of flipped AFM order parameter, one can reconstruct the original symmetry broken state with long-range order by flipping the spins within each closed loop, as illustrated in Fig. 7.14 (b). Using spin- and charge-resolved snapshots, cold-atom quantum simulators at state-of-the-art temperatures can directly search for these structures by evaluating Eq. (7.38), which highlights the potential of exploring the intermediate temperature regime of doped antiferromagnets with ultracold atoms.

The phase diagram of the Hamiltonian Eq. (7.35) is shown in Fig. 7.15, featuring an Ising* transition from an AFM to hidden AFM phase at $T_c/h = 2.27$, see the black line in Fig. 7.15. We propose that this mechanism of hidden AFM correlations ultimately leads to the fast disappearance of the AFM phase in doped cuprates. At elevated temperatures, the Ising* criticality drives a transition from the AFM phase with long-range order to the hidden AFM phase with only short-range correlations in real space. A schematic phase diagram of doped cuprates at

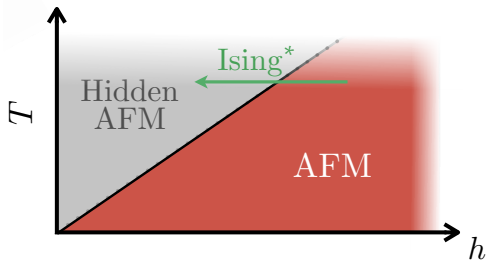

Figure 7.15: **Classical phase diagram of fluctuating domain walls.** Schematic phase diagram of Eq. (7.35). We propose a scenario in which doping leads to the formation of fluctuating closed loop domain walls across which the AFM order parameter switches its sign, leading to an extended phase that features *hidden order*. At elevated temperatures, we argue that thermal fluctuations of string loops are captured by the (classical) Hamiltonian Eq. (7.35), which features a dual Ising criticality (Ising*) that describes a transition from long-range AFM to hidden AFM order due to percolating string nets (green arrow). This corresponds to the regime in the T-h plane where $T_c/h = \text{const.}$, illustrated by the dotted grey line.

strong magnetic fields, i.e. where the d-wave superconducting phase is suppressed, is presented in Fig. 7.13. Starting at half-filling, doping leads to an increase of string density Eq. (7.36), in turn reducing the string tension in the loop gas. We can therefore expect that the doping level δ of the microscopic system and the string tension h of the effective classical model Eq. (7.35) are inversely related, resulting in a sharp drop of the critical temperature of the AFM phase in Fig. 7.13. The transition to the hidden order phase at elevated temperatures is then governed by the same Ising* criticality as in Eq. (7.35), as indicated in both Fig. 7.13 and Fig. 7.15 by the green horizontal line. This picture is consistent with experimental signatures of an Ising-type order parameter found in the pseudogap regime [295].

Upon decreasing temperature, we propose that a transition from hidden order to long-range, incommensurate stripe order appears, whereby individual stripes lock into place and break both translational and rotational lattice symmetries. This corresponds to an ordering transition of the $\hat{\tau}^z$ fields, and is akin to mean-field ground state considerations in Ref. [288].

To summarize, the partition function $\mathcal{Z}$ in Eq. (7.10) so far is expressed in terms of a path integral over fermions c coupled to the Néel-order parameter $\mathbf{\Omega}$. Above we have argued that the relevant low-energy configurations in the pseudogap regime correspond to domain-wall lines of the Néel order, supplemented by long-wavelength fluctuations of the hidden AFM state. This motivates the expression of the partition function, after integrating out fermions, as

$$\mathcal{Z} = \int \prod_{\mathbf{i}} \mathcal{D}\tilde{\mathbf{\Omega}}_{\mathbf{i}}(\tau) \prod_{\ell} \mathcal{D}\tau^z_{\ell}(\tau) e^{S_{\text{eff}}}. \tag{7.39}$$

Here $\tilde{\mathbf{\Omega}}$ is the hidden Néel order field in (the 2D generalization of) squeezed space, and τ^z describes the line-like AFM domain wall defects; together these determine $\mathbf{\Omega}$. So far the effective action S_{eff} consists of the NLSM for $\tilde{\mathbf{\Omega}}$ and the thermal fluctuations governed by the classical loop-gas Hamiltonian from Eq. (7.35).

In the above discussion of the loop gas, we have focused on zero matter density, i.e., we

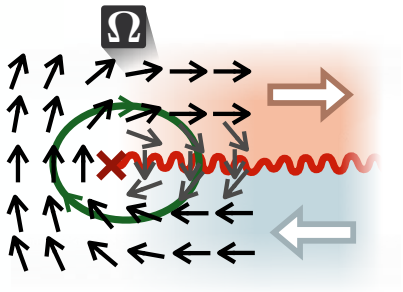

Figure 7.16: **Half-vortex excitation.** Winding of the $\mathbf{\Omega}$ field around an open domain wall string, corresponding to a half-vortex excitation. We identify these excitations as magnetic visons in the effective toric code description. Across the domain wall, the discontinuity of $\mathbf{\Omega}$ is described by a rotation in the continuum limit on scales around the lattice spacing, see the grey arrows. When adiabatically following a closed path that encircles an open string end, the field performs a full 2π rotation - leading to a Berry phase of π when a spin-1/2 defect (e.g. a magnetic polaron) winds around an open domain wall end (along the green circle).

excluded open ends of domain wall strings in our description. In this setting, the percolating (hidden order) phase extends up to infinite temperature, though the stiffness and correlation length of the underlying SU(2) symmetry broken state (governed by a NLSM) is reduced with rising temperature. In particular at elevated temperatures (and akin to previous considerations of fluctuating stripes [287–290]), we expect that including open domain wall string excitations constitutes an important step towards a more accurate description of the fluctuating stripe scenario. Ends of strings then correspond to topological half-vortices of the $\mathbf{\Omega}$ field, illustrated in Fig. 7.16. We speculate that explicitly taking into account open ends and their interactions may lead to a BKT-type transition from the hidden order to a disordered phase, driven by the unbinding of (half) vortex-antivortex pairs connected by domain wall strings. Such a transition would mark the edge of the pseudogap phase observed at T^*.

7.5.2 Berry phases and emergent toric code

Although we restricted our considerations to closed domain wall loops so far, analyzing the braiding statistics of topological vortex charges will give us important insights into the nature of gauge fluctuations that need to be included in the effective low-temperature theory that we construct next. This will ultimately lead us to a $\mathbb{Z}_2$ lattice gauge theory (LGT) with unit background charge, in turn realizing an odd $\mathbb{Z}_2$ quantum spin liquid in the ground state.

As a starting point, we revisit the step from Eq. (7.10) to Eq. (7.39) in which we have focused on classical terms and ignored Berry phase effects. While this is justified at elevated temperatures, including Berry phase terms associated with topological defects of $\mathbf{\Omega}$ is crucial to obtain the correct low-temperature description. As above, our goal is to express the microscopic field $\mathbf{\Omega}$ in terms of the smoothly varying hidden Néel field $\tilde{\mathbf{\Omega}}$—for which Berry phases are not important at low doping—and the fluctuating string field τ^z describing domain walls. The latter contains information about topological excitations of $\mathbf{\Omega}$ and must therefore reflect the associated quantized Berry phases.

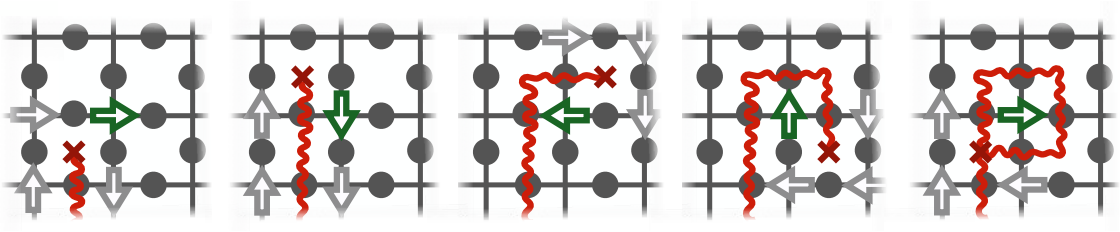

Figure 7.17: **Berry phase.** Effect of adiabatically moving an open string end (unit $\mathbb{Z}_2$ magnetic charge) around a lattice site. Encircled microscopic spins perform an in-plane rotation by 2π. This leads to the lattice sites carrying a $\mathbb{Z}_2$ electric charge, i.e., there exists a background unit charge that ultimately leads to the formation of an odd $\mathbb{Z}_2$ spin liquid.

To understand how this can be achieved, we discuss the gauge structure of τ^z and clarify how it relates to $\mathbf{\Omega}$. In our description of string configurations τ^z, domain wall lines can be interpreted as $\mathbb{Z}_2$ magnetic field lines on the dual lattice. Ends of domain wall lines give rise to topological half-vortex excitations of the $\mathbf{\Omega}$ field, where the parity of the AFM order parameter continuously changes its sign. This is depicted in Fig. 7.16 for a particular rotation direction on the Bloch sphere (we note, however, that in the path integral, the field is integrated over all rotation directions, which restores the global S^z_{tot} symmetry via NLSM thermal fluctuations of the hidden antiferromagnet).

We therefore identify the ends of domain wall lines as vison excitations (or $\mathbb{Z}_2$ magnetic charges) of an effective $\mathbb{Z}_2$ LGT theory. We now ask what happens when adiabatically moving such a vison around a site $\mathbf{i}$ of the physical lattice, see Fig. 7.17. Due to the vortex structure of the associated $\mathbf{\Omega}$-configuration, this winds the spin on site $\mathbf{i}$ once around itself, Fig. 7.17. Thereby, the many-body wave function picks up a topological Berry phase of $\varphi_B = \Omega_S/2 = \pi$, as one microscopic spin-1/2 completes a full rotation around the Bloch sphere and hence encloses a solid angle of $\Omega_S = 2\pi$.

Next we construct the effective action of the τ^z field. To this end we include quantum fluctuations and make sure that the ground state of the field τ^z inherits the π-Berry phase derived above, produced by the microscopic field $\mathbf{\Omega}$ that we integrate out in going from Eq. (7.10) to Eq. (7.39). Microscopically, quantum fluctuations of domain wall loops originate from fluctuating mobile dopants; here we capture them by the simplest effective Hamiltonian consistent with the topology of closed loops.

We introduce the operator $\hat{\tau}^x_\ell$ conjugate to the $\hat{\tau}^z_\ell$ that flips the $\mathbb{Z}_2$ degree of freedom, $\hat{\tau}^x_\ell |1\rangle_\ell = |0\rangle_\ell$. Including terms $\prod_{\ell\in+_\mathbf{i}} \hat{\tau}^x_\ell$ in the Hamiltonian, where $+_\mathbf{i}$ includes all links around a site $\mathbf{i}$, thus constitutes a minimal scenario: When applying flips on the purple links in Fig. 7.14 (c), the red domain wall loop is extended to surround the site connected by the purple links—thus allowing the domain wall to fluctuate without introducing open strings. Within this scenario, fluctuating stripes are described by a perturbed toric code Hamiltonian [281],

$$\hat{\mathcal{H}}_{\text{TC}} = -K_\square \sum_\square \prod_{\ell\in\square} \hat{\tau}^z_\ell - h\sum_\ell \hat{\tau}^z_\ell + K_+ \sum_+ \prod_{\ell\in+} \hat{\tau}^x_\ell - \lambda \sum_\ell \hat{\tau}^x_\ell. \tag{7.40}$$

As in the case of classical fluctuations, we in this work focus on the limit of fully closed domain-

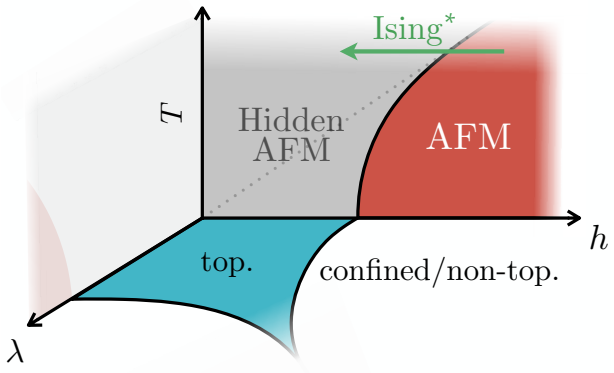

Figure 7.18: **Phase diagram of the perturbed toric code Hamiltonian.** (a) Schematic phase diagram of Eq. (7.40). At elevated temperatures, we argue that thermal fluctuations of string loops are captured by the (classical) Hamiltonian Eq. (7.35), which features a dual Ising criticality (Ising*) that describes a transition from long-range AFM to hidden AFM order due to percolating string nets (green arrow). This corresponds to the regime in the T-h plane where $T_c/h = \text{const.}$, illustrated by the dotted grey line. At low temperatures, quantum fluctuations stabilize the hidden order phase, characterized by loop condensation (blue area).

wall loops. Therefore we set $\lambda = 0$ in the following, although we note that small non-vanishing λ would not change our conclusions below.

What remains to be clarified is the sign of K_+. To this end we note that the choice $K_+ > 0$ that we make fixes the gauge sector to $\prod_{\ell\in+} \hat{\tau}^x_\ell = -1$, ensuring a unit $\mathbb{Z}_2$ electric background charge. The mutual braiding statistics of a vison around a $\mathbb{Z}_2$ electric charge corresponds to a π-Berry phase in the topologically ordered ground state of the perturbed toric code Hamiltonian Eq. (7.40). Therefore we conjecture that integrating out $\mathbf{\Omega}$-configurations associated with AFM domain wall defects introduces a large, positive K_+ term in the effective Hamiltonian of the fluctuating domain-wall field τ^z that correspond to a topologically ordered ground state whose vison excitations carry the required π-Berry phase of half-vortex defects, see Fig. 7.17.

The well-known phase diagram of Hamiltonian Eq. (7.40) as a function of λ, h and T (assuming $K_\square = K_+$) is shown in Fig. 7.18—see also Refs. [296–299]. Within the blue region at $T = 0$, the ground state features topological order, realizing an odd $\mathbb{Z}_2$ spin liquid due to the non-vanishing background charge [123]. In particular, this regime corresponds to a deconfined phase characterized by loop gas condensation [296, 297], whereby quantum fluctuations lead to the extension of the hidden AFM phase to the ground state. At elevated temperatures, quantum fluctuations are negligible, and the system is effectively described by the classical Hamiltonian Eq. (7.35).

While stripes are expected to be stabilized by weak string-string interactions (not explicitly included in Eq. (7.40)) at zero temperature, we propose that the normal state with a small Fermi surface observed around optimal doping (and in the presence of a magnetic field to suppress superconductivity) [96] realizes a topologically ordered hidden AFM as described above, see Fig. 7.13.

7.5.3 Geometric FL*

This finally brings us to the analysis of charge carriers in the hidden AFM phase. We argue that these are constituted by magnetic (or spin-) polaron excitations [265,272–279] of the hidden AFM, with a charge carrier density given by the number of free dopants δ. This suggests that they form a small Fermi surface, and as we will show next by analyzing their coupling to gauge fluctuations, this is in accordance with the generalized Luttinger theorem for fractionalized Fermi liquids [101, 122, 280] when the AFM domain walls τ^z form a topologically ordered string-net condensate.

From this perspective, the ordered stripe phase breaking the translational symmetry gaps out the small Fermi suface and can lead to the formation of charge- and (incommensurate) spin-density wave orders [79–81, 121]. Note that even in the hidden AFM phase with fluctuating AFM domain walls we expect strong spin-charge correlations to stabilize such domain walls. However, this does not require the charge carriers to be bound into these fluctuating structures, see also Ref. [147]; our picture is rather that they simultaneously participate in a small-FS Fermi sea while stabilizing the loop gas of the domain wall strings.

Our effective field theory in Eq. (7.39) is still lacking the degrees of freedom associated with mobile dopants. At very low doping, before domain-wall strings proliferate, the AFM breaks the SU(2) and translational symmetries of the system, and its elementary charged excitations correspond to magnetic polarons. In the following we will denote them by fermionic operators $\hat{f}_{\mathbf{i},\sigma}$ carrying spin-1/2 and charge e, and include them in the partition function in Eq. (7.10) by introducing an additional path integration $\int \prod_{\mathbf{i}} \mathcal{D} f_{\mathbf{i},\sigma}(\tau)$. In the parent AFM, corresponding to $\hat{\tau}^z \equiv 1$ everywhere, magnetic polarons gain kinetic energy through spin-exchange processes in the underlying quantum magnet, leading to effective next-to-nearest neighbor (NNN) hopping and a corresponding dispersion that has its minimum around $[\pi/2, \pi/2]$ [265, 272–279]. Note that, since we start in a state with broken translational symmetry, opposite spin states live on opposite sub-lattices.

Moving through a non-uniform AFM, the spin of a magnetic polaron adiabatically follows the surrounding Néel field $\mathbf{\Omega}(\mathbf{x})$. This has important consequences when AFM domain walls, described by the field τ^z, proliferate, and dictates the coupling of $\hat{f}$-fermions to $\hat{\tau}$. To understand this, we perform another Berry-phase analysis. As before, our starting point is an open domain wall end, see Fig. 7.16. Across the domain wall, the continuous $\mathbf{\Omega}$ field experiences a π-phase slip; in a continuum description, this can be described by an in-plane rotation of the $\mathbf{\Omega}$ field on scales comparable to the lattice constant, illustrated by grey arrows in Fig. 7.16. Therefore, when a magnetic polaron encircles the end of an open domain wall string its spin orientation adiabatically follows the direction of the $\mathbf{\Omega}$ field, and correspondingly it picks up a Berry phase of $\varphi_B = \pi$ (Fig. 7.16). Meanwhile, closed paths that do not encircle the end of an open string result in a vanishing Berry phase.

Thus we find that magnetic polarons and open domain wall ends are mutual semions. Since we identified the latter with $\mathbb{Z}_2$ magnetic excitations (visons) of the fluctuating string field $\hat{\tau}$, we conclude that magnetic polarons must carry the corresponding $\mathbb{Z}_2$ electric charge: The mutual semionic braiding statistics of $\mathbb{Z}_2$ electric and magnetic excitations reflects the topological π-Berry phase of magnetic polarons that needs to be taken into account when expressing the

microscopic field $\mathbf{\Omega}$ by the AFM domain-wall strings $\hat{\tau}$.

These new insights lead us to the following effective Hamiltonian capturing the motion of magnetic polarons in a quantum loop gas of fluctuating domain walls,

$$\hat{\mathcal{H}} = \hat{\mathcal{H}}_{\mathrm{TC}} + \sum_{\substack{\langle\langle \mathbf{i},\mathbf{k}\rangle\rangle \\ \mathbf{j}\in \mathrm{NN}\{\mathbf{i},\mathbf{k}\}}} \left[t^{\mathrm{MP}}_{\langle\langle \mathbf{i},\mathbf{k}\rangle\rangle} \hat{f}^{\dagger}_{\mathbf{i}} \hat{\tau}^{z}_{\ell=\langle \mathbf{i},\mathbf{j}\rangle} \hat{\tau}^{z}_{\ell=\langle \mathbf{j},\mathbf{k}\rangle} \hat{f}_{\mathbf{k}} + \mathrm{H.c.} \right]. \tag{7.41}$$

Here, fermionic operators $\hat{f}^{(\dagger)}_{\mathbf{i}}$ create (remove) magnetic polarons on site $\mathbf{i}$ and $\langle\langle \mathbf{i},\mathbf{k}\rangle\rangle$ are NNN pairs on the square lattice; the sum over $\mathbf{j}$ includes both NNN paths when coupling sites $\mathbf{i} \leftrightarrow \mathbf{k}$ with hopping strength $t^{\mathrm{MP}}_{\langle\langle \mathbf{i},\mathbf{k}\rangle\rangle}$. The latter is proportional to the superexchange energy of the bare Hubbard model, t^2/U [265]. Note that we dropped the spin index of the polarons $\hat{f}_{\mathbf{i}}$ since the latter is fixed by the sublattice of $\mathbf{i}$ together with the domain wall configuration $\{\hat{\tau}^z_\ell\}$. To capture the semionic statistics between magnetic polarons and open string ends, the polarons couple to electric field lines $\hat{\tau}^z$ when hopping on the lattice. In particular, this coupling to gauge fluctuations does not disrupt the fermionic quasiparticle nature of magnetic polarons. Consequently, both fermionic quasiparticles and the topological quantum field theory describing the $\mathbb{Z}_2$ spin liquid contribute with a direct sum to Oshikawa's momentum balance argument, as described in Sec. 7.4.3. Repeating the arguments for an FL*, the spin liquid absorbs flux that corresponds to unit density, which results in the formation of a small Fermi surface with carrier density δ constituted by magnetic polarons.

The above arguments are akin to the doped quantum dimer scenario introduced in Sec. 7.4.3, where the background spins form a quantum spin liquid that preserves the spin's underlying SU(2) symmetry. In this scenario, holon-spinon bound states that carry the same quantum numbers as fermionic holes then form a small Fermi surface. We emphasize that in our case, the background spins break the SU(2) symmetry. Their order is not disrupted by magnetic frustration but instead by fluctuating domain walls, which form a string-net condensate with $\mathbb{Z}_2$ topological order and fractionalized excitations: The broken symmetry together with the sublattice fluctuations defines the geometric nature of the FL* in our scenario.

Finally, let us briefly recapitulate on the logic of our arguments: We started with the microscopic FH Hamiltonian, and—motivated by experimental and numerical evidence—argued that the important low-energy contributions to the path integral in Eq. (7.10) are given by fermions coupled to closed loop configurations of domain walls. By going to the continuum limit, we argued how microscopic Berry phase effects of fermionic as well as excitations of the closed domain wall structure naturally emerge. For this, it is important to assume that domain walls are never sharp objects, but are smoothed out due to microscopic fluctuations. The $\mathbf{\Omega}$ field hence smoothly varies across domain walls and around half-vortex excitations, which directly influence the Berry phase effects. Finally, we wrote down an effective model that described (now again sharp) fluctuating domain walls through an effective $\mathbb{Z}_2$ degree of freedom on the links of the lattice, which captures the microscopic Berry phase effects. This model, in turn, has nontrivial topological properties that lead to the formation of a small Fermi surface.

7.5.4 Hidden quantum criticality

When suppressing superconductivity in hole-doped cuprates using strong magnetic fields, the pseudogap persists at low temperatures up to a critical doping of $\delta_c \sim 19\%$, see Sec. 7.3. Around this doping level, non-Fermi liquid transport characteristics have been observed, whereby the resistivity grows linearly with temperature (strange metal) [300]. The location of the strange metal phase in the phase diagram suggests that the non-Fermi liquid behavior is caused by a quantum critical point [301], where the pseudogap metal becomes unstable and turns into a plain-vanilla Fermi liquid, see Fig. 7.13. This transition is accompanied by a change of the Fermi surface volume, and is hence believed to be of topological nature.

Within our fluctuating domain wall picture, we propose the following scenario for the appearance of a quantum critical point as a function of doping: For low dopings, in the pseudogap regime, the ground state is characterized by hidden AFM order in (the 2D generalization of) squeezed space, i.e. the state spontaneously breaks the SU(2) symmetry but long-range AFM correlations are hidden by the proliferation of AFM domain walls. Eventually the SU(2) symmetry of the underlying spins must be fully restored, as in the Fermi liquid (with large Fermi surface) observed beyond $\delta_c \sim 19\%$ doping. In between, this necessitates the existence of a quantum critical point associated with the formation of the SU(2) broken AFM in squeezed space. Due to the nature of correlations in the original lattice model, which are short-ranged on both sides of this transition, the quantum critical point itself is "hidden" (hQCP) and cannot be directly associated with a diverging correlation length.

To understand the microscopic origin of the hQCP, let us consider the effective Hamiltonian describing spins in 2D squeezed space. Since we work in the strong- coupling regime of the Hubbard model, the tunneling energy of the mobile dopants, t, exceeds the AFM superexchange coupling, J, which introduces significant charge fluctuations. Both, for dopants bound into stripe-like structures as well as mobile holes forming magnetic polarons, this has been argued to create significant frustration in the surrounding spin background [135,265,288,302]. As we saw in a quantitative analysis in a mixed-dimensional setting in Chap. 6, the effective spin system in squeezed space can be accurately described by a J_1-J_2-type Heisenberg antiferromagnet, with a ratio J_2/J_1 that is doping dependent. It was argued that as hole-doping increases, the effective squeezed spin system can be driven into a highly frustrated phase in the J_1-J_2 phase diagram.

We propose that at the critical doping value $\delta_c \sim 19\%$, the frustrating effect of charge fluctuations becomes too large. In terms of our field theory, this means that the spin stiffness ρ_s associated with the NLSM describing the AFM $\tilde{\mathbf{\Omega}}$ in squeezed space, Eq. (7.39), becomes small: quantum fluctuations restore the hidden SU(2) symmetry. Without the diverging correlation length in squeezed space, the fluctuating domain wall field τ^z, Eq. (7.34), becomes ill-defined and our field theoretic description is no longer valid at higher dopings.

The hQCP itself can only be detected through highly non-local observables that capture correlations in squeezed space. However, non-Fermi liquid behavior around the critical point can still be observed in transport measurements, consistent with extensive experimental evidence [303, 304]. In particular, we expect signatures of a quantum critical fan emerging from

the hQCP with increasing temperature. It is also conceivable that right at the hQCP the spins in squeezed space form an SU(2) symmetric quantum spin liquid, turning magnetic polarons into a more conventional (non-geometric) FL* before topological order is lost in the FL regime. This scenario is reminiscent of the physics of a doped quantum dimer model featuring an FL* at the Rokhsar-Kivelson point [114], and suggests that the hQCP itself may be described by the field theory of an FL* [122].

This points to an intricate relationship between QCP signatures in hole-doped cuprates and those found in electron-doped cuprates [75], heavy-fermion metals [305], iron-based superconductors [306], and quasi-1D organic conductors [307]. In the latter systems, the QCP scenario is well established, where the AFM phase terminates and a d-wave superconducting dome emerges around the QCP [308–311]. In hole-doped cuprates, while strong evidence suggests that the pseudogap critical point is a QCP based on specific heat and transport measurements, no diverging length scale related to quantum criticality has been identified thus far [311], see also Sec. 7.3. In our domain wall scenario, hidden AFM correlations are implicated in the formation of the pseudogap in hole-doped cuprates. We propose that these fluctuations lead to the hQCP located within the T_c dome, which potentially offers new insights into the origin of superconductivity in these materials, driven by AFM spin fluctuations in squeezed space. This includes scenarios where superconductivity has been proposed to arise from magnon exchange [312,313], the spin-bag mechanism [276,314], or an emergent Feshbach resonance [315].

7.6 Discussion

We proposed a theoretical framework for hole-doped cuprates where fluctuations of closed, stripe-like structures give rise to hidden AFM order. At elevated temperatures and very low doping $\delta \sim 5\%$, we suggest that a transition occurs from long-range AFM to hidden order, driven by an Ising* criticality where string nets percolate. In the ground state, we argue that quantum fluctuations extend the hidden order phase down to $T = 0$, with topological properties naturally emerging from a minimal model – leading to magnetic (or spin-) polarons forming a small Fermi surface coupled to topological excitations of a string-net condensate. At a critical doping, we propose that hidden order vanishes, resulting in a transition from a geometric fractionalized Fermi liquid (GFL*) to a conventional Fermi liquid at a hidden quantum critical point (hQCP), which furthermore constitutes a scenario that explains signatures of quantum criticality observed in hole-doped cuprates. These results are summarized in Fig. 7.13.

Our scenario unifies several puzzles in the cuprates, including the relation of the pseudogap phase to stripes and antiferromagnetism, and paves the way for intriguing future directions. One avenue involves exploring half-vortex excitations linked by domain wall strings (open string ends), which could drive a Berezinskii-Kosterlitz-Thouless (BKT)-type transition; we speculate that this might be related to the physics associated with the temperature scale T^* revealed in various observables [24,72,101,316,317]. Running semi-classical numerical simulations that incorporate their structure and interactions may shed light on the fate of hidden order at higher temperatures. Another promising direction is to quantify the frustration in squeezed space caused

by fluctuations of closed loops within the hidden order phase. By employing Hamiltonian reconstruction methods as discussed in the previous Chap. 6, this could provide deeper insights into the nature of a possible quantum phase transition at the hidden critical doping δ_c.

In the hidden order phase, the SU(2) symmetry of the underlying local moments is spontaneously broken, possibly explaining signatures of time-reversal symmetry-breaking in certain families of cuprates [295,318,319]. This scenario is supported by the observation of pronounced paramagnon peaks up to high doping values beyond the pseudogap regime [103–105]. However, we note that our scenario does not directly account for the missing backside of the Fermi pockets, cf. Sec. 7.3. We propose that the suppression of spectral weight on the backside is of a more subtle origin, which future experiments with high energy and momentum resolution may be able to clarify [90]. We can summarize our findings in light of the experimental characteristics of the pseudogap outlined in Sec. 7.3:

- ☑ Short-range antiferromagnetic (AFM) correlations are present, but there is no evidence of long-range AFM order.
- ☑ Well-defined paramagnons, or spin-wave-like excitations, are observed.
- ☒ A partial suppression of the single-particle spectral function occurs, manifesting as the emergence of Fermi arcs.
- ☑ Coherent fermionic quasiparticles are evident.
- ☑ The system exhibits plain Fermi liquid behavior with a small Fermi surface area scaling as $V_{\mathrm{FS}} \propto \delta$.
- ☑ No local order parameter has been identified that drives a thermal or quantum phase transition into or out of the pseudogap phase.

We note that our picture of fluctuating stripe-like structures differs fundamentally from other proposals in e.g. Ref. [320], where thermodynamic and transport anomalies in cuprates are attributed to Fermi surface reconstruction by static stripe order (see also Ref. [106]). Since quantum oscillations and d.c. transport measurements are essentially static probes, fluctuating stripes (in terms of symmetry-breaking order) likely do not lead to observable features in the pseudogap phase of cuprates. In contrast, in our scenario, these features naturally arise from the topological geometric structure of fluctuating stripes.

Finally, we highlight once more that ultracold atom simulation platforms offer a unique opportunity to test our hidden order scenario. By analyzing spin- and charge-resolved snapshots, evidence of our extended definition of squeezed space in two dimensions could be explored, possibly at temperatures which are within immediate reach of current experiments. If such patterns are observed, the real-space nature of many-body snapshots allows for a direct calculation of spin-spin correlations within squeezed space, which could be used to identify the transition from the pseudogap to the Fermi liquid phase. Moreover, DMDs can be used to effectively decouple a 2D system into two parts. Sharp boundaries are expected to expel domain wall lines,

leading to the reappearance of long-range spin-spin correlations. True long-range order is anticipated to emerge along these 1D boundary lines, contrasting the power-law decay expected in 1D systems. This will constitute the ultimate test of our proposed theoretical scenario, and underlines ultracold atom experiments as unique tools to test and compare various microscopic theories.

8 Superconductivity in bilayer t-J models

Summary. In this chapter, we investigate a minimal single-band bilayer FH model to describe the essential physics of the high-temperature bilayer nickelates superconductor $La_3Ni_2O_7$ (LNO). We will utilize DMRG and analytically tractable perturbative limits to establish a thorough understanding of the model and the magnetically induced pairing through comparison to the perturbative limit of dominating inter-layer spin couplings. In particular, this allows us to explain appearing finite-size effects, firmly establishing the existence of long-range superconducting order in the thermodynamic limit. By analyzing binding energies, we predict a BEC-BCS crossover as a function of the Hamiltonian parameters, whereas LNO is anticipated to lie on the BCS side in vicinity of the transition. We find large binding energies of the order of the inter-layer coupling that suggest strikingly high critical temperatures of the Berezinskii-Kosterlitz-Thouless transition, setting the stage for the quantum simulation of unconventional superconductivity and raising the question whether bilayer materials possibly facilitate critical temperatures above room temperature.

8.1 Introduction

In the past chapters, we have put our focus on the 2D FH model, the phases appearing in hole-doped cuprates, and their quantum simulation. Very recently, in May 2023, the Ruddlesen-Popper bilayer perovskite nickelate $La_3Ni_2O_7$ (LNO) has joined the family of bulk superconductors above the boiling point of liquid nitrogen, with extraordinarily high critical temperatures of $T_c = 80$ K at applied pressures above 14 GPa [70, 166, 321]. As discussed in detail in Sec. 2.3, density functional theory (DFT) calculations suggest that the active degrees of freedom near the Fermi energy in the layered LNO structure are given by the $3d_{x^2-y^2}$ and $3d_{z^2}$ Ni or-

bitals [322–328], whereby the four $3d$ orbitals in each unit cell (two in each layer) share three electrons. The $3d$ character of the electronic structure together with the absence of perfect nesting in the non-interacting model indicates the necessity of strong coupling approaches for an accurate description of LNO [329], in line with recent experiments suggesting the vicinity of LNO to a Mott transition [330].

In the limit of strong on-site repulsion and considering inter-atomic effects such as Hund's coupling, a minimal, single-band model can be derived from the electronic structure of LNO, as outlined in Sec. 2.3. For readability, we here reprint the mixed-dimensional (mixD) bilayer $t_\parallel$-$J_\perp$-$J_\parallel$ model for describing the essential low-energy physics of LNO,

$$\begin{aligned}\hat{\mathcal{H}}_{\mathrm{BL}} = -t_\parallel \sum_{\langle \mathbf{i},\mathbf{j}\rangle,\sigma,\alpha} \hat{\mathcal{P}}_{GW}\left(\hat{c}^\dagger_{\mathbf{i},\sigma,\alpha}\hat{c}_{\mathbf{j},\sigma,\alpha} + \mathrm{h.c.}\right)\hat{\mathcal{P}}_{GW} + J_\parallel \sum_{\langle \mathbf{i},\mathbf{j}\rangle,\alpha} \left(\hat{\mathbf{S}}_{\mathbf{i},\alpha}\cdot\hat{\mathbf{S}}_{\mathbf{j},\alpha} - \frac{\hat{n}_{\mathbf{i},\alpha}\hat{n}_{\mathbf{j},\alpha}}{4}\right) \\ + J_\perp \sum_{\mathbf{i}} \left(\hat{\mathbf{S}}_{\mathbf{i},1}\cdot\hat{\mathbf{S}}_{\mathbf{i},2} - \frac{\hat{n}_{\mathbf{i},1}\hat{n}_{\mathbf{i},2}}{4}\right).\end{aligned} \tag{8.1}$$

In particular, the quarter filled $d_{x^2-y^2}$ band corresponds to a doping level of $\delta = 0.5$ in the mixD $t_\parallel$-$J_\perp$-$J_\parallel$ model compared to the half-filled state with one particle per site, cf. Sec. 2.3.

In this chapter, we use matrix product state methods to study pair-pair correlations as well as binding energies in the Hamiltonian Eq. (8.1) on finite width bilayer geometries. By comparison to the limit of strong inter-layer spin-spin interactions, where the model can be mapped to a spin-1/2 XXZ model, we gain a detailed understanding of the mixD $t_\parallel$-$J_\perp$-$J_\parallel$ model even away from this perturbative limit. In particular, this allows us to understand appearing finite-size effects and the influence of the various coupling parameters on the long-range pairing order, where the latter might permit to realize a certain tunability of experimental probes to favorable situations.

Through the computation of binding energies, we anticipate the emergence of a crossover from a Bose-Einstein condensate (BEC) to Bardeen-Cooper-Schrieffer (BCS) state in the mixD bilayer model as a function of $t_\parallel/J_\perp$, characterized by extended, overlapping pairs. We estimate critical temperatures of the superfluid transition to be of the order of the magnetic coupling, hence possibly facilitating superconductivity at temperatures beyond room temperature in mixD bilayer systems. In addition, as the effective model of tightly-bound pairs in the limit of strong spin couplings $J_\perp \gg t_\parallel, J_\parallel$ yields a linear resistivity as a function of temperature above the superconducting phase, we speculate that the resistivity in the bilayer model in vicinity to the crossover is governed by the conduction of pairs.

We will present the perturbative limit of dominating inter-layer spin couplings as an important case study that allows for an understanding of qualitative physical features even away from this limit. This is in stark contrast to the Fermi-Hubbard model, where such controlled perturbative limits are absent, and large scale numerical simulations are necessary to resolve the small energy differences of competing phases, as discussed in Sec. 2.2.

Though the single-band model, Eq. (8.1), is not believed to quantitatively describe e.g. transition temperatures of pressurized bilayer nickelates, establishing a microscopic understanding of simplified models by fully taking into account their correlation structure is an important step towards developing a theory of bilayer superconductors. Our calculations suggest high critical

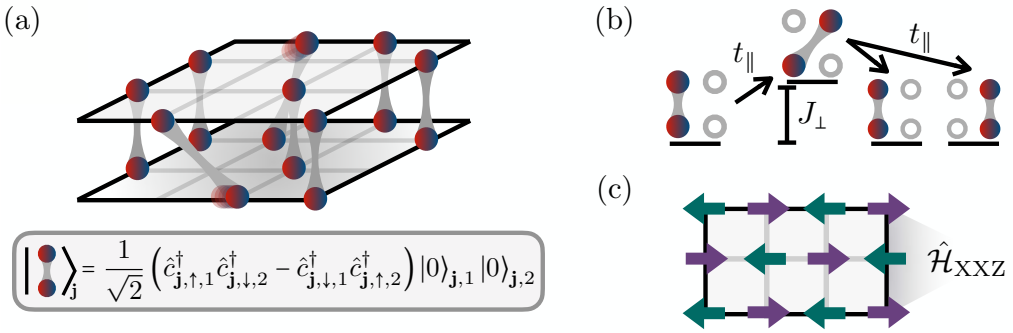

Figure 8.1: **Perturbative model.** (a) In the limit $J_\perp \gg t_\parallel, J_\parallel$, the bilayer mixD $t_\parallel$-$J_\perp$-$J_\parallel$ model, Eq. (8.1), reduces to a model of hopping singlets. Singlets hop on the bilayer structure via second order processes (b), leading to a single layer interacting hard-core bosonic system, Eq. (8.2), in the perturbative limit. A further mapping to a spin system yields an effective 2D XXZ model, Eq. (8.4), where spin-spin correlations in the xy-plane map to coherent pair-pair correlations in the bilayer system, (c).

temperatures of the single-band model, which facilitates the preparation of a state with (quasi) long-range superconducting order in ultracold atom experiments with currently realistic temperatures. This, in turn, may allow for a systematic exploration of novel materials using analog quantum simulation platforms, and is discussed in Chapter 9 in detail.

The content of this chapter, including the above introduction, is largely based on the following publication, partially with textual overlap:

> [5] **HS**, U. Schollwöck, F. Grusdt, and A. Bohrdt. **Superconductivity in the pressurized nickelate $La_3Ni_2O_7$ in the vicinity of a BEC-BCS crossover**, Communications Physics 7, 366 (2024)

This chapter is structured as follows. In Sec. 8.2, we analyze the perturbative limit of strong inter-layer spin couplings, which will serve as a guide throughout the succeeding sections. In Sec. 8.3, we will look at numerical calculations of pair-pair correlations and analyze finite-size effects in shallow systems. In Sec. 8.4, we compute binding energies of hole pairs, and estimate critical temperatures to be expected in the thermodynamic limit. In Sec. 8.5, we propose a mechanism for the observed strange metal phase in LNO, based on the intuition of conducting hard-core bosons.

8.2 Perturbative limit

In the case of dominating spin couplings $J_\perp \gg t_\parallel, J_\parallel$, the fermions pair into tightly bound inter-layer singlets, where breaking apart a singlet is associated with energy cost $J_\perp$ (Fig. 8.1). In this limit, the low-energy physics of Eq. (8.1) is described by the restricted local basis consisting of empty sites on site $\mathbf{j}$ in both layers, $|0\rangle_{\mathbf{j}} = |0\rangle_{\mathbf{j},1}\,|0\rangle_{\mathbf{j},2}$ (a chargon-chargon pair), as well as paired singlets, $|1\rangle_{\mathbf{j}} = \hat{b}^\dagger_{\mathbf{j}}\,|0\rangle_{\mathbf{j}}$, where the (hard-core) bosonic operator $\hat{b}^\dagger$ creates an inter-layer spin singlet, $\hat{b}^\dagger_{\mathbf{j}}\,|0\rangle_{\mathbf{j}} = \frac{1}{\sqrt{2}}\left(\hat{c}^\dagger_{\mathbf{j},\uparrow,1}\hat{c}^\dagger_{\mathbf{j},\downarrow,2} - \hat{c}^\dagger_{\mathbf{j},\downarrow,1}\hat{c}^\dagger_{\mathbf{j},\uparrow,2}\right)|0\rangle_{\mathbf{j}}$. By considering virtual processes to

spinon-chargon states $c^\dagger_{\mathbf{j},\sigma,\alpha}|0\rangle_\mathbf{j}$ in second order perturbation theory, and restricting the effective Hamiltonian to the low-energy subspace, the mixD bilayer model reduces to an interacting hard-core bosonic system in a single 2D plane illustrated in Fig. 8.1. Let us go through the various terms in the Hamiltonian Eq. (8.1) and see how they map to the effective low-energy space (see also [40, 331, 332]):

- ▷ **Hopping of singlets:** Singlets can hop perturbatively. Through second-order processes involving the constituents of the singlets, they can hop from site $\mathbf{i} \to \mathbf{j}$ with an amplitude $2t_\parallel^2/J_\perp$ (since both the upper and lower particles in the singlet can initiate the hop), Fig. 8.1 (b). The hopping term is thus given by $-\frac{K}{2}\sum_{\langle\mathbf{i},\mathbf{j}\rangle}\left(\hat{b}^\dagger_\mathbf{i}\hat{b}_\mathbf{j} + \text{h.c.}\right)$, where $K = 4t_\parallel^2/J_\perp$.

- ▷ **Recombination of constituents:** Constituents of a singlet can hop one site before recombining into a singlet at the same site again, see also Fig. 8.1 (b). This results in the terms $-\frac{K}{2}\sum_{\langle\mathbf{i},\mathbf{j}\rangle}\left(\hat{b}^\dagger_\mathbf{i}\hat{b}_\mathbf{i} + \hat{b}^\dagger_\mathbf{j}\hat{b}_\mathbf{j}\right)$.

- ▷ **Blocked kinetic energy:** When two singlets occupy neighboring sites, they cannot gain kinetic energy through delocalization. This costs an energy $K\sum_{\langle\mathbf{i},\mathbf{j}\rangle}\hat{b}^\dagger_\mathbf{i}\hat{b}_\mathbf{i}\hat{b}^\dagger_\mathbf{j}\hat{b}_\mathbf{j}$, which must be added to the kinetic terms above.

- ▷ **Interlayer interactions:** The spin-spin interaction term $J_\perp\sum_\mathbf{i}\left(\hat{\mathbf{S}}_{\mathbf{i},1}\cdot\hat{\mathbf{S}}_{\mathbf{i},2} - \frac{\hat{n}_{\mathbf{i},1}\hat{n}_{\mathbf{i},2}}{4}\right)$ leads to an energy of $-J_\perp$ per singlet. This contributes the term $-J_\perp\sum_\mathbf{i}\hat{b}^\dagger_\mathbf{i}\hat{b}_\mathbf{i}$.

- ▷ **Intralayer interactions:** The density-density interaction term $-\frac{J_\parallel}{4}\sum_{\langle\mathbf{i},\mathbf{j}\rangle,\alpha}\hat{n}_{\mathbf{i},\alpha}\hat{n}_{\mathbf{j},\alpha}$ contributes an additional nearest-neighbor (NN) interaction $-\frac{J_\parallel}{2}\sum_{\langle\mathbf{i},\mathbf{j}\rangle}\hat{b}^\dagger_\mathbf{i}\hat{b}_\mathbf{i}\hat{b}^\dagger_\mathbf{j}\hat{b}_\mathbf{j}$. The factor of two arises because the summation is over both layers; the spin-spin interaction $\propto J_\parallel$ does not contribute, as two neighboring singlet states are disjoint.

Summing over all terms, we end up with the following Hamiltonian,

$$\hat{\mathcal{H}}_{\text{HCB}} = -\frac{K}{2}\sum_{\langle\mathbf{i},\mathbf{j}\rangle}\hat{\mathcal{P}}_{GW}(\hat{b}^\dagger_\mathbf{i}\hat{b}_\mathbf{j} + \text{h.c.})\hat{\mathcal{P}}_{GW} - J_\perp\sum_\mathbf{i}\hat{b}^\dagger_\mathbf{i}\hat{b}_\mathbf{i} + K\sum_{\langle\mathbf{i},\mathbf{j}\rangle}\left(\Delta\hat{b}^\dagger_\mathbf{i}\hat{b}_\mathbf{i}\hat{b}^\dagger_\mathbf{j}\hat{b}_\mathbf{j} - \frac{\hat{b}^\dagger_\mathbf{i}\hat{b}_\mathbf{i}}{2} - \frac{\hat{b}^\dagger_\mathbf{j}\hat{b}_\mathbf{j}}{2}\right), \tag{8.2}$$

where we introduced the anisotropy $\Delta = 1 - J_\parallel/2K$.

We can now associate the chargon-chargon pair and interlayer singlet with two spin states described by spin-1/2 operators $\hat{J}^\mu_\mathbf{i}$, $\mu = x, y, z$ (see e.g. Ref. [16]),

$$\begin{aligned}\hat{J}^+_\mathbf{i} = \eta_\mathbf{i}\hat{b}^\dagger_\mathbf{i}, \quad \hat{J}^-_\mathbf{i} = \eta_\mathbf{i}\hat{b}_\mathbf{i}\\ \hat{J}^z_\mathbf{i} = \hat{b}^\dagger_\mathbf{i}\hat{b}_\mathbf{i} - 1/2,\end{aligned} \tag{8.3}$$

where $\eta_\mathbf{i}$ is 1 (-1) on the A (B) sublattice. The effective boson model Eq. (8.2) can then be mapped to a 2D XXZ spin system,

$$\hat{\mathcal{H}}_{\text{XXZ}} = K\sum_{\langle\mathbf{i},\mathbf{j}\rangle}\left(\hat{J}^x_\mathbf{i}\hat{J}^x_\mathbf{j} + \hat{J}^y_\mathbf{i}\hat{J}^y_\mathbf{j} + \Delta\hat{J}^z_\mathbf{i}\hat{J}^z_\mathbf{j}\right) - J_\perp\sum_\mathbf{i}\hat{J}^z_\mathbf{i} - \frac{J_\parallel}{4}\sum_{\langle\mathbf{i},\mathbf{j}\rangle}\left(\hat{J}^z_\mathbf{i} + \hat{J}^z_\mathbf{j}\right), \tag{8.4}$$

where trivial constant terms have been dropped. $\hat{J}^{\mu}_{\mathbf{i}}$, $\mu = x, y, z$ are spin-1/2 operators—not to be confused with the spin operators $\hat{S}^{\mu}_{\mathbf{i}}$ of the fermionic bilayer Hamiltonian, Eq. (8.1). The magnetization m of the spin model Eq. (8.4) maps to the filling δ of the bilayer model Eq. (8.1) as

$$m = \delta - 1/2. \tag{8.5}$$

Note specifically that the density-density term of the in-plane Heisenberg interactions in Eq. (8.1) leads to the appearance of an anisotropy $\Delta < 1$. The last term in Eq. (8.4) is constant in periodic systems, however induces non-trivial effects for open boundaries that we will discuss in the upcoming section. For $J_{\parallel} = 0$, Eq. (8.4) reduces to the Heisenberg model with a Zeeman field.

In the perturbative regime, the bilayer system is hence a *bona fide* superconductor, featuring long-range pairing order in the ground state that translates to long-range antiferromagnetic order in the xy-plane of the XXZ model, see Fig. 8.1 (c). The controlled connection to the XXZ model in the perturbative limit will prove to be useful in the following analysis of the appearing phases in the mixD bilayer model.

8.3 Pair correlations and finite-size effects

We simulate the bilayer $t_{\parallel}$-$J_{\perp}$-$J_{\parallel}$ system, Eq. (8.1), in the ground state using DMRG for various parameters $J_{\perp}/t_{\parallel}$ at $J_{\parallel} = 0$ and doping $\delta = 0.5$. We focus on systems of size $l \times w \times 2$, where w and l are the width and length of each layer in the bilayer system, respectively. As in Chapters 5 and 6, we exploit the full U(1) symmetries in each layer and conserve the total magnetization, such that the symmetry of the system is given by $\mathrm{U}(1)^{\alpha=1} \otimes \mathrm{U}(1)^{\alpha=2} \otimes \mathrm{U}(1)^{S^z_{\mathrm{tot}}}$.

Fig. 8.2 shows coherent pair-pair correlations $\langle \hat{\Delta}^{\dagger}_{\mathbf{i}} \hat{\Delta}_{\mathbf{j}} \rangle$ as a function of distance along the long direction x of the bilayer system, for varying $J_{\perp}/t_{\parallel}$ and for widths $w = 1, 2, 3, 5$. We apply open boundary conditions in all directions. In the ladder systems ($w = 1$), we find pronounced algebraic signals of pair-pair correlations throughout the whole system for all parameters (Fig. 8.2 (a)), in line with previous findings presented in [170]. When tuning the system towards the perturbative limit, pair-pair correlations are seen to converge towards spin-spin correlations $\langle \hat{J}^{+}_{\mathbf{i}} \hat{J}^{-}_{\mathbf{j}} \rangle$ of the mapped XXZ model (with $\hat{J}^{\pm}_{\mathbf{i}} = \hat{J}^{x}_{\mathbf{i}} \pm i \hat{J}^{y}_{\mathbf{i}}$).

Notably, while the absolute values of pair-pair correlations rise for increasing $J_{\perp}/t_{\parallel}$, their corresponding decay exponent remains almost unchanged even down to $J_{\perp}/t_{\parallel} \sim 1$, which is the relevant regime for LNO [323]. In particular, fitted Luttinger exponents K_{sc} (with $\langle \hat{\Delta}^{\dagger}_{\mathbf{i}} \hat{\Delta}_{\mathbf{j}} \rangle \propto |\mathbf{i} - \mathbf{j}|^{-K_{sc}}$) are $K_{sc} = 1.211(18)$ for $J_{\perp}/t_{\parallel} = 1$ and $K_{sc} = 0.946(3)$ for $J_{\perp}/t_{\parallel} = 20$. Similarly to the ladders, algebraic decay is observed for $w = 3$ throughout the range of $J_{\perp}/t_{\parallel}$, cf. Fig. 8.2 (c). Here, the fitted Luttinger exponents are given by $K_{sc} = 0.82(2)$ for $J_{\perp}/t_{\parallel} = 5$ and $K_{sc} = 0.89(1)$ for $J_{\perp}/t_{\parallel} = 20$.

For $w = 5$, we show results for $\delta = 0.5$ and in the perturbative regime $J_{\perp}/t_{\parallel} = 20$ for varying bond dimensions in Fig. 8.2 (e). While insufficient bond dimensions lead to a natural exponential decay of correlations, the extrapolation shows an algebraic signal that matches spin-spin correlations of the perturbative XXZ model. Though going significantly away from the perturbative regime is intractable for wide systems such as $w = 5$ with current state-of-the-art

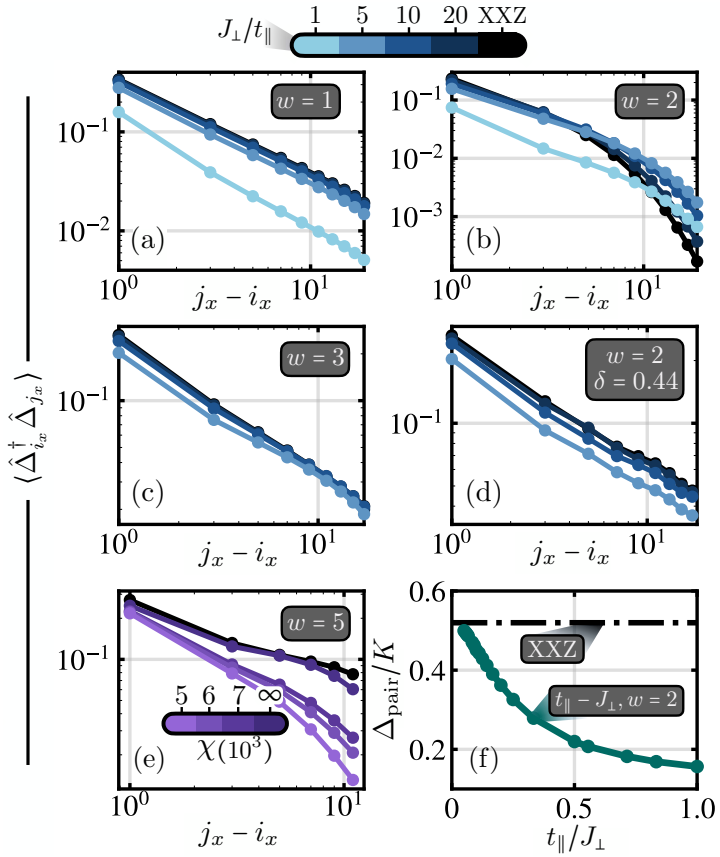

Figure 8.2: **Pair correlations.** Pair-pair correlation function $\langle \hat{\Delta}^\dagger_{\mathbf{i}} \hat{\Delta}_{\mathbf{j}} \rangle$ in the $t_\parallel$-$J_\perp$ model ($J_\parallel = 0$) for varying $J_\perp/t_\parallel$ and width w; $\delta = 0.5$ is used if not indicated differently. For $w = 1$ (a) and $w = 3$ (c), correlations show algebraic signals, with increasing magnitudes for growing $J_\perp/t_\parallel$ while the decay exponents stay almost constant. Pair-pair correlations converge towards spin-spin correlations $\langle \hat{J}^+_{\mathbf{i}} \hat{J}^-_{\mathbf{j}} \rangle$ of the XXZ model in the perturbative limit (black data). For $w = 5$, an extrapolation to large bond dimension for $J_\perp/t_\parallel = 20$ is shown, matching the prediction from the XXZ model. For $w = 2$ at $\delta = 0.5$ (b), the decay of $\langle \hat{\Delta}^\dagger_{\mathbf{i}} \hat{\Delta}_{\mathbf{j}} \rangle$ is exponential for all values of $J_\perp/t_\parallel$, with decreasing correlation lengths for increasing $J_\perp/t_\parallel$. This is explained by a finite pair charge gap Δ_{pair} that corresponds to the spin gap of the SU(2) symmetric Heisenberg model in the perturbative limit (f). Away from $\delta = 0.5$ and for $w = 2$ (d), correlations decay algebraically for all values of $J_\perp/t_\parallel$, as expected from the Heisenberg model at finite magnetization. We choose reference sites $\mathbf{i} = [i_x = 10, i_y = 1]$ ($l = 32$) for $w = 1, 2$, $\mathbf{i} = [i_x = 4, i_y = 2]$ ($l = 24$) for $w = 3$ and $\mathbf{i} = [i_x = 2, i_y = 3]$ ($l = 16$) for $w = 5$.

techniques, the correspondence between the mixD bilayer $t_\parallel$-$J_\perp$-$J_\parallel$ model and the XXZ model for $J_\perp/t_\parallel = 20$ and $w = 5$ suggests long-range pairing order also away from $J_\perp/t_\parallel \gg 1$.

In stark contrast to systems of odd widths, for $w = 2$ at $\delta = 0.5$ we find at distances $j_x - i_x \gtrsim 10$ exponential behavior of pair-pair correlations, which, notably, has not been mentioned in previous numerical studies of the mixD bilayer t-J model [170]. A comparison with the perturbative XXZ model turns out as a useful tool to understand the origin of exponentially decaying pair correlations: In SU(2) symmetric Heisenberg ladders of even width and at zero magnetization, the formation of rung-singlets opens a spin-gap Δ_s, which in turn leads to an exponential suppression of spin-spin correlations. In contrast, odd-width ladders have a vanishing

spin-gap, and long-range correlations are observed [263, 333, 334]. Similarly, we demonstrate in the following that the exponential decay of pair-pair correlations (even away from the perturbative limit) is an artifact of finite-size effects along the y-direction, driven by a finite charge pair gap Δ_{pair}.

The spin gap is given by the singlet-triplet gap of the effective spin-1/2 model, i.e.

$$\Delta_s = E(S_{\text{tot}} = 1) - E(S_{\text{tot}} = 0). \tag{8.6}$$

In the limit of vanishing in-plane spin interactions $J_{\parallel} = 0$ and magnetization $m = 0$, Eq. (8.4) reduces to the Heisenberg model with an emergent SU(2) symmetry, where both the total spin S_{tot} as well as the total magnetization along z, S^z_{tot}, commute with the Hamiltonian and are good quantum numbers. However, the effective Zeeman field $\propto J_{\perp} \sum_{\mathbf{i}} \hat{f}^z_{\mathbf{i}}$ in Eq. (8.4) splits the energy levels for total spin $S_{\text{tot}} = 1$. In order to calculate the genuine singlet-triplet spin gap, we explicitly remove the Zeeman contribution, and compute $\Delta_s = E(S^z_{\text{tot}} = 1) - E(S^z_{\text{tot}} = 0)$ of the Heisenberg model,

$$\hat{\mathcal{H}}_{\text{Heis}} = K \sum_{\langle \mathbf{i},\mathbf{j} \rangle} \left(\hat{f}^x_{\mathbf{i}} \hat{f}^x_{\mathbf{j}} + \hat{f}^y_{\mathbf{i}} \hat{f}^y_{\mathbf{j}} + \hat{f}^z_{\mathbf{i}} \hat{f}^z_{\mathbf{j}} \right), \tag{8.7}$$

where $\Delta_s / K = const$. Accordingly, to compare Δ_s to the pair charge gap in the bilayer model, we account for the above by computing

$$\Delta_{\text{pair}} = E(N) - E(N+2) + J_{\perp}. \tag{8.8}$$

Here, $E(N)$ is the ground state energy at $\delta = 0.5$, i.e., with a total particle number of $N = l \times w$, and $E(N+2)$ corresponds to the energy of the system with one more particle in each layer compared to $\delta = 0.5$.

Indeed, the charge pair gap is seen to be finite throughout the whole parameter regime for $w = 2$ at $\delta = 0.5$, as illustrated in Fig. 8.2 (f). Particularly, Δ_{pair} falls below the singlet-triplet spin gap in the Heisenberg model (where $\Delta_s \propto K$) for increasing $t_{\parallel} / J_{\perp}$, signaling a weaker exponential decay of pair-pair correlations when tuning the model away from the tightly-bound limit, matching observations in Fig. 8.2 (b).

Away from $\delta = 0.5$, a finite magnetization in the effective model in the perturbative limit prevents the formation of a spin-singlet state, which in turn results in algebraic decay of spin-spin correlations even for finite, even-width systems. Likewise, pair-pair correlations in the bilayer model are seen to decay algebraically for $\delta \neq 0.5$, as shown for $\delta = 0.44$ in Fig. 8.2 (d). We note that in LNO, the coexistence of a strongly correlated state and a hole pocket in the d_{z^2} band has been proposed to lead to self-doping between the d_{z^2} and $d_{x^2-y^2}$ orbitals, which is likely to slightly shift the doping in the $d_{x^2-y^2}$ away from $\delta = 0.5$ [171, 328]. In this case, the appearance of long-range pair-pair correlations is expected for all system widths in the single-band description.

From our considerations, we conclude that in the thermodynamic limit, the model (with $J_{\parallel} \neq 0$ to break the emergent SU(2) symmetry) features quasi long-range pairing correlations up to a critical temperature determined by the Berezinskii-Kosterlitz-Thouless (BKT) transition T_{BKT} where phase coherence occurs. We stress the direct correspondence of the decay of corre-

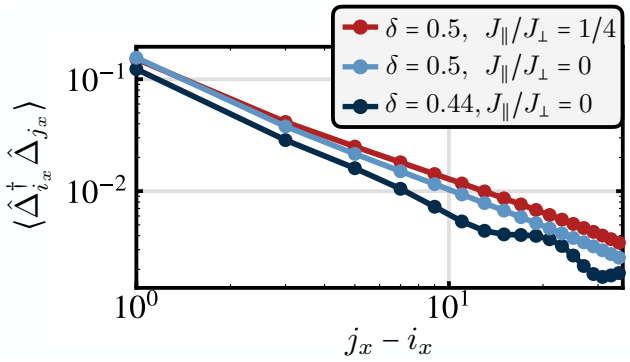

Figure 8.3: **Tuning pair correlations.** Dependence of pair-pair correlations when tuning the filling δ and the ratio $J_\parallel/J_\perp$, for fixed $J_\perp/t_\parallel = 1$ (here shown for a system of size $w = 1, l = 64$). Finite in-plane AFM spin interactions $J_\parallel$ lead to an increase of pair-pair correlations. Doping the system away from $\delta = 0.5$ decreases pairing order and induces oscillatory boundary effects.

lations in the mixD bilayer and XXZ model: When the effective model in the perturbative limit features an emerging SU(2) symmetry and forms spin singlets, correlations are exponential in the mixD model even away from $J_\perp/t_\parallel \gg 1$; however, when a finite magnetization prevents the formation of spin-singlets, correlations decay algebraically throughout the whole range of $J_\perp/t_\parallel$. Furthermore, there is only an insignificant change of the decay of pair-pair correlations when leaving the perturbative limit towards experimentally relevant regimes of $J_\perp/t_\parallel \sim 1$, strongly suggesting that the key pairing physics of superconductivity in LNO is described by the XXZ universality class of hard-core bosons constituted by s-wave singlet pairs. Such controlled limits that capture the essential physics are absent in the plain-vanilla 2D Fermi-Hubbard model, where the ground state (not to mention the finite temperature phase diagram) is still under active debate due to the intricate competition between various phases, see also Sec. 2.2.

The comparison to the perturbative limit of tightly bound inter-layer pairs $J_\perp \gg t_\parallel, J_\parallel$ further gives us an intuitive understanding of all appearing terms in the mixD $t_\parallel$-$J_\perp$-$J_\parallel$ Hamiltonian, Eq. (8.1). Due to the in-plane magnetic interactions, an anisotropy $\Delta < 1$ is introduced in the effective XXZ model. This strengthens superconducting correlations compared to the isotropic case $\Delta = 1$: for small Δ, the Luttinger decay exponent of correlations $\langle \hat{J}^+_{i_x} \hat{J}^-_{j_x} \rangle$ is proportional to $1 + 2\Delta/\pi$, i.e., smaller anisotropies Δ lead to slower power-law decay of correlations. Furthermore, doping the bosonic model away from $\delta = 0.5$ translates to finite magnetizations along z in the XXZ model, leading to suppressed pair-pair correlations. We confirm these tendencies in DMRG simulations of the mixD bilayer model for experimentally relevant parameters, shown in Fig. 8.3. Note that the oscillatory behavior of correlations for $\delta = 0.44$ stem from Friedel modulations of the density that decay away from the open boundaries, and do not indicate charge order in the system.

In the above, we have carefully checked convergence of our results. In particular, let us take a closer look at the on-site particle density as well as pair-pair correlations in the bilayer systems. Fig. 8.4 shows $\langle \hat{n}_{i_x} \rangle$ as well as $\langle \hat{\Delta}^\dagger_{i_x} \hat{\Delta}_{j_x} \rangle$ for bond dimensions $\chi = 2000, \ldots, 6000$. We see that both observables converge for all considered system widths ($\chi = 4000$ and $\chi = 6000$ are indistinguishable on the plot).

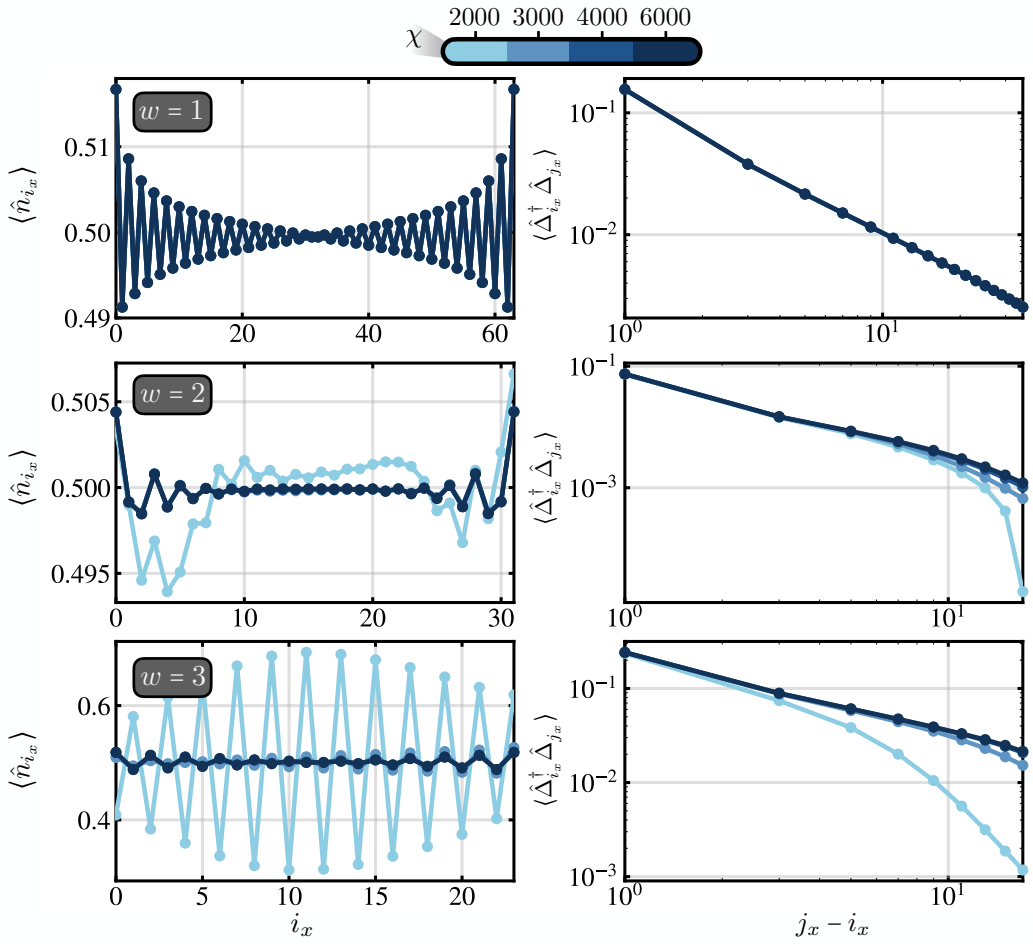

Figure 8.4: **DMRG Convergence.** Convergence of the on-site particle density $\langle \hat{n}_{i_x} \rangle$ (left panels) as well as pair-pair correlations $\langle \hat{\Delta}^\dagger_{i_x} \hat{\Delta}_{j_x} \rangle$ (right panels) in the bilayer system for $w = 1, 2, 3$. $t_\parallel / J_\perp = 1$ for $w = 1, 2$, and $t_\parallel / J_\perp = 10$ for $w = 3$. In all cases, the particle densities as well as pair-pair correlations are observed to converge for $\chi > 4000$ ($\chi = 4000$ and $\chi = 6000$ are indistinguishable on the plot).

Let us do some further comparison between the bilayer $t_\parallel$-$J_\perp$-$J_\parallel$ model to the effective spin description. Fig. 8.5 (a) shows the local expectation values of on-site pairs, $\langle \hat{\Delta}^\dagger_{i_x} \hat{\Delta}_{i_x} \rangle$ for varying $J_\perp / t_\parallel$, $J_\parallel = 0$ and widths $w = 1, 2$, as well as $\langle \hat{S}^z_{i_x} \rangle + 0.5$ in the XXZ model. For $w = 1$, the number of on-site pairs is seen to converge towards the Heisenberg limit more quickly than for $w = 2$.

Lastly, we compute the on-site number of pairs for the mixD $t_\parallel$-$J_\perp$-$J_\parallel$ model for $l = 32$, $w = 1$, $J_\perp / t_\parallel = 5$, and finite in-plane coupling $J_\parallel / t_\parallel = 0.3$, as shown in Fig. 8.5 (b). In the effective XXZ description, this leads to coupling parameters $K / t_\parallel = 0.8$ and an anisotropy of $\Delta = 0.8125$. On-site magnetizations $\langle \hat{S}^z_{i_x} \rangle + 0.5$ are shown in Fig. 8.5 (b) by black data points. The last term in Eq. (8.4) leads to oscillations of the magnetization in the vicinity of the boundary, visible also for the number of on-site pairs in the mixD $t_\parallel$-$J_\perp$-$J_\parallel$ model. We stress that these effects are an artefact of open boundaries imposed by our DMRG simulations, and disappear in the thermodynamic limit. Nevertheless, the above further underlines our understanding of the appearing structure

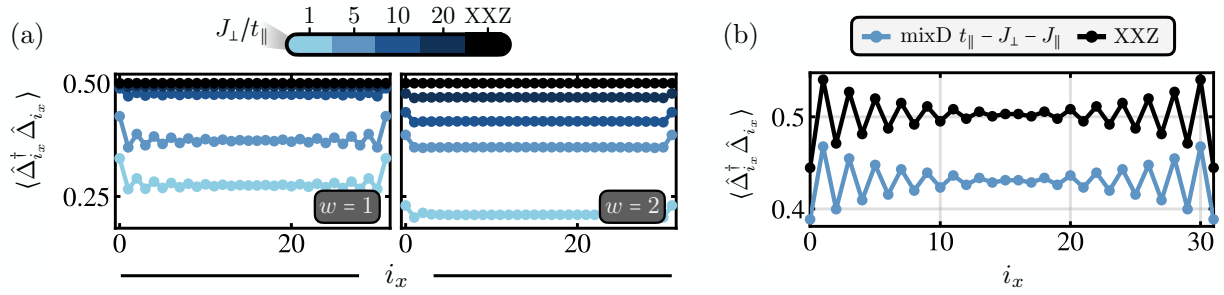

Figure 8.5: **On-site pairs.** (a) Number of on-site pairs $\langle \hat{\Delta}^\dagger_{i_x} \hat{\Delta}_{i_x} \rangle$ for varying $J_\perp/t_\parallel$ and for $w = 1$ (left) and $w = 2$ (right), both for $l = 32$. In the perturbative regime, the number of pairs converges to the density $\delta = 0.5$, corresponding to $m + 1/2$ where m is the magnetization of the mapped Heisenberg model. (b) $\langle \hat{\Delta}^\dagger_{i_x} \hat{\Delta}_{i_x} \rangle$ in the $t_\parallel$-$J_\perp$-$J_\parallel$ for $J_\perp/t_\parallel = 5$, $J_\parallel/t_\parallel = 0.3$ and for $w = 1$. Oscillatory effects of the pair density in the vicinity of the boundary are captured within the effective XXZ model, and stem from the last term in Eq. (8.4) (black data).

of pair densities in the $t_\parallel$-$J_\perp$-$J_\parallel$ by mapping to the effective XXZ spin-1/2 system.

8.4 Binding energies and critical temperatures

Though long-range pair-pair correlations are necessary for any superconductor, their presence does not give any further insights into the nature and structure of the ground state. For this purpose, we compute inter-layer binding energies at $\delta = 0.5$ by evaluating

$$E_b = 2E(N+1) - E(N) - E(N+2), \tag{8.9}$$

and compare them to the spin gap

$$\Delta_s = E(N; S^z_{\text{tot}} = 1) - E(N; S^z_{\text{tot}} = 0). \tag{8.10}$$

The left panel in Fig. 8.6 shows results for mixD ladders, i.e. $w = 1$. In the perturbative regime $t_\parallel/J_\perp \ll 1$, $E_b \approx \Delta_s \approx J_\perp$; each chargon-chargon as well as chargon-spinon pair is associated with energy $J_\perp$, while breaking up a singlet with fixed particle number also costs energy $J_\perp$. Away from the tightly-bound limit, the spin gap monotonously decreases, as growing sizes of the chargon-chargon bound states induce increasing frustration in the spin background, see Chap. 6. However, similar to the case of zero doping [69], where we compute $E_b = 2E(1) - E(0) - E(2)$ for a single hole pair (see grey solid lines in Fig. 8.6), the binding energy is observed to have a minimum around $t_\parallel/J_\perp \approx 0.5$, after which it starts to increase for further rising $t_\parallel/J_\perp$. In the low doping limit, it has been shown by some of us that this behavior is accurately captured within the string picture [265,278,302] of the mesonic bound states: an increasing mobility of the dopants leads to a significant kinetic contribution to the binding energy, resulting in an asymptotic scaling $E_b/J_\perp \sim (t_\parallel/J_\perp)^{1/3}$ [69]. Away from the perturbative limit, the monotonously descreasing spin-gap hence falls below the binding energy. Our numerical results demonstrate that the phenomenology is the same even at high doping $\delta = 0.5$ of the mixD ladders, though binding energies are renormalized to smaller values due to doping.

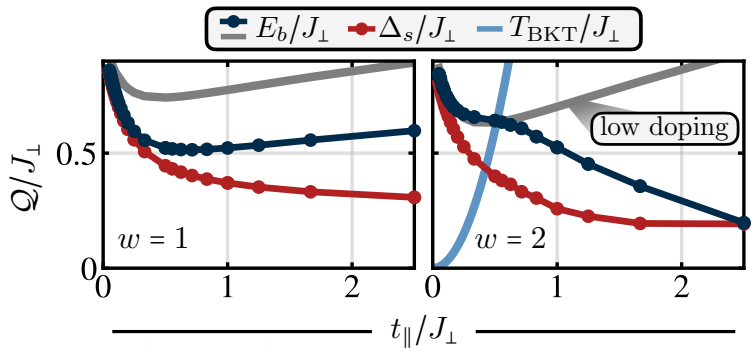

Figure 8.6: **Binding energies.** Binding energies $E_b/J_\perp$ (dark blue) and spin gap $\Delta_s/J_\perp$ (red) as a function of $t_\parallel/J_\perp$ at $\delta = 0.5$ and $J_\parallel = 0$, for $w = 1$ (left) and $w = 2$ (right). For mixD ladders $w = 1$, binding energies behave as predicted in the string picture [69], where a large mobility of pairs for increasing $t_\parallel/J_\perp$ leads to enhanced binding energies. As a reference, binding energies in the dilute limit of a single hole pair are shown by grey solid lines. Meanwhile, due to the frustrating effect of moving charges, the spin gap decreases monotonously. For $w = 2$, the binding energy in the zero doping limit features a similar structure as in the ladders. In contrast, large doping levels $\delta = 0.5$ permit the appearance of strongly overlapping chargon-chargon pairs, leading to a distinct drop of E_b for $t_\parallel/J_\perp \gtrsim 0.6$. The crossing point of estimated critical temperatures of the BKT transition (corresponding to $w \to \infty$) in the perturbative regime (light blue line) with the binding energy coincides with the point of qualitative change of E_b, suggesting a BEC-BCS crossover as $t_\parallel/J_\perp$ is tuned.

When considering bilayer systems with widths $w > 1$, the structure of the pairs fundamentally changes. In contrast to $w = 1$ ladders, where the chargon-chargon bound states may overlap without destroying their confining strings, adding a second dimension allows for string-breaking processes. This is illustrated in Fig. 8.7: In Fig. 8.7 (a), two hole pairs are doped into the interlayer singlet background for a ladder system, shown by the orange and blue circles. When the orange pair is separated, singlets are tilted in between the two holes, leading to the formation of a geometric string with linearly growing energy cost (orange wiggly line, left panel of Fig. 8.7 (a)). When a chargon of a second pair (blue circles) follows the path shown by the blue line in the left panel in Fig. 8.7 (a), the bound states can overlap, but strings are not allowed to cross and hence cannot break (Fig. 8.7 (a), right panel).

This structural restriction of strings appearing in ladders is lifted for $w > 1$. Here, strings from separate chargon-chargon pairs can cross, as illustrated in Fig. 8.7 (b). For instance, if the lower blue hole on the left-hand side in Fig. 8.7 (b) follows the path shown by the blue line, the tilted singlets in between the extended orange pair can be re-traced, resulting in the state shown in the right panel of Fig. 8.7 (b).

In particular, this effect is expected to strongly influence the physics when the size of the bound pairs becomes comparable to the inter-pair distance for a given doping, where the string picture based on linearly growing string energies breaks down and has to be extended to include these processes. Results for the binding energy and spin gap are shown for $w = 2$ in the right panel of Fig. 8.6. In the dilute limit with only two holes (grey line), the binding energy is observed to feature a string-like behavior as expected. Likewise, in the perturbative regime $t_\parallel \ll J_\perp$ at

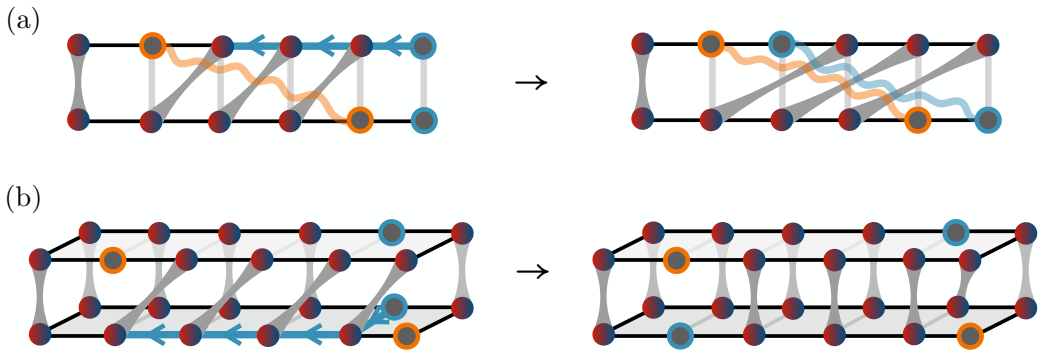

Figure 8.7: **Re-traced strings.** An initially extended (orange) and localized (blue) chargon-chargon pair is shown both for a ladder, (a), and a system with width $w = 2$, (b). In the case of the ladder, the upper blue hole can follow the orange string along the blue solid line, however the resulting strings (wiggly lines) do not cross and hence do not break. In extended systems along a second dimension, self-retracing paths are possible, leading to a fundamentally different structure and ultimately driving a BEC-BCS crossover.

doping $\delta = 0.5$, we find binding energies following the string prediction since string lengths $d \lesssim 1$ remain small compared to the average distance between hole pairs. Strikingly, this behavior extends well beyond the perturbative limit, where binding energies at $\delta = 0.5$ are seen to match predictions in the dilute limit up to $t_\parallel/J_\perp \approx 0.6$. However, for $t_\parallel/J_\perp \gtrsim 0.6$—where $d \gtrsim 1$ [69]—the binding energy starts to decrease for growing $t_\parallel/J_\perp$, approximately approaching the spin gap for large $t_\parallel/J_\perp$, which is expected in a BCS-like state. This, in turn, suggests the appearance of a BCS phase beyond $t_\parallel/J_\perp \gtrsim 0.6$, consisting of spatially extended pairs of holes.

We note that the above results are independent on the symmetries that we implement in our MPS calculations. With the implemented $\mathrm{U}(1)^{\alpha=1}\otimes\mathrm{U}(1)^{\alpha=2}\otimes\mathrm{U}(1)^{S^z_{\mathrm{tot}}}$ symmetry, $E(N+1)$ corresponds to a system with an additional particle in one layer compared to $\delta = 0.5$, while the other layer is doped with $N/2$ holes. We now compare resulting binding energies to a system where only the total number of particles is conserved in the bilayer system, i.e., with a $\mathrm{U}(1)^{\alpha=1,2}\otimes\mathrm{U}(1)^{S^z_{\mathrm{tot}}}$ symmetry. When simulating the mixD model with the latter (reduced) symmetry, we add a small perpendicular hopping $t_\perp/t_\parallel = 0.01$ between the planes, such that we calculate ground state energies of the Hamiltonian

$$\begin{aligned}\hat{\mathcal{H}} = -t_\parallel \sum_{\langle \mathbf{i},\mathbf{j}\rangle,\sigma,\alpha} \hat{\mathcal{P}}_{GW}\left(\hat{c}^\dagger_{\mathbf{i},\sigma,\alpha}\hat{c}_{\mathbf{j},\sigma,\alpha} + \mathrm{h.c.}\right)\hat{\mathcal{P}}_{GW} - t_\perp \sum_{\mathbf{i},\sigma} \hat{\mathcal{P}}_{GW}\left(\hat{c}^\dagger_{\mathbf{i},\sigma,1}\hat{c}_{\mathbf{i},\sigma,2} + \mathrm{h.c.}\right)\hat{\mathcal{P}}_{GW} \\ + J_\parallel \sum_{\langle \mathbf{i},\mathbf{j}\rangle,\alpha} \left(\hat{\mathbf{S}}_{\mathbf{i},\alpha}\cdot\hat{\mathbf{S}}_{\mathbf{j},\alpha} - \frac{\hat{n}_{\mathbf{i},\alpha}\hat{n}_{\mathbf{j},\alpha}}{4}\right) + J_\perp \sum_{\mathbf{i}} \left(\hat{\mathbf{S}}_{\mathbf{i},1}\cdot\hat{\mathbf{S}}_{\mathbf{i},2} - \frac{\hat{n}_{\mathbf{i},1}\hat{n}_{\mathbf{i},2}}{4}\right).\end{aligned} \tag{8.11}$$

Results for the binding energies and particle densities are presented in Fig. 8.8 (a) and (b), respectively, with $\chi = 6000$ ($\chi = 5000$) for the calculations with implemented $\mathrm{U}(1)^{\alpha=1}\otimes\mathrm{U}(1)^{\alpha=2}\otimes\mathrm{U}(1)^{S^z_{\mathrm{tot}}}$ ($\mathrm{U}(1)^{\alpha=1,2}\otimes\mathrm{U}(1)^{S^z_{\mathrm{tot}}}$) symmetry. While the density distributions are different due to the odd number of particles in the system, binding energies are almost indistinguishable.

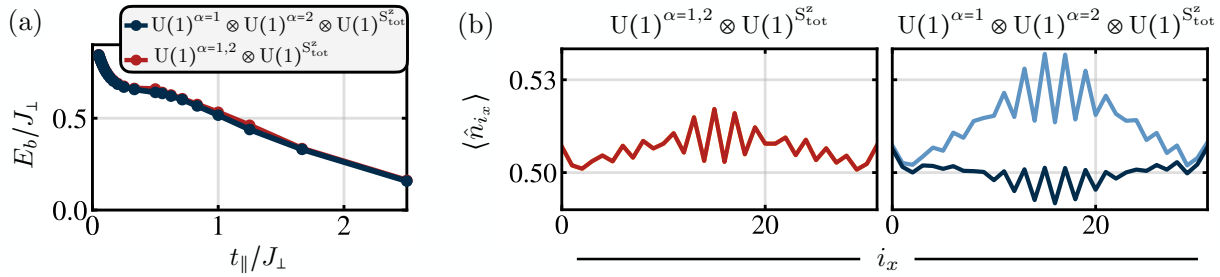

Figure 8.8: **Different symmetries in DMRG calculations.** (a) Binding energies as a function of $t_\parallel/J_\perp$ when conserving the particle number in each layer (blue) compared to conserving only the total number of particles in the system (red). In the latter case, a small $t_\perp/t_\parallel$ is added to reach convergence. (b) Local densities $\langle\hat{n}_{i_x}\rangle$ for $J_\perp/t_\parallel = 1.6$ and particle number $N+1$. In the left panel, the total number of particles is conserved, such that the densities in the lower (dark red) and upper (light red—invisible) layers are identical. In the right panel, the particle number in each layer is conserved; the upper layer (light blue) has one hole less compared to $\delta = 0.5$, i.e., $N/2+1$ particles.

Critical temperature estimation

We further corroborate the appearance of a BEC-BCS crossover by estimating critical temperatures of the BKT phase ordering transition in the perturbative limit. In the 2D XXZ model with coupling K, extensive quantum Monte Carlo studies have quantified the phase transition, finding $T_{\mathrm{BKT}}/K \approx 0.7$ (0.6) for $\Delta = 0$ (0.95) [335,336]. We estimate critical temperatures in the mixD bilayer model by assuming a small in-plane superexchange coupling $J_\parallel$, leading to an anisotropy close to the Heisenberg point in the effective XXZ description, $\Delta \lesssim 1.0$. Hence, following Eq. (8.4) and assuming $\Delta = 0.95$, the BKT transition temperature is estimated by $T_{\mathrm{BKT}}/J_\perp \approx 2.4\left(t_\parallel/J_\perp\right)^2$, shown by the blue solid line in the right panel of Fig. 8.6. Indeed, we find that the critical temperature T_{BKT} for phase coherence surpasses the binding energy at $t_\parallel/J_\perp \approx 0.6$, matching the point of qualitative change of E_b. Beyond this point, the superconducting transition is no longer driven by phase fluctuations and should be of BCS-type. In the BCS regime, the binding energy of a Cooper pair is given by $E_b = 2\Delta$ (with Δ the superconducting gap in the ground state), which implies critical temperatures of $T_c \sim 0.28E_b$ for $t_\parallel/J_\perp \gtrsim 0.6$.

The resulting phase diagram of the mixD bilayer model is schematically shown in Fig. 8.9, which is the main result of this chapter. In LNO, depending on the strength of the on-site Coulomb repulsion $U/t_\parallel \sim 5-10$, the predicted range of superexchange interactions is given by $t_\parallel/J_\perp \sim 0.7-1.5$ [323], such that we predict the superconductor to be of BCS-type (though multi-band effects may renormalize the energy scales [171,337]). We note that a complementary mean-field study of a related model found a similar BEC-BCS crossover phenomenology, however with quantitatively different results [338]. In order to experimentally verify the nature of the condensate, we propose to measure the specific heat of LNO under pressure, where a symmetric (asymmetric) shape is expected in a BEC-like (BCS-like) state as a function of the temperature [339,340]. Measuring the shift of spectral weight of the optical conductivity across the superconducting phase transition may give additional insights into the nature of the condensate [338].

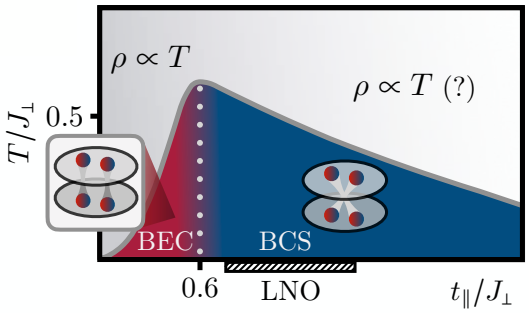

Figure 8.9: **Schematic phase diagram and effective model.** (a) Schematic phase diagram of the mixD $t_\parallel$-$J_\perp$-$J_\parallel$ model, Eq. (8.1), at doping $\delta = 50\%$ relevant to LNO. In the limit of dominating inter-layer magnetic interactions, a BEC-type superfluid of tightly bound pairs is realized. When the average sizes of pairs become larger, spatially extended pairs form a BCS-like superconducting state. Binding energies and estimated critical temperatures in vicinity of the crossover are of the order of the magnetic coupling $J_\perp$. In the BEC regime, the model shows linear in T resistivity ($\rho \propto T$) above the superconducting phase, which may extend to larger values of $t_\parallel/J_\perp$ above the BCS regime. The relevant parameter regime for LNO depending on the strength of the on-site repulsion is shown by the black hatched area, where $t_\parallel/J_\perp \sim 0.7 - 1.5$ (which may however be renormalized when taking into account multi-band effects).

We speculate that the in-plane hopping $t_\parallel$ for systems of widths $w > 1$ plays a similar role as nearest-neighbor particle repulsion in mixD ladders, where a related crossover from tightly bound pairs of holes (closed channel) at small repulsion to more spatially extended, correlated pairs of individual holes (open channel) at large repulsion has been proposed and studied in detail in [331, 332, 337]. There, it was argued that the attraction of holes is ultimately mediated by the closed channel in analogy to a Feshbach resonance [315]. Our simulations of extended systems similarly suggests Feshbash mediated pairing in bilayer nickelates, resulting in an effective attraction of spinon-chargon pairs due to the presence of the closed chargon-chargon channel.

Regardless of whether the constituents of the superfluid are tightly bound chargon-chargon pairs (BEC) or overlapping Cooper pairs (BCS), binding energies of the order of the coupling $J_\perp$ suggest extraordinarily high critical temperatures in bilayer systems. Assuming an inter-layer coupling of $J_\perp \approx 0.3$ eV [323], our results propose transition temperatures of the order of $T_c \approx 1000$ K in the region of the BEC-BCS crossover, which is an order of magnitude larger than measured in LNO. We note however that the multi-band nature of LNO likely leads to strong suppressions of the condensation temperatures. For instance, a more sophisticated two-band model that takes into account Hund's coupling in a more rigorous manner has been shown to effectively reduce the coupling $J_\perp$ by a factor of four, which shifts the system deeper into the BCS phase and reduces its critical temperature [171]. Nevertheless, we stress that the physics in the perturbative limit (i.e. a description by an effective XXZ model) stays identical up to renormalization of the parameters, supporting the view that the single-band model captures the essential pairing physics. Considering both an effective reduction of $J_\perp$ due to the multi-band nature of LNO as well as the BCS prediction for T_c leads to estimated critical temperatures of the mixD bilayer model that are indeed of the same order of magnitude as measured in LNO. Disorder effects may further suppress T_c in bilayer nickelate materials, such that higher critical temper-

atures may be reached for cleaner samples. Though the above effects likely play a major role in determining the exact quantitative transition temperature of LNO, the high T_c of the order of $J_\perp/2$ in the single-band, mixD bilayer model Hamiltonian near the crossover is very striking in its own right, and may open the path towards a more targeted design of materials possibly facilitating superconductivity above room temperature.

Lastly, we note that there exist intriguing similarities between the condensation of electron-hole pairs (excitons) [341, 342] in bilayer semiconductors and superconductivity in bilayer nickelates. For example, high-temperature condensation of inter-layer excitons with large binding energies of $E_b \gtrsim 100$ meV has been demonstrated in bilayer transition metal dichalcogenide (TMD) semiconductors [343]. Additionally, a BEC-BCS crossover between tightly and weakly bound electron-hole pairs has been observed in bilayer quantum Hall systems by continuously tuning the pairing strength through variation of the layer separation [344].

8.5 Strange metallicity

Above the superconducting critical temperature of LNO, an extended region of strange metallicity with linear resistivity $\rho \propto T$ has been reported [70, 166]. Indeed, it has been shown that hard-core bosons on the 2D square lattice show a very similar behavior, with zero resistivity for $T < T_{\mathrm{BKT}}$ and asymptotic linear resistivity $d\rho/dT \propto 1/\rho_s$ above T_{BKT}, with ρ_s the phase stiffness in the ground state [345]. We note that this is in stark contrast to weakly interacting Bose gases, where the resistivity saturates at high temperatures. This shows that, within the perturbative limit, the extended regime of linear in T resistivity above the superconducting transition temperature as measured in LNO is captured in the effective model of tightly bound pairs, see Fig. 8.9.

We propose that, away from the perturbative limit but in vicinity of the conjectured BEC-BCS crossover, the behavior of the conductivity is nevertheless dominantly dictated by the conduction of pairs, conceivably leading to linear in T resistivity in the bilayer system at experimentally relevant parameters $J_\perp/t_\parallel \sim 1$, cf. Fig. 8.9. Further studies of the mixD bilayer system are, however, necessary to pin down its properties away from the BEC-like limit.

8.6 Discussion

We have presented an extensive analysis of superconductivity in mixD bilayer systems by studying the single band $t_\parallel$-$J_\perp$-$J_\parallel$ model. By carefully analyzing finite size effects, we demonstrated that long-range pairing correlations emerge in the ground state, and quasi-long range power-law correlations below $T < T_{\mathrm{BKT}}$, in the thermodynamic limit. We presented an analytically accessible limit of dominant inter-layer couplings, in which the model can be described by an effective spin-1/2 XXZ model. This allowed us to make predictions even away from this limit. Specifically, we proposed that the resistivity of the mixD bilayer system in the vicinity of the perturbative regime is dictated by the conduction of pairs, possibly explaining the linear in temperature resistivity measured in LNO above T_c.

Our study of binding energies at $\delta = 0.5$ proposes the appearance of a BEC-BCS crossover as the ratio $t_\parallel / J_\perp$ is tuned. This may lead to unexpected similarities with underdoped cuprates, where a similar Feshbach scenario has recently been proposed [315]. With our understanding of all appearing terms in the mixD model Hamiltonian, we suggest to tune bilayer nickelates towards the BEC-BCS crossover point, e.g. through rare-earth substitutions as proposed in [346]. Recent experiments suggest the appearance of superconductivity in trilayer nickelate compounds [347–349]. Performing a similar analysis for minimal models to trilayer systems and identifying relevant mechanisms may help to obtain a unified understanding of nickelate superconductors [350, 351].

We note that in the plain-vanilla Fermi-Hubbard model, which has been in the spotlight of fermionic quantum simulators in recent years, the strong competition between different phases, low T_c's or even absence of superconductivity in the ground state [145] renders an observation of long-ranged pairing order with ultracold atoms a real challenge. The mixD bilayer model, in turn, facilitates such an observation in state-of-the-art experiments owing to its large tunability and high predicted critical temperatures of the order of $J_\perp/2$. Furthermore, transport properties can be measured by relaxation of an imposed density modulation [49], enabling a direct observation of the strange metal and superconducting phases in the mixD $t_\parallel$-$J_\perp$-$J_\parallel$ model. This would allow for the simulation of 2D bilayer systems for a generic choice of Hamiltonian parameters, ultimately enabling realistic simulations of materials using analog quantum machines. A detailed experimental proposal will be discussed in the upcoming chapter.

9 

Exploring superconductivity in optical lattices

Summary. The simulation of high-temperature superconducting materials by implementing strongly correlated fermionic models in optical lattices is one of the major objectives in the field of analog quantum simulation. In this chapter we show that local control and optical bilayer capabilities combined with spatially resolved measurements create a versatile toolbox to study fundamental properties of both nickelate and cuprate high-temperature superconductors. Building on the previous chapter, on the one hand we present a scheme to implement a bilayer model that captures the essential pairing physics of pressurized bilayer nickelates. This allows for the long-sought realization of a state with long-range superconducting order in current lattice quantum simulation machines. On the other hand, we demonstrate that control of local gates enables the observation of *d*-wave pairing order in the two-dimensional (single-layer) repulsive FH model through the simulation of a system with attractive interactions. Lastly, we introduce a scheme to measure momentum-resolved dopant densities, providing access to observables complementary to solid-state experiments—which is of particular interest for future studies of the enigmatic pseudogap phase appearing in cuprates.

9.1 Introduction

The exploration of unconventional superconductivity and exotic normal phases, such as the pseudogap, using ultracold atoms in optical lattices is a major objective in the field of quantum simulation. Although the original vision of studying superfluid states in ultracold, repulsively interacting fermionic gases was first proposed in 2002 [68], their realization remains elusive to this day. What makes this observation so challenging?

1. Small energy differences between various collectively ordered phases lead to extremely

low critical temperatures [144, 145, 228], which are currently out of reach for state-of-the-art quantum simulators. As discussed in the introduction (Chap. 1), reaching temperatures below $T/J \sim 0.5$ presents significant technological challenges. Moreover, as mentioned in Sec. 2.2, in the plain-vanilla square lattice Fermi-Hubbard (FH) model, superconducting order is absent, with stripe order being dominant [145]. Although this balance can be shifted by introducing next-to-nearest neighbor terms [146, 147], critical temperatures are expected to remain on the order of a few percent of the hopping energy scale.

2. Even if a state with long-range pairing order were to be realized experimentally, measuring it remains highly challenging. Superconducting order in quantum many-body states cannot be directly probed using local densities, as the corresponding observables are off-diagonal in the Fock basis. This requires the ability to coherently add and remove singlet pairs from the system, posing a significant experimental hurdle.

3. For studying the exotic normal phases of cuprate superconductors, momentum-resolved observables of dopants are crucial [24, 101, 316]. While momentum-space densities of particles can be accessed via time-of-flight measurements, this method is not applicable for resolving the momentum of the system's dopants.

As discussed in detail in Sec. 5.3, mixed-dimensional (mixD) systems that can be engineered in optical lattices subject to potential gradients have emerged as a compelling tool to energetically favor and study collective phenomena in strongly correlated models. The experimental setup to engineer mixD systems consists of an optical superlattice, i.e. coupled double wells, with tunable energy offset Δ [see e.g. the left-hand side of Fig. 9.2 for an illustration]. This allows for the realization of meta-stable states where the hopping along the potential gradient is suppressed, while spin-exchange remains finite.

With the discovery of high-temperature superconductivity at $T_c \sim 80$ K in pressurized bilayer nickelates, mixD systems have gained broad attention also in the condensed matter community. As discussed in previous chapters (see i.p. Sec. 2.3 and Chap. 8), mixed dimensions are widely believed to play an essential role in the formation of superconductivity in the bilayer nickelate $La_3Ni_2O_7$ (LNO). Indeed, our simulations of minimal, single-band models in Chap. 8 suggest astonishingly high critical temperatures of the order of the magnetic coupling $J_\perp/2$ in certain parameter regimes, which are readily achievable in state-of-the-art quantum simulation experiments.

In this chapter, we present how local control of gates and bilayer optical lattice capabilities can be independently utilized to simulate minimal models and measure observables relevant to both nickelate and cuprate high-temperature superconductors. In particular, we argue that these methods overcome the challenges in microscopically studying superconducting and exotic normal phases: We show how current state-of-the-art quantum simulators can be used to (i) prepare and observe a state with superconducting order, i.e. (quasi) long-range pair coherence, at realistic temperatures in the mixD bilayer t-J model, (ii) measure d-wave pairing correlations in the 2D FH model, and (iii) access momentum-resolved dopant distribution functions in the 2D t-J model. This directly facilitates complementary measurements to solid-state experiments

of both bilayer nickelate and cuprate high-temperature superconductors using analog quantum simulation. After giving a brief overview and introduction in the following, the corresponding proposals (i)-(iii) are detailed in Secs. 9.2,9.3,9.4.

In the context of nickelate superconductors, we present a scheme to simulate the 2D mixD bilayer t-J model on the square lattice and adiabatically prepare states that feature quasi long-range pairing correlations,

$$\langle \hat{\Delta}_{\mathbf{i}}^{\dagger} \hat{\Delta}_{\mathbf{j}} \rangle \simeq \begin{cases} |\mathbf{i}-\mathbf{j}|^{-\alpha} & 0 < T < T_c \\ \text{const} & T = 0, \end{cases} \tag{9.1}$$

where $\hat{\Delta}_{\mathbf{i}}^{\dagger} = \frac{1}{\sqrt{2}} \left(\hat{c}_{\mathbf{i},\uparrow,\alpha=1}^{\dagger} \hat{c}_{\mathbf{i},\downarrow,\alpha=2}^{\dagger} - \hat{c}_{\mathbf{i},\downarrow,\alpha=1}^{\dagger} \hat{c}_{\mathbf{i},\uparrow,\alpha=2}^{\dagger} \right)$ creates an interlayer singlet between layers $\alpha = 1,2$ on site $\mathbf{i}$. The experimental setup consists of two FH layers with energy offset Δ in the strong-coupling limit, giving rise to interlayer magnetic interactions, as well as intralayer tunneling and magnetic coupling; hopping of particles between the two layers, however, is suppressed, making the system mixed-dimensional. The setup is summarized in Fig. 9.1. An essential ingredient that allows for the measurement of pair-pair correlations is to hole-dope one layer, while doublon-doping the other layer (see also Refs. [331, 332] for related setups), illustrated on the left-hand side of Fig. 9.1. In Sec. 9.2, we start by showing that, on bipartite lattices, the doublon-hole-doped bilayer mixD t-J system is equivalent (up to tunable interlayer density-density interactions) to a fully hole-doped description by a partial particle-hole transformation applied to one layer only [see the right-hand side of Fig. 9.1].

We then present a minimal adiabatic preparation scheme of a quantum state featuring pair-coherence. We propose a measurement protocol involving resonant global interlayer tunneling $\pi/2$ pulses, which allows to access superconducting (pair-pair) correlations in the particle-hole transformed Hamiltonian. These correlations map to density-density correlations in the physically implemented doublon-hole-doped system and are hence readily accessible, without requiring to change the number of fermions. We propose to apply this scheme also to experimentally accessible 2D mixD bilayers, in which the Berezinskii–Kosterlitz–Thouless (BKT) transition to a superconducting state with quasi long-range pairing correlations around $T_c \sim J_{\perp}/2$ can be explored, see Chap. 8.

In connection with cuprates, in Sec. 9.3 we present a related scheme that allows to measure coherent pairing correlations in the 2D FH model on the square lattice. Following the ideas of Ho, Cazalilla and Giamarchi [352], we consider an implementation of the FH model with strong attractive interactions [353], which is equivalent to the repulsive system through a partial particle-hole transformation, summarized in Fig. 9.9. Coherent pairing order in the repulsive FH model can then be accessed through local basis-rotations in the implemented (attractive) model. In particular, we show that local control of tunneling gates allows for the observation of pairing correlations with different symmetries, e.g., the state can be probed on both s-wave and d-wave pairing order. Thereby we extend the ideas from Ref. [352], where noise-correlation measurements have been proposed to analyze the antiferromagnetic state on the attractive side. With recent advances in local control in optical lattices [354], our scheme paves the way for the

long-sought demonstration of d-wave pairing correlations in the plain-vanilla Hubbard model.

The toolbox of doped mixD bilayers additionally allows for the exploration of momentum-resolved observables of mobile holes in 2D t-J models. In particular, in Sec. 9.4 we present a protocol to measure the free-hole (dopant) density in an effective 2D t-J model in momentum-space, $\langle \hat{n}_h(\mathbf{k}) \rangle$, which is a particularly relevant observable for revealing the properties of exotic normal phases (such as the appearance of a small Fermi surface in the pseudogap phase) of cuprates. We note that this is in contrast to direct implementations of the hole-doped 2D t-J model, which give access to momentum resolved particle—but not dopant densities.

To this end, we propose to implement a mixD bilayer system in the limit of strong interlayer Kondo-type couplings, i.e. strong spin exchange $J_\perp$ without tunneling $t_\perp$ between the layers, where mobile singlets can be mapped to holes in an effective 2D model, summarized in Fig. 9.11. By coherently driving tunneling transitions between interlayer singlets and doublon-hole pairs and the subsequent removal of one spin species, the momentum distribution of dopants $\langle \hat{n}_h(\mathbf{k}) \rangle$ can be accessed through time-of-flight measurements. In particular, $\langle \hat{n}_h(\mathbf{k}) \rangle$ does not depend on the spectral weight at the respective momentum $\mathbf{k}$, which can be advantageous compared to angle-resolved photoemission spectroscopy (ARPES) in regions of the Brillouin zone with low spectral weight, such as the backside of the Fermi arcs [87]. Furthermore, the effective 2D t-J model features hopping and spin interaction amplitudes that originate from different layers. This allows for an independent tuning of these parameters, and hence to simulate regimes that cannot be accessed through a direct implementation of a 2D layer.

9.2 Measuring pairing correlations: Mixed-dimensional bilayers

In the following, we present how states with quasi long-range superconducting order can be prepared and how coherent pairing correlations can be measured in realistic experimental setups by implementing the mixD bilayer t-J model in a transformed basis, summarized in Fig. 9.1.

An essential ingredient to measure pairing correlations in the mixD bilayer t-J model is to experimentally implement a partially particle-hole transformed Hamiltonian. Therefore, before precisely defining the proposed model, we review the particle-hole symmetry of the standard t-J model on bipartite lattices, retrieved from perturbation theory from the FH model. We note that relevant models for bilayer nickelates are defined on the (bipartite) square lattice, where the particle-hole symmetry and hence our proposed measurement scheme holds.

9.2.1 Particle-hole symmetry of the conventional t-J model

When hole-doping the FH model away from one particle per site and projecting out states with double occupancy (valid in the strongly interacting limit $U \gg t$), the Hamiltonian reads (neglecting three-site, next-nearest neighbor terms $\sim J$)

$$\hat{\mathcal{H}} = -t \sum_{\langle \mathbf{i},\mathbf{j} \rangle, \sigma} \hat{\mathcal{P}}_{GW} \left(\hat{c}^\dagger_{\mathbf{i},\sigma} \hat{c}_{\mathbf{j},\sigma} + \text{h.c.} \right) \hat{\mathcal{P}}_{GW} + J \sum_{\langle \mathbf{i},\mathbf{j} \rangle} \left(\hat{\mathbf{S}}_\mathbf{i} \cdot \hat{\mathbf{S}}_\mathbf{j} - \frac{\hat{n}_\mathbf{i} \hat{n}_\mathbf{j}}{4} \right). \tag{9.2}$$

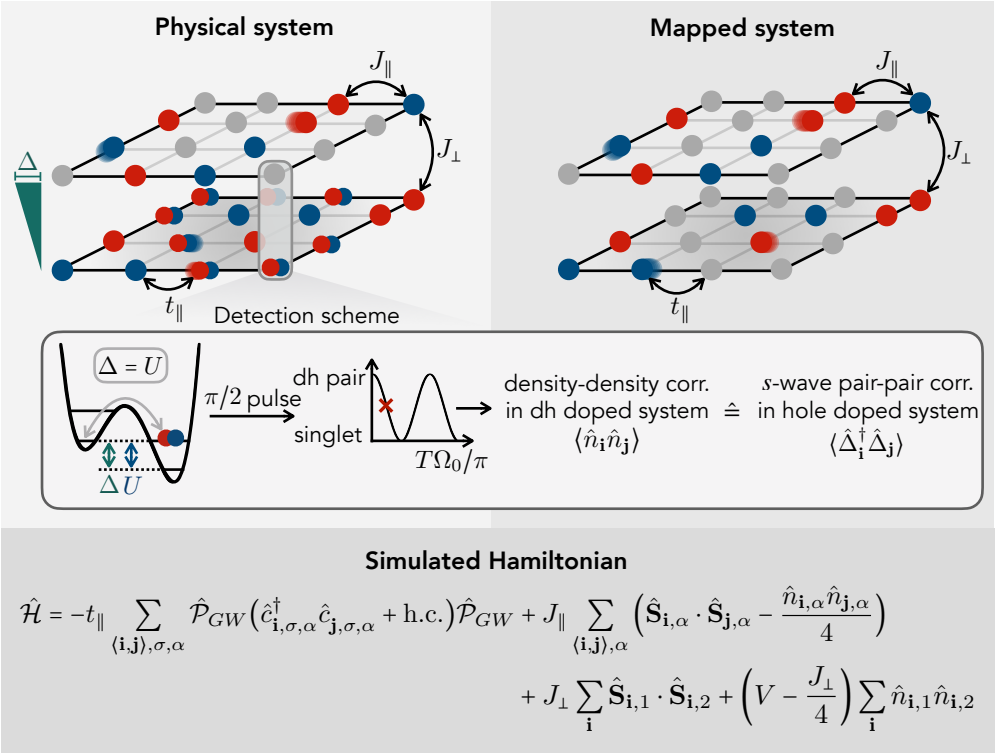

Figure 9.1: **Exploring high-temperature superconductivity in mixD with optical lattices.** Scheme how to measure coherent pairing correlations in the mixD bilayer $t-J$ model. We propose to implement the Fermi-Hubbard model in the strong-coupling limit on a bilayer geometry (physical system). By applying a potential gradient Δ between the two layers, interlayer tunneling is suppressed, such that $t_\perp = 0$, but $J_\perp > 0$. Up to tunable interlayer density-density interactions, the model relates to a fully hole-doped mixD bilayer t-J model through a partial particle-hole transformation (mapped system). In the physical, doublon-hole-doped system, performing a global resonant tunneling pulse ($\Delta = U$) after ramping up the lattice depth results in Rabi oscillations with frequency Ω_0 between singlets and doublon-hole (dh) pairs on the rungs. In a $\pi/2$ rotated basis (red cross), density-density correlations in the doublon-hole-doped system then correspond to coherent pair-pair correlations in the fully hole-doped system.

Let us explicitly write out the Gutzwiller projector $\hat{\mathcal{P}}_{GW}$ that removes states with double occupancy,

$$\hat{\mathcal{P}}_{GW} = \prod_\mathbf{i} \left(1 - \hat{n}_{\mathbf{i},\uparrow}\hat{n}_{\mathbf{i},\downarrow}\right). \tag{9.3}$$

The total particle number is given by $\hat{N} = \sum_\mathbf{i} \hat{n}_{\mathbf{i},\uparrow} + \hat{n}_{\mathbf{i},\downarrow} = L - d$, where L and d are the number of sites and (hole) dopants in the system, respectively.

Similarly, we can consider doublon-doping the FH model. The perturbation theory works identically, however now we project out empty states, denoted by the projector $\hat{\tilde{\mathcal{P}}}_{GW}$,

$$\hat{\tilde{\mathcal{P}}}_{GW} = \prod_\mathbf{i} \Big(1 - (1 - \hat{n}_{\mathbf{i},\uparrow})(1 - \hat{n}_{\mathbf{i},\downarrow})\Big). \tag{9.4}$$

Up to an overall doping dependent energy shift due to double occupancies, the Hamiltonian

reads

$$\hat{\tilde{\mathcal{H}}} = -t \sum_{\langle \mathbf{i},\mathbf{j}\rangle,\sigma} \hat{\tilde{\mathcal{P}}}_{GW} \left(\hat{c}^\dagger_{\mathbf{i},\sigma}\hat{c}_{\mathbf{j},\sigma} + \text{h.c.}\right)\hat{\tilde{\mathcal{P}}}_{GW} + J \sum_{\langle \mathbf{i},\mathbf{j}\rangle} \left(\hat{\mathbf{S}}_\mathbf{i}\cdot\hat{\mathbf{S}}_\mathbf{j} - \frac{\hat{\tilde{n}}_\mathbf{i}\hat{\tilde{n}}_\mathbf{j}}{4}\right), \tag{9.5}$$

where $\hat{\tilde{n}}_\mathbf{i} = 2 - \hat{n}_{\mathbf{i},\downarrow} - \hat{n}_{\mathbf{i},\uparrow} = 0\,(1)$ for doublons (singly occupied sites).

We now map the doublon-doped t-J model, Eq. (9.5), to the hole-doped system, Eq. (9.2), and describe both in the same Hilbert space. Consider for this the charge conjugation transformation $\hat{C}$, which maps particle creation to annihilation operators and vice versa,

$$\begin{aligned} \hat{C}\hat{c}_{\mathbf{i},\sigma}\hat{C}^{-1} &= \hat{c}^\dagger_{\mathbf{i},\sigma} \\ \hat{C}\hat{c}^\dagger_{\mathbf{i},\sigma}\hat{C}^{-1} &= \hat{c}_{\mathbf{i},\sigma}. \end{aligned} \tag{9.6}$$

Let us evaluate how the single particle states $\{|0\rangle, |\uparrow\rangle, |\downarrow\rangle\}$ behave under the transformation $\hat{C}$. First, consider the action on the vacuum state, which is defined by $\hat{c}_{\mathbf{i},\sigma}|0\rangle = 0$ for all $\mathbf{i},\sigma$. Applying the transformation yields

$$0 = \hat{C}\hat{c}_{\mathbf{i},\sigma}|0\rangle = \hat{C}\hat{c}_{\mathbf{i},\sigma}\hat{C}^{-1}\hat{C}|0\rangle = \hat{c}^\dagger_{\mathbf{i},\sigma}\hat{C}|0\rangle, \tag{9.7}$$

such that the transformed vacuum state is the fully occupied state, $\hat{C}|0\rangle = \prod_{\mathbf{i},\sigma} c^\dagger_{\mathbf{i},\sigma}|0\rangle$. Furthermore, we get for each $\mathbf{i}$ (we omit the lattice site index $\mathbf{i}$ for simplicity)

$$\hat{C}|\uparrow\rangle = \hat{C}\hat{c}^\dagger_\uparrow|0\rangle = \hat{C}\hat{c}^\dagger_\uparrow\hat{C}^{-1}\hat{C}|0\rangle = \hat{c}_\uparrow\hat{c}^\dagger_\uparrow\hat{c}^\dagger_\downarrow|0\rangle = \hat{c}^\dagger_\downarrow|0\rangle = |\downarrow\rangle \tag{9.8}$$

and

$$\hat{C}|\downarrow\rangle = \hat{C}\hat{c}^\dagger_\downarrow|0\rangle = \hat{C}\hat{c}^\dagger_\downarrow\hat{C}^{-1}\hat{C}|0\rangle = \hat{c}_\downarrow\hat{c}^\dagger_\uparrow\hat{c}^\dagger_\downarrow|0\rangle = -\hat{c}^\dagger_\uparrow|0\rangle = -|\uparrow\rangle. \tag{9.9}$$

The spin flips of the single particle states under the transformation as seen above are intuitive when considering a state in the subspace of single and double occupancies, $|\uparrow,\downarrow,\uparrow\downarrow,\uparrow\rangle$. Applying the hopping term $\hat{c}^\dagger_{2,\uparrow}\hat{c}_{3,\uparrow}|\uparrow,\downarrow,\uparrow\downarrow,\uparrow\rangle = -|\uparrow,\uparrow\downarrow,\downarrow,\uparrow\rangle$, we see that the hopping of the $\uparrow$-spin maps to a hopping of a $\downarrow$-spin in the subspace of empty and singly occupied sites, $\hat{c}^\dagger_{3,\downarrow}\hat{c}_{2,\downarrow}|\uparrow,\downarrow,0,\uparrow\rangle = |\uparrow,0,\downarrow,\uparrow\rangle$. Note that there is an additional sign change of the hopping term after the transformation, as $\hat{C}\hat{c}^\dagger_{\mathbf{i},\sigma}\hat{c}_{\mathbf{j},\sigma}\hat{C}^{-1} = \hat{c}_{\mathbf{i},\sigma}\hat{c}^\dagger_{\mathbf{j},\sigma} = -\hat{c}^\dagger_{\mathbf{j},\sigma}\hat{c}_{\mathbf{i},\sigma}$ (for $\mathbf{i}\neq\mathbf{j}$).

To account for the appearing spin and phase flips, we redefine the charge conjugation operation $\hat{C}$ and make it site- and spin-dependent (i.e., we add a unitary transformation to the charge conjugation Eq. (9.6), $\hat{\mathcal{U}}\hat{C}\hat{\mathcal{U}}^\dagger = \hat{\mathcal{C}}$, representing another possible particle-hole transformation),

$$\begin{aligned} \hat{\mathcal{C}}\hat{c}_{\mathbf{i},\sigma}\hat{\mathcal{C}}^{-1} &= \eta_\mathbf{i}\,\mathrm{sgn}(\bar{\sigma})\hat{c}^\dagger_{\mathbf{i},\bar{\sigma}} \\ \hat{\mathcal{C}}\hat{c}^\dagger_{\mathbf{i},\sigma}\hat{\mathcal{C}}^{-1} &= \eta_\mathbf{i}\,\mathrm{sgn}(\bar{\sigma})\hat{c}_{\mathbf{i},\bar{\sigma}}. \end{aligned} \tag{9.10}$$

Here, the sign factor $\eta_\mathbf{i} = e^{i\boldsymbol{\pi}\cdot\mathbf{i}}$ with $\boldsymbol{\pi} = [\pi,\pi]$ is positive (negative) on sublattice A (B) on the square lattice; note that $\hat{\mathcal{C}}$ also switches spins $\sigma \leftrightarrow \bar{\sigma}$.

Applying the transformation to single particle states on a given site ($\hat{\mathcal{C}}|0\rangle = \prod_{\mathbf{i},\sigma}\hat{c}^\dagger_{\mathbf{i},\sigma}|0\rangle$ still

holds),

$$\begin{aligned}\hat{\mathcal{C}}\,|0\rangle &= \hat{c}^\dagger_\uparrow \hat{c}^\dagger_\downarrow\,|0\rangle = |\uparrow\downarrow\rangle \\ \hat{\mathcal{C}}\,|\uparrow\rangle &= \hat{\mathcal{C}}\hat{c}^\dagger_\uparrow\hat{\mathcal{C}}^{-1}\hat{\mathcal{C}}\,|0\rangle = -\hat{c}_\downarrow \hat{c}^\dagger_\uparrow \hat{c}^\dagger_\downarrow\,|0\rangle = |\uparrow\rangle \\ \hat{\mathcal{C}}\,|\downarrow\rangle &= \hat{\mathcal{C}}\hat{c}^\dagger_\downarrow\hat{\mathcal{C}}^{-1}\hat{\mathcal{C}}\,|0\rangle = \quad \hat{c}_\uparrow \hat{c}^\dagger_\uparrow \hat{c}^\dagger_\downarrow\,|0\rangle = |\downarrow\rangle\,,\end{aligned} \tag{9.11}$$

such that the singly occupied states map onto themselves, while doublons map to holes and vice versa. Transforming the relevant operators in the Hamiltonian Eq. (9.5) for nearest neighbor pairs $\langle \mathbf{i}, \mathbf{j}\rangle$ yields

$$\begin{aligned}\hat{\mathcal{C}}\hat{n}_{\mathbf{i},\sigma}\hat{\mathcal{C}}^{-1} &= \hat{c}_{\mathbf{i},\bar{\sigma}}\hat{c}^\dagger_{\mathbf{i},\bar{\sigma}} = 1 - \hat{n}_{\mathbf{i},\bar{\sigma}} \\ \hat{\mathcal{C}}\hat{n}_{\mathbf{i}}\hat{\mathcal{C}}^{-1} &= \hat{\bar{n}}_{\mathbf{i}} \\ \hat{\mathcal{C}}\hat{\mathcal{P}}_{GW}\hat{\mathcal{C}}^{-1} &= \hat{\bar{\mathcal{P}}} \\ \hat{\mathcal{C}}\hat{c}^\dagger_{\mathbf{i},\sigma}\hat{c}_{\mathbf{j},\sigma}\hat{\mathcal{C}}^{-1} &= -\hat{c}_{\mathbf{i},\bar{\sigma}}\hat{c}^\dagger_{\mathbf{j},\bar{\sigma}} = \hat{c}^\dagger_{\mathbf{j},\bar{\sigma}}\hat{c}_{\mathbf{i},\bar{\sigma}} \\ \hat{\mathcal{C}}\hat{S}^z_{\mathbf{i}}\hat{\mathcal{C}}^{-1} &= \frac{1}{2}\hat{\mathcal{C}}(\hat{n}_{\mathbf{i},\uparrow} - \hat{n}_{\mathbf{i},\downarrow})\hat{\mathcal{C}}^{-1} = \hat{S}^z_{\mathbf{i}} \\ \hat{\mathcal{C}}\hat{S}^x_{\mathbf{i}}\hat{\mathcal{C}}^{-1} &= \frac{1}{2}\hat{\mathcal{C}}(\hat{c}^\dagger_{\mathbf{i},\uparrow}\hat{c}_{\mathbf{i},\downarrow} + \hat{c}^\dagger_{\mathbf{i},\downarrow}\hat{c}_{\mathbf{i},\uparrow})\hat{\mathcal{C}}^{-1} = \hat{S}^x_{\mathbf{i}} \\ \hat{\mathcal{C}}\hat{S}^y_{\mathbf{i}}\hat{\mathcal{C}}^{-1} &= \frac{1}{2}i\hat{\mathcal{C}}(\hat{c}^\dagger_{\mathbf{i},\downarrow}\hat{c}_{\mathbf{i},\uparrow} - \hat{c}^\dagger_{\mathbf{i},\uparrow}\hat{c}_{\mathbf{i},\downarrow})\hat{\mathcal{C}}^{-1} = \hat{S}^y_{\mathbf{i}}.\end{aligned} \tag{9.12}$$

Furthermore, the total particle number transforms as $\hat{\mathcal{C}}\hat{N}\hat{\mathcal{C}}^{-1} = \sum_{\mathbf{i}} \left(2 - \hat{n}_{\mathbf{i},\uparrow} - \hat{n}_{\mathbf{i},\downarrow}\right) = L - d$, such that $\sum_{\mathbf{i}} \hat{n}_{\mathbf{i},\uparrow} + \hat{n}_{\mathbf{i},\downarrow} = L + d$, i.e., the transformed system has a total of $L + d$ particles (d doublons).

Using Eq. (9.12), transforming the relevant operators in the Hamiltonian Eq. (9.5) for nearest neighbor pairs $\langle \mathbf{i}, \mathbf{j}\rangle$ ultimately yields

$$\hat{\mathcal{C}}\hat{\bar{\mathcal{H}}}\hat{\mathcal{C}}^{-1} = \hat{\mathcal{H}}, \tag{9.13}$$

such that the description of the doublon-doped system in the subspace of singly and doubly occupied sites is manifestly equivalent to a hole-doped description in the Hilbert space of singly occupied and empty sites (i.e., the t-J Hamiltonian is particle-hole symmetric). Note that this is relying on the fact that the underlying lattice is bipartite (hence, including the additional 3-site term in the t-J model does not change this result); non-bipartite lattices (e.g. when considering diagonal couplings t' [147]) yield different signs in the hopping term after the charge-conjugation operation, and are hence not particle-hole symmetric.

9.2.2 Partial particle-hole mapping of the mixD t-J model

We now consider the hole-doped mixD bilayer $t_\parallel$-$J_\perp$-$J_\parallel$ model, which we propose to simulate,

$$\hat{\mathcal{H}} = \sum_{\alpha=1,2} \hat{\mathcal{H}}_\alpha + \hat{\mathcal{H}}_{12}. \tag{9.14}$$

Here, $\hat{\mathcal{H}}_\alpha$ denotes the Hamiltonian in layer $\alpha = 1, 2$ alone,

$$\hat{\mathcal{H}}_\alpha = -t_\parallel \sum_{\langle \mathbf{i},\mathbf{j}\rangle,\sigma} \hat{\mathcal{P}}_{GW} \left(\hat{c}^\dagger_{\mathbf{i},\sigma,\alpha} \hat{c}_{\mathbf{j},\sigma,\alpha} + \text{h.c.}\right) \hat{\mathcal{P}}_{GW} + J_\parallel \sum_{\langle \mathbf{i},\mathbf{j}\rangle} \left(\hat{\mathbf{S}}_{\mathbf{i},\alpha} \cdot \hat{\mathbf{S}}_{\mathbf{j},\alpha} - \frac{\hat{n}_{\mathbf{i},\alpha}\hat{n}_{\mathbf{j},\alpha}}{4}\right), \tag{9.15}$$

and $\hat{\mathcal{H}}_{12}$ is their interlayer Kondo-type coupling $\propto J_\perp$,

$$\hat{\mathcal{H}}_{12} = J_\perp \sum_{\mathbf{i}} \left(\hat{\mathbf{S}}_{\mathbf{i},1} \cdot \hat{\mathbf{S}}_{\mathbf{i},2} - \frac{\hat{n}_{\mathbf{i},1}\hat{n}_{\mathbf{i},2}}{4}\right). \tag{9.16}$$

As discussed in Chap 8, this model features (quasi) long-range s-wave pairing order, with expected critical temperatures of $T_c \sim J_\perp/2$ for $t_\parallel/J_\perp \sim 0.6$ in the 2D limit.

The Hamiltonian Eq. (9.14) can be simulated in bilayer optical lattices described by the on-site interaction U, intralayer (interlayer) tunnel couplings $\tilde{t}_\parallel$ ($\tilde{t}_\perp$), and a potential offset between the two layers Δ [2,57,355]. When choosing $\tilde{t}_\parallel, \tilde{t}_\perp \ll \Delta < U$, the mixD setting in Eq. (9.14) is realized, with effective parameters $t_\parallel = \tilde{t}_\parallel$, $t_\perp = 0$, $J_\parallel = 4\tilde{t}^2_\parallel/U$ and $J_\perp = 2\tilde{t}^2_\perp/(U+\Delta) + 2\tilde{t}^2_\perp/(U-\Delta)$, cf. Sec. 5.3.

Experimentally, we argue below that it is advantageous to simulate a closely related mixD bilayer model, with hole-doping in one and doublon-doping in the other layer. Using the notation from above, this model is described by the Hamiltonian

$$\hat{\tilde{\mathcal{H}}} = \hat{\mathcal{H}}_1 + \hat{\tilde{\mathcal{H}}}_2 + \hat{\tilde{\mathcal{H}}}'_{12}. \tag{9.17}$$

Here, layer 1 (2) is hole (doublon) doped and the coupling $\hat{\tilde{\mathcal{H}}}'_{12}$ contains additional interlayer density-density interactions arising from the mapping of a Hubbard model with a strong potential gradient between the layers, as discussed in more detail next. A similar setup has been analyzed in Refs. [331, 332], where the original motivation was to utilize the additional interlayer density-density interactions in the doublon-hole-doped model to tune the system through a crossover associated with a Feshbach resonance. Here we demonstrate another useful feature of this setting that readily allows to measure coherent pairing correlations.

From now on, we assume that layer 1 is energetically offset from layer 2, i.e., holes (doublons) are doped in layer 1 (2). We shall denote the layer with larger (smaller) on-site energy as upper (lower) layer. On the left-hand side of Fig. 9.2, we schematically show a single double well with energy offset Δ, where $\alpha = 1$ ($\alpha = 2$) correspond to the lower (upper) layer. We note that the situation of doublon (hole) doping the upper (lower) layer instead leads to the same conclusions as discussed in the following, however with a different sign of the additional density-density interactions.

Density-density interactions

Before we apply a particle-hole mapping $\hat{\mathcal{C}}$ in the doublon-doped layer in order to relate $\hat{\tilde{\mathcal{H}}}$ to a mixD bilayer system with hole-doping ($\hat{\mathcal{H}}$), we describe the origin of the additional interactions

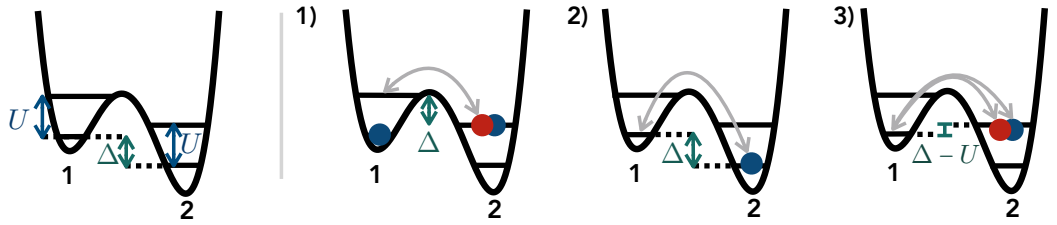

Figure 9.2: **Interlayer interactions.** Left panel: illustration of the double well geometry with on-site interaction U and energy offset Δ; here, layer 1 (2) is the energetically upper (lower) layer. In the doublon-hole-doped setting, virtual processes lead to the appearance of nearest-neighbor interlayer interactions between particles. Contributions come from **1)** a particle in the upper ($\alpha = 1$) and a doublon in the lower ($\alpha = 2$) layer, **2)** a hole in the upper and a particle in the lower layer, and **3)** a hole in the upper and a doublon in the lower layer.

in $\hat{\tilde{\mathcal{H}}}$,

$$\hat{\tilde{\mathcal{H}}}'_{12} = J_\perp \sum_{\mathbf{i}} \hat{\mathbf{S}}_{\mathbf{i},1} \cdot \hat{\mathbf{S}}_{\mathbf{i},2} + \left(V - \frac{J_\perp}{4}\right) \sum_{\mathbf{i}} \hat{n}_{\mathbf{i},1} \hat{\tilde{n}}_{\mathbf{i},2}. \tag{9.18}$$

Virtual tunnel couplings between the doublon and hole-doped layer lead to the appearance of nearest neighbor (interlayer) interactions between dopants. The following contributions appear when doublon-doping the energetically lower layer ($\alpha = 2$) and hole-doping the upper layer ($\alpha = 1$) [331, 332], see Fig. 9.2 (we note that we always imply $0 < \Delta < U$):

1) $-\frac{\tilde{t}_\perp^2}{\Delta} \hat{n}_{\mathbf{i},1}(1 - \hat{\tilde{n}}_{\mathbf{i},2})$ for a particle in the upper and a doublon in the lower layer,

2) $-\frac{\tilde{t}_\perp^2}{\Delta}(1 - \hat{n}_{\mathbf{i},1})\hat{\tilde{n}}_{\mathbf{i},2}$ for a hole in the upper and a particle in the lower layer,

3) $-2\frac{\tilde{t}_\perp^2}{\Delta - U}(1 - \hat{n}_{\mathbf{i},1})(1 - \hat{\tilde{n}}_{\mathbf{i},2})$ for a hole in the upper and a doublon in the lower layer.

Here, $\tilde{t}_\perp$ denotes the hopping between layers in the bilayer Fermi-Hubbard model with a gradient. Adding up the above contributions, we find an effective interlayer nearest neighbor interaction of the form

$$V \sum_{\mathbf{i}} \hat{n}_{\mathbf{i},1} \hat{\tilde{n}}_{\mathbf{i},2}, \tag{9.19}$$

with $V = 2\tilde{t}_\perp^2 \left(\frac{1}{\Delta} + \frac{1}{U-\Delta}\right)$. For $\Delta < U$, interactions are repulsive, $V > 0$. The sign of V changes when doublon (hole) doping the energetically upper (lower) layer instead: In this case, $V = -2\tilde{t}_\perp^2 \left(\frac{1}{\Delta} - \frac{1}{U+\Delta}\right) < 0$ for all values of $\Delta, U > 0$.

Now we apply the partial particle-hole mapping $\hat{\mathcal{C}}_2 \equiv \mathbb{1}_1 \otimes \hat{\mathcal{C}}_2$, acting only on the doublon-doped layer 2, in order to obtain the effective Hamiltonian in the Hilbert space with hole dopants only. Since we are in mixed dimensions, no hopping terms $t_\perp$ exist in the effective t-J description: Hence after applying the transformation $\hat{\mathcal{C}}$ from Eq. (9.10), the doublon-doped layer changes to an equivalent hole-doped layer, $\hat{\mathcal{C}}_2 \hat{\tilde{\mathcal{H}}}_2 \hat{\mathcal{C}}_2^{-1} = \hat{\mathcal{H}}_2$. Moreover, using $\hat{\mathcal{C}}_2 \hat{\tilde{n}}_{\mathbf{i},2} \hat{\mathcal{C}}_2^{-1} = \hat{n}_{\mathbf{i},2}$, the coupling $\hat{\tilde{\mathcal{H}}}'_{12}$ transforms and we obtain

$$\hat{\mathcal{C}}_2 \hat{\tilde{\mathcal{H}}} \hat{\mathcal{C}}_2^{-1} = \hat{\mathcal{H}}_1 + \hat{\mathcal{H}}_2 + \hat{\mathcal{H}}_{12} + V \sum_{\mathbf{i}} \hat{n}_{\mathbf{i},1} \hat{n}_{\mathbf{i},2}. \tag{9.20}$$

Therefore, the physical implementation of the doublon-hole-doped mixD bilayer FH model after the particle-hole mapping corresponds to a fully hole-doped mixD bilayer system with interlayer hole-hole interactions, i.e., the simulated Hamiltonian reads

$$\begin{aligned}\hat{\mathcal{H}} = -t_{\parallel} \sum_{\langle \mathbf{i},\mathbf{j}\rangle,\sigma,\alpha} \hat{\mathcal{P}}_{GW} \left(\hat{c}^{\dagger}_{\mathbf{i},\sigma,\alpha}\hat{c}_{\mathbf{j},\sigma,\alpha} + \text{h.c.}\right)\hat{\mathcal{P}}_{GW} + J_{\parallel} \sum_{\langle \mathbf{i},\mathbf{j}\rangle,\alpha} \left(\hat{\mathbf{S}}_{\mathbf{i},\alpha}\cdot\hat{\mathbf{S}}_{\mathbf{j},\alpha} - \frac{\hat{n}_{\mathbf{i},\alpha}\hat{n}_{\mathbf{j},\alpha}}{4}\right) \\ + J_{\perp}\sum_{\mathbf{i}} \hat{\mathbf{S}}_{\mathbf{i},1}\cdot\hat{\mathbf{S}}_{\mathbf{i},2} + \left(V - \frac{J_{\perp}}{4}\right)\sum_{\mathbf{i}} \hat{n}_{\mathbf{i},1}\hat{n}_{\mathbf{i},2}.\end{aligned} \tag{9.21}$$

After the partial particle-hole transformation as specified above, the interactions in Eq. (9.19) correspond to tunable interlayer density-density interactions. We note that in the case of hole or doublon-doping both layers in the physical implementation, virtual tunnel couplings between the two energetically offset layers merely lead to a constant energy shift; Hence, tunable density-density interactions V are a particular feature of the doublon-hole-doped mixD bilayer system.

9.2.3 Phase-coherent pairing correlations

Finally we explain why working with a doublon and a hole-doped layer provides a major experimental advantage. To this end, we note that resonant tunnel couplings between the two layers, if added again, lead to the appearance of terms like $\hat{c}^{\dagger}_{\mathbf{i},\sigma,1}\hat{c}_{\mathbf{i},\sigma,2}$. In the particle-hole transformed basis, these become $\hat{\mathcal{C}}_2\hat{c}^{\dagger}_{\mathbf{i},\sigma,1}\hat{c}_{\mathbf{i},\sigma,2}\hat{\mathcal{C}}_2^{-1} \propto \hat{c}^{\dagger}_{\mathbf{i},\sigma,1}\hat{c}^{\dagger}_{\mathbf{i},\bar{\sigma},2}$, which create and destroy pairs in the effective description of holes and singly occupied sites. In the mixD setting $\tilde{t}_{\parallel}, \tilde{t}_{\perp} \ll \Delta < U$, such pair-creation and annihilation terms do not appear. By explicitly tunnel coupling the two layers, the particle-hole transformed basis can be exploited to measure coherent pair-pair correlations in the mixD bilayer model without changing the total number of fermions, which we demonstrate in more detail in Sec. 9.2.5. In the following, we argue that the effective model Eq. (9.21) features long-range pairing order for a wide range of parameters in the ground state (as well as quasi long-range order at finite $T < T_c$). We then explain explicitly how pairing correlations can be measured for a simple double-well building block, before presenting state preparation and measurement protocols for mixD systems.

Long-range superconducting order in the simulated model: numerical results

In the following, we present numerical results for the ground state of mixD ladders across a range of coupling strengths $J_{\perp}/t_{\parallel}$ and $V/t_{\parallel}$. These simulations were done by Hannah Lange and are included here for completeness.

For a typical experimental value of $\Delta = U/2$, we obtain $|V| = 1.5J_{\perp}$. In the following, we show that this is a moderate repulsion which does not qualitatively change the physics and superconducting properties of the mixD model. To this end, DMRG calculations of Eq. (9.21) are performed on a ladder geometry, for varying $t_{\parallel}/J_{\perp}$, $V/J_{\perp}$ and hole doping $\delta = 0.5$ in both layers. The $U(1)^{\alpha=1} \times U(1)^{\alpha=2}$ charge conservation symmetry is explicitly exploited in each leg.

Fig. 9.3 (a) shows pair-pair correlations $\langle \hat{\Delta}^{\dagger}_i \hat{\Delta}_{i+x}\rangle$ for a ladder of length $L_x = 60$, with

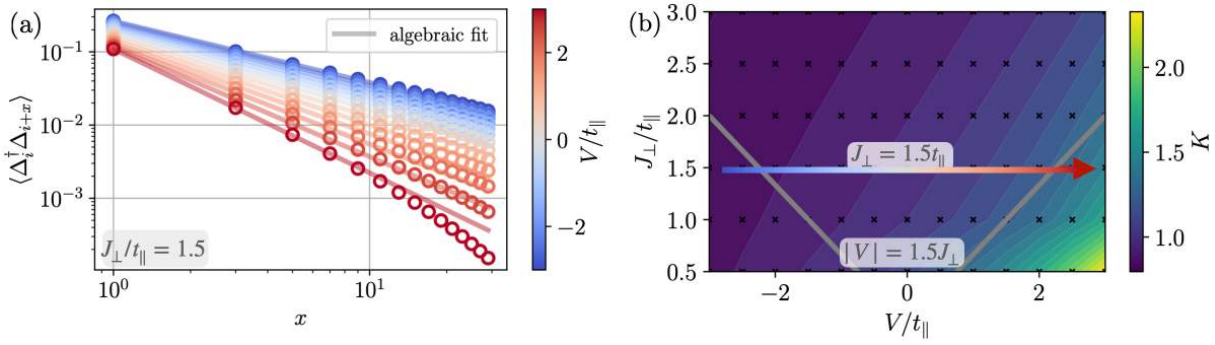

Figure 9.3: **DMRG simulations.** (a) Coherent pairing correlations $\langle \hat{\Delta}_i^\dagger \hat{\Delta}_{i+x} \rangle$ in the ground state of a mixD ladder of length $L_x = 60$ at hole doping $\delta = 0.5$, for experimentally relevant couplings $J_\parallel/t_\parallel = 0.5$ and $J_\perp/t_\parallel = 1.5$ [57] and for various interaction strengths $V/t_\parallel$. Fits to algebraic decay functions are shown by solid lines; for illustrative reasons, only odd distances are shown. (b) Luttinger decay exponents K as a function of $J_\perp/t_\parallel$ and $V/t_\parallel$. Contours denote extrapolated lines of constant K, black dots the points evaluated for the extrapolation. The arrow with the color gradient indicates the $V/t_\parallel$ scan in (a) from attractive (blue) to repulsive (red) interactions. Gray lines show typical interaction strengths for $\Delta = U/2$, $V = 1.5J_\perp$, see Eq. (9.21). These calculations were performed by Hannah Lange, and are included here for completeness.

$J_\perp/t_\parallel = 1.5$ as approximately realized in Ref. [57] and for varying interlayer density-density interactions $V/t_\parallel = -3\ldots3$. In a gapless 1D system, pairing correlations decay algebraically, $\langle \hat{\Delta}_i^\dagger \hat{\Delta}_{i+x} \rangle \sim x^{-K}$, with K the Luttinger parameter. Corresponding fits for $i = 10$ and $x = 1,\ldots,42$ are shown by solid lines in Fig. 9.3 (a). For a broad range of interaction strengths $V/t_\parallel$, clear algebraic signals are found. Only for strong repulsive interactions $V > V_c \approx 2.5t_\parallel \approx 1.7J_\perp$, the onset of an exponential decay for $\langle \hat{\Delta}_i^\dagger \hat{\Delta}_{i+x} \rangle$ is observed at large distances x. This is in agreement with previous observations of a pair charge gap opening at commensurate doping $\delta = 0.5$ and intermediate repulsion V [332], see also Chap. 8.

Fig. 9.3 (b) presents K as a function of both $V/t_\parallel$ and $J_\perp/t_\parallel$. Again, for most considered values of $V/t_\parallel$ and $J_\perp/t_\parallel$, Luttinger parameters $K \approx 1$ are found. Only for large $V > V_c \approx 3.0t_\parallel = 2.0J_\perp$ and $J_\perp/t_\parallel < 1.5$, K becomes significantly larger before the onset of an exponential decay. The Kondo coupling $J_\perp/t_\parallel = 1.5$ and the corresponding $|V| = 1.5J_\perp$ (indicated by the gray lines in Fig. 9.3 (b)) realized in the experiment [57] are deep in the $K \approx 1$ regime for attractive V (i.e. doublon-doping the energetically upper layer), and for repulsive interactions (i.e. doublon-doping the energetically lower layer) $K \approx 1.5$. Note that it is possible to tune $J_\perp/t_\parallel$ and $V/t_\parallel$, e.g. via the potential offset Δ, to the regime with smaller K, i.e. longer-ranged correlations.

We note that at finite temperature, correlations decay exponentially in ladder systems due to their one-dimensional nature [356]. Nevertheless, in the same spirit as early observations of antiferromagnetic order [41, 51, 62, 65, 242], measurable finite-range correlations are expected in regimes realistically accessible to ultracold atom experiments. In particular, in Sec. 8.4 it was shown that binding energies in ladder systems exceed $E_b/J_\perp > 0.5$ for all values of $t_\parallel/J_\perp$. Therefore, for temperatures $T/E_b \lesssim 1$, we expect sizable pairing correlations in ladder systems. In contrast, in the 2D bilayer limit, we expect algebraic correlations up to relatively high critical BKT temperatures even in the presence of interlayer density repulsions.

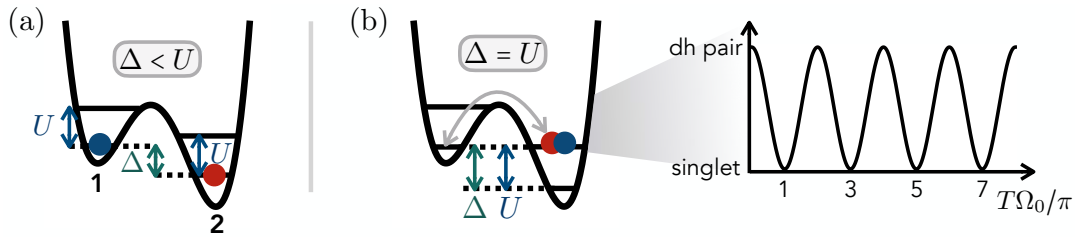

Figure 9.4: **Double well Rabi oscillations.** (a) A single double well building block with energy shift $\Delta < U$. The ground state with one particle per site is a singlet state. (b) When tuning $\Delta = U$ to resonance, coherent Rabi oscillations (in time T) between singlets and doublon-hole pairs are induced, with holes (doublons) situated in the energetically upper (lower) site, labeled site 1 (2).

A single double well

As an experimental building block, consider a single double well with energy offset $\Delta < U$, loaded with two fermions ($N_\uparrow = N_\downarrow = 1$). The ground state corresponds to a spin singlet, $|\mathrm{s}\rangle = \frac{1}{\sqrt{2}}(|\uparrow\rangle_1 |\downarrow\rangle_2 - |\downarrow\rangle_1 |\uparrow\rangle_2)$, see Fig. 9.4 (a). When tuning the tunneling transition between doublon-hole pairs $|\mathrm{dh}\rangle = |0\rangle_1 |\uparrow\downarrow\rangle_2$ and singlets $|\mathrm{s}\rangle$ into resonance, i.e. setting $\Delta = U$, hopping transitions are induced,

$$\sum_\sigma \hat{c}^\dagger_{\sigma,2}\hat{c}_{\sigma,1}|\mathrm{s}\rangle = \frac{1}{\sqrt{2}}\Big(\hat{c}^\dagger_{\uparrow,2}\hat{c}_{\uparrow,1}|\uparrow\rangle_1|\downarrow\rangle_2 \underbrace{-\hat{c}^\dagger_{\downarrow,2}\hat{c}_{\downarrow,1}|\downarrow\rangle_1|\uparrow\rangle_2}_{=+|0\rangle_1|\uparrow\downarrow\rangle_2}\Big) \propto |\mathrm{dh}\rangle\,. \tag{9.22}$$

Similarly,

$$\sum_\sigma \hat{c}^\dagger_{\sigma,1}\hat{c}_{\sigma,2}|\mathrm{dh}\rangle = \frac{1}{\sqrt{2}}\Big(\hat{c}^\dagger_{\uparrow,1}\hat{c}_{\uparrow,2}|0\rangle_1|\uparrow\downarrow\rangle_2 + \underbrace{\hat{c}^\dagger_{\downarrow,1}\hat{c}_{\downarrow,2}|0\rangle_1|\uparrow\downarrow\rangle_2}_{=-|\downarrow\rangle_1|\uparrow\rangle_2}\Big) \propto |\mathrm{s}\rangle\,. \tag{9.23}$$

This gives rise to Rabi oscillations between singlets and doublon-hole pairs, Fig. 9.4 (b). Double well Rabi oscillations of single particles have been demonstrated with high fidelity in Refs. [354, 355, 357, 358].

When mapping the doublon-hole-doped system to the fully hole-doped mixD t-J basis via the partial particle-hole transformation, we now see that the tunneling operations in Eqs. (9.22),(9.23) formally correspond to spin-singlet creation and annihilation operators,

$$\begin{aligned}\hat{\mathcal{C}}_2(\hat{c}^\dagger_{\uparrow,1}\hat{c}_{\uparrow,2} + \hat{c}^\dagger_{\downarrow,1}\hat{c}_{\downarrow,2})\hat{\mathcal{C}}_2^{-1} &= \underbrace{\hat{c}^\dagger_{\downarrow,1}\hat{c}^\dagger_{\uparrow,2} - \hat{c}^\dagger_{\uparrow,1}\hat{c}^\dagger_{\downarrow,2}}_{\propto\hat{\Delta}^\dagger}\\ \hat{\mathcal{C}}_2(\hat{c}^\dagger_{\uparrow,2}\hat{c}_{\uparrow,1} + \hat{c}^\dagger_{\downarrow,2}\hat{c}_{\downarrow,1})\hat{\mathcal{C}}_2^{-1} &= \underbrace{\hat{c}_{\downarrow,1}\hat{c}_{\uparrow,2} - \hat{c}_{\uparrow,1}\hat{c}_{\downarrow,2}}_{\propto\hat{\Delta}}\,.\end{aligned} \tag{9.24}$$

Therefore, the Rabi oscillations between doublon-hole and singlet states in the physical system map onto coherent oscillations between a rung-singlet and a paired state of two holes after applying the partial particle-hole transformation $\hat{\mathcal{C}}_2$ on the second (doublon-doped) layer. Thus, measurements of singlet-to-doublon-hole oscillations in the physical system provide a direct measurement of coherent pair creation in the corresponding $\hat{\mathcal{C}}_2$-transformed system that we

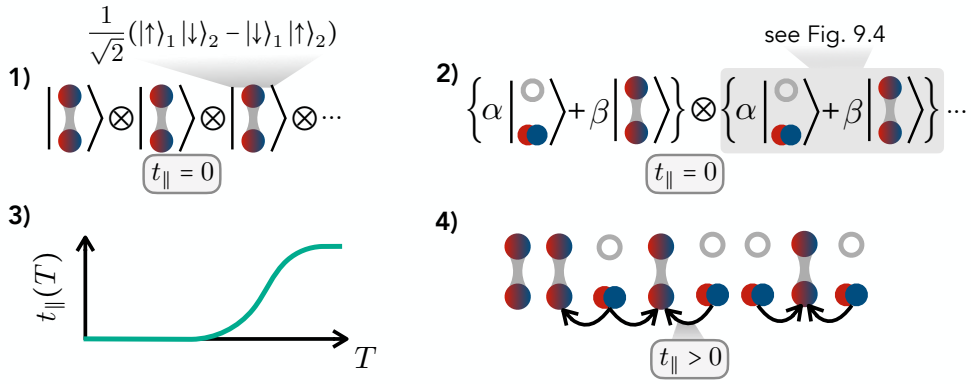

Figure 9.5: **State preparation scheme.** State preparation for simulating the mixD t-J model on a ladder. **1)** A band insulating state is prepared in deep double wells with $\Delta > U$. **2)** Tuning $\Delta = U$ for a given amount of time, singlets are created with a certain average density $|\beta|^2$ (where still $t_\parallel = 0$), cf. Fig. 9.4. Afterwards, Δ is tuned to $\Delta < U$. **3)** Hopping between double wells is adiabatically turned on by ramping down the lattice potentials, which enables the simulation of the mixD bilayer model on a ladder geometry in step **4)**.

ultimately propose to investigate. We finally note that tuning Δ of the optical superlattice to resonance has the advantage of high control, while avoiding lattice shaking induced transitions which cause heating.

9.2.4 State preparation scheme

Based on coupled double-wells as building blocks, in the following we present a state preparation scheme for simulating the mixD system. We note that ultimately, the simulation of the full 2D bilayer model Eq. (9.21) is desirable. For this purpose, bilayer capabilities of existing quantum gas microscope experiments [359, 360] used e.g. for spin-resolved imaging [66, 361] can be utilized. Offsetting the two layers by an energy Δ then implements the mixD model on a 2D square lattice geometry. However, as a first step, we argue that implementing mixD ladders as in Ref. [57] already constitutes a valuable setup that is readily available to measure coherent pairing correlations in 1D systems. For this purpose, the state preparation consists of the following steps, summarized in Fig. 9.5:

1) Loading doublon-hole pairs into multiple (separate) double wells with strong potential gradients $\Delta > U$ realizes the product state

$$\bigotimes_{\mathbf{i}} |0, \uparrow\downarrow\rangle_{\mathbf{i}}\,, \tag{9.25}$$

where $\mathbf{i}$ denotes the index of the double wells. Lattice potentials are sufficiently deep, such that $t_\parallel = 0$. This can be achieved with low entropy starting from a band insulating state [362] in the lower layer.

2) By globally tuning the optical superlattice to resonance ($\Delta = U$), singlets are coherently created. The fraction of doublon-hole pairs compared to singlets can be controlled depend-

ing on the time T_{res} for which resonant tunneling is switched on. After T_{res}, Δ is further ramped down to $\Delta < U$. This allows for the preparation of e.g. a 50:50 mixture (50% doublon/hole doping) as present in LNO.

3) When adiabatically ramping down the lattice depth, in-plane hopping $t_\parallel$ is induced, simulating the mixD bilayer system Eq. (9.21). When considering a ladder geometry, adiabatic ramping of $t_\parallel$ guarantees that a low-temperature Luther-Emery liquid of phase-coherent pairs [331,332] is realized.

This scheme can also be directly applied to a mixD bilayer constituted by two coupled 2D layers. Note that the phase-coherent creation of pairs in step **2)** readily realizes the product state $\bigotimes_{\mathbf{i}} (\alpha \left|0,\uparrow\downarrow\right\rangle_{\mathbf{i}} + \beta \left|s\right\rangle_{\mathbf{i}})$, which has long-range pairing correlations and is hence adiabatically connected to low-energy states of the mixD t-J model. We expect that after sufficient thermalization times, the system reaches an equilibrium steady-state whose correlation functions correspond to those of the mixD system, Eq. (9.21). This suggests high fidelities reachable in step **3)**.

The accuracy of the global $\pi/2$ pulse ultimately sets the doping value of the simulated mixD bilayer model. We note that away from 50% doping, the system remains superconducting, with only slight renormalization of pair-pair correlations [5]. Thus, we expect that the measurement output is stable against infidelities of the state preparation scheme, e.g. due to local fluctuations of the Hamiltonian parameters.

9.2.5 Measurement protocol

After the adiabatic state preparation of the doublon-hole-doped mixD system, coherent pair-pair correlations can be measured. In particular, in the fully hole-doped target system that we propose to realize in a particle-hole transformed basis, we would like to directly measure correlations $\langle \hat{\Delta}_{\mathbf{i}}^\dagger \hat{\Delta}_{\mathbf{j}} \rangle$, where $\hat{\Delta}_{\mathbf{i}}^\dagger = \frac{1}{\sqrt{2}}(\hat{c}_{\mathbf{i},\uparrow,1}^\dagger \hat{c}_{\mathbf{i},\downarrow,2}^\dagger - \hat{c}_{\mathbf{i},\downarrow,1}^\dagger \hat{c}_{\mathbf{i},\uparrow,2}^\dagger)$ creates an interlayer singlet on site $\mathbf{i}$. This requires measuring $\hat{\mathcal{C}}_2 \hat{\Delta}_{\mathbf{i}}^\dagger \hat{\Delta}_{\mathbf{j}} \hat{\mathcal{C}}_2^{-1}$ in the physical system with doublon (hole) doping in the lower (upper) layer.

In the following, we first describe the protocol in the limit of strong Kondo-couplings $J_\perp \gg t_\parallel, J_\parallel$, where a mapping to an effective spin-1/2 system reveals how coherent pairing correlations can be accessed through a basis rotation in the subspace of singlets and doublon-hole pairs. Subsequently, we extend the discussion to situations away from the perturbative regime.

Perturbative limit

In the case of strong Kondo-couplings $J_\perp \gg t_\parallel, J_\parallel$, fermions pair into tightly bound interlayer singlets with associated binding energies $J_\perp$. As described in Sec. 8.2, in this limit, the low-energy Hilbert space of Eq. (9.14) is spanned by chargon-chargon pairs (i.e., holes on site $\mathbf{i}$ in both layers, $\left|0\right\rangle_{\mathbf{i}} = \left|0\right\rangle_{\mathbf{i},1} \left|0\right\rangle_{\mathbf{i},2}$), and rung-singlets, $\left|1\right\rangle_{\mathbf{i}} = \hat{b}_{\mathbf{i}}^\dagger \left|0\right\rangle_{\mathbf{i}}$.

Describing these states through a spin-1/2 degree of freedom, the bilayer system at dominat-

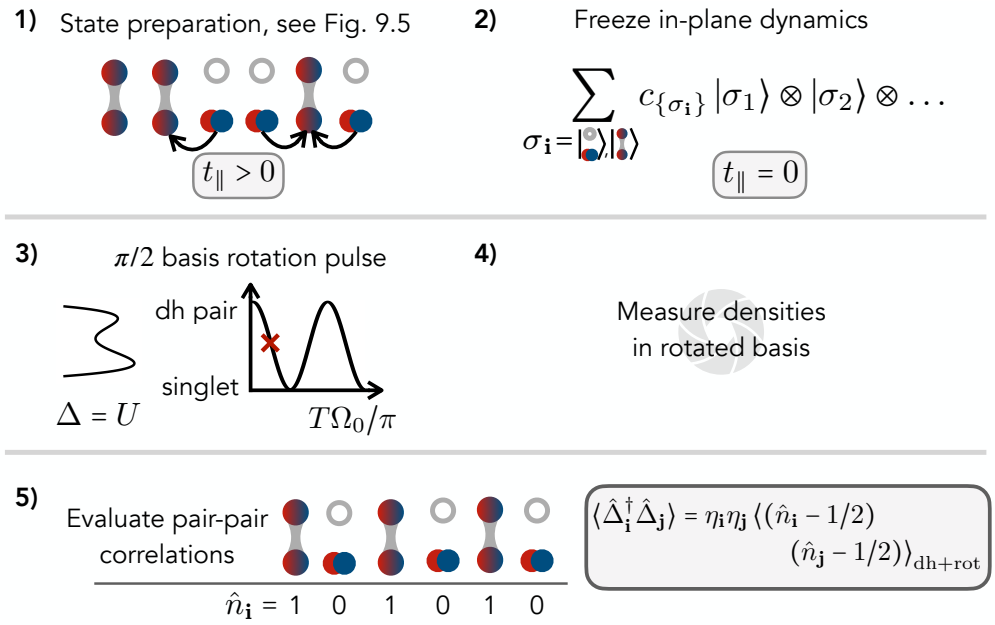

Figure 9.6: **Measurement protocol.** After state preparation (cf. Fig. 9.5) in step **1)**, lattice potentials are ramped up to freeze out $t_\parallel = 0$, **2)**. A $\pi/2$ basis rotation by tuning $U = \Delta$ **3)** and consecutively measuring densities of singlets and doublon-hole pairs **4)** then allows for evaluation of pair-pair correlations in step **5)**.

ing interlayer couplings is effectively described by the XXZ Heisenberg model (see Sec. 8.2),

$$\hat{\mathcal{H}}_{\mathrm{XXZ}} = K \sum_{\langle \mathbf{i},\mathbf{j} \rangle} \left(\hat{J}_\mathbf{i}^x \hat{J}_\mathbf{j}^x + \hat{J}_\mathbf{i}^y \hat{J}_\mathbf{j}^y + \Delta_{\mathrm{ani}} \hat{J}_\mathbf{i}^z \hat{J}_\mathbf{j}^z \right), \tag{9.26}$$

where $K = 4t_\parallel^2/J_\perp$ and $\Delta_{\mathrm{ani}} = 1 - J_\parallel/2K$[1]. We note that in Eq. (9.26), constant terms that arise have been dropped.

Pair-pair correlations in the mixD t-J model map to in-plane spin-spin correlations of the XXZ Hamiltonian, $\langle \hat{\Delta}_\mathbf{i}^\dagger \hat{\Delta}_\mathbf{j} \rangle \rightarrow \eta_\mathbf{i}\eta_\mathbf{j} \langle \hat{J}_\mathbf{i}^+ \hat{J}_\mathbf{j}^- \rangle$, where $\eta_\mathbf{i}$ is 1 (-1) on the A (B) sublattice. These can be accessed through a basis rotation in the subspace of singlets and hole pairs, in analogy to measurements of in-plane (off-diagonal) spin-spin correlations in the FH model [50], $\langle \hat{J}_\mathbf{i}^+ \hat{J}_\mathbf{j}^- \rangle = 2 \langle \hat{J}_\mathbf{i}^x \hat{J}_\mathbf{j}^x \rangle = 2 \langle \hat{J}_\mathbf{i}^z \hat{J}_\mathbf{j}^z \rangle_{\mathrm{rot}}$. In particular, we propose the following measurement scheme, summarized in Fig. 9.6:

1) State preparation, see Fig. 9.5.

2) Ramp up lattice depth to freeze in-plane degrees of freedom, $t_\parallel = 0$.

3) Rotate basis by a global $\pi/2$ tunneling pulse, see Fig. 9.4.

4) Measure densities (which corresponds to a measurement of the mapped spin $\hat{\mathbf{J}}$ in the XXZ model in the z-basis after the rotation (3), i.e., either a doublon-hole pair or singlet is measured at each site $\mathbf{i}$).

[1] As we denote energy tilts in optical lattices by Δ, we have here added the subscript in the anisotropy for clarity.

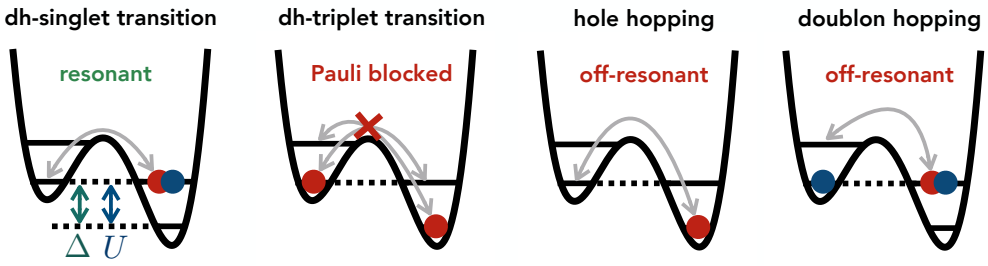

Figure 9.7: **Allowed and blocked transitions.** Applying a $\pi/2$ pulse by tuning $\Delta = U$ leads to the following effect depending on the local configuration: Transitions between local rung-singlets and doublon-hole pairs are resonant. Meanwhile, transitions between local rung-triplets and doublon-hole pairs are Pauli-blocked and interlayer hopping of single holes and doublons is off-resonant.

5) Using Eq. (8.3), evaluate pair-pair correlations via

$$\langle \hat{\Delta}_{\mathbf{i}}^{\dagger} \hat{\Delta}_{\mathbf{j}} \rangle = 2\eta_{\mathbf{i}}\eta_{\mathbf{j}} \Big\langle (\hat{n}_{\mathbf{i}} - 1/2) \times (\hat{n}_{\mathbf{j}} - 1/2) \Big\rangle_{\text{dh+rot}} \tag{9.27}$$

Here, $\langle \circ \rangle_{\text{dh+rot}}$ denotes measurement of the doublon-hole-doped system in the rotated basis and $\hat{n}_{\mathbf{i}} = 1\ (0)$ for a measured singlet (doublon-hole pair) on site $\mathbf{i}$ in the rotated basis.

Away from the perturbative limit

When tuning the system away from the perturbative limit, hopping processes can break interlayer singlets. The basis states of a single rung hence not only include singlets and doublon-hole pairs, but consist of $d = 9$ states $\{|0\rangle_1 |\uparrow\downarrow\rangle_2, |\sigma\rangle_1 |\uparrow\downarrow\rangle_2, |0\rangle_1 |\sigma\rangle_2, |\mathrm{s}\rangle, |\mathrm{t}_{1,2,3}\rangle\}$, where $|\mathrm{s}\rangle, |\mathrm{t}_{1,2,3}\rangle$ denote the rung singlet and three triplet states, respectively. A global $\pi/2$ tunneling pulse as described above realizes a basis rotation only in the subspace of the states $\{|\mathrm{dh}\rangle, |\mathrm{s}\rangle\}$, as all other transitions are either Pauli blocked or off-resonant as shown in Fig. 9.7.

When taking snapshots in the rotated basis, only contributions from singlets and doublon-hole pairs contribute to Eq. (9.27). The two triplet states $|\uparrow\rangle_1 |\uparrow\rangle_2$, $|\downarrow\rangle_1 |\downarrow\rangle_2$ as well as the states $|\sigma\rangle_1 |\uparrow\downarrow\rangle_2$, $|0\rangle_1 |\sigma\rangle_2$ are trivially identified in spin-resolved snapshots and have zero contribution to Eq. (9.27). Spin-resolved measurements in the mixD setting have been demonstrated on ladder geometries in Ref. [57], which can be extended to 2D bilayers with current technologies.

In order to also distinguish the triplet $|\uparrow\rangle_1 |\downarrow\rangle_2 + |\downarrow\rangle_1 |\uparrow\rangle_2$ from the singlet $|\uparrow\rangle_1 |\downarrow\rangle_2 - |\downarrow\rangle_1 |\uparrow\rangle_2$, we propose to adiabatically ramp up a magnetic field gradient, which has the following effect: Consider the Hamiltonian

$$\hat{\mathcal{H}}(B_z) = \hat{\mathcal{H}}_{\text{FH}}(t, U) + B_z \hat{S}_2^z, \tag{9.28}$$

where $\hat{\mathcal{H}}_{\text{FH}}(t, U)$ is the FH model with hopping (on-site repulsion) t (U), and B_z denotes the magnetic field gradient strength. If B_z is ramped up adiabatically, $|t_1\rangle = |\downarrow\downarrow\rangle$ and $|t_3\rangle = |\uparrow\uparrow\rangle$ stay eigenstates of the Hamiltonian throughout the transformation. On the other hand, the singlet state will adiabatically transform to $|s\rangle \to |\uparrow\downarrow\rangle$, and the triplet state $|t_2\rangle$ transforms to the remaining product state $|\downarrow\uparrow\rangle$. This is illustrated in Fig. 9.8 (a), where we show the instantaneous eigenenergies of $\hat{\mathcal{H}}(B_z)$ as a function of B_z/t for $U/t = 12$. Spin-resolved snapshots after rapidly

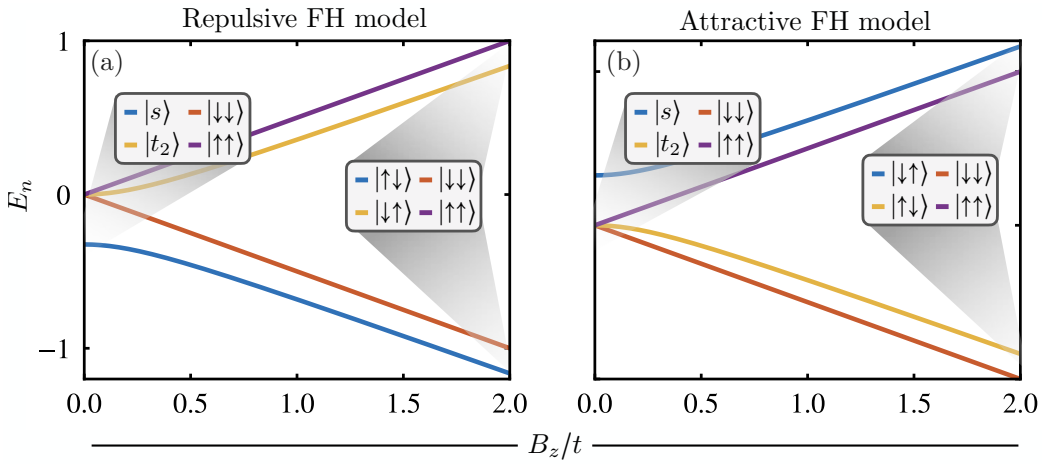

Figure 9.8: **Adiabatic magnetic field gradient ramp.** Evolution of instantaneous eigenstate energies of Hamiltonian Eq. (9.28) as a function of B_z/t, with $U/t = 12$ [$U/t = -12$] in (a) [(b)]. For $B_z/t = 0$, triplet states are degenerate and energetically offset from the singlet state. While $|\uparrow\uparrow\rangle$ and $|\downarrow\downarrow\rangle$ stay invariant under the adiabatic transformation, the singlet state transforms to $|\uparrow\downarrow\rangle$ ($|\downarrow\uparrow\rangle$), and the triplet state to $|\downarrow\uparrow\rangle$ ($|\uparrow\downarrow\rangle$) in the repulsive (attractive) case. This allows to (i) distinguish singlet from triplet states in spin-resolved snapshots, as required in measurement scheme Sec. 9.2.5, and (ii) apply the transformation $|\uparrow\downarrow\rangle \rightarrow |t_2\rangle$ through a reversed adiabatic protocol as proposed in measurement scheme Sec. 9.3.3.

turning off the field then allow to distinguish between states that have originally been in a spin-singlet and spin-triplet state. We note that (after freezing in-plane dynamics) the Hamiltonian conserves S_z^{tot} in each double well, such that diabatic transitions to other states in the triplet manifold, e.g. $|\uparrow\downarrow\rangle \rightarrow |\downarrow\downarrow\rangle$, are suppressed. Thus, up to overall phases, applying the magnetic field gradient has the following effect on the singlet and triplet states,

$$\begin{aligned} \frac{1}{\sqrt{2}}\left(|\uparrow\rangle_1|\downarrow\rangle_2 - |\downarrow\rangle_1|\uparrow\rangle_2\right) &\rightarrow |\uparrow\rangle_1|\downarrow\rangle_2 \\ \frac{1}{\sqrt{2}}\left(|\uparrow\rangle_1|\downarrow\rangle_2 + |\downarrow\rangle_1|\uparrow\rangle_2\right) &\rightarrow |\downarrow\rangle_1|\uparrow\rangle_2 , \end{aligned} \tag{9.29}$$

while all other configurations remain unaffected.

We note that the adiabatic process is in contrast to singlet-triplet oscillations, where the state is quenched under the magnetic field gradient Hamiltonian (i.e., the process is non-adiabatic). In this case, the relative phase between the states $|\uparrow\downarrow\rangle$ and $|\downarrow\uparrow\rangle$ is dynamically changed, $|\uparrow\downarrow\rangle + e^{i\varphi(t)}|\downarrow\uparrow\rangle$, leading to coherent oscillations between singlet and triplet states [51, 240, 357, 363].

During the measurement scheme, infidelities of global basis rotations and adiabatic ramping of the magnetic field gradient lead to quantitative deviations of the measurement signal to the true pair-pair correlations. However, we stress that signals consistent with finite values away from zero constitute evidence for the existence of pair-pair correlations in the system. Therefore we argue that, while ultimately obtaining quantitatively accurate results is desirable, the qualitative interpretation of non-zero signals influenced by infidelities remains the same. This paves the way towards a systematic exploration of superconducting phases in inherently repulsively

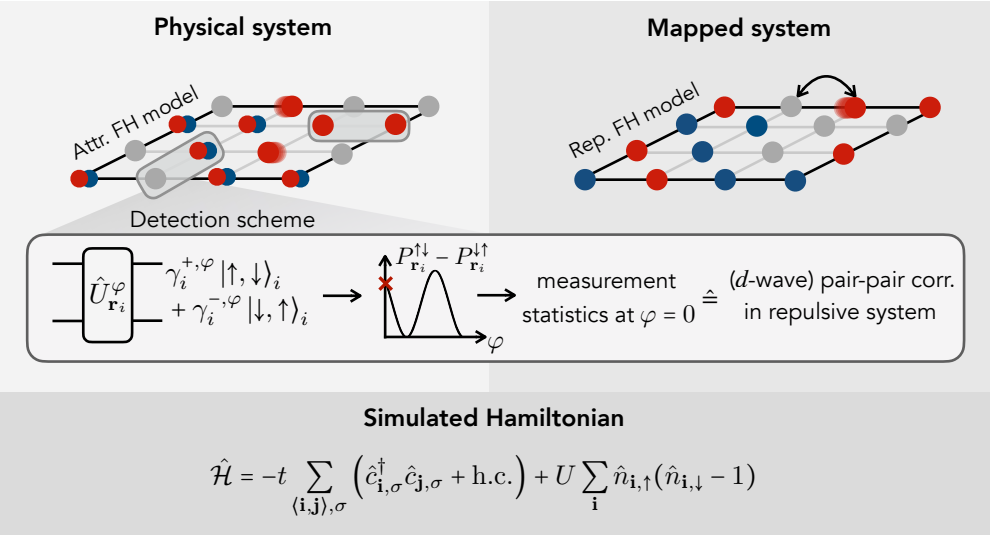

Figure 9.9: **Exploring high-temperature superconductivity in the 2D FH model with optical lattices.** In a similar spirit to the mixD setting, the 2D repulsive FH model relates to its attractive counterpart by a partial particle-hole transformation. To measure pairing correlations of various symmetries (including d-wave) $\langle \hat{\Delta}^\dagger_{\mathbf{r}_1}\hat{\Delta}_{\mathbf{r}_2}\rangle$ between bonds $\mathbf{r}_1$ and $\mathbf{r}_2$, we propose to implement the attractive FH model and apply local gates with unitaries $\hat{U}^{\varphi}_{\mathbf{r}_i}$ acting on bonds $\mathbf{r}_i$. This gives rise to a Ramsey interferometer as a function of a controlled phase dependency φ, from which pairing correlations can be accessed in the repulsive model. In particular, probabilities $P^{\sigma_1\sigma_2}_{\mathbf{r}_i}$ of measuring $|\uparrow,\downarrow\rangle$ and $|\downarrow,\uparrow\rangle$ states after applying the local gates correspond to pairing correlations in the repulsive model.

interacting fermionic systems with state-of-the-art ultracold atom simulators.

9.3 Measuring pairing correlations: 2D Fermi-Hubbard model

We have demonstrated that in the mixD setting, coherent pair-creation and annihilation processes can be naturally implemented through tunneling transitions between doublon- and hole-doped layers. We now show that related ideas allow for the measurement of pairing correlations in the 2D (single-layer) FH model, through a partial particle-hole transformation that maps the attractive to the repulsive FH model. In particular, we show that local control enables access to spin-singlet pairing correlations between both horizontal and vertical bonds, $P^{\alpha,\beta}_{\mathbf{i},\mathbf{j}} = \langle \hat{\Delta}^\dagger_{\mathbf{i},\alpha}\hat{\Delta}_{\mathbf{j},\beta}\rangle$, where $\hat{\Delta}^\dagger_{\mathbf{i},\mu} = \frac{1}{\sqrt{2}}\left(\hat{c}^\dagger_{\mathbf{i},\uparrow}\hat{c}^\dagger_{\mathbf{i}+\hat{\mathbf{e}}_\mu,\downarrow} - \hat{c}^\dagger_{\mathbf{i},\downarrow}\hat{c}^\dagger_{\mathbf{i}+\hat{\mathbf{e}}_\mu,\uparrow}\right)$ with $\hat{\mathbf{e}}_\mu$ the unit lattice vectors along $\mu = x, y$. For s-wave pairing, all combinations of α, β yield the same sign in the correlator, whereas a d-wave pairing structure features different signs of P^{xy} compared to P^{xx}, P^{yy}. This way, our scheme allows for a direct observation of the sign and nodal structure of the pair-pair correlations in the 2D doped FH model, which can be identified as a superconducting order parameter.

We note that pairing correlations between parallel bonds, i.e. $\alpha = \beta$, are easier to access experimentally compared to the case $\alpha \neq \beta$, where in the latter two optical superlattices with different orientations need to be realized, e.g. by using local addressability. Nevertheless, independent of the pairing symmetry, $P^{\alpha=\beta}_{\mathbf{i},\mathbf{j}} \neq 0$ at large distances $|\mathbf{i} - \mathbf{j}| \gg 1$ if the system fea-

tures superconducting order. Hence, working with a superlattice with one orientation and fixing $\alpha = \beta$, pairing correlations (including d-wave) can be detected in the 2D FH model (though the symmetry can not be uniquely specified in this case).

Our proposed measurement scheme relies on a particle-hole symmetry of the 2D FH model, which in turn requires the underlying lattice to be bipartite. State-of-the-art numerical calculations suggest the absence of long-range superconducting order in the ground state of the plain-vanilla 2D Fermi-Hubbard model on the square lattice (i.e. without next-nearest neighbor terms t') [145]. While finite values of t' are believed to stabilize superconductivity [147] in the ground state, at typical temperatures of quantum simulation platforms correlations are expected to decay exponentially in both the plain-vanilla and finite t' FH model. Therefore, independent on the (short- or long-range) pairing structure of the ground state, at first only exponentially decaying pair-pair correlations can be accessed with currently available technologies. We argue that it is these short-range correlations (including their symmetry) that can be probed with our measurement scheme, which, in turn, constitutes first valuable steps towards simulating and probing superconductivity in 2D FH-type models. Furthermore, we stress that even in this regime many open questions can be addressed, including the microscopic nature of the formation of pairs and the relation between the pseudogap and superconductivity. The scheme is summarized in Fig. 9.9.

9.3.1 Partial particle-hole mapping of the 2D Fermi-Hubbard model

Consider the repulsive ($U > 0$) 2D FH model on the square lattice at finite doping which we would ultimately like to simulate,

$$\hat{\mathcal{H}}(t,U) = -t \sum_{\langle \mathbf{i},\mathbf{j}\rangle,\sigma} \left(\hat{c}^\dagger_{\mathbf{i},\sigma}\hat{c}_{\mathbf{j},\sigma} + \text{h.c.}\right) + U\sum_{\mathbf{i}} \hat{n}_{\mathbf{i},\uparrow}\hat{n}_{\mathbf{i},\downarrow}. \tag{9.30}$$

On a bipartite lattice, a partial particle-hole mapping of one spin-species

$$\hat{\mathcal{C}}\hat{c}_{\mathbf{i},\sigma}\hat{\mathcal{C}}^{-1} = \begin{cases} \hat{c}_{\mathbf{i},\uparrow} & \text{for } \sigma = \uparrow \\ \eta_{\mathbf{i}}\hat{c}^\dagger_{\mathbf{i},\downarrow} & \text{for } \sigma = \downarrow \end{cases} \tag{9.31}$$

transforms (up to an overall constant) the repulsive to the attractive FH model [352] (see also Refs. [54, 353]), i.e.,

$$\hat{\mathcal{C}}^{-1}\hat{\mathcal{H}}(t,U)\hat{\mathcal{C}} = \hat{\mathcal{H}}(t,-U) + U\sum_{\mathbf{i}} n_{\mathbf{i},\uparrow}. \tag{9.32}$$

Note that from Eq. (9.31) follows that the vacuum state of the repulsive model $|0\rangle$ transforms as $\hat{\mathcal{C}}\,|0\rangle = \prod_{\mathbf{i}} \hat{c}^\dagger_{\mathbf{i},\downarrow}\,|0\rangle$. Thus, a hole-pair $|0\rangle_1\,|0\rangle_2 = |0,0\rangle$ on neighboring sites $1,2$ in the repulsive model corresponds to a spin-down pair $\hat{\mathcal{C}}\,|0\rangle_1\,|0\rangle_2 = |\downarrow\rangle_1\,|\downarrow\rangle_2 = |\downarrow,\downarrow\rangle$ in the attractive model. Accordingly, hole doping the repulsive system translates to a finite magnetization on the attractive side, $\hat{\mathcal{C}}^{-1}\hat{N}_h\hat{\mathcal{C}} = \hat{N}_\downarrow - \hat{N}_\uparrow$, where $N_{h,\uparrow,\downarrow}$ denote the total number of holes, up- and down-spins, respectively.

Furthermore, the spin-singlet state $|s\rangle$ in the repulsive Hamiltonian maps to

$$|\tilde{s}\rangle = \hat{\mathcal{C}}\,|s\rangle = \frac{1}{\sqrt{2}}\left(|\uparrow\downarrow\rangle_1\,|0\rangle_2 + |0\rangle_1\,|\uparrow\downarrow\rangle_2\right) \tag{9.33}$$

in the attractive model.

In the following, we show how the application of local unitary gates which map $|t_1\rangle = |\downarrow\rangle_1\,|\downarrow\rangle_2$ and $|\tilde{s}\rangle$ to the unmagnetized spin-triplet and singlet state, respectively, allows to measure the pairing operator. In particular, spin-resolved measurement statistics in the z-basis after applying the gates give access to pair-pair correlations in the repulsive FH model.

9.3.2 Measurement protocol

Starting from a low-temperature state of the attractive FH model ($U < 0$) in an optical lattice, lattice depths are ramped up globally to freeze any dynamics. The goal is to measure the pair correlator in the repulsive FH model $\langle\hat{\Delta}^\dagger_{\mathbf{r}_1}\hat{\Delta}_{\mathbf{r}_2}\rangle$ on bonds $\mathbf{r}_1 = (\mathbf{i}, \mathbf{i}+\hat{\mathbf{e}}_\mu)$ and $\mathbf{r}_2 = (\mathbf{j}, \mathbf{j}+\hat{\mathbf{e}}_{\mu'})$, each of them aligned along the unit vectors $\hat{\mathbf{e}}_{\mu^{(\prime)}}$.

To understand how this can be achieved we find it convenient to decompose the quantum many-body wave function into the following (orthogonal) contributions: (i) States with two holes at bond $\mathbf{r}_i$ in the repulsive model, corresponding to $|\downarrow,\downarrow\rangle_i$ in the attractive model, (ii) the states with a singlet pair at bond $\mathbf{r}_i$, corresponding to $|\tilde{s}\rangle_i = \frac{1}{\sqrt{2}}\left(|\uparrow\downarrow,0\rangle_i + |0,\uparrow\downarrow\rangle_i\right)$ in the attractive model, and (iii) orthogonal contributions $|\phi\rangle$. Notably, applications of $\hat{\Delta}_{\mathbf{r}_i}$ only act within the subspace spanned by (i) and (ii).

Therefore, a general pure state on bond $\mathbf{r}_i$ in the repulsive model reads

$$|\psi\rangle_i = \alpha_i\,|0,0\rangle_i + \beta_i\,|s\rangle_i + |\phi\rangle\,. \tag{9.34}$$

Correspondingly, we get in the attractive model

$$|\tilde{\psi}\rangle_i = \alpha_i\,|\downarrow,\downarrow\rangle_i + \beta_i\,|\tilde{s}\rangle_i + |\tilde{\phi}\rangle\,. \tag{9.35}$$

To motivate how our measurement scheme works, we assume a product state $|\Psi\rangle = |\psi\rangle_1\,|\psi\rangle_2$ that explicitly breaks the U(1) particle conservation symmetry next. Afterwards, we will provide a proof for arbitrary correlated states; the scheme still works in the latter case since we only employ unitary operations acting independently on the different bonds $\mathbf{r}_i$.

Expectation values of the pairing fields in the repulsive model yield

$$\begin{aligned} {}_i\langle\psi|\hat{\Delta}^\dagger_{\mathbf{r}_i}|\psi\rangle_i &= \alpha_i\beta_i^*, \\ {}_i\langle\psi|\hat{\Delta}_{\mathbf{r}_i}|\psi\rangle_i &= \alpha_i^*\beta_i, \end{aligned} \tag{9.36}$$

and therefore

$$\langle\Psi|\left(\hat{\Delta}^\dagger_{\mathbf{r}_1} + \hat{\Delta}_{\mathbf{r}_1}\right)\left(\hat{\Delta}^\dagger_{\mathbf{r}_2} + \hat{\Delta}_{\mathbf{r}_2}\right)|\Psi\rangle = (\alpha_1\beta_1^* + \alpha_1^*\beta_1)(\alpha_2\beta_2^* + \alpha_2^*\beta_2). \tag{9.37}$$

Hence, by measuring certain products of $\alpha_1^{(*)}, \alpha_2^{(*)}, \beta_1^{(*)}, \beta_2^{(*)}$ in the attractive model, pairing correlations in the repulsive model can be accessed.

In the following, we introduce a measurement circuit that realizes a unitary $\hat{U}^\varphi = \prod_i \hat{U}^\varphi_{\mathbf{r}_i}$, which allows to extract such products $\alpha_i^{(*)}\beta_i^{(*)}$ from Fock-basis snapshots of the transformed state. We design the measurement protocol such that the action of this unitary on the state realizes a Ramsey-type interferometer,

$$\hat{U}^\varphi_{\mathbf{r}_i} |\tilde{\psi}\rangle_i = \left(\gamma_i^{+,\varphi} |\uparrow,\downarrow\rangle_i + \gamma_i^{-,\varphi} |\downarrow,\uparrow\rangle_i\right) + |\phi\rangle\,, \tag{9.38}$$

with $\gamma_i^{\pm,\varphi} = \frac{1}{\sqrt{2}}(\alpha_i \pm \mathrm{e}^{i\varphi}\beta_i)$.

Before we discuss the experimental realization of $\hat{U}^\varphi$ in Sec. 9.3.3, we explain how it gives access to the pair correlations Eq. (9.37): Consider the probability to measure $|\uparrow,\downarrow\rangle_{\mathbf{r}_i}$ after applying $\hat{U}^\varphi_{\mathbf{r}_i}$,

$$P^{\uparrow\downarrow}_{\mathbf{r}_i}(\varphi) = |_i\langle\uparrow,\downarrow|\hat{U}^\varphi_{\mathbf{r}_i}|\tilde{\psi}\rangle_i|^2 = \frac{1}{2}|\alpha_i + \mathrm{e}^{i\varphi}\beta_i|^2, \tag{9.39}$$

and $P^{\downarrow\uparrow}_{\mathbf{r}_i}$ defined in analogy. The difference between these probabilities,

$$P_{\mathbf{r}_i}(\varphi) = (P^{\uparrow\downarrow}_{\mathbf{r}_i} - P^{\downarrow\uparrow}_{\mathbf{r}_i})(\varphi) = 2\mathrm{e}^{-i\varphi}\left(\alpha_i\beta_i^* + \mathrm{e}^{2i\varphi}\alpha_i^*\beta_i\right), \tag{9.40}$$

evaluated at each of the two bonds $\mathbf{r}_i$ hence gives, via Born's rule, access to $\langle\hat{\Delta}^\dagger_{\mathbf{r}_i} + \hat{\Delta}_{\mathbf{r}_i}\rangle$ from the measurement statistics of $\downarrow\uparrow$ and $\uparrow\downarrow$ configurations.

The phase dependency $P_{\mathbf{r}_i}(\varphi)$ gives rise to Ramsey fringes, i.e. oscillations between $\pm 4|\alpha_i||\beta_i|$, with $P_{\mathbf{r}_i}(\varphi = 0) = \alpha_i\beta_i^* + \alpha_i^*\beta_i = \langle\hat{\Delta}^\dagger_{\mathbf{r}_i} + \hat{\Delta}_{\mathbf{r}_i}\rangle$. Correspondingly, by computing $P_{\mathbf{r}_1}P_{\mathbf{r}_2} = \langle\Psi|\left(\hat{\Delta}^\dagger_{\mathbf{r}_1} + \hat{\Delta}_{\mathbf{r}_1}\right)\left(\hat{\Delta}^\dagger_{\mathbf{r}_2} + \hat{\Delta}_{\mathbf{r}_2}\right)|\Psi\rangle$, pair-pair correlations can be computed.

We note that when the U(1) particle conservation symmetry is spontaneously broken, the order parameter averaged over many independent experimental realizations vanishes, $_i\langle\psi|\hat{\Delta}^{(\dagger)}_{\mathbf{r}_i}|\psi\rangle_i = 0$, and $P_{\mathbf{r}_i} = 0$. Nevertheless, for general correlated states, the product of the probabilities $P_{\mathbf{r}_i}P_{\mathbf{r}_j}$ (corresponding to pair-pair correlations $\langle\hat{\Delta}^\dagger_{\mathbf{r}_i}\hat{\Delta}_{\mathbf{r}_j} + \text{h.c.}\rangle$) is finite at large distances $|\mathbf{r}_i - \mathbf{r}_j|$ for states with superconducting order.

Let us look at this in more detail. For a general correlated state, expectation values are given by $\langle\hat{\Delta}^\dagger_{\mathbf{r}_1}\hat{\Delta}_{\mathbf{r}_2}\rangle = \mathrm{tr}\left(\hat{\rho}^{sh}_{12}\hat{\Delta}^\dagger_{\mathbf{r}_1}\hat{\Delta}_{\mathbf{r}_2}\right)$, where $\hat{\rho}^{sh}_{12}$ is the reduced density matrix in the subspace of hole-pairs and singlets on bonds $\mathbf{r}_1, \mathbf{r}_2$ (as $\hat{\Delta}^{(\dagger)}_{\mathbf{r}_i}$ only acts on this subspace). The most general form of $\hat{\rho}^{sh}_{12}$ in the basis $\{|00\rangle_1|00\rangle_2, |s\rangle_1|00\rangle_2, |00\rangle_1|s\rangle_2, |s\rangle_1|s\rangle_2\}$ reads (note that fermion number conservation implies $a_1 = a_2 = b_1 = b_2 = c_2 = 0$),

$$\hat{\rho}^{sh}_{12} = \begin{bmatrix} p_1 & a_2^* & a_1^* & c_2^* \\ a_2 & p_2 & c_1^* & b_1^* \\ a_1 & c_1 & p_3 & b_2^* \\ c_2 & b_1 & b_2 & p_4 \end{bmatrix}, \tag{9.41}$$

with $\sum_{j=1}^{4} p_j = 1$. Thus, pairing correlations are given by the anti-diagonal elements,

$$\mathrm{tr}\left[\hat{\rho}_{12}^{sh}\left(\hat{\Delta}_{\mathbf{r}_1}^{\dagger}+\hat{\Delta}_{\mathbf{r}_1}\right)\left(\hat{\Delta}_{\mathbf{r}_2}^{\dagger}+\hat{\Delta}_{\mathbf{r}_2}\right)\right] = c_1 + c_1^* + c_2 + c_2^*. \tag{9.42}$$

As we show now, these elements can be accessed by taking snapshots in the rotated basis (i.e. after applying the attractive-to-repulsive mapping and the unitary $\hat{U}^{\varphi}$). Specifically, in analogy to the strategy for a product state as outlined in the main text, we calculate the probability of measuring the transformed state as $|\uparrow\downarrow\rangle_1 |\uparrow\downarrow\rangle_2$,

$$P_{\mathbf{r}_1,\mathbf{r}_2}^{\uparrow\downarrow,\uparrow\downarrow} = \mathrm{tr}\left[\hat{\rho}_{12}^{sh}\hat{U}^{\varphi}|\uparrow\downarrow\rangle_1|\uparrow\downarrow\rangle_2\langle\uparrow\downarrow|_2\langle\uparrow\downarrow|_1\hat{U}^{\varphi\dagger}\right]. \tag{9.43}$$

For $\varphi = 0$, the transformed state $\hat{U}^{\varphi=0}|\uparrow\downarrow\rangle_1|\uparrow\downarrow\rangle_2 \propto \hat{U}^{\varphi=0}(|t_2\rangle_1|t_2\rangle_2 + |t_2\rangle_1|s\rangle_2 + |s\rangle_1|t_2\rangle_2 + |s\rangle_1|s\rangle_2)$ corresponds to the equal superposition $|00\rangle_1|00\rangle_2 + |00\rangle_1|s\rangle_2 + |s\rangle_1|00\rangle_2 + |s\rangle_1|s\rangle_2$ in the repulsive model. Extending this to the other possible states in the rotated basis, we find

$$\begin{aligned}
\hat{U}^{\varphi=0}|\uparrow\downarrow\rangle_1|\uparrow\downarrow\rangle_2 &\tilde{\propto} |00\rangle_1|00\rangle_2 + |00\rangle_1|s\rangle_2 + |s\rangle_1|00\rangle_2 + |s\rangle_1|s\rangle_2,\\
\hat{U}^{\varphi=0}|\uparrow\downarrow\rangle_1|\downarrow\uparrow\rangle_2 &\tilde{\propto} |00\rangle_1|00\rangle_2 + |00\rangle_1|s\rangle_2 - |s\rangle_1|00\rangle_2 - |s\rangle_1|s\rangle_2,\\
\hat{U}^{\varphi=0}|\downarrow\uparrow\rangle_1|\uparrow\downarrow\rangle_2 &\tilde{\propto} |00\rangle_1|00\rangle_2 - |00\rangle_1|s\rangle_2 + |s\rangle_1|00\rangle_2 - |s\rangle_1|s\rangle_2,\\
\hat{U}^{\varphi=0}|\downarrow\uparrow\rangle_1|\downarrow\uparrow\rangle_2 &\tilde{\propto} |00\rangle_1|00\rangle_2 - |00\rangle_1|s\rangle_2 - |s\rangle_1|00\rangle_2 + |s\rangle_1|s\rangle_2.
\end{aligned} \tag{9.44}$$

From this, it is straight-forward to show that

$$P_{\mathbf{r}_1,\mathbf{r}_2}^{\uparrow\downarrow,\uparrow\downarrow} + P_{\mathbf{r}_1,\mathbf{r}_2}^{\downarrow\uparrow,\downarrow\uparrow} - P_{\mathbf{r}_1,\mathbf{r}_2}^{\downarrow\uparrow,\uparrow\downarrow} - P_{\mathbf{r}_1,\mathbf{r}_2}^{\uparrow\downarrow,\downarrow\uparrow} \sim c_1 + c_1^* + c_2 + c_2^*, \tag{9.45}$$

which extends the results presented in the main text to arbitrary correlated many body states.

In particular, in this case $P_{\mathbf{r}_i}P_{\mathbf{r}_j}$ only depends on the overall phase difference picked up during the measurement scheme on the two bonds. When applying a control phase $\varphi_{\mathrm{control}}$ to one of the two bonds, Ramsey fringes as a function of $\varphi_{\mathrm{control}}$ can be observed in $P_{\mathbf{r}_i}P_{\mathbf{r}_j}(\varphi_{\mathrm{control}})$. Though pairing correlations can be directly accessed by setting $\varphi_{\mathrm{control}} = 0$, observation of the Ramsey fringes constitutes a valuable experimental verification of the coherence of the interferometer.

9.3.3 The measurement circuit

The measurement protocol that we propose consists of a sequence of unitaries that is applied locally on all bonds $\mathbf{r}_i$ independently. We focus on the states that contribute to the pair correlations, namely $|\downarrow,\downarrow\rangle_{\mathbf{r}_i}$ and $|\tilde{s}\rangle_{\mathbf{r}_i}$, that correspond to hole and singlet pairs on bond $\mathbf{r}_i$ in the repulsive model. The general idea of the measurement protocol is to apply a unitary $\hat{U}_{\mathbf{r}_i}^{\varphi}$ that transforms the states $|\downarrow,\downarrow\rangle_i$ and $|\tilde{s}\rangle_i$ to spin-singlets and triplets (up to a controlled overall phase difference φ), respectively, from which pair-pair correlations can be accessed by taking spin-resolved measurements in the z-basis. Note that all other contributions are orthogonal and remain orthorgonal during the sequence due to the unitarity of $\hat{U}_{\mathbf{r}_i}^{\varphi}$. The gate sequence that realizes $\hat{U}_{\mathbf{r}_i}^{\varphi}$ consists of the following steps, summarized in Fig. 9.10 (a).

1) First, by locally turning on tunneling (i.e. by reducing the lattice depth of double wells

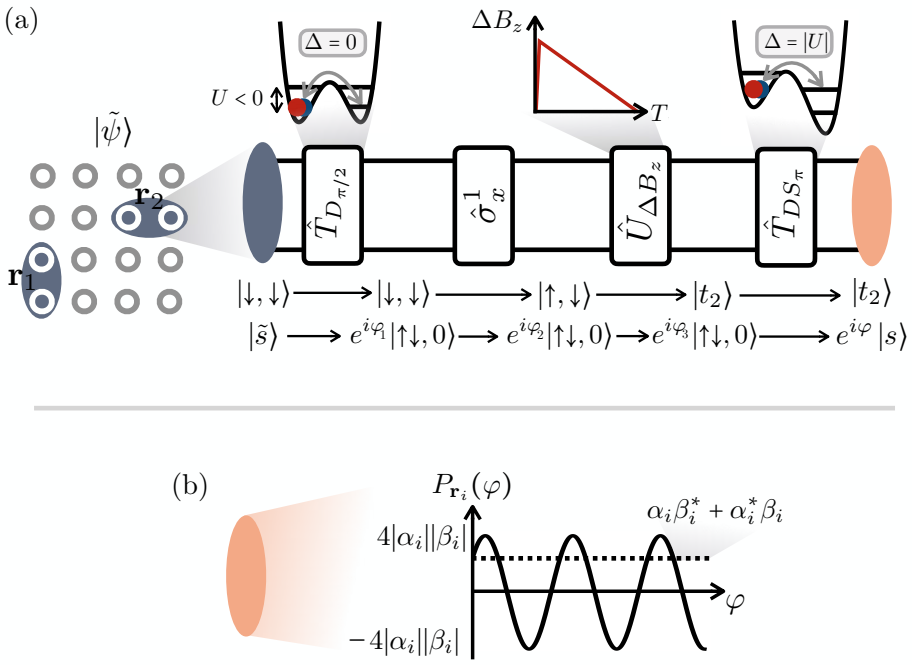

Figure 9.10: **Measuring pairing correlations in the plain-vanilla FH model.** (a) Circuit that allows to measure coherent pair-pair correlations in the repulsive FH model between bonds $\mathbf{r}_1$, $\mathbf{r}_2$ through implementation of the attractive FH model. The shown sequence in (a) consists of a combination of local tunneling and spin gates. The former are realized by locally reducing the lattice depth and tuning the superlattice offset Δ. Adiabatic tuning of a magnetic field gradient ΔB_z allows to map $|\downarrow,\downarrow\rangle$ (corresponding to the hole-pair state in the repulsive model) to a spin-triplet, whereas $|\tilde{s}\rangle$ (corresponding to $|s\rangle$ in the repulsive model) is transformed to a spin-singlet. After each step, relative phases between the two input states are picked up, with an overall phase shift of φ by the end of the sequence. Spin-resolved measurements after applying the unitary allow for the evaluation of pairing correlations $P^{\alpha,\beta}_{\mathbf{i},\mathbf{j}}$ in the repulsive FH model. (b) The overall phase difference φ between the final output states gives rise to oscillations of measurement probabilities $P_{\mathbf{r}_i}$, from which $\langle(\hat{\Delta}^\dagger_{\mathbf{r}_1}+\hat{\Delta}_{\mathbf{r}_1})(\hat{\Delta}^\dagger_{\mathbf{r}_2}+\hat{\Delta}_{\mathbf{r}_2})\rangle = (\alpha_1\beta_1^*+\alpha_1^*\beta_1)(\alpha_2\beta_2^*+\alpha_2^*\beta_2)$ can be reconstructed.

on sites connected by bonds $\mathbf{r}_i$), Rabi oscillations between the states $|\uparrow\downarrow,0\rangle$ and $|0,\uparrow\downarrow\rangle$ are induced with effective doublon tunneling rate $4t^2/|U|$. Starting from $|\tilde{s}\rangle$, a $\pi/2$ tunneling pulse $\hat{T}_{D_{\pi/2}}$ transforms the state to $|\uparrow\downarrow,0\rangle$. Meanwhile, tunneling transitions of $|\downarrow,\downarrow\rangle$ are Pauli blocked, i.e. the state stays invariant (up to an overall dynamical phase) under $\hat{T}_{D_{\pi/2}}$.

2) Spin-flip pulses σ^1_x on the first sites of the respective double wells (i.e. on sites $\mathbf{i}$, $\mathbf{j}$) transforms $|\downarrow,\downarrow\rangle \to |\uparrow,\downarrow\rangle$, while $|\uparrow\downarrow,0\rangle$ remains unchanged.

3) By applying an adiabatic magnetic field gradient ramp along z, the transformation $|\uparrow,\downarrow\rangle \to |t_2\rangle = \frac{1}{\sqrt{2}}(|\uparrow,\downarrow\rangle + |\downarrow,\uparrow\rangle)$ is performed. In particular, the above can be realized through a reversed adiabatic protocol as described in Sec. 9.2: A magnetic field gradient is rapidly turned on, and then ramped down adiabatically to $B_z \to 0$. The instantaneous eigenenergies of the double-well Hamiltonian Eq. (9.28) as a function of B_z are shown for $U/t = -12$ in Fig. 9.8 (b). During the adiabatic process, $|\uparrow\downarrow\rangle \to |t_2\rangle$, while the doublon-hole state

$|\uparrow\downarrow, 0\rangle$ remains unaffected.

4) Lastly, resonant oscillations between doublons and singlets ($\Delta = |U|$) allow to realize a π-pulse between the doublon-hole and singlet state, $\hat{T}_{DS_\pi}|\uparrow\downarrow, 0\rangle \propto |s\rangle$. The triplet state t_2, on the other hand, is Pauli-blocked from corresponding tunnel transitions.

During this sequence, a relative phase φ between the final singlet and triplet states is picked up. By applying a potential gradient after the first tunneling unitary, this overall relative phase φ can be varied and the Ramsey fringes observed, Fig. 9.10 (b). This, in turn, ultimately allows to measure pair-pair correlations $\langle \hat{\Delta}^\dagger_{\mathbf{r}_1}\hat{\Delta}_{\mathbf{r}_2} + \hat{\Delta}_{\mathbf{r}_1}\hat{\Delta}^\dagger_{\mathbf{r}_2}\rangle$. In particular, by varying μ, μ' for a given pair of sites $\mathbf{i}, \mathbf{j}$, d-wave pairing correlations can be measured by evaluating

$$\langle \hat{\Delta}^\dagger_{\mathbf{i},x}\hat{\Delta}_{\mathbf{j},x} + \hat{\Delta}^\dagger_{\mathbf{i},y}\hat{\Delta}_{\mathbf{j},y} - \hat{\Delta}^\dagger_{\mathbf{i},x}\hat{\Delta}_{\mathbf{j},y} - \hat{\Delta}^\dagger_{\mathbf{i},y}\hat{\Delta}_{\mathbf{j},x} + \text{h.c.}\rangle. \tag{9.46}$$

9.4 Measuring dopant properties in the 2D t-J model

While Secs. 9.2 and 9.3 focused on the preparation and observation of superconducting states, studying exotic normal phases appearing in unconventional superconductors, such as the pseodogap (see i.p. Chap. 7), is another central area of research. Here, we argue how a tilted bilayer setup as used to realize the mixD setting in Sec. 9.2 allows to study properties of hole dopants in the 2D t-J model, which in turn can give insights into the enigmatic properties of the pseudogap phase. The following ideas were mainly developed by Hannah Lange, such that we only very briefly sketch out the main ideas in the following. For more details, we refer to the publication Ref. [6].

The main idea is that we use an enlarged Hilbert space comprising one mixD rung per site, whose low energy states in the large $J_\perp, U \gg t_\parallel$ limit can be mapped to the states of a 2D t-J model. The scheme is summarized conceptually in Fig. 9.11.

In order to map the mixD bilayer to a 2D t-J model, we consider the mixD bilayer with layer-dependent parameters U_α and $t^\alpha_\parallel$ in the large $U_\alpha, J_\perp \gg t^\alpha_\parallel$ limit. This realized the formation of a Mott insulating state in one layer, coupled strongly with the dopants in the other later to form singlets. To this end, we use the capability that the filling in each layer can be controlled individually. Here, we consider an (energetically) upper layer at one particle per site ($\hat{n}_{\mathbf{i},\alpha=1} = 1$), and $\hat{n}_{\mathbf{i},\alpha=2} \leq 1$. In this case, the low energy states are either the (bosonic) rung singlets $\hat{b}^\dagger_{\mathbf{i}}$ or singly occupied rungs with an empty site in layer $\alpha = 2$, represented by fermionic operators $\hat{\tilde{c}}^\dagger_{\mathbf{i},\sigma} = \hat{c}^\dagger_{\mathbf{i},\sigma,1}\hat{b}_{\mathbf{i}}$.

Through perturbative arguments, this leads to the following low-energy, effective single-layer description of the system,

$$\hat{\mathcal{H}}_{\text{eff}} = -\tilde{t}\sum_{\langle \mathbf{i},\mathbf{j}\rangle}\hat{\mathcal{P}}_{GW}\left(\hat{\tilde{c}}^\dagger_{\mathbf{i}\sigma}\hat{\tilde{c}}_{\mathbf{j}\sigma} + \text{h.c.}\right)\hat{\mathcal{P}}_{GW} + \tilde{J}\sum_{\langle \mathbf{i},\mathbf{j}\rangle}\left[\tilde{\mathbf{S}}_{\mathbf{i}}\cdot\tilde{\mathbf{S}}_{\mathbf{j}} - \frac{\gamma}{4}\hat{\tilde{n}}_i\hat{\tilde{n}}_j\right] + \frac{J^{\alpha=2}_\parallel}{2}\sum_{\mathbf{i}}\hat{\tilde{n}}_{\mathbf{i}}, \tag{9.47}$$

with $\tilde{t} = t^{\alpha=2}_\parallel/2$, $\tilde{J} = J^{\alpha=1}_\parallel$ and $\gamma = \frac{J^{\alpha=2}_\parallel}{\tilde{J}}$, see Fig. 9.11. Here, the modified spin operators

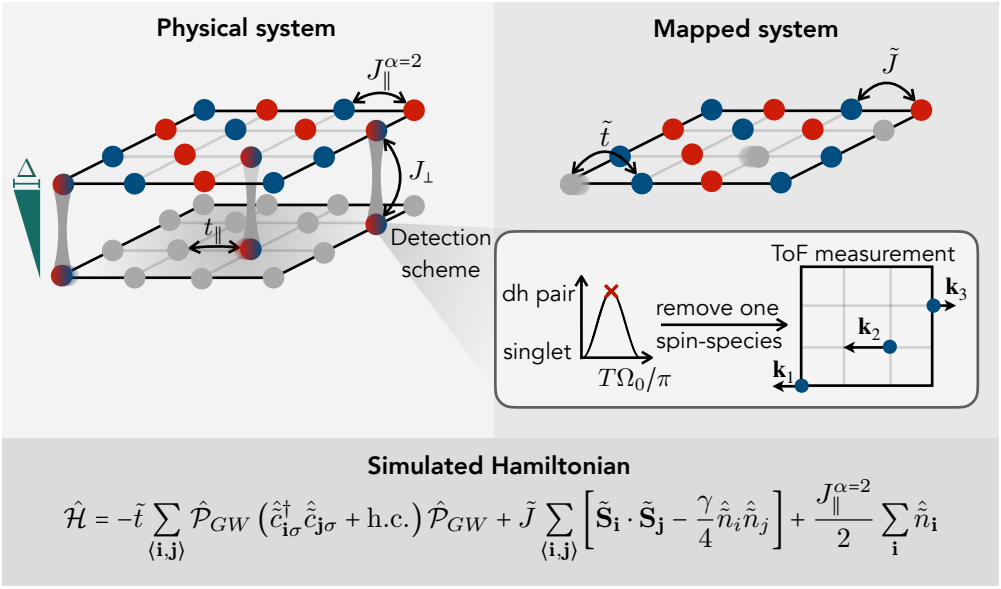

Figure 9.11: **Measuring dopant properties in the 2D t-J model.** By preparing the upper layer of a mixD setup at half-filling and loading (particle) dopants into the (initially empty) lower layer, singlets can be mapped to holes in an effective 2D t-J model for $J_\perp \gg t_\parallel, J_\parallel^{\alpha=1,2}$. Singlet-to-dh transitions then give access to momentum-resolved hole densities via time-of-flight measurements in the lower layer.

correspond to

$$\hat{\tilde{\mathbf{S}}}_\mathbf{i} = \hat{\tilde{c}}^\dagger_{\mathbf{i},\mu}\frac{\sigma_{\mu\nu}}{2}\hat{\tilde{c}}_{\mathbf{i}\nu} = \hat{\mathbf{S}}_{\mathbf{i},1}(1-\hat{b}^\dagger_\mathbf{i}\hat{b}_\mathbf{i}), \tag{9.48}$$

which only act on the singly occupied rungs and not on the singlets.

In the effective t-J model, holes or dopants are represented by particles in an auxiliary layer, allowing for a direct measurement of hole-related properties, such as the momentum-resolved hole density $\langle \hat{n}_h(\mathbf{k})\rangle$. This is particularly compelling because $\langle \hat{n}_h(\mathbf{k})\rangle$ is independent of the spectral weight at momentum $\mathbf{k}$, providing access to regions of the Brillouin zone that are inaccessible to ARPES, such as the backside of the Fermi arcs [87]. In contrast, direct realizations of the 2D t-J model are restricted to measuring momentum-resolved particle densities.

The fact that doped holes in the t-J monolayer Eq. (9.47) correspond to particles in the physical bilayer model allows to measure the momentum-resolved density of holes $\langle \hat{n}_h(\mathbf{k})\rangle$ through the following measurement sequence:

1) After state preparation, the dynamics is frozen by ramping up a deep lattice to start the measurement procedure.

2) Similar to Sec. 9.2.5, the rung singlets are brought into resonance with doublons in the lower layer for $\Delta = U$, see Fig. 9.7. Using a π tunneling pulse, singlets are transformed into doublons in the lower layer. Then, the upper layer is spatially removed from the lower $\alpha = 2$ layer.

3) The remaining $\alpha = 2$ layer consists only of doublons or empty sites. Upon removing one spin species from this layer and ramping down the intralayer lattice depth, the remaining indistinguishable particles move freely, allowing for a time-of-flight (TOF) measurement similar to Ref. [364] in order to determine their momentum resolved density $\hat{n}_h(\mathbf{k})$.

As a slight modification of the above protocol, we note that it is also possible to prepare a doublon-doped FH system in the (initially) energetically lower layer, while the other one is empty. Doublons are then transferred to the other layer via two consecutive π-pulses (where in the second step the sign of the energy offset is switched). In analogy to the above scheme, one spin-species is removed to ensure indistinguishability and TOF measurements can be performed. This way, the implementation of strong interlayer couplings $J_\perp$ can be avoided; however, virtual doublon-hole fluctuations may have notable effects for moderately strong repulsions.

9.5 Discussion

Motivated by recent studies of high-temperature superconductivity in bilayer nickelates, we have proposed a scheme to prepare and measure a state with (quasi) long-range pair coherence in ultracold atom simulators. With estimated critical temperatures on the order of $J_\perp/2$ in the mixD bilayer t-J model, see Chap. 8 ,our scheme provides a directly realizable protocol for the observation of superconducting correlations in a system with strongly repulsively interacting fermions with current state-of-the-art experimental platforms. Additionally, simulating minimal models of bilayer nickelates may allow for an experimental observation of BEC-BCS-type crossovers as a function of $t_\parallel/J_\perp$. Furthermore, differences between single- and multi-band models can be studied by engineering tailored bilayer and ladder systems that mimic multiple orbitals. This opens the door to directly simulate strongly correlated materials with ultracold atoms in optical lattices, and may be a major step towards designing new materials with high critical temperatures.

Moreover, local addressability of spin-flip and tunneling gates allows to measure both coherent pairing correlations and momentum-resolved dopant densities in 2D FH models. While the former utilizes a mapping of the repulsive FH to its closely related attractive cousin, the latter is achieved by projecting mobile holes to interlayer singlets, whose momentum can be accessed through time-of-flight measurements in the auxiliary layer. These capabilities directly bridge solid-state and cold atom experiments, and may help to microscopically study the enigmatic (normal and superconducting) phases appearing in copper-oxide compounds. Our work also paves the way for a direct measure of d-wave pairing fluctuations in the plain-vanilla Hubbard model using ultracold atoms in optical lattices, positioning digital-analog hybrid techniques and access to only a few gates as promising future directions to enhance the scope of quantum simulation platforms.

10

Doped frustrated lattices

Summary. On top of the competition between kinetic and many-body interaction energies, introducing geometric frustration leads to the appearance of additional, exotic effects. In this chapter, we first study the singly doped *t*-*J* model on the triangular lattice, focusing on the competition between kinetic and magnetic frustration as a function of temperature. In doublon-doped systems, we uncover a crossover between Nagaoka-type ferromagnetic correlations at high temperatures and exchange-mediated antiferromagnetic order around the doublon at low temperatures. We then discuss how frustrated FH physics can be explored in moiré materials. For a bilayer $MoSe_2/WS_2$ stacked in a specific alignment, a unique charging behavior emerges, leading to the realization of an effective bilayer triangular FH model. We discuss the main experimental results and build a theoretical understanding of the observed magnetic structures.

10.1 Introduction

The study of strong correlations on frustrated geometries has a long history, dating back to Anderson's proposal that quantum magnets on triangular lattices form states of resonating spin singlets [258], now known as a $\mathbb{Z}_2$ quantum spin liquid (see also Sec. 7.5). Although Anderson's idea has profoundly influenced modern condensed matter physics, the RVB state as the ground state of the Heisenberg model on the triangular lattice was later shown to be incorrect. Instead, as in classical systems, a long-range ordered magnetic spiral state with 120° order forms [365].

Numerous works have demonstrated that doping frustrated quantum magnets in the absence of particle-hole symmetry can lead to unique physical phenomena [67, 366–374], which, with successful implementations of optical triangular lattices, can now be explored experimentally [375–379]. In addition to ultracold atom experiments, solid-state platforms based on

moiré heterostructures provide a promising complementary approach for quantum simulation of Hubbard physics on triangular lattice geometries [38], as outlined in Sec. 4.2.

In this chapter, in Sec. 10.2, we give an overview of a particular form of magnetic order arising through kinetic effects on non-bipartite lattices, called kinetic magnetism. In Sec. 10.3, we then study a single hole doped into the triangular lattice t-J model. Secs. 10.2 and 10.3 are based on the following publication, partially with textual overlap:

> [7] **HS**, U. Schollwöck, A. Bohrdt, and F. Grusdt. **Kinetic-to-magnetic frustration crossover and linear confinement in the doped triangular t-J model**, Phys. Rev. B 110, L041117 (2024)

In Sec. 10.4, we introduce how kinetic effects play a role in moiré materials, before studying in detail a particular heterostructure, which gives rise to peculiar triangular lattice bilayer physics. Sec. 10.4 is the result of an experimental collaboration lead by Borislav Polovnikov and Alexander Högele, who the author of this thesis specifically acknowledges. Further acknowledgements go to Johannes Scherzer, Subhradeep Misra, and the rest of the moiré team in the group of Alexander Högele. The author of this thesis has significantly contributed to the modeling and theoretical interpretation of the measurements, which Sec. 10.4 focuses on. It is based on the following preprint, partially with textual overlap in the theory discussion:

> [8] Borislav Polovnikov*, Johannes Scherzer*, Subhradeep Misra*, **Henning Schlömer**, Julian Trapp, Xin Huang, Christian Mohl, Zhijie Li, Jonas Göser, Jonathan Förste, Ismail Bilgin, Kenji Watanabe, Takashi Taniguchi, Annabelle Bohrdt, Fabian Grusdt, Anvar S. Baimuratov, and Alexander Högele, **Implementation of the bilayer Hubbard model in a moiré heterostructure**, arXiv 2404.05494

10.2 Kinetic magnetism

The delocalization of particles associated with kinetic energy gain is of fundamental importance when describing itinerant magnetism in strongly correlated systems. Effective antiferromagnetic (AFM) spin-spin interactions arise in the Hubbard model via virtual exchange processes, which favor Néel order in undoped and weakly doped systems on bipartite lattices [191].

In the infinitely interacting limit—where exchange processes are fully suppressed—kinetic effects lead to interesting, and contrasting, magnetic ordering tendencies for single dopants. To see this, consider the Hamiltonian of a doped system in the infinitely interacting limit,

$$\hat{\mathcal{H}} = -t \sum_{\sigma,\langle \mathbf{i},\mathbf{j}\rangle} \hat{\mathcal{P}}_{GW} \left(\hat{c}^\dagger_{\mathbf{i},\sigma}\hat{c}_{\mathbf{j},\sigma} + \text{h.c.}\right)\hat{\mathcal{P}}_{GW}, \tag{10.1}$$

for now on an arbitrary lattice with connectivity z. In the following, we fix the total particle number to $N = N_L - N_d$, with N_L the number of lattice sites and N_d the number of dopants[1]. For $t > 0$, Eq. (10.1) then describes a single hole hopping through a Mott insulator on the triangular lattice.

[1] We will in the following often consider the case of a single dopant, $N_d = 1$.

Doublon doping, on the other hand, is described by Eq. (10.1) still at $N = N_L - N_d$ but with $t < 0$, which arises from a particle-hole transformation of the Hamiltonian Eq. (10.1). This can be explicitly demonstrated by writing down the FH Hamiltonian with infinite interactions for a doublon-doped system. Here, the perturbation mechanism works identically to the hole-doped case, resulting in Eq. (10.1), with the only difference being [380]

$$\hat{\mathcal{P}}_{\mathrm{GW}} \to \hat{\tilde{\mathcal{P}}}_{\mathrm{GW}}. \tag{10.2}$$

The Gutzwiller operator $\hat{\mathcal{P}}_{\mathrm{GW}}$ that projects out double occupancies is replaced by $\hat{\tilde{\mathcal{P}}}_{\mathrm{GW}}$, which projects out empty sites. The Hilbert space therefore consists of single and double occupancies only.

We can now apply the particle-hole transformation (see also Sec. 9.2.1),

$$\hat{c}_{\mathbf{i},\sigma} \to \hat{c}^{\dagger}_{\mathbf{i},\sigma} \quad \hat{c}^{\dagger}_{\mathbf{i},\sigma} \to \hat{c}_{\mathbf{i},\sigma}, \tag{10.3}$$

which reverses the sign of the hopping term $t \to -t$.[2] Under this transformation, the total particle number changes as

$$N = N_L - N_d \to N_L + N_d. \tag{10.4}$$

Thus, both doublon and hole doping in the strongly correlated FH model can be simulated through the Hamiltonian Eq. (10.1) with a filling of $N = N_L - N_d$. For hole doping, we set $t > 0$, while for doublon doping, we set $t < 0$.

We can now analyze how the kinetic motion of dopants influences the magnetic environment. In the following, we focus on a single dopant, $N_d = 1$. Consider first a single hole hopping on a square lattice as depicted in Fig. 10.1 (a), i.e., we analyze Eq. (10.1) with $t > 0$. Starting at the hole's initial position and considering different paths to reach a final position (marked by the red cross), we observe that whether reaching the final point requires an even or odd number of hopping events depends solely on the final position and is independent of the chosen path. This enables constructive interference of various paths with the same initial and final positions, thereby lowering the hole's kinetic energy. These interference effects are maximized when all spins in the background are polarized in the same direction, rendering them indistinguishable.

By applying a particle-hole transformation that maps the hole to a particle and the polarized background spins to the vacuum, the single hole can be described as a free particle on the square lattice[3]. The resulting band structure for the single hole in a polarized background, along high-symmetry points, is shown in Fig. 10.1 (b). The kinetic energy reaches its minimum of $E_{\mathrm{kin}} = -zt$ at the M point, where z is the coordination number of the lattice ($z = 4$ for the square lattice).

Due to the particle-hole symmetry of the FH model on the square lattice, analogous arguments apply to a hopping doublon. As argued above, the only difference lies in the overall sign of the dopant's hopping, which is swapped for doublons. This shifts the kinetic energy mini-

[2] Note that when performing the particle-hole transformation on the more general t-J model with finite J, the Heisenberg spin-spin interactions remain invariant.

[3] Note that this second transformation introduces another minus sign in the hopping term. Consequently, the band structure corresponds to the standard triangular tight-binding solution with an overall positive hopping amplitude.

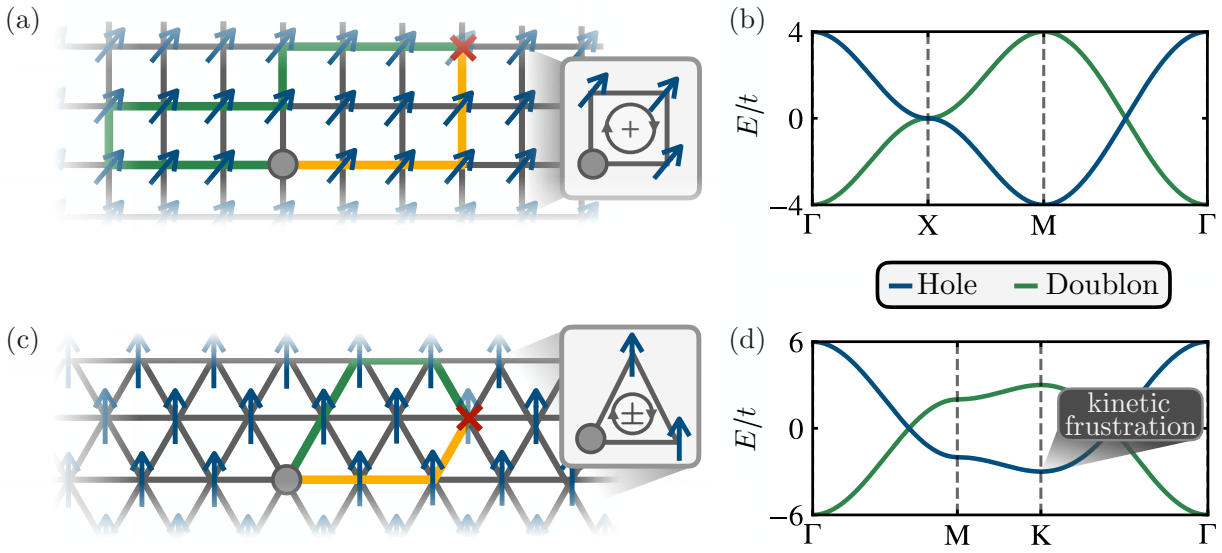

Figure 10.1: **Kinetic magnetism**. (a) On a square lattice, all possible paths from an initial position (grey dot) to a final position (red cross) have the same path parity; for the shown example, all paths are of odd length. Regardless of the overall hopping sign, this results in constructive interference when all spins are aligned. Consequently, the motion of the dopant induces a fully polarized, ferromagnetic spin environment (Nagaoka FM). (b) Single particle dispersion on the square lattice, for a single hole (blue) and doublon (green). In both cases, the maximum kinetic energy of $E_{\text{kin}}/t = -4$ is reached at the M and Γ point, respectively. (c) On a triangular lattice, different paths can have different parities. For the doublon (overall positive hopping), Nagaoka FM appears. However, for the doped hole, destructive interference happens as the overall hopping sign is negative. As a result, the dopant cannot fully exploit the kinetic energy associated with the geometry, see (d). Kinetic frustration can be relieved by ordering the spins in the background into an AFM 120° pattern (Haerter-Shastry AFM).

mum of the single doublon in a fully polarized background to the Γ point, where it minimizes its energy, see Fig. 10.1 (b). Therefore, for both a single hole and doublon, and in the limit $U \to \infty$, kinetic effects favor ferromagnetic order in the spins. This phenomenon is known as the Nagaoka effect [381–383], which can indeed be proven analytically in this limit (and generally on bipartite lattices) for single dopants [381].

However, on non-bipartite lattices, destructive interference of dopant paths can lead to the phenomenon of kinetic frustration. For example, consider the above arguments on the triangular lattice in Fig. 10.1 (c). Here, the non-bipartite nature of the underlying lattice allows for paths between a fixed initial and final position with differing path parities (i.e., paths can have both even and odd lengths). If the *overall* hopping is positive (as in the case of doublons, $t < 0$), this does not have any effect, and the doublon's paths can interfere constructively in a fully polarized background. This is supported by the corresponding band structure of the doublon, shown in Fig. 10.1 (d), which achieves the minimal kinetic energy of $E_{\text{kin}} = -zt = -6t$.

In contrast, for the case of the doped hole, various paths can interfere destructively (as they can have different associated signs). This quantum effect, termed kinetic frustration, prevents the mobile dopants from minimizing their kinetic energy in a fully spin-polarized background. This becomes evident from the effective band structure of the single hole in a polarized background,

which only reaches a minimum of $E_{\text{kin}} = -3t > -zt$, Fig. 10.1 (d). Note that this is a direct consequence of the lack of particle-hole symmetry in the FH model on the triangular lattice, where the upper and lower band edges have different (absolute) energies.

What is the resulting effect of this kinetic frustration on the background spins? Instead of favoring indistinguishable spins, as in the case of Nagaoka ferromagnetism (FM), kinetic frustration can be released by making the spin background as distinguishable as possible. This reduces the amount of destructive interference among various hole paths, allowing the hole to achieve energies in the range $-6t < E_{\text{kin}} < -3t$. This effect is maximized for (classical) antiferromagnetic alignment of the spins, a phenomenon referred to as Haerter-Shastry magnetism [366, 368, 384]. On the triangular lattice, this corresponds to 120° order of the background spins. In Ref. [67], both Nagaoka-type FM and Haerter-Shastry-type AFM has been observed numerically in the single doped triangular lattice at $U \to \infty$.

10.3 The single-hole doped triangular lattice

Though in the limit of $U \to \infty$ (or, equivalently, $J \to 0$ in the t-J model), magnetic ordering driven by kinetic effects has been studied in detail, the question arises as to how these kinetically driven effects compete with or support the superexchange mechanism, which (independent on the hopping sign and hence the nature of the dopant) favors AFM order. In this section, we study this interplay between kinetic and exchange mechanisms for itinerant magnetism in the triangular t-J model for the experimentally relevant regime of finite temperature and interaction strengths, focusing on single hole and doublon doping.

For hole doping, exchange and kinetic processes are in synergy with each other, both favoring 120° Néel order in the magnetic background, which strengthens AFM correlations. For doublon doping, we find that the competition between Nagaoka-type FM and Heisenberg AFM gives rise to crossovers between FM and AFM spin correlations around the doublon as a function of temperature. Our results are summarized in Fig. 10.2.

In the ground state, where magnetic correlations are governed by exchange-mediated Heisenberg interactions, we firmly establish the Brinkman-Rice picture [272, 385] of linear confining potentials arising from the antiferromagnetically ordered spin background (geometric string theory, see also Chap. 11 for more detail) for the doped doublon. For the doped hole, our results are also consistent with the string picture, although the signatures we find are less striking. We map out the various regimes using ground state and finite temperature MPS techniques on cylinders of the t-J model.

We consider the t-J Hamiltonian on the triangular lattice,

$$\hat{\mathcal{H}} = -t \sum_{\sigma,\langle \mathbf{i},\mathbf{j}\rangle} \hat{\mathcal{P}}_{GW} \left(\hat{c}^{\dagger}_{\mathbf{i},\sigma}\hat{c}_{\mathbf{j},\sigma} + \text{h.c.}\right)\hat{\mathcal{P}}_{GW} + J \sum_{\langle \mathbf{i},\mathbf{j}\rangle} \left(\hat{\mathbf{S}}_{\mathbf{i}} \cdot \hat{\mathbf{S}}_{\mathbf{j}} - \frac{\hat{n}_{\mathbf{i}}\hat{n}_{\mathbf{j}}}{4}\right), \tag{10.5}$$

in the symmetry sector of $N = N_L - 1$ particles, and focus on a single hole ($t > 0$) and a single doublon ($t < 0$). To reduce notational complexity, from this point onward, we will denote the hopping strength as t for both hole- and doublon-doped systems, implicitly assuming the

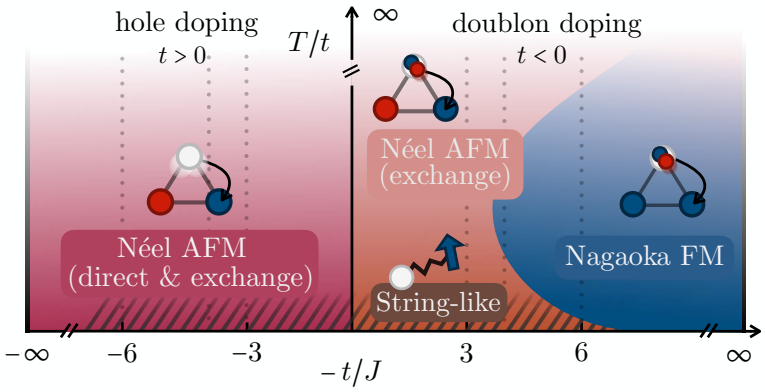

Figure 10.2: **Phase diagram.** Schematic phase diagram of the triangular t-J model, indicating different regimes of itinerant magnetism for a single dopant. For hole doping, both direct and exchange mechanisms favor 120° Néel order (light red area). On the doublon doped side, Nagaoka FM and kinetic frustration compete, leading to AFM (FM) spin correlations around the dopant in the orange (blue) regions. Dashed lines illustrate parameters of our numerical simulations. At low temperatures, singly doublon doped systems are well described by geometric strings (grey hatched area; for holes at low temperatures the signatures of strings are less striking). At high temperatures, small AFM correlations are present for all values of t/J, leading to reentrance phenomena between AFM and FM correlations on the doublon doped side.

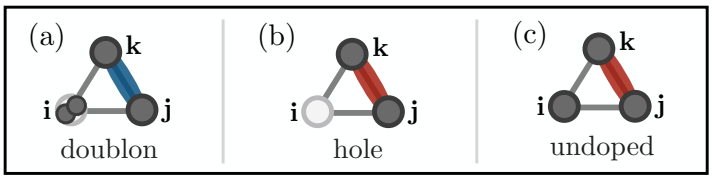

Figure 10.3: **Considered correlators.** Illustration of evaluated correlators $\mathcal{C}_\triangle = \langle \hat{P}^h_{\mathbf{i}} \hat{\mathbf{S}}_{\mathbf{j}} \cdot \hat{\mathbf{S}}_{\mathbf{k}} \rangle_T / \langle \hat{P}^h_{\mathbf{i}} \rangle_T$ for (a) the doublon-doped and (b) the hole-doped triangular lattice, as well as for (c) the undoped Heisenberg system, where $\mathcal{C}_\triangle = \langle \hat{\mathbf{S}}_{\mathbf{j}} \cdot \hat{\mathbf{S}}_{\mathbf{k}} \rangle_T$.

appropriate sign as per Eq. (10.5).

10.3.1 Finite temperature correlations

We simulate the doped triangular t-J model, Eq. (10.5), at finite temperature using imaginary time evolution schemes. As in previous chapters, we implement the U(1) particle conservation symmetry, but allow for thermal spin fluctuations. We simulate a cylinder of size $L_x \times L_y = 9 \times 3$, and apply open (periodic) boundaries along the x- (y-) direction, which can resolve 120° Néel order.

We focus on spin correlations around the dopant, and calculate the following thermal average at temperature T,

$$\mathcal{C}_\triangle = \frac{\langle \hat{P}^h_{\mathbf{i}} \hat{\mathbf{S}}_{\mathbf{j}} \cdot \hat{\mathbf{S}}_{\mathbf{k}} \rangle_T}{\langle \hat{P}^h_{\mathbf{i}} \rangle_T}, \tag{10.6}$$

where $\hat{P}^h_{\mathbf{i}}$ is a local projection onto the hole (dopant) at site $\mathbf{i}$, i.e., $\hat{P}^h_{\mathbf{i}} = |0\rangle_{\mathbf{i}} \langle 0|_{\mathbf{i}}$. We choose indices $(\mathbf{i}, \mathbf{j}, \mathbf{k})$ to lie on a triangular plaquette in the bulk of the system, i.e., we focus on spin-

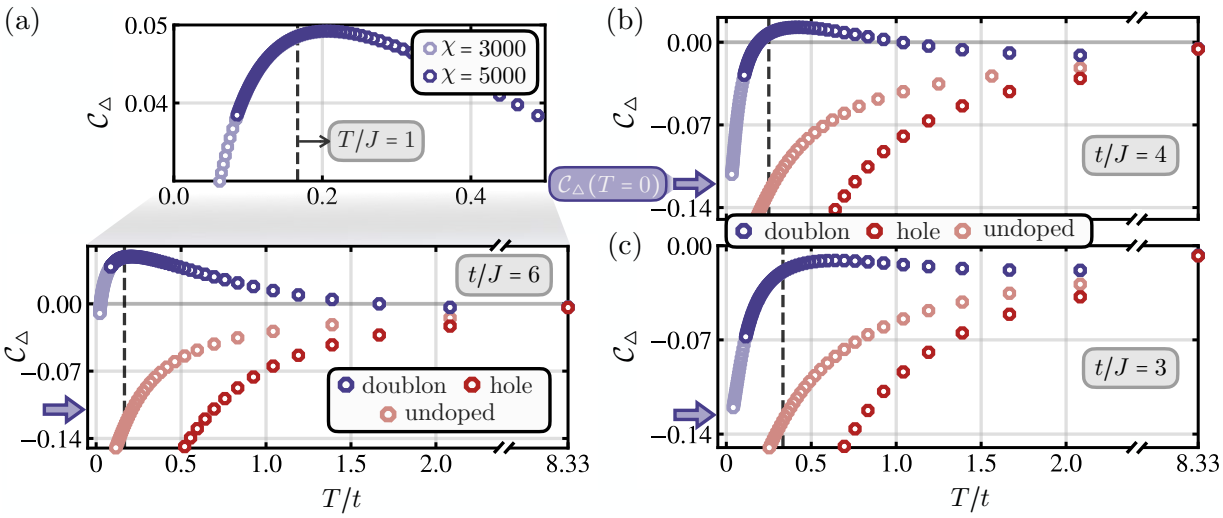

Figure 10.4: **Finite temperature calculations.** (a) We compute thermally averaged charge-spin-spin correlations around the dopant, Eq. (10.6), as a function of temperature T/t, and for $\mathbf{i} = [x = 5, y = 2]$. (b) For $t/J = 6$ and doublon doping (blue data points), Nagaoka-type kinetic FM leads to positive correlations at temperatures $T \sim t$. At $T \sim J$ (grey dashed line), a maximum of correlations is observed as exchange processes start to win over Nagaoka-type FM. Ground state results of $\mathcal{C}_\triangle$ for doublon doping are shown by blue arrows on the left. The inset shows the region around the maximum for MPS calculations with bond dimensions $\chi = 3000$ and $\chi = 5000$, demonstrating convergence down to $T/t \sim 0.1$. Two-point correlations in the undoped case are shown in salmon. Upon hole doping the system, both exchange and the release of kinetic frustration favor 120° order, strengthening AFM correlations (red dots). For $t/J = 4$, (c), correlations around the doublon are positive in the range $0.3 \lesssim T/t \lesssim 1$, whereas for $t/J = 3$, (d), AFM correlations win over Nagaoka-type FM and $\mathcal{C}_\triangle$ is negative for all temperatures. Nevertheless, kinetic effects manifest in the doublon case through a maximum of the correlator at $T/J \sim 1$. We do not show the full range of correlations for the hole doped case for illustrative reasons, and show their convergence behavior down to low temperatures in Fig. 10.5.

spin correlations in the direct vicinity of the dopant, see Fig. 10.3. To compare to the undoped case, we further calculate finite temperature two-point correlations of the Heisenberg model on the triangular lattice, where $\mathcal{C}_\triangle$ reduces to $\langle \hat{\mathbf{S}}_\mathbf{j} \cdot \hat{\mathbf{S}}_\mathbf{k} \rangle_T$, as illustrated on the right-hand side of Fig. 10.3. Full spatial and spin resolution techniques in quantum gas microscopy allow for a direct access of spin correlations around the mobile dopant [65, 66, 361].

Results showing $\mathcal{C}_\triangle(T)$ for $t/J = 6, 4, 3$ are presented in Fig. 10.4 (a)-(c). Two-point correlations in the undoped Heisenberg model are shown in each case with salmon dots, where Heisenberg interactions cause AFM correlations to build up as the temperature is lowered. In Fig. 10.4 (a), $t/J = 6$ is simulated. When doping a hole into the system, both direct (t) and indirect (J) kinetic mechanisms are in synergy with each other, i.e., 120° Néel order is favored. In particular, stronger AFM signals are visible in the hole doped system compared to its undoped analog, shown by red data points in Fig. 10.4.

When instead doping a single doublon into the system, Nagaoka-type kinetic FM starts to develop and overpower weak AFM correlations at $T/t \lesssim 1$. FM correlations increase with decreasing temperature, until they reach a maximum at $T/J \lesssim 1$, where Heisenberg interactions

favoring AFM alignment visibly suppress positive correlations. In fact, in the ground state, correlations around the hole are negative, as indicated by the blue arrow in Fig. 10.4 (a). The zoom-in panel in Fig. 10.4 (a) shows the peak region for TDVP-2 calculations with maximal bond dimensions $\chi = 3000$ and $\chi = 5000$. We observe that the peak is well converged for the two given bond dimensions down to $T/t \sim 0.1$. We note that the sharp drop of the correlator $\mathcal{C}_\triangle$ towards the ground state value at low temperatures is particularly hard to resolve using purification. Nevertheless, energies are found to converge towards the ground state results at low temperatures, as we will discuss later.

The competition between Nagaoka-type kinetic FM and Heisenberg AFM on the doublon doped side is underlined in Fig. 10.4 (b) for $t/J = 4$. Here, next to an apparent maximum at $T/J \sim 1$ of $\mathcal{C}_\triangle$, a sign change of these charge-spin-spin correlations around the doublon is observed at $T/J < 1$. Small residual negative correlations at high temperatures, positive correlations at $T/t \sim 1$ and negative correlations at low temperatures hence lead to reentrance phenomena of the Nagaoka-type regime as a function of temperature, see Figs. 10.2 and 10.4. For $t/J = 3$, correlations are observed to be negative throughout all temperatures, as presented in Fig. 10.4 (c). Nevertheless, kinetic effects and their interplay with Heisenberg-type AFM are clearly visible—i.e., AFM correlations around a doublon are weakened and show a maximum at $T/J \sim 1$.

As in previous chapters, we start with two global Krylov steps with $\Delta\tau = 0.01$, after which we switch to the local two-site TDVP method with $\Delta\tau = 0.02$. At $\tau = 2.0$, we increase the imaginary time step to $\Delta\tau = 0.1$ in order to evolve the system down to low temperatures and compare to ground state properties. For our calculations, we fix weight cutoffs to $w_{\text{Kry}} = 10^{-7}$ and $w_{\text{TDVP}} = 10^{-9}$ for the Krylov and TDVP imaginary time evolution, respectively, and limit maximum bond dimensions to $\chi_{\text{Kry}} = 1024$, $\chi_{\text{TDVP}} = 3000$ and $\chi_{\text{TDVP}} = 5000$ to test convergence.

Convergence of the energy as a function of temperature T/t is shown for the 9×3 systems in Fig. 10.5 (a)-(c). Energies are seen to converge towards the ground state results (dashed lines) both for the hole (red data) and doublon (blue data) doped systems. The insets are zoom-in panels showing the low-temperature region $T/t = 0 \ldots 0.1$, where in particular for $t/J = 3$ convergence towards the ground state can be clearly established.

Fig. 10.5 (d)-(f) show spin-spin correlations around the dopant, $\mathcal{C}_\triangle$, as a function of temperature, where again convergence towards the ground state is established. However, we observe that capturing the turnover from increasingly FM signals caused by kinetic effects to strong AFM correlations on the doublon doped side is a difficult task. In the insets of Fig. 10.5 (d)-(f), we show zoom-ins into the peak region—showing convergence down to $T/t \sim 0.1$.

10.3.2 Ground state: linear confinement

We now turn to the ground state of the system. Using DMRG, we simulate Eq. (10.5) on a cylinder and employ $U(1)$ symmetries both in particle number and total magnetization. We focus on system sizes $L_x \times L_y = 12 \times 6$ with open (periodic) boundaries along the x- (y-) direction, and use bond dimensions of $\chi = 5500$.

Fig. 10.6 (a) shows $\mathcal{C}_\triangle$ as a function of t/J. In the hole doped case, AFM correlations are

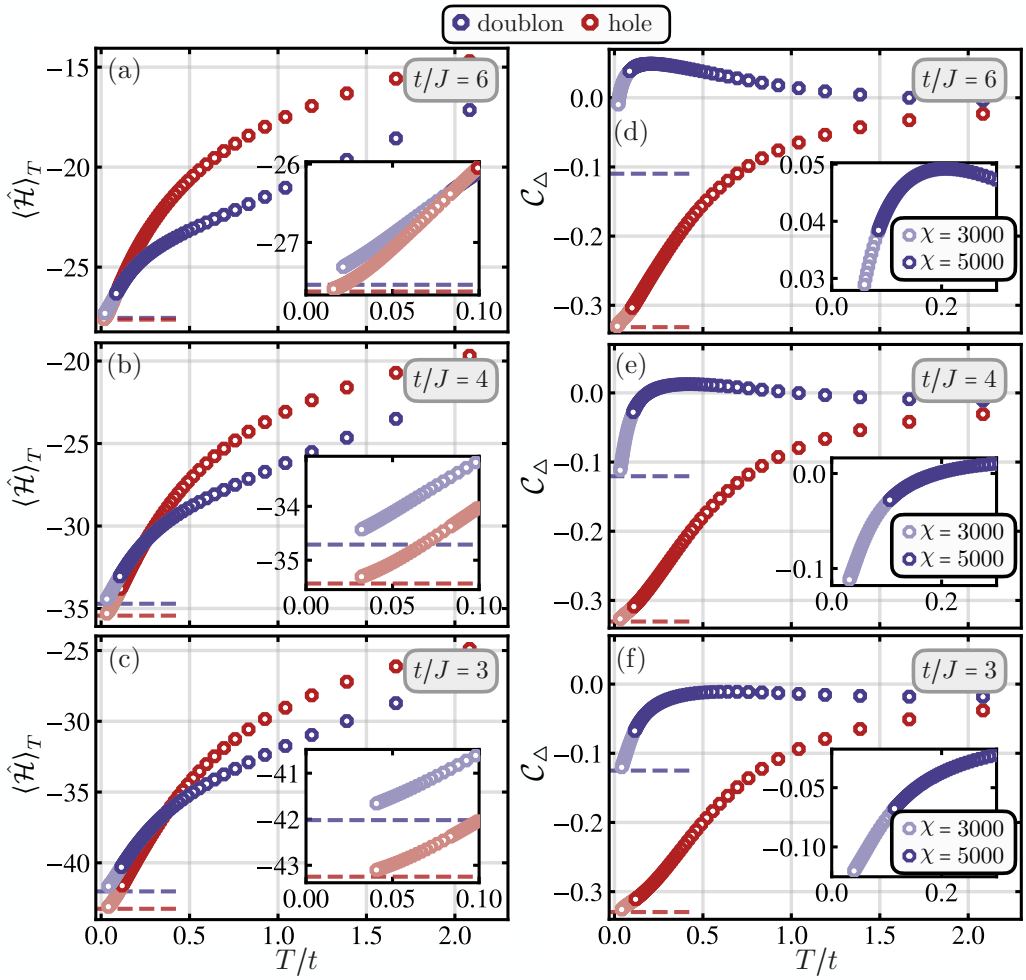

Figure 10.5: **Convergence of finite temperature calculations.** (a)-(c) Thermally averaged energy $\langle \hat{\mathcal{H}} \rangle_T$ as a function of temperature T/t for (a) $t/J = 6$, (b) $t/J = 4$, and (c) $t/J = 3$, for both a doped hole (red) and doublon (blue). In all cases, convergence towards the ground state energies (dashed red and blue lines) can be observed, underlined by the zoom-in panels showing the low temperature regime. (d)-(f) Local charge-spin-spin correlator $\mathcal{C}_\triangle$ as a function of T/t, evaluated for $\mathbf{i} = [x = 4, y = 2]$ in the physical system. Down to $T/t \sim 0.1$, convergence of maximal bond dimensions $\chi = 3000$ and $\chi = 5000$ is observed, as illustrated by the insets.

significantly stronger compared to corresponding two-point spin correlations in the undoped case (grey dashed line), with a subtle tendency towards weaker correlations for decreasing t/J. On the doublon doped side (and away from the Nagaoka regime at $t/J \gg 1$), strong AFM correlations quickly develop for decreasing t/J, complementing the results at finite temperature. In the limit $t/J \to 0$, i.e. an immobile defect doped into a Mott insulator, surrounding AFM correlations are expected to be stronger compared to the undoped case due to a local reduction of frustration around the defect [373], see the dark blue diamond in Fig. 10.6 (a).

The observed strong AFM correlations in the ground state for both hole and doublon doping and for a large range of t/J suggest linear confinement of the dopant, illustrated in Fig. 10.6 (b). In particular, when hopping through a 120° ordered, frozen spin background, each hopping process causes a magnetic energy cost of order J and creates a (partial) memory of the chosen

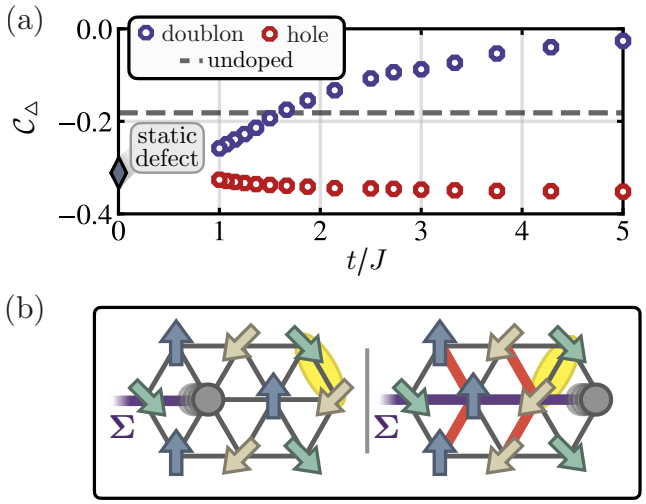

Figure 10.6: **Ground state calculations.** (a) Ground state spin-spin correlations around the dopant, $\mathcal{C}_\triangle$, as a function of t/J for a doped hole (red) and doublon (blue), evaluated for $\mathbf{i} = [x = 4, y = 3]$. Two-point correlations in the triangular Heisenberg model are shown by the grey dashed line; the blue diamond shows $\mathcal{C}_\triangle$ surrounding an immobile dopant ($t/J \to 0$). (b) AFM correlations around the dopant in the ground state suggests a linear confining potential imposed by the spin background. When the dopant hops through the system, it displaces the spins, leading to a linearly growing energy penalty (red lines) as a function of the string length $|\Sigma|$ (purple line) and strong AFM correlations around the dopant (indicated by yellow ellipses).

trajectory. This is expected to lead to the formation of a geometric string Σ along which pairs of spins are locally aligned. A hallmark of such string formation is the resulting scaling of the dopant's energy when $J/t \ll 1$ as [272,385]

$$E/t = -2\sqrt{z-1} + const.\,(J/t)^{2/3} + \mathcal{O}(J/t), \tag{10.7}$$

with z the connectivity of the underlying lattice. An intuitive proof of Eq. (10.7) is presented in Ref. [386]. When assuming orthogonal states generated by the hopping of the hole, we can model the dopant as a hopping particle on the Bethe lattice. Through unitary transformations and by using the radial symmetry of the system (i.e. the string energy does not depend on the direction that the hole hops), this problem can be reduced to an infinite collection of 1D chains, where the on-site energies are given by the string tension and the effective hoppings depend on the connectivity of the underlying lattice. Through a continuum approximation and re-scaling of length and energy scales, Eq. (10.7) is obtained.

In order to test the prediction Eq. (10.7), we calculate ground state energies of a single dopant as a function of $(J/t)^{2/3}$, presented in Fig. 10.7 (a). For $(J/t)^{2/3} \gtrsim 0.2$, both hole and doublon energies seem to be well approximated by a linear scaling law. Fig. 10.8 (a) corroborates the scaling of the doublon energy by plotting the data against $(J/t)^\alpha$, for both $\alpha = 1, 2/3$. In the case of $\alpha = 1$ (light blue triangles), positive curvature clearly remains visible, as underlined by the solid line connecting the first and last data point in the plot. For $\alpha = 2/3$, in turn, the curvature almost completely vanishes (dark blue dots). Indeed, when treating α as an independent fit

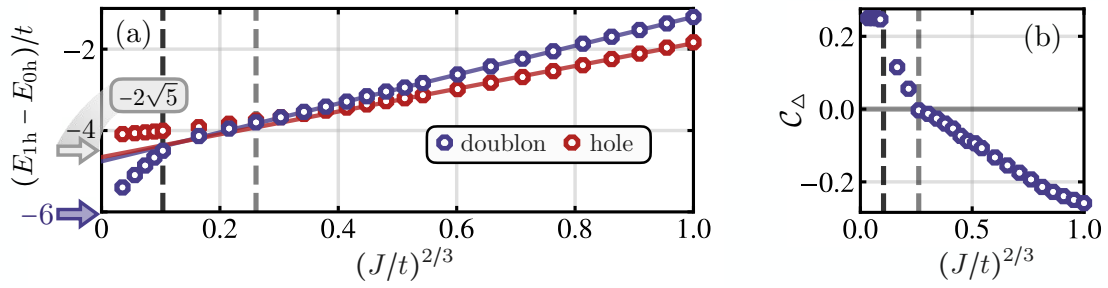

Figure 10.7: **Ground state calculations.** (a) Ground state hole and doublon energies in the singly doped triangular t-J model as a function of $(J/t)^{2/3}$. E_{1h} (E_{0h}) denotes the energy of the singly doped (undoped) system. For intermediate J/t, both ground state energy curves show linear behavior with extrapolated y-intercept close to $-2\sqrt{5}$ (grey arrow), as predicted by geometric string theory, Eq. (10.7). At small values of J/t, the formation of the Nagaoka polaron is observed for doublons by a kink in the energy, which is now approaching $-6t$ for $J/t \to 0$ (blue arrow). The transition is underlined in (b), where $\mathcal{C}_\triangle$ changes sign at around $(J/t)^{2/3} \sim 0.25$ (light grey dashed lines) followed by a sudden jump to strong FM signals at $(J/t)^{2/3} \sim 0.1$ (dark grey dashed lines).

parameter, we find $\alpha = 0.67$, further stressing the predicted $2/3$ scaling of the doublon energy.

The data for the hole doped system, Fig. 10.8 (a), is seen to be more consistent with $\alpha = 1$, whereby the energies plotted against $(J/t)^{2/3}$ shows noticeable negative curvature. We speculate that higher order terms $\mathcal{O}(J/t)$ in Eq. (10.7) may contribute stronger to the hole's energy, making it more difficult to isolate a possible $\alpha = 2/3$ contribution. Finite size effects might further lead to pronounced influences on the observed energies, such that we can not rule out a scaling of the form Eq. (10.7) in the thermodynamic limit. For instance, the close proximity of the y-intercept assuming a scaling of the form $\alpha = 2/3$ to the theoretically predicted value $-2\sqrt{5}$ is in strong support of major characteristics of the string theory prediction, Eq. (10.7).

Furthermore, in the relevant regime for geometric strings, $0.2 \lesssim (J/t)^{2/3} \lesssim 1.0$, we observe that both doublon and hole energies match up to only minor discrepancies. This, in turn, corroborates linear confining behavior also for hole doped systems, as in first approximation the string picture is independent of the hopping sign and only relies on locally present AFM correlations around the dopant. For growing J/t, however, where the dispersion of spinons becomes more prominent [302, 372], corrections are expected from the scaling behavior that do depend on the dopant species, as also seen here for $(J/t)^{2/3} \gtrsim 0.5$.

In the doublon doped system, the onset of Nagaoka FM for $J/t \to 0$ reveals itself by a clearly visible kink of the doublon energy away from the string picture scaling at around $(J/t)^{2/3} = 0.1$ ($J/t \sim 30$), see the dark dashed line in Fig. 10.7 (a). Once the Nagaoka polaron builds up around the doublon, it can gain kinetic energy that, in case of a fully polarized background for $J/t \to 0$, approaches the value of a free dopant, $E_{\text{kin}} = -6t = -zt$.

For the hole doped system, in contrast, the minimal kinetic energy in a fully polarized spin background is given by $E_{\text{kin}} = -3t > -zt$, i.e., it is kinetically frustrated. This limit lies above the asymptotic value $-2\sqrt{5}t \approx -4.47t$ expected from the string picture. This is in agreement with our numerics, which confirm hole energies $< -3t$ for $(J/t)^{2/3} \lesssim 0.6$ (where AFM correlations

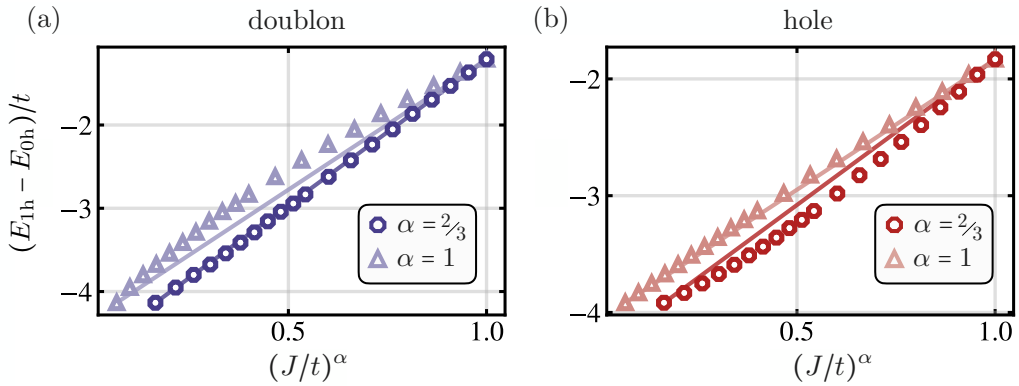

Figure 10.8: **Single dopant energy scaling.** Energies of a single dopant as a function of $(J/t)^\alpha$ for $\alpha = 1$, $\alpha = 2/3$ for a doped doublon, (a), and hole, (b). For doublons (a) the power-law scaling $\sim (J/t)^{2/3}$ matches the string prediction, Eq. (10.7) to remarkable precision. The ground state energies are shown as a function of $(J/t)^\alpha$ for both $\alpha = 1$ and $\alpha = 2/3$. In the former case, curvature is clearly visible, indicated by the solid light blue line connecting the first and last data point in the plot. For $\alpha = 2/3$, the curvature disappears. For hole doping, (b), our results are more consistent with $\alpha = 1$, though a scaling of the form Eq. (10.7) can not be ruled out in the thermodynamic limit.

are present around the dopant), demonstrating that the hole can gain more kinetic energy by instead moving in an AFM spin environment. For $J/t \to 0$, the hole's energy reaches roughly $-4.1t$, supplementing numerical predictions presented in [366, 368].

Fig. 10.7 (b) shows charge-spin-spin correlations $\mathcal{C}_\triangle$ for the doublon doped system. For decreasing J/t, we observe that $\mathcal{C}_\triangle$ changes sign at around $(J/t)^{2/3} \sim 0.25$ ($t/J \sim 8$), before suddenly jumping to strongly positive FM correlations at $(J/t)^{2/3} \sim 0.1$ ($J/t \sim 30$)—coinciding with notable deviations from the predicted energy scaling, see the dark and light grey dashed lines in Fig. 10.7 (a) and (b). Pictorially, a Nagaoka bubble of positive correlations around the hole forms, which grows with decreasing J/t until the fully polarized state is achieved (the radius of the Nagaoka bubble roughly scales as $\propto (t/J)^{1/4}$, as can be seen from variational arguments [383]). In the thermodynamic limit, the local correlator $\mathcal{C}_\triangle$ is expected to feature a similar behavior with an observable sign change of correlations in direct vicinity of the dopant at intermediate J/t, smoothly evolving towards the Nagaoka phase at $J \to 0$, whereby the total spin of the system S continuously grows from $S = 0$ to $S = S_{\max}$ in a series of phase transitions.

Finite size effects

In the above discussion, systems of widths $L_y = 6$ were analyzed for the ground state calculations. By comparing to systems of width $L_y = 3$, we here analyze trends when going towards the thermodynamic limit. In Fig. 10.9 (a), we show the charge-spin-spin correlator $\mathcal{C}_\triangle$ as a function of $(J/t)^{2/3}$, cf. Fig. 10.7 (b). We see that the sign change of $\mathcal{C}_\triangle$ coincides both for $L_y = 3$ as well as $L_y = 6$ at approximately $(J/t)^{2/3} \sim 0.25$ (corresponding to $t/J \sim 8$).

Shown in Fig. 10.9 (b) and (c) are the results of the doublon and hole energies, respectively, as a function of $(J/t)^{2/3}$ and for systems sizes $L_x \times L_y = 9 \times 3$ (light colors) and $L_x \times L_y = 12 \times 6$

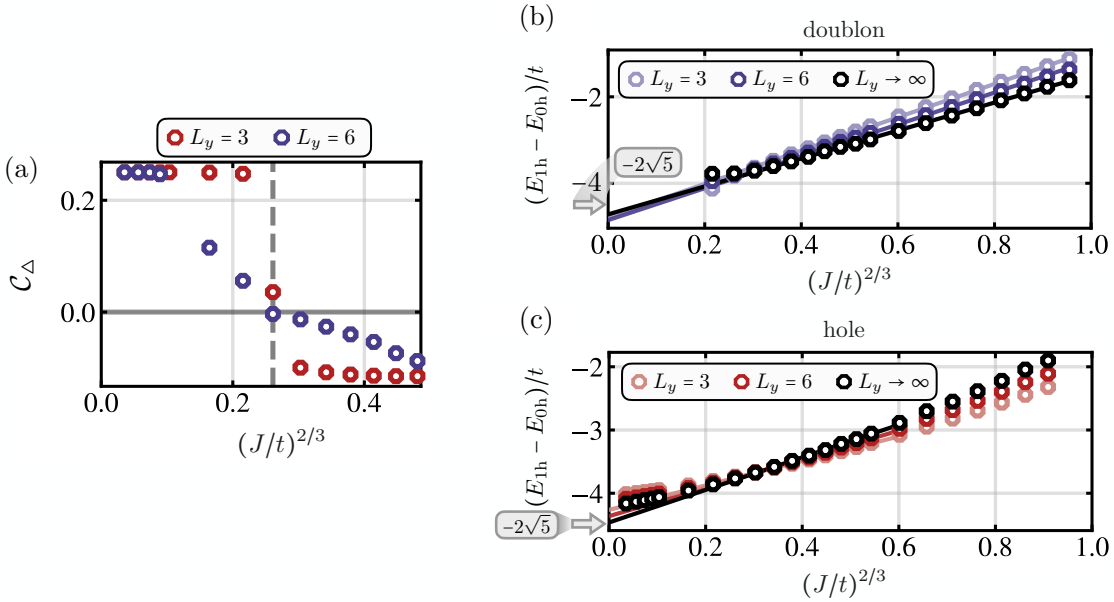

Figure 10.9: **Finite size effects.** (a) Charge-spin-spin correlations $\mathcal{C}_\triangle$ for systems of sizes $L_x \times L_y = 9 \times 3$ (red) and $L_x \times L_y = 6 \times 12$ (blue), evaluated for $\mathbf{i} = [x = 4, y = 2]$ and $\mathbf{i} = [x = 4, y = 3]$, respectively. The dashed line indicates the sign changes of both systems, coinciding at $(J/t)^{2/3} \sim 0.25$, cf. Fig. 10.7 (b). Doublon, (b), and hole, (c), energies as a function of $(J/t)^{2/3}$ and for system sizes $L_x \times L_y = 9 \times 3$ (light colors) and $L_x \times L_y = 12 \times 6$ (dark colors). Extrapolations to infinite system sizes are shown by black data points. Linear fits show corrections towards the universal prediction of $-2\sqrt{5}$ for $J/t \to 0$. Linear fits are done for $(J/t)^{2/3} > 0.3$ for doublons and $0.3 < (J/t)^{2/3} < 0.6$ for holes.

(dark colors). Extrapolations to infinite system sizes by a $1/L_y$ expansion are shown by black data points. We note that the extrapolation to infinite system sizes by two cylinder widths is a very crude procedure, and must be interpreted with lots of caution. Though a slight negative curvature trend is visible in the extrapolation of the doublon energies, the presence of the Nagaoka regime at $J/t \to 0$ suggests a dip towards energies $-6t$ also in the thermodynamic limit. This trend is, however, not visible in the extrapolation, and hence we attribute the slight positive curvature to the rudimentary finite size extrapolation. In the thermodynamic limit, we hence do not rule out a linear scaling of the doublon's energy as a function of $(J/t)^{2/3}$.

Though the data for the doped hole is more consistent with a linear scaling, we plot the hole's energy as a function of $(J/t)^{2/3}$ in Fig. 10.9 (c) in order to identify possible trends when increasing the system's width. Though a slight negative curvature is still observable in the extrapolated thermodynamic limit, we nevertheless see corrections of the y-intercept of fitted linear curves in the approximatelty linear regime towards the universal prediction in Eq. (10.7). However, more detailed work and larger system sizes are needed to distill the true scaling behavior of the doped hole.

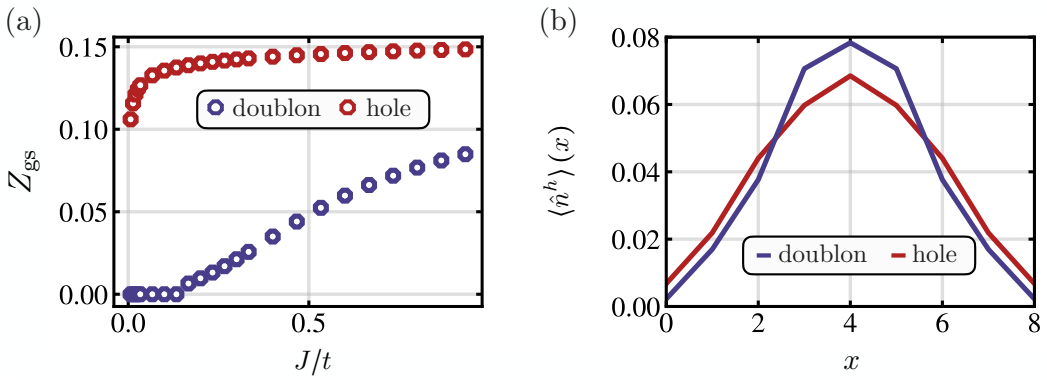

Figure 10.10: **Quasiparticle weight and hole density** (a) Ground state quasiparticle weight Z_{gs} as a function of J/t for a single doped hole (red) and doublon (blue). For doublons, the Nagaoka regime leads to strong suppression of the quasiparticle weight, suggesting a flat quasiparticle dispersion. (b) This is underlined by the hole density $\langle \hat{n}^h \rangle (x)$, showing enhanced localization of the doublon compared to the hole, here shown for $J/t = 0.2$.

Quasiparticle spectral weight and self-localization

In Ref. [372], it has been demonstrated that the quasiparticle properties of the magnetic polarons in the hole and doublon doped triangular lattice significantly differ from one another. In the hole doped case, the quasiparticle was found to be dispersive, while the magnetic polaron in the doublon doped case is nearly flat with strongly suppressed quasiparticle weight $Z(\mathbf{k})$. We calculate Z_{gs} for the ground state as a function of J/t, which can be accessed through the DMRG MPS ground states by evaluation of

$$Z_{gs} = \sum_{\sigma} \sum_{\mathbf{i}} | \langle \psi_{1h} | \hat{c}_{\mathbf{i},\sigma} | \psi_{0h} \rangle |^2, \tag{10.8}$$

where $|\psi_{1h}\rangle$ ($|\psi_{0h}\rangle$) denote the ground state with a single and no hole, respectively.

Results are shown in Fig. 10.10 (a). In the hole doped case, strong AFM correlations (cf. Fig. 10.6) suggest a large quasiparticle weight, as confirmed by our numerics. For doublons, on the other hand, the quasiparticle weight is strongly suppressed at low J/t, where the build up of Nagaoka FM leads to a vanishing overlap between $|\psi_{1h}\rangle$ and $\hat{c}_{\mathbf{i},\sigma} |\psi_{0h}\rangle$.

The hole density distribution, $\langle \hat{n}^h \rangle (x)$, is shown for $J/t = 0.2$ in Fig. 10.10 (b). In the case of doublon doping, the density is noticeably more localized compared to hole doping, corroborating the picture of a heavy Nagaoka magnetic polaron on the doublon doped side and supplementing results presented in Ref. [372].

Density profiles

Fig. 10.11 (a) shows the dopant's density distribution both for the doped hole (grey) as well as doublon (blue) for the $L_x \times L_y = 6 \times 12$ system, for $J/t = 0.2$. Shown are cuts at constant y (where all values of y are equivalent due to applied periodic boundary conditions). In contrast to the doped hole, the doublon's density distribution is seen to be asymmetric around the center of the system, which does not significantly change upon increasing the bond dimension further

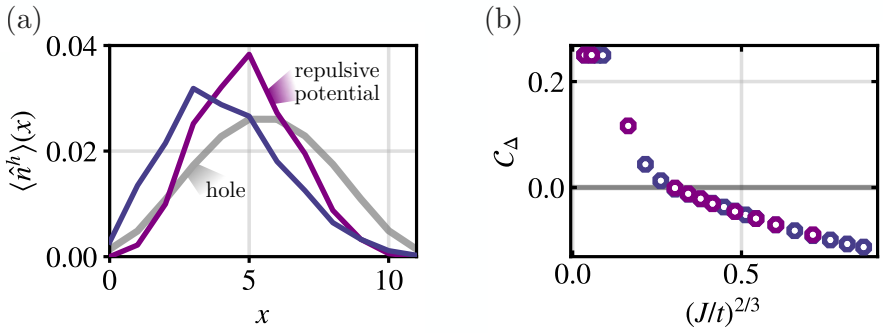

Figure 10.11: **Density profiles and hole-spin-spin correlations.** (a) Density profiles for the single hole (grey) and doublon (blue) for the $L_x \times L_y = 6 \times 12$ system, at $J/t = 0.2$ along $y = 2$. The doublon's density distribution is observed to be asymmetric around the center of the system. We apply strong repulsive potentials at the open edges along x of the system (with strength $100J$), which shifts the distribution closer to the center (though a slight asymmetry is still observed). Spin-spin correlations around the dopant at the maximum of the distribution is shown with and without repulsive potentials in blue and purple, respectively, in (b)—which are seen to remain unchanged in the two cases.

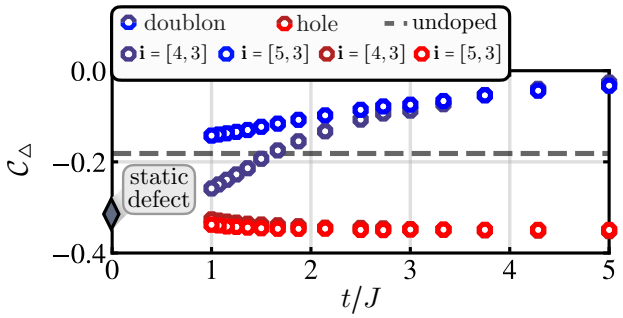

Figure 10.12: **Odd-even effects.** Charge-spin-spin correlations, $\mathcal{C}_\triangle$ for doublon (blue colors) and hole (red colors) doping, on two triangular plaquettes with $\mathbf{i} = [x = 4, y = 3]$ (dark colors) and $\mathbf{i} = [x = 5, y = 3]$ (light colors). Notable effects are visible for $t/J \lesssim 2.5$, presumably stemming from the broken translational symmetry in the system.

(shown are results with $\chi = 5500$). We apply strong repulsive potentials for the hole density along the open edges of the system (with strength $100J$), which shifts the distribution closer to the center, see the purple curve in Fig. 10.11 (a). However, spin correlations around the dopant remain unchanged, as shown in Fig. 10.11 (b), where we choose the reference site $\mathbf{i}_0$ to coincide with the maximum doublon density along x. We note that for systems of width $L_y = 3$, the doublon's density does converge to a symmetric distribution, see Fig. 10.10 (b)—underlining that there is no qualitative change expected from the asymmetry of the doublon's density for $L_y = 6$.

Odd-even effects of $\mathcal{C}_\triangle$

Lastly, for the charge-spin-spin correlator $\mathcal{C}_\triangle$, we take a look at its dependence on the position of the triangular plaquette along the long side of the cylinder. Results for $\mathbf{i} = [x = 4, y = 3]$

(as shown previously) and $\mathbf{i} = [x = 5, y = 3]$ are shown in Fig. 10.12. For $t/J \lesssim 2.5$, notable odd-even modulations are visible in the correlator. We believe that these modulations of the observable along the long direction originate from the broken translational symmetry, which mixes the degenerate ground states existing at dispersion minima in the thermodynamic limit.

10.3.3 Kinetic magnetism in ultracold atoms in optical lattices

The emergence of Nagaoka polarons has recently been realized and analyzed in quantum gas microscope experiments that realize the strongly interacting FH model on the triangular lattice. In particular, in Refs. [55, 56], extended ferromagnetic bubbles around doublon dopants were directly observed, whereas AFM polarons were seen to be promoted around hole dopants. Higher-order correlations functions were further analyzed to give insights into the contributions of superexchange and kinetic mechanisms, in-line with our theoretical predictions in this section. In both Refs. [55, 56], ultracold ^{6}Li atoms were used. The triangular lattice was generated through a combination of two non-interfering lattices of different polarizations in [56], whereas in Ref. [55], two interfering, actively phase-stabilized beams were used.

10.4 Bilayer triangular Fermi-Hubbard model in moiré materials

As introduced in Sec. 4.2, moiré heterostructures of transition metal dichalcogenides (TMDs) provide a versatile platform to simulate the physics of the single-band FH model in the strongly correlated regime $U \gg t$. Due to the non-bipartite nature of most effective moiré lattices in TMD materials, these systems also enable the study and probe the physics of geometric and kinetic frustration effects as discussed in detail in the previous section.

For instance, in a parallel stacking of $MoSe_2/WS_2$ (commonly referred to as R-type stacking), a deep moiré potential minimum arises at points in real space where the transition metal atoms align. This forms a moiré triangular lattice, effectively realizing an FH model in the strongly interacting regime when the moiré conduction band is doped [387]. By measuring the spin susceptibilities at various temperatures and fitting them to the Curie-Weiss law[4], the strength and sign of magnetic interactions can be extracted. For $n = 1 + \epsilon$ (doping doublons into the Mott insulating state at one particle per site), positive Curie temperatures are observed [387], consistent with our theoretical considerations in Sec. 10.3, where doublon doping leads to Nagaoka ferromagnetism. This is further supported by the suppression of ferromagnetic (FM) correlations at commensurate fillings, where the system forms a Wigner crystal; in these insulating states, kinetic effects are significantly suppressed.

In contrast, hole doping the Mott insulator in R-stacked $MoSe_2/WS_2$ ($n = 1 - \epsilon$) reveals paramagnetic responses [387]. It has been argued that the absence of clear antiferromagnetic (AFM) signals at unit filling ($n = 1$) and slight hole doping arises from weak exchange interactions as $U \gg t$; higher moiré potential depths than theoretically expected may further contribute to the suppression of AFM correlations at $n = 1$ and at slight hole doping [387].

[4] When charging the HBL, dopants can form trion states (bound states of dopant charges and excitons) in the potential minima; probing these excitations provides access to the spin susceptibility of the underlying moments, see also Sec. 4.2.

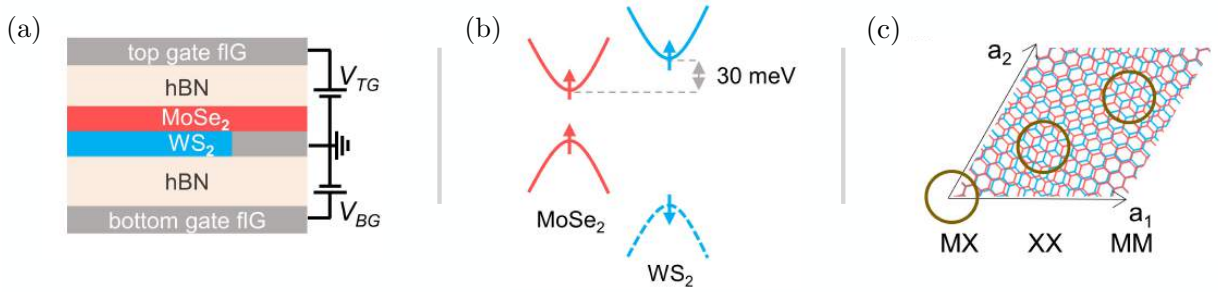

Figure 10.13: **Antiparallel $MoSe_2/WS_2$.** (a) Experimental setup: Stacked $MoSe_2/WS_2$ placed on hBN, with top and bottom gates enabling the tuning of gate biases and electric fields. (b) Type-I band structure alignment of $MoSe_2/WS_2$. (c) Atomic structure of the moiré unit cell in antiparallel $MoSe_2/WS_2$, with highlighted zones of high symmetry: XX, MM, and MX. Figure adapted from Ref. [8].

In the following section, we analyze $MoSe_2/WS_2$ with an antiparallel alignment. Here, one layer is inverted relative to the other, such that the transition metal and chalcogen atoms in one layer are aligned differently with those in the adjacent layer compared to a parallel stacking. As we will see, this stacking configuration leads to drastically different physics compared to R-stacked $MoSe_2/WS_2$ heterobilayers (HBLs). One particularly notable feature of the antiparallel stacking is its charging behavior. In this configuration, the $MoSe_2$ layer is charged first until the moiré lattice reaches one particle per unit cell, at which point the WS_2 layer begins to charge a vertically offset and laterally staggered secondary moiré lattice. This section is based on an experimental collaboration lead by Borislav Polovnikov and Alexander Högele. In the following, we will summarize their main experimental results, and then focus on a theoretical scenario to explain the peculiar physics found in antiparallel $MoSe_2/WS_2$. For more details in particular regading the experimental measurements, we refer to the preprint Ref. [8]. The theoretical discussion will closely follow Ref. [8], partially with textual overlap.

10.4.1 Charging behavior of antiparallel $MoSe_2/WS_2$

In the experiment, a WS_2 layer is stacked on top of a hexagonal boron nitride (hBN) dielectric spacing substrate; a $MoSe_2$ layer is then stacked antiparallel to the WS_2 layer. Another hBN spacer is placed on top, and separate top and bottom gate voltages connected to few-layer graphene allow the application of bias voltages and electric fields between the two layers, as illustrated in Fig. 10.13 (a). The band structure of antiparallel $MoSe_2/WS_2$ is shown in Fig. 10.13 (b). Without applied fields, this system follows a type-I band alignment[5]. Notably, the conduction band edges exhibit a small energy difference $\Delta_C \approx 30\,\text{meV}$, which is smaller than the on-site Coulomb repulsion of the effective FH model when doping the $MoSe_2$ conduction band, where $U \approx 60\,\text{meV}$. As we will describe below, this leads to a peculiar charging sequence in the heterobilayer (HBL). Fig. 10.13 (c) depicts the atomic alignment in the sample, highlighting regions where transition metal (M) and/or chalcogen (X) atoms align (MM, XX, and MX alignment).

[5] A type-I band alignment corresponds to the situation where the valence and conduction band of one layer is energetically in between those of the other layer, see Fig. 10.13 (b)

To analyze the charging behavior, we consider measurements of the reflection spectrum of the $MoSe_2$ layer as a function of photon energy and gate voltage V_G at zero electric field (i.e., equal top and bottom voltages), shown in Fig. 10.14 (a). For $V_G = -7 \ldots 0.6$ V, the HBL is in the band gap of both layers (corresponding to a doping density per moiré unit cell of $\nu = 0$, see the right axis of Fig. 10.14 (a)), and three prominent excitons produce peaks in the differential reflection spectrum. Previously, it has been argued that these excitons correspond to distinct real-space positions in the moiré potential [388–390]: The M_1 exciton is located near XX stacking points, while the M_2 exciton is associated with the shallow local minimum around MM alignment points, see Fig. 10.14 (b). These M exciton energies closely resemble those of monolayer $MoSe_2$, corroborating that they represent intralayer excitations within the $MoSe_2$ layer, modulated by the moiré potential.

When the system is hole-doped (into the valence band of $MoSe_2$ at $V_G \lesssim -7$ V), holes form charged (positive) trion bound states with the M_1 exciton ($\tilde{M}_1^+$), which rapidly lose oscillator strength with increasing bias. However, electron doping in the $MoSe_2$ conduction band produces much richer signals. The M_1 exciton transitions into a charged (negative) electron-exciton trion (M_1^-), while the M_2 peak evolves smoothly into a slightly red-shifted peak $\tilde{M}_2^-$. The abrupt oscillator strength transfer from M_1 to M_1^- signals electron doping in the $MoSe_2$ layer, i.e., dopants form bound states in the XX moiré pockets. At $\nu = 1$, the M_1 exciton completely loses its oscillator strength, marking unit filling of the $MoSe_2$ layer (upper orange line in Fig. 10.14 (a)). This is schematically corroborated in the charging diagram in Fig. 10.14 (c), where ν_{Mo} rises linearly to unity, while ν_W stays at zero doping.

For $1 < \nu < 2$, both M_1^- and $\tilde{M}_2^-$ resonances remain largely unchanged. This behavior contrasts with the first charging step ($0 < \nu < 1$), indicating that doping proceeds in the WS_2 layer, see Fig. 10.14 (c), leaving excitations in the $MoSe_2$ layer unchanged. In particular, this suggests that moiré minima for WS_2 electrons are spatially shifted from the XX and MM points, forming a moiré bilayer system. This charging behavior aligns with the HBL's band structure: As the on-site repulsion U exceeds the conduction band edge difference between $MoSe_2$ and WS_2, electron filling transitions from the $MoSe_2$ layer (one particle per site) to the WS_2 layer[6].

Further doping reveals a transition from the $\tilde{M}_2^-$ peak to the charged trion M_2^-, accompanied by the simultaneous emergence of a new trion peak, M_3^-, see Fig. 10.14 (a). This indicates additional charging of the $MoSe_2$ layer (as well as the WS_2 layer where the two trion peaks remain constant as a function of V_G), see also Fig. 10.14 (c). Eventually, the oscillators lose their strengths and are red-shifted, signaling further doping of the layer(s).

The physical understanding of the emerging bilayer is illustrated in Fig. 10.15. Two laterally (and, in the physical system, also vertically) shifted triangular lattices lead to the formation of

[6] Applying an electric field between the layers modifies this behavior by altering the relative conduction band positions. At a critical field, a transition occurs from a type-I to type-II band alignment, where the WS_2 conduction band edge falls below that of $MoSe_2$. In this scenario, the M_1 exciton persists until electron doping begins in the $MoSe_2$ layer, where it transitions to a trion. Conversely, further separating the conduction bands beyond the on-site interaction energy causes electrons to fill only the $MoSe_2$ layer. This latter behavior mirrors that of P-stacked $MoSe_2/WS_2$, where charging occurs exclusively in the $MoSe_2$ layer. Tracking the binding energy of the $\tilde{M}_2^-$ trion further supports the picture of a bilayer moiré system. For a more detailed discussion and corresponding data, we refer to Ref. [8], and shall not go deeper into the specifics beyond the intuitive picture outlined above.

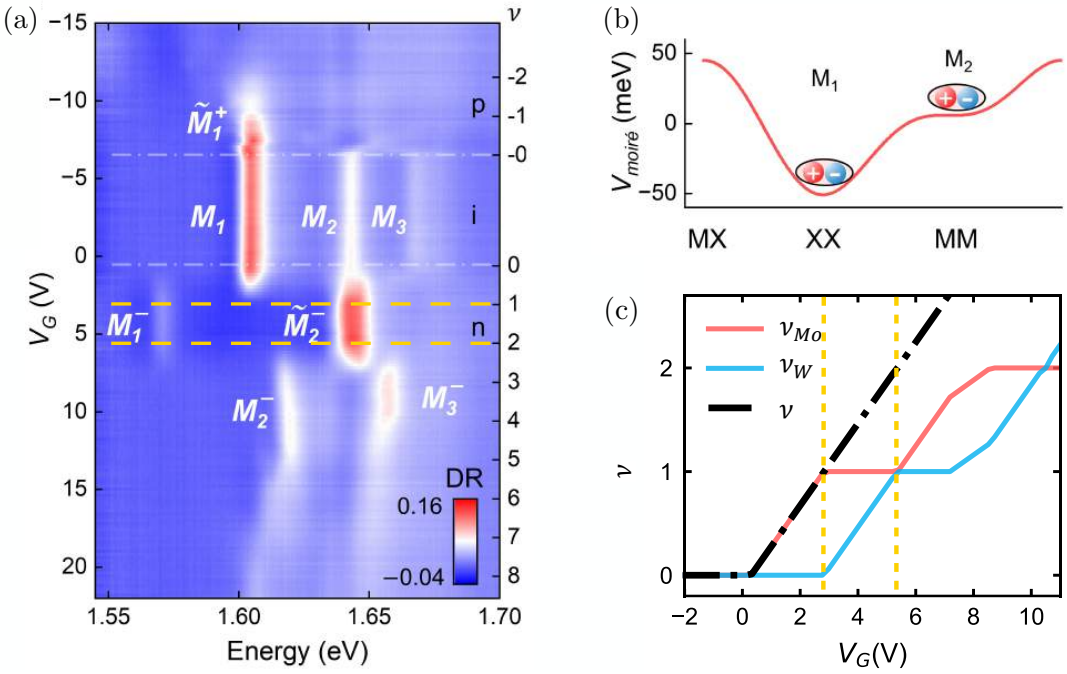

Figure 10.14: **Charging behavior.** Charging behavior of antiparallel $MoSe_2/WS_2$ under applied gate voltage (at zero electric field, i.e., with equal top and bottom voltages). (a) Differential reflection spectrum; peaks indicate excitonic resonances. Within the band gap of both layers (between the grey dashed-dotted lines), three prominent excitons are observed, originating from $MoSe_2$ monolayer excitations subject to the moiré potential. These excitons correspond to distinct spatial regions of the potential, with M_1 (M_2) excitons residing in the moiré pockets around XX (MM) alignments, as illustrated in (b). Electron doping (positive bias voltages) and tracking trion bound states of excitons and dopants reveal an intriguing bilayer charging behavior (see text). Positions where the total particle number per moiré unit cell ν satisfies $\nu = 1, 2$ are indicated by orange dashed lines. (c) Schematic depiction of the charging behavior in the $MoSe_2$ and WS_2 layers. Orange lines correspond to the same positions as in (a). The invariance of $MoSe_2$ trions during WS_2 layer charging in (a) suggests a lateral displacement of the two moiré lattices, resulting in the realization of a bilayer FH system with various layer-imbalanced fillings. Figure adapted from Ref. [8].

a bilayer. Due to the above discussed charging sequence, one of the two layers is doped until unit filling; succeeding doping will start to fill the second layer, until at $\nu = 2$ both are in a Mott insulating regime with one particle per site.

10.4.2 Strongly correlated bilayer physics

Having established the charging behavior of the $MoSe_2/WS_2$ HBL, we would like to probe the correlated physics for the whole range of ν. Particularly interesting here is the range $1 < \nu < 2$, where one of the moiré bilayers is in a Mott insulating state, while the other is itinerant and partially filled. To analyze spin correlations in the $MoSe_2$ layer, the $\tilde{M}_2^-$ peak can be used as a sensor for its magnetic environment, i.e., intralayer excitons act as probes of local magnetization; the latter can be measured through renormalized exciton g-factors. In particular, by measuring the valley Zeeman effect by probing the HBL with exclusively right- or left-handed light gives

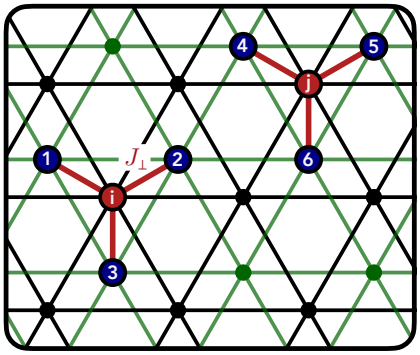

Figure 10.15: **Moiré bilayer.** Emerging bilayer triangular lattice in antiparallel $MoSe_2/WS_2$. The bilayer consists of two laterally shifted triangular lattices. The black layer is filled first up to $\nu = 1$, at which point the second (green) lattice is filled until $\nu = 2$, where in each layer there is one particle per moiré site. RKKY interactions: Two local spins at sites **i** and **j** in the Mott insulating (black) layer interact by inducing a local magnetization profile in the metallic (green) layer. Each site in the MI layer has three nearest neighbors in the metallic layer, such that a total of nine terms contribute to RKKY contributions to magnetic interactions, see also Eq. (10.14).

access to the g-factors and hence the susceptibility.

Fig. 10.16 (a) shows the the g-factors for different temperatures. For all temperatures, we observe a quick rise of $|g|$ between $0 < \nu < 1$, until it reaches a maximum at one electron per moiré cell in $MoSe_2$. To qualitatively describe the first charging stage of $MoSe_2$ ($0 < \nu < 1$), we simulate a single triangular lattice using the two-particle self-consistent theory, outlined in Sec. 3.2. Specifically, we implement the triangular lattice by simulating a square lattice with NNN interactions along a single diagonal.

Results for the spin susceptibility (which is proportional to the g-factor) are shown in the inset of Fig. 10.16 (a) for $0 < \nu < 1$. As expected, when filling the lattice with electrons, the susceptibility rises monotonously. This qualitatively explains the rise of $|g|$ in the experimental data in the regime $0 < \nu < 1$. However, TPSC does not capture the more subtle structures of the g-factor. At filling factors ν between 0.7 and 0.9, we observe a small sub-plateau below 1 K in the HBL, which vanishes at higher temperatures, see Fig. 10.16 (a). Similar to the R-type stacked $MoSe_2/WS_2$, where kinetic magnetism has been observed for $\nu = 1 + \epsilon$ [387], the release of kinetic magnetism via Haeter-Shastry type AFM in the $\nu = 1 - \epsilon$ regime is a plausible candidat to explain the observed behavior: At $\nu \approx 2/3$, the electrons in the $MoSe_2$ layer become increasingly frustrated, leading to a saturation of g. However, once kinetic effects become relevant for $\nu \gtrsim 0.9$, strong AFM correlations build up, which in turn boost the g-factor up to significantly higher values.

We now analyze the g-factor in the regime $1 < \nu < 2$. Remarkably, in contrast to other heterostructures, g reaches a maximum value around $\nu \approx 1$, after which it saturates for the whole region where the sensing peak $\tilde{M}_2^-$ is present. Throughout the plateau, the values of the g-factors exhibit variations on the order of 10 - 15%, which we interpret as effects coming from the emerging second, laterally shifted lattice. As can be seen in Fig. 10.16 (a), this behavior is robust across all temperatures (and across various samples [8]), indicating a physical origin of

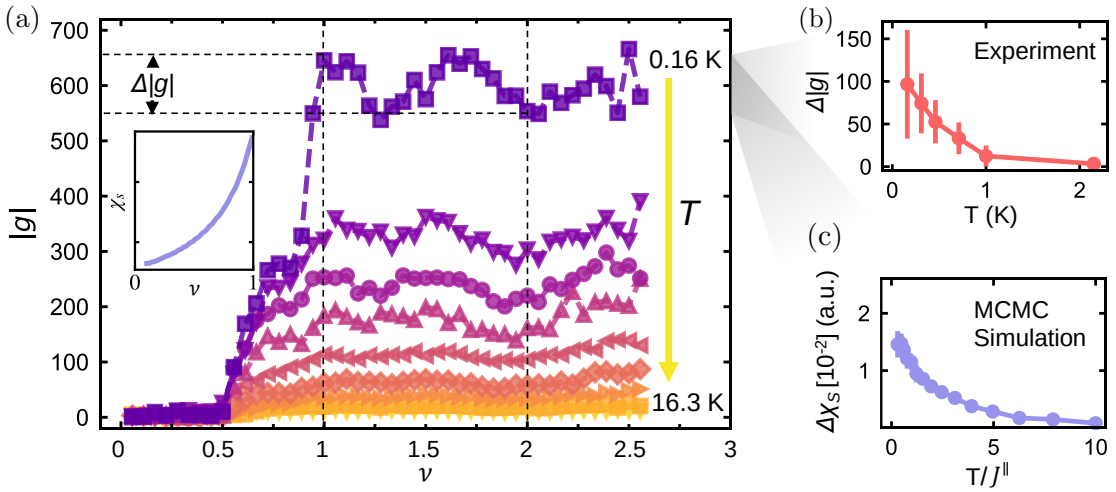

Figure 10.16: **Strongly correlated bilayer physics.** (a) Filling-factor dependent g-factor in the regime where the $\tilde{M}_2^-$ charged trion has pronounced peaks. The g-factor rises strongly when willing the $MoSe_2$ layer ($0 < \nu < 1$), which is captures qualitatively by theory calculations: The inset shows χ_s in arbitrary units of the FH model on the triangular lattice using TPSC (at $U/t = 9.5$, $T/t = 0.1$). For $\nu \gtrsim 1$, a local maximum of the spin-susceptibility is followed by a decrease on the order of 10 - 15 %; there is a subsequent increase to the maximum value around $\nu = 1.6 - 1.7$, and another decrease to a local minimum around $\nu = 2$. (b) Difference of the g-factors Δg as a function of temperature in the Mott-insulating regimes $\nu = 1, 2$. (c) Difference of spin susceptibilities χ_s (arb. units) calculated from classical Monte Carlo simulations of mono- and bilayer triangular Heisenberg models. For $\nu = 2$, the presence of inter-layer couplings $J_\perp$ leads to an out-of-plane tilt of the magnetic order which results in a reduction of χ_s and g compared to $\nu = 1$. Figure adapted from Ref. [8].

the observed fluctuations.

To get a qualitative understanding of the observations, we shall first focus on the two cases $\nu = 1, 2$. Here, the system is in a fully Mott-insulating state and can be described by a spin model with localized moments at every site of the triangular monolayer ($\nu = 1$) and bilayer ($\nu = 2$). Fig. 10.16 (b) shows the difference of the g-factors, $\Delta g = g(\nu = 1) - g(\nu = 2)$, of both Mott insulating regimes as a function of temperature. For $T \lesssim 1$ K, the g-factor of the $\nu = 2$ filled system is seen to consistently fall below the one at $\nu = 1$. We qualitatively model the Mott insulating regimes by classical Heisenberg models on the corresponding lattices. In particular, for $\nu = 1$ we model the system by a classical Heisenberg spin model on the triangular lattice with Hamiltonian

$$H_{\nu=1} = J_{\parallel} \sum_{\langle \mathbf{i},\mathbf{j} \rangle} \mathbf{S_i} \cdot \mathbf{S_j}. \tag{10.9}$$

Here, $\mathbf{S_i}$ are classical vectors of length $|\mathbf{S_i}| = 1$ living at lattice site $\mathbf{i}$. To compare this to the bilayer case ($\nu = 2$), we additionally define a Heisenberg Hamitonian defined on the triangular bilayer lattice as presented in Fig. 10.15,

$$H_{\nu=2} = \sum_{\alpha=1,2} J_{\parallel} \sum_{\langle \mathbf{i},\mathbf{j} \rangle_{\alpha,\alpha}} \mathbf{S_i} \cdot \mathbf{S_j} + J_\perp \sum_{\langle \mathbf{i},\mathbf{j} \rangle_{1,2}} \mathbf{S_i} \cdot \mathbf{S_j}. \tag{10.10}$$

Here, $\langle \mathbf{i}, \mathbf{j} \rangle_{\alpha,\alpha'}$ denote NN between layers α, α', see also Fig. 10.15.

Using Markov chain Monte Carlo methods, we compute the susceptibility, which can be calculated by

$$\chi_s = \beta V(\langle m^2 \rangle - \langle m \rangle^2), \tag{10.11}$$

where β is the inverse temperature and V is the number of lattice sites (we simulate a grid of $V = L_x \times L_y \times = 32 \times 32$ lattice sites with periodic boundary conditions); m is the absolute value of the magnetization averaged over a snapshot, i.e.

$$m = \sqrt{\sum_{\mu=x,y,z} m_\mu^2}, \quad m_\mu = \frac{1}{V} \sum_{\mathbf{i}} S_{\mathbf{i}}^\mu. \tag{10.12}$$

We calculate the magnetic susceptibility for both cases $\nu = 1$ and $\nu = 2$ and evaluate their difference $\Delta\chi = \chi(\nu = 1) - \chi(\nu = 2)$, shown in Fig. 10.16 (c). In agreement with the measured g-factors, the magnetic susceptibility of the bilayer at $\nu = 2$ is consistently lower compared to $\nu = 1$. This aligns with intuitive expectations of the magnetic structure in the respective models: Coupling two triangular lattices (where each layer is initially in a 120° state) by an inter-layer coupling $J_\perp$ results in an enhancement of frustration between the magnetic moments, tilting the 120°-ordered spins out-of-plane. This suppresses correlations within each layer, which in turn results in a reduction of the susceptibility (and correspondingly the g-factors) compared to the case of a single Mott-insulating plane. This qualitative comparison of classical spin models with the observed physics at $\nu = 1$ and $\nu = 2$ suggests a significant coupling $J_\perp$ between the layers, and supports the view that the material at hand is governed by bilayer Fermi-Hubbard physics.

We corroborate the above picture by explicitly looking at spin-spin correlations $\langle \mathbf{S_i} \cdot \mathbf{S_j} \rangle$ in the classical simulations of a 16×16 lattice, see Fig. 10.17 (a) for $\nu = 1$ and Fig. 10.17 (b) for $\nu = 2$. In the latter, we only show correlations within the plane of one of the two layers—this allows for an evaluation on how the second lattice affects in-pane correlations. While 120° magnetic order spans the whole system in the case $\nu = 1$, correlations are much shorter range for $\nu = 2$, where tilting the spins reduces the in-plane correlations. We further underline the above by performing ground state DMRG calculations of a bilayer $t_\parallel$-$J_\parallel$-$J_\perp$ model, i.e., a system where one triangular layer is filled with one particle per site and the filling in the other layer is varied from empty to one particle per site (realizing the scenario $1 < \nu < 2$). Similarly, we see how doping the second lattice to unit filling leads to a reduction of in-plane correlations, shown in Fig. 10.17 (c).

From the g-factor data at various temperatures in Fig. 10.16 (a), fitting the data to a Curie Weiss law gives access to the nature of spin correlations in the system. The extracted Curie temperatures θ as a function of filling factor are shown in Fig. 10.18 (a). Just as in the case of the g-factors, θ presents pronounced variations across the range $1 < \nu < 2$ with two distinct maxima around $\nu = 1$ and $\nu \approx 1.8$. Physically, a negative θ is associated with an antiferromagnetic (AFM) 120° state; an increase of θ towards 0 mK indicates a weakening of the AFM state and is highlighted by the grey areas in Fig. 10.18 (a).

For $1 < \nu < 2$, the $MoSe_2$ layer is in a Mott-insulating state, while the WS_2 layer is partially filled. In the regime of light WS_2 particle doping ($\nu \gtrsim 1$), the system can be described by a weakly interacting Fermi-liquid coupled to local moments in a Mott-insulator. Here, inter-layer

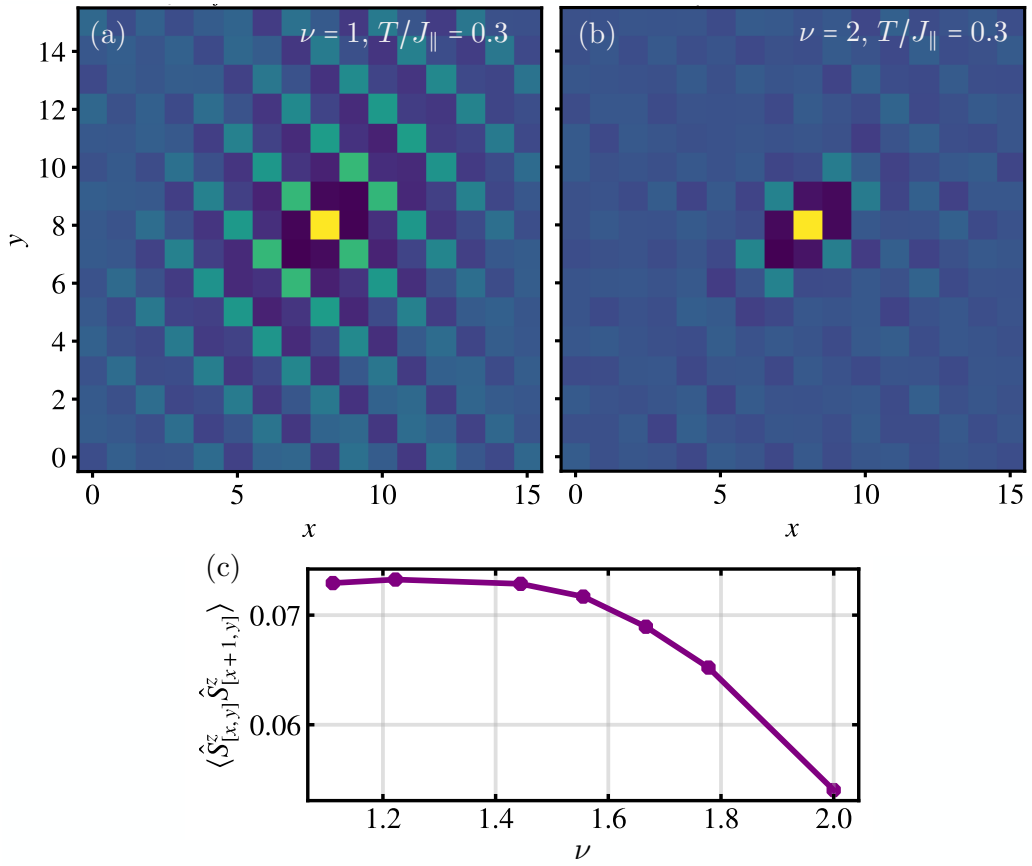

Figure 10.17: **Spin correlations in single and bilayer triangular lattices.** (a) Spin-spin correlations $\langle \mathbf{S}_{\mathbf{i}_0} \mathbf{S}_{\mathbf{j}} \rangle_T$ at temperature T, mapped on a square lattice, for the classical triangular lattice Heisenberg model. Strong 120° correlations are observed. (b) The same correlations in the triangular lattice layer when coupling an additional, laterally offset triangular lattice to the Heisenberg model with coupling $J_\perp$. Shown correlations correspond to only a single layer; tilting of the classical spins due to the second lattice leads to a reduction of correlations. (c) DMRG calculations in the ground state of a $L_x \times L_y \times L_z = 6 \times 3 \times 2$ bilayer triangular lattice t-J model. We choose $t/J_\perp = 2$, and $J_\perp/J_\parallel = 1$. While one layer is filled, the other is ranging between zero and unit filling, i.e., we simulate the range $\nu \in [1, 2]$. We then assess spin-spin correlations in the Mott insulating layer, which are seen to be decreased in a monotonic fashion as ν approaches the bilayer Heisenberg model, corroborating the frustrating effect of the second lattice on the first lattice.

couplings $J_\perp$ lead to the appearance of RKKY-type intra-layer interactions J^{RKKY} [71,391] within the $MoSe_2$ layer (which are mediated by the metallic WS_2 electrons). In particular, a magnetic moment in the $MoSe_2$ layer at site $\mathbf{i}$ induces a magnetization profile of the metal, which in turn couples to another localized spin at position $\mathbf{j}$. This results in the emergence of long-range interactions between the localized spins, described by the Hamiltonian[7] [71,391],

$$\hat{\mathcal{H}}^{\mathrm{RKKY}} = \frac{1}{2} \sum_{\mathbf{i},\mathbf{j}} J^{\mathrm{RKKY}}_{\mathbf{ij}} \hat{\mathbf{S}}_{\mathbf{i}} \cdot \hat{\mathbf{S}}_{\mathbf{j}}. \tag{10.13}$$

[7] The factor of $1/2$ makes sure to avoid double counting.

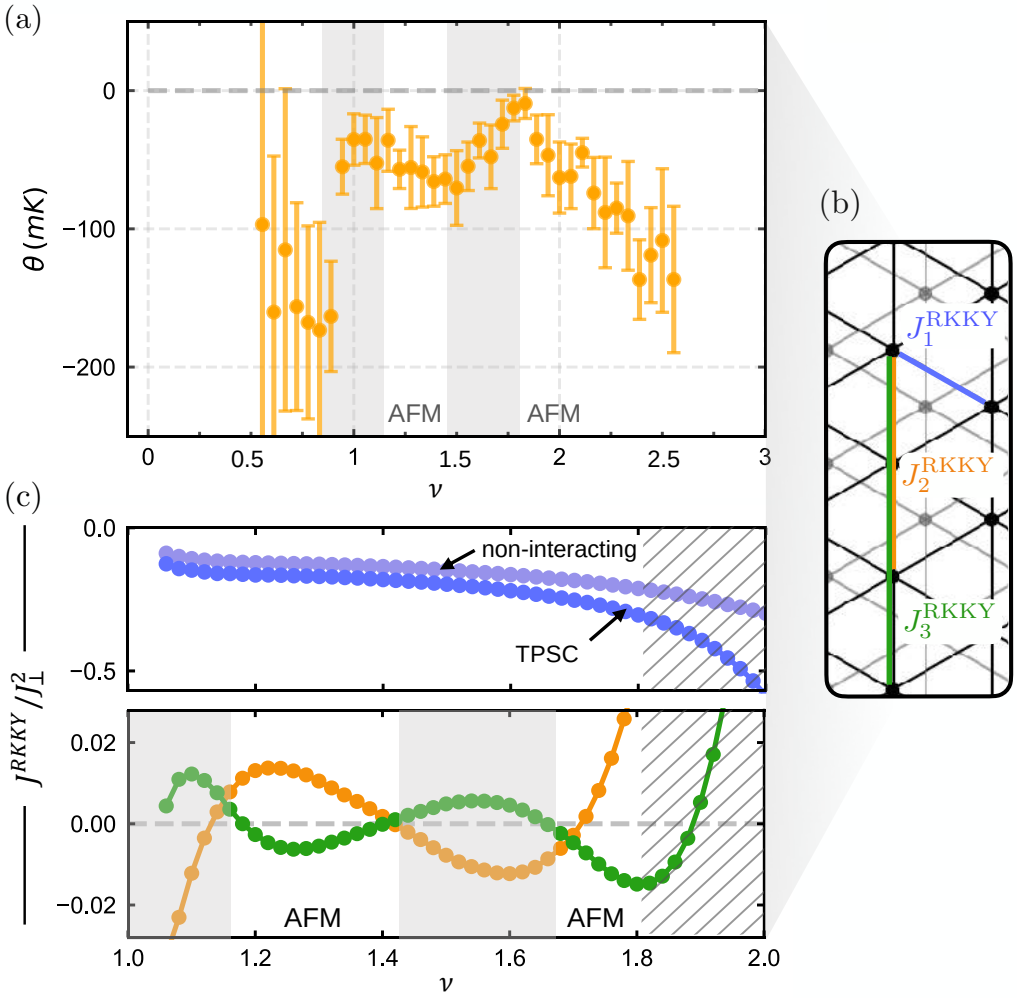

Figure 10.18: **Curie temperature and TPSC.** (a) Curie-Weiß temperatures θ extracted from the data in Fig. 10.16 (a), showing similar oscillations as the g-factor. The filling-factors where θ increases towards 0 mK (shaded in grey) correspond to a weakening of the 120° antiferromagnetic (AFM) order, whereas a decrease of θ to higher negative values indicates a strengthening of the 120° state. (b) Schematic of RKKY-type interactions in the $MoSe_2$ layer mediated by the metallic WS_2 electrons, see also Fig. 10.15. (c) Top panel: nearest-neighbor RKKY interactions in the $MoSe_2$ layer calculated from the susceptibility of the WS_2 layer using free fermions (light blue) and with TPSC (dark blue). The sharp correction of NN couplings for $\nu \gtrsim 1$ leads to a distinct drop of θ as seen in (a). Lower panel: Longer-range RKKY interactions can act against (or in favor of) the AFM 120° state depending on the filling factor and are highlighted by the grey (white) areas in the lower panel as in (a). Close to the Mott insulating regime $\nu = 2$, the perturbative picture breaks down and other effects (such as kinetic magnetism) are likely to dominate, illustrated by the hatched area in (c). Figure adapted from Ref. [8].

The interaction $J_{\mathbf{ij}}^{\mathrm{RKKY}}$ is calculated from the susceptibility of the metal. As each site in the $MoSe_2$ layer interacts with three sites in the WS_2 layer (assuming NN inter-layer couplings), the contributions to $J_{\mathbf{ij}}^{\mathrm{RKKY}}$, see Fig. 10.18 (b), read

$$J_{\mathbf{ij}}^{\mathrm{RKKY}} = -J_{\perp}^{2} \sum_{\mathbf{a}\in\{1,2,3\}} \sum_{\mathbf{b}\in\{4,5,6\}} \chi(\mathbf{a}-\mathbf{b}), \tag{10.14}$$

with

$$\chi(\mathbf{x}) = \int_{\mathbf{q}} d\mathbf{q} e^{i\mathbf{q}\cdot\mathbf{x}} \chi(i\omega_n = 0, \mathbf{q}). \tag{10.15}$$

We approximate the strength of RKKY interactions using the picture of free fermions in the WS_2 layer as well as by using TPSC approach. The upper panel in Fig. 10.18 (c) shows RKKY corrections J_1^{RKKY} to nearest-neighbor (NN) intra-layer interactions $J_{\parallel}^{1}$ (i.e. the effective NN interactions in the $MoSe_2$ are given by $\tilde{J}_{\parallel}^{1} = J_{\parallel}^{1} + J_1^{\mathrm{RKKY}}$). For small doping $\nu \gtrsim 1$, a rapid drop of J_1^{RKKY} is observed. We argue that the sudden reduction of magnetic interaction strength $\tilde{J}_{\parallel}^{1}$ likely causes the jump of the Curie temperature around $\nu = 1$, see Fig. 10.18 (a). This is consistent with the observed initial drop of the g-factor for $\nu \gtrsim 1$: When $\tilde{J}_{\parallel}^{1}$ is reduced, the effective temperature of the spins in the $MoSe_2$ layer is increased, leading to a drop of the g-factor.

At larger doping $\nu \gtrsim 1.5$, NN interactions are further renormalized, suggesting a strong rise of θ as observed in Fig. 10.18 (a) towards 0 K. Comparison between free fermion and TPSC calculations show that interactions in the WS_2 layer further enhance this effect, see the light and dark blue data in Fig. 10.18 (c). In between $1 < \nu \lesssim 1.8$, the Curie temperature is non-monotonic and shows an additional minimum at $\nu \approx 1.4$, which is in contrast to the behavior of NN RKKY interactions. A possible scenario for this effect is the relevance of longer-range RKKY interactions, shown in Fig. 10.18 (c) (lower panel) for second- and third-nearest neighbors J_2^{RKKY}, J_3^{RKKY}. Indeed, the induced interactions show distinct oscillations that can act towards (de-)stabilizing the 120° magnetic order. In particular, positive (negative) second- (third-) neighbor interactions act in favor of the 120° state and imply a decrease in θ, whereas a reversed sign inhibits the 120° order as highlighted by the shaded areas in Fig. 10.18 (a) and (c). For $1.15 \lesssim \nu \lesssim 1.4$, AFM correlations are favored, possibly leading to a reduction of θ in this regime as observed in Fig. 10.18 (a).

Close to the regime $\nu \lesssim 2$ (grey hatched area in Fig. 10.18 (c)), the Fermi-liquid picture breaks down and a bilayer Mott-insulator forms. Here, other effects of strongly-correlated origin likely take over and dominate the physics. In particular, as demonstrated in the previous section, when slightly hole doping a Mott insulator on a triangular lattice, kinetic effects lead to Hearter-Shastry type antiferromagnetism which strongly favors the formation of a classical 120° state to minimize the dopant's kinetic energy. The sharp turnaround of θ at $\nu \approx 1.8$ may thus be the result of these kinetic effects, which overcomes the trend of weakening couplings due to RKKY interactions and pushes θ back to AFM signals when $\nu \to 2$. This argument is in-line with the observations of the g-factor close to the bilayer Mott insulator: For $\nu \lesssim 2$, kinetic magnetism leads to a strengthening of AFM correlations which in turn enhances g.

10.5 Discussion

In the first part of this chapter, we have analyzed the competing interplay between kinetic and magnetic frustration in the singly doped triangular t-J model, associated with energy scales t and J, respectively, and at temperature T. We unveiled regimes of itinerant magnetism in the vicinity of the dopant, which can directly be accessed and observed using state-of-the-art quantum gas microscopy of ultracold atoms on triangular optical lattices. Remarkably, we predict an increased stability of Nagaoka ferromagnetism at elevated temperatures, potentially facilitating its observation with ultracold atoms. Studying Nagaoka FM at finite doping as well as on other non-bipartite lattices are interesting directions for further research [392].

At low temperatures, we have presented strong evidence for the existence of linear confinement of the dopants surrounded by 120° ordered spins on the triangular lattice. The strikingly accurate scaling of the doublon's energy $\sim (J/t)^{2/3}$ firmly establishes the picture of geometric strings for frustrated systems. The role of enhanced quantum fluctuations as well as the non-othogonality of classically ordered 120° spin states on the geometric string basis construction is an interesting topic for future research. Particularly, our work further advocates a possible significance of strings for pairing [57,393] and ro-vibrational excitations [265] in doped AFMs—hinting towards a possible universal picture of the physics in doped Mott insulators.

In the second part of the chapter, we turned towards the analysis of a $MoSe_2/WS_2$ HBL. By stacking the 2D sheets in an anti-parallel alignment, a unique charging behavior leads to the formation of an effective bilayer FH model on the triangular lattice. These considerations motivate H-type $MoSe_2/WS_2$ as a candidate system for manifestations of kinetic magnetism, providing compelling motivation for future experimental and theoretical work on many-body phenomena and magnetism in antiparallel $MoSe_2/WS_2$ heterostacks. We have proposed a theoretical scenario where kinetic effects and induced RKKY interactions lead to magnetic tendencies that align with the observations—nevertheless, further quantitative numerical studies are needed to fully pin down the physical origin of the observed effects. Other possible scenarios include the formation of Wigner crystal-type electronic charge order, which may lead to pronounced maxima of the g-factor at certain doping values.

11

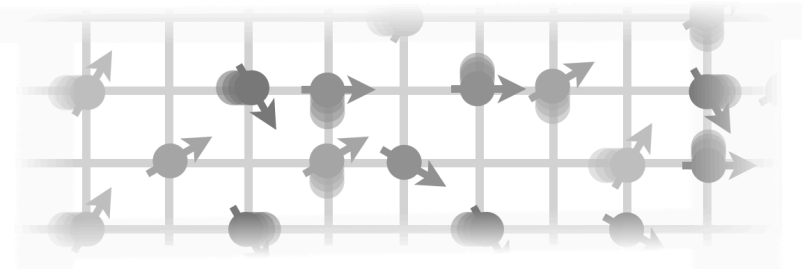

SU(N) symmetric systems

Summary. The FH model with higher SU(N) spin symmetries gives rise to rich magnetic ground states at a filling of one particle per site compared to the case of SU(2) spins. In this chapter, we address the question of doping these systems by studying a single hole in the SU(3) t-J model. By analyzing both ground state and dynamical properties utilizing DMRG, we establish the appearence of magnetic polarons consisting of chargons and flavor defects, whose dynamics is constrained to a single effective dimension along the ordered diagonal. We will semi-analytically describe the system using geometric string theory, where paths of hole motion are the fundamental degrees of freedom. We will see that at $N > 2$, intricate ground states at finite doping are expected, which opens future directions towards exploring a wealth of physics in doped SU(N) Fermi-Hubbard models on various geometries. Lastly, we will use TPSC to gain insights into the thermodynamic behavior of the SU(N) symmetric FH model, and compare results to determinant quantum Monte Carlo calculations.

11.1 Introduction

As introduced in Sec. 2.2.2, FH models with higher spin symmetries, realized by SU($N > 2$) invariant models, promise rich physics beyond the SU(2) paradigm [394–403]. Indeed, they have established as important generalizations of the SU(2) symmetric FH model to describe systems with, e.g., orbital degeneracy. In particular, $N > 2$ models are relevant to capture the essential physics of transition-metal oxides [404–406], the Kondo effect [407, 408] and heavy fermion compounds [71, 409], as well as single and twisted bilayer graphene [410–413].

In addition to novel magnetic states and enhanced quantum fluctuations, SU(N) symmetric models separate features that are linked in the vanilla SU(2) Hubbard model: perfect nesting and van Hove singularities at one particle per site are absent, in contrast to the SU(2) FH model,

see also the discussion in Sec. 2.2.2.

At unit filling $\langle \hat{n} \rangle = 1$, the SU(3) FH model has been shown to feature rich magnetic structures of various translation symmetry breaking patterns, where in particular finite repulsive interactions $U > 0$ are necessary to open a charge gap and observe magnetically ordered Mott insulating (MI) states [158, 162, 398, 399, 414]. This is in contrast to the SU(2) FH model, where metal-to-MI transitions are absent. In the strongly coupled regime of the SU(3) FH model, effective mappings to SU(3) Heisenberg models at $\langle \hat{n} \rangle = 1$ reveal a 3-sublattice (3-SL), diagonally striped magnetic order, stabilized by quantum fluctuations through an order by disorder mechanism [159, 415].

An important setting for the SU(N) FH model is ultracold alkaline-earth-atoms (AEAs), where a highly precise SU(N) symmetry arises from the near-perfect decoupling of nuclear spins from the electronic structure due to their closed shells [208, 416–419], as we discussed in Sec. 4.1.3 in more detail. Using fermionic isotopes of ^{87}Sr and ^{173}Yb, recent ultracold atom experiments have successfully observed Mott insulating states [58, 213, 214], nearest-neighbor (NN) antiferromagnetic correlations [59, 60], as well as measured the equation of state in the SU(6) FH model [61].

While the intricate magnetic structures of SU(N) Heisenberg magnets have been studied with increased interest [160, 161, 163–165], the physics of doped SU(N) Mott insulators remains widely unexplored. Studying doped Mott insulators with higher spin symmetries promises novel insights into the competition between spin and motional degrees of freedom, possibly helping to unravel the microscopic nature of hole pairing in strongly correlated electronic systems.

In this chapter, we take a first step in this direction: in Secs. 11.2 and 11.3, we utilize tensor network methods to study the undoped and singly doped SU(3) t-J model, the latter both in and out of equilibrium. We establish the appearence of magnetic polarons consisting of chargons and flavor defects (SU(3) spinons), whose dynamics is constrained to a single effective dimension along the ordered diagonal. We demonstrate how this sub-dimensional phenomenology is qualitatively captured within non-linear geometric string theory after including both chargon and spinon fluctuations of the magnetic polaron. Our results can be directly probed with ultracold AEAs paired with quantum gas microscopes with single-site resolution [420–422], paving the way towards exploring a wealth of exotic physics in doped SU(N) symmetric systems.

In Sec. 11.4, we will use the two-particle self-consistent theory to gain insights into the thermodynamic properties of the SU(N) FH model at one particle per site. After generalizing the TPSC equations to SU(N) symmetric systems, we apply them to compute relevant quantities such as the number of on-site pairs as a function of temperature. By comparing to determinant quantum Monte Carlo and RPA calculations, we establish that while (standard) TPSC can capture essential features of thermodynamic observables, it cannot capture the true SU(N) symmetric nature of the model.

This chapter is based on the results of a collaboration with Kaden Hazzard at Rice University. Special acknowledgments go to Kaden for his hospitality during my stay and for his continuous support beyond our collaboration. The following contents, along with the above introduction,

are based on the following publication, with partial textual overlap:

> [9] **HS**, F. Grusdt, U. Schollwöck, K. R. A. Hazzard, and A. Bohrdt. **Sub-dimensional magnetic polarons in the one-hole doped SU(3) t-J model**, Phys. Rev. B 110, 125134 (2024)

11.2 Magnetic order in the undoped system

Before analyzing the effect of doping, let us consider magnetic ordering in the undoped model. To this end, consider the SU(N) Heisenberg model,

$$\hat{\mathcal{H}} = \frac{J}{2}\sum_{\langle \mathbf{i},\mathbf{j}\rangle}\sum_{\alpha,\beta} |\mathbf{i}\alpha,\mathbf{j}\beta\rangle\langle \mathbf{i}\beta,\mathbf{j}\alpha| = \frac{J}{2}\sum_{\langle \mathbf{i},\mathbf{j}\rangle}\sum_{\alpha,\beta} \hat{\mathcal{P}}_{\mathrm{GW}}\hat{c}^{\dagger}_{\mathbf{i},\alpha}\hat{c}_{\mathbf{i},\beta}\hat{c}^{\dagger}_{\mathbf{j},\beta}\hat{c}_{\mathbf{j},\alpha}\hat{\mathcal{P}}_{\mathrm{GW}}. \tag{11.1}$$

The former Hamiltonain corresponds to the SU(N) Heisenberg model in first quantization, where indices $\alpha,\beta = 1\ldots N$ correspond to the flavor index. The Hamiltonian consists of exchange terms that swap the flavors of two adjacent sites $\mathbf{i},\mathbf{j}$. The factor of $1/2$ is added for reasons that become clear later on. In the latter formulation, we have introduced fermionic creation (annihilation) operators $\hat{c}^{\dagger}_{\mathbf{i},\alpha}$ ($\hat{c}_{\mathbf{i},\alpha}$) of flavor α on site $\mathbf{i}$, and $\hat{\mathcal{P}}_{\mathrm{GW}}$ is the Gutzwiller operator projecting out states with local occupancy > 1. From now on, we will focus on $N = 3$, and label the flavors as $\alpha = \{\mathrm{R},\mathrm{G},\mathrm{B}\}$. Furthermore, we define $\hat{n}^{\alpha}_{\mathbf{i}}$ as the local occupation number of flavor α at site $\mathbf{i}$.

In the following, we numerically implement the model using DMRG, on systems of size $L_x \times L_y = 9 \times 5$, and use open boundaries along both directions. We explicitly break the SU(3) symmetry of the Hamiltonian Eq. (11.1) by adding flavor-dependent pinning potentials along the (short) edges of the system. We choose the potential to pin a 3-sublattice (3-SL) structure of the spins, as has been established to correspond to the lowest energy state in previous works [415]. In particular, the Hamiltonian reads

$$\hat{\mathcal{H}} = \frac{J}{2}\sum_{\langle \mathbf{i},\mathbf{j}\rangle}\sum_{\alpha,\beta} \hat{\mathcal{P}}_{\mathrm{GW}}\hat{c}^{\dagger}_{\mathbf{i},\alpha}\hat{c}_{\mathbf{i},\beta}\hat{c}^{\dagger}_{\mathbf{j},\beta}\hat{c}_{\mathbf{j},\alpha}\hat{\mathcal{P}}_{\mathrm{GW}} - \mu_p \sum_{i\in\mathrm{edge}} \hat{n}^{\alpha_{\mathbf{i}}}_{\mathbf{i}}, \tag{11.2}$$

where $\alpha_{\mathbf{i}}$ is chosen such that it corresponds to a 3-SL order.

We now calculate the resulting magnetic order for varying pinning field strength. To this end, we evaluate on-site flavor occupations $\langle \hat{n}^{\alpha}_{\mathbf{i}}\rangle$ in the undoped Heisenberg model for $\mu_p/J = 0.5$ and $\mu_p/J = 1.0$. Fig. 11.1 shows the full occupations on the 9×5 lattice (left-hand side) as well as a cut through the central rung of the system (right-hand side). In both cases, clear spin-stripe ordering along the diagonals is visible, cf. the schematic illustration of spin-stripes in Fig. 2.4. Though directly at the boundaries (where the pinning field is finite) flavor occupations vary as μ_p/J is changed, in the bulk of the system they are indistinguishable. Hence, we conclude that the long-range order of the magnetic background and hence the physics of the magnetic polaron in the bulk is independent on the pinning strength—it is merely needed to break the SU(3) symmetry and pin the order.

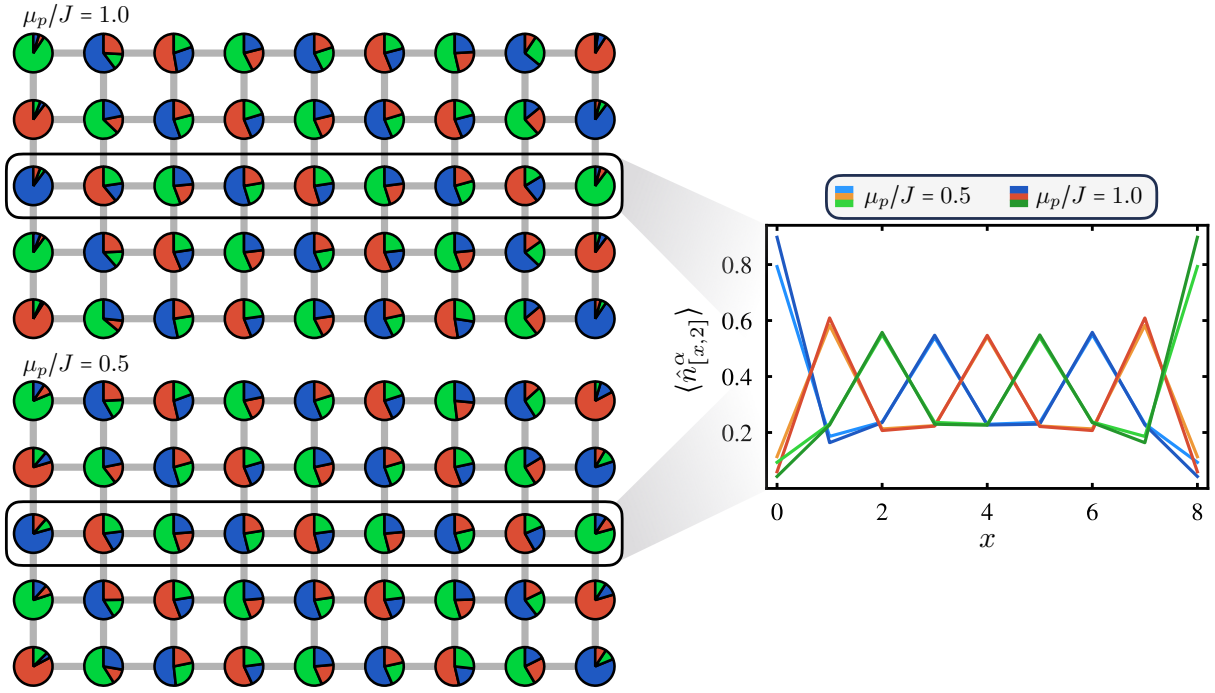

Figure 11.1: **Varying pinning field.** On-site flavor occupations $\langle \hat{n}^{\alpha}_{\mathbf{i}} \rangle$ in the undoped SU(3) symmetric Heisenberg model for $\mu_p/J = 0.5$ and $\mu_p/J = 1.0$, with OBCs. The colors in the pie diagram correspond to the flavors R (red), G (green), and B (blue). Full occupations are shown on the left-hand side, where the 3-SL order along the diagonals becomes evident. A cut through the central rung of the system is shown on the right-hand side. While at the boundaries occupations vary, the center of the system is independent on the pinning strength. Hence, while the applied fields pin the order, they do not influence the physics in the bulk.

11.2.1 Role of boundary conditions in the SU(3) Heisenberg model

In the above, we have focused on OBCs in both directions in our simulations. Indeed, we find that for the accessible system sizes OBCs are crucial to observe the three sublattice diagonal stripe order in the ground state of SU(3) Heisenberg model, consistent with what was mentioned in Ref. [415]. Fig. 11.2 (a) shows the on-site moments of the three flavors for a system of size $L_x \times L_y = 8, 6$ with periodic boundaries (PBC) applied along the short (y-) direction. Even with the applied pinning (shown in Fig. 11.2 for $\mu_p/J = 1$), the order rapidly disappears away from the boundaries. Moreover, we have carefully checked that full projections of real-space patterns do further not reveal any ordered state.

For the system widths considered here, the entanglement entropy reveals that the ground state converges to a state of weakly coupled 1D (periodic) chains, as shown in Fig. 11.2 (b). We conclude that the appearance of weakly coupled chains in periodic systems is an artifact of finite-size effects, and that we expect diagonal stripe order to appear when $L_y \gg 1$ becomes much larger—which is, however, not accessible with current numerical techniques. Therefore, in the following discussion of the doped SU(3) t-J model, we will keep OBCs in all our simulations.

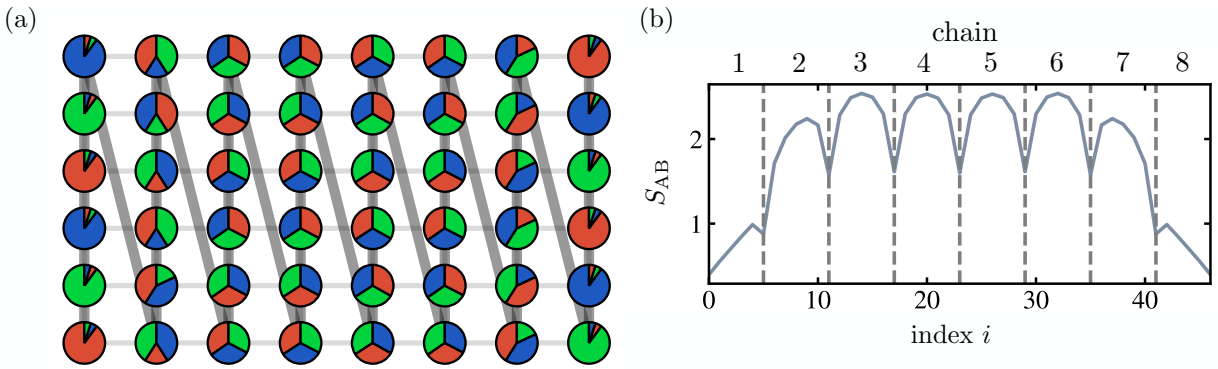

Figure 11.2: **Periodic boundary conditions.** On-site moments (a) and entanglement entropy (b) for a system of size $L_x \times L_y = 8 \times 6$ with periodic boundaries along the y-direction. Both boundaries pin the 3-SL diagonal order, with pinning strength $\mu_p/J = 1$. The site index in (b) indicates the border of the subsystem, following the standard snake indexing as illustrated by dark gray lines in (a). Both entanglement entropy and on-site moments imply the absence of magnetic order despite the applied pinning, and instead suggest the appearance of coupled 1D (periodic) chains.

11.3 The one-hole doped SU(3) t-J model

In the limit of strong on-site repulsion, the hole-doped 2D SU(3) symmetric FH model as realized by AEAs in sufficiently deep lattices at density $\langle n \rangle \leq 1$ reduces to the SU(3) symmetric t-J model on the square lattice. Neglecting three-site terms[1], the corresponding Hamiltonian reads

$$\hat{\mathcal{H}} = -t \sum_{\langle \mathbf{i},\mathbf{j}\rangle,\alpha} \hat{\mathcal{P}}_{GW} \left(\hat{c}^\dagger_{\mathbf{i},\alpha} \hat{c}_{\mathbf{j},\alpha} + \text{h.c.} \right) \hat{\mathcal{P}}_{GW} + \frac{J}{2} \sum_{\langle \mathbf{i},\mathbf{j}\rangle} \left(\sum_{\alpha,\beta} \hat{\mathcal{P}}_{GW} \hat{c}^\dagger_{\mathbf{i},\alpha} \hat{c}_{\mathbf{i},\beta} \hat{c}^\dagger_{\mathbf{j},\beta} \hat{c}_{\mathbf{j},\alpha} \hat{\mathcal{P}}_{GW} - \hat{n}_\mathbf{i} \hat{n}_\mathbf{j} \right). \tag{11.3}$$

where $\hat{n}_\mathbf{i}$ are the local particle densities given by $\hat{n}_\mathbf{i} = \sum_\alpha \hat{n}^\alpha_\mathbf{i}$.

We note that in the case of $N = 2$, Eq. (11.3) is equivalent to the standard t-J model without next-nearest neighbor terms,

$$\hat{\mathcal{H}} = -t \sum_{\langle \mathbf{i},\mathbf{j}\rangle,\alpha} \hat{\mathcal{P}}_{GW} \left(\hat{c}^\dagger_{\alpha,\mathbf{i}} \hat{c}_{\alpha,\mathbf{j}} + \text{h.c.} \right) \hat{\mathcal{P}}_{GW} + J \sum_{\langle \mathbf{i},\mathbf{j}\rangle} \left(\hat{S}^x_\mathbf{i} \hat{S}^x_\mathbf{i} + \hat{S}^y_\mathbf{i} \hat{S}^y_\mathbf{i} + \hat{S}^z_\mathbf{i} \hat{S}^z_\mathbf{i} - \frac{1}{4} \hat{n}_\mathbf{i} \hat{n}_\mathbf{j} \right). \tag{11.4}$$

Using $\hat{S}^\mu_\mathbf{i} = \frac{1}{2} \sum_{\alpha\alpha'} \hat{c}^\dagger_{\mathbf{i},\alpha} \sigma^\mu_{\alpha\alpha'} \hat{c}_{\mathbf{i},\alpha'}$ with σ^μ ($\mu = x, y, z$) the Pauli matrices, the second part of Eq. (11.4) reads

$$\begin{aligned} &\frac{J}{4} \sum_{\langle \mathbf{i},\mathbf{j}\rangle} (\hat{c}^\dagger_{\mathbf{i},\uparrow} \hat{c}_{\mathbf{i},\downarrow} + \hat{c}^\dagger_{\mathbf{i},\downarrow} \hat{c}_{\mathbf{i},\uparrow})(\hat{c}^\dagger_{\mathbf{j},\uparrow} \hat{c}_{\mathbf{j},\downarrow} + \hat{c}^\dagger_{\mathbf{j},\downarrow} \hat{c}_{\mathbf{j},\uparrow}) + (\hat{c}^\dagger_{\mathbf{i},\uparrow} \hat{c}_{\mathbf{i},\downarrow} - \hat{c}^\dagger_{\mathbf{i},\downarrow} \hat{c}_{\mathbf{i},\uparrow})(\hat{c}^\dagger_{\mathbf{j},\downarrow} \hat{c}_{\mathbf{j},\uparrow} - \hat{c}^\dagger_{\mathbf{j},\uparrow} \hat{c}_{\mathbf{j},\downarrow}) \\ &\quad + (\hat{c}^\dagger_{\mathbf{i},\uparrow} \hat{c}_{\mathbf{i},\uparrow} - \hat{c}^\dagger_{\mathbf{i},\downarrow} \hat{c}_{\mathbf{i},\downarrow})(\hat{c}^\dagger_{\mathbf{j},\uparrow} \hat{c}_{\mathbf{j},\uparrow} - \hat{c}^\dagger_{\mathbf{j},\downarrow} \hat{c}_{\mathbf{j},\downarrow}) - (\hat{c}^\dagger_{\mathbf{i},\uparrow} \hat{c}_{\mathbf{i},\uparrow} + \hat{c}^\dagger_{\mathbf{i},\downarrow} \hat{c}_{\mathbf{i},\downarrow})(\hat{c}^\dagger_{\mathbf{j},\uparrow} \hat{c}_{\mathbf{j},\uparrow} + \hat{c}^\dagger_{\mathbf{j},\downarrow} \hat{c}_{\mathbf{j},\downarrow}), \end{aligned} \tag{11.5}$$

[1] At low doping as considered here, three-site terms are expected to have only a minor effect on the appearing physics [423]. However, at finite doping, a systematic analysis of the terms may be necessary to draw direct connections to ultracold atom experiments.

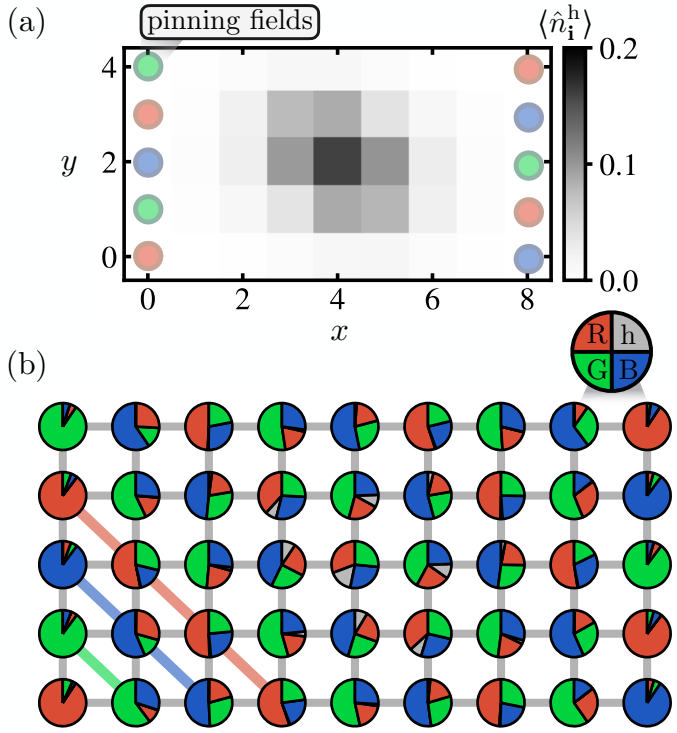

Figure 11.3: **Single hole ground state.** (a) DMRG results of the hole density distribution $\langle \hat{n}^h_{\mathbf{i}} \rangle$ for a single hole (missing red atom) doped into a magnetic background pinned at the edges (indicated by the colored circles along the edges), for a $L_x \times L_y = 9 \times 5$ system with open boundaries, $t/J = 1.5$, and pinning fields $\mu_p/J = 1$. The hole distribution is anisotropic, such that the hole spreads further along the diagonal spin stripes than perpendicular to them. The full on-site moment distributions $\langle \hat{n}^f_{\mathbf{i}} \rangle$, $f =$ h,R,G,B, are shown in gray, red, green and blue, respectively, in (b). The 3-SL diagonal stripe order pinned by the local chemical potentials on the boundaries is indicated by the solid colored lines in (b).

which can be rewritten to

$$\frac{J}{2} \sum_{\langle \mathbf{i},\mathbf{j} \rangle} \hat{c}^\dagger_{\mathbf{i},\uparrow} \hat{c}_{\mathbf{i},\downarrow} \hat{c}^\dagger_{\mathbf{j},\downarrow} \hat{c}_{\mathbf{j},\uparrow} + \hat{c}^\dagger_{\mathbf{i},\downarrow} \hat{c}_{\mathbf{i},\uparrow} \hat{c}^\dagger_{\mathbf{j},\uparrow} \hat{c}_{\mathbf{j},\downarrow} + \hat{c}^\dagger_{\mathbf{i},\uparrow} \hat{c}_{\mathbf{i},\uparrow} \hat{c}^\dagger_{\mathbf{j},\uparrow} \hat{c}_{\mathbf{j},\uparrow} + \hat{c}^\dagger_{\mathbf{i},\downarrow} \hat{c}_{\mathbf{i},\downarrow} \hat{c}^\dagger_{\mathbf{j},\downarrow} \hat{c}_{\mathbf{j},\downarrow} - (\hat{n}_{\mathbf{i},\uparrow} \hat{n}_{\mathbf{j},\downarrow} + \hat{n}_{\mathbf{i},\downarrow} \hat{n}_{\mathbf{j},\uparrow} + \hat{n}_{\mathbf{i},\uparrow} \hat{n}_{\mathbf{j},\uparrow} + \hat{n}_{\mathbf{i},\downarrow} \hat{n}_{\mathbf{j},\downarrow}). \tag{11.6}$$

This , in turn, corresponds to the interaction term in Eq. (11.3).

11.3.1 Ground state

We simulate the ground state of the one-hole doped SU(3) t-J model, Eq. (11.3), using DMRG. For a single hole, the density-density interaction in Eq. (11.3) merely leads to a constant energy shift (up to boundary effects) and is neglected in the following. We implement separate U(1) particle conservation symmetries for each flavor, and simulate systems of size $L_x \times L_y = 9 \times 5$. As discussed in Sec. 11.2, we focus on OBC along both x- and y- directions in the following. As in the undoped scenario, by introducing local chemical potentials $-\mu_p \sum_{i \in \mathrm{edge}} \hat{n}^{\alpha_i}_{\mathbf{i}}$ at the short edges of the system, we explicitly break the SU(3) symmetry and pin a 3-sublattice (3-SL) stripe order

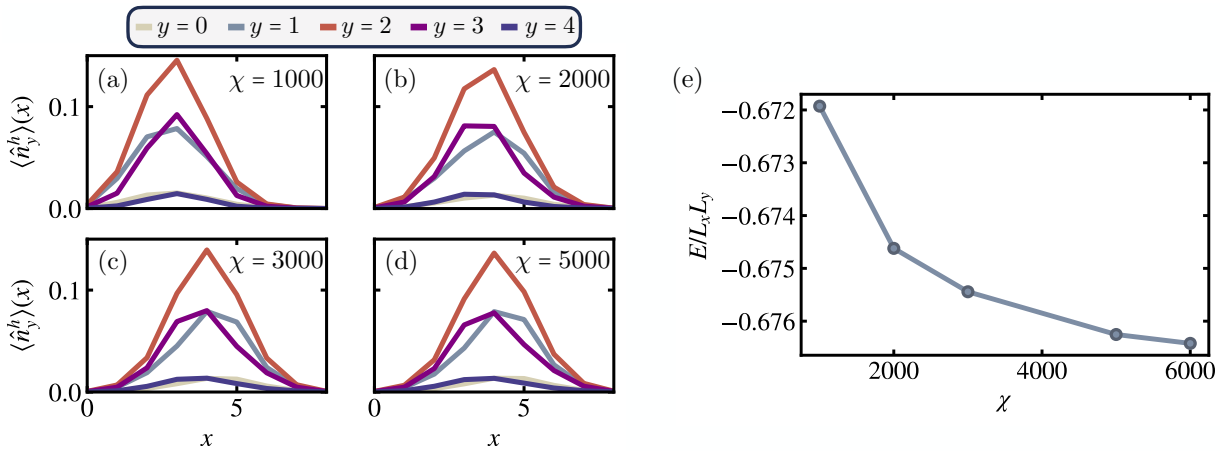

Figure 11.4: **Ground state DMRG convergence.** Hole densities $n_y^h(x)$ for horizontal cuts $y = 0,\ldots,4$ and bond dimensions $\chi = 1000$ (a), $\chi = 2000$ (b), $\chi = 3000$ (c) and $\chi = 5000$ (d). Convergence is reached for $\chi > 3000$. (e) Convergence of the energy per site, $\mathrm{E}/(L_x L_y)$, as a function of bond dimension. Between $\chi = 5000$ and $\chi = 6000$, the relative difference in energies is of the order of a tenth of a percent.

along the diagonal, indicated by colored lines in Fig. 11.3 (a). We here fix $\mu_p/J = 1$; however, as discussed in Sec. 11.2, magnetic correlations are independent of the pinning potential in the bulk of the system. We introduce a single hole into the system by removing a particle corresponding to the flavor of the central site $\mathbf{i}_0$ in a (classically) ordered background. For the pinning shown in Fig. 11.3, this corresponds to the symmetry sector $N_\mathrm{G} = N_\mathrm{B} = L_x L_y/3$, $N_\mathrm{R} = L_x L_y/3 - 1$, where N_α is the total particle number of flavor $\alpha = \mathrm{R}$ (red), G (green), B (blue).

The hole density distribution of the ground state determined by DMRG, $\langle \hat{n}_\mathbf{i}^h \rangle = 1 - \sum_\alpha \langle \hat{n}_\mathbf{i}^\alpha \rangle$, is shown in Fig. 11.3 (a) for $t/J = 1.5$. The hole density features a pronounced anisotropy, whereby its distribution has enhanced weight on the diagonals aligning with the pinned order. On the other hand, the hole density is suppressed on the anti-diagonals, i.e, directions that are perpendicular to the 3-SL order. This is corroborated in Fig. 11.3 (b), where the full on-site moments $\langle \hat{n}_\mathbf{i}^f \rangle$, for $f = \mathrm{h}$ (hole), R (red), G (green) and B (blue) are shown. Importantly, the delocalization of the hole only slightly disturbs the magnetic background in its vicinity, leaving the overall 3-SL order intact, as illustrated by the solid colorful lines in the lower left corner of Fig. 11.3 (b).

Before proceeding to describe the single hole in the 3-SL background using non-linear string theory, let us look at the convergence of the ground state results in Fig. 11.3. Fig. 11.4 (a)-(d) shows the hole densities along horizontal cuts of the system with $t/J = 3$ for increasing bond dimension $\chi = 1000,\ldots,5000$. We observe convergence of the local hole density for bond dimensions $\chi > 3000$, and use $\chi = 5000$ throughout the calculations shown in the main text. Similarly, we observe convergence of the energy per site with increasing bond dimension, shown in Fig. 11.4 (e).

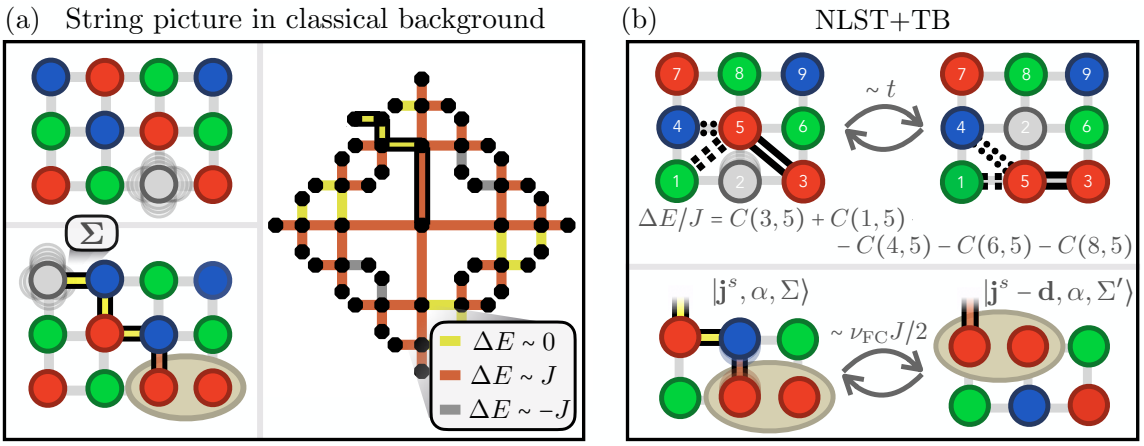

Figure 11.5: **Non-linear string theory.** (a) Illustration of hole motion through a classically ordered SU(3) background. When hopping, the hole leaves behind a string Σ of displaced spins. The first hop is confining due to positive spin-spin correlations along the diagonal – leading to the formation of a spinon, see the ocher ellipse in the lower left panel. Subsequent hops along the diagonals, however, lead to classically degenerate configurations and paths of no additional energy cost (yellow). The full energy landscape is illustrated on the Bethe lattice in the right panel. (b) We describe chargon fluctuations within the FSA. String state energies are determined by a sum of particle exchange correlations $C(\mathbf{i},\mathbf{j})$ of the undoped ground state, where $\mathbf{i},\mathbf{j}$ become neighbors after the hole is displaced through the string (upper panel). Spinon fluctuations are included by considering dominant off-diagonal couplings (lower panel), leading to an effective 1D spinon Hamiltonian on the diagonal.

11.3.2 Geometric string theory

In the following, we describe the doped hole in the 3-SL background using non-linear geometric string theory (NLST) [265, 302] and establish the formation of a sub-dimensional magnetic polaron whose motion is predominantly aligned with the ordered background. The starting point is a parton representation of the SU(3) t-J model, where the creation and annihilation operators are decomposed into bosonic chargons ($\hat{h}_\mathbf{i}$) and fermionic spinons ($\hat{f}_{\mathbf{i},\alpha}$),

$$\hat{c}_{\mathbf{i},\alpha} = \hat{h}^\dagger_\mathbf{i} \hat{f}_{\mathbf{i},\alpha}. \tag{11.7}$$

The spinon label α corresponds to the flavor of the particle that has been removed. The single occupancy constraint in the t-J model is ensured via $\sum_\alpha \hat{f}^\dagger_{\alpha,\mathbf{i}} \hat{f}_{\alpha,\mathbf{i}} + \hat{h}^\dagger_\mathbf{i} \hat{h}_\mathbf{i} = 1$ for all $\mathbf{i}$.

We describe the magnetic polaron within the geometric string basis: By doping a single hole at position $\mathbf{j}^s$ into the ground state $|\Psi_0\rangle$ of the undoped SU(3) Heisenberg Hamiltonian, we define the state

$$|\mathbf{j}^s, \alpha, \Sigma = 0\rangle = \hat{c}_{\alpha,\mathbf{j}^s} |\Psi_0\rangle . \tag{11.8}$$

To describe the partons, we work in the regime $t/J \gg 1$, where fluctuations of the chargon and the ordered background approximately decouple. In a first step, we fix the initial hole position $\mathbf{j}^s$, and describe the fast chargon fluctuations on time scales $\sim 1/t$. Motivated by the separation of energy scales, we work in the frozen spin approximation (FSA): When the hole fluctuates,

the background spins are displaced and their positions change, however their quantum state is assumed to remain unaffected. This generalizes the notion of squeezed space [236, 237, 288] to two dimensions. By displacing particles in real space, the hole motion changes the underlying geometry of the lattice in squeezed space, whereby nearest neighbor (NN) pairs in squeezed space can become next-nearest neighbor (NNN) or even larger-distance pairs. String states are defined by

$$|\mathbf{j}^s, \alpha, \Sigma\rangle = \hat{G}_\Sigma \, |\mathbf{j}^s, \alpha, \Sigma = 0\rangle \,, \tag{11.9}$$

where the string operator

$$\hat{G}_\Sigma = \prod_{\langle \mathbf{i},\mathbf{j}\rangle \in \Sigma} \left(\hat{h}^\dagger_\mathbf{i} \hat{h}_\mathbf{j} \sum_\alpha \hat{f}^\dagger_{\mathbf{j},\alpha} \hat{f}_{\mathbf{i},\alpha} \right) \tag{11.10}$$

displaces the background spins along string Σ.

The string states and the tunnel coupling between them can be mapped to a Bethe lattice, illustrated in Fig. 11.5 (a) for a classical spin background. In particular, each string of displaced particles Σ can be associated with a corresponding potential energy on the Bethe lattice, $E(\mathbf{j}^s, \Sigma)$[2]. Alignment of flavors along the diagonals surrounding the hole leads to an energy penalty $\Delta E \sim J$ when the hole leaves its initial position and moves by one lattice site, leaving behind a flavor defect (spinon) at $\mathbf{j}^s$ (see the ocher ellipse in the lower left panel of Fig. 11.5 (a)). After its initial hop, however, the energy landscape for subsequent chargon motion loses its isotropy. In particular, paths along the diagonally ordered background merely lead to local flavor exchanges along the string, which is classically degenerate with the initial 3-SL order. This, in turn, leads to the existence of string segments of no additional energy cost, illustrated by yellow paths on the Bethe lattice in the right panel of Fig. 11.5 (a). Directions perpendicular to the diagonal stripe order, in contrast, are associated with linearly growing magnetic energy (linear confinement), shown by red paths in Fig. 11.5 (a). Negative energy differences (gray lines) result from loop effects.

In the case of a classical background, string states $|\mathbf{j}^s, \alpha, \Sigma\rangle$ are mutually orthonormal except for special loop configurations which restore the ordered background, known as Trugman loops [424]. In the case of a (classical) diagonally striped background, these configurations involve at least 12 string segments (corresponding to three loops around a square plaquette), and are hence negligible compared to the exponential number of string states. Due to strong diagonal-order correlations in the undoped SU(3) t-J model (see Sec. 11.2), we expect that the approximation of mutual orthonormality of string states remains accurate away from the classical limit.

We include quantum fluctuations in two stages: First, we describe fluctuations of the chargon moving in a frozen spin background. In a second step, we include fluctuations of the spinon through a tight-binding description. The formalism is summarized in Fig. 11.5 (b) and explained in detail in the following.

[2]Note that in the SU(2) case, where the background is ordered according to a 2-SL structure, all directions are equally confining, i.e., the string energy only depends on the absolute length of the string, $E(\Sigma) = E(|\Sigma|)$.

Chargon motion

Our first step to go beyond the classically ordered magnetic background is to use the FSA: Upon creation of the hole, the background spins are labeled according to their original positions. When the hole moves, the particles are displaced and their positions change, resulting in energies $E(\mathbf{j}^s, \Sigma)$ of string states $|\mathbf{j}^s, \alpha, \Sigma\rangle$. The crucial ingredient in order to describe fluctuations of the chargon around its initial position $\mathbf{j}^s$ within NLST are magnetic correlations of the undoped system,

$$C(\mathbf{i}, \mathbf{j}) = \sum_{\alpha,\beta} \langle \Psi_0 | \hat{\mathcal{P}}_{GW} \hat{c}^\dagger_{\alpha,\mathbf{i}} \hat{c}_{\beta,\mathbf{i}} \hat{c}^\dagger_{\beta,\mathbf{j}} \hat{c}_{\alpha,\mathbf{j}} \hat{\mathcal{P}}_{GW} | \Psi_0 \rangle \, /2, \tag{11.11}$$

where $|\Psi_0\rangle$ is the ground state with one particle per site. Fig. 11.6 shows correlations for a fixed reference site $\mathbf{i} = [x = 4, y = 2]$ in the center of the finite-size system we study with DMRG. Following the 3-SL order of the ground state, sites are correlated positively along every third diagonal; nearest neighbor correlations, in contrast, show strong negative signals. When a hole is added at initial position $\mathbf{j}^s$ and then hops away, assuming a frozen spin background it reshuffles the particles in its vicinity, leading to an energy cost that can directly be evaluated from correlations given by Eq. (11.11).

For instance, if a hole initially placed in the center $\mathbf{j}^s = [4, 2]$ moves up by one lattice site, the corresponding change in magnetic energy is given by (see also Fig. 11.5) $\Delta E/J = C(\mathbf{i} = [3, 2], \mathbf{j} = [4, 3]) + C(\mathbf{i} = [5, 2], \mathbf{j} = [4, 3]) + C(\mathbf{i} = [4, 1], \mathbf{j} = [4, 3]) - C(\mathbf{i} = [4, 4], \mathbf{j} = [4, 3]) - C(\mathbf{i} = [5, 3], \mathbf{j} = [4, 3]) - C(\mathbf{i} = [3, 3], \mathbf{j} = [4, 3]) = 0.97$. Using correlations Eq. (11.11), all energies on the Bethe lattice are calculated this way, depicted in Fig. 11.6 (b) for $\mathbf{j}^s = [4, 2]$. Note that this includes the effect of open boundary conditions within NLST: if the hole moves outside the finite system's frame, the site is cut off from the Bethe lattice (in Fig. 11.6 (b), a Bethe lattice depth of $d = 3$ is considered. The two sites corresponding to strings [up, up, up] and [down, down, down] lie outside the frame and are thus cut off). Energies of string configurations (diagonal matrix elements of a string configuration with itself) using the system's correlations follow the structure of a classical background as illustrated in Fig. 11.5 (a), whereby string energies along the diagonal are lower compared to other paths.

The Hamiltonian of the chargon for an initial hole position $\mathbf{j}^s$ is then expressed within the geometric string basis on the Bethe lattice,

$$\begin{aligned} \hat{\mathcal{H}}_{\text{charge}}(\mathbf{j}^s, \alpha) = -t \sum_{\langle \Sigma, \Sigma' \rangle} & |\mathbf{j}^s, \alpha, \Sigma\rangle \langle \mathbf{j}^s, \alpha, \Sigma'| + \text{ h.c.} \\ & + \sum_{\Sigma} E(\mathbf{j}^s, \Sigma) \, |\mathbf{j}^s, \alpha, \Sigma\rangle \langle \mathbf{j}^s, \alpha, \Sigma| \, . \end{aligned} \tag{11.12}$$

The Hamiltonian Eq. (11.12) is diagonalized, yielding

$$|\Psi_{\text{charge}}(\mathbf{j}^s, \alpha)\rangle = \sum_{\Sigma} \psi^{\text{charge}}_{\mathbf{j}^s, \Sigma} \, |\mathbf{j}^s, \alpha, \Sigma\rangle \, , \tag{11.13}$$

as its ground state with eigenenergy $E^0_{\text{charge}}(\mathbf{j}^s)$. Mapping the hole density back to real space, $\langle \hat{n}^h_{\mathbf{j}} \rangle = \sum_{\Sigma \in Q_{\mathbf{j}}} |\psi^{\text{charge}}_{\mathbf{j}^s, \Sigma}|^2$ where $Q_{\mathbf{j}}$ is the set of paths leading from a hole initially at $\mathbf{j}^s$ to be located

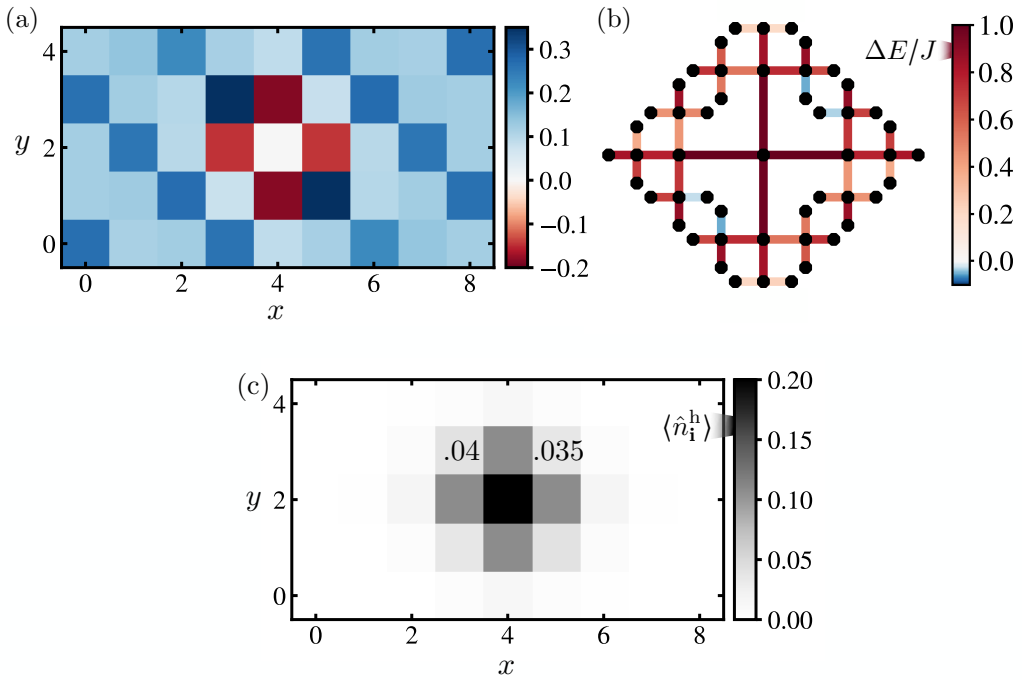

Figure 11.6: **Chargon fluctuations within NLST.** (a) Correlations $C(\mathbf{i}, \mathbf{j})$, Eq. (11.11), for a fixed reference site $\mathbf{i} = [4, 2]$ calculated with DMRG with the same pinning fields as described in the main text. These correlations are the essential ingredient for calculating the energy of string states on the Bethe lattice, presented for lattice depth $d = 3$ in (b). The structure follows the classical picture illustrated in Fig. 11.5 (a) in the main text. Finite size effects are taken into account by cutting off sites on the Bethe lattice that do not lie within the finite system's frame. (c) Density distribution in real space after diagonalizing the hopping Hamiltonian on the Bethe lattice, Eq. (11.12). Though the anisotropic energy distribution on the Bethe lattice leads to slightly larger hole densities on the diagonals compared to the anti-diagonals, differences are small (see the numerical values).

at $\mathbf{j}$, results in the density distribution shown in Fig. 11.6 (c) for $\mathbf{j}^s = [4, 2]$. Though the anisotropic energy distribution on the Bethe lattice leads to slightly larger hole densities on the diagonals compared to the anti-diagonals, differences are small (see the numerical values in Fig. 11.6 (c)).

Comparing the result to the densities as acquired from DMRG calculations (Fig. 11.3), this suggests that the magnetic polaron itself (built up from fast chargon fluctuations centered around the fixed spinon) is only slightly influenced by the anisotropic energies on the Bethe lattice, but instead the motion of the composite chargon-spinon object induces the observed anisotropy.

Spinon fluctuations

In the following we demonstrate that is the effect of spinon fluctuations on time scales $\propto 1/J$ that lead to the observed alignment along the diagonal in Fig. 11.3 (a), which we include on top of chargon fluctuations by using a tight-binding description of spinon motion (NLST+TB). Concretely, we consider off-diagonal couplings $J_s(\mathbf{j}^s, \mathbf{j}^{s'}; \Sigma, \Sigma') = \langle \mathbf{j}^{s'}, \alpha, \Sigma' | \hat{\mathcal{H}} | \mathbf{j}^s, \alpha, \Sigma \rangle$ within the geometric string basis construction to describe spinon fluctuations. In the case of the SU(2) symmetric t-J model, major contributions are given by next-nearest neighbor (NNN) spinon hopping

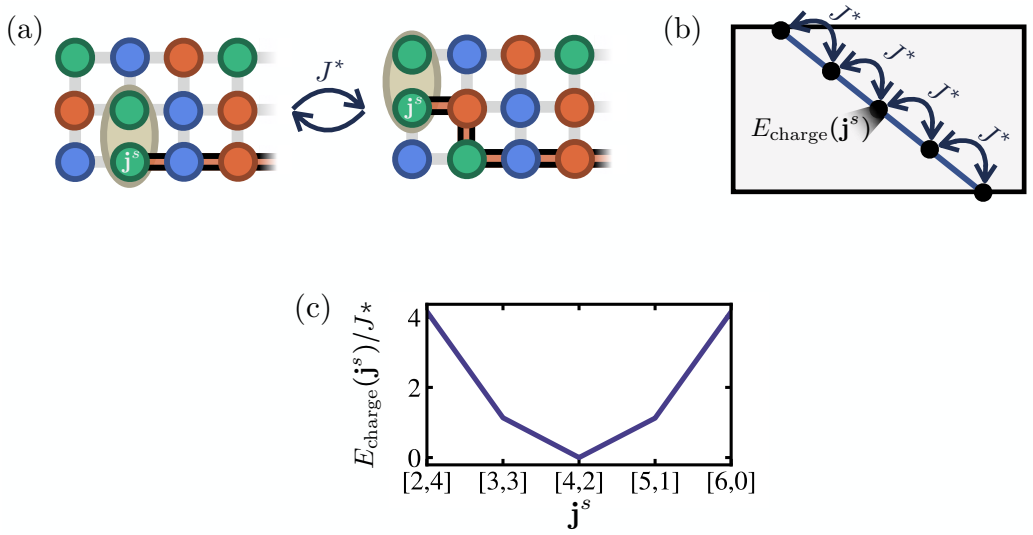

Figure 11.7: **Spinon tight-binding description.** Exchange processes as appearing in the Hamiltonian of the SU(3) t-J model lead to hopping processes of the spinon, as illustrated in (a). Dominant contributions come from diagonal spinon hopping events, (b), resulting in a string state $|\Sigma', \mathbf{j}^s + \mathbf{d}\rangle$ of length $|\Sigma'| = |\Sigma| \pm 2$. The on-site energy $E_{\text{charge}}(\mathbf{j}^s)$ defines an effective potential seen by the spinon, (c), here shown for $\nu_{\text{FC}} = 0.1$.

processes isotropically in all spatial directions. In contrast, in the SU(3) t-J model, dominant contributions are restricted to diagonal NNN spinon hopping processes along the 3-SL order. This is owing to the Hamiltonian's $\text{U}(1)^{\otimes \text{N}}$ particle conservation symmetry: applying $\hat{\mathcal{H}}$ to string states $|\mathbf{j}^s, \alpha, \Sigma\rangle$ conserves the flavor of the removed particle α.

Fig. 11.7 (a) illustrates the process. For a given string configuration $|\mathbf{j}^s, \alpha = \text{R}, \Sigma\rangle$, exchange of two neighboring particles (here given by the green and red flavors at the left edge of the central leg) leads to a string configuration $|\mathbf{j}^s - \mathbf{e}_x + \mathbf{e}_y, \alpha = \text{R}, \Sigma'\rangle$, with a resulting string length $|\Sigma'| = |\Sigma| + 2$ and unit vectors $\mathbf{e}_x, \mathbf{e}_y$. More generally, the Hamiltonian couples off-diagonal string states $\langle \mathbf{j}^s, \alpha, \Sigma | \hat{\mathcal{H}} | \mathbf{j}^s \pm \mathbf{d}, \alpha, \Sigma' \rangle$ with $|\Sigma'| = |\Sigma| \pm 2$ and $\mathbf{d} = \mathbf{e}_x - \mathbf{e}_y$ pointing along the diagonal stripe order, see also Fig. 11.5 (b).

Owing to the finite overlap of string states with different initial hole positions $\mathbf{j}^s$, the effective spinon hopping is given by

$$J^*(\mathbf{j}^s, \mathbf{j}^{s'}) = \sum_{\Sigma,\Sigma'} J_s(\mathbf{j}^s, \mathbf{j}^{s'}; \Sigma, \Sigma') \psi^{\text{charge}*}_{\mathbf{j}^{s'},\Sigma'} \psi^{\text{charge}}_{\mathbf{j}^s,\Sigma}. \tag{11.14}$$

In the classical limit and for large system sizes, $J_s(\mathbf{j}^s, \mathbf{j}^{s'}, \Sigma, \Sigma') = J/2$ if a single particle exchange relates the two string states $|\mathbf{j}^s, \alpha, \Sigma\rangle$ and $|\mathbf{j}^{s'}, \alpha, \Sigma'\rangle$. As the exact evaluation of $J_s(\mathbf{j}^s, \mathbf{j}^{s'}, \Sigma, \Sigma')$ is cumbersome, we approximate $J^*(\mathbf{j}^s, \mathbf{j}^{s'}) \approx \nu_{\text{FC}} J/2$, where we treat the Franck-Condon factor ν_{FC} as an effective fit parameter of the geometric string theory. In the limit of weak coupling, $t \ll J$, the Franck-Condon factor approaches $\nu_{\text{FC}} = 0$. In the strong coupling regime, $t \gg J$, $\nu_{\text{FC}} \to 0.5$ [302].

We model diagonal hopping of the heavy polaron by an effectively 1D tight-binding system, with hopping parameter $J^* = \nu_{\text{FC}} J/2$ and on-site energies $E^0_{\text{charge}}(\mathbf{j}^s)$ calculated via NLST, with

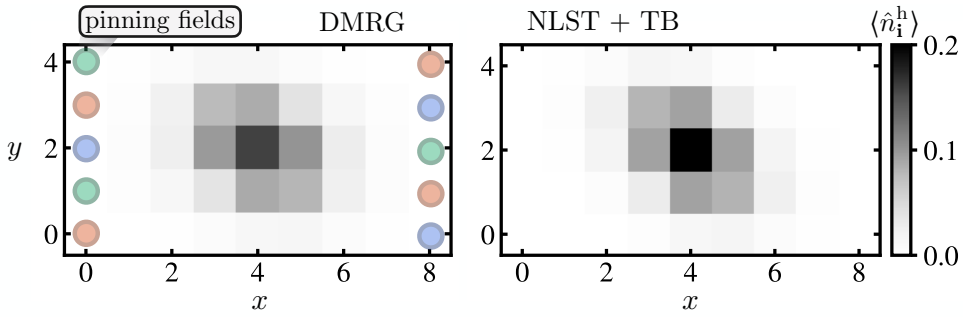

Figure 11.8: **DMRG and non-linear string theory.** The resulting hole density distribution when including both chargon and spinon fluctuations in the NLST ansatz with $\nu_{\mathrm{FC}} = 0.1$ matches DMRG results remarkably well. DMRG results are the same as in Fig. 11.3.

$\mathbf{j}^s$ lying on the diagonal $\mathcal{D}$ that includes the central site—illustrated in Fig. 11.7 (b) and (c). The Hamiltonian is given by

$$\hat{\mathcal{H}}_{\mathrm{spinon}} = J^* \Big(\sum_{\langle \mathbf{i},\mathbf{j} \rangle \in \mathcal{D}} c_{\mathbf{i}}^\dagger c_{\mathbf{j}} + \mathrm{h.c.} \Big) + \sum_{\mathbf{j} \in \mathcal{D}} E^0_{\mathrm{charge}}(\mathbf{j}) c_{\mathbf{j}}^\dagger c_{\mathbf{j}}, \tag{11.15}$$

yielding coefficients $\psi^{\mathrm{spinon}}_{\mathbf{j}^s}$ for spinon positions $\mathbf{j}^s$. We note that, as both ν_{FC} and J are positive, the effective spinon hopping is positive, $J^* > 0$, resulting in a dispersion minimum of the spinon at $k = \pi$ reminiscent to 2D quantum magnets [238, 302]. Finally, we combine charge and spinon parts by a plane-wave ansatz, arriving at

$$|\Psi\rangle = \sum_{\mathbf{j}^s \in \mathcal{D}} \psi^{\mathrm{spinon}}_{\mathbf{j}^s} |\Psi_{\mathrm{charge}}(\mathbf{j}^s, \alpha)\rangle = \sum_{\mathbf{j}^s \in \mathcal{D}} \psi^{\mathrm{spinon}}_{\mathbf{j}^s} \sum_{\Sigma} \psi^{\mathrm{charge}}_{\mathbf{j}^s,\Sigma} |\mathbf{j}^s, \alpha, \Sigma\rangle \,. \tag{11.16}$$

The total hole distribution is given by a weighed sum with coefficients $|\psi^{\mathrm{spinon}}_{\mathbf{j}^s}|^2$ of hole distributions $|\psi^{\mathrm{charge}}_{\mathbf{j}^s,\Sigma}|^2$ for each mean chargon position $\mathbf{j}^s$, i.e., it is determined by mapping $|\psi^{\mathrm{spinon}}_{\mathbf{j}^s} \psi^{\mathrm{charge}}_{\mathbf{j}^s,\Sigma}|^2$ back to the original real space lattice.

We note again that we treat ν_{FC} as an effective free parameter of the theory, matching DMRG results strikingly well for $\nu_{\mathrm{FC}} = 0.1$, see Fig. 11.8. This agreement corroborates the validity of NLST+TB, and supports the existence of a sub-dimensional magnetic polaron in the singly doped SU(3) t-J model. Additional DMRG simulations presented in Fig. 11.9 further support this picture, whereby the anisotropy in the hole density is seen to increase for rising exchange interactions J/t, while a dominating hopping $J/t \ll 1$ leads to the formation of a broad, isotropic polaron cloud. Lastly, we note that while the Hilbert space spanned by the string states grows exponentially, a systematic cutoff of chargon states far away from their initial position on the Bethe lattice allows for an efficient calculation of hole density distributions. This ultimately allows us to make concrete comparisons between the phenomenological geometric string theory and finite-size numerical calculations. While the latter is only possible for small system sizes, our effective description provides strong evidence that the qualitative influence of the magnetic structure on the polaron distribution survives in the thermodynamic limit. This is further corroborated by large-scale calculations of the SU(3) FH model at one particle per site, which establish that the

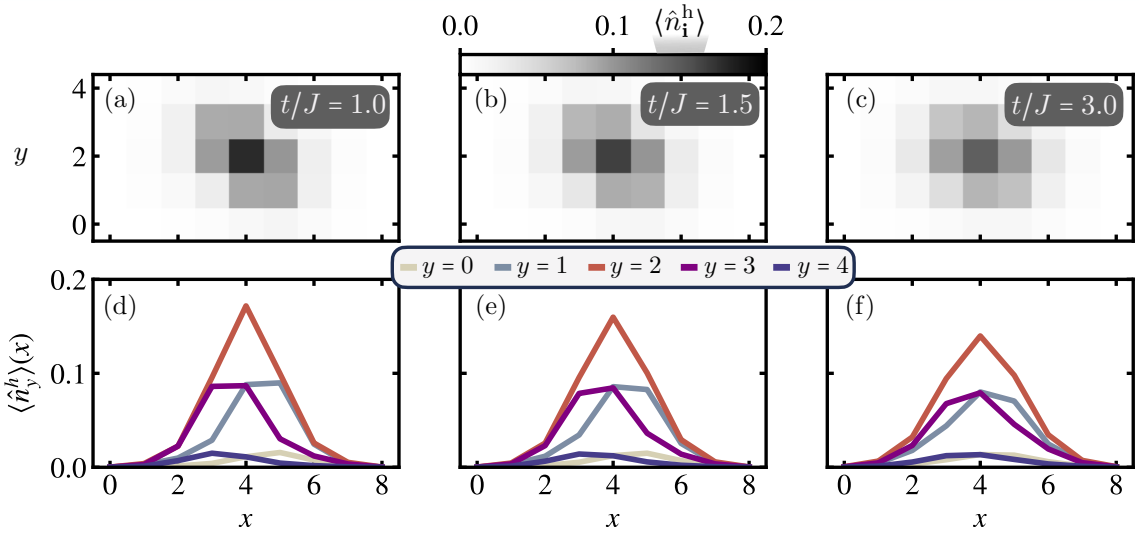

Figure 11.9: **Varying t/J.** (a)-(c) 2D hole density distributions for $t/J = 1.0, 1.5, 3.0$, respectively, calculated with DMRG for $L_x \times L_y = 9 \times 5$ systems with OBC. (d)-(f) Hole densities along the x-direction, for each of the five legs. When increasing t/J (i.e. increasing the ratio of hole fluctuations compared to magnetic coupling strength), the anisotropy in the density is observed to monotonously decrease.

magnetic order is present also in large systems [162].

11.3.3 Dynamics

To further study the behavior of the magnetic polaron in the SU(3) t-J model, we analyze quenched hole dynamics, which is particularly accessible to ultracold atom experiments and has been probed for a single hole doped into an SU(2) AFM background [44]. Specifically, we analyze the hole's dynamics after doping it in the center $\mathbf{i}_0$ of the undoped ground state, i.e., at time $T = 0$, the initial state is $|\Psi(T = 0)\rangle = |\mathbf{i}_0, \alpha, \Sigma = 0\rangle$. We note that global Krylov schemes have trouble in capturing the fast entanglement growth of the charge sector (while the entanglement in the spin sector is large already in the initial state). Global subspace expansion methods [185] show much better convergence[3], which we use for a single time step before switching to TDVP calculations. During the time evolution, we track the Manhattan distance $\langle \hat{x}_m \rangle$ from $\mathbf{i}_0$ along the diagonal and anti-diagonal.

At short times, fast chargon fluctuations lead to a symmetric, ballistic expansion of the hole, see Fig. 11.10. At times $Tt \sim 1$, a rapid slow down and apparent saturation of the hole's spread is observed, reminiscent of dynamics in the SU(2) t-J model [44, 425–427]. Here, it has been established that the hole's long-time dynamics is governed by spinon dynamics, i.e., by the motion of the heavy composite magnetic polaron itself. The strong splitting between diagonal and anti-diagonal distances appearing in the SU(3) system at times $Tt \sim 1$, shown in Fig. 11.10, further underlines the role of spinon delocalization in the observed anisotropy.

Fig. 11.11 shows the dynamics presented in Fig. 11.10 for the various bond dimensions. Along

[3] We choose a Krylov subspace order of 3, time steps $\Delta TJ = 0.02$, and bond dimensions $\chi_{\max} = 5000$.

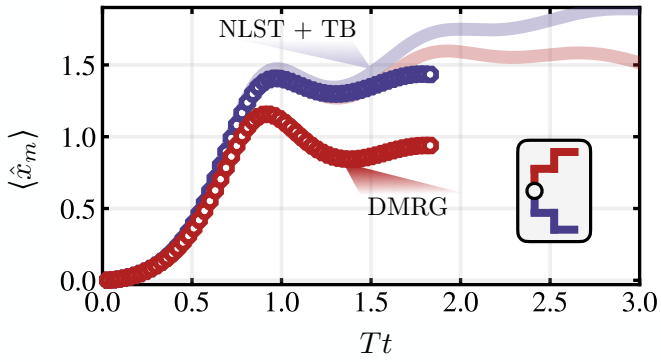

Figure 11.10: **Hole dynamics.** Time evolution of an initially localized hole at $\mathbf{i}_0 = [4, 2]$. Mean Manhattan distances along the diagonal (anti-diagonal) are shown in blue (red) for a $L_x \times L_y = 9 \times 5$ system. Light red and blue lines show NLST+TB results for an infinite system with $\nu_{\mathrm{FC}} = 0.5$.

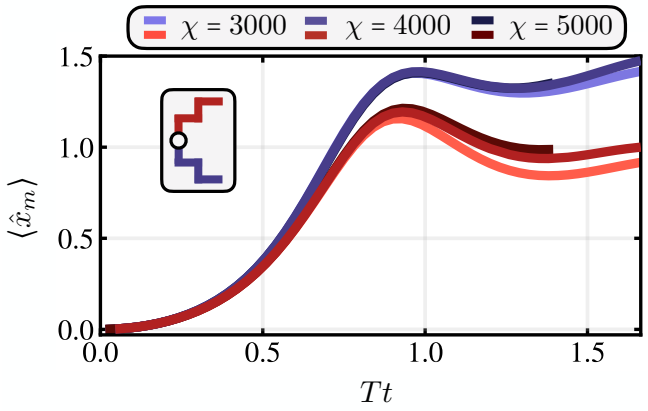

Figure 11.11: **Convergence of DMRG dynamics.** Mean Manhattan distances along the diagonal and anti-diagonal in a $L_x \times L_y = 9 \times 5$ system with $t/J = 1.5$ as a function of time, for maximum bond dimensions $\chi = 3000, 4000, 5000$. While the mean Manhattan distance converges along the diagonal, slight differences between $\chi = 4000$ and $\chi = 5000$ are seen along the anti-diagonal. Nevertheless, the dynamical formation of the sub-dimensional magnetic polaron that leads to the appearance of the anisotropy at early times is identical for all bond dimensions.

the diagonal, the mean Manhattan distance is seen to converge up to times $Tt \sim 1.3$. Minor deviations between bond dimensions $\chi = 4000$ and $\chi = 5000$ are visible starting from times $Tt \sim 1.0$ along the anti-diagonal. Nevertheless, the early time dynamics including the dynamical appearance of the anisotropy between the diagonal and anti-diagonal mean distances is well converged.

We describe the dynamics of the magnetic polaron within geometric string theory by again assuming a product state ansatz with effective Hamiltonian

$$\hat{\mathcal{H}}_{\mathrm{eff}} = \hat{\mathcal{H}}_{\mathrm{charge}} + \hat{\mathcal{H}}_{\mathrm{spinon}}, \tag{11.17}$$

such that dynamical properties are evaluated by calculating $\exp\left(-i\hat{\mathcal{H}}_{\mathrm{eff}}T\right)|\mathbf{j}^s, \alpha, \Sigma = 0\rangle$; here, $\hat{\mathcal{H}}_{\mathrm{spinon}}$ only acts on the spinon degree of freedom $|\mathbf{j}^s\rangle$, whereas $\hat{\mathcal{H}}_{\mathrm{charge}}$ generates chargon dy-

namics for a given spinon position. As the MPS calculations are limited to small system sizes with OBC, we here focus on infinite systems (i.e. we do not consider the open boundaries when constructing the string basis) to make predictions of the dynamical formation and motion of the polaron in the thermodynamic limit.

Results are shown in Fig. 11.10 with blue and red solid lines, where all qualitative features are in line with finite-size MPS simulations. At short times we find quantitative agreement. However, the anisotropy developing later in time is seen to be underestimated within the string theory, which is likely caused by significant finite size effects in the MPS dynamics (being particularly prominent as we are focusing on observables along the diagonal). In fact, motivated by the picture of a polaron effectively constrained to 1D, in the thermodynamic limit we expect a linear expansion (saturation) of $\hat{x}_m$ along the diagonal (anti-diagonal) at large times, which is, however, out of reach to simulate with current methods.

11.4 TPSC for the SU(N) symmetric Fermi-Hubbard model

In the previous section, we numerically studied small system sizes of the SU(3) symmetric t-J model in the ground state. At finite temperature, methods like determinant quantum Monte Carlo (DQMC)[4] yield accurate results, which however become intractable below $T/J \lesssim 1$ (with $J = 4t^2/U$ the superexchange energy as usual). In particular, the sign problem is present even at one particle per site for $N > 2$ (in fact becoming worse with increasing N), severely limiting calculations at low to intermediate temperatures. This corroborates how in SU(N) symmetric systems, numerical studies both at one particle per site and at finite doping pose a true challenge to any known technique. This calls for testing and benchmarking approximative methods, such as the random-phase approximation (RPA) and two-particle self-consistent theory (TPSC). In particular, this could allow to learn about qualitative thermodynamic features of the SU(N) FH model without the need of immensely expensive numerical computations.

In Appendix A.2, we generalize the TPSC equations introduced in Sec. 3.2 and derived in Sec. A.1 to the case of the SU(N) Hubbard model, where N spin flavors (denoted by $\sigma, \tau = 1 \dots N$) enter the Hamiltonian,

$$\hat{\mathcal{H}} = -t \sum_{\langle i,j \rangle} \sum_{\sigma=1}^{N} \left(\hat{c}_i^\dagger \hat{c}_j + \text{H.c.} \right) + \frac{U}{2} \sum_i \sum_{\sigma \neq \tau} \hat{n}_{i,\sigma} \hat{n}_{i,\tau} - \mu \sum_i \sum_\sigma \hat{n}_{i,\sigma}. \tag{11.18}$$

In particular, when using the Bethe-Salpeter equations for generalized susceptibilities of the SU(N) symmetric system, we will find the following TPSC equation in the spin sector,

$$\frac{T}{N_{\mathbf{q}}} \sum_{\mathbf{q}, i\omega_n} \frac{\chi_0(\mathbf{q}, i\omega_n; N)}{1 - \frac{1}{N} U_{\text{sp}} \chi_0(\mathbf{q}, i\omega_n; N)} = N[\langle \hat{n}_\sigma \rangle - \langle \hat{n}_\sigma \hat{n}_\tau \rangle] = n - N \langle \hat{n}_\sigma \hat{n}_\tau \rangle . \tag{11.19}$$

[4] For SU(N) symmetric systems, $N(N-1)/2$ auxiliary Hubbard-Stratonovich fields can be introduced to obtain averages of the thermal equilibrium observables

Here, we defined

$$\chi_0(\mathbf{q}, i\omega_n; N) = -N\frac{T}{N_\mathbf{k}}\sum_\mathbf{k}\frac{n_F(\epsilon_\mathbf{k}-\mu)-n_F(\epsilon_{\mathbf{k}+\mathbf{q}}-\mu)}{i\omega_n+\epsilon_\mathbf{k}-\epsilon_{\mathbf{k}+\mathbf{q}}}. \tag{11.20}$$

Note that the TPSC equation for the N-component system, Eq. (11.19), is equivalent to the SU(2) symmetric case, when replacing all factors arising from spin degeneracies with $2 \to N$.

When using the same ansatz as in the two-component case,

$$\langle \hat{n}_\sigma \hat{n}_\tau \rangle = \frac{U_{\mathrm{sp}}}{U} n_\sigma^2, \tag{11.21}$$

we see how the TPSC equation becomes N-independent,

$$\frac{T}{N_\mathbf{q}}\sum_{\mathbf{q}, i\omega_n}\frac{\chi_0(\mathbf{q}, i\omega_n; 1)}{1-U_{\mathrm{sp}}\chi_0(\mathbf{q}, i\omega_n; 1)} = n_\sigma - \frac{U_{\mathrm{sp}}}{U} n_\sigma^2. \tag{11.22}$$

In particular, Eq. (11.22) only depends on the filling per spin flavor $n_\sigma = \langle \hat{n}_\sigma(\mathbf{r}, \tau)\rangle$. Consider, for instance, a SU(6) system at $n = 1$, i.e., $n_\sigma = 1/6$. The solution of the TPSC equation (11.19) will be equivalent to a SU(2) system at filling $n = 1/3$, corresponding to the same filling per flavor $n_\sigma = 1/6$. Thus, the equation does not capture the true SU(N) nature of the system, but rather solves the problem by effectively scaling down to two spin-components at a lower filling. Ultimately, the N-dependence cancels out due to the form of the the ansatz made for $\langle \hat{n}_\sigma \hat{n}_\tau \rangle = \frac{U_{\mathrm{sp}}}{U} n_\sigma^2$. It remains to be found out whether a different ansatz might be better suited to capture the differences between various N. As Trembley and Vilk said themselves: *We want to stress, however, that this ansatz is not a rigorous result like sum rules* [189]. Let us take a closer look into the performance of the N-component TPSC, and try to collect possible ideas to make predictions for the SU(N) system more accurate.

Comparison of TPSC with DQMC

We start by solving the "simple upscaling" of the TPSC equations, Eq. (11.19), and compare to DQMC results presented in [428]. The latter has been produced by E. Ibarra-García-Padilla, who kindly provided the data for the following comparison. Before comparing the methods, let us briefly discuss the qualitative physics of the number of on-site pairs, $\mathcal{D} = \frac{N(N-1)}{2}\langle \hat{n}_\sigma \hat{n}_\tau \rangle$, as a function of temperature and N, as calculated using DQMC [428]. Fig. 11.12 shows $\mathcal{D}$ as a function of temperature T/t for $N = 2, 3, 4, 6$. Starting at high temperatures, DQMC demonstrates that for $N > 2$, $\mathcal{D}$ initially decreases, reaches a minimum around $T/t \sim 1$, and then saturates at a constant value.

As detailed in Ref. [428], this behavior can be explained as follows. At $T/U \gtrsim 1$, double occupancies can be thermally excited, resulting in a large value of $\mathcal{D}$ at high temperatures. Upon cooling, single occupancies begin to dominate, as they acquire significantly higher Boltzmann weights, leading to a depletion of double occupancies. In this regime, where the physics is primarily governed by singly occupied states, nearest neighbors can form either singlet or triplet states. Singlet states include an admixture of doubly occupied states (with a weight proportional

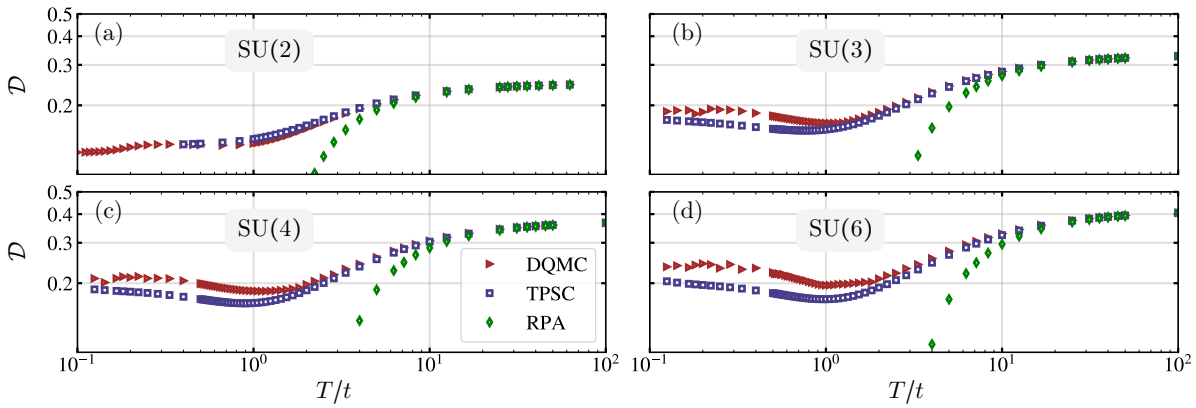

Figure 11.12: Comparison of the N-component TPSC (blue squares) and plain RPA (green diamonds) with DQMC data (red triangles) for the number of on-site pairs $\mathcal{D} = \frac{N(N-1)}{2}\langle \hat{n}_\sigma \hat{n}_\tau \rangle$, for $N = 2, 3, 4, 6$ in panels (a), (b), (c), (d), respectively. DQMC data was taken from [428].

to t^2/U^2), which facilitates delocalization and a corresponding kinetic energy gain. Conversely, triplet states exclude any doublon formation. As the temperature approaches the energy difference between singlet and triplet states, singlet states are favored, and hence double occupancy increases. This effect corresponds to the development of local AFM correlations, which has been directly observed through singlet-triplet oscillations in ultracold atom experiments [60].

Moreover, at high temperatures, the number of doublons increases with N, which can be attributed to simple combinatorics: For larger N, there is a higher number of possible two-flavor combinations for the formation of a doublon, leading to higher values of $\mathcal{D}$.

Fig. 11.12 further shows corresponding TPSC results for the number of on-site pairs, $\mathcal{D}$. For high temperatures, both methods show a quantitative match—as expected for $T/U \gg 1$, where interaction effects are negligible and SU(N) systems are indeed equivalent to a SU(2) model at a correspondingly lower filling. In the case of two spin-components, there is a quantitatively good match down to rather low temperatures, in-line with results presented in Refs. [188, 189, 191]. Note, however, that we are here looking at the particularly difficult case of the SU(2) model at half-filling, reducing the prediction accuracy at temperatures well below $T/t \ll 1$ due to entering the renormalized classical regime (where antiferromagnetic correlations grow exponentially) [188]. For $N > 2$, deviations between TPSC and DQMC start to be noticeable at around $T/t \sim 3$ for e.g. $N = 3$. For increasing N, these deviations start to appear at growing temperatures. For $N = 4$ ($N = 6$), discrepancies between TPSC and DQMC become visible at $T/t \sim 5$ ($T/t \sim 7$).

For further comparison, results when merely using the bare Hubbard-U (RPA) are shown by green diamonds. Due to finite temperature phase transitions predicted within the RPA framework, strong deviations to the DQMC data appear already at high temperatures, similar to the high-temperature expansion used for comparison in [428].

On a qualitative level, TPSC seems to capture the appearing minimum of $\mathcal{D}$ with a succeeding rise when lowering the temperature. However, we observe that the number of on-site pairs is in general underestimated within TPSC. A possible explanation for this effect is that, becuase

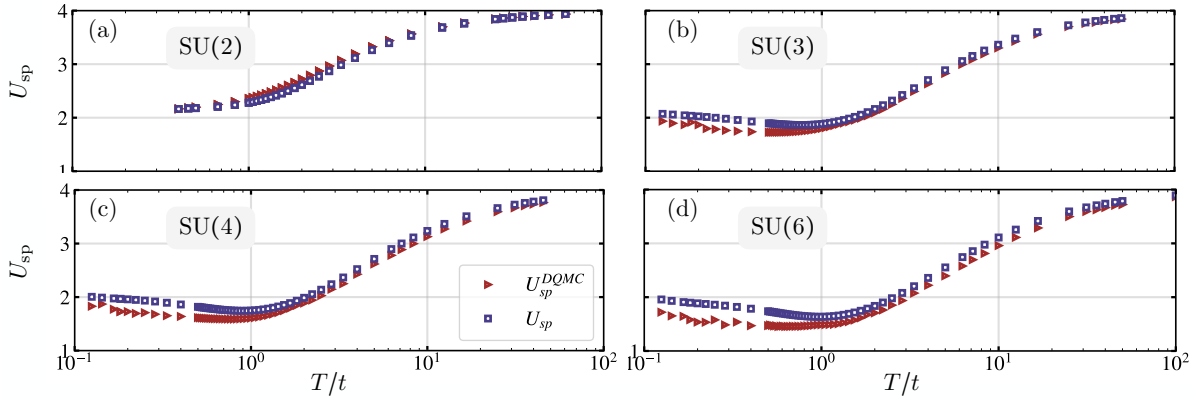

Figure 11.13: Comparison of the effective spin vertex U_{sp} using the simple ansatz N-component TPSC (blue squares) with fits of Eq. (11.19) to the DQMC data, resulting in the red triangles. Data is shown for $N = 2, 3, 4, 6$ in panels (a), (b), (c), (d), respectively. The N-component TPSC is seen to consistently overestimate the effective interaction U_{sp}.

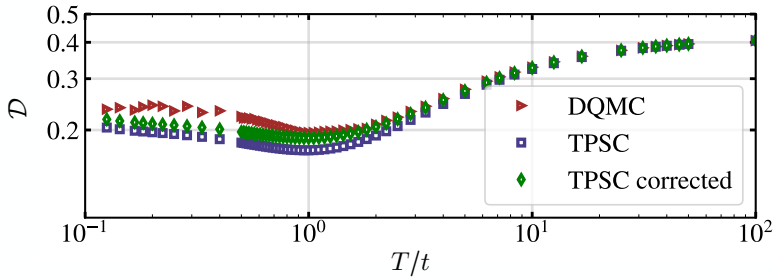

Figure 11.14: After solving the TPSC equations, we subtract a constant correction term from the self-consistently found effective interaction vertex, here we choose $U_{\mathrm{sp}} \to U_{\mathrm{sp}} - 0.1$. After having done so, the number of on-site pairs $\mathcal{D}$ is re-calculated with the updated effective U_{sp}, yielding the green diamond data points. Data presented here corresponds to SU(6), $n = 1$, cf. Fig. 11.12 (d).

the TPSC generalization to N spin-components is equivalent to a SU(2) system at lower filling, the effective interaction U_{sp} tends to be overestimated. Using Eq. (11.19) without any ansatz for $\langle \hat{n}_\sigma \hat{n}_\tau \rangle$, but rather feeding into the TPSC equation the data for $\mathcal{D}$ from DQMC, we can find the values U_{sp} that reproduce the output of DQMC. Results for this fit are compared to solutions using the simple ansatz in Fig. 11.13. As anticipated from the data shown in Fig. 11.12, effective interactions are observed to be overestimated in TPSC for $N \geq 3$.

A straight forward way to account for the overestimation of U_{sp} would be to slightly shift the self-consistent TPSC results by a constant correction term, and then re-calculate $\langle \hat{n}_\sigma \hat{n}_\tau \rangle$ with the updated effective interaction. Looking at Fig. 11.13 (d), it indeed seems like between $T/t = 1 \ldots 10$, the offset between TPSC and target solutions is approximately constant ~ 0.1. Doing this simple subtraction scheme for $N = 6$ and an offset of 0.1 results in Fig. 11.14. Though quantitative improvements can be seen (the DQMC and corrected TPSC curves now noticeably deviate at lower temperatures around $T/t \sim 2$ instead of $T/t \sim 7$), the above scheme is far from being universally applicable, as it is unclear how to choose the shift. Apart from that,

qualitatively we can not expect to gain any additional insights from this shift.

It could be insightful to check how well the SU(2) TPSC away from one particle per site matches (quasi-) exact numerical methods. For instance, it would be interesting to see if the SU(6) TPSC curve in Fig. 11.12 for $n = 1$ matches DQMC data for SU(2) at $n = 1/3$. If there is a good match, the deviations we see really show the differences between SU(2) and SU(N) physics. In particular, it is tempting to think that certain qualitative features—like the appearance of a maximum of $\langle \hat{n}_\sigma \hat{n}_\tau \rangle$ at low temperatures—arise only in SU(N) systems and are absent for their corresponding SU(2) cousin at lower filling. Furthermore, an open question in particular regarding the SU(N) symmetric system is whether one can find a better ansatz for $\langle \hat{n}_\sigma \hat{n}_\tau \rangle$, with an explicit non-trivial dependence on N.

11.5 Discussion

In the first part of this chapter we have studied the one-hole doped SU(3) t-J model both in- and out of equilibrium. In the ground state, we observed anisotropic hole delocalization, and established the formation of a sub-dimensional polaron by combining chargon and spinon fluctuations in an effective theory. This picture was further corroborated in calculations of the dynamics initiated from a localized hole, which can provide a direct probe of the polaron physics in SU(N) ultracold atom experiments once single-site resolution becomes available. In our setting of a doped SU(3) AFM, we have demonstrated how sub-dimensional excitations naturally emerge, reminiscent of mobility restricted fractons as appearing e.g. in three dimensional X-cube models [429, 430].

Based on our study of a single hole, we propose that SU(3) AFMs on the square lattice at finite doping are described by weakly coupled Tomonaga-Luttinger (TL) liquids of bound spinon-chargon polarons along the diagonals,

$$\hat{\mathcal{H}}_{\text{eff}} = \sum_{\mathcal{D}_i} \hat{\mathcal{H}}_{\mathcal{D}_i} + \sum_{\mathcal{D}_i \neq \mathcal{D}_j} \hat{\mathcal{H}}^{\text{int}}_{\mathcal{D}_i,\mathcal{D}_j} + \sum_{k_n} \sum_{\mathcal{D}_i \neq \mathcal{D}_j} t_{\mathcal{D}_i,\mathcal{D}_j} \hat{c}^\dagger_{k_n,\mathcal{D}_i} \hat{c}_{k_n,\mathcal{D}_j} + \text{h.c.}, \tag{11.23}$$

where $\hat{\mathcal{H}}_{\mathcal{D}_i}$ is the Hamiltonian of a 1D TL liquid [431] on the i'th diagonal $\mathcal{D}_i$, $\hat{\mathcal{H}}^{\text{int}}_{\mathcal{D}_i,\mathcal{D}_j}$ is the (weak) interaction between chains $\mathcal{D}_i$ and $\mathcal{D}_j$, and the last term describes particles with quasi-momentum k_n hopping between the diagonals. In particular, in the absence of inter-chain couplings in Eq. (11.23) we predict the appearance of power-law correlations of charges along the diagonal order, $\langle \hat{n}^h_{x+\ell,y-\ell} \hat{n}^h_{x,y} \rangle \propto \ell^{-\alpha}$, while correlations perpendicular to the stripe order are short-range with exponential decay, $\langle \hat{n}^h_{x+\ell,y+\ell} \hat{n}^h_{x,y} \rangle \propto e^{-\ell}$. Though inter-chain interactions are a relevant perturbation of the TL liquid, we still expect these scalings over intermediate length scales for finite couplings.

In the second part of this chapter, we focused on the thermodynamic properties of SU(N) symmetric systems and benchmarked the TPSC approach against DQMC results. Specifically, we examined the number of on-site pairs $\mathcal{D}$ and found that TPSC qualitatively captures all main physical features. However, we demonstrated that a straightforward generalization of the TPSC equations does not fully account for the SU(N) symmetric nature of the interactions. Future

directions could include developing a more suitable, potentially physically motivated ansatz for $\langle \hat{n}_\sigma \hat{n}_\tau \rangle$ to better reflect the SU(N) symmetry. This can then be tested against experimental data obtained e.g. in Ref. [60], in particular in regimes where state-of-the-art quantum Monte Carlo methods fail.

12

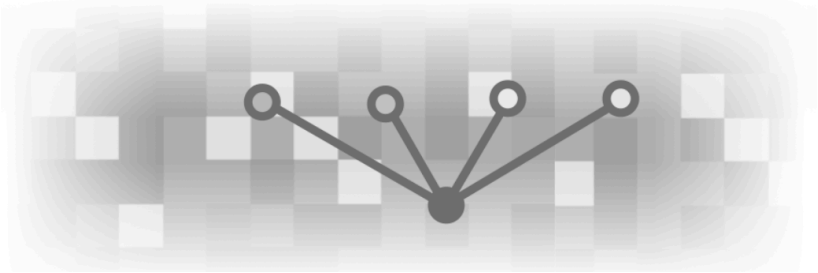

Machine learning assisted snapshot analysis

Summary. Quantum many-body snapshots contain an extensive amount of information, calling for the use of advanced analysis methods. In this chapter, we introduce three strategies based on neural networks to analyze many-body snapshots in an interpretable way. First, we combine confusion learning with correlation convolutional neural networks, and study thermodynamic properties of the 2D Heisenberg model. The trained network is shown to pick up qualitative changes in the snapshots above and below a characteristic temperature where magnetic correlations become significantly long-range. We identify the full counting statistics of nearest neighbor spin correlations as the most important quantity for the decision process of the neural network, which go beyond averages of local observables. We then introduce an interpretable architecture based on the transformer attention mechanism, which can inherently capture non-local correlations. Finally, we discuss an autoencoder model that allows to learn characterizing patterns of symmetry-broken states, which we exemplify with snapshots taken in the ground state of the frustrated J_1-J_2 model.

12.1 Introduction

Next to revolutionizing applications in image and sequence processing, in recent years neural networks have gained tremendous interest also in the field of quantum many-body physics [432–435]. In strongly correlated systems, complex phases of matter can emerge in seemingly simple models – which, in many settings, still lack microscopic understanding [24, 72]. With their powerful abstraction tools, neural networks have quickly opened a novel paradigm of analyzing many-body phases of matter, which may help to gain deeper understanding of appearing phases in strongly correlated systems [43, 436, 437], as well as act toward experimental image reconstruc-

tion [438], enhanced Monte Carlo sampling [439–442], and efficient representations of quantum states [443–445].

As a concrete example, deep neural networks have been increasingly utilized to predict phase transitions in physical systems, the model's input data types ranging from entanglement entropy spectra [446–449] to quantum image data generated numerically [450–455] and experimentally [43,456–458]. However, one major drawback of the neural network toolbox is their inherent black-box nature, which limits interpretation—and in turn restricts their applicability towards developing microscopic theories of yet unsolved physical regimes. For phase classification tasks using standard feed forward neural networks, for instance, the models represent complicated non-linear functions that are optimized to best represent the conditional probability $P(y|\mathbf{s})$ of assigning phase label y to data input $\mathbf{s}$, however mostly without any deeper insights into the decision making process of the network. This significant pitfall of neural networks in quantum physics has triggered intensified research regarding reliable interpretability, such as for linear and kernel [459–461], shallow [462,463] and engineered [436,464,465] models, as well as by using Hessian based similarity measures [466,467] and optimal prediction methods [468,469].

Highly controllable analog quantum simulation platforms—e.g. via ultracold atoms—allow for a systematic experimental exploration of paradigmatic Hamiltonians with strong correlations like the Fermi-Hubbard model. As discussed in Sec. 4.1, these setups allow to perform genuine quantum projective measurements and sample snapshots of the many-body state in the Fock basis, which in turn allow for insights into the wave function beyond averages and local observables [242,470], see also Chap. 6. Nonetheless, if order parameters are unknown or the physics goes beyond the Landau paradigm of phase transitions, it is a difficult task to differentiate between different phases of matter when a whole zoo of possible correlation functions needs to be considered.

To this end, neural network processing of quantum snapshots can act as a guiding hand, where architectures are desirable that, apart from detecting qualitatively different physical regimes, let us know which physical correlations are crucial to base a reliable decision on. For this purpose, unsupervised-supervised hybrid machine learning approaches based on correlation convolutional neural networks (CCNN) [436] have been proposed, where interpretable phase detection has been demonstrated via data clustering and subsequent filtering of important correlations in each cluster [437].

In this chapter, we propose and benchmark three methods for interpretable phase detection, based on (i) the combination of confusion learning training schemes [446] with CCNNs (coCCNN), (ii) tailored transformer neural networks, and (iii) autoencoders (AE).

We start by describing the coCCNN in Sec. 12.2, and study numerically generated snapshots of the Heisenberg model, whose temperature dependent magnetic properties share many similarities with the low-energy features of the Fermi-Hubbard model at half filling. In this case, a characteristic temperature T^* exists where spin correlations become significantly long-range, replacing Fermi-liquid quasiparticles by a single-particle pseudogap [189,471]. In the Heisenberg model, though no quasiparticle interpretation exists, a suppression of the spin susceptibility can be observed below a characteristic temperature $T^* \sim J$ [472–474] in analogy to the half filled

Fermi-Hubbard model [475,476]. Similarly, both the Heisenberg and Fermi-Hubbard model feature a maximum of the specific heat at $T_C \sim 2J/3$ [477–479], signaling the thermal activation of the spin degrees of freedom. We show that the trained confusion correlator convolutional neural network is able to pick up upon qualitative changes of these thermodynamic properties in the Heisenberg snapshot data sets above and below a characteristic temperature, broadly matching both the peak of the susceptibility as well as the specific heat. We find that the network classifies snapshots by analyzing the full counting statistics of nearest neighbor spin correlations, which directly contain information about higher moments of the distributions. By evaluating the fluctuations of nearest neighbor correlators, the network uses indirect access to four-point correlations to assess long-range properties of the snapshots.

Initiating the step towards fully long-range capabilities, in Sec. 12.3 we demonstrate that similar features can be detected using transformer vision networks, which incorporate an attention mechanism and capture correlations across the entire snapshot. Moreover, we discuss the Correlater Transformer (CoTra) architecture, whose simplified and tailored attention mechanism allows for an efficient extraction of important correlations of the system.

Lastly, in Sec. 12.4, we analyze an autoencoder model trained to efficiently compress snapshots of the frustrated J_1-J_2 model. By training the model in specific parameter regimes and testing it across a broad range that spans several phases of matter, we observe that the model effectively learns the order parameter corresponding to the phase it was trained in. We show that as a result, AE networks naturally filter out important physical patterns of ordered many-body phases.

The methods discussed in this chapter may help towards gaining deeper microscopic insights into strongly correlated phases. In particular, application of the fluctuation based detection scheme and the transformer based approaches promises novel perspectives onto non-local properties of many-body systems. One particular example is the geometric fractionalized Fermi liquid, which is characterized by hidden correlations, see Chap. 7.

Large parts of this chapter, including the above introduction, is based on the following publication, partially with textual overlap:

> [10] **HS** and A. Bohrdt. **Fluctuation based interpretable analysis scheme for quantum many-body snapshots**, SciPost Phys. 15, 099 (2023)

Part of Sec. 12.3, which (briefly) introduces the Correlator Transformer architecture, is based on the following preprint:

> [12] A. Suresh, **HS**, B. Hashemi, and A. Bohrdt. **Interpretable correlator Transformer for image-like quantum matter data**, arXiv 2407.21502 (2024)

12.2 Correlation based confusion learning

Confusion learning is a training scheme which aims to identify phase transitions by learning the best labeling of data, where the labeling is originally unknown [446]. Given an input dataset in

some parameter space $p \in [p_1, p_2]$, purposely mislabeling the data into two subsets and evaluating the performance of the network to distinguish between the two labels can give insights into whether and where a phase transition occurs. Concretely, consider a physical system with a phase transition at point p_c. Within the confusion learning scheme, a neural network is trained to distinguish whether the input is taken from $p_1 \leq p \leq p'$ or $p' < p \leq p_2$, with p' an arbitrary decision boundary. If we choose, for instance, $p' = p_2$, we train the model to assign label "A" to the full dataset, which is a trivial task for the neural network and results in 100% accuracy. The same argument holds if we choose $p' < p_1$, where now all inputs are predicted to belong to label "B". Furthermore, assuming the model is capable of perfectly distinguishing the two phases, we reach ideal performance also at $p' = p_c$. In between, the model is assigned to label data from the same phase as coming from qualitatively different regimes, leading to a majority decision and a reduced accuracy (hence the confusion of the network). As a result, a characteristic W-shape of the network's performance as a function of p is expected[1]. By identifying the maximum of the network's performance $p'_{\max}$ upon varying the decision boundary, the critical parameter $p_c = p'_{\max}$ can be estimated. If, on the other hand, no transition exists in the system, the network will always make a majority decision – resulting instead in a V-shape of the accuracy.

12.2.1 Network architecture

With increasing efforts to interpret machine learning in the context of physical observables, a neural network architecture based on non-linearities that directly correspond to measurable correlations has been proposed in [436]. In particular, the uncontrolled mixing of correlations that appears when using standard non-linearities is explicitly replaced by interpretable correlation maps in the correlation convolutional neural network (CCNN) architecture. Here, by combining correlation based convolutions with confusion learning (co-CCNN), we detect qualitative variations of quantum many-body snapshots while having direct access to the model's decision making process.

The network's architecture is schematically illustrated in Fig. 12.1 (a). Many-body snapshots for a range of parameters are divided into two subsets—i.e., above and below a given decision boundary p'. In order to perform interpretable classification, convolutional filters generate a first order correlation map of the snapshot (C^1), from which higher order (i.e. non-linear) correlations are evaluated up to order M (C^n, $1 < n \leq M$). In particular, for a snapshot with pixels $S_c(\mathbf{x})$ for channels $c = \{\uparrow, \downarrow\}$ and filter weights $f_c(\mathbf{x})$, the correlation maps are given by [436]

$$C^n(\mathbf{x}) = \sum_{(\mathbf{a}_1, c_1) \neq \ldots \neq (\mathbf{a}_n, c_n)} \prod_{j=1}^{n} f_{c_j}(\mathbf{a}_j) S_{c_j}(\mathbf{x} + \mathbf{a}_j), \tag{12.1}$$

where $\mathbf{a}_j$ refers to the positions of the convolution window[2]. Hence, the n'th order correlation map corresponds to n-point correlations within a given fixed convolutional window. Note

[1] Note that, in most realistic applications, the model is not perfectly able to distinguish between the two phases, leading to a smeared out W-shape in the accuracy [446].

[2] C^1 thus corresponds to the feature map of a standard convolutional operation; the non-linear part of the model corresponds to all higher orders, C^n, $n > 1$.

that the above can be easily generalized to multiple filters. However, for the sake of simplicity and easier interpretability, we here restrict ourselves to a single filter per channel[3]. After post-processing the correlation maps by normalizing and averaging[4], the M-dimensional output is fed into a single fully connected layer with weights $w^{(n)}$, which then makes a binary classification based on the measured correlations. As the filters are trainable, the CCNN hence learns which correlations give key information about the two subsets of snapshots when attempting to distinguish between them. Upon sweeping the decision boundary through parameter space, this allows for interpretable classification of snapshots within a single-step protocol in a fully automated manner, whereby the model outputs regions of qualitatively differing snapshot sets while at the same time yielding insights into which correlations are important to distinguish these sets.

12.2.2 Application to the Heisenberg model

Using stochastic series expansion quantum Monte Carlo techniques [42, 480, 481], we take snapshots of the antiferromagnetic (AFM) Heisenberg model at temperature T, described by the Hamiltonian

$$\mathcal{H} = J \sum_{\langle \mathbf{i},\mathbf{j} \rangle} \hat{\mathbf{S}}_\mathbf{i} \cdot \hat{\mathbf{S}}_\mathbf{j}, \tag{12.2}$$

where $\hat{\mathbf{S}}$ is a spin-1/2 operator and $\langle \mathbf{i}, \mathbf{j} \rangle$ denotes nearest neighbor pairs on the 2D square lattice. Though long-range antiferromagnetic (AFM) order is only present in the ground state ($T = 0$) and there exists no phase transition at finite temperature, the 2D Heisenberg model features interesting thermodynamic properties. For instance, a typical temperature scale T^* exists at which magnetic correlations become significantly long-range, indicated by a sudden suppression of the uniform spin susceptibility [472–474],

$$\chi_s = \frac{1}{NT} \sum_{\mathbf{i},\mathbf{j}} \langle \hat{S}^z_\mathbf{i} \hat{S}^z_\mathbf{j} \rangle \,, \tag{12.3}$$

where N the number of spins in the system. The Heisenberg model is an effective low energy description of the Fermi-Hubbard model at half filling and strong repulsion, where a similar phenomenology of the spin susceptibility is observed [189, 475]. Here, it has been proposed that at T^*, the exponentially growing correlation length of spin fluctuations becomes comparable to the quasiparticle de Broglie wavelength $\lambda_B \sim v_F / T$ (with v_F the Fermi velocity)—leading to the formation of precursor AFM bands and the depletion of the electronic density of states at the Fermi level (i.e., the pseudogap) [189]. Though subtle differences between the actual opening of the pseudogap at the Fermi surface in the Fermi-Hubbard model and the peak of the magnetic susceptibility exist in cuprate materials [482], T^*—in this chapter defined as the maximum of the susceptibility—constitutes a characteristic temperature below which significant magnetic correlations develop.

[3] When including multiple filters, our findings do not change qualitatively.

[4] We assume translational invariance of the system, such that we can get meaningful quantities (i.e. measurable n-point correlations) by spatially averaging over the correlation maps.

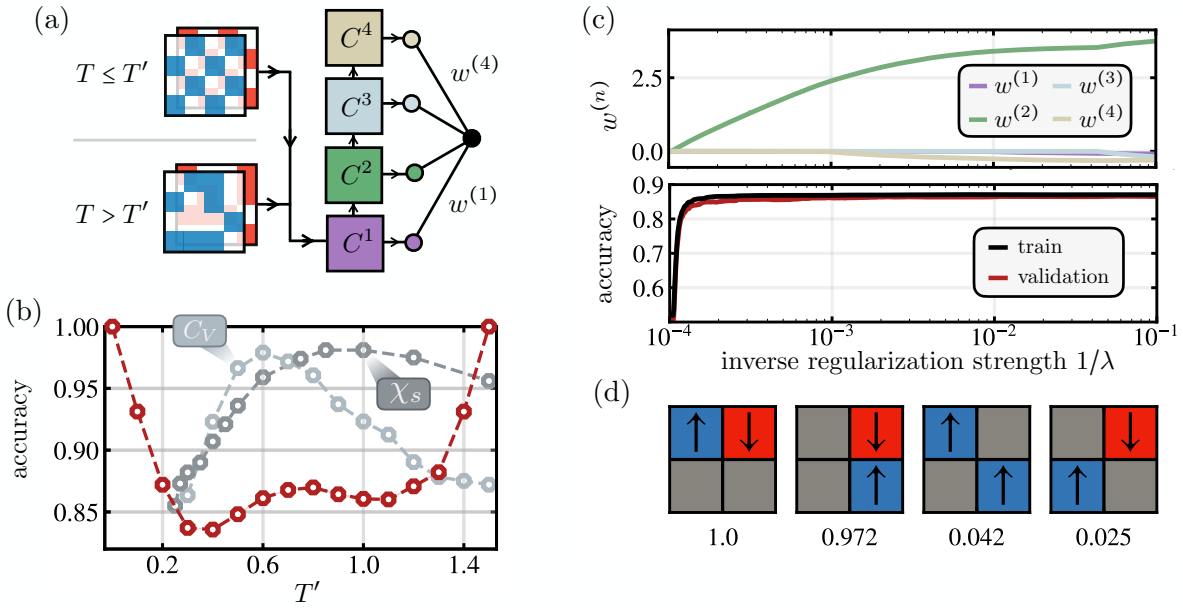

Figure 12.1: **Correlator based confusion learning.** (a) Schematic architecture of the confusion based [446] CCNN [436] network (co-CCNN). Correlation maps are computed via convolution with learnable filters, which a coupled fully-connected discriminator bases its binary decision on. We use a single 2×2 filter for each channel, and cascade the first order correlation map to fourth order, $M = 4$. (b) When changing the decision boundary T' in the confusion learning scheme, the network's accuracy features a W-shape, signaling that two qualitatively differing regimes are present in the data (red data points). Accuracies are averaged over 20 runs; errors are negligible on the scale of the plot. The performance maximum at $T'_{\text{max}} \sim 0.8$ is found to broadly match peaks of the specific heat C_V at $T_C \sim 0.6$ (light blue data points) and magnetic susceptibility χ_s at $T^* \sim 0.9$ (light blue data points, taken from [472]). Values for χ_s and C_V are re-scaled and shifted to match the axis frame. (c) Top panel: regularization path analysis of the weights $w^{(n)}$ at $T' = 0.7$. Second order correlations are found to set in earliest, while all other correlations stay insignificant for the whole range of λ. Lower panel: accuracy of the discriminator upon tuning the regularization strength λ. When significant weight is on the second order correlation neuron, maximum accuracy is reached. (d) The four most relevant two-point correlations that the network utilizes to make its decision, with weights given by $f_{c_1}(\mathbf{a}_1) f_{c_2}(\mathbf{a}_2)$ (normalized by the highest value), cf. Eq. (12.1). Nearest neighbor correlators are seen to single out as the important correlations.

Moreover, large correlation lengths at low temperatures and random, uncorrelated spins at high temperatures lead to the appearance of a maximum of the specific heat at $T_C \sim 2J/3$ both in the Heisenberg as well as Fermi-Hubbard model,

$$C_V = \left(\langle \hat{\mathcal{H}}^2 \rangle - \langle \hat{\mathcal{H}} \rangle^2 \right) / T^2 = \frac{\partial}{\partial T} \langle \hat{\mathcal{H}} \rangle \,, \tag{12.4}$$

constituting a characteristic energy scale where spin degrees of freedom are thermally activated [477, 479]. At low temperature, it has been shown that $C_V \propto T^2$ [478], as anticipated from spin-wave theory.

The close correspondence of the low energy physics between the Heisenberg and the Hubbard model at half filling together with its non-trivial thermodynamic behavior render the

Heisenberg model a valuable and, importantly, verifiable testing ground for machine learning applications. In the following, we analyze simulated snapshots of the Heisenberg model at various temperatures using the co-CCNN scheme. We demonstrate that the network is capable of picking up qualitative thermodynamic changes of the model, which we fully interpret in terms of full counting statistics of correlation functions – paving the way to analyze many-body snapshots in, e.g., temperature and density scans in the Fermi-Hubbard model away from half filling.

In our simulations, we take snapshots of the thermal ensemble of a 40×40 Heisenberg model, but use only the central 16×16 region for further processing to minimize boundary effects. In the following, all energies are given in units of J, where we set $J = 1$. According to the scheme outlined in Sec. 12.2.1, we train a CCNN to discriminate between temperatures $T \leq T'$ and $T > T'$ using binary cross entropy (BCE) loss and 2×2 convolutional filters. We use 2,000 snapshots for each temperature value between $T = 0.1$ and $T = 1.5$ in increments of $\Delta T = 0.1$. We utilize 90% of the data set for training; the remaining 10% is used for validation.

The accuracy after 50 training epochs averaged over 20 runs is shown in Fig. 12.1 (b). In immediate vicinity to the boundaries $T' \gtrsim 0.1$ and $T' \lesssim 1.5$, we see a linear reduction of accuracy, signaling that the network makes a majority decision. At intermediate decision boundaries, however, the network's performance reaches a local maximum located at $T'_{\text{max}} \sim 0.8$—being in broad agreement with both the maximum of the spin susceptibility at $T^* \sim 0.9$ (dark grey data points in Fig. 12.1 (b)) as well as the peak of the specific heat at $T_C \sim 0.6$ (light grey data points in Fig. 12.1 (b), evaluated by numerical differentiation of $\langle \hat{\mathcal{H}} \rangle$). As we show later, our results to not alter qualitatively when choosing larger convolutional windows. However, generally, the filter size shall be treated as a tunable hyperparameter of the CCNN, whereby the maximum order of correlations accessible to the model is limited by the size of the kernel.

The observed performance maximum at T'_{max} suggests that the network picks up upon the qualitative change of thermodynamic properties of the spin system below and above characteristic energy scales T_C, T^*, where magnetic correlations become significantly long-range. Importantly, we note that quantities such as C_V and χ_s explicitly include long-range contributions, cf. Eqs. (12.3), (12.4); the network, however, is restricted to evaluating local correlations within the convolutional filter. Thus, the question arises how the model makes its decision and which qualitative changes precisely the co-CCNN scheme detects.

Regularization path analysis

To classify which correlation maps are important for the decision process, we retrain the fully connected layer of the model that directly leads to the decision neuron [436]. By explicitly adding a $\mathcal{L}_1$ penalty to the weights $w^{(n)}$ between the post-processed correlation maps and the interpretation bottleneck (see Fig. 12.1 (a)), we perform a regularization path that allows us to analyze which correlation map is used first to reach maximum discrimination accuracies. In particular, the retraining loss reads

$$\mathcal{L}_{\text{reg}} = \mathcal{L}_{\text{BCE}} + \lambda \sum_{n=1}^{N} |w^{(n)}|, \tag{12.5}$$

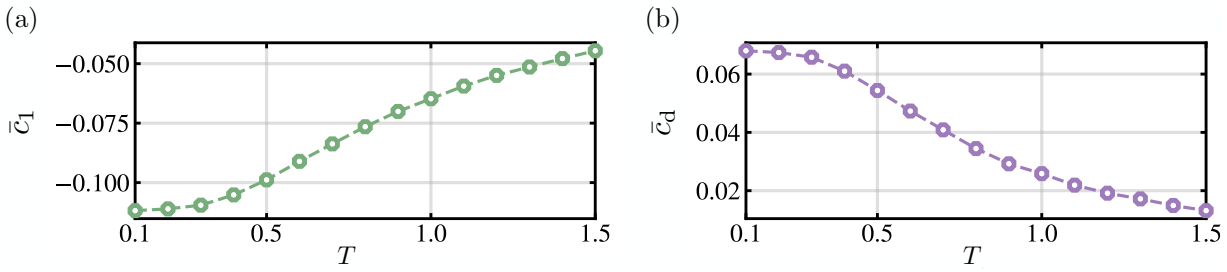

Figure 12.2: **Two-point correlations of the Heisenberg model.** Nearest neighbor correlations $\bar{c}_1$, (a), as well as diagonal correlations $\bar{c}_\mathrm{d}$, (b), in the Heisenberg model as a function of temperature. Correlations are approximated by evaluating c_1, c_d in each shot and averaging over all snapshots, cf. Eq. (12.7). Both correlations show a monotonous behavior, with no qualitative differences above and below $T'_\mathrm{max} \sim 0.8$.

where $\mathcal{L}_\mathrm{BCE}$ is the binary cross entropy loss that was used to train the convolutional filters and λ is the regularization strength.

Weights $w^{(n)}$ for a given λ are shown in the top panel of Fig. 12.1 (c) for decision boundary $T' = 0.7$. We observe that for $1/\lambda \sim 10^{-4}$, weights for the second order correlations first start to deviate from zero. At the same time, the accuracy of the network shoots from $\sim 50\%$ to $\sim 85\%$, see the lower panel in Fig. 12.1 (c). Note that all other weights are vanishingly small throughout the whole range of λ, and even when slightly deviating from zero do not lead to a performance increase of the network. Hence, we conclude that it is indeed correlations of second order that let the network reach its maximal accuracy shown in Fig. 12.1 (b).

To make it explicit which two-point correlators precisely the network measures, we plot the four correlations with highest weights $f_{c_1}(\mathbf{a}_1) f_{c_2}(\mathbf{a}_2)$ (normalized by the largest correlation weight) when applying the learned convolutional filter, Fig. 12.1 (d). Nearest neighbor spin-spin correlations in horizontal and vertical direction single out by their strong weights. Diagonal correlations are found to be further calculated and analyzed by the network, however only with marginal weight (around 5%) compared to the nearest neighbor correlations. Note that for all decision boundaries T', the results shown above are qualitatively identical—that is, second order nearest-neighbor correlations are found to be used by the network to make its decision.

Full counting statistics

Based on these insights, we take a look at nearest neighbor and diagonal spin-spin correlations,

$$\langle \hat{c}_1 \rangle = \left\langle \frac{1}{N_b} \sum_{\langle \mathbf{i},\mathbf{j} \rangle} \hat{S}^z_\mathbf{i} \hat{S}^z_\mathbf{j} \right\rangle \qquad \langle \hat{c}_d \rangle = \left\langle \frac{1}{N_b} \sum_{\langle\langle \mathbf{i},\mathbf{j} \rangle\rangle_\mathrm{diag}} \hat{S}^z_\mathbf{i} \hat{S}^z_\mathbf{j} \right\rangle, \tag{12.6}$$

where N_b is the total number of nearest neighbor (diagonal) pairs $\langle \mathbf{i},\mathbf{j} \rangle$ ($\langle\langle \mathbf{i},\mathbf{j} \rangle\rangle_\mathrm{diag}$). We evaluate correlations Eq. (12.6) by averaging over N_s snapshots,

$$\bar{c}_1 = \frac{1}{N_s} \sum_{s=1}^{N_s} c_1^{(s)} \qquad \bar{c}_\mathrm{d} = \frac{1}{N_s} \sum_{s=1}^{N_s} c_d^{(s)}, \tag{12.7}$$

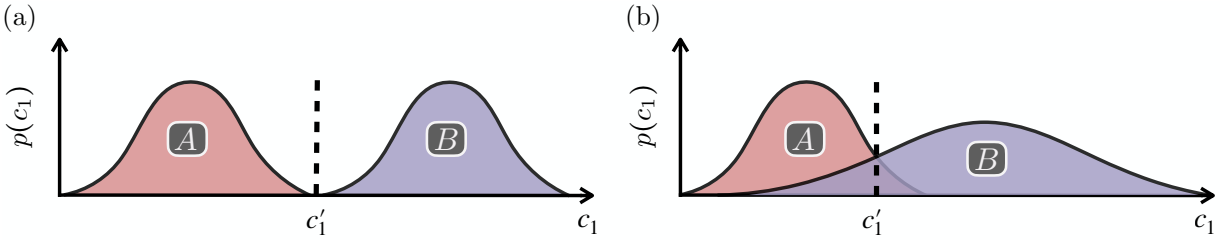

Figure 12.3: **Illustration of the network's learning process.** By analyzing the full counting statistics of sets $A = \{c_1 \,|\, T \leq T'\}$ and $B = \{c_1 \,|\, T > T'\}$, the network learns a threshold c_1'. For a given, unseen snapshot with $c_1^{(s)}$, the network then classifies it as belonging to $T \leq T'$ ($T > T'$) for $c_1 \leq c_1'$ ($c_1 > c_1'$). When both distributions have no overlap, the network has perfect accuracy, (a); for finite overlap, the network's performance decreases, (b). The ideal choice of c_1' that maximizes the accuracy explicitly depends on the full distributions of A and B, including their means and widths.

where $c_{1/d}^{(s)}$ is the approximation of the correlator $c_{1/d}$ using snapshot s,

$$c_1^{(s)} = \frac{1}{N_b} \sum_{\langle \mathbf{i},\mathbf{j} \rangle} S_{\mathbf{i}}^{z,s} S_{\mathbf{j}}^{z,s} \qquad c_d^{(s)} = \frac{1}{N_b} \sum_{\langle\langle \mathbf{i},\mathbf{j} \rangle\rangle_{\text{diag}}} S_{\mathbf{i}}^{z,s} S_{\mathbf{j}}^{z,s}, \tag{12.8}$$

with $S_{\mathbf{i}}^{z,s}$ denoting the spin orientation of spin $\mathbf{i}$ in snapshot s. As depicted in Fig. 12.2, both correlator strengths show a monotonous increase with decreasing temperature with no qualitative difference above or below the temperature of maximum network accuracy.
If no structural change in the two-point correlators can be seen when passing T'_{max}, but the network only utilizes nearest neighbor two-point correlations when learning to label the data, what is it then that the network bases its decision upon?

To answer this question, we analyze the full counting statistics (FCS) of c_1, given by the total distribution $\{c_1\} = \{c_1^{(1)}, c_1^{(2)}, \dots\}$, cf. Eq. (12.8). In contrast to merely using averages, Eq. (12.7), the FCS directly gives information about higher moments of the distribution, such as its width and skewness. In particular, given a bipartition of the data set with boundary T', a corresponding boundary c_1' can be learned by the network which assigns label $T \leq T'$ ($T > T'$) to all snapshots fulfilling $c_1^{(s)} \leq c_1'$ ($c_1^{(s)} > c_1'$) such that its accuracy is maximized. If the network indeed estimates c_1 for each snapshot and bases its decision on the result, its accuracy will be flawless if the two sets $A = \{c_1 \,|\, T \leq T'\}$ and $B = \{c_1 \,|\, T > T'\}$ have no overlap, as illustrated in Fig. 12.3 (a). On the other hand, increasing overlaps will result in decreasing accuracy of the network as a hard decision boundary c_1' will inevitably lead to uncertain label predictions, cf. Fig. 12.3 (b).

For each shot, we calculate the snapshot's approximation of c_1, Eq. (12.8), and explicitly differentiate whether or not the network makes a correct decision, $C = \{c_1 \,|\, \text{correct categorization}\}$ and $F = \{c_1 \,|\, \text{false categorization}\}$, shown in Fig. 12.4 (a) in blue and red, respectively. The accuracy of the classifier is hence given by $a = |C|/(|C|+|F|)$, with $|C|$ ($|F|$) referring to the total instances of correctly (incorrectly) categorized snapshots. Accuracies a as a function of T' are shown on the right hand side of Fig. 12.4 (a), matching Fig. 12.1 (b)[5].

[5]Note that in Fig. 12.4 (a) we are showing the accuracy after a single run, whereas Fig. 12.1 (b) presents the mean

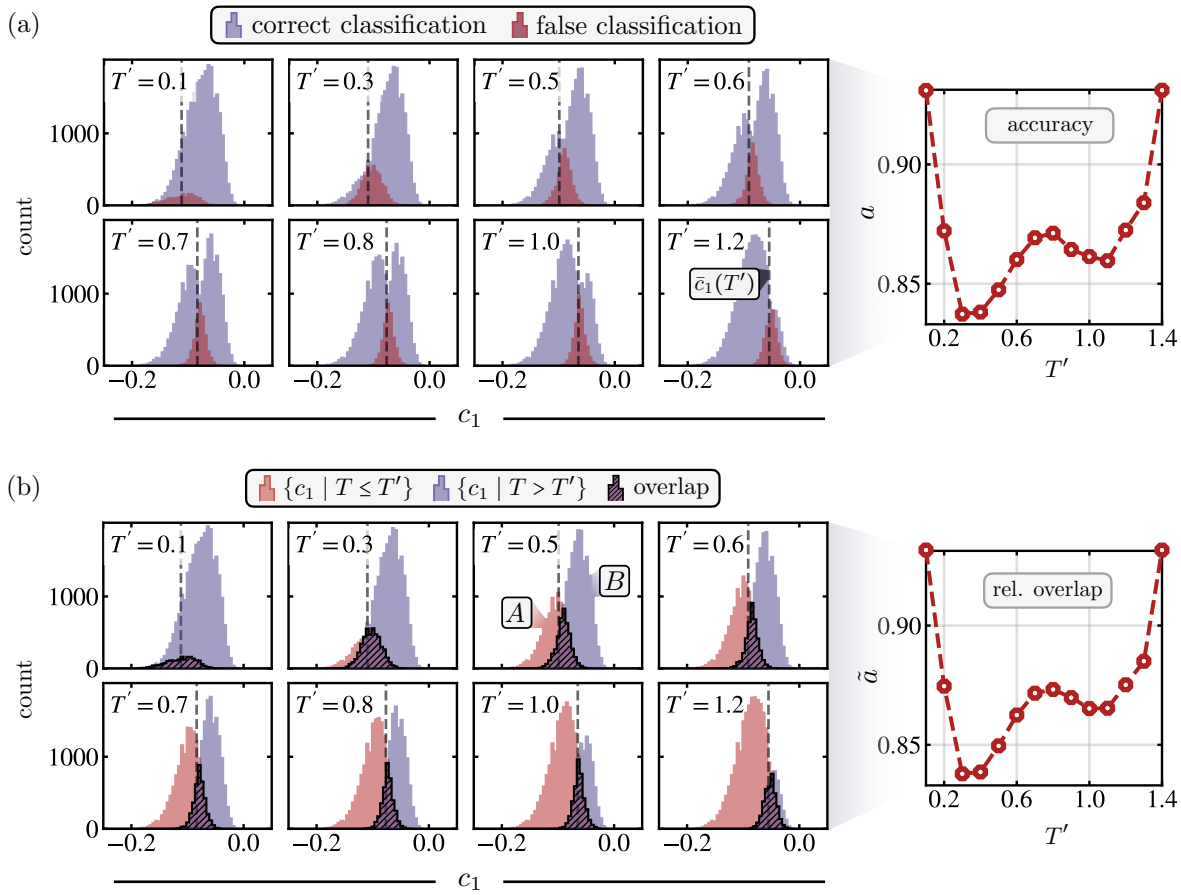

Figure 12.4: **Full counting analysis.** (a) We approximate the nearest neighbor correlator for each snapshot, Eq. (12.8), and analyze whether the network correctly labels it for a given decision boundary T' after training. Shown are the full counting statistics, where blue (red) indicates a correct (wrong) decision by the network. The right panel shows the total accuracy of the network, cf. Fig. 12.1 (b). (b) Full counting statistics of c_1 directly calculated from the Heisenberg snapshot data for a given bipartition $T \leq T'$ (red), $T > T'$ (blue). If basing the labeling decision on c_1, finite errors are expected when both distributions overlap (hatched areas). The shapes of the hatched and non-hatched areas precisely match the FCS of the network's performance as a function of c_1 in (a), underlining the interpretation of the network's decision making. The right panel shows the ratio $\tilde{a}$ between the area spanned by the non-hatched distributions to the total area below both hatched and non-hatched distributions, reproducing the W-shape of the network's accuracy.

We now perform a similar analysis of the FCS of c_1 directly from the raw Heisenberg snapshot data. To this end, we create bipartitions $A = \{c_1 \,|\, T \leq T'\}$ and $B = \{c_1 \,|\, T > T'\}$ of the snapshots and plot the corresponding distributions, in analogy to Fig. 12.3. Results are shown in Fig. 12.4 (b), where A (B) is shown in red (blue). Overlaps of both distributions are illustrated by hatched areas. Comparing the histograms in Fig. 12.4 (a) and (b), we find that the distributions match up almost perfectly. In particular, the hatched overlap of A and B in Fig. 12.4 (b) corresponds to the distribution of false classifications of the network, F, see Fig. 12.4 (a). Correct instances C, in turn, match the distribution $(A \backslash B) \cup (B \backslash A)$, i.e., the non-hatched areas in

accuracy over multiple optimizations—leading to the two curves not to be identical.

Fig. 12.4 (b). Indeed, when computing the accuracy analog of the raw Heisenberg histograms by evaluating the ratio $\tilde{a} = {}^{|A\setminus B|+|B|}/_{|A|+|B|} = {}^{|B\setminus A|+|A|}/_{|A|+|B|}$, the characteristic W-shape of the confusion learning scheme is reproduced—even matching quantitatively the accuracy of the neural network up to high precision, see the right panel in Fig. 12.4 (b).

For a given snapshot s to be categorized, we conclude that the network makes a majority decision that is based on the snapshot's nearest neighbor correlation estimate c_1. In particular, the network learns a threshold c_1' according to which it classifies a given snapshot with $c_1^{(s)}$ as $T \leq T'$ or $T > T'$ for $c_1^{(s)} \leq c_1'$ and $c_1^{(s)} > c_1'$, respectively. We note that, as the network has no information about the temperature of the snapshots, it can not, for instance, estimate averages $\bar{c}_1(T')$ and make a corresponding decision according to $c_1' = \bar{c}_1(T')$. Instead, the network leverages the FCS of the distributions A and B, choosing c_1' in order to maximize the classification accuracy. Specifically, c_1' corresponds to the point where the distributions $A = \{c_1 \,|\, T \leq T'\}$ and $B = \{c_1 \,|\, T > T'\}$ have maximum overlap, cf. Figs. 12.3 and 12.4. The learned threshold c_1' explicitly depends on the widths σ of distributions A and B, which directly include information of the fluctuations of nearest neighbor correlations c_1. We note that the learned decision thresholds closely (though not exactly) match the values of $\bar{c}_1(T')$, as illustrated in Fig. 12.4 by grey dashed lines.

To underline the network's decisive mechanism, we compute c_1 for each snapshot and create two corresponding subsets by distinguishing between the two classification outcomes by the network after training. Fig. 12.5 shows the distributions of c_1 when being classified as $T \leq T'$ (red) and $T > T'$ (blue) for $T' = 0.1 \ldots 1.2$. For T' close to the lower boundary of simulated temperatures, $T' = 0.1$, we see how the network classifies (almost) all snapshots as $T > T'$, hence locking in on a majority decision. However, for intermediate temperatures $0.3 \lesssim T' \lesssim 1.2$, a sharp cutoff between samples classified as $T \leq T'$ and $T > T'$ in terms of c_1 is observed. Indeed, the cutoff matches quantitatively the averages $\bar{c}_1(T')$, underlining that the network makes its decision solely by comparing $c_1^{(s)}$ with (a learned) cutoff value given by $c_1' = \bar{c}_1(T')$.

Having identified the FCS of c_1 as the decisive mechanism of the network to detect qualitatively differing snapshots in the Heisenberg model, we take a closer look at the widths σ_1 of the distributions $\{c_1\}$ as a function of temperature, i.e., we study the fluctuations of c_1,

$$\sigma_1^2 = \langle \hat{c}_1^2 \rangle - \langle \hat{c}_1 \rangle^2 . \tag{12.9}$$

Results are shown in Fig. 12.6 (a). We observe that at high temperatures, the width of the distributions stay relatively constant. At roughly $T \sim T'_{\text{max}} \sim 0.8$, however, the standard deviation starts to significantly increase, consistent with magnetic fluctuations becoming more prominent at temperatures below T^*. As shown in Fig. 12.6 (a), this holds for both nearest neighbor as well as diagonal two-point correlations.

Explicitly writing out Eq. (12.9),

$$\sigma_1^2 = \frac{1}{N_b^2} \sum_{\langle \mathbf{i},\mathbf{i}' \rangle} \sum_{\langle \mathbf{j},\mathbf{j}' \rangle} \langle \hat{S}_{\mathbf{i}}^z \hat{S}_{\mathbf{i}'}^z \hat{S}_{\mathbf{j}}^z \hat{S}_{\mathbf{j}'}^z \rangle - \langle \hat{c}_1 \rangle^2 , \tag{12.10}$$

we see that σ_1 in fact includes four-point correlations over two nearest neighbor spin pairs—

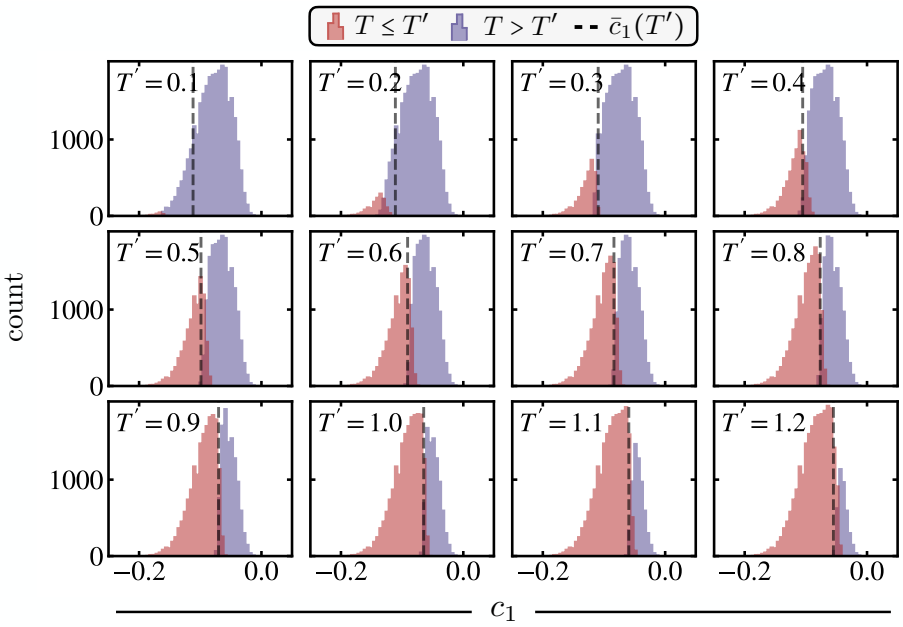

Figure 12.5: **Classification boundary c_1'.** After training, c_1 is calculated and sorted into two sets corresponding to their classification. Approximations c_1 of snapshots classified as $T \leq T'$ ($T > T'$) are shown in red (blue) for $T' = 0.1 \ldots 1.2$. For $T' = 0.1$, (almost) all snapshots are classified to belong to $T > T'$. For $T' \geq 0.3$, maximum accuracy is instead achieved by learning a boundary c_1', below (above) which all snapshots are classified as $T \leq T'$ ($T > T'$) – underlining that the decisive process of the network is solely based on evaluation of c_1. Though not exactly, these cutoffs match averages of c_1 at the decision boundary temperature, i.e., $\bar{c}_1(T')$ (grey dashed lines).

which, for a given configuration of indices $\langle \mathbf{i}, \mathbf{i}' \rangle, \langle \mathbf{j}, \mathbf{j}' \rangle$ might lie far apart from each other. Hence, the width of the distribution of c_1 directly includes information about long-range properties of the spin-spin correlations. Note that, while nearest neighbor two-point correlations show monotonous behavior as a function of temperature, long-range two-point correlations as appearing in the susceptibility, Eq. (12.3), *do* show signals of changes of the thermodynamic properties, cf. Fig. 12.1 (b). However, as the network is by construction restricted to analyze local correlations only, it has no access to evaluate these long range properties. By instead considering the FCS of c_1, the network finds a back door to analyze long-range correlations via the four-point correlator appearing in Eq. (12.10), which enables it to detect qualitatively different thermodynamic characteristics of snapshots above and below T'_{max}.

In fact, the width of c_1, Eq. (12.9), very closely resembles the form of the specific heat C_V, Eq. (12.4). Concretely, σ_1^2 corresponds to the Ising part of $T^2 C_V$, where in particular cross-terms such as $\sim \langle \hat{S}^x_{\mathbf{i}} \hat{S}^x_{\mathbf{i}'} \hat{S}^z_{\mathbf{j}} \hat{S}^z_{\mathbf{j}'} \rangle$ as appearing in C_V are not present. Though there exists no pronounced peak of σ_1 as observed for the specific heat at $T_C \sim 0.6$, its strong alternation for $T \lesssim 0.8$ is highly suggestive of corresponding thermodynamic features appearing in C_V, cf. Fig. 12.1 (b). However, though similarities are present, there exists no direct correspondence between the FCS signatures the network utilizes and thermodynamic properties such as C_V or χ_s. By indirectly evaluating long-range properties (as appearing in χ_s and C_V) of four-point correlations

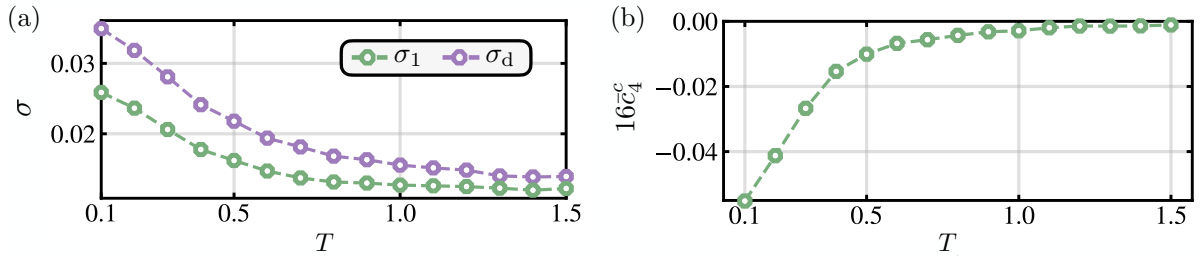

Figure 12.6: **Standard deviations and connected four-point correlations.** (a) The empirical standard deviation $\sigma_{1/\mathrm{d}}$, Eq. (12.9), of c_1, c_d, showing a sharp increase below temperature $T'_{\mathrm{max}} \sim 0.8$. (b) Averaged connected four-point correlator, Eq. (12.11), as a function of T. While being vanishingly small for $T \gtrsim T'_{\mathrm{max}}$, for $T \lesssim T'_{\mathrm{max}}$ the connected correlator gains significant weight.

(as appearing in C_V), the network succeeds in detecting qualitative changes in the snapshots as a function of temperature. These detected changes cannot, however, directly be attributed to originating from the peak in C_V or χ_s, and shall rather be interpreted as a related but independent indicator of qualitative change close to the pseudogap regime—as also suggested by the position of the performance maximum lying in between the peaks of C_V and χ_s. Nevertheless, the presence of pronounced signatures of σ_1 as a function of temperature is very intriguing by itself, in turn strongly encouraging the observation of similar indications at finite doping in spin-resolved occupation number snapshots as accessed through quantum gas microscopes.

We conclude the above discussion by calculating explicitly the connected four-point spin correlator,

$$\begin{aligned}\langle \bar{c}_4^c \rangle = \frac{1}{N_b^2} \sum_{\langle \mathbf{i},\mathbf{i}' \rangle} \sum_{\langle \mathbf{j},\mathbf{j}' \rangle} \Big[&\langle \hat{S}^z_{\mathbf{i}} \hat{S}^z_{\mathbf{i}'} \hat{S}^z_{\mathbf{j}} \hat{S}^z_{\mathbf{j}'} \rangle - \langle \hat{S}^z_{\mathbf{i}} \hat{S}^z_{\mathbf{i}'} \rangle \langle \hat{S}^z_{\mathbf{j}} \hat{S}^z_{\mathbf{j}'} \rangle \\ &- \langle \hat{S}^z_{\mathbf{i}} \hat{S}^z_{\mathbf{j}} \rangle \langle \hat{S}^z_{\mathbf{i}'} \hat{S}^z_{\mathbf{j}'} \rangle - \langle \hat{S}^z_{\mathbf{i}} \hat{S}^z_{\mathbf{j}'} \rangle \langle \hat{S}^z_{\mathbf{i}'} \hat{S}^z_{\mathbf{j}} \rangle \Big],\end{aligned} \tag{12.11}$$

which we again approximate using the Heisenberg snapshots, $\bar{c}_4^c$. Eq. (12.11) gives information about the genuine four-point correlations in the system, that in particular go beyond merely the correlation length of the two-point correlators. Evaluation of $\bar{c}_4^c$ shows vanishingly small values for $T > T'_{\mathrm{max}}$, shown in Fig. 12.6 (b). However, as T drops below T'_{max}, $\bar{c}_4^c(T)$ experiences a sharp increase, indicating how long-range, four-point correlations gain significant weight below T'_{max}—and correspondingly below the characteristic temperature, T^*, and the maximum of the specific heat, T_C.

Filter size

In the above discussion, we have focused on fixed convolutional filter sizes of 2×2 and demonstrated that the FCS of two-point correlations enable the network to classify snapshots. To analyze possible dependencied on the filter size, we now retrain the model with a single 3×3 filter, and again analyze the network's performance and regularization path; results are illustrated in Fig. 12.7. Though showing slight deviations in the network's accuracy as a function of T' from 2×2 filters, the qualitative W-shape including the position of T'_{max} remains unchanged when considering larger filter sizes, Fig. 12.7 (a). As for the 2×2 filter, including solely two-point cor-

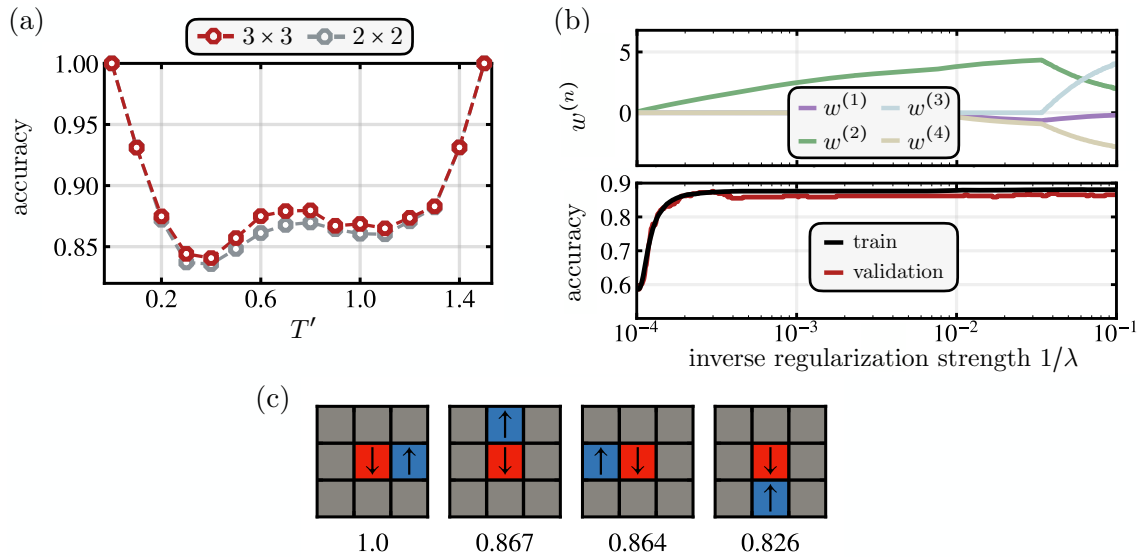

Figure 12.7: **Larger filter sizes.** (a) The network's performance as a function of decision boundary T' for 3×3 (red) as well as 2×2 filters as presented in the main text (grey). Though slight quantitative differences are present, the qualitative shape including the position of the maximum remains unchanged. (b) Regularization path analysis for 3×3 convolutional filters. Inclusion of two-point correlations lead to a saturation of the accuracy. Finite weights of higher-order correlations as present at large $1/\lambda$ have no effect on the performance on the network, highlighting the importance of the regularization path analysis to isolate the most important contributions. (c) Two-point correlations of highest weights $f_{c_1}(\mathbf{a}_1) f_{c_2}(\mathbf{a}_2)$, normalized by the maximum value. As for the 2×2 filter, nearest neighbor correlations single out as the most important contributions for the network's decision.

relations leads to maximum accuracy as a function of regularization strength λ, see Fig. 12.7 (b). Note that, with increasing inverse regularization strength $1/\lambda$, weights corresponding to higher order correlations also light up, however without any noticeable effect on the network's performance. This highlights the importance of the regularization strength analysis, whereby solely looking at weights of the last dense layer for $\lambda = 0$ is generally not sufficient to reliably learn which correlations are important. In Fig. 12.7 (c), we show the four two-point correlations with highest weights (corresponding to $f_{c_1}(\mathbf{a}_1) f_{c_2}(\mathbf{a}_2)$, normalized by the highest value). As for the 2×2 filter, nearest neighbor spin-spin correlations single out as the most important contributions.

12.3 Transformer architectures

A general concern when using convolutional neural networks to classify phases as presented above is the limitation of correlations to the convolutional window, which seemingly excludes sensibility to long-range order. As seen above, performant characterization can nevertheless be achieved by the network via analysis of the FCS of local correlations, which implicitly includes longer-range contributions. Nevertheless, a network architecture that is able to intrinsically capture long-range correlations is desirable for future applications of machine vision techniques in

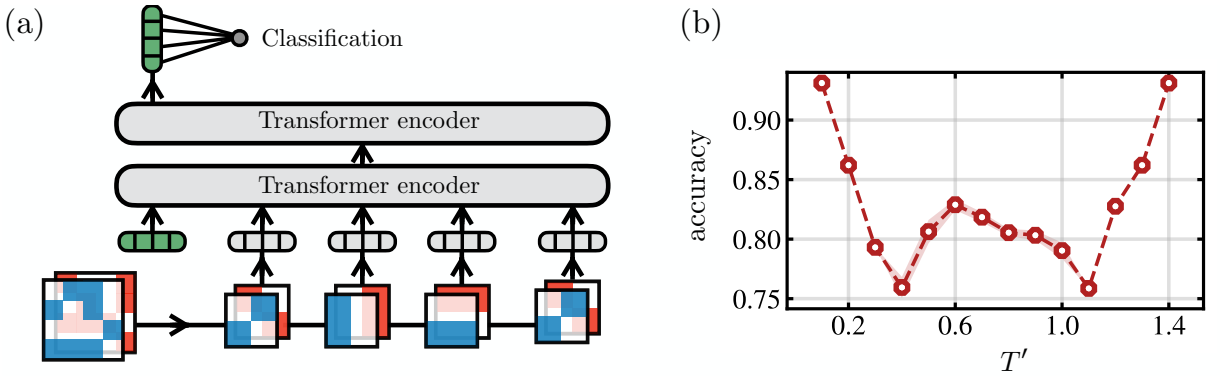

Figure 12.8: **Confusion transformer.** (a) Schematic illustration of the transformer architecture coupled to a confusion learning scheme. Snapshots are cut into small patches and linearly embedded via learnable matrices. The classification token (shown in green) as well as positional encodings are added to the sequence, before being encoded in two transformer blocks. The classification token – now including information of all patches – is retrieved after the last self-attention encoder and classified to belong to $T \leq T'$ or $T > T'$. (b) Classification accuracy as a function of T'. The W-shape signals detection of qualitative change between the regions $T \lesssim 0.6$, $T \gtrsim 0.6$. Light red areas correspond to the error to the mean of 20 repetitions.

many-body physics. Transformers are a promising candidate for this purpose, taking advantage of non-local (and i.p. long-range) self-attention originally designed to capture interdependencies in natural language processing (NLP) [483]. In particular, and in stark contrast to e.g. recurrent neural networks (RNN) and long short-term memory models (LSTM) [484], transformer architectures explicitly avoid recurrent processing of sequential data. Instead, they compute similarity scores between all constituents of a given input sequence (self-attention), allowing to capture long-range dependencies by processing the input as a whole—i.e., they do not rely solely on past hidden states in the sequence.

In the past years, extension of transformers to image processing (vision transformers) has proven itself to be comparably powerful to convolutions [485], opening possible routes toward their application in many-body physics [486–488]. The architecture of a vision transformer is schematically illustrated in Fig. 12.8 (a). In the first step, input images are cut into smaller patches. These patches are subsequently linearly transformed, i.e., d-dimensional representations of the input patches, called tokens, are computed[6]. Importantly, as transformers do not sequentially process the input, the tokens are further positionally encoded, i.e., the position of the patch within the original image is stored. Thereafter follows the self-attention encoder, where all-to-all inter-dependencies between tokens are computed. In particular, three linear transformations are learned, resulting in three feature vectors per token, referred to as query, key and value (QKV). Evaluation of dot-products between query-key pairs results in attention scores between corresponding pairs of tokens, which is then used to efficiently store inter-dependencies of a given token with the remaining sequence. By feeding the encoded output of a single transformer block into another, independent encoder, this process is repeated multiple times. Additionally, multiple QKV transformations can be learned and applied in parallel in each transformer block,

[6] In NLP, these tokens correspond to encodings of words.

resulting in multi-head attention encodings.

In addition to the data tokens, a randomized classification token is added to the beginning of the sequence, which, via the self-attention mechanism, stores all inter-dependencies between tokens while being processed through the various layers. After application of the encoding blocks, the classification token is passed to a standard classifier. For a more detailed discussion of vision transformer networks, we refer to its original proposal in [485]. For quantum-image processing, the vision transformer's intrinsic capability of capturing long-range dependencies promises sensitivity to long-range and non-local (e.g. topological) order, potentially leading to significant advantages over standard, convolutional approaches.

12.3.1 Confusion Transformer

We implement a vision transformer and combine it with the same confusion learning scheme outlined in Sec. 12.2. The original snapshot images are cut into 4×4 patches, and are fed into the first transformer encoder after a learnable linear embedding and positional encoding[7] is applied. In particular, the 32-dimensional sequences (16 entries for each channel) are embedded into an 8-dimensional space (tokens), and a classification token is inserted at the beginning of the sequence (green box in Fig. 12.8 (a)). For simplicity, we use a single head within the encoder, and limit the network to two transformer blocks. After applying self-attention and classifying the auxiliary classification token, accuracies after training are presented in Fig. 12.8. Similarly to using convolutional neural networks, a clear W-shape is visible in the accuracy as a function of decision boundary T', with a pronounced maximum at $T'_{\text{max}} \sim 0.6$—suggesting that also the vision transformer detects the alternations of thermodynamic properties. Through accessing the model's learned attention maps between various patches, their inter-dependencies can be analyzed. In particular, tailored encoding blocks could allow for interpretation in terms of correlation functions similar in spirit to CCNNs, whereby the order of encoded correlations increases with each encoding layer in the transformer architecture. Importantly, the all-to-all self-attention mechanism could surpass convolution based approaches, in particular when facing systems characterized by long-range and non-local properties.

12.3.2 Correlator Transformer

Although the above architecture demonstrated the ability to differentiate between distinct regimes, the interpretability of the transformer's output remains challenging. This is primarily due to the complex encoding layers, which do not directly compute physical correlation functions. Consequently, there is a need for tailored architectures inspired by the transformer's attention mechanism but simplified to allow for physical interpretability. In the following, we briefly outline the main idea and working principle of the Correlator Transformer (CoTra), developed by Abhinav Suresh during his Master's thesis in Regensburg, under the supervision of Annabelle Bohrdt and co-supervised by the author of this thesis.

The working principle of the CoTra is summarized in Fig. 12.9. As in the architecture outlined

[7] We use the same positional encoding as proposed in [483].

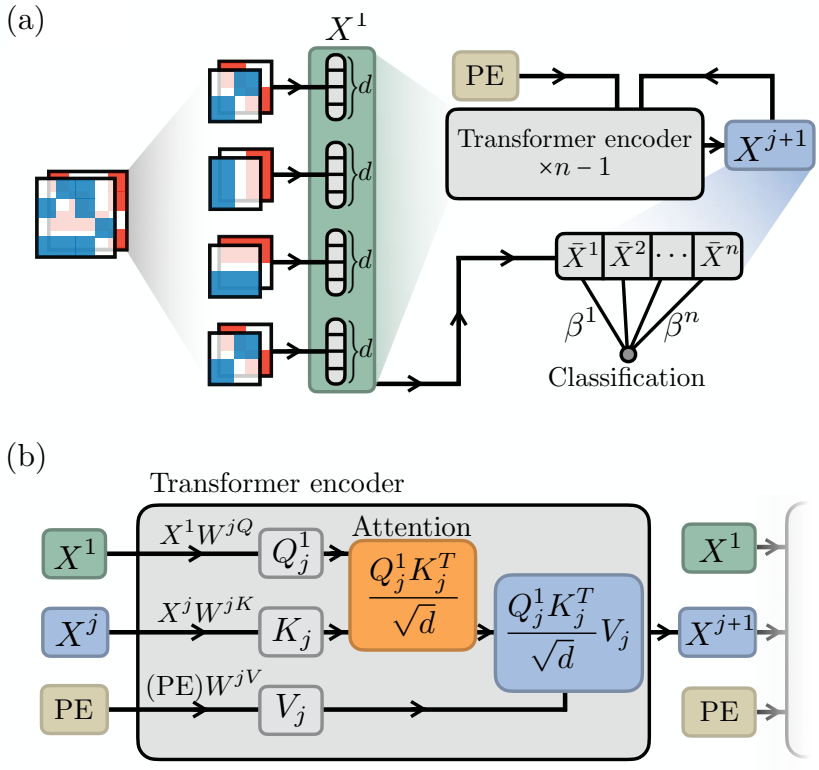

Figure 12.9: **The correlator Transformer.** (a) The overall flow starts from the 2D input data, here illustrated by a snapshot with two channels. After cutting the input into patches, they are linearly embedded to dimension d. The collection of d-dimensional vector tokens is denoted by X^1 (green box). Higher-order correlations are then generated in the Transformer encoder. To analyze n^{th} order correlations, $n-1$ encoding steps are carried out. While the query remains identical throughout all layers, keys (K_j) and values (V_j) are learned and computed in each layer, shown in panel (b). In the j^{th} layer, the attention then includes correlations up to order $j+1$. By multiplying with the value V_j, X^{j+1} is computed. PE denotes the absolute positional encoding. Averaging the outputs results in the vector $[\bar{X}^1, \bar{X}^2, \ldots, \bar{X}^n]$, which is then used for classification. Through a regularization path analysis, weights $\beta^\ell, \ell = 1, \ldots, n$ of the final layer give information about which correlations are important for successful classification.

in Fig. 12.8, the snapshot is divided into patches and linearly embedded into vectors of dimension d. This embedding corresponds to a linear transformation of the snapshot itself and can be interpreted as a sum over individual pixels, i.e., first-order correlations. The main idea of the subsequent steps is to generate maps of second, third, and higher-order correlations through a tailored transformer encoder.

Initially, query and key matrices are applied to the embedded patches, denoted as X_1. By incorporating positional embeddings (see Ref. [12] for details), a second-order attention map X_2 is constructed. This map represents a superposition of second-order terms, weighted according to the learned key, query, and embedding matrices. Feeding X_2 and X_1 into the encoder produces a third-order attention map X_3, and this process can be iterated to generate higher-order maps. The resulting maps X_j are then averaged, and a simple linear regression network performs classification. Similar to the CCNN network, a regularization path analysis distills

the most important correlations that the network uses for its decision-making. Importantly, the attention maps provide insights into the explicit correlations utilized by the network.

The network reveals two types of contributions: intra-patch correlations, which arise from correlations within individual patches of the snapshot, and inter-patch correlations, corresponding to correlations between different patches. While the former highlights significant local information in the data, the latter enables the detection of long-range dependencies in the snapshots.

As detailed in Ref. [12], the CoTra architecture is capable of learning various phenomena, such as local AFM order, global gauge constraints in lattice gauge theories, and non-local structures like the formation of Cooper pairs in momentum snapshots or distinguishing percolating from non-percolating images. Due to the direct interpretability of the network, different correlation orders can be characterized and identified in an unsupervised manner.

12.4 Autoencoders

Techniques initially created for data compression have further developed into popular tools to analyze data of quantum systems. As an example, autoencoders (AE) have been proposed as an unsupervised way to study the occurrence of phase transitions of quantum many-body systems [448, 449]. Here, the network is exposed and trained to compress and reconstruct certain physical features in a given parameter regime. When then showing the model data from a different phase, it fails to reconstruct the data and hence notices sudden changes of physical properties. In this context, autoencoders so far primarily focused on quantities like the entanglement spectrum [448, 449], which contains a large amount of information about the quantum state and hence qualifies as a good candidate to study sudden changes in the many-body wave function when passing a phase transition. However, the entanglement spectrum is quite a theoretical object, which lacks experimental accessibility.

Here, we propose the use of an autoencoder architecture to directly analyze many-body snapshots. For a certain parameter configuration of an underlying Hamiltonian, snapshots X (following the probability distribution $P(X)$) are fed into the network, see Fig. 12.10 (a). They are then compressed, with the goal that during training the model learns an abstract representation of the probability distribution within the dimensionally reduced latent space. When again being upscaled to the original size, the model is trained such that reconstruction losses between the original and output snapshots are minimal, see Fig. 12.10 (a).

12.4.1 The J_1-J_2 Heisenberg model

We here study the frustrated J_1-J_2 Heisenberg model, given by the Hamiltonian

$$\hat{H} = J_1 \sum_{\langle \mathbf{i},\mathbf{j} \rangle} \hat{\mathbf{S}}_\mathbf{i} \cdot \hat{\mathbf{S}}_\mathbf{j} + J_2 \sum_{\langle\langle \mathbf{i},\mathbf{j} \rangle\rangle_{\text{diag}}} \hat{\mathbf{S}}_\mathbf{i} \cdot \hat{\mathbf{S}}_\mathbf{j}, \tag{12.12}$$

where $\langle \mathbf{i},\mathbf{j} \rangle$ ($\langle\langle \mathbf{i},\mathbf{j} \rangle\rangle_{\text{diag}}$) signals nearest neighbors (diagonal next-to-nearest neighbors) on the square lattice. The model features antiferromagnetic (AFM) ordering for $J_2/J_1 \lesssim 0.41$, a stripe

AFM phase for $J_2/J_1 \gtrsim 0.61$, and a non-magnetic region in between, being a promising candidate for a quantum spin liquid [252–257], see also Chap. 6.

We simulate a 4×8 $J_1 - J_2$ Heisenberg system DMRG with periodic (open) boundaries along x- and y- direction. In order to project to the z-spin basis, we implement a global spin U(1) symmetry instead of utilizing the full SU(2) invariance of Eq. (12.12). We take uncorrelated snapshots of the converged matrix product state via the perfect sampling approach in the z-basis, $\{|\uparrow\rangle, |\downarrow\rangle\}$. Hence, our snapshots consist of a single channel (one-hot-vectors) with values $0, 1$ for $|\downarrow\rangle, |\uparrow\rangle$, respectively.

We start by analyzing the snapshots using a fully connected autoencoder with two en- and decoding stages, as depicted in Fig. 12.10 (a). In each encoding step, we reduce the number of nodes by a factor of two, leading to a latent space dimension of $\mathcal{D}_Z = \mathcal{D}_X/4$. The goal of the network is to be able to reconstruct the snapshots within the training region.

We further add a skip connections between symmetric layers with equivalent dimensions, allowing for the efficient transfer of encoded information [449]. We train the model to minimize the mean square error (MSE) between input and reconstructed snapshot, given by

$$\mathcal{L}_{\text{rec}} = \sum_{\mathbf{i}} (X_{\mathbf{i}} - Y_{\mathbf{i}})^2. \tag{12.13}$$

During training, the model learns to represent the distribution of snapshots in the training set in a low-dimensional latent space in an abstract way. Ideally, it picks up which patterns and correlations are important to accurately represent the data set in a low-dimensional space. Hence, if these correlations appear in a previously unseen snapshot of the same distribution as the training set, the network will be able to spot and reconstruct these features, leading to a high reconstruction quality. On the contrary, when input snapshots are sampled from a different distribution in a different physical phase, the network will fail to reconstruct the key features of the input data and hence suffer from large reconstruction errors.

The upper panel in Fig. 12.10 (a) shows the dense AE architecture, where (i) the data is flattened, (ii) compressed via two fully connected layers to latent dimension $\mathcal{D}_z = 8$, and (iii) symmetrically upscaled to the input dimension. The mean square error loss is then computed between the input and output snapshots and used as a base for an ADAM gradient descent. A typical loss progression is shown in Fig. 12.10 (b), where we train the model for $J_2/J_1 = 0.05 \ldots 0.2$.

After 50 epochs, we stop training and evaluate the MSE for the each J_2/J_1, shown in Fig. 12.10 (c). The anomaly loss is defined as the MSE offset by the mean error in the training region, and afterwards rescaled to a maximum of unity. When training in the AFM region ($J_2/J_1 = 0.05 \ldots 0.2$), the anomaly score stays almost constant up until $J_2/J_1 \sim 0.4$, where a sharp rise signals a transition to a different regime. After this sharp rise, between $J_2/J_1 = 0.6 \ldots 0.95$ the loss is again relatively flat, suggesting that there are in total three distinct regimes in the considered parameter span. When instead training the model to reconstruct snapshots within the stripe AFM phase, similar features of the loss curve can be observed.

We evaluate the order parameters of the AFM and stripe AFM phases using the MPS, given

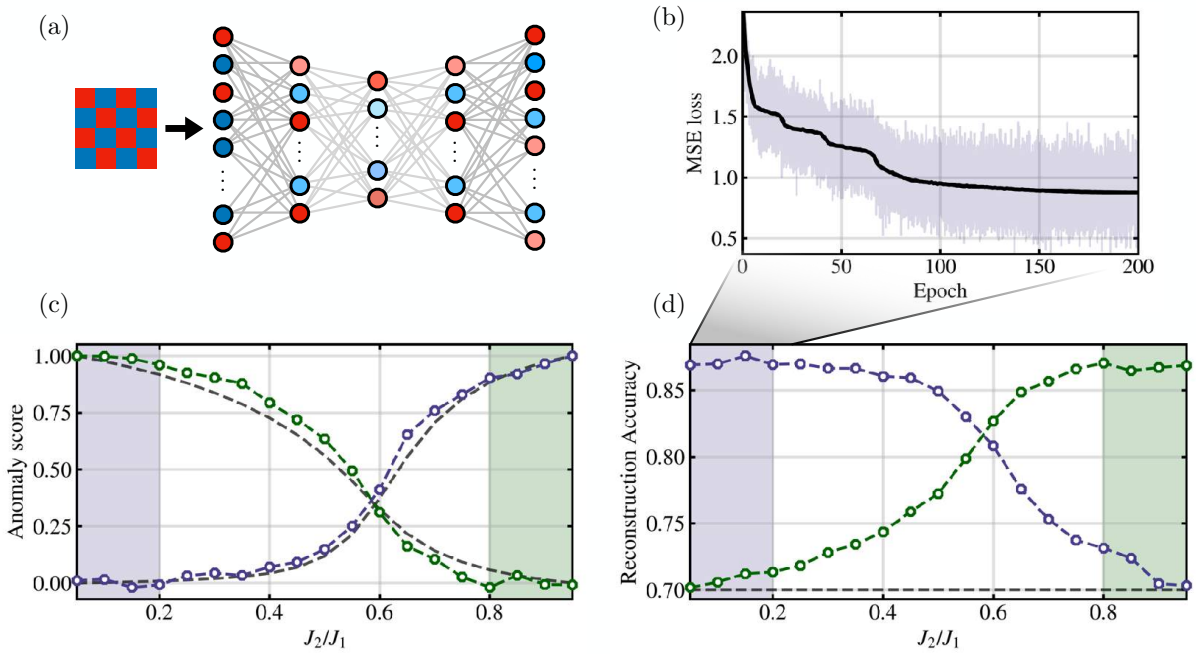

Figure 12.10: **Anomaly detection using dense Autoencoders.** (a) Network architecture of a plain dense AE. The data is flattened, downscaled in two steps to latent dimension $\mathcal{D}_z = \mathcal{D}_{\text{image}}/4$, and upscaled in a symmetric fashion. To test the AE, we use 2,000 snapshots of a 4×8 frustrated $J_1 - J_2$ Heisenberg model on the square lattice. We use ReLu nonlinearities in down- and upscaling layers, except for the last layer, where a sigmoid function results in an output $\in [0, 1]$ for each lattice site. We use pixel wise mean square error loss and measure the accuracy by how many pixels are reconstructed accurately (with pixel $= |\uparrow\rangle, |\downarrow\rangle$ if the output is > 0.5 and < 0.5, respectively). (b) Loss progression during training. The black solid line shows averages over one epoch, blue lines in the background show losses per mini-batch (of size 24). (c) Anomaly score when training the network in regions $J_2/J_1 = 0.05 \ldots 0.2$ ($J_2/J_1 = 0.05 \ldots 0.2$) shown in blue (green). The MSE loss normalized to the respective maximum of the loss, and the mean reconstruction error of the training set is subtracted. Grey dashed lines show the order parameters in the AFM and stripe AFM phases, given by $S(\pi, \pi)$ and $S(0, \pi)$, respectively. (d) The same as in (c), with the reconstruction accuracy shown for the two different training regimes. The grey dashed line is the reconstruction accuracy of random snapshots.

by the spin-structure factor

$$S(\mathbf{q}) = \frac{1}{L_x L_y} \sum_{\mathbf{i},\mathbf{j}} e^{i(\mathbf{i}-\mathbf{j})\mathbf{q}} \langle \hat{\mathbf{S}}_\mathbf{i} \cdot \hat{\mathbf{S}}_\mathbf{j} \rangle \tag{12.14}$$

at $\mathbf{q} = (\pi, \pi)$ for AFM, and $\mathbf{q} = (0, \pi)$ for stripe AFM order. The order parameters (normalized by their maximum values) are shown by black dashed lines in Fig. 12.10 (c). We observe a qualitative, but also astoundingly well quantitative match, between the anomaly loss and the order parameter of the system. When plotting the reconstruction accuracy (that is, the ratio of pixels that are predicted correctly by the network after rounding the output to one-hot-vectors) instead of the anomaly score, we see how the reconstruction accuracy reaches $\sim$ 90% in the training regime, and drops to $\sim$ 70% in the correspondingly "opposite" phase. Similarly, when feeding

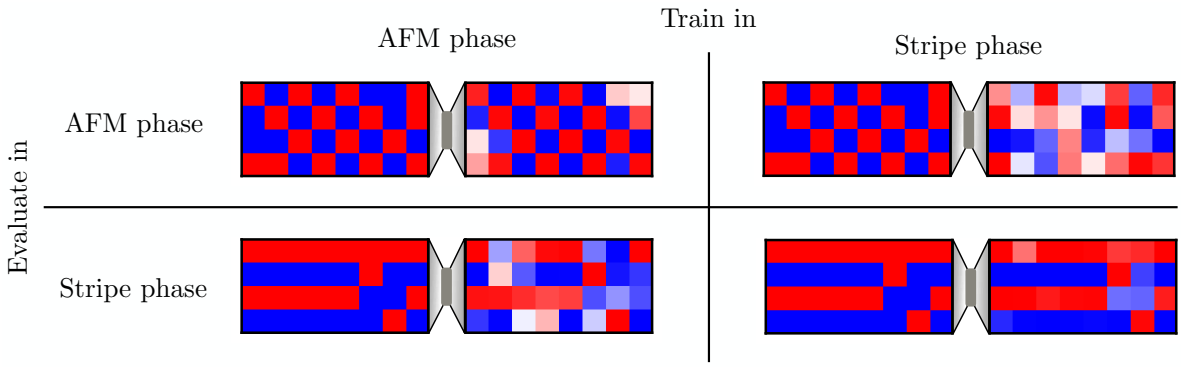

Figure 12.11: **Reconstruction of the AE.** Performance of the AE when training and evaluating it in the AFM and stripe AFM phases. For each case, we look specifically at the reconstruction of a snapshot for $J_2/J_1 = 0.1, 0.9$. During training, the network learns which patterns and correlations are important when compressing the snapshot. Upon decoding, these patterns are correctly reconstructed, whereas fluctuations from the corresponding patterns are blurry after upscaling the compressed image. The autoencoder hence naturally acts as a highlighter of the important patterns and correlations in a given phase.

random data into the network, a reconstruction accuracy of $\sim 70\%$ is achieved[8], underlined by the black dashed line in Fig. 12.10 (d).

By choosing representative snapshots in both the AFM and stripe AFM regimes, we visualize the network's performance in Fig. 12.11 after training in both phases. Specifically, we show input snapshots together with their corresponding output of the autoencoder after training in a specific phase. When training the system with snapshots in the AFM phase, the autoencoder picks up the checkerboard pattern characterizing the phase, and reconstructs to high accuracy all patches in the original snapshot that follow the AFM alternating pattern. Fluctuations from the Néel state result in blurry pixels in the reconstruction, i.e., the network is not able to predict the patches governed by fluctuations. When showing the autoencoder snapshots of the stripe phase after training in the AFM regime, it further fails to reconstruct the stripy magnetic pattern, and instead only is able to capture the local AFM features in the snapshot.

The same holds when reversing the training, i.e., stripe features can be reconstructed when training inside the stripe AFM regime, whereas the network is not able to compress AFM type patterns for low J_2/J_1. The above discussion suggests that the autoencoder—while accurately predicting qualitative changes in physical properties—can further be used to highlight patterns and correlations that the encoder picks up as common and important features within the trained regime.

The above results position the AE as a promising toolkit to analyze data of FH quantum gas simulators, and can be used to act as a marking tool that highlights characterizing patterns in the snpshots. Depending on the use case, a variety of adjustments to the AE come to mind: making the AE variational allows for a regularization of latent space, which may give interpretable insights into the network's mechanism. Training the AE in an adversarial way may further en-

[8]This is due to skip connections, which transport some extend of information between the encoding and decoding layers. Hence, random snapshots have a reconstruction accuracy of >50%.

hance its capabilites, at the same time reducing the focus on the network to output the exact same snapshot, but rather comparing two snapshots that come from the same or different distributions. However, in the latter case, we have not found any significant performance differences to the standard AE, and hence refrain from showing the results here.

12.5 Discussion

In the first part of this chapter, we proposed the co-CCNN scheme as an approach based on interpretable neural networks to detect distinct regimes in quantum many-body snapshots. Specifically, by utilizing correlation-based convolutions in conjunction with a confusion learning scheme, it is possible to identify parameter regions that exhibit significant differences, while maintaining complete interpretability through correlation functions.

We have applied the method to snapshots of a 2D Heisenberg spin system, where the build up of magnetic correlations as the temperature is decreased leads to the appearance of, e.g., pronounced peaks of the specific heat and spin susceptibility. Using our method, we found that the network categorizes the snapshots into two regimes $T \lessgtr T'_{\mathrm{max}}$, whereby T'_{max} was found to broadly match temperatures of maximal specific heat and susceptibility—thus capturing the variation of thermodynamic properties. We found that the network bases its decision solely on nearest neighbor correlations, which by itself have featureless, monotonic characteristics as a function of temperature. However, we presented strong evidence that the network indirectly accesses long-range, four-point correlations in the system by analyzing the full counting statistics of nearest neighbor correlations. This enables the network to detect alternations of thermodynamic quantities, such as the peak of the specific heat and suppression of spin susceptibility, which directly include contributions from long-range correlations.

With even subtle alternations being detected by the network, this opens up insightful future directions in interpretable quantum image processing. With regard to analog simulation of strongly correlated systems with quantum gas microscopes, the presented method can be directly applied to detect regions of differing phases, with immediate access to correlation functions which are important to characterize the respective regimes. Concretely, in the FH model our work suggests to directly look for the four-point spin correlator identified here, both as a function of doping and as a function of temperature at finite doping.

We note that for our numerical experiments, which consist of data sets similar in size to realistic quantum gas microscope experiments, the confusion learning scheme demands only low computational resource. Nevertheless, for larger data sets, the retraining for all possible decision boundaries can quickly become expensive, for which extended schemes as proposed in [489] combined with interpretable CCNN architectures pose a possible extension of our work.

Building a bridge toward networks with intrinsic capabilities for capturing long-range dependencies, in the second part of this chapter we demonstrated that training a standard vision transformer using the confusion learning scheme further supports the categorization $T \lessgtr T'_{\mathrm{max}}$. To enhance the interpretability of the transformer network, we summarized the working principle of the Convolutional Transformer (CoTra), whose attention maps can be directly interpreted

as physical correlations. With its successful classification performance and the corresponding physical interpretation of lattice gauge theories and snapshots characterized by non-local correlations, it will be insightful to test this architecture in more complex scenarios, including snapshots of the FH model. Regarding the geometric fractionalized Fermi liquid discussed in Chap. 7, the CoTra model can be directly applied to uncover potentially existing hidden order structures. In particular, the attention mechanism may enable the identification of the best matching strings of holes that form domain walls of the background antiferromagnet.

In the last part of this chapter, we benchmarked an autoencoding architecture applied to snapshots of the frustrated J_1-J_2 Heisenberg model. By learning to compress snapshots of various phases, the AE naturally highlighted significant structures, which were successfully reconstructed, while fluctuations away from these structures appeared as blur. This capability allows the separation of patterns from fluctuations, providing interpretable physical features in symmetry-broken phases.

13

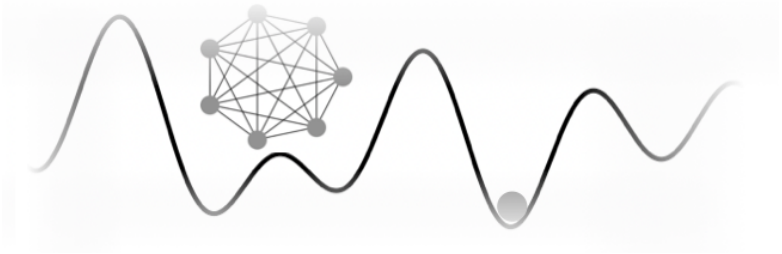

Beyond Fermi-Hubbard: Quantum annealing with chaotic driver Hamiltonians

Summary. Quantum annealing is a computational approach designed to leverage quantum fluctuations for solving large-scale classical optimization problems. Although incorporating standard transverse field terms in the annealing process can help navigate sharp minima, the potential for achieving a scalable quantum advantage for general optimization problems remains uncertain. In this chapter, we examine the effectiveness of including chaotic quantum driver Hamiltonians in the annealing dynamics. Specifically, we investigate driver Hamiltonians based on a bosonic spin version of the Sachdev-Ye-Kitaev (SYK) model, which features a high degree of non-locality and non-commutativity. Focusing on MaxCut instances on regular graphs, we find that a considerable proportion of SYK model instances demonstrate significant speedups, especially for challenging graph configurations. Additionally, our analysis of time-to-solution scalings for the low autocorrelation binary sequence (LABS) problem suggests that SYK-type fluctuations can outperform traditional transverse field annealing schedules in large-scale optimization tasks. Lastly, we evaluate the gate complexity of simulating dynamics under (various forms) of SYK-like Hamiltonians using digital schemes.

13.1 Introduction

In this thesis, we have provided a range of perspectives on the low-temperature physics of Fermi-Hubbard models. In this final chapter, we will extend our discussion beyond models with local interactions to consider highly non-local systems, such as the Sachdev-Ye-Kitaev model. While its unique physical properties give rise to a plethora of exotic and intriguing phenomena, our focus here will shift to a different perspective: exploring whether non-local, chaotic systems can

aid in solving classical optimization problems within quantum annealing setups.

This chapter is based on the results of an independent collaboration with Subir Sachdev at Harvard University. Special acknowledgments go to Subir for his hospitality during my stay and for his continuous support beyond our collaboration. In particular, the content presented in this chapter is to large parts based on the following preprint, partially with textual overlap:

> [11] **HS** and S. Sachdev **Quantum Annealing with chaotic driver Hamiltonians**, arXiv 2409.20538 (2024)

We begin by providing an introduction to quantum annealing in Sec. 13.2. Next, we introduce the Sachdev-Ye-Kitaev (SYK) model and its bosonic descendants in Sec. 13.3. In Sec. 13.4, we use a simple toy model to illustrate how the terms appearing in the SYK model can be advantageous for quantum annealing. Subsequently, we apply these ideas to challenging MaxCut optimization problems in Sec. 13.5 and to the Low Autocorrelation Binary Sequence (LABS) problem in Sec. 13.6. Finally, in Sec. 13.7, we discuss the gate complexity of digitally simulating the SYK model (including fermionic, bosonic, and sparse variants) and provide an outlook on potential future experiments.

13.2 Quantum Annealing

Physically-inspired annealing approaches aim to use fluctuations as a resource to solve classical optimization problems with highly complex energy landscapes and many local minima. Historically, the concept of "simulated annealing" was proposed as a numerical tool to optimize a classical cost function with many independent parameters by performing Metropolis Monte Carlo simulations of an Ising model (whose energy landscape maps to the classical cost function [490]) at finite temperature. Systematically lowering the temperature by an annealing schedule then utilizes thermal fluctuations to escape local minima, ideally freezing the system in the ground state [491].

Kadowaki and Nishimori proposed to replace thermal by quantum fluctuations [492], where a time-dependent transverse field (TF), called the driver Hamiltonian, is added to the Ising Hamiltonian that describes the optimization problem. Indeed, it has been established that quantum annealing shows convergence to the optimal (ground) state with larger probability than simulated annealing in a variety of cases if the same annealing schedule is used [492–500]. The intuition for the enhanced performance is that quantum fluctuations allow for tunneling events through particularly spiky peaks of the energy landscape [501, 502], which in contrast are not possible when using classical simulated annealing.

The typical time-dependent Hamiltonian that evolves according to a specified annealing schedule $s(t)$ as a function of time t reads

$$\hat{H}_{\mathrm{QA}} = s\hat{H}_{\mathrm{C}} + (1-s)\hat{H}_{\mathrm{D}}. \tag{13.1}$$

Here, $\hat{H}_{\mathrm{C}}$ is the classical Ising Hamiltonian whose ground state corresponds to the solution of an optimization problem, and $\hat{H}_{\mathrm{D}}$ is the driver Hamiltonian that, importantly, does not commute

with $\hat{H}_C$. The annealing schedule $s(t)$ for a given total annealing time T is chosen such that $s(0) = 0$ and $s(T) = 1$. Ideally, the time evolution is adiabatic, i.e. when starting in the ground state of the driver Hamiltonian, the system stays in the instantaneous ground state of the system and finally evolves into a state that has large overlap with the ground state of the target Hamiltonian.

Naturally, the performance of the quantum annealing algorithm depends on the minimum (instantaneous) gap of the system during the evolution. In particular, according to the quantum adiabatic theorem [503], the annealing time T relates to the minimum instantaneous energy gap Δ as $T \sim 1/\Delta^2$. Fully solving the time-dependent Schrödinger equation for Sherrington-Kirkpatrick (SK) spin glasses and evaluating their performance for different annealing times reveals strong correlations between instances of the SK model that are particularly hard to solve (from now on called "hard instances") and their corresponding minimum instantaneous energy gap [504].

Following the definition in [505], such a hard instance is characterized by a "diabatic bump", where the success probability to end up in the ground state of the optimization Hamiltonian features a local maximum at intermediate annealing times, before increasing towards unity in the adiabatic regime $T \sim 1/\Delta^2$ (see also Ref. [504]). Intuitively, diabatic transitions that happen at short annealing times partially deplete the ground state occupancy *before* the instantaneous gap minimum, hence reducing the transition probability from the ground to the excited state at the gap closing. In contrast, for longer annealing times (but shorter than needed to be in the adiabatic regime), the ground state occupancy before the instantaneous gap minimum stays constant, and transitions to the first excited states are highly probable when approaching the minimum energy gap.

Recent technological advances in designing and engineering special purpose quantum annealing machines has sparked additional interest in quantum annealing, with the ultimate goal of building a scalable quantum device that implements coherent and adiabatic time evolution for Hamiltonians with flexible interactions [506]. With major efforts invested in superconducting qubit devices [502,507–512], neutral atom [513,514] and trapped ion [515,516] annealers are promising alternative architectures offering several advantages, including long coherence times and all-to-all connectivities.

The transverse field driver $\hat{H}_X = \sum_i \hat{\sigma}_i^x$ (with $\hat{\sigma}_i^x$ the Pauli-x matrix on site i) constitutes the Hermitian complete combination of operators that couple all binary sequences of the classical problem, and has established as the paradigmatic choice both in theoretical and experimental considerations [506]. However, a transverse field only couples states with Hamming distance $d_H = 1$, i.e., application of the driver results in a superposition of single spin flips for a given product state. This, in turn, opens the question whether driver Hamiltonians that include (non-local) multi-point interactions of degree > 1 may help to escape local minima and anneal to the ground state more efficiently in complicated optimization landscapes.

Moreover, the transverse field is a "stoquastic" Hamiltonian, which results in all path integral configurations to have real and positive weight, ultimately rendering the system sign-problem free [517]. Hence, properties of the annealing Hamiltonian can be efficiently calculated using classical techniques. Though Monte Carlo is designed to simulate the equilibrium

Boltzmann distribution (and hence only equilibrium properties can be directly computed), it has been shown that it can capture features of quantum dynamics and hence of the annealing process [502,518,519]. Indeed, identical scalings of computational time with system size for genuine and Monte Carlo simulated quantum annealing have been reported [502,518,519]. This may suggest that if an instance of a problem is particularly hard to solve using classical Monte Carlo methods, it is also hard to solve using quantum annealing with a TF driver. Utilizing driver Hamiltonians that can not be efficiently simulated classically may hence enable performance enhancements in particular for hard instances [520].

The effects of using non-stoquastic annealing schedules have been numerically analyzed in Refs. [521, 522]. Hormozi *et al.* demonstrated that adding non-stoquastic terms to the driver Hamiltonian can enhance the performance of hard instances by promoting diabatic transitions at short annealing times (i.e. away from the adiabatic regime) [522]. Crosson *et al.* reported similar findings, demonstrating that non-stoquastic terms do enhance the success rate, although not significantly more than the addition of stoquastic terms [521]. Furthermore, it was shown that by including non-stoquastic drivers that add antiferromagnetic quantum fluctuations to the annealing schedule, first order phase transitions can be reduced to be of second order for specific problems [523–526], enhancing the time to solution from scaling exponentially to polynomially with system size. From a different perspective, it has been demonstrated that tailored (generally non-stoquastic) Hamiltonians can be used to solve optimization problems with additional constraints, whereby the driver Hamiltonian is to be constructed such that it commutes with the constraint operators [527,528].

While progress has been made in understanding the effect of certain additional terms in the driver Hamiltonian, analyzing which type of fluctuations leads to the best performance for general optimization problems remains an open question. Following intuitive reasoning one may argue that the inclusion of non-local terms that couple states with larger Hamming distance $d_H > 1$ can allow for a more efficient exploration of the optimization landscape, hence leading to a computational advantage compared to the regular transverse field. This is in particular motivated by recent progress in neutral atom and trapped ion setups, which allow for the implementation of long-range interactions [529,530]. Additional quantum fluctuations by making the driver Hamiltonian itself quantum may further enhance the annealing performance. This motivates us to study optimization performances when implementing Sachdev-Ye-Kitaev-type fluctuations into the annealing schedule, whose nature are highly chaotic. We demonstrate that drastic computational enhancements can be achieved for general hard optimization problems.

13.3 The (bosonic) SYK model

Before analyzing the performance of quantum annealing with SYK-like driver Hamiltonians, let us give a brief introduction to the SYK model itself. The SYK model is a strongly correlated quantum many-body system that features highly entangled, non-Fermi liquid low-energy states [531,532] . It is chaotic, nearly conformally invariant, and exactly solvable in the thermodynamic limit. Specifically, the SYK model constitutes a concrete model Hamiltonian that fea-

tures many-body quantum chaos, which is characterized by fast scrambling of quantum information [533–535] that saturates universal bounds (formalized by the Lyapunov exponent) [536,537].

On the one hand, these special features allowed for valuable insights into the behavior of non-Fermi liquid phases in solid state materials, e.g. strange metals [538]. On the other hand, the SYK model is a non-relativistic, non-supersymmetric model that has been conjectured to be holographically dual to charged black holes with 2D anti-de Sitter (AdS2) horizons [539], making it a promising candidate to gain a consistent ultraviolet completion of classical gravity. In particular, simulating the system for a large but finite number of particles, which is not tractable with current classical numerical techniques, may give insights into $(1/N)$ quantum corrections of gravity due to the effect of loops of strings [540,541].

The particle-hole symmetric Majorana formulation of the SYK model with q-local interactions reads

$$\hat{H}_{\text{SYK}} = \sum_{i_1<\cdots<i_q} J_{i_1\ldots i_q}\hat{\chi}_{i_1}\cdots\hat{\chi}_{i_q}. \tag{13.2}$$

Here, $\hat{\chi}_i$ are N (hermitian) Majorana operators and $J_{i_1\ldots i_q}$ are independent Gaussian random variables with zero mean and variance

$$\text{Var}[J_{i_1\ldots i_4}] = \frac{(q-1)!}{N^{q-1}}. \tag{13.3}$$

The latter ensures that the bandwidth of the model is of order unity for all N.

Due to its broad applications, there has been increasing interest in performing digital quantum simulations of the SYK model on Noisy Intermediate-Scale Quantum (NISQ) processors, which are, however, heavily limited by their gate error rates and coherence times. Nevertheless, there have been recent attempts to simulate dynamics under (variants of) the SYK Hamiltonian for small system sizes [542–544], with up to $N = 8$ Majorana fermions. To this end, the SYK Hamiltonian Eq. (13.2) can be mapped to spin models that are implementable on quantum computers through the Jordan-Wigner [545] or other non-local (e.g. the Bravyi-Kitaev [546]) transformations. For instance, for the former, N Majorana operators can be represented by $N_s = N/2$ spin-1/2 operators through

$$\begin{aligned}\hat{\chi}_{2k-1} &\propto \left(\bigotimes_{j=1}^{k-1}\hat{\sigma}_j^z\right)\otimes\hat{\sigma}_k^x\otimes\mathbb{1}^{\otimes(N-2k)/2},\\ \hat{\chi}_{2k} &\propto \left(\bigotimes_{j=1}^{k-1}\hat{\sigma}_j^z\right)\otimes\hat{\sigma}_k^y\otimes\mathbb{1}^{\otimes(N-2k)/2}.\end{aligned} \tag{13.4}$$

However, due to the overhead of encoding fermionic degrees of freedom in bosonic qubit systems, studying bosonic versions[1] of the SYK model has been discussed as a promising avenue simulate chaotic models with quantum computers [547,548]. Following Refs. [549–551], we de-

[1] By bosonic we specifically mean that the system's Hilbert space has a tensor product structure whereby operators from different sites commute.

fine the bosonic SYK model with q-local all-to-all interactions (from now on denoted by bSYK$_q$)[2],

$$\hat{H}_{\text{bSYK}_q} = \sum_{i_1<\cdots<i_q} \sum_{\alpha_1,\ldots,\alpha_q} J_{i_1\ldots i_q}^{\alpha_1\ldots\alpha_q} \hat{\sigma}_{i_1}^{\alpha_1} \ldots \hat{\sigma}_{i_q}^{\alpha_q}. \tag{13.5}$$

Here, $\alpha_i = x, y, z$; $J_{i_1\ldots i_q}^{\alpha_1\ldots\alpha_q}$ are again (real) random Gaussian variables with vanishing mean and variance

$$\text{Var}[J_{i_1\ldots i_q}^{\alpha_1\ldots\alpha_q}] = \frac{(q-1)!}{N^{q-1}}. \tag{13.6}$$

It has been shown that many of the defining features of the SYK model, such as power law correlation functions and an extensive low-temperature entropy, are present also in the above bosonic formulation [548]. Furthermore, at large q, the bSYK$_q$ model features the same four-point functions as those of the SYK$_q$ Hamiltonian, leading to maximal chaos at low temperature [548]. This makes it an attractive candidate to study emergent gravitational descriptions and quantum chaos using quantum computers, primarily because it removes the issue of non-local operators when mapping fermionic degrees of freedom to spins. We will come back and address the gate complexity of simulating various forms of SYK-type models in Sec. 13.7.

With implementations of (variants of) the SYK model becoming more realistic, in the main part of this chapter we ask the following question: Can the chaotic and fast scrambling nature of the system enhance quantum annealing approaches to solve classical optimization problems? Building on the intuition above, non-locality combined with a high degree of non-commutativity of the SYK model may lead to higher probabilities to escape local minima and find the global minimum of the energy landscape. In Sec 13.4, we present a simple two-qubit energy landscape that illustrates the advantage of the above on an intuitive basis.

In the following, we will focus on two ways of including SYK-type driver Hamiltonians into the annealing schedule:

1. First, we study an annealing process where we start in the ground state of the bosonic SYK model, which is then annealed to the classical optimization Hamiltonian, i.e.,

$$\hat{H}_{\text{QA}}^{(1)} = s\hat{H}_{\text{C}} + (1-s)\hat{H}_{\text{bSYK}_q}, \tag{S1}$$

   with linear ramp $s(t) = t/T$. We note that the ground state preparation of $\hat{H}_{\text{bSYK}_q}$ is experimentally challenging. However, including the chaotic driver in various ways allows us to compare different settings of adding non-local fluctuations to the annealing process.

2. Second, we study the performance when adding SYK-type fluctuations on top of the TF schedule,

$$\begin{aligned}\hat{H}_{\text{QA}}^{(2)} = s\hat{H}_{\text{C}} + (1-s)\hat{H}_X \\ + 4s(1-s)\hat{H}_{\text{bSYK}_q}.\end{aligned} \tag{S2}$$

   In particular, here the system starts in the product state of the transverse field at $s = 0$.

[2] We note that a variety of bosonic versions of the SYK model have been proposed, including a two-component spin model [547]. However, we expect that our results largely don't depend on the details of the spin model; see also the discussion in Ref. [548]

Fluctuations of the SYK-type model are then added to the Hamiltonian (where the corresponding strengths of the TF and SYK model are equal at $s = 1/2$), ending at the classical Ising Hamiltonian at $s = 1$ (see also Refs. [521,522]). This approach is specifically motivated by the design of hardware annealers, where the system is initialized in a product state and then evolves dynamically under a time-dependent Hamiltonian, which can potentially be engineered to include more terms beyond the transverse field.

Both schedules (S1) and (S2) are compared to the standard TF annealing approach,

$$\hat{H}^X_{\mathrm{QA}} = s\hat{H}_C + (1-s)\hat{H}_X. \tag{TF}$$

Specifically, we test the performance of SYK-type drivers for two classical optimization problems: In Section 13.5, we look at MaxCut problems on random d-regular graphs, which can be mapped to an Ising model with 2-body interactions on the respective graphs. We demonstrate that for hard optimization problems, the SYK driver has a finite probability of performing significantly better than the TF driver. In Section 13.6, we look at the Low Autocorrelation Binary Sequence (LABS) problem, which aims to find a sequence of binary numbers with minimal autocorrelations. In this case, the classical optimization problem can be encoded in an Ising Hamiltonian that consists of non-local 4-body terms. All classical (exact and heuristic) algorithms known scale exponentially with system size for LABS. By solving the time-dependent Schrödinger equation for small system sizes, our results suggest that using chaotic drivers may lead to a scaling advantage compared to conventional annealing schedules.

13.4 Toy model

We start by constructing a simple energy landscape example that illustrates the advantage of (i) non-localilty and (ii) additional quantum fluctuations. To illustrate how non-local interactions can enhance the performance of quantum annealing, consider a system of two qubits and a classical energy landscape described by the Hamiltonian

$$\hat{\mathcal{H}}_C = -\Delta\hat{\sigma}^z_1\hat{\sigma}^z_2 + \delta(\hat{\sigma}^z_1 + \hat{\sigma}^z_2), \tag{13.7}$$

with $\hat{\sigma}^z_i$ the Pauli-z matrix on site i. For $\Delta/\delta \gg 1$, the energy landscape consists of sharp peaks for states $|\uparrow\downarrow\rangle$ and $|\downarrow\uparrow\rangle$, while $|\downarrow\downarrow\rangle$ is the ground state with a gap of 4δ to the first excited state $|\uparrow\uparrow\rangle$ (see Fig. 13.1 (a)). The transverse field ground state, $|{+}{+}\rangle = \frac{1}{2}(|\uparrow\uparrow\rangle + |\downarrow\downarrow\rangle + |\uparrow\downarrow\rangle + |\downarrow\uparrow\rangle)$, has an equal weight on all four basis states. When using solely the transverse field driver (which connects states with Hamming distance $d_H = 1$), dynamically shifting the weight to the ground state requires to pass through the spiky peaks. On the other hand, when additionally allowing fluctuations of the form $\hat{\sigma}^x_1\hat{\sigma}^x_2$, a direct connection between the two low-lying states $|\uparrow\uparrow\rangle$ and $|\downarrow\downarrow\rangle$ exists, which can help to find the ground state faster.

We first focus on the following annealing path akin to schedule (S2),

$$\hat{\mathcal{H}}_{\mathrm{QA}} = s\hat{\mathcal{H}}_C + (1-s)\hat{\mathcal{H}}_X \pm 4s(1-s)\hat{\sigma}^x_1\hat{\sigma}^x_2, \tag{13.8}$$

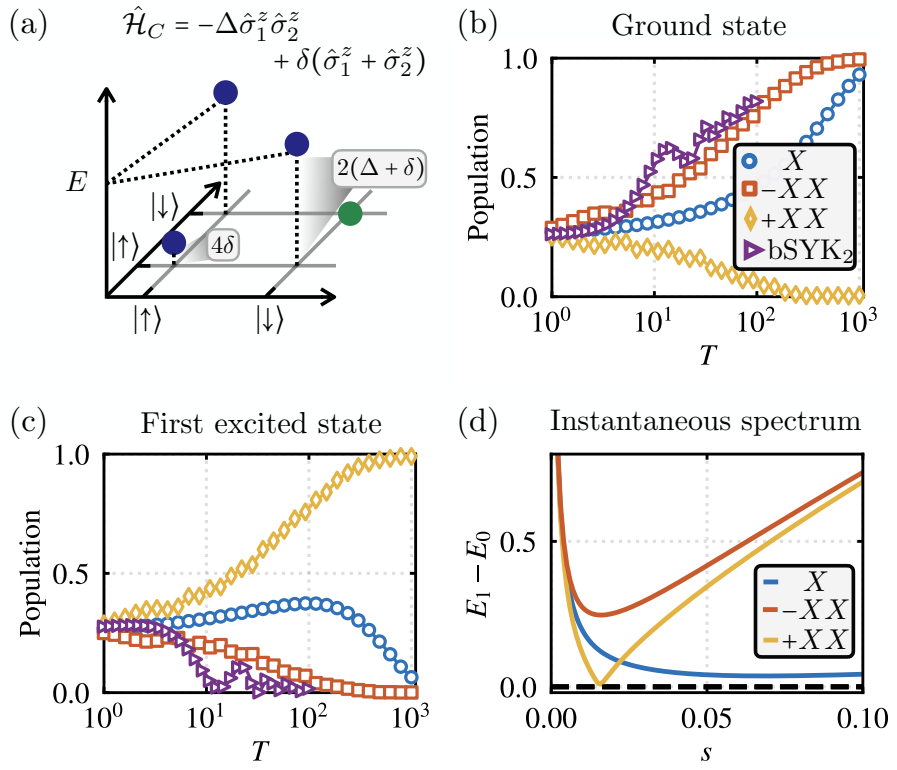

Figure 13.1: **2-qubit toy model.** (a) Energy landscape of Hamiltonian Eq. (13.7) for $\Delta/\delta \gg 1$. Relative to the ground state $|\downarrow\downarrow\rangle$, states with Hamming distance $d_H = 1$ are largely gapped out, while a small splitting to $|\uparrow\uparrow\rangle$ exists. (b) Ground state population after annealing schedule Eq. (13.8) when including only the TF driver (blue circles), and when addition additional terms $\pm XX$ (yellow diamonds and orange squares, respectively). Purple triangles show results for a particular instance of the bSYK$_2$ model. (c) The same as (b) for the first excited state. (d) Instantaneous eigenspectrum showing the gap to the first excited state, $E_1 - E_0$, for the different annealing scenarios. While the $-XX$ driver gaps out the spectrum, a gap closing exists for $+XX$.

where we choose additional drivers $\pm\hat{\sigma}_1^x\hat{\sigma}_2^x$. The above schedule starts in the ground state of the TF Hamiltonian; additional 2-point interactions are then added smoothly to the Hamiltonian. At $s = 1/2$, the strength of both the TF and $\pm\hat{\sigma}_1^x\hat{\sigma}_2^x$ terms are equal. At $s = 1$, the Hamiltonian corresponds to the classical model Eq. (13.7). We solve the time-dependent Schrödinger equation governed by Eq. (13.8) of two spins with $\Delta = 10^3$, $\delta = 10^{-1}$, and annealing time T (with parameterization $s = t/T$).

The ground state (first excited state) population after the schedule with annealing time T for the different paths is shown in Fig. 13.1 (a) (Fig. 13.1 (b)). Without additional driver Hamiltonians (i.e. a schedule given by Eq. (13.1)), the population of both $|\uparrow\uparrow\rangle$ and $|\downarrow\downarrow\rangle$ slowly rise simultaneously, before splitting at larger annealing times and reaching the adiabatic regime at times of the order of $T = \mathcal{O}(100)$ (blue dots in Figs. 13.1 (a) and (b)). This is corroborated in the instantaneous eigenspectrum as a function of annealing parameter s, shown in Fig. 13.1 (d). A small instantaneous energy gap $\Delta_X \sim 0.04$ leads to long annealing times where the process is adiabatic, i.e. $T_X \gtrsim 600$. In contrast, when adding the additional driver $-\hat{\sigma}_1^x\hat{\sigma}_2^x$, the energy gap of the instantaneous eigenspectrum is significantly opened ($\Delta_{-XX} \sim 0.25$), leading to a faster entrance

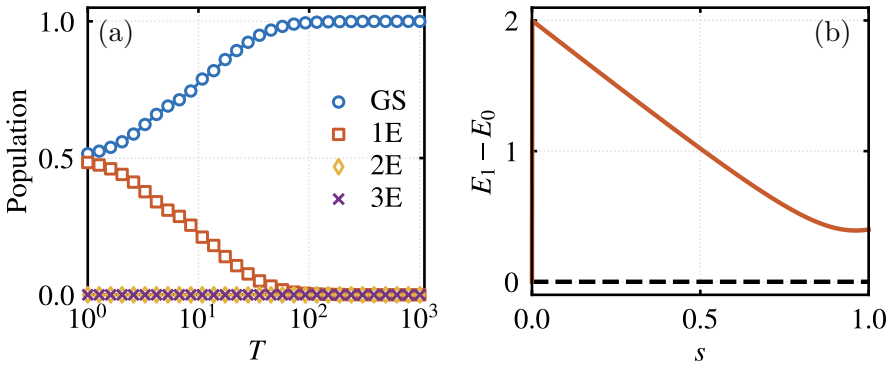

Figure 13.2: **2-qubit toy model.** (a) Ground state and excited state populations after the annealing schedule using Eq. (13.10). The initial state has weight only on the two low-energy states, which are directly coupled by the driver Hamiltonian. We note that in this case, using both signs ($\pm\hat{\sigma}_1^x\hat{\sigma}_2^x$) in the annealing schedule leads to identical results. (b) Instantaneous eigenspectrum. While the state at $s = 0$ is two-fold degenerate, the spectrum features a large energy gap for any $0 < s \leq 1$.

into the adiabatic regime for $T_{-XX} \sim \mathcal{O}(10)$ (orange squares in Fig. 13.1 (b)). We note that the annealing performance of the additional driver strongly depends on its sign: For $\hat{\mathcal{H}}_D = +\hat{\sigma}_1^x\hat{\sigma}_2^x$, a gap closing emerges at $s \sim 0.02$, leading to a large population of the first excited state instead (while the ground state population depletes)—see the yellow diamonds in Fig. 13.1 (c).

The sign of the interactions are seen to play an important role in the above example. In a more general setting, adding additional terms to the driver with randomly assigned weights may lead to further quantum interferences that result in a faster convergence to the ground state. For the simple 2-qubit landscape, we replace the $\hat{\sigma}_1^x\hat{\sigma}_2^x$ term by

$$\sum_{\alpha_1,\alpha_2} J^{\alpha_1,\alpha_2}\hat{\sigma}_1^{\alpha_1}\hat{\sigma}_2^{\alpha_2}, \tag{13.9}$$

which precisely corresponds to the bosonic SYK Hamiltonian Eq. (13.5) for $q = 2$ and $N = 2$ spins. Indeed, for a subset of randomly drawn prefactors, the annealing performance can be further enhanced, as illustrated in Fig. 13.1 (purple data). The (bosonic) SYK model with its random combination of q-body spin interaction terms thus emerges as a natural candidate to study in quantum annealing protocols.

Lastly, we look at performances when annealing schedule (S1),

$$\hat{\mathcal{H}}_{\mathrm{QA}} = s\hat{\mathcal{H}}_{\mathrm{C}} \pm (1-s)\hat{\sigma}_1^x\hat{\sigma}_2^x. \tag{13.10}$$

Here, we start in the ground state of the Hamiltonian $\pm\hat{\sigma}_1^x\hat{\sigma}_2^x$ and linearly anneal to the classical Hamiltonian. We note that the ground state of $\pm\hat{\sigma}_1^x\hat{\sigma}_2^x$ is two-fold degenerate. In the following, we choose as initial states $|\uparrow\uparrow\rangle \pm |\downarrow\downarrow\rangle$. Annealing performances for varying T are shown in Fig. 13.2 (a).

Due to the structure of the initial state, the ground state population at $t = 0$ has a large overlap with the target state of 50%. The driver Hamiltonian then directly couples the two populated

states, leading to a fast annealing to the ground state. This is corroborated in Fig. 13.2 (b), which shows that the spectrum (apart from the degeneracy at $t = 0$) is fully gapped out throughout the annealing schedule. We note that in the above example, a combination of large overlap of the initial state with the target state together with the introduced coupling constitutes a highly idealized scenario for quantum annealing. Nevertheless, it underlines and motivates our perspective that non-local terms can help to navigate through spiky energy landscapes.

13.5 MaxCut

Our first test case is the MaxCut optimization problem, where one aims to maximize the number of weighted edges (given by the set $E = \{(\langle i, j\rangle, w_{ij})\}$) in a graph that are "cut" by a given partition of the vertices ($V = 1, 2, \ldots, N$) into two sets. For a given graph with edges E and vertices V, the problem can be mapped to finding the ground state $\hat{H}_{\mathrm{MC}} |\Psi_0\rangle = E_{\mathrm{GS}} |\Psi_0\rangle$ of the following Ising Hamiltonian,

$$\hat{H}_{\mathrm{MC}} = \sum_{\langle i,j\rangle} w_{ij} \hat{\sigma}_i^z \hat{\sigma}_j^z. \tag{13.11}$$

Here, $\hat{\sigma}_i^z$ is the z-component of the spin-1/2 Pauli operator. While finding exact solutions for general graphs is exponentially hard with increasing system size N, many heuristic algorithms have been proposed. Here, one aims to design an algorithm that finds a bit string $\mathbf{z}$ with energy $E(\mathbf{z})$ such that

$$E(\mathbf{z})/E_{\mathrm{GS}} \geq r^*. \tag{13.12}$$

Indeed, it has been rigorously shown that beyond a certain approximation ratio r^*, MaxCut is NP-hard [552]. The currently best known algorithm is the one by Goemans and Williamson, with $r^* \approx 0.88$ [553]. When restricting the edges of the graph to be bimodal, this bound is raised to $r^* \approx 0.93$ [554]. Farhi, Goldstone, and Gutman showed that the quantum approximate algorithm (QAOA) has a guaranteed minimum approximation ratio of $r^* \gtrsim 0.69$, and can in principle reach $r^* = 1$ for infinite depth [555]. Similarly, $r^* \to 1$ for the quantum annealing approach at infinite annealing times, which makes MaxCut a promising testing ground for a potential quantum advantage [556].

Here, we focus on the performance of quantum annealing when using both the paradigmatic transverse field driver Hamiltonian as well as bSYK$_q$ drivers with schedules (S1) and (S2). We shall restrict our considerations to hard instances of the MaxCut problem on d-regular graphs, where every vertex is connected to d other vertices; specifically, we choose $d = 3$.

For a given graph size $N = 14$, we draw $N_g = 3050$ random instances, where the weights w_{ij} are randomly chosen from a uniform distribution $\in [0, 1]$. To isolate the hard instances, we calculate the instantaneous eigenspectrum of the annealing schedule using the TF driver (TF) as a function of annealing parameter s and extract the minimum instantaneous energy gap Δ. The resulting distribution of Δ is shown in Fig. 13.3 (a). While most graph instances have an instantaneous gap $\Delta > 10^{-2}$, we isolate those configurations with $\Delta < 10^{-2}$. As an example, we show the instantaneous eigenspectrum decomposition for one random graph in Fig. 13.3 (b). The minimum instantaneous gap is $\Delta \approx 2 \cdot 10^{-3}$, which appears at $s \approx 0.85$. The corresponding value

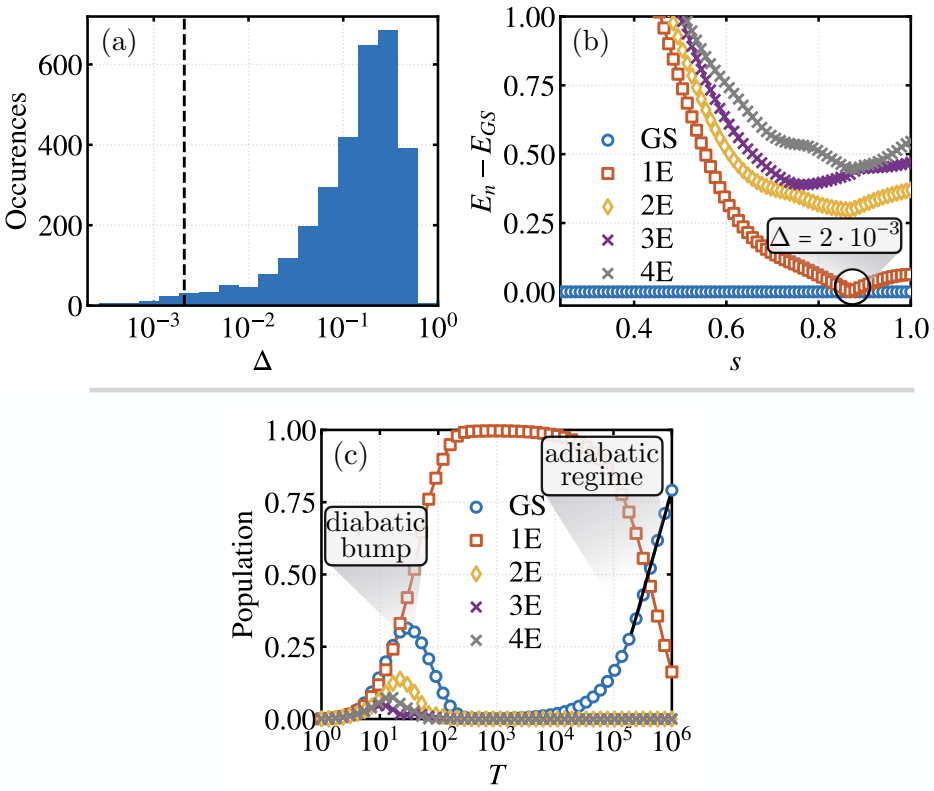

Figure 13.3: **MaxCut with transverse field driver.** (a) Distribution of minimum instantaneous energy gaps Δ during adiabatic evolution under annealing schedule (TF) for $N_g = 3050$ random instances of 3-regular MaxCut graphs with $N = 14$ vertices. (b) The instantaneous eigenspectrum (relative to the ground state energy) as a function of annealing parameter s for a single hard graph instance. The corresponding minimum instantaneous energy gap of $\Delta \approx 2 \cdot 10^{-3}$ at $s \approx 0.85$ is indicated by the black dashed line in the distribution of Δ in (a). (c) Decomposition of the dynamically evolved state with annealing time T into the eigenstates of the MaxCut Ising Hamiltonian. Hard instances are characterized by a diabatic bump of the ground state weight at small times. At times $T \gtrsim \Delta^{-2}$, the ground state weight approaches unity exponentially (adiabatic regime, indicated by the black solid line).

of Δ of the shown graph is underlined by the black dashed line in the distribution in Fig. 13.3 (a).

For all graph instances with small instantaneous gaps $\Delta < 10^{-2}$, we calculate the annealing performance for varying annealing time T. We note that the Hamiltonian (TF) commutes with the parity operator $\hat{P} = \sum_i \hat{\sigma}^x$, which we conserve during our simulations. For the random seed presented in Fig. 13.3 (b), annealing results are shown for $10 \leq T \leq 10^6$ in Fig. 13.3 (c).

A typical hard instance is characterized by a diabatic bump for short annealing times T, where diabatic transitions during the annealing sweep lead to enhanced ground state populations by the end of the protocol. For times $T > \Delta^{-2}$, the annealing schedule reaches the adiabatic regime, whereby the ground state population exponentially approaches unity (indicated by the black solid line in Fig. 13.3 (c)). These observations are in line with previous definitions of hard instances of MaxCut problems, see e.g. [504, 505].

For hard instances, we now compare the annealing performance of the TF driver to schedules (S1) and (S2) that include the bosonic SYK model in the driver Hamiltonian. In contrast to

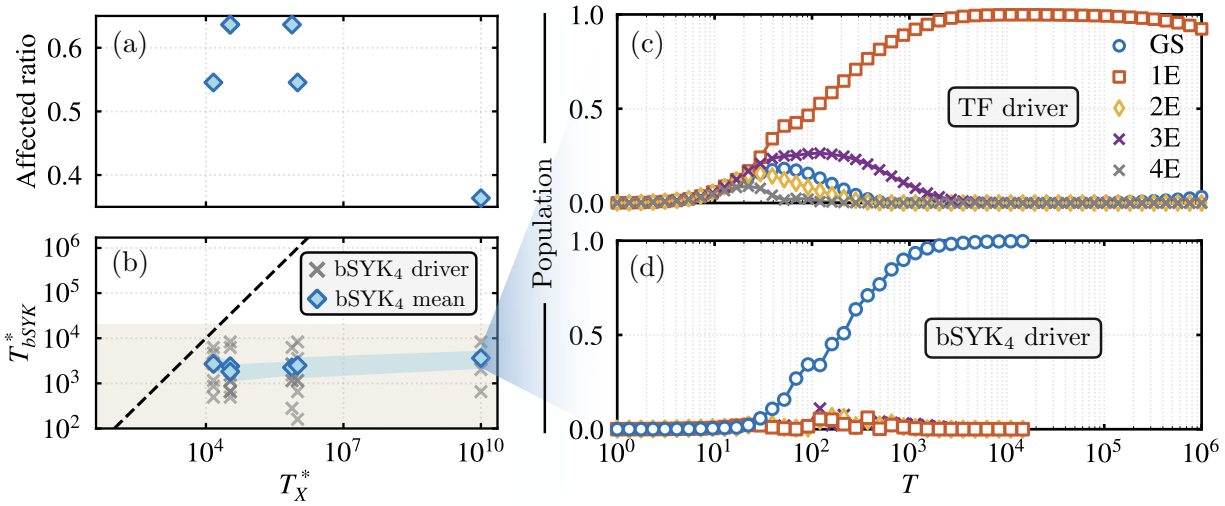

Figure 13.4: **TF vs. bSYK drivers with annealing schedule** (S1). (a) The ratio of bSYK$_4$ instances that lie within the considered numerical annealing time window and that show better performance compared to the TF driver. (b) $T^*_{\text{bSYK}_4}$ for the successful instances (grey dots) in comparison to T^*_X when using the TF driver. Mean values of T^* for the bSYK$_4$ driver are shown with blue diamonds; the shaded blue region illustrates the error to the mean. The dashed line is a guide to the eye signaling $T^*_X = T^*_{\text{bSYK}_4}$, and the beige region corresponds to the range we consider numerically, i.e., $T^*_{\text{bSYK}_4} \leq 2 \cdot 10^4$. (c) Annealing performance for a particularly hard instance using the TF model. Around the longest considered annealing times, the ground state population is barely entering the adiabatic regime. (d) An exemplary successful bSYK$_4$ instance showing significant enhancement of the annealing performance for the same MaxCut problem as considered in (c). As parity is not conserved for the bSYK driver, the shown ground state population in (d) corresponds to the sum over both minimal energy parities of the classical MaxCut Hamiltonian; in (c), only one parity sector is shown.

the TF schedule (TF), we need to solve the time-dependent Schrödinger equation for varying annealing times T in the full Hilbert space of N spins, as no symmetries can be exploited for the SYK model; furthermore, the matrices are dense, such that methods for sparse Hamiltonians can't be used. Therefore, in the following we focus on six representative hard graph instances, and analyze the annealing performance for $N_{\text{bSYK}_q} = 12$ SYK realizations for annealing times $10 \leq T \leq 2 \cdot 10^4$. In particular, we use Runge-Kutta and exact diagonalization methods available in the `QuSpin` package [557, 558].

As a metric to compare the annealing performance of the TF and bSYK driver, we extract the time T for which the ground state population reaches a value $p_{\text{GS}}(T^*) = 0.9$ after the diabatic bump. We note that this is in contrast to e.g. Ref. [522], where a short fixed annealing time of $T = 100$ was chosen for all graph instances. In particular, our metric relies entirely on adiabadicity of the annealing schedule, i.e., enhanced success probabilities due to promoted diabatic transitions before the gap closing are excluded.

Annealing schedule (S1). We start by analyzing the case where the initial state of the annealing schedule is the ground state of the bSYK$_q$ model, i.e., the Hamiltonian as a function of annealing parameter s is $\hat{H}^{(1)}_{\text{QA}} = s\hat{H}_{\text{MC}} + (1-s)\hat{H}_{\text{bSYK}_q}$. We denote the bSYK$_4$ realizations which result in a $T^*_{\text{bSYK}_4}$ that is lower than T^*_X and below our numerical time evolution threshold of $2 \cdot 10^4$ as

successful instances. For $q = 4$, the fraction of successful instances is shown in Fig. 13.4 (a) as a function of T_X^* for various hard graph instances. For graphs with solution times $T_X^* \lesssim 10^6$, success ratios are relatively constant and range between $\sim 55 - 65\%$. For the hardest considered instance, the success ratio is found to be considerably lower, with $\sim 35\%$ of the bSYK realizations leading to faster annealing.

For the successful instances, times $T^*_{\text{bSYK}_4}$ are compared to corresponding times T_X^* when using the TF driver in Fig. 13.4 (b). Grey crosses show results for various bSYK_4 driver realizations, blue dots show the mean over the successful instances. The black dashed line shows where $T^*_{\text{bSYK}_4} = T_X^*$, and the beige shading displays our numerically considered range of $T^*_{\text{bSYK}_4} \leq 2 \cdot 10^4$. Indeed, successful instances are seen to result in solution times that stay approximately constant of the order $\bar{T}^*_{\text{bSYK}_4} \sim \mathcal{O}(10^3)$, independent on the solution time T_X^* when using the TF driver.

This is corroborated in Fig. 13.4 (c), which shows the eigenstate populations of the MaxCut problem for varying T for a particularly hard instance using the TF driver. Around the largest considered annealing times, the TF driver barely starts to gain a visible ground state population. In stark contrast, for the bSYK_4 driver, the optimal solution is found with high probability $p(T^*) = 0.9$ already for $T^*_{\text{bSYK}_4} \approx 2 \cdot 10^3$ (Fig. 13.4 (d)). We crudely extrapolate T_X^* to be 10^{10} for the shown example, which corresponds to the outer right data point in Fig. 13.4 (b). The exact time T_X^* is, however, only of secondary importance, the takeaway being that if an instance of the bSYK model is successful, it allows to reach large ground state probabilities on significantly shorter time scales. However, we note that smaller success ratios are observed for the hardest considered optimization problem (though the small sample size of SYK instances lead to only coarse resolutions).

The behavior of $T^*_{\text{bSYK}_4}$ as a function of T_X^* suggests that a critical level of graph difficulty exists where the bSYK driver starts to outperform the mere use of TF fluctuations. For the considered 3-regular MaxCut problem with $N = 14$ vertices, we read off an approximate threshold of $T_X^* \sim 10^3$, see Fig. 13.4 (b). This aligns with the intuition given above: For comparably easy instances with large gaps, the transverse field efficiently navigates through the optimization landscape and quickly finds optimal solutions. However, for hard instances with complex energy landscapes, the non-local nature of the SYK model offers an advantage over the TF, whereby it can find the global minimum more efficiently.

The enhanced adiabatic performance when using the SYK-type driver suggests that the gap of the instantaneous eigenspectrum is widened (see also the simple toy model we presented in Sec 13.4). Fig. 13.5 (a) and (b) show the instantaneous eigenspectrum of the annealing schedule (S1) for two different random instances of the bSYK driver for the hardest considered MaxCut graph, cf. Fig. 13.4. As the bosonic SYK Hamiltonian does not commute with $\hat{P} = \sum_i \hat{\sigma}_i^x$, it can couple states of different parities $\hat{P}$. This is in contrast to the TF driver, which preserves the parity during time evolution. Hence, in our numerical time evolution, the final states at $s = 1$ are two-fold degenerate in the case of the bSYK driver, as seen in Fig. 13.5 (a) and (b). Correspondingly, by the end of the annealing schedule, the ground state population corresponds to the sum over the degenerate ground state subspace.

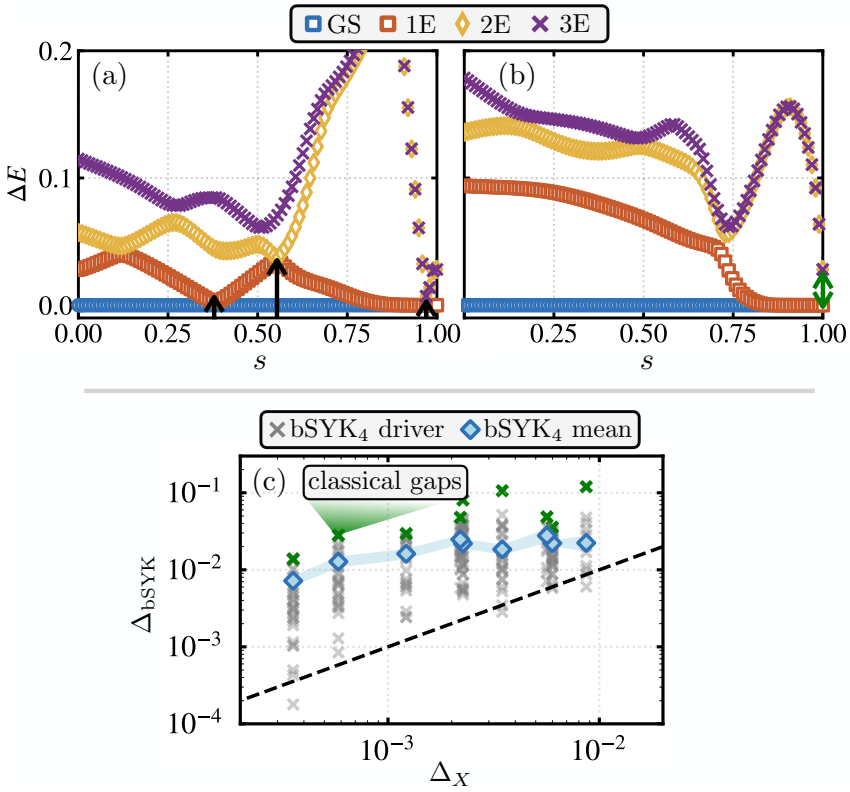

Figure 13.5: **Instantaneous spectra and minimum gaps for annealing schedule** (S1)**.** (a) and (b) show the instantaneous eigenspectrum of (S1) as a function of annealing parameter s for two random bSYK$_4$ instances. In (a), a series of avoided crossings (indicated by the left and center arrow) as well as a small instantaneous gap $\Delta_{\text{bSYK}_q} = E_2 - E_{\text{GS}}$ (right arrow) can lead to a depletion of the ground state population. (b) shows the same random bSYK$_4$ instance as in Fig. 13.4 (d), where a wide gap opening of the instantaneous spectrum leads to an ideal annealing performance. The classical gap of the MaxCut optimization problem at $s = 1$ is indicated by the green arrow. (c) Comparison of the minimum instantaneous energy gaps when using the TF and bSYK$_4$ driver. Grey crosses show individual instances of the SYK-type driver, solid diamonds show corresponding mean values. Green crosses indicate the classical gaps at $s = 1$, which is an upper bound for the instantaneous gap Δ_{bSYK_4}. Due to different conserved symmetries, $\Delta_{\text{bSYK}_4} = E_2 - E_{\text{GS}}$, while $\Delta_X = E_1 - E_{\text{GS}}$ (see main text). In almost all cases, instantaneous gaps are significantly opened.

The ground state population can thus be depleted via two main mechanisms: (i) The gap between the ground and second excited state closes, as seen exemplary at the right arrow in Fig. 13.5 (a). (ii) The appearance of a series of avoided crossings between the ground, first and second excited state, see the left and center arrow in Fig. 13.5 (a). However, we find that in many driver realizations, neither of the above appear and instantaneous gaps are significantly opened. Fig. 13.5 (b) shows the spectrum for the bSYK driver realization presented in Fig. 13.4 (d). Indeed, there is no avoided crossing of the ground and first excited state and a large instantaneous gap is present throughout the whole range of $0 \leq s \leq 1$. The minimum instantaneous energy gap appears at $s = 1$, i.e., it is determined by the classical gap of the MaxCut spectrum itself (see the green arrow in Fig. 13.5 (b)). This, in turn, leads to an ideal annealing performance presented in

Fig. 13.4 (d).

In Fig. 13.5 (c), we compare the minimum instantaneous energy gaps $\Delta_{\text{bSYK}_q} = \min_s(E_2 - E_{\text{GS}})$ when using schedule (S1) to $\Delta_X = \min_s(E_1 - E_{\text{GS}})$ when using the TF driver (TF), for nine hard instances and 50 bSYK realizations each. We see that for almost all instances of the SYK model, the minimum instantaneous energy gap is indeed significantly widened. Mean values are shown by blue diamonds, which, in line with calculations of T^* in Fig. 13.4 (b), stay almost constant independent of Δ_X. Corresponding classical gaps of the MaxCut problems (i.e. the instantaneous gap at $s = 1$) are shown by green crosses, which is an upper bound of Δ_{bSYK_q} that indeed is saturated for a finite number of bSYK_4 driver instances. Nevertheless, we again note that a series of avoided crossings can lead to a depletion of the ground state population, even for large minimum instantaneous gaps Δ_{bSYK_q}. As a result, this leads to lower fractions of bSYK instances to be successful in our annealing simulations in Fig. 13.4.

Annealing schedule (S2). Experimental preparation of the bSYK_q ground state with high fidelity is a very challenging task. Furthermore, the low-energy level spacings of the SYK model become exponentially small for large N, rendering annealing schedules following Eq. (S1) unrealistic for large-scale optimization problems with $N \gg 1$. Therefore, we now analyze annealing schedule (S2), i.e., we implement time evolution under the Hamiltonian $\hat{H}^{(2)}_{\text{QA}} = s\hat{H}_{\text{MC}} + (1-s)\hat{H}_{\text{TF}} + 4s(1-s)\hat{H}_{\text{bSYK}_q}$ with $s(t) = t/T$.

Fig. 13.6 shows our numerical results for the same hard MaxCut graphs as in Fig 13.4, with $N_{\text{bSYK}_q} = 24$ driver instances each. For $q = 4$, $T^*_{\text{bSYK}_4}$ is shown in Fig. 13.6 (b), which features a very similar behavior as the results for schedule (S1). It therefore seems like the details of adding SYK-like fluctuations to the driver Hamiltonian play only a secondary role in the annealing outcome: In both cases (S1) and (S2), significant ratios of SYK instances show enhanced performances for all considered hard graphs.

Varying degree of interactions

We now analyze if the performance depends on the degree of interactions q. In Ref. [548], it has been argued that for $q > 4$, the bSYK model features power-law correlation functions and an extensive low temperature entropy, akin to the fermionic SYK model. For $q = 2, 3$, the ground state is a spin glass; $q = 4$ has been identified as a marginal case. We analyze annealing schedule (S2) with $q = 2$, i.e., we restrict the all-to-all interactions in the bosonic SYK Hamiltonian to two-body terms[3]. Results are presented in Fig. 13.6 (a) and (c) with orange data points.

Successful instances of the bSYK_2 driver show very similar performances compared to $q = 4$, see Fig. 13.6 (b). For MaxCut instances with moderate $10^4 \lesssim T^*_X \lesssim 10^6$, a seemingly larger variation of $T^*_{\text{bSYK}_2}$ leads to overall lower affected ratios, see Fig. 13.6 (a). This is corroborated by the gap structure of the instantaneous eigenspectrum: Fig. 13.7 shows a comparison between $q = 4$ (a) and $q = 2$ (b). As previously, we focus on $\Delta_{\text{bSYK}_q} = \min_s(E_2 - E_{\text{GS}})$ and $\Delta_X = \min_s(E_1 - E_{\text{GS}})$ due to the different conserved symmetries. While $\Delta_{\text{bSYK}_q} > \Delta_X$ for most instances with both $q = 2$ and $q = 4$, the case of two-body interactions has notably larger variations in particular for

[3] We here only consider annealing schedule (S2). However, akin to the results for $q = 4$, we expect similar results to hold for general annealing schedules.

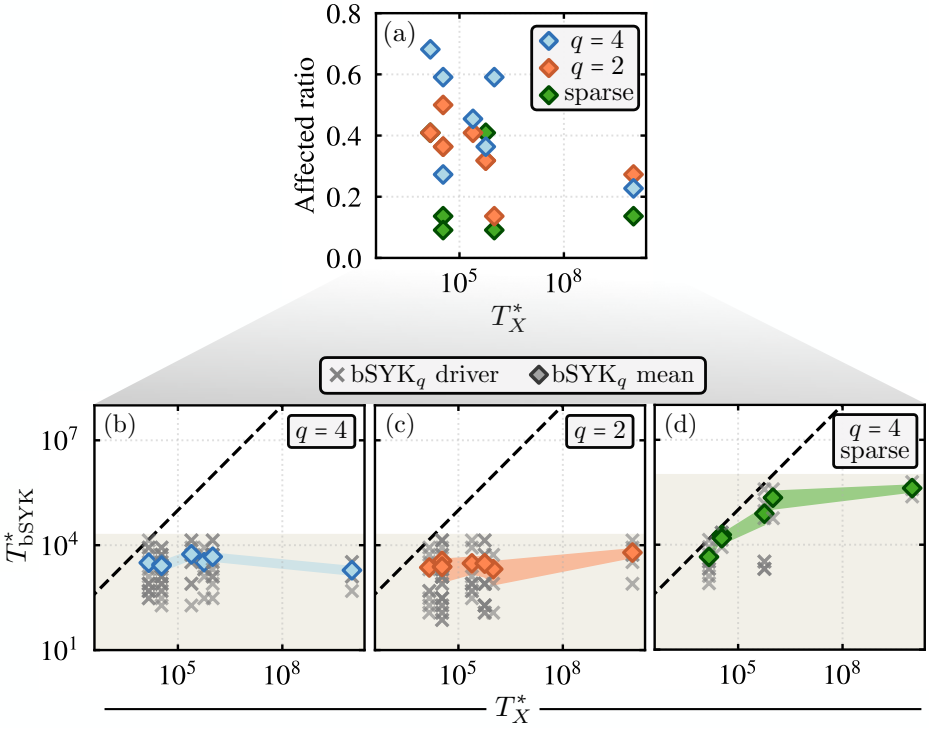

Figure 13.6: **TF vs. bSYK drivers with annealing schedule** (S2)**.** (a) The ratio of instances that lie within the considered numerical annealing time window and that show better performance compared to the TF driver. We consider $N_{\mathrm{bSYK}_q} = 24$ driver instances for each hard graph, for $q = 4$ (blue), $q = 2$ (orange), and a sparsified bSYK$_4$ model that keeps only $4N$ interactions terms (green). (b) T^* for the successful instances (grey dots) in comparison to TF drivers for $q = 4$. Mean values of T^* for successful instances are shown in blue. The dashed line indicates where $T^*_{\mathrm{bSYK}_q} = T^*_X$, and the beige shading shows our numerically considered annealing time range for the bSYK driver. The performance of driver (S2) is comparable to (S1), whereby the average T^* over successful instances remains approximately constant. (c) T^* for $q = 2$. A larger variation of T^* leads to slightly lower success ratios, see (a). Nevertheless, the performance is comparable to the case where $q = 4$. (c) T^* for the sparse bSYK$_4$ model. Only very few driver realizations lead to an enhanced annealing performance, with notably larger T^* for most MaxCut graphs.

moderately small gaps Δ_X. This underlines results of T^* (see Fig. 13.6), where larger variations for $q = 2$ lead to smaller success ratios within the considered annealing time windows.

Sparse drivers

Motivated by classical and quantum computational accessibility, next to the bSYK model there has been a recent focus on sparse versions of the (fermionic) SYK model. Here, from all original interaction terms in the Hamiltonian, only kN are chosen to be present in the sparse model. Indeed, it has been shown that above a certain threshold $k_{\mathrm{crit}} = \mathcal{O}(1)$, strong quantum chaos and holographic properties of the model survive [559–561]. We finally study the quantum annealing performance when using sparse versions of the bSYK model, and may focus here on $q = 4$ and $k = 4$. Results are shown in Fig. 13.6 (a) and (c). Although we consider larger annealing

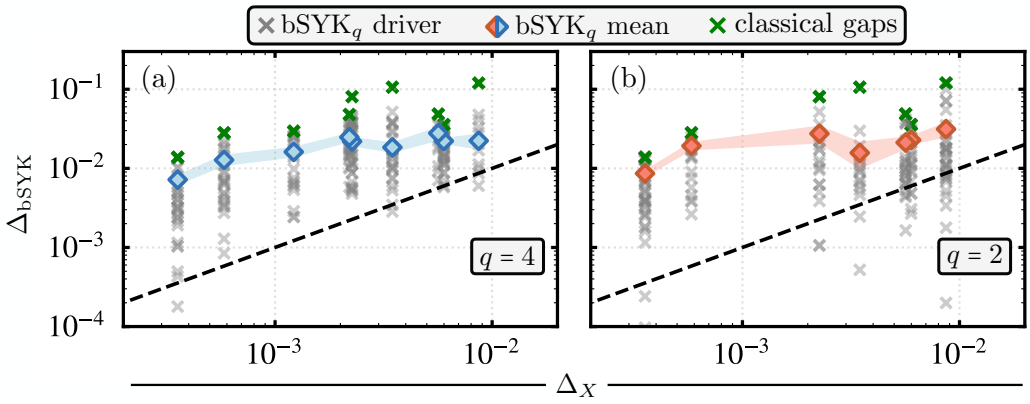

Figure 13.7: **Minimum instantaneous energy gaps.** Comparison of minimum instantaneous energy gaps when using the TF and bSYK$_4$ driver (S1) for $q = 4$ (a) and $q = 2$ (b). (a) is the same as in Fig. 13.5, and is reprinted here for easier comparison. Grey crosses show individual instances of the SYK-type driver, solid diamonds show corresponding mean values (with their error given by the shaded lines). Green crosses indicate the classical gaps at $s = 1$, which is an upper bound for the instantaneous gap Δ_{bSYK_q}. Due to different conserved symmetries, $\Delta_{\text{bSYK}_q} = E_2 - E_{\text{GS}}$, while $\Delta_X = E_1 - E_{\text{GS}}$ (see the discussion in the text). While gaps are significantly opened in both cases, $q = 2$ features notably wider distributions in particular for problems with moderately small gap sizes Δ_X.

time windows $10 \leq T \leq 10^6$ for the sparse bSYK model, very few instances result in an enhanced annealing performance. Furthermore, T^* for the sparse bSYK realizations that do show an enhancement are, in most cases, orders of magnitude larger compared to typical successful instances for the dense drivers.

While the dependence of the annealing performance on the degree of interactions q was found to be negligible, sparsifying the bSYK Hamiltonian significantly weakens the driver's capabilities to navigate through complicated energy landscapes. We therefore speculate that is it primarily the non-locality of the SYK-type drivers that lead to more efficient quantum annealing solutions. Nevertheless, it is an interesting future research direction to study in more depth the connections between annealing performances and quantum scrambling and chaos.

From a more practical point of view and assuming that all-to-all interactions can be engineered in hardware setups, our perspective is that a cyclic annealing algorithm leads to best results, akin to what has been proposed in [562, 563]: A given graph is repeatedly annealed with randomly drawn bSYK$_q$ instances, where as many terms of the bSYK model as feasible are included in the time evolution. From a large number of anneal results, the bit string that corresponds to the lowest classical energy is then chosen as the annealing solution. We found that the performance only weakly depends on how the bSYK model is included in the driver, i.e., the exact functional form of the annealing schedule is only of minor importance and can be adapted to what may be experimentally most feasible.

13.6 LABS

Though finding optimal solutions of MaxCut problems is generally an NP-hard problem, solutions can be found very efficiently for typical instances. In contrast, the low autocorrelation binary sequence (LABS) problem does not feature such efficient heuristic algorithms. LABS was originally developed to reduce the peak power of radiation and sonar pulses [564–567], which has been used to e.g. optimize interplanetary radar measurements of spacetime curvature [568]. The objective of the LABS optimization is to minimize the so-called sidelobe energy of a binary sequence, which can be found by finding the ground state of the classical Hamiltonian

$$\hat{H}_{\text{LABS}} = \sum_{j=1}^{N-1} \hat{\mathcal{C}}^2(j) = \sum_{j=1}^{N-1} \left(\sum_{i=1}^{N-j} \hat{\sigma}_i^z \hat{\sigma}_{i+j}^z \right)^2 . \tag{13.13}$$

Here, $\hat{\mathcal{C}}(j) = \sum_{i=1}^{N-j} \hat{\sigma}_i^z \hat{\sigma}_{i+j}^z$ is the autocorrelation operator at distance j. The Hamiltonian Eq. (13.13) features long-range 4-body interactions, but is fully deterministic, i.e., there is no disorder as in glassy systems. Nevertheless, the energy landscape is highly complex, and the system has similarities with disordered systems (i.e. it features self-induced disorder) [569]. At high temperatures, variations of the replica method allow for an analytic treatment of the system [570, 571]. However, at low energy (and in particular in the ground state at $T = 0$), exact properties are not known.

All known classical algorithms feature an exponential run time in system size, and getting exact (approximate) solutions are computationally possible for only $N \leq 66$ ($N \lesssim 200$). The best known exact (heuristic) algorithm[4] scales with system size as 1.73^N (1.34^N) [567]. In Ref. [572], the LABS problem was studied using QAOA. Indeed, it was shown that when combining a constant depth QAOA routine with quantum minimum-finding, the scaling of the time-to-solution (TTS) with system size is 1.21^N, which is lower than the best known classical heuristic.

Here, we study the performance of quantum annealing when applied to the LABS problem. We again focus on varying annealing times and corresponding time-to-solutions, and compare their scaling with N when using transverse field and SYK-type driver Hamiltonians. To approximate the scaling of the annealing algorithm as N is varied, we calculate for each annealing time T the time-to-solution,

$$\text{TTS} \propto \frac{T}{\log\left(1 - p_{\text{GS}}(T)\right)}. \tag{13.14}$$

Here, $p_{\text{GS}}(T)$ is the probability to be in the ground state of the LABS Hamiltonian by the end of an annealing schedule of length T. The derivation of Eq. (13.14) is straightforward: The probability of failing to find the optimal state after R repetitions with annealing time T is $(1 - p_{\text{GS}}(T))^R$; the probability of succeeding at least once within the R repetitions is hence $1 - (1 - p_{\text{GS}}(T))^R$. Given a target probability $p_T \equiv 1 - (1 - p_{\text{GS}}(T))^R$ (often taken to be 99%) and considering that each repetition takes time T to run, Eq. (13.14) follows, see also Ref. [490].

We note that solutions to the LABS problem have varying degrees of degeneracy (D) for

[4] For a full survey of classical algorithms, see in particular the supplementary materials of Ref. [572].

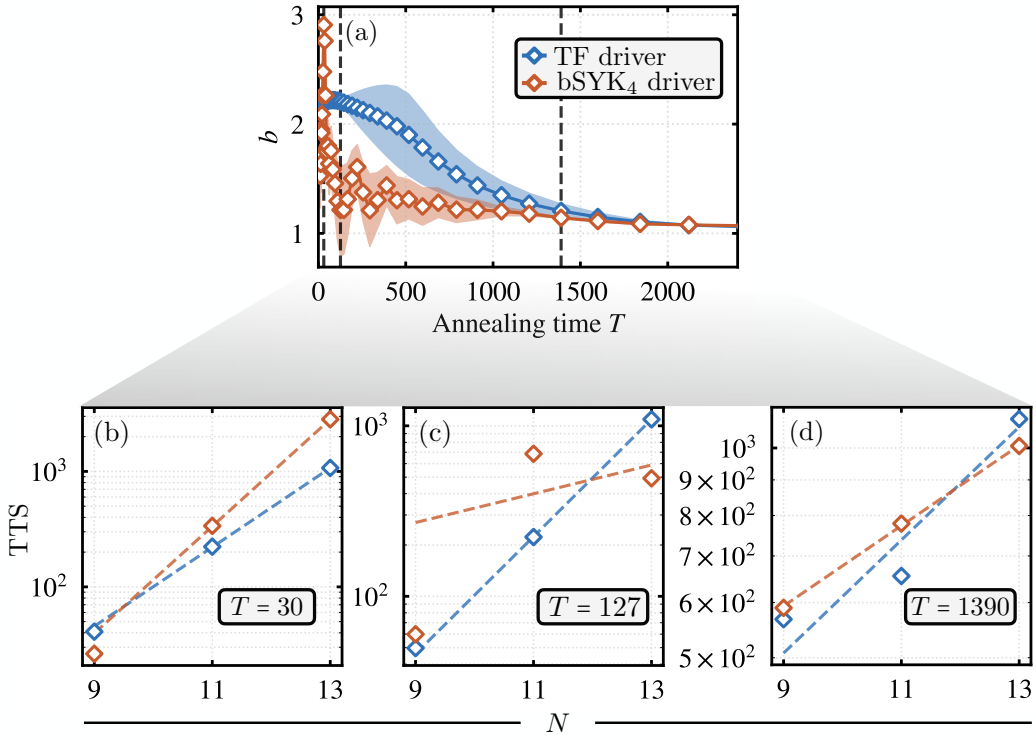

Figure 13.8: **Solving LABS with quantum annealing.** (a) Fitted scalings of the time-to-solution TTS$\sim b^N$ for varying annealing time T. When fitting for a range of $N = 9, 11, 13$, at intermediate T the SYK-type driver has a scaling advantage over TF driver schedules. The shaded regions correspond to the uncertainty of the fits, which is notably large in the intermediate T region. (b), (c), (d) show the TTS as a function of N for three annealing times $T = 30, 127, 1390$ (see the grey dashed lines in (a)). Scaling fits are shown by the dashed lines.

varying system size. Therefore, we define $p_{\text{GS}} = \sum_{i=1}^{D} p_{\text{GS}}^{(i)}$, with $p_{\text{GS}}^{(i)}$ the wave function's weight on the i'th degenerate bit string of the classical Hamiltonian.

For varying annealing time T, we calculate the TTS for systems of sizes $N = 9, 11, 13$. An exponential fit to the TTS as a function of N then yields the scaling TTS $\sim b^N$. The dependency $b(T)$ is shown in Fig. 13.8 (a). For three different annealing times, we show the dependence of TTS on N together with the scaling fits in Fig. 13.8 (b)-(d). In particular for intermediate times, the fits are very limited in accuracy, in particular as only three data points have been used. Comparisons between the two different drivers should thus be interpreted as rough trends: While in the limit of long annealing times both TF and bSYK$_q$ drivers reach the same value of $b \sim 1.1$, at short times the scaling of the bSYK$_q$ driver is advantageous over the TF schedule[5].

While the TTS scaling of the two different drivers can be compared, we stress that a meaningful comparison to classical heuristic algorithms is impossible with our considered system sizes. To extract the scaling of the classical algorithms, $N > 40$ spins were used, whereas our system sizes are significantly smaller. Larger systems and more data points are needed for the annealing results to see which algorithm decisively performs better at scale. Nevertheless, our results

[5]We note that we here focus on annealing schedule defined in Eq. (S1) with $q = 4$; however, akin to the above discussion, we expect similar results to hold for other annealing schemes.

corroborate that the use of non-local, chaotic Hamiltonians in quantum annealing can lead to a computational speedup compared to standard TF drivers when solving classical optimization problems.

13.7 Digital simulation

As mentioned previously, due to the overhead of implementing Jordan-Wigner strings to ensure fermionic commutation relations, there has been increased recent interest in studying bosonic versions of the SYK model [547,549–551], where the Hilbert space has a tensor product structure such that operators from different sites commute. In particular, these models have been argued to constitute a realistic path towards simulating minimal holographic models using quantum computers. In Ref. [547], a particular bosonic model with q-local all-to-all interactions has been studied, where Jordan-Wigner strings in Eq. (13.2) are replaced by unit matrices,

$$\begin{aligned} \hat{\chi}'_{2k-1} &\propto \mathbb{1}^{\otimes(k-1)} \otimes \hat{\sigma}^x_k \otimes \mathbb{1}^{\otimes(N-2k)/2}, \\ \hat{\chi}'_{2k} &\propto \mathbb{1}^{\otimes(k-1)} \otimes \hat{\sigma}^y_k \otimes \mathbb{1}^{\otimes(N-2k)/2}. \end{aligned} \tag{13.15}$$

Constructing a Hamiltonian in analogy to Eq. (13.2) leads to (with $\eta_{i_1\ldots i_q}$ a properly chosen normalization to ensure hermiticity of the Hamiltonian)

$$\hat{H}_{\text{bSYK}} = \sum_{i_1<\cdots<i_q} J_{i_1\ldots i_q} \eta_{i_1\ldots i_q} \hat{\chi}'_{i_1} \cdots \hat{\chi}'_{i_q}, \tag{13.16}$$

which has been shown to capture the essential features of the SYK model. Specifically, it does not feature a spin-glass ground state, and its spectroscopic signatures are similar of those of the full fermionic SYK model [547]. We note that this bosonic spin formulations slightly differs from the one we used in the previous sections (see i.p. Eq. (13.5)), which also include Pauli-z terms in the Hamiltonian[6]. However, we here focus on the formulation in Eq. (13.16), primarily because it allows for a more intuitive comparison of the quantum computing resources needed for digital time evolution, and for convenience, denote it by bSYK$_q$ in the following as well.

Similarly motivated by classical and quantum computational accessibility, next to the bSYK model there has been a focus on sparse versions of the (fermionic) SYK model. Here, from the original $\binom{N}{4}$ interacting terms in the Hamiltonian, only kN are chosen to be present in the sparse model. Indeed, it has been shown that above a certain threshold $k_{\text{crit}} = \mathcal{O}(1)$, strong quantum chaos and holographic properties of the model survive [559–561]. In particular, above the critical level of sparsity the two models share the same four-point functions in the limit of large q [559].

The combination of a sparse, bosonic model for $k = N$ has been analyzed numerically in [559]. In particular, it was found that the Edwards-Anderson order parameter (which, if finite, signals the existence of a spin glass) vanishes in the thermodynamic limit for $q \geq q_{\text{crit}} = 4$ (i.e., the ground state is not a spin glass). Consequently, it has been argued that the sparse bosonic SYK model Hamiltonian thus constitutes a minimal model to study quantum holography.

[6] These models feature a total number of terms of $\binom{N}{4}3^q$ instead of $\binom{N}{4}$ terms.

We now aim to give realistic resource estimates for the simulation of both fermionic and bosonic, dense and sparse SYK models. In particular, we will in the following consider (i) the fermionic SYK model with q-body interactions (denoted by SYK_q), (ii) the bosonic SYK model (denoted by bSYK_q), (iii) the sparse fermionic SYK model (denoted by $\mathrm{s}_k\mathrm{SYK}_q$) as well as (iv) the sparse bosonic SYK model (denoted by $\mathrm{s}_k\mathrm{bSYK}_q$). We use a tailored optimization strategy to obtain the necessary entangling gate operations per Trotter step, and comment on feasibility using various quantum computing platforms.

In the following, we restrict ourselves to the simulation of quantum dynamics under the SYK-type Hamiltonians introduced above, which can be decomposed as a sum of Pauli strings $\hat{\mathcal{H}} = \sum_{j=1}^{M} w_j \hat{P}_j$. Quantum time evolution can then be simulated through the first-order Lie-Trotter decomposition[7],

$$e^{i\hat{\mathcal{H}}t} = \lim_{k\to\infty} \left(\prod_{j=1}^{M} e^{iw_j \hat{P}_j t/k} \right)^k . \tag{13.17}$$

Though there are various modalities of gate-based quantum computation, in all cases two-qubit entangling gates constitute the ingredient with the highest error source. To make realistic estimates for implementing SYK-type models on digital machines, we therefore seek to minimize the number of entangling gates. In particular, we focus on minimizing the total application of (i) CNOT (or equivalently CZ) and (ii) R_{ZZ} gates, which correspond to the native two-qubit gates in (i) superconducting qubit and neutral atom and (ii) trapped ion devices.

13.7.1 Optimization strategies

Dense SYK models with four-body, all-to-all connectivity consist of $\binom{N}{4} \approx N^4/4!$ Pauli strings. It has been established that grouping terms into mutually commuting clusters and simultaneously diagonalizing the clusters can lead to a substantial reduction of circuit depths [544,573,574]. We closely adhere to the protocols presented in Refs. [573,574] and use the following optimization strategy for minimizing the number of entangling gates (summarized in Fig. 13.9):

- ▷ The set of Pauli strings for a given Hamiltonian is grouped into commuting clusters, where within each cluster each terms commutes with all other terms. This can be done using standard graph coloring techniques, where two nodes (corresponding to two Pauli terms) share an edge if and only if they do not commute. Using the package NetworkX [575], we utilize several greedy graph coloring schemes, including `largest_first`, `independent_set`, and `DSATUR`.

- ▷ After grouping, each cluster is diagonalized by the algorithms devoloped in Ref. [573]. This results in the Pauli strings only consisting of identity and Pauli-z matrices, allowing for efficient cancellations in quantum circuits. In particular, we utilize algorithms `cz`, `greedy1` and `greedy2` from Ref. [573], and compare their performance for each graph coloring algorithm.

[7] Though higher-order approximations can be applied, we here restrict our discussion to the first-order expression.

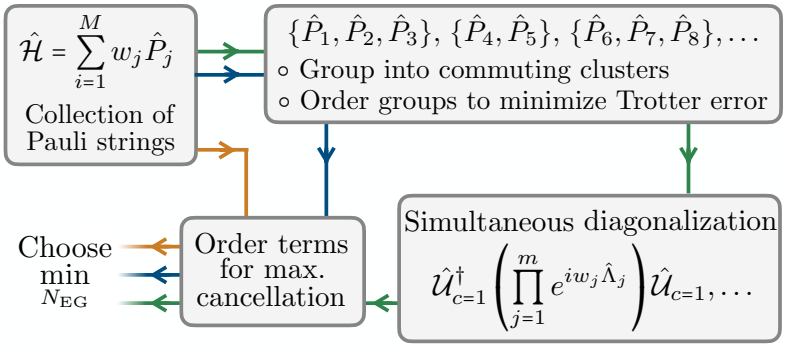

Figure 13.9: **Optimization strategy.** Scheme to minimize the number of entangling gates. The Pauli strings in the Hamiltonian are first grouped into commuting clusters. Each cluster is then diagonalized and ordered such that the maximal number of entangling gates cancel (green path). We compare this to re-ordering the terms directly (orange path) and within each cluster without diagonalization (blue path). The latter two strategies are found to be beneficial when clusters of commuting Pauli strings are small, as e.g. the case for sparse formulations of the SYK model. From the three paths, the one that minimizes the number of entangling gates N_{EG} is chosen.

- ▷ The ordering in each cluster can be freely chosen without altering the Trotter error. We use traveling salesperson heuristics as used in Ref. [574] to order the terms such that the maximal number of entangling gates cancel. Slight variations of the algorithm let us minimize the number of CNOT (or CZ) gates as well as R_{ZZ} gates.

- ▷ The different clusters can then be ordered such that it minimizes the Trotter error, as elaborated in Ref. [574].

We compare the above to the scenarios where we directly order terms according to the traveling salesperson heuristics before and after clustering, i.e., without diagonalizing each cluster (see the orange and blue paths in Fig. 13.9, respectively). As we will see, this is beneficial in particular for the sparse versions of the SYK model, where cluster sizes are small and direct reordering may lead to enhanced gate cancellations. From these three protocols, for each case the one that minimizes the number of entangling gates N_{EG} is chosen.

13.7.2 Resource estimates

We first focus on the sparse fermionic and bosonic SYK models, i.e., Eqs. (13.2) and (13.16). To understand the amount of resources needed for the diagonalization and Pauli string implementation respectively, we count the number of CNOT gates needed for the two separately. In particular, we sum the number of CNOTs needed over all clusters after optimizing the circuit for the total number of entangling gates. Results are shown in the left panel of Fig. 13.10. While resources to implement the diagonalized Pauli strings are seen to scale similarly for both bosonic and fermionic versions, the diaginalization unitaries show clear differences. For the bosonic SYK model, the lack of long Pauli strings leads to a roughly constant number of entangling gates for implementing the diagonalization unitaries. In contrast, diagonalizing the full SYK clusters requires more complex unitaries, leading to the scaling observed in the left panel of Fig. 13.10

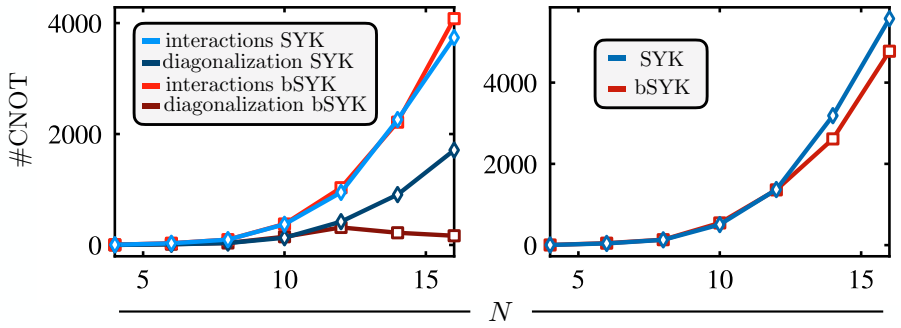

Figure 13.10: **Optimized circuits of dense SYK models.** CNOT count for a single Trotter step using the optimizations scheme outlined in Fig. 13.9 as a function of N, where N corresponds to the number of Majorana fermions in the standard SYK model Eq. (13.2). Left panel: CNOTs needed for diagonalization (dark colors) and implementing the diagonalized Pauli strings (light colors), for the fermionic SYK model Eq. (13.2) (blue) and the bosonic SYK model Eq. (13.16) (red). While implementing the diagonalized Pauli strings uses roughly the same resources, the diagonalization routine is significantly cheaper for the bSYK model for $N \geq 14$. Right panel: The total number of CNOT operations needed per Trotter step for the SYK and bosonic SYK model.

(dark colors).

Adding the cost of both diagonalization and implementing the Pauli strings is shown in the right panel of Fig. 13.10. Though the scaling of the bosonic SYK model is favorable, significant enhancements are only seen for system sizes $N \geq 14$. Here, the number of needed CNOT gates is already beyond $N_{\text{EG}} > 1000$ per Trotter step. We thus conclude that bosonic verisons of the SYK model do not help significantly in realizing near-term digital simulations, which are restricted to a total circuit depth of roughly 1000.

It therefore seems essential to sparsify the model for realistic large-scale applications. We here focus on randomly pruning all but $k = 4$ and $k = N$ terms in the Hamiltonian, both for the fermionic and bosonic SYK model. Results are presented in Fig. 13.11. For $N > 10$, the advantages of the bosonic over the fermionic model become apparent. In particular, as expected, the scaling for the sparse bosonic SYK model is linear in system size, with roughly $N_{\text{EG}} = 500$ CNOT gates needed for a trotter step with $N = 30$. The green background signals an entangling gate count of $N_{\text{EG}} < 333$, such that at least three trotter steps can be computed with less than 1000 CNOT gates. More detailed numbers are displayed in Tab. 13.1.

13.8 Discussion

We have numerically studied the scenario of adding chaotic driver Hamiltonians to quantum annealing protocols, and compared resulting performances in a variety of settings to the standard transverse field. In particular, we focused on hard instances of classical optimization problems, and showed that chaotic drivers can indeed significantly enhance the annealing performance when compared to plain transverse field annealing.

While not all instances of SYK Hamiltonians were successful in reducing the annealing time, those that do show an advantage were seen to reach high ground state populations independent

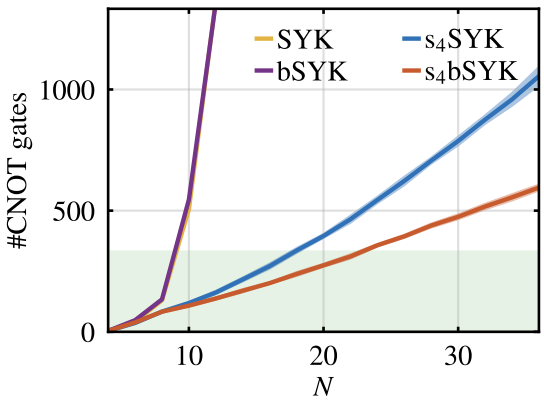

Figure 13.11: **Optimized circuits of dense and sparse SYK models.** CNOT count for a single Trotter step using the optimizations scheme outlined in Fig. 13.9 as a function of N, where N corresponds to the number of Majorana fermions in the standard SYK model Eq. (13.2). Shown are the fermionic and bosonic SYK models as well as their sparsified versions.

N	SYK	bSYK	s_4SYK	s_4bSYK
4	4	4	4	4
6	42	48	36	38
8	130	134	83	83
10	506	546	119	108
12	1368	1360	162	137
14	3186	2614	216	169
16	5574	4772	271	201
18	-	-	335	238
20	-	-	395	274
22	-	-	464	311
24	-	-	544	357
26	-	-	622	394
28	-	-	706	438
30	-	-	787	474
32	-	-	875	517
34	-	-	959	555
36	-	-	1055	595
38	-	-	1147	-
40	-	-	1244	-

Table 13.1: **Entangling gates.** Number of two-qubit entangling gates needed for a single Trotter step for the full fermionic SYK model (SYK), its bosonic spin formulation (bSYK), as well as corresponding sparse models with $k = 4$ (s_4SYK, s_4bSYK). In each case, various gate optimization strategies were used, and the minimum CNOT gate number is shown. Highlighted in green are models for which each Trotter step consumes less than 333 CNOT operations, such that at least three time steps can be computed with less than 1000 entangling gates.

on the instantaneous minimum energy gap when using the transverse field. For practical applications of large-scale optimization problems, it is an interesting question how these success rates scale as a function of graph size N. Furthermore, it could be insightful to analyze the performance of other quantum alhorithms, e.g. QAOA, when using chaotic driver Hamiltonians.

For the MaxCut problem on regular graphs, we have found comparable results for varying degree of interactions q, while sparsifying the Hamiltonian matrix led to significantly less efficient annealing performances. It is an interesting future research direction to study if any more direct connections between our numerical observations and the quantum chaotic and fast scrambling nature of the SYK model, as well as the degree of sparsity can be drawn.

For practical quantum annealing setups, our results suggest that implementing additional non-local fluctuations of degree $q \geq 2$ to the transverse field lead to an enhanced performance, even if implementing the fully dense bSYK model is currently out of reach. We have given estimates for the number of entangling gate operations needed to simulate SYK-like models in Sec. 13.7.

With Rydberg atom arrays naturally implementing the TF Ising model in analog mode, hybrid digital-analog techniques could be used to implement quantum annealing with additional (digitally engineered) terms. To this end, multiple particles could be brought into the same entangling zone in a dynamic manner, allowing for an efficient implementation of multi-body interactions (hence drastically reducing the number of gates as estimated in Sec. 13.7). Thus, with recent advances in the control and coherence of neutral atom quantum processors, a digitized annealing approach that includes SYK-like Hamiltonians during trotterized time evolution may constitute a promising path towards practical quantum advantage.

14

Discussion and future directions

This thesis has focused on the exploration of strongly correlated phases of matter in the low-temperature regimes of doped Hubbard models, with an emphasis on their implementation using ultracold atoms in optical lattices. We began by analyzing modified Fermi-Hubbard models, and in an experimental collaboration reported on the observation of emergent collective stripe order in doped Mott insulators in Chap. 5. This observation of fluctuating stripes motivated the development of a theory for the pseudogap in Chap. 7, wherein fluctuating domain walls obscure magnetic order and lead to the formation of a small Fermi surface.

With efficient entropy redistribution schemes and decoupling of charge reservoirs from the physical system, achieving much lower temperatures ($T/t \lesssim 0.1$) is now within reach for analog quantum simulators. This advancement will enable the study of regimes where stripes melt in fully 2D settings, allowing our hypothesis of fluctuating domain walls causing the peculiar pseudogap physics to be rigorously tested. In particular, we propose the use of DMDs to effectively decouple a 2D system into two parts. Sharp boundaries are expected to expel domain wall lines, leading to the reappearance of long-range spin-spin correlations. True long-range order is anticipated to emerge along these 1D boundary lines, contrasting the power-law decay expected in 1D systems. This makes it feasible to test our scenario in detail.

Our proposed hidden order scenario opens up a range of future research directions. With our microscopically motivated model of domain walls coupled to gauge fields, the study of various toy models can be envisioned. For instance, coupling Ising or XY spin models to toric code gauge fluctuations can provide deeper theoretical insights into hidden order and hidden criticality. In particular, theoretical and experimental studies of these systems may enable novel perspectives on the interplay between symmetry-broken and topological order.

Furthermore, by incorporating Higgs fields that carry gauge charges into the theory, intriguing analogies to orthogonal semi-metals (OSMs) [576–578] can be explored. It would be particularly interesting to investigate whether, similar to OSMs, convolutions of the Higgs and fermionic dispersions give rise to Fermi arcs in our GFL* scenario of the pseudogap [578].

Another focus of this thesis has been the exploration of superconductivity in analog quantum simulators, a long-standing goal that has driven and inspired research in ultracold atoms in the past decades. As we demonstrated in Chapters 8 and 9, measuring (quasi-)long-range coherent pair-pair correlations is now directly feasible using state-of-the-art quantum gas simulators. These systems can simulate the minimal physics of nickelate superconductors, enabling the study of intriguing BEC-BCS crossovers in *repulsively* interacting fermionic systems. This paves the way for studying unconventional superconductivity in optical lattice experiments, and may ultimately potentially help in designing novel materials with high critical temperatures.

Moreover, we demonstrated that the measurement schemes to access pairing order in bilayer systems can be generalized to the 2D FH model using local superlattice control and global gate techniques. These hybrid analog-digital approaches open new possibilities: One the one hand, they allow access to observables off-diagonal in the Fock basis, such as coherent pair-pair correlations; on the other hand, hybrid approaches enable the digital engineering of additional Hamiltonian terms. Applications include adding next-to-nearest neighbor hoppings to the analog FH model or incorporating non-local terms like SYK-type interactions. Using Rydberg atom arrays in analog mode to simulate the transverse-field Ising model, SYK-type interactions could be sequentially engineered digitally, rendering annealing schemes as outlined in Chap. 13 realistic in the near future. Fully universal fermionic quantum computing also presents a promising direction for simulating strongly correlated fermionic phases of matter [199–201].

Studying doped systems with higher symmetries, such as SU(N), in ultracold atom experiments offers another promising path to gaining deeper insights into the low-temperature physics of doped Mott insulators. Our theoretical considerations in Chap. 11 predict the emergence of exotic physics in these systems. With ongoing efforts to develop quantum gas microscopes for alkaline-earth atoms, these intriguing systems could soon be studied microscopically. As the local Hilbert space dimension of SU($N > 2$) systems grows much faster than that of SU(2) systems, AEAs in optical latttices represent analog quantum simulators that offer substantial quantum advantage. Combined with the ultra-low temperatures achievable in AEA Fermi gases, this may uncover a vast range of exotic physics much beyond current numerical capabilities.

Machine learning, with its powerful capabilities, finds applications across almost all scientific fields. It is natural to apply machine learning approaches in the context of analog quantum simulation. In this thesis, we (i) employed Hamiltonian reconstruction to quantitatively understand the interplay between spin and motional degrees of freedom in Chap. 6, and (ii) utilized and developed imaging-processing networks to analyze many-body snapshots in Chap. 12. Applying these techniques to analyze the FH model in interesting regimes, such as the pseudogap, is a promising avenue for future research, possibly unraveling non-local, hidden structures.

This thesis marks a step in a new era of quantum gas microscopy, where collective orders such as stripes and superconductivity, exotic phases like the pseudogap, and intriguing ground states in SU(N) symmetric systems can be studied in microscopic detail. The combination of novel theoretical phenomenological theories, enhanced measurement schemes, and the prospect to achieve colder temperatures paves the way for further extensive exploration of the low-temperature regime of doped Hubbard models.

A

TPSC equations

In Sec. 3.2, we gave an intuitive derivation of the TPSC equations. For completeness, we here derive then from a more fundamental point of view, based on Luttinger-Ward functionals and Bethe-Salpeter equations. Closely following Ref. [188], we will start from general (non-perturbative) many-body arguments, and then do appropriate approximations for the Hubbard model. We first focus on the SU(2) symmetric case in Sec. A.1, before generalizing to SU(N) symmetric systems in Sec. A.2. Finally, in Sec. A.3, we give details regarding the self-consistent numerical implementation of the TPSC equations.

A.1 SU(2) FH model

In the following, we will use the notation of $1 = (\mathbf{r}_1, \tau_1)$ in position-imaginary time space, where barred indices $\bar{1}$ indicate integration over space and imaginary time, $f(\bar{1})g(\bar{1}) = \int d1 f(1)g(1) \propto \int d^3\mathbf{r} \int d\tau f(\mathbf{r},\tau)g(\mathbf{r},\tau)$ [188]. We will separate out the spin indices σ to make them stand out explicitly. The single-particle Green's function reads

$$G_\sigma(1,2) = -\left\langle T_\tau \hat{c}_\sigma(1)\hat{c}^\dagger_\sigma(2)\right\rangle, \tag{A.1}$$

with $\langle\circ\rangle$ the thermal ensemble average and T_τ the imaginary time-ordering operator (lowest times to the right).

We will be interested in calculating response functions to external perturbations. Consider for this the generating functional of the Green's function, given by

$$\ln Z[\phi] = \ln\left\langle T_\tau \exp\left(-\hat{c}^\dagger_{\bar{\sigma}}(\bar{1})\phi_{\bar{\sigma}}(\bar{1},\bar{2})\hat{c}_{\bar{\sigma}}(\bar{2})\right)\right\rangle. \tag{A.2}$$

The single-particle Green's function is calculated via functional derivatives,

$$G_\sigma(1,2;[\phi]) = -\frac{\delta \ln Z[\phi]}{\delta\phi_\sigma(2,1)}. \tag{A.3}$$

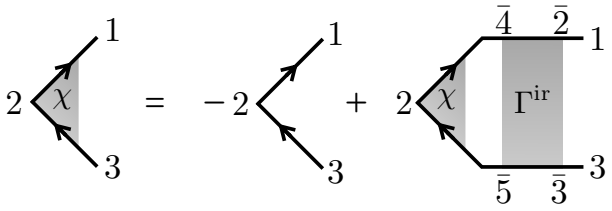

Figure A.1: **Bethe-Salpeter equation.** Diagrammatic representation of the Bethe-Salpeter equation, Eq. (A.9).

$G_\sigma(1,2)$ in Eq. (A.1) can then be retrieved by setting $G_\sigma(1,2;[\phi\equiv 0])$. The two-point susceptibility $\chi_{\sigma\tau}(1,2)$ is defined as

$$\chi_{\sigma\tau}(1,2) = -\frac{\delta G_\sigma(1,1^+;[\phi])}{\delta\phi_\tau(2^+,2)}\bigg|_{\phi=0}. \tag{A.4}$$

Using Eq. (A.2), (A.3) and (A.4) we find

$$\begin{aligned}\chi_{\sigma\tau}(1,2) &= -\langle T_\tau \hat{c}_\sigma(1)\hat{c}^\dagger_\sigma(1^+)\hat{c}^\dagger_\tau(2^+)\hat{c}_\tau(2)\rangle - \langle\hat{n}_\sigma(1)\rangle\langle\hat{n}_\tau(2)\rangle \\ &= \langle T_\tau \hat{n}_\sigma(1)\hat{n}_\tau(2)\rangle - \langle\hat{n}_\sigma(1)\rangle\langle\hat{n}_\tau(2)\rangle \\ &= \langle T_\tau \hat{n}_\sigma(1)\hat{n}_\tau(2)\rangle - n_\sigma^2,\end{aligned} \tag{A.5}$$

where we defined $n_\sigma = \langle\hat{n}_\sigma(1)\rangle = \langle\hat{n}_\tau(2)\rangle$ as the occupation per spin-species. For the case of SU(2), we have $n_\uparrow = n_\downarrow = n/2$, where $n = \langle\hat{n}_\uparrow\rangle + \langle\hat{n}_\downarrow\rangle$. From these definitions, we can calculate spin- and charge response functions $\chi_{\mathrm{ch/sp}}(1,2)$, given in particular for a two-spin species system by

$$\begin{aligned}\chi_{\mathrm{ch}}(1,2) &= 2\big[\chi_{\uparrow\uparrow}(1,2)+\chi_{\uparrow\downarrow}(1,2)\big] = 2\big[\,\langle T_\tau\hat{n}_\uparrow(1)\hat{n}_\uparrow(2)\rangle + \langle T_\tau\hat{n}_\uparrow(1)\hat{n}_\downarrow(2)\rangle\,\big] - n^2, \\ \chi_{\mathrm{sp}}(1,2) &= 2\big[\chi_{\uparrow\uparrow}(1,2)-\chi_{\uparrow\downarrow}(1,2)\big] = 2\big[\,\langle T_\tau\hat{n}_\uparrow(1)\hat{n}_\uparrow(2)\rangle - \langle T_\tau\hat{n}_\uparrow(1)\hat{n}_\downarrow(2)\rangle\,\big].\end{aligned} \tag{A.6}$$

Note that the above defined response functions (and when implying spin-rotational symmetry) indeed correspond to density-density and spin-spin correlation functions,

$$\begin{aligned}\chi_{\mathrm{ch}}(1,2) &= \langle T_\tau\big[\hat{n}_\uparrow(1)+\hat{n}_\downarrow(1)\big]\big[\hat{n}_\uparrow(2)+\hat{n}_\downarrow(2)\big]\rangle - n^2 = \langle T_\tau\hat{n}(1)\hat{n}(2)\rangle - n^2 \\ \chi_{\mathrm{sp}}(1,2) &= \langle T_\tau\big[\hat{n}_\uparrow(1)-\hat{n}_\downarrow(1)\big]\big[\hat{n}_\uparrow(2)-\hat{n}_\downarrow(2)\big]\rangle = \langle T_\tau\hat{S}^z(1)\hat{S}^z(2)\rangle\,,\end{aligned} \tag{A.7}$$

where $\hat{S}^z(1) = \hat{n}_\uparrow(1) - \hat{n}_\downarrow(1)$ is the spin-polarization in $z-$direction.

Let us now consider generalized three-point susceptibilities $\chi_{\sigma\tau}(1,3;2)$,

$$\chi_{\sigma\tau}(1,3;2) = -\frac{\delta G_\sigma(1,3)}{\delta\phi_\tau(2^+,2)}. \tag{A.8}$$

The two-point susceptibility as introduced in Eq. (A.4) and used in Eq. (A.6) is then retrieved

upon choosing $3 = 1^+$. For $\chi_{\sigma\tau}(1,3;2)$, we can write down the Bethe-Salpeter equation (BSE)[1] in the particle-hole channel, see Fig. A.1,

$$\chi_{\sigma\tau}(1,3;2) = -G_\sigma(1,2)G_\tau(2,3)\delta_{\sigma\tau} + G_\sigma(1,\bar{2})\Gamma^{\mathrm{ir}}_{\sigma\bar{\nu}}(\bar{2},\bar{3};\bar{4},\bar{5})\chi_{\bar{\nu}\tau}(\bar{4},\bar{5};2)G_\sigma(\bar{3},3). \tag{A.9}$$

Here, $\Gamma^{\mathrm{ir}}_{\sigma\tau}$ is the irreducible vertex generated from the Luttinger-Ward functional $\Phi[G]$,

$$\Gamma^{\mathrm{ir}}_{\sigma\tau}(1,2;3,4) = \frac{\delta^2\Phi[G]}{\delta G_\sigma(2,1)\delta G_\tau(3,4)}, \tag{A.10}$$

which is calculated via a Legendre transform on the generating functional $\ln Z[\phi]$ using the Kadanoff-Baym relation between the Green's function and the self energy[2]. The sign of the first term in the BSE, Eq. (A.9), is chosen as convention. With definition Eq. (A.6), we get for the spin channel

$$\begin{aligned}\chi_{\mathrm{sp}}(1,3;2) = 2[\chi_{\uparrow\uparrow}(1,3;2) - \chi_{\uparrow\downarrow}(1,3;2)] = -2G_\uparrow(1,2)G_\uparrow(2,3) + G_\uparrow(1,\bar{2}) \times \dots \\ \cdots \times 2\Big\{\Gamma^{\mathrm{ir}}_{\uparrow\uparrow}(\bar{2},\bar{3};\bar{4},\bar{5})\chi_{\uparrow\uparrow}(\bar{4},\bar{5};2) + \Gamma^{\mathrm{ir}}_{\uparrow\downarrow}(\bar{2},\bar{3};\bar{4},\bar{5})\chi_{\downarrow\uparrow}(\bar{4},\bar{5};2) \\ - \Gamma^{\mathrm{ir}}_{\uparrow\uparrow}(\bar{2},\bar{3};\bar{4},\bar{5})\chi_{\uparrow\downarrow}(\bar{4},\bar{5};2) - \Gamma^{\mathrm{ir}}_{\uparrow\downarrow}(\bar{2},\bar{3};\bar{4},\bar{5})\chi_{\downarrow\downarrow}(\bar{4},\bar{5};2)\Big\}G_\uparrow(\bar{3},3).\end{aligned} \tag{A.11}$$

Exploiting $\chi_{\sigma\tau} = \chi_{-\sigma-\tau}$[3] as a result from the SU(2) symmetry, the part in the brackets (including the factor of 2) reads

$$2\big\{\Gamma^{\mathrm{ir}}_{\uparrow\uparrow}\chi_{\uparrow\uparrow} + \Gamma^{\mathrm{ir}}_{\uparrow\downarrow}\chi_{\uparrow\downarrow} - \Gamma^{\mathrm{ir}}_{\uparrow\uparrow}\chi_{\uparrow\downarrow} - \Gamma^{\mathrm{ir}}_{\uparrow\downarrow}\chi_{\uparrow\uparrow}\big\} = 2[\chi_{\uparrow\uparrow} - \chi_{\uparrow\downarrow}] \times [\Gamma^{\mathrm{ir}}_{\uparrow\uparrow} - \Gamma^{\mathrm{ir}}_{\uparrow\downarrow}] = -\chi_{\mathrm{sp}}\Gamma_{\mathrm{sp}}, \tag{A.12}$$

where in the last step we have defined $\Gamma_{\mathrm{sp}} = \Gamma^{\mathrm{ir}}_{\uparrow\downarrow} - \Gamma^{\mathrm{ir}}_{\uparrow\uparrow}$. Hence, the BSE for the spin susceptibility reads

$$\chi_{\mathrm{sp}}(1,3;2) = -2G_\uparrow(1,2)G_\uparrow(2,3) - \Gamma_{\mathrm{sp}}(\bar{2},\bar{3};\bar{4},\bar{5})G_\uparrow(1,\bar{2})G_\uparrow(\bar{3},3)\chi_{\mathrm{sp}}(\bar{4},\bar{5};2). \tag{A.13}$$

Similarly, for the charge susceptibility we get

$$\chi_{\mathrm{ch}}(1,3;2) = -2G_\uparrow(1,2)G_\uparrow(2,3) + \Gamma_{\mathrm{ch}}(\bar{2},\bar{3};\bar{4},\bar{5})G_\uparrow(1,\bar{2})G_\uparrow(\bar{3},3)\chi_{\mathrm{ch}}(\bar{4},\bar{5};2), \tag{A.14}$$

where $\Gamma_{\mathrm{ch}} = \Gamma^{\mathrm{ir}}_{\uparrow\downarrow} + \Gamma^{\mathrm{ir}}_{\uparrow\uparrow}$.

We can now make an explicit approximation for the form of the irreducible vertices, which, in their simplest form, are only parametrized by two constants, $\Gamma^{\mathrm{ir}}_{\uparrow\downarrow}$ and $\Gamma^{\mathrm{ir}}_{\uparrow\uparrow}$. In other words, the irreducible vertex is chosen to be independent of momentum and frequency, corresponding to

$$\Gamma^{\mathrm{ir}}_{\sigma\tau}(2,3;4,5) = \delta(3-4)\delta(2-5)\delta(4^+-5)\Gamma^{\mathrm{ir}}_{\sigma\tau}. \tag{A.15}$$

[1] In its original formulation, the BSE considers generalized four-point susceptibilities, $\chi_{\sigma\tau}(1,3;4,2) = -\frac{\delta G_\sigma(1,3)}{\delta\phi_\tau(4,2)}$, which are equivalent to our case by choosing $4 = 2^+$. When reducing to the two-point susceptibility after solving the BSE, both give the same result. However, three-point susceptibilites already introduce some Kronecker-Deltas in the equations, simplifying the expressions at an earlier stage.

[2] The Kadanoff-Baym relation reads $G^{-1} = G_0^{-1} + \phi + \Sigma$, with Σ the self-energy.

[3] Indices with a $(-)$ sign correspond to the opposite spin, i.e., $-\uparrow=\downarrow$, $-\downarrow=\uparrow$.

Inserting into Eq. (A.13) and denoting $G_\uparrow = G_\downarrow = G$, we find for the two-point susceptibility

$$\chi_{\rm sp}(1;2) = -2G(1,2)G(2,1) - U_{\rm sp}G(1,\bar{4})G(\bar{4},1)\chi_{\rm sp}(\bar{4};2), \tag{A.16}$$

where we defined $U_{\rm sp} = \Gamma^{\rm ir}_{\uparrow\downarrow} - \Gamma^{\rm ir}_{\uparrow\uparrow}$. With $\chi_0(1,2) = -2G(1,2)G(2,1)$, we arrive at the Dyson equation for the two-point susceptibility,

$$\chi_{\rm sp}(1;2) = \chi_0(1,2) + \frac{1}{2}U_{\rm sp}\chi_0(1,\bar{4})\chi_{\rm sp}(\bar{4};2). \tag{A.17}$$

In Matsubara-Fourier space, Eq. (A.17) turns into[4]

$$\sum_q e^{-iq(1-2)}\chi_{\rm sp}(q) = \sum_q e^{-iq(1-2)}\chi_0(q) + \sum_q e^{-iq(1-2)}\frac{1}{2}U_{\rm sp}\chi_0(q)\chi_{\rm sp}(q). \tag{A.18}$$

By approximating $\chi_0(q) = -2\frac{T}{N_{\mathbf{k}}}\sum_k G(k)G(k+q) \approx -2\frac{T}{N_{\mathbf{k}}}\sum_k G_0(k)G_0(k+q)$ with $G_0(k)$ the non-interacting Green's function $G_0(k) = (i\omega_n - \epsilon_{\mathbf{k}})^{-1}$ with single-particle dispersion $\epsilon_{\mathbf{k}}$, we have for $\chi_0(q)$

$$\chi_0(q) = -2\frac{T}{N_{\mathbf{k}}}\sum_k G(k)G(k+q) = -2\frac{T}{N_{\mathbf{k}}}\sum_{\mathbf{k}}\frac{n_F(\epsilon_{\mathbf{k}}-\mu) - n_F(\epsilon_{\mathbf{k}+\mathbf{q}}-\mu)}{i\omega_n + \epsilon_{\mathbf{k}} - \epsilon_{\mathbf{k}+\mathbf{q}}}. \tag{A.19}$$

Here, $N_{\mathbf{k}}$ is the number $\mathbf{k}$-points in the BZ (= number of lattice sites), $n_F(x) = (e^{x/T}+1)^{-1}$ is the Fermi-Dirac distribution, and μ is chosen such that the particle density per spin flavor n_σ is given by

$$n_\sigma = \frac{1}{N_{\mathbf{k}}}\sum_{\mathbf{k}} n_F(\epsilon_{\mathbf{k}} - \mu). \tag{A.20}$$

The non-interacting susceptibility is thus determined by T, $\epsilon_{\mathbf{k}}$ and n_σ. Finally, with Eq. (A.18), we arrive at

$$\chi_{\rm sp}(q) = \frac{\chi_0(q)}{1 - \frac{1}{2}U_{\rm sp}\chi_0(q)}. \tag{A.21}$$

Similarly, for the charge sector, we get

$$\chi_{\rm ch}(q) = \frac{\chi_0(q)}{1 + \frac{1}{2}U_{\rm ch}\chi_0(q)}, \tag{A.22}$$

with $U_{\rm ch} = \Gamma^{\rm ir}_{\uparrow\downarrow} + \Gamma^{\rm ir}_{\uparrow\uparrow}$. In a final step to get to the TPSC equations, we enforce Pauli's principle on a two-particle level, i.e., we impose that $\langle \hat{n}_\sigma(\mathbf{r},\tau)\hat{n}_\sigma(\mathbf{r},\tau)\rangle = \langle \hat{n}_\sigma(\mathbf{r},\tau)\rangle$. In Eq. (A.6), we see that we can exploit Pauli's principle for the equal-time, equal-space response $\chi_{\rm sp/ch}(1,1^+)$, yielding

$$\begin{aligned}
\chi_{\rm sp}(1,1^+) &= \frac{T}{N_{\mathbf{q}}}\sum_{\mathbf{q},i\omega_n}\chi_{\rm sp}(\mathbf{q},i\omega_n) = n - 2\langle \hat{n}_\uparrow\hat{n}_\downarrow\rangle, \\
\chi_{\rm ch}(1,1^+) &= \frac{T}{N_{\mathbf{q}}}\sum_{\mathbf{q},i\omega_n}\chi_{\rm ch}(\mathbf{q},i\omega_n) = n - n^2 + 2\langle \hat{n}_\uparrow\hat{n}_\downarrow\rangle,
\end{aligned} \tag{A.23}$$

[4] We use the notation $q = (\mathbf{q}, i\omega_n)$.

where $N_{\mathbf{q}}$ is the number of lattice sites, $\hat{n}_\sigma = \hat{n}_\sigma(\mathbf{r},\tau)$ and we used that $\langle \hat{n}_\uparrow \rangle = \langle \hat{n}_\downarrow \rangle = n/2$. Together with the ansatz

$$\frac{U_{\mathrm{sp}}}{U} = \frac{\langle \hat{n}_\uparrow \hat{n}_\downarrow \rangle}{n_\sigma^2}, \tag{A.24}$$

this defines the TPSC theory.

A.2 SU(N) FH model

We now aim to generalize the TPSC equations derived in the previous section to the case of the SU(N) Hubbard model, where N spin flavors enter the Hamiltonian,

$$\hat{\mathcal{H}} = -t \sum_{\langle i,j \rangle} \sum_{\sigma=1}^{N} \left(\hat{c}_i^\dagger \hat{c}_j + \mathrm{H.c.} \right) + \frac{U}{2} \sum_i \sum_{\sigma \neq \tau} \hat{n}_{i,\sigma} \hat{n}_{i,\tau} - \mu \sum_i \sum_\sigma \hat{n}_{i,\sigma}. \tag{A.25}$$

We will be interested in computing the generalized spin-susceptibility χ_{sp} (see also Ref. [158]), given by

$$\begin{aligned} \chi_{\mathrm{sp}}(1,2) &= N(N-1)\left[\langle T_\tau \hat{n}_\sigma(1) \hat{n}_\sigma(2) \rangle - \langle T_\tau \hat{n}_\sigma(1) \hat{n}_{\tau \neq \sigma}(2) \rangle \right] \\ &= N(N-1)\left[\chi_{\sigma\sigma}(1,2) - \chi_{\sigma\tau\neq\sigma}(1,2) \right]. \end{aligned} \tag{A.26}$$

Note that Eq. (A.26) reduces to the spin-susceptibility in Eq. (A.6) for the case $N = 2$. We can now write down the Bethe-Salpeter equation, see Eq. (A.9), for the three-point susceptibilities, leading to

$$\begin{aligned} \chi_{\mathrm{sp}}(1,3;2) = N(N-1)[\chi_{\sigma\sigma}(1,3;2) - \chi_{\sigma\tau}(1,3;2)] &= -N(N-1)G(1,2)G(2,3) + G(1,\bar{2}) \times \dots \\ \cdots \times N(N-1)\Big\{ \Gamma^{\mathrm{ir}}_{\sigma\sigma}(\bar{2},\bar{3};\bar{4},\bar{5}) \chi_{\sigma\sigma}(\bar{4},\bar{5};2) &+ (N-1)\Gamma^{\mathrm{ir}}_{\sigma\tau}(\bar{2},\bar{3};\bar{4},\bar{5}) \chi_{\tau\sigma}(\bar{4},\bar{5};2) \\ - \Gamma^{\mathrm{ir}}_{\sigma\sigma}(\bar{2},\bar{3};\bar{4},\bar{5}) \chi_{\sigma\tau}(\bar{4},\bar{5};2) &- (N-2)\Gamma^{\mathrm{ir}}_{\sigma\tau}(\bar{2},\bar{3};\bar{4},\bar{5}) \chi_{\sigma\tau}(\bar{4},\bar{5};2) \\ - \Gamma^{\mathrm{ir}}_{\sigma\tau}(\bar{2},\bar{3};\bar{4},\bar{5}) \chi_{\tau\tau}(\bar{4},\bar{5};2) &\Big\} G(\bar{3},3). \end{aligned} \tag{A.27}$$

Defining $\Gamma_{\mathrm{sp}} = \Gamma^{\mathrm{ir}}_{\sigma\tau} - \Gamma^{\mathrm{ir}}_{\sigma\sigma}$ and $\chi_0(1,3;2;N) = -NG(1,2)G(2,3)$, we get

$$\chi_{\mathrm{sp}}(1,3;2) = (N-1)\chi_0(1,3;2;N) - \Gamma_{\mathrm{sp}}(\bar{2},\bar{3};\bar{4},\bar{5}) G(1,\bar{2}) G(\bar{3},3) \chi_{\mathrm{sp}}(\bar{4},\bar{5};2). \tag{A.28}$$

Similarly to the case for two spin flavors, we make the same simplified ansatz for the irreducible vertex, Eq. (A.15). This leads to the Dyson equation for the SU(N) symmetric FH model,

$$\chi_{\mathrm{sp}}(1;2) = (N-1)\chi_0(1,2;N) + \frac{1}{N} U_{\mathrm{sp}} \chi_0(1,\bar{4};N) \chi_{\mathrm{sp}}(\bar{4};2), \tag{A.29}$$

where $U_{\mathrm{sp}} = \Gamma^{\mathrm{ir}}_{\sigma\tau} - \Gamma^{\mathrm{ir}}_{\sigma\sigma}$. Evaluating again the equal-time and equal-space correlation function

$\chi_{\rm sp}(1,1^+)$ from Eq. (A.26), we find the TPSC equation for the spin susceptibility

$$\chi_{\rm sp}(1,1^+) = \frac{T}{N_{\mathbf{q}}}\sum_{\mathbf{q},i\omega_n}\frac{\chi_0(\mathbf{q},i\omega_n;N)}{1-\frac{1}{N}U_{\rm sp}\chi_0(\mathbf{q},i\omega_n;N)} = N[\langle\hat{n}_\sigma\rangle - \langle\hat{n}_\sigma\hat{n}_\tau\rangle] = n - N\langle\hat{n}_\sigma\hat{n}_\tau\rangle\,. \tag{A.30}$$

Note that the TPSC equation for the N-component system, Eq. (A.30), is equivalent to the SU(2) symmetric case, with $2 \to N$. When using the same ansatz as in the two-component case, $\langle\hat{n}_\sigma\hat{n}_\tau\rangle = \frac{U_{\rm sp}}{U}n_\sigma^2$, we see how the TPSC equation becomes N-independent,

$$\chi_{\rm sp}(1,1^+) = \frac{T}{N_{\mathbf{q}}}\sum_{\mathbf{q},i\omega_n}\frac{\chi_0(\mathbf{q},i\omega_n;1)}{1-U_{\rm sp}\chi_0(\mathbf{q},i\omega_n;1)} = n_\sigma - \frac{U_{\rm sp}}{U}n_\sigma^2. \tag{A.31}$$

In particular, Eq. (A.31) only depends on the filling per spin flavor $n_\sigma = \langle\hat{n}_\sigma(\mathbf{r},\tau)\rangle$, see also the discussion presented in Sec. 11.4.

A.3 Numerical implementation

From Eq. (3.40), it is evident that only the non-interacting susceptibility is needed to self-consistently solve the equations for $U_{\rm sp}, U_{\rm ch}$. Hence, for a given grid in Matsubara-Fourier space $(\mathbf{q},i\omega_n)$, $\chi_0(\mathbf{q},i\omega)$ is computed and tabulated. This process scales as $\mathcal{O}(N_{\mathbf{k}}^2 N_\omega)$, with $N_{\mathbf{k}}$ and N_ω the number of points in the BZ mesh and number of Matsubara frequencies, respectively.

As a concrete example, let us specify for the case of the square lattice. For the summation, we use the mesh by Monkhorst and Pack [579], whereby we choose to exclude all high-symmetry points from the summation. Note that due to the symmetry $\chi_{\rm sp}(\mathbf{q}=[q_x,q_y],i\omega) = \chi_{\rm sp}(\mathbf{q}=[\sigma q_x,\sigma' q_y],i\omega)$ for $\sigma=\pm1,\sigma'=\pm1$, only $1/4$ of the Brillouin zone (BZ) needs to be computed (however, the $\mathbf{k}-$sum in the definition of $\chi_0(\mathbf{q},i\omega_n)$ needs to span the entire BZ). Furthermore, we only have to sum over positive Matsubara frequencies (plus the contribution from $i\omega_n=0$), as $\chi_{\rm sp}(\mathbf{q},i\omega_n) = \chi^*_{\rm sp}(\mathbf{q},-i\omega_n)$. Hence, we need to tabulate $\mathbf{q}\in 1\mathrm{Q}, i\omega_n \geq 0$ and compute

$$\sum_{\mathbf{q}}\sum_{i\omega_n}\chi_{\rm sp}(\mathbf{q},i\omega_n) = \sum_{\mathbf{q}\in 1\mathrm{Q}}\chi_{\rm sp}(\mathbf{q},i\omega_n=0) + 8\mathrm{Re}\Big[\sum_{\mathbf{q}\in 1\mathrm{Q}}\sum_{i\omega_n>0}\chi_{\rm sp}(\mathbf{q},i\omega_n)\Big], \tag{A.32}$$

where 1Q denotes a single quadrant in the BZ. In order to approximate the Matsubara sum, we evaluate Eq. (A.32) for various cutoffs N_ω, and extrapolate the result linearly in $1/N_\omega$ to $N_\omega\to\infty$.

We then compute Eq. (A.32) for a given interaction $U_{\rm sp}$, and self-consitently solve Eq. (3.40) with the ansatz Eq. (3.44). In order to update $U_{\rm sp}$ in each iteration, a simple mixing scheme $U_{\rm sp}^{n+1} = \alpha\tilde{U}_{\rm sp}^{n+1} + (1-\alpha)U_{\rm sp}^n$ is employed that ensures fast convergence, where

$$\tilde{U}_{\rm sp}^{n+1} = \frac{U}{2n_\sigma^2}\left[n - \chi_{\rm sp}(1,1^+;U_{\rm sp}^n)\right]. \tag{A.33}$$

Note that the numerical complexity of solving the self-consistency equations is negligible compared to tabulating the non-interacting susceptibilities. When doing so, the iteration over $\mathbf{q}$ (which is usually the bigger mesh compared to the frequencies) can be parallelized.

Acknowledgements

Many people have played a part in making the past years both scientifically successful and so enjoyable.

Fabian and Annabelle—you're incredible physicists and mentors. You've taught me so much, and your passion for research is contagious. The supportive, collaborative environment you create is the definition of an academic family, and I couldn't have been luckier to be a part of it. Many Cambridge Common playground discussions (with Mariella leading the way!), dinners at your place, soccer and hockey matches, and all the exciting projects we worked on together have made my PhD such an enjoyable journey. Learning from you and watching all of us grow over the years—in Munich, Boston, Houston, and everywhere in between—has been amazing. I'll always treasure those memories, and the immense support and freedom you've given me every step of the way.

I also had the privilege of spending time at ITAMP, Harvard, and Rice University during my PhD. Huge thanks to Kaden Hazzard, Hossein Sadeghpour, and Subir Sachdev—your generosity and hospitality gave me the chance to learn a lot, meet incredible people, and grow as a scientist. I'll always be grateful for the doors you opened for me and the encouragement you gave, and I look forward to continuing to work with you in the future.

Many thanks to Uli Schollwöck for the hospitality at his chair and for always offering helpful advice whenever I needed his experience, insight, or support. Thanks also to Lode Pollet for sharing his immense physical intuition and giving me many valuable insights. A special thanks to Cordula Weber and Kathrin Higgen for always helping with all bureaucratic matters.

A big thanks to Kaden Hazzard for his continuous support over the past years and for co-supervising this thesis, and to Immanuel Bloch, Steffen Rulands and Dmitri Efetov for being part of my PhD committee.

To my current and former colleagues in Munich: From endless discussions and Mensa lunches to fun conferences and trips, you were always there. Mattia, Matjaž, Tim, Felix, Giovanni, Simon, Lukas, Hannah, and Reja—you made every day on the fourth floor and beyond enjoyable. Special thanks to Mattia, Tim, Felix and Matjaž for reading parts of this thesis.

Thank you Sebastian, Sam, and Martin, for always offering a helping hand regarding the `SyTen` toolkit whenever I needed it.

To the Lithium team at MPQ: Working so close with you in the past years and learning many things about your experiment has been a highlight of my PhD. Big thanks to Dominik, Titus, Timon, Thomas, Petar, Si, Sarah, and Immanuel.

Thank you Borislav Polovnikov, Alexander Högele and the moiré team—learning about

moiré systems and developing theoretical scenarios for your bilayer system has been great fun.

To the colleagues and friends I met abroad, and all the discussions we had both in and out of work. The Harvard and ITAMP crew: Pietro, Elisa, Oriana, Christian, Rudi, Anant, Martin, Lev, Symeon, Vasil, Valentin, Ceren, Francisco. And the Rice crew: Eduardo, Diego, Haotian, Sohail, Zewen, Dorian.

An meine Freunde und Familie außerhalb der Forschung: Eure Unterstützung und Liebe haben mir immer die Stärke und den Mut gegeben, neue Wege zu gehen. Es ist so wertvoll, Menschen um sich zu haben, auf die man sich immer verlassen kann. Danke von Herzen an meine Familie—Anne, Bettina und Frank—ihr seid mein Anker, egal wo ich bin. Und natürlich ein riesiges Danke an dich, Julia, dafür, dass du immer an meiner Seite stehst, egal was passiert. Ohne euch wäre das alles nicht möglich gewesen.

Bibliography

[1] Henning Schlömer, Annabelle Bohrdt, Lode Pollet, Ulrich Schollwöck, and Fabian Grusdt. Robust stripes in the mixed-dimensional $t - J$ model. *Phys. Rev. Res.*, 5:L022027, May 2023. Referenced on pages xi, 6, and 67.

[2] Dominik Bourgund, Thomas Chalopin, Petar Bojović, Henning Schlömer, Si Wang, Titus Franz, Sarah Hirthe, Annabelle Bohrdt, Fabian Grusdt, Immanuel Bloch, and Timon A. Hilker. Formation of individual stripes in a mixed-dimensional cold-atom Fermi-Hubbard system. *Nature*, 637(8044):57–62, 2025. Referenced on pages xi, 3, 6, 67, 82, 83, 84, 85, 86, 87, 91, 93, 94, and 180.

[3] Henning Schlömer, Timon A. Hilker, Immanuel Bloch, Ulrich Schollwöck, Fabian Grusdt, and Annabelle Bohrdt. Quantifying hole-motion-induced frustration in doped antiferromagnets by Hamiltonian reconstruction. *Communications Materials*, 4(1):64, 2023. Referenced on pages xi, 6, and 98.

[4] Henning Schlömer, Annabelle Bohrdt, and Fabian Grusdt. Geometric fractionalized Fermi liquids: Hidden antiferromagnetism and pseudogap from fluctuating stripes, 2024. Referenced on pages xi, 7, 18, and 120.

[5] Henning Schlömer, Ulrich Schollwöck, Fabian Grusdt, and Annabelle Bohrdt. Superconductivity in the pressurized nickelate La3Ni2O7 in the vicinity of a BEC–BCS crossover. *Communications Physics*, 7(1):366, 2024. Referenced on pages xi, 7, 159, and 186.

[6] Henning Schlömer, Hannah Lange, Titus Franz, Thomas Chalopin, Petar Bojović, Si Wang, Immanuel Bloch, Timon A. Hilker, Fabian Grusdt, and Annabelle Bohrdt. Local Control and Mixed Dimensions: Exploring High-Temperature Superconductivity in Optical Lattices. *PRX Quantum*, 5:040341, Dec 2024. Referenced on pages xi, 7, and 196.

[7] Henning Schlömer, Ulrich Schollwöck, Annabelle Bohrdt, and Fabian Grusdt. Kinetic-to-magnetic frustration crossover and linear confinement in the doped triangular $t - J$ model. *Phys. Rev. B*, 110:L041117, Jul 2024. Referenced on pages xii, 7, and 200.

[8] Borislav Polovnikov, Johannes Scherzer, Subhradeep Misra, Henning Schlömer, Julian Trapp, Xin Huang, Christian Mohl, Zhijie Li, Jonas Göser, Jonathan Förste, Ismail Bilgin, Kenji Watanabe, Takashi Taniguchi, Annabelle Bohrdt, Fabian Grusdt, Anvar S. Baimuratov, and Alexander Högele. Implementation of the bilayer Hubbard model in a moiré heterostructure, 2024. Referenced on pages xii, 8, 200, 215, 216, 217, 218, 219, and 222.

[9] Henning Schlömer, Fabian Grusdt, Ulrich Schollwöck, Kaden R. A. Hazzard, and Annabelle Bohrdt. Subdimensional magnetic polarons in the one-hole doped SU(3) $t-J$ model. *Phys. Rev. B*, 110:125134, Sep 2024. Referenced on pages xii, 8, and 227.

[10] Henning Schlömer and Annabelle Bohrdt. Fluctuation based interpretable analysis scheme for quantum many-body snapshots. *SciPost Phys.*, 15:099, 2023. Referenced on pages xii, 8, and 249.

[11] Henning Schlömer and Subir Sachdev. Quantum Annealing with chaotic driver Hamiltonians, 2024. Referenced on pages xii, 9, and 272.

[12] Abhinav Suresh, Henning Schlömer, Baran Hashemi, and Annabelle Bohrdt. Interpretable correlator Transformer for image-like quantum matter data, 2024. Referenced on pages xii, 249, 263, and 264.

[13] Annika Böhler, Henning Schlömer, Ulrich Schollwöck, Annabelle Bohrdt, and Fabian Grusdt. Probing a Modified Luttinger Sum Rule in the Strongly Interacting 1D Fermi-Hubbard Model, 2024. Referenced on page xii.

[14] Henning Schlömer, Chunyu Tan, Stephan Haas, and Hubert Saleur. Parity effects and universal terms of $\mathcal{O}(1)$ in the entanglement near a boundary. *SciPost Phys.*, 13:110, 2022. Referenced on page xii.

[15] Gautam Rai, Henning Schlömer, Chris Matsumura, Stephan Haas, and Anuradha Jagannathan. Bulk topological signatures of a quasicrystal. *Phys. Rev. B*, 104:184202, Nov 2021. Referenced on page xii.

[16] Subir Sachdev. *Quantum Phases of Matter*. Cambridge University Press, Cambridge, 2023. Referenced on pages 1, 2, 19, 120, 129, 130, 136, and 160.

[17] Jun Kondo. Resistance minimum in dilute magnetic alloys. *Progress of theoretical physics*, 32(1):37–49, 1964. Referenced on page 2.

[18] G. R. Stewart. Heavy-fermion systems. *Rev. Mod. Phys.*, 56:755–787, Oct 1984. Referenced on page 2.

[19] F. Steglich, J. Aarts, C. D. Bredl, W. Lieke, D. Meschede, W. Franz, and H. Schäfer. Superconductivity in the Presence of Strong Pauli Paramagnetism: $CeCu_2Si_2$. *Phys. Rev. Lett.*, 43:1892–1896, Dec 1979. Referenced on page 2.

[20] Maxim Dzero, Jing Xia, Victor Galitski, and Piers Coleman. Topological Kondo Insulators. *Annual Review of Condensed Matter Physics*, 7(Volume 7, 2016):249–280, 2016. Referenced on page 2.

[21] G. R. Stewart. Non-Fermi-liquid behavior in d- and f-electron metals. *Rev. Mod. Phys.*, 73:797–855, Oct 2001. Referenced on page 2.

[22] Horst L. Stormer, Daniel C. Tsui, and Arthur C. Gossard. The fractional quantum Hall effect. *Rev. Mod. Phys.*, 71:S298–S305, Mar 1999. Referenced on page 2.

[23] J. G. Bednorz and K. A. Müller. Possible high Tc superconductivity in the Ba−La−Cu−O system. *Zeitschrift für Physik B Condensed Matter*, 64(2):189–193, 1986. Referenced on pages 2 and 14.

[24] Patrick A. Lee, Naoto Nagaosa, and Xiao-Gang Wen. Doping a Mott insulator: Physics of high-temperature superconductivity. *Rev. Mod. Phys.*, 78:17–85, Jan 2006. Referenced on pages 2, 19, 98, 123, 124, 154, 174, and 247.

[25] Kenneth G. Wilson. The renormalization group: Critical phenomena and the Kondo problem. *Rev. Mod. Phys.*, 47:773–840, Oct 1975. Referenced on page 2.

[26] N. Andrei, K. Furuya, and J. H. Lowenstein. Solution of the Kondo problem. *Rev. Mod. Phys.*, 55:331–402, Apr 1983. Referenced on page 2.

[27] David P. Landau, Steven P. Lewis, and Heinz-Bernd Schüttler, editors. *Quantum Simulations of Strongly Correlated Electron Systems*, Berlin, Heidelberg, 2000. Springer Berlin Heidelberg. Referenced on page 2.

[28] Steven R. White. Density matrix formulation for quantum renormalization groups. *Phys. Rev. Lett.*, 69:2863–2866, Nov 1992. Referenced on page 2.

[29] Ulrich Schollwöck. The density-matrix renormalization group in the age of matrix product states. *Annals of Physics*, 326(1):96–192, 2011. January 2011 Special Issue. Referenced on pages 2, 32, and 33.

[30] U. Schollwöck. The density-matrix renormalization group. *Rev. Mod. Phys.*, 77:259–315, Apr 2005. Referenced on page 2.

[31] Antoine Georges, Gabriel Kotliar, Werner Krauth, and Marcelo J. Rozenberg. Dynamical mean-field theory of strongly correlated fermion systems and the limit of infinite dimensions. *Rev. Mod. Phys.*, 68:13–125, Jan 1996. Referenced on page 2.

[32] Hannah Lange, Anka Van de Walle, Atiye Abedinnia, and Annabelle Bohrdt. From architectures to applications: a review of neural quantum states. *Quantum Science and Technology*, 9(4):040501, 2024. Referenced on page 2.

[33] Richard P. Feynman. Simulating physics with computers. *International Journal of Theoretical Physics*, 21(6):467–488, 1982. Referenced on page 2.

[34] Immanuel Bloch, Jean Dalibard, and Wilhelm Zwerger. Many-body physics with ultracold gases. *Rev. Mod. Phys.*, 80:885–964, Jul 2008. Referenced on page 2.

[35] Tilman Esslinger. Fermi-Hubbard Physics with Atoms in an Optical Lattice. *Annual Review of Condensed Matter Physics*, 1(1):129–152, 2010. Referenced on page 2.

[36] Michael Foss-Feig, Guido Pagano, Andrew C. Potter, and Norman Y. Yao. Progress in Trapped-Ion Quantum Simulation. *Annual Review of Condensed Matter Physics*, 2024. Referenced on page 2.

[37] Morten Kjaergaard, Mollie E. Schwartz, Jochen Braumüller, Philip Krantz, Joel I.-J. Wang, Simon Gustavsson, and William D. Oliver. Superconducting Qubits: Current State of Play. *Annual Review of Condensed Matter Physics*, 11(Volume 11, 2020):369–395, 2020. Referenced on page 2.

[38] Dante M. Kennes, Martin Claassen, Lede Xian, Antoine Georges, Andrew J. Millis, James Hone, Cory R. Dean, D. N. Basov, Abhay N. Pasupathy, and Angel Rubio. Moiréheterostructures as a condensed-matter quantum simulator. *Nature Physics*, 17(2):155–163, 2021. Referenced on pages 2, 58, 59, 60, 62, and 200.

[39] T. D. Ladd, F. Jelezko, R. Laflamme, Y. Nakamura, C. Monroe, and J. L. O'Brien. Quantum computers. *Nature*, 464(7285):45–53, 2010. Referenced on page 3.

[40] Annabelle Bohrdt, Lukas Homeier, Christian Reinmoser, Eugene Demler, and Fabian Grusdt. Exploration of doped quantum magnets with ultracold atoms. *Annals of Physics*, 435:168651, 2021. Special issue on Philip W. Anderson. Referenced on pages 3, 4, and 160.

[41] Anton Mazurenko, Christie S. Chiu, Geoffrey Ji, Maxwell F. Parsons, Márton Kanász-Nagy, Richard Schmidt, Fabian Grusdt, Eugene Demler, Daniel Greif, and Markus Greiner. A cold-atom Fermi–Hubbard antiferromagnet. *Nature*, 545(7655):462–466, 2017. Referenced on pages 3, 4, 54, 77, and 183.

[42] Christie S. Chiu, Geoffrey Ji, Annabelle Bohrdt, Muqing Xu, Michael Knap, Eugene Demler, Fabian Grusdt, Markus Greiner, and Daniel Greif. String patterns in the doped Hubbard model. *Science*, 365(6450):251–256, 2019. Referenced on pages 3, 4, and 251.

[43] Annabelle Bohrdt, Christie S. Chiu, Geoffrey Ji, Muqing Xu, Daniel Greif, Markus Greiner, Eugene Demler, Fabian Grusdt, and Michael Knap. Classifying snapshots of the doped Hubbard model with machine learning. *Nature Physics*, 15(9):921–924, 2019. Referenced on pages 3, 4, 247, and 248.

[44] Geoffrey Ji, Muqing Xu, Lev Haldar Kendrick, Christie S. Chiu, Justus C. Brüggenjürgen, Daniel Greif, Annabelle Bohrdt, Fabian Grusdt, Eugene Demler, Martin Lebrat, and Markus Greiner. Coupling a Mobile Hole to an Antiferromagnetic Spin Background: Transient Dynamics of a Magnetic Polaron. *Phys. Rev. X*, 11:021022, Apr 2021. Referenced on pages 3, 4, and 238.

[45] Maxwell F. Parsons, Anton Mazurenko, Christie S. Chiu, Geoffrey Ji, Daniel Greif, and Markus Greiner. Site-resolved measurement of the spin-correlation function in the Fermi-Hubbard model. *Science*, 353(6305):1253–1256, 2016. Referenced on pages 3, 4, and 56.

[46] Joannis Koepsell, Jayadev Vijayan, Pimonpan Sompet, Fabian Grusdt, Timon A. Hilker, Eugene Demler, Guillaume Salomon, Immanuel Bloch, and Christian Gross. Imaging magnetic polarons in the doped Fermi–Hubbard model. *Nature*, 572(7769):358–362, 2019. Referenced on pages 3, 4, and 95.

[47] Guillaume Salomon, Joannis Koepsell, Jayadev Vijayan, Timon A. Hilker, Jacopo Nespolo, Lode Pollet, Immanuel Bloch, and Christian Gross. Direct observation of incommensurate magnetism in Hubbard chains. *Nature*, 565(7737):56–60, 2019. Referenced on pages 3 and 4.

[48] Joannis Koepsell, Dominik Bourgund, Pimonpan Sompet, Sarah Hirthe, Annabelle Bohrdt, Yao Wang, Fabian Grusdt, Eugene Demler, Guillaume Salomon, Christian Gross, and Immanuel Bloch. Microscopic evolution of doped Mott insulators from polaronic metal to Fermi liquid. *Science*, 374(6563):82–86, 2021. Referenced on pages 3, 4, and 95.

[49] Peter T. Brown, Debayan Mitra, Elmer Guardado-Sanchez, Reza Nourafkan, Alexis Reymbaut, Charles-David Hébert, Simon Bergeron, A.-M. S. Tremblay, Jure Kokalj, David A. Huse, Peter Schauß, and Waseem S. Bakr. Bad metallic transport in a cold atom Fermi-Hubbard system. *Science*, 363(6425):379–382, 2019. Referenced on pages 3, 4, and 172.

[50] Peter T. Brown, Debayan Mitra, Elmer Guardado-Sanchez, Peter Schauß, Stanimir S. Kondov, Ehsan Khatami, Thereza Paiva, Nandini Trivedi, David A. Huse, and Waseem S. Bakr. Spin-imbalance in a 2D Fermi-Hubbard system. *Science*, 357(6358):1385–1388, 2017. Referenced on pages 3, 4, and 187.

[51] Daniel Greif, Thomas Uehlinger, Gregor Jotzu, Leticia Tarruell, and Tilman Esslinger. Short-Range Quantum Magnetism of Ultracold Fermions in an Optical Lattice. *Science*, 340(6138):1307–1310, 2013. Referenced on pages 3, 4, 183, and 189.

[52] Lawrence W. Cheuk, Matthew A. Nichols, Katherine R. Lawrence, Melih Okan, Hao Zhang, Ehsan Khatami, Nandini Trivedi, Thereza Paiva, Marcos Rigol, and Martin W. Zwierlein. Observation of spatial charge and spin correlations in the 2D Fermi-Hubbard model. *Science*, 353(6305):1260–1264, 2016. Referenced on pages 3, 4, and 56.

[53] Matthew A. Nichols, Lawrence W. Cheuk, Melih Okan, Thomas R. Hartke, Enrique Mendez, T. Senthil, Ehsan Khatami, Hao Zhang, and Martin W. Zwierlein. Spin transport in a Mott insulator of ultracold fermions. *Science*, 363(6425):383–387, 2019. Referenced on pages 3 and 4.

[54] M. Gall, C. F. Chan, N. Wurz, and M. Köhl. Simulating a Mott Insulator Using Attractive Interaction. *Phys. Rev. Lett.*, 124:010403, Jan 2020. Referenced on pages 3, 4, and 191.

[55] Martin Lebrat, Muqing Xu, Lev Haldar Kendrick, Anant Kale, Youqi Gang, Pranav Seetharaman, Ivan Morera, Ehsan Khatami, Eugene Demler, and Markus Greiner. Observation of Nagaoka polarons in a Fermi–Hubbard quantum simulator. *Nature*, 629(8011):317–322, 2024. Referenced on pages 3, 5, and 214.

[56] Max L. Prichard, Benjamin M. Spar, Ivan Morera, Eugene Demler, Zoe Z. Yan, and Waseem S. Bakr. Directly imaging spin polarons in a kinetically frustrated Hubbard system. *Nature*, 629(8011):323–328, 2024. Referenced on pages 3, 5, and 214.

[57] Sarah Hirthe, Thomas Chalopin, Dominik Bourgund, Petar Bojović, Annabelle Bohrdt, Eugene Demler, Fabian Grusdt, Immanuel Bloch, and Timon A. Hilker. Magnetically mediated hole pairing in fermionic ladders of ultracold atoms. *Nature*, 613(7944):463–467, 2023. Referenced on pages 3, 7, 26, 55, 56, 81, 180, 183, 185, 188, and 224.

[58] Christian Hofrichter, Luis Riegger, Francesco Scazza, Moritz Höfer, Diogo Rio Fernandes, Immanuel Bloch, and Simon Fölling. Direct Probing of the Mott Crossover in the SU(N) Fermi-Hubbard Model. *Phys. Rev. X*, 6:021030, Jun 2016. Referenced on pages 3, 5, 57, and 226.

[59] Hideki Ozawa, Shintaro Taie, Yosuke Takasu, and Yoshiro Takahashi. Antiferromagnetic Spin Correlation of SU($\mathcal{N}$) Fermi Gas in an Optical Superlattice. *Phys. Rev. Lett.*, 121:225303, Nov 2018. Referenced on pages 3, 5, 57, 58, and 226.

[60] Shintaro Taie, Eduardo Ibarra-García-Padilla, Naoki Nishizawa, Yosuke Takasu, Yoshihito Kuno, Hao-Tian Wei, Richard T. Scalettar, Kaden R. A. Hazzard, and Yoshiro Takahashi. Observation of antiferromagnetic correlations in an ultracold SU(N) Hubbard model. *Nature Physics*, 18(11):1356–1361, 2022. Referenced on pages 3, 5, 57, 58, 226, 242, and 245.

[61] G. Pasqualetti, O. Bettermann, N. Darkwah Oppong, E. Ibarra-García-Padilla, S. Dasgupta, R. T. Scalettar, K. R. A. Hazzard, I. Bloch, and S. Fölling. Equation of State and Thermometry of the 2D SU(N) Fermi-Hubbard Model. *Phys. Rev. Lett.*, 132:083401, Feb 2024. Referenced on pages 3, 5, 57, 58, and 226.

[62] Russell A. Hart, Pedro M. Duarte, Tsung-Lin Yang, Xinxing Liu, Thereza Paiva, Ehsan Khatami, Richard T. Scalettar, Nandini Trivedi, David A. Huse, and Randall G. Hulet. Observation of antiferromagnetic correlations in the Hubbard model with ultracold atoms. *Nature*, 519(7542):211–214, 2015. Referenced on pages 3, 96, and 183.

[63] Hou-Ji Shao, Yu-Xuan Wang, De-Zhi Zhu, Yan-Song Zhu, Hao-Nan Sun, Si-Yuan Chen, Chi Zhang, Zhi-Jie Fan, Youjin Deng, Xing-Can Yao, Yu-Ao Chen, and Jian-Wei Pan. Antiferromagnetic phase transition in a 3D fermionic Hubbard model. *Nature*, 632(8024):267–272, 2024. Referenced on page 3.

[64] Jonathan Simon, Waseem S. Bakr, Ruichao Ma, M. Eric Tai, Philipp M. Preiss, and Markus Greiner. Quantum simulation of antiferromagnetic spin chains in an optical lattice. *Nature*, 472(7343):307–312, 2011. Referenced on page 4.

[65] Martin Boll, Timon A. Hilker, Guillaume Salomon, Ahmed Omran, Jacopo Nespolo, Lode Pollet, Immanuel Bloch, and Christian Gross. Spin- and density-resolved microscopy of antiferromagnetic correlations in Fermi-Hubbard chains. *Science*, 353(6305):1257–1260, 2016. Referenced on pages 4, 183, and 205.

[66] Christian Gross and Waseem S. Bakr. Quantum gas microscopy for single atom and spin detection. *Nature Physics*, 17(12):1316–1323, 2021. Referenced on pages 4, 185, and 205.

[67] Ivan Morera, Márton Kanász-Nagy, Tomasz Smolenski, Livio Ciorciaro, Ataç Imamoğlu, and Eugene Demler. High-temperature kinetic magnetism in triangular lattices, Jun 2022. Referenced on pages 5, 199, and 203.

[68] W. Hofstetter, J. I. Cirac, P. Zoller, E. Demler, and M. D. Lukin. High-Temperature Superfluidity of Fermionic Atoms in Optical Lattices. *Phys. Rev. Lett.*, 89:220407, Nov 2002. Referenced on pages 7 and 173.

[69] Annabelle Bohrdt, Lukas Homeier, Immanuel Bloch, Eugene Demler, and Fabian Grusdt. Strong pairing in mixed-dimensional bilayer antiferromagnetic Mott insulators. *Nature Physics*, 2022. Referenced on pages 7, 26, 166, 167, and 168.

[70] Hualei Sun, Mengwu Huo, Xunwu Hu, Jingyuan Li, Zengjia Liu, Yifeng Han, Lingyun Tang, Zhongquan Mao, Pengtao Yang, Bosen Wang, Jinguang Cheng, Dao-Xin Yao, Guang-Ming Zhang, and Meng Wang. Signatures of superconductivity near 80 K in a nickelate under high pressure. *Nature*, 621(7979):493–498, 2023. Referenced on pages 7, 26, 27, 157, and 171.

[71] Piers Coleman. *Introduction to many-body physics*. Cambridge University Press, 2015. Referenced on pages 13, 14, 221, and 225.

[72] B. Keimer, S. A. Kivelson, M. R. Norman, S. Uchida, and J. Zaanen. From quantum matter to high-temperature superconductivity in copper oxides. *Nature*, 518(7538):179–186, 2015. Referenced on pages 15, 98, 154, and 247.

[73] Richard L. Greene, Pampa R. Mandal, Nicholas R. Poniatowski, and Tarapada Sarkar. The Strange Metal State of the Electron-Doped Cuprates. *Annual Review of Condensed Matter Physics*, 11(Volume 11, 2020):213–229, 2020. Referenced on pages 15, 17, and 18.

[74] T. Sato, T. Kamiyama, T. Takahashi, K. Kurahashi, and K. Yamada. Observation of d(x2-y2)-Like Superconducting Gap in an Electron-Doped High-Temperature Superconductor. *Science*, 291(5508):1517–1519, 2001. Referenced on page 17.

[75] N. P. Armitage, P. Fournier, and R. L. Greene. Progress and perspectives on electron-doped cuprates. *Rev. Mod. Phys.*, 82:2421–2487, Sep 2010. Referenced on pages 18 and 154.

[76] V. J. Emery, S. A. Kivelson, and J. M. Tranquada. Stripe phases in high-temperature superconductors. *Proceedings of the National Academy of Sciences*, 96(16):8814–8817, 1999. Referenced on page 18.

[77] S. A. Kivelson, I. P. Bindloss, E. Fradkin, V. Oganesyan, J. M. Tranquada, A. Kapitulnik, and C. Howald. How to detect fluctuating stripes in the high-temperature superconductors. *Rev. Mod. Phys.*, 75:1201–1241, Oct 2003. Referenced on page 18.

[78] Matthias Vojta. Lattice symmetry breaking in cuprate superconductors: stripes, nematics, and superconductivity. *Advances in Physics*, 58(6):699–820, 11 2009. Referenced on page 18.

[79] J. M. Tranquada, B. J. Sternlieb, J. D. Axe, Y. Nakamura, and S. Uchida. Evidence for stripe correlations of spins and holes in copper oxide superconductors. *Nature*, 375(6532):561–563, 1995. Referenced on pages 18, 65, 143, and 151.

[80] J. M. Tranquada, J. D. Axe, N. Ichikawa, Y. Nakamura, S. Uchida, and B. Nachumi. Neutron-scattering study of stripe-phase order of holes and spins in $La_{1.48}Nd_{0.4}Sr_{0.12}CuO_4$. *Phys. Rev. B*, 54:7489–7499, Sep 1996. Referenced on pages 18, 65, 143, and 151.

[81] P. Abbamonte, A. Rusydi, S. Smadici, G. D. Gu, G. A. Sawatzky, and D. L. Feng. Spatially modulated 'Mottness' in La2-xBaxCuO4. *Nature Physics*, 1(3):155–158, 2005. Referenced on pages 18, 65, 143, and 151.

[82] C. Howald, H. Eisaki, N. Kaneko, M. Greven, and A. Kapitulnik. Periodic density-of-states modulations in superconducting $Bi_2Sr_2CaCu_2O_{8+\delta}$. *Phys. Rev. B*, 67:014533, Jan 2003. Referenced on page 18.

[83] Michael Vershinin, Shashank Misra, S. Ono, Y. Abe, Yoichi Ando, and Ali Yazdani. Local Ordering in the Pseudogap State of the High-Tc Superconductor Bi2Sr2CaCu2O8+δ. *Science*, 303(5666):1995–1998, 2004. Referenced on page 18.

[84] Colin V. Parker, Pegor Aynajian, Eduardo H. da Silva Neto, Aakash Pushp, Shimpei Ono, Jinsheng Wen, Zhijun Xu, Genda Gu, and Ali Yazdani. Fluctuating stripes at the onset of the pseudogap in the high-Tc superconductor Bi2Sr2CaCu2O8+x. *Nature*, 468(7324):677–680, 2010. Referenced on page 18.

[85] Tao Wu, Hadrien Mayaffre, Steffen Krämer, Mladen Horvatić, Claude Berthier, W. N. Hardy, Ruixing Liang, D. A. Bonn, and Marc-Henri Julien. Magnetic-field-induced charge-stripe order in the high-temperature superconductor YBa2Cu3Oy. *Nature*, 477(7363):191–194, 2011. Referenced on page 18.

[86] J. Chang, N. B. Christensen, Ch. Niedermayer, K. Lefmann, H. M. Rønnow, D. F. McMorrow, A. Schneidewind, P. Link, A. Hiess, M. Boehm, R. Mottl, S. Pailhés, N. Momono, M. Oda, M. Ido, and J. Mesot. Magnetic-Field-Induced Soft-Mode Quantum Phase Transition in the High-Temperature Superconductor $La_{1.855}Sr_{0.145}CuO_4$: An Inelastic Neutron-Scattering Study. *Phys. Rev. Lett.*, 102:177006, Apr 2009. Referenced on page 18.

[87] Kyle M. Shen, F. Ronning, D. H. Lu, F. Baumberger, N. J. C. Ingle, W. S. Lee, W. Meevasana, Y. Kohsaka, M. Azuma, M. Takano, H. Takagi, and Z.-X. Shen. Nodal Quasiparticles and Antinodal Charge Ordering in $Ca_{2-x}Na_xCuO_2Cl_2$. *Science*, 307(5711):901–904, February 2005. Referenced on pages 18, 124, 125, 126, 127, 176, and 197.

[88] A. Kanigel, M. R. Norman, M. Randeria, U. Chatterjee, S. Souma, A. Kaminski, H. M. Fretwell, S. Rosenkranz, M. Shi, T. Sato, T. Takahashi, Z. Z. Li, H. Raffy, K. Kadowaki,

D. Hinks, L. Ozyuzer, and J. C. Campuzano. Evolution of the pseudogap from Fermi arcs to the nodal liquid. *Nature Physics*, 2(7):447–451, 2006. Referenced on pages 18 and 124.

[89] H.-B. Yang, J. D. Rameau, Z.-H. Pan, G. D. Gu, P. D. Johnson, H. Claus, D. G. Hinks, and T. E. Kidd. Reconstructed Fermi Surface of Underdoped $Bi_2Sr_2CaCu_2O_{8+\delta}$ Cuprate Superconductors. *Phys. Rev. Lett.*, 107:047003, Jul 2011. Referenced on pages 18 and 124.

[90] Kifu Kurokawa, Shunsuke Isono, Yoshimitsu Kohama, So Kunisada, Shiro Sakai, Ryotaro Sekine, Makoto Okubo, Matthew D. Watson, Timur K. Kim, Cephise Cacho, Shik Shin, Takami Tohyama, Kazuyasu Tokiwa, and Takeshi Kondo. Unveiling phase diagram of the lightly doped high-Tc cuprate superconductors with disorder removed. *Nature Communications*, 14(1):4064, 2023. Referenced on pages 18, 124, and 155.

[91] Nicolas Doiron-Leyraud, Cyril Proust, David LeBoeuf, Julien Levallois, Jean-Baptiste Bonnemaison, Ruixing Liang, D. A. Bonn, W. N. Hardy, and Louis Taillefer. Quantum oscillations and the Fermi surface in an underdoped high-Tc superconductor. *Nature*, 447(7144):565–568, 2007. Referenced on pages 18, 126, and 127.

[92] B. Vignolle, A. Carrington, R. A. Cooper, M. M. J. French, A. P. Mackenzie, C. Jaudet, D. Vignolles, Cyril Proust, and N. E. Hussey. Quantum oscillations in an overdoped high-Tc superconductor. *Nature*, 455(7215):952–955, 2008. Referenced on pages 18 and 126.

[93] E. A. Yelland, J. Singleton, C. H. Mielke, N. Harrison, F. F. Balakirev, B. Dabrowski, and J. R. Cooper. Quantum Oscillations in the Underdoped Cuprate $YBa_2Cu_4O_8$. *Phys. Rev. Lett.*, 100:047003, Feb 2008. Referenced on pages 18 and 126.

[94] B. J. Ramshaw, Baptiste Vignolle, James Day, Ruixing Liang, W. N. Hardy, Cyril Proust, and D. A. Bonn. Angle dependence of quantum oscillations in YBa2Cu3O6.59 shows free-spin behaviour of quasiparticles. *Nature Physics*, 7(3):234–238, 2011. Referenced on pages 18 and 126.

[95] Yoichi Ando, Y. Kurita, Seiki Komiya, S. Ono, and Kouji Segawa. Evolution of the Hall Coefficient and the Peculiar Electronic Structure of the Cuprate Superconductors. *Phys. Rev. Lett.*, 92:197001, May 2004. Referenced on pages 18 and 127.

[96] S. Badoux, W. Tabis, F. Laliberté, G. Grissonnanche, B. Vignolle, D. Vignolles, J. Béard, D. A. Bonn, W. N. Hardy, R. Liang, N. Doiron-Leyraud, Louis Taillefer, and Cyril Proust. Change of carrier density at the pseudogap critical point of a cuprate superconductor. *Nature*, 531(7593):210–214, 2016. Referenced on pages 18, 127, and 150.

[97] C. Collignon, S. Badoux, S. A. A. Afshar, B. Michon, F. Laliberté, O. Cyr-Choinière, J.-S. Zhou, S. Licciardello, S. Wiedmann, N. Doiron-Leyraud, and Louis Taillefer. Fermi-surface transformation across the pseudogap critical point of the cuprate superconductor $La_{1.6-x}Nd_{0.4}Sr_xCuO_4$. *Phys. Rev. B*, 95:224517, Jun 2017. Referenced on pages 18 and 127.

[98] Seyed Iman Mirzaei, Damien Stricker, Jason N. Hancock, Christophe Berthod, Antoine Georges, Erik van Heumen, Mun K. Chan, Xudong Zhao, Yuan Li, Martin Greven, Neven Barišić, and Dirk van der Marel. Spectroscopic evidence for Fermi liquid-like energy and temperature dependence of the relaxation rate in the pseudogap phase of the cuprates. *Proceedings of the National Academy of Sciences*, 110(15):5774–5778, 2013. Referenced on pages 18 and 128.

[99] M. K. Chan, M. J. Veit, C. J. Dorow, Y. Ge, Y. Li, W. Tabis, Y. Tang, X. Zhao, N. Barišić, and M. Greven. In-Plane Magnetoresistance Obeys Kohler's Rule in the Pseudogap Phase of Cuprate Superconductors. *Phys. Rev. Lett.*, 113:177005, Oct 2014. Referenced on pages 18 and 128.

[100] J. M. Luttinger. Fermi Surface and Some Simple Equilibrium Properties of a System of Interacting Fermions. *Phys. Rev.*, 119:1153–1163, Aug 1960. Referenced on pages 19 and 120.

[101] Debanjan Chowdhury and Subir Sachdev. *The Enigma of the Pseudogap Phase of the Cuprate Superconductors*, pages 1–43. World Scientific, 2015. Referenced on pages 19, 20, 123, 129, 130, 132, 133, 140, 142, 143, 151, 154, and 174.

[102] Guangyong Xu, G. D. Gu, M. Hücker, B. Fauqué, T. G. Perring, L. P. Regnault, and J. M. Tranquada. Testing the itinerancy of spin dynamics in superconducting Bi2Sr2CaCu2O8+δ. *Nature Physics*, 5(9):642–646, 2009. Referenced on page 19.

[103] M. Le Tacon, G. Ghiringhelli, J. Chaloupka, M. Moretti Sala, V. Hinkov, M. W. Haverkort, M. Minola, M. Bakr, K. J. Zhou, S. Blanco-Canosa, C. Monney, Y. T. Song, G. L. Sun, C. T. Lin, G. M. De Luca, M. Salluzzo, G. Khaliullin, T. Schmitt, L. Braicovich, and B. Keimer. Intense paramagnon excitations in a large family of high-temperature superconductors. *Nature Physics*, 7(9):725–730, 2011. Referenced on pages 19, 124, and 155.

[104] M. P. M. Dean, G. Dellea, R. S. Springell, F. Yakhou-Harris, K. Kummer, N. B. Brookes, X. Liu, Y-J. Sun, J. Strle, T. Schmitt, L. Braicovich, G. Ghiringhelli, I. Božović, and J. P. Hill. Persistence of magnetic excitations in La2−xSrxCuO4 from the undoped insulator to the heavily overdoped non-superconducting metal. *Nature Materials*, 12(11):1019–1023, 2013. Referenced on pages 19, 124, and 155.

[105] M. Guarise, B. Dalla Piazza, H. Berger, E. Giannini, T. Schmitt, H. M. Rønnow, G. A. Sawatzky, J. van den Brink, D. Altenfeld, I. Eremin, and M. Grioni. Anisotropic softening of magnetic excitations along the nodal direction in superconducting cuprates. *Nature Communications*, 5(1):5760, 2014. Referenced on pages 19, 124, and 155.

[106] Matthias Vojta. Stripes and electronic quasiparticles in the pseudogap state of cuprate superconductors. *Physica C: Superconductivity*, 481:178–188, 2012. Referenced on pages 19, 132, and 155.

[107] Mehdi Frachet, Igor Vinograd, Rui Zhou, Siham Benhabib, Shangfei Wu, Hadrien Mayaffre, Steffen Krämer, Sanath K. Ramakrishna, Arneil P. Reyes, Jérôme Debray, Tohru Kuro-

sawa, Naoki Momono, Migaku Oda, Seiki Komiya, Shimpei Ono, Masafumi Horio, Johan Chang, Cyril Proust, David LeBoeuf, and Marc-Henri Julien. Hidden magnetism at the pseudogap critical point of a cuprate superconductor. *Nature Physics*, 16(10):1064–1068, 2020. Referenced on pages 19 and 66.

[108] I. Vinograd, R. Zhou, H. Mayaffre, S. Krämer, S. K. Ramakrishna, A. P. Reyes, T. Kurosawa, N. Momono, M. Oda, S. Komiya, S. Ono, M. Horio, J. Chang, and M.-H. Julien. Competition between spin ordering and superconductivity near the pseudogap boundary in $La_{2-x}Sr_xCuO_4$: Insights from NMR. *Phys. Rev. B*, 106:054522, Aug 2022. Referenced on pages 19 and 66.

[109] A. Missiaen, H. Mayaffre, S. Krämer, D. Zhao, Y. B. Zhou, T. Wu, X. H. Chen, S. Pyon, T. Takayama, H. Takagi, D. LeBoeuf, and M. H. Julien. Spin-stripe order tied to the pseudogap phase in La1.8-xEu0.2SrxCuO4, 2024. Referenced on pages 19, 66, and 143.

[110] Andrew J. Millis and M. R. Norman. Antiphase stripe order as the origin of electron pockets observed in 1/8-hole-doped cuprates. *Phys. Rev. B*, 76:220503, Dec 2007. Referenced on page 19.

[111] Ivailo Dimov, Pallab Goswami, Xun Jia, and Sudip Chakravarty. Competing order, Fermi surface reconstruction, and quantum oscillations in underdoped high-temperature superconductors. *Phys. Rev. B*, 78:134529, Oct 2008. Referenced on page 19.

[112] M. R. Norman, Jie Lin, and A. J. Millis. Lifshitz transition in underdoped cuprates. *Phys. Rev. B*, 81:180513, May 2010. Referenced on page 19.

[113] Hong Yao, Dung-Hai Lee, and Steven Kivelson. Fermi-surface reconstruction in a smectic phase of a high-temperature superconductor. *Phys. Rev. B*, 84:012507, Jul 2011. Referenced on page 19.

[114] Matthias Punk, Andrea Allais, and Subir Sachdev. Quantum dimer model for the pseudogap metal. *Proceedings of the National Academy of Sciences*, 112(31), 2015. Referenced on pages 19, 20, 132, 133, 139, 140, 142, and 154.

[115] Yayu Wang, Lu Li, and N. P. Ong. Nernst effect in high-T_c superconductors. *Phys. Rev. B*, 73:024510, Jan 2006. Referenced on pages 19 and 133.

[116] H. B. Yang, J. D. Rameau, P. D. Johnson, T. Valla, A. Tsvelik, and G. D. Gu. Emergence of preformed Cooper pairs from the doped Mott insulating state in Bi2Sr2CaCu2O8+δ. *Nature*, 456(7218):77–80, 2008. Referenced on pages 19 and 133.

[117] A. Kanigel, U. Chatterjee, M. Randeria, M. R. Norman, G. Koren, K. Kadowaki, and J. C. Campuzano. Evidence for Pairing above the Transition Temperature of Cuprate Superconductors from the Electronic Dispersion in the Pseudogap Phase. *Phys. Rev. Lett.*, 101:137002, Sep 2008. Referenced on pages 19 and 133.

[118] Jiasen Niu, Maialen Ortego Larrazabal, Thomas Gozlinski, Yudai Sato, Koen M Bastiaans, Tjerk Benschop, Jian-Feng Ge, Yaroslav M Blanter, Genda Gu, Ingmar Swart, et al. Equivalence of pseudogap and pairing energy in a cuprate high-temperature superconductor. *arXiv:2409.15928*, 2024. Referenced on pages 19 and 133.

[119] I. Battisti, K. M. Bastiaans, V. Fedoseev, A. de la Torre, N. Iliopoulos, A. Tamai, E. C. Hunter, R. S. Perry, J. Zaanen, F. Baumberger, and M. P. Allan. Universality of pseudogap and emergent order in lightly doped Mott insulators. *Nature Physics*, 13(1):21–25, 2017. Referenced on pages 19 and 133.

[120] Yu-Te Hsu, Andreas Rydh, Maarten Berben, Caitlin Duffy, Alberto de la Torre, Robin S. Perry, and Nigel E. Hussey. Carrier density crossover and quasiparticle mass enhancement in a doped 5d Mott insulator. *Nature Physics*, 2024. Referenced on pages 19 and 133.

[121] Debanjan Chowdhury and Subir Sachdev. Density-wave instabilities of fractionalized Fermi liquids. *Phys. Rev. B*, 90:245136, Dec 2014. Referenced on pages 20, 133, and 151.

[122] T. Senthil, Subir Sachdev, and Matthias Vojta. Fractionalized Fermi Liquids. *Phys. Rev. Lett.*, 90:216403, May 2003. Referenced on pages 20, 133, 139, 151, and 154.

[123] N. Read and Subir Sachdev. Large-N expansion for frustrated quantum antiferromagnets. *Phys. Rev. Lett.*, 66:1773–1776, Apr 1991. Referenced on pages 20, 133, and 150.

[124] X. G. Wen. Mean-field theory of spin-liquid states with finite energy gap and topological orders. *Phys. Rev. B*, 44:2664–2672, Aug 1991. Referenced on pages 20 and 133.

[125] Ribhu K. Kaul, Alexei Kolezhuk, Michael Levin, Subir Sachdev, and T. Senthil. Hole dynamics in an antiferromagnet across a deconfined quantum critical point. *Phys. Rev. B*, 75:235122, Jun 2007. Referenced on pages 20 and 133.

[126] Yang Qi and Subir Sachdev. Effective theory of Fermi pockets in fluctuating antiferromagnets. *Phys. Rev. B*, 81:115129, Mar 2010. Referenced on pages 20, 133, and 142.

[127] Eun Gook Moon and Subir Sachdev. Underdoped cuprates as fractionalized Fermi liquids: Transition to superconductivity. *Phys. Rev. B*, 83:224508, Jun 2011. Referenced on pages 20, 133, and 142.

[128] Jia-Wei Mei, Shinji Kawasaki, Guo-Qing Zheng, Zheng-Yu Weng, and Xiao-Gang Wen. Luttinger-volume violating Fermi liquid in the pseudogap phase of the cuprate superconductors. *Phys. Rev. B*, 85:134519, Apr 2012. Referenced on pages 20 and 133.

[129] Matthias Punk and Subir Sachdev. Fermi surface reconstruction in hole-doped $t-J$ models without long-range antiferromagnetic order. *Phys. Rev. B*, 85:195123, May 2012. Referenced on pages 20 and 133.

[130] Subir Sachdev and Debanjan Chowdhury. The novel metallic states of the cuprates: Topological Fermi liquids and strange metals. *Progress of Theoretical and Experimental Physics*, 2016(12):12C102, 2016. Referenced on pages 20, 120, 133, 138, and 142.

[131] Gabriel Kotliar and Jialin Liu. Superexchange mechanism and d-wave superconductivity. *Phys. Rev. B*, 38:5142–5145, Sep 1988. Referenced on pages 20, 106, and 133.

[132] C. Castellani, C. Di Castro, and M. Grilli. Singular Quasiparticle Scattering in the Proximity of Charge Instabilities. *Phys. Rev. Lett.*, 75:4650–4653, Dec 1995. Referenced on pages 20 and 132.

[133] S. A. Kivelson, E. Fradkin, and V. J. Emery. Electronic liquid-crystal phases of a doped Mott insulator. *Nature*, 393(6685):550–553, 1998. Referenced on pages 20 and 132.

[134] J. Hubbard and Brian Hilton Flowers. Electron correlations in narrow energy bands. *Proceedings of the Royal Society of London. Series A. Mathematical and Physical Sciences*, 276(1365):238–257, 1963. Referenced on page 21.

[135] P. W. Anderson. The Resonating Valence Bond State in La2CuO4 and Superconductivity. *Science*, 235(4793):1196–1198, 1987. Referenced on pages 21, 106, and 153.

[136] Kazushige Machida. Magnetism in La2CuO4 based compounds. *Physica C: Superconductivity*, 158(1):192–196, 1989. Referenced on page 21.

[137] Masaru Kato, Kazushige Machida, Hiizu Nakanishi, and Mitsutaka Fujita. Soliton Lattice Modulation of Incommensurate Spin Density Wave in Two Dimensional Hubbard Model -A Mean Field Study. *Journal of the Physical Society of Japan*, 59(3):1047–1058, 1990. Referenced on page 21.

[138] Jan Zaanen and Olle Gunnarsson. Charged magnetic domain lines and the magnetism of high-T_c oxides. *Phys. Rev. B*, 40:7391–7394, Oct 1989. Referenced on pages 21, 143, and 144.

[139] Antoine Georges, Gabriel Kotliar, Werner Krauth, and Marcelo J. Rozenberg. Dynamical mean-field theory of strongly correlated fermion systems and the limit of infinite dimensions. *Rev. Mod. Phys.*, 68:13–125, Jan 1996. Referenced on pages 21 and 143.

[140] Steven R. White and D. J. Scalapino. Density Matrix Renormalization Group Study of the Striped Phase in the 2D $t - J$ Model. *Phys. Rev. Lett.*, 80:1272–1275, Feb 1998. Referenced on pages 21 and 143.

[141] Steven R. White and D. J. Scalapino. Stripes on a 6-Leg Hubbard Ladder. *Phys. Rev. Lett.*, 91:136403, Sep 2003. Referenced on pages 21 and 143.

[142] Edwin W. Huang, Christian B. Mendl, Hong-Chen Jiang, Brian Moritz, and Thomas P. Devereaux. Stripe order from the perspective of the Hubbard model. *npj Quantum Materials*, 3(1):22, 2018. Referenced on pages 21 and 143.

[143] Yi-Fan Jiang, Jan Zaanen, Thomas P. Devereaux, and Hong-Chen Jiang. Ground state phase diagram of the doped Hubbard model on the four-leg cylinder. *Phys. Rev. Research*, 2:033073, Jul 2020. Referenced on pages 21 and 143.

[144] Bo-Xiao Zheng, Chia-Min Chung, Philippe Corboz, Georg Ehlers, Ming-Pu Qin, Reinhard M. Noack, Hao Shi, Steven R. White, Shiwei Zhang, and Garnet Kin-Lic Chan. Stripe order in the underdoped region of the two-dimensional Hubbard model. *Science*, 358(6367):1155–1160, 2017. Referenced on pages 21, 76, 143, and 174.

[145] Mingpu Qin, Chia-Min Chung, Hao Shi, Ettore Vitali, Claudius Hubig, Ulrich Schollwöck, Steven R. White, and Shiwei Zhang. Absence of Superconductivity in the Pure Two-Dimensional Hubbard Model. *Phys. Rev. X*, 10:031016, Jul 2020. Referenced on pages 21, 66, 143, 172, 174, and 191.

[146] Steven R. White and D. J. Scalapino. Competition between stripes and pairing in a $t - t' - J$ model. *Phys. Rev. B*, 60:R753–R756, Jul 1999. Referenced on pages 21 and 174.

[147] Hao Xu, Chia-Min Chung, Mingpu Qin, Ulrich Schollwöck, Steven R. White, and Shiwei Zhang. Coexistence of superconductivity with partially filled stripes in the Hubbard model. *Science*, 384(6696):eadh7691, 2024. Referenced on pages 21, 143, 151, 174, 179, and 191.

[148] R. Preuss, W. Hanke, C. Gröber, and H. G. Evertz. Pseudogaps and Their Interplay with Magnetic Excitations in the Doped 2D Hubbard Model. *Phys. Rev. Lett.*, 79:1122–1125, Aug 1997. Referenced on pages 21 and 143.

[149] Alexandru Macridin, M. Jarrell, Thomas Maier, P. R. C. Kent, and Eduardo D'Azevedo. Pseudogap and Antiferromagnetic Correlations in the Hubbard Model. *Phys. Rev. Lett.*, 97:036401, Jul 2006. Referenced on pages 21 and 143.

[150] B. Kyung, S. S. Kancharla, D. Sénéchal, A.-M. S. Tremblay, M. Civelli, and G. Kotliar. Pseudogap induced by short-range spin correlations in a doped Mott insulator. *Phys. Rev. B*, 73:165114, Apr 2006. Referenced on pages 21 and 143.

[151] Michel Ferrero, Pablo S. Cornaglia, Lorenzo De Leo, Olivier Parcollet, Gabriel Kotliar, and Antoine Georges. Pseudogap opening and formation of Fermi arcs as an orbital-selective Mott transition in momentum space. *Phys. Rev. B*, 80:064501, Aug 2009. Referenced on pages 21 and 143.

[152] G. Sordi, P. Sémon, K. Haule, and A.-M. S. Tremblay. Strong Coupling Superconductivity, Pseudogap, and Mott Transition. *Phys. Rev. Lett.*, 108:216401, May 2012. Referenced on pages 21 and 143.

[153] Wei Wu, Mathias S. Scheurer, Shubhayu Chatterjee, Subir Sachdev, Antoine Georges, and Michel Ferrero. Pseudogap and Fermi-Surface Topology in the Two-Dimensional Hubbard Model. *Phys. Rev. X*, 8:021048, May 2018. Referenced on pages 21 and 143.

[154] Fedor Šimkovic, Riccardo Rossi, Antoine Georges, and Michel Ferrero. Origin and fate of the pseudogap in the doped Hubbard model. *Science*, 385(6715), 2024. Referenced on pages 21, 66, and 143.

[155] Ian Osborne, Thereza Paiva, and Nandini Trivedi. Fermi-surface Reconstruction in the Repulsive Fermi-Hubbard Model, 2020. Referenced on pages 21 and 143.

[156] Hao Xu, Hao Shi, Ettore Vitali, Mingpu Qin, and Shiwei Zhang. Stripes and spin-density waves in the doped two-dimensional Hubbard model: Ground state phase diagram. *Phys. Rev. Res.*, 4:013239, Mar 2022. Referenced on pages 21 and 66.

[157] Alexander Altland and Ben D. Simons. *Condensed Matter Field Theory*. Cambridge University Press, 2 edition, 2010. Referenced on pages 23 and 43.

[158] Eduardo Ibarra-García-Padilla, Chunhan Feng, Giulio Pasqualetti, Simon Fölling, Richard T. Scalettar, Ehsan Khatami, and Kaden R. A. Hazzard. Metal-insulator transition and magnetism of SU(3) fermions in the square lattice, 2023. Referenced on pages 23, 226, and 303.

[159] Tamás A. Tóth, Andreas M. Läuchli, Frédéric Mila, and Karlo Penc. Three-Sublattice Ordering of the SU(3) Heisenberg Model of Three-Flavor Fermions on the Square and Cubic Lattices. *Phys. Rev. Lett.*, 105:265301, Dec 2010. Referenced on pages 24, 25, and 226.

[160] Philippe Corboz, Andreas M. Läuchli, Karlo Penc, Matthias Troyer, and Frédéric Mila. Simultaneous Dimerization and SU(4) Symmetry Breaking of 4-Color Fermions on the Square Lattice. *Phys. Rev. Lett.*, 107:215301, Nov 2011. Referenced on pages 24, 25, and 226.

[161] Pierre Nataf and Frédéric Mila. Exact Diagonalization of Heisenberg SU(N) Models. *Phys. Rev. Lett.*, 113:127204, Sep 2014. Referenced on pages 24, 25, and 226.

[162] Chunhan Feng, Eduardo Ibarra-García-Padilla, Kaden R. A. Hazzard, Richard Scalettar, Shiwei Zhang, and Ettore Vitali. Metal-insulator transition and quantum magnetism in the SU(3) Fermi-Hubbard model. *Phys. Rev. Res.*, 5:043267, Dec 2023. Referenced on pages 24, 226, and 238.

[163] Salvatore R. Manmana, Kaden R. A. Hazzard, Gang Chen, Adrian E. Feiguin, and Ana Maria Rey. SU(N) magnetism in chains of ultracold alkaline-earth-metal atoms: Mott transitions and quantum correlations. *Phys. Rev. A*, 84:043601, Oct 2011. Referenced on pages 24 and 226.

[164] Pierre Nataf, Miklós Lajkó, Philippe Corboz, Andreas M. Läuchli, Karlo Penc, and Frédéric Mila. Plaquette order in the SU(6) Heisenberg model on the honeycomb lattice. *Phys. Rev. B*, 93:201113, May 2016. Referenced on pages 24 and 226.

[165] Christian Romen and Andreas M. Läuchli. Structure of spin correlations in high-temperature SU(N) quantum magnets. *Phys. Rev. Res.*, 2:043009, Oct 2020. Referenced on pages 24 and 226.

[166] Yanan Zhang, Dajun Su, Yanen Huang, Zhaoyang Shan, Hualei Sun, Mengwu Huo, Kaixin Ye, Jiawen Zhang, Zihan Yang, Yongkang Xu, Yi Su, Rui Li, Michael Smidman, Meng Wang, Lin Jiao, and Huiqiu Yuan. High-temperature superconductivity with zero resistance and

strange-metal behaviour in La3Ni2O7. *Nature Physics*, 2024. Referenced on pages 27, 157, and 171.

[167] Danfeng Li, Kyuho Lee, Bai Yang Wang, Motoki Osada, Samuel Crossley, Hye Ryoung Lee, Yi Cui, Yasuyuki Hikita, and Harold Y. Hwang. Superconductivity in an infinite-layer nickelate. *Nature*, 572(7771):624–627, 2019. Referenced on page 26.

[168] Grace A. Pan, Dan Ferenc Segedin, Harrison LaBollita, Qi Song, Emilian M. Nica, Berit H. Goodge, Andrew T. Pierce, Spencer Doyle, Steve Novakov, Denisse Córdova Carrizales, Alpha T. N'Diaye, Padraic Shafer, Hanjong Paik, John T. Heron, Jarad A. Mason, Amir Yacoby, Lena F. Kourkoutis, Onur Erten, Charles M. Brooks, Antia S. Botana, and Julia A. Mundy. Superconductivity in a quintuple-layer square-planar nickelate. *Nature Materials*, 21(2):160–164, 2022. Referenced on page 26.

[169] Chen Lu, Zhiming Pan, Fan Yang, and Congjun Wu. Interlayer-Coupling-Driven High-Temperature Superconductivity in $La_3Ni_2O_7$ under Pressure. *Phys. Rev. Lett.*, 132:146002, Apr 2024. Referenced on page 29.

[170] Xing-Zhou Qu, Dai-Wei Qu, Jialin Chen, Congjun Wu, Fan Yang, Wei Li, and Gang Su. Bilayer $t - J - J_\perp$ Model and Magnetically Mediated Pairing in the Pressurized Nickelate $La_3Ni_2O_7$. *Phys. Rev. Lett.*, 132:036502, Jan 2024. Referenced on pages 29, 161, and 162.

[171] Hanbit Oh and Ya-Hui Zhang. Type-II $t - J$ model and shared superexchange coupling from Hund's rule in superconducting $La_3Ni_2O_7$. *Phys. Rev. B*, 108:174511, Nov 2023. Referenced on pages 29, 163, 169, and 170.

[172] W. Kohn. Nobel Lecture: Electronic structure of matter—wave functions and density functionals. *Rev. Mod. Phys.*, 71:1253–1266, Oct 1999. Referenced on page 31.

[173] M B Hastings. An area law for one-dimensional quantum systems. *Journal of Statistical Mechanics: Theory and Experiment*, 2007(08):P08024, aug 2007. Referenced on page 31.

[174] J. Ignacio Cirac, David Pérez-García, Norbert Schuch, and Frank Verstraete. Matrix product states and projected entangled pair states: Concepts, symmetries, theorems. *Rev. Mod. Phys.*, 93:045003, Dec 2021. Referenced on page 32.

[175] G. Vidal. Class of Quantum Many-Body States That Can Be Efficiently Simulated. *Phys. Rev. Lett.*, 101:110501, Sep 2008. Referenced on page 32.

[176] Román Orús. Tensor networks for complex quantum systems. *Nature Reviews Physics*, 1(9):538–550, 2019. Referenced on page 32.

[177] Sebastian Paeckel, Thomas Köhler, Andreas Swoboda, Salvatore R. Manmana, Ulrich Schollwöck, and Claudius Hubig. Time-evolution methods for matrix-product states. *Annals of Physics*, 411:167998, 2019. Referenced on pages 32, 39, 40, 41, and 42.

[178] Claudius Hubig, Felix Lachenmaier, Nils-Oliver Linden, Teresa Reinhard, Leo Stenzel, Andreas Swoboda, Martin Grundner, and Sam Mardazad. The SyTen Toolkit. Referenced on page 32.

[179] Claudius Hubig. Symmetry-Protected Tensor Networks, 2017. Referenced on pages 32 and 39.

[180] J. Sakurai and Jim Napolitano. *Modern Quantum Mechanics : Pearson New International Edition*. Pearson Deutschland, 08 2013. Referenced on page 37.

[181] Gene H. Golub and Charles F. Van Loan. *Matrix Computations - 4th Edition*. Johns Hopkins University Press, Philadelphia, PA, 2013. Referenced on page 37.

[182] C. Hubig, I. P. McCulloch, U. Schollwöck, and F. A. Wolf. Strictly single-site DMRG algorithm with subspace expansion. *Phys. Rev. B*, 91:155115, Apr 2015. Referenced on page 37.

[183] Sukhwinder Singh, Robert N. C. Pfeifer, and Guifre Vidal. Tensor network states and algorithms in the presence of a global U(1) symmetry. *Phys. Rev. B*, 83:115125, Mar 2011. Referenced on page 39.

[184] Cornelius Lanczos. An iteration method for the solution of the eigenvalue problem of linear differential and integral operators. 1950. Referenced on page 41.

[185] Mingru Yang and Steven R. White. Time-dependent variational principle with ancillary Krylov subspace. *Phys. Rev. B*, 102:094315, Sep 2020. Referenced on pages 42 and 238.

[186] Steven R. White. Minimally Entangled Typical Quantum States at Finite Temperature. *Phys. Rev. Lett.*, 102:190601, May 2009. Referenced on page 42.

[187] A. Nocera and G. Alvarez. Symmetry-conserving purification of quantum states within the density matrix renormalization group. *Phys. Rev. B*, 93:045137, Jan 2016. Referenced on pages 42 and 73.

[188] Y.M. Vilk and A.-M.S. Tremblay. Non-Perturbative Many-Body Approach to the Hubbard Model and Single-Particle Pseudogap. *J. Phys. I France*, 7(11):1309–1368, 1997. Referenced on pages 43, 45, 242, and 299.

[189] Y.M. Vilk and A.-M.S. Tremblay. Non-Perturbative Many-Body Approach to the Hubbard Model and Single-Particle Pseudogap. *J. Phys. I France*, 7(11):1309–1368, 1997. Referenced on pages 43, 45, 241, 242, 248, and 251.

[190] André-Marie S. Tremblay. *Two-Particle-Self-Consistent Approach for the Hubbard Model*, pages 409–453. Springer Berlin Heidelberg, Berlin, Heidelberg, 2012. Referenced on page 45.

[191] Thomas Schäfer, Nils Wentzell, Fedor Simkovic, Yuan-Yao He, Cornelia Hille, Marcel Klett, Christian J. Eckhardt, Behnam Arzhang, Viktor Harkov, Francois-Marie Le Régent, Alfred Kirsch, Yan Wang, Aaram J. Kim, Evgeny Kozik, Evgeny A. Stepanov, Anna Kauch, Sabine

Andergassen, Philipp Hansmann, Daniel Rohe, Yuri M. Vilk, James P. F. LeBlanc, Shiwei Zhang, A.-M. S. Tremblay, Michel Ferrero, Olivier Parcollet, and Antoine Georges. Tracking the Footprints of Spin Fluctuations: A MultiMethod, MultiMessenger Study of the Two-Dimensional Hubbard Model. *Phys. Rev. X*, 11:011058, Mar 2021. Referenced on pages 45, 200, and 242.

[192] Rudolf Grimm, Matthias Weidemüller, and Yurii B. Ovchinnikov. *Optical Dipole Traps for Neutral Atoms*, volume 42, pages 95–170. Academic Press, 2000. Referenced on page 48.

[193] Immanuel Bloch. Ultracold quantum gases in optical lattices. *Nature Physics*, 1(1):23–30, 2005. Referenced on page 48.

[194] Christian Gross and Immanuel Bloch. Quantum simulations with ultracold atoms in optical lattices. *Science*, 357(6355):995–1001, 2017. Referenced on page 48.

[195] Timon Hilker. Spin-resolved microscopy of strongly correlated fermionic many-body states, November 2017. Referenced on page 48.

[196] Andrew John Daley. *Manipulation and simulation of cold atoms in optical lattices*. 2005. Referenced on pages 48 and 49.

[197] Joannis Koepsell. *Quantum simulation of doped two-dimensional Mott insulators*. PhD thesis, Ludwig Maximilians Universität München, 2021. Referenced on pages 48, 52, and 81.

[198] Maxwell F. Parsons, Florian Huber, Anton Mazurenko, Christie S. Chiu, Widagdo Setiawan, Katherine Wooley-Brown, Sebastian Blatt, and Markus Greiner. Site-Resolved Imaging of Fermionic ^{6}Li in an Optical Lattice. *Phys. Rev. Lett.*, 114:213002, May 2015. Referenced on pages 51 and 55.

[199] D. González-Cuadra, D. Bluvstein, M. Kalinowski, R. Kaubruegger, N. Maskara, P. Naldesi, T. V. Zache, A. M. Kaufman, M. D. Lukin, H. Pichler, B. Vermersch, Jun Ye, and P. Zoller. Fermionic quantum processing with programmable neutral atom arrays. *Proceedings of the National Academy of Sciences*, 120(35):e2304294120, 2023. Referenced on pages 52 and 298.

[200] Alexander Schuckert, Eleanor Crane, Alexey V. Gorshkov, Mohammad Hafezi, and Michael J. Gullans. Fermion-qubit fault-tolerant quantum computing, 2024. Referenced on pages 52 and 298.

[201] Robert Ott, Daniel González-Cuadra, Torsten V. Zache, Peter Zoller, Adam M. Kaufman, and Hannes Pichler. Error-corrected fermionic quantum processors with neutral atoms, 2024. Referenced on pages 52 and 298.

[202] R Onofrio. Physics of our Days: Cooling and thermometry of atomic Fermi gases. *Physics-Uspekhi*, 59(11):1129, nov 2016. Referenced on page 54.

[203] Paul Hamilton, Geena Kim, Trinity Joshi, Biswaroop Mukherjee, Daniel Tiarks, and Holger Müller. Sisyphus cooling of lithium. *Phys. Rev. A*, 89:023409, Feb 2014. Referenced on page 54.

[204] C. Monroe, D. M. Meekhof, B. E. King, S. R. Jefferts, W. M. Itano, D. J. Wineland, and P. Gould. Resolved-Sideband Raman Cooling of a Bound Atom to the 3D Zero-Point Energy. *Phys. Rev. Lett.*, 75:4011–4014, Nov 1995. Referenced on page 55.

[205] S. E. Hamann, D. L. Haycock, G. Klose, P. H. Pax, I. H. Deutsch, and P. S. Jessen. Resolved-Sideband Raman Cooling to the Ground State of an Optical Lattice. *Phys. Rev. Lett.*, 80:4149–4152, May 1998. Referenced on page 55.

[206] A. M. Kaufman, B. J. Lester, and C. A. Regal. Cooling a Single Atom in an Optical Tweezer to Its Quantum Ground State. *Phys. Rev. X*, 2:041014, Nov 2012. Referenced on page 55.

[207] Eduardo Ibarra-García-Padilla and Sayan Choudhury. Many-body physics of ultracold alkaline-earth atoms with SU(N)-symmetric interactions. *Journal of Physics: Condensed Matter*, 37(8):083003, 2025. Referenced on page 57.

[208] A. V. Gorshkov, M. Hermele, V. Gurarie, C. Xu, P. S. Julienne, J. Ye, P. Zoller, E. Demler, M. D. Lukin, and A. M. Rey. Two-orbital S U(N) magnetism with ultracold alkaline-earth atoms. *Nature Physics*, 6(4):289–295, 2010. Referenced on pages 57 and 226.

[209] Michael E Gehm. Properties of 6Li. *Jetlab,*, 2003. Referenced on page 57.

[210] Andrew D. Ludlow, Martin M. Boyd, Jun Ye, E. Peik, and P. O. Schmidt. Optical atomic clocks. *Rev. Mod. Phys.*, 87:637–701, Jun 2015. Referenced on page 57.

[211] Andrew J. Daley, Martin M. Boyd, Jun Ye, and Peter Zoller. Quantum Computing with Alkaline-Earth-Metal Atoms. *Phys. Rev. Lett.*, 101:170504, Oct 2008. Referenced on page 57.

[212] Shintaro Taie, Yosuke Takasu, Seiji Sugawa, Rekishu Yamazaki, Takuya Tsujimoto, Ryo Murakami, and Yoshiro Takahashi. Realization of a $SU(2) \times SU(6)$ System of Fermions in a Cold Atomic Gas. *Phys. Rev. Lett.*, 105:190401, Nov 2010. Referenced on pages 57 and 58.

[213] Shintaro Taie, Rekishu Yamazaki, Seiji Sugawa, and Yoshiro Takahashi. An SU(6) Mott insulator of an atomic Fermi gas realized by large-spin Pomeranchuk cooling. *Nature Physics*, 8(11):825–830, 2012. Referenced on pages 57 and 226.

[214] D. Tusi, L. Franchi, L. F. Livi, K. Baumann, D. Benedicto Orenes, L. Del Re, R. E. Barfknecht, T. W. Zhou, M. Inguscio, G. Cappellini, M. Capone, J. Catani, and L. Fallani. Flavour-selective localization in interacting lattice fermions. *Nature Physics*, 18(10):1201–1205, 2022. Referenced on pages 57 and 226.

[215] Sandra Buob, Jonatan Höschele, Vasiliy Makhalov, Antonio Rubio-Abadal, and Leticia Tarruell. A Strontium Quantum-Gas Microscope. *PRX Quantum*, 5:020316, Apr 2024. Referenced on page 58.

[216] Ryuta Yamamoto, Jun Kobayashi, Takuma Kuno, Kohei Kato, and Yoshiro Takahashi. An ytterbium quantum gas microscope with narrow-line laser cooling. *New Journal of Physics*, 18(2):023016, 2016. Referenced on page 58.

[217] Bijit Mukherjee, Jeremy M Hutson, and Kaden R A Hazzard. SU(N) magnetism with ultracold molecules. *New Journal of Physics*, 27(1):013013, 2025. Referenced on page 58.

[218] Kin Fai Mak and Jie Shan. Semiconductor moirématerials. *Nature Nanotechnology*, 17(7):686–695, 2022. Referenced on pages 59 and 60.

[219] Fengcheng Wu, Timothy Lovorn, Emanuel Tutuc, and A. H. MacDonald. Hubbard Model Physics in Transition Metal Dichalcogenide Moiré Bands. *Phys. Rev. Lett.*, 121:026402, Jul 2018. Referenced on page 60.

[220] C. R. Dean, L. Wang, P. Maher, C. Forsythe, F. Ghahari, Y. Gao, J. Katoch, M. Ishigami, P. Moon, M. Koshino, T. Taniguchi, K. Watanabe, K. L. Shepard, J. Hone, and P. Kim. Hofstadter's butterfly and the fractal quantum Hall effect in moirésuperlattices. *Nature*, 497(7451):598–602, 2013. Referenced on page 60.

[221] Yuan Cao, Valla Fatemi, Ahmet Demir, Shiang Fang, Spencer L. Tomarken, Jason Y. Luo, Javier D. Sanchez-Yamagishi, Kenji Watanabe, Takashi Taniguchi, Efthimios Kaxiras, Ray C. Ashoori, and Pablo Jarillo-Herrero. Correlated insulator behaviour at half-filling in magic-angle graphene superlattices. *Nature*, 556(7699):80–84, 2018. Referenced on page 60.

[222] Yuan Cao, Valla Fatemi, Shiang Fang, Kenji Watanabe, Takashi Taniguchi, Efthimios Kaxiras, and Pablo Jarillo-Herrero. Unconventional superconductivity in magic-angle graphene superlattices. *Nature*, 556(7699):43–50, 2018. Referenced on page 60.

[223] Yanhao Tang, Lizhong Li, Tingxin Li, Yang Xu, Song Liu, Katayun Barmak, Kenji Watanabe, Takashi Taniguchi, Allan H. MacDonald, Jie Shan, and Kin Fai Mak. Simulation of Hubbard model physics in WSe2/WS2 moirésuperlattices. *Nature*, 579(7799):353–358, 2020. Referenced on pages 60 and 61.

[224] Yang Xu, Song Liu, Daniel A. Rhodes, Kenji Watanabe, Takashi Taniguchi, James Hone, Veit Elser, Kin Fai Mak, and Jie Shan. Correlated insulating states at fractional fillings of moirésuperlattices. *Nature*, 587(7833):214–218, 2020. Referenced on page 61.

[225] Philippe Corboz, T. M. Rice, and Matthias Troyer. Competing States in the *t-J* Model: Uniform *d*-Wave State versus Stripe State. *Phys. Rev. Lett.*, 113:046402, Jul 2014. Referenced on page 66.

[226] Bo-Xiao Zheng and Garnet Kin-Lic Chan. Ground-state phase diagram of the square lattice Hubbard model from density matrix embedding theory. *Phys. Rev. B*, 93:035126, Jan 2016. Referenced on page 66.

[227] Mingpu Qin. Stripes versus superconductivity in the doped Hubbard model on the honeycomb lattice. *Phys. Rev. B*, 105:035111, Jan 2022. Referenced on page 66.

[228] Alexander Wietek, Yuan-Yao He, Steven R. White, Antoine Georges, and E. Miles Stoudenmire. Stripes, Antiferromagnetism, and the Pseudogap in the Doped Hubbard Model at

Finite Temperature. *Phys. Rev. X*, 11:031007, Jul 2021. Referenced on pages 68, 74, 76, and 174.

[229] H. J. Schulz. Correlation exponents and the metal-insulator transition in the one-dimensional Hubbard model. *Phys. Rev. Lett.*, 64:2831–2834, Jun 1990. Referenced on page 70.

[230] Fabian Grusdt and Lode Pollet. $\mathbb{Z}_2$ Parton Phases in the Mixed-Dimensional $t - J_z$ Model. *Phys. Rev. Lett.*, 125:256401, Dec 2020. Referenced on pages 71, 76, 78, and 96.

[231] VJ Emery, SA Kivelson, and JM Tranquada. Stripe phases in high-temperature superconductors. *Proceedings of the National Academy of Sciences*, 96(16):8814–8817, 1999. Referenced on page 77.

[232] Oron Zachar, S. A. Kivelson, and V. J. Emery. Landau theory of stripe phases in cuprates and nickelates. *Phys. Rev. B*, 57:1422–1426, Jan 1998. Referenced on page 77.

[233] Andrew J. Ferris and Guifre Vidal. Perfect sampling with unitary tensor networks. *Phys. Rev. B*, 85:165146, Apr 2012. Referenced on page 77.

[234] Maximilian Buser, Ulrich Schollwöck, and Fabian Grusdt. Snapshot-based characterization of particle currents and the Hall response in synthetic flux lattices. *Phys. Rev. A*, 105:033303, Mar 2022. Referenced on page 77.

[235] Yu-Rong Shu, Maxime Dupont, Dao-Xin Yao, Sylvain Capponi, and Anders W. Sandvik. Dynamical properties of the $S = \frac{1}{2}$ random Heisenberg chain. *Phys. Rev. B*, 97:104424, Mar 2018. Referenced on page 78.

[236] H. V. Kruis, I. P. McCulloch, Z. Nussinov, and J. Zaanen. Geometry and the hidden order of Luttinger liquids: The universality of squeezed space. *Phys. Rev. B*, 70:075109, Aug 2004. Referenced on pages 78, 93, 98, and 233.

[237] Masao Ogata and Hiroyuki Shiba. Bethe-ansatz wave function, momentum distribution, and spin correlation in the one-dimensional strongly correlated Hubbard model. *Phys. Rev. B*, 41:2326–2338, Feb 1990. Referenced on pages 78, 111, and 233.

[238] Fabian Grusdt, Zheng Zhu, Tao Shi, and Eugene Demler. Meson formation in mixed-dimensional t-J models. *SciPost Phys.*, 5:057, 2018. Referenced on pages 78 and 237.

[239] L.-M. Duan, E. Demler, and M. D. Lukin. Controlling Spin Exchange Interactions of Ultracold Atoms in Optical Lattices. *Phys. Rev. Lett.*, 91:090402, Aug 2003. Referenced on page 80.

[240] S. Trotzky, P. Cheinet, S. Fölling, M. Feld, U. Schnorrberger, A. M. Rey, A. Polkovnikov, E. A. Demler, M. D. Lukin, and I. Bloch. Time-Resolved Observation and Control of Superexchange Interactions with Ultracold Atoms in Optical Lattices. *Science*, 319(5861):295–299, 2008. Referenced on pages 80 and 189.

[241] Ivana Dimitrova, Niklas Jepsen, Anton Buyskikh, Araceli Venegas-Gomez, Jesse Amato-Grill, Andrew Daley, and Wolfgang Ketterle. Enhanced Superexchange in a Tilted Mott Insulator. *Phys. Rev. Lett.*, 124:043204, Jan 2020. Referenced on page 80.

[242] Timon A. Hilker, Guillaume Salomon, Fabian Grusdt, Ahmed Omran, Martin Boll, Eugene Demler, Immanuel Bloch, and Christian Gross. Revealing hidden antiferromagnetic correlations in doped Hubbard chains via string correlators. *Science*, 357(6350):484–487, 2017. Referenced on pages 93, 98, 107, 111, 112, 183, and 248.

[243] Thomas Hartke, Botond Oreg, Ningyuan Jia, and Martin Zwierlein. Doublon-Hole Correlations and Fluctuation Thermometry in a Fermi-Hubbard Gas. *Phys. Rev. Lett.*, 125:113601, Sep 2020. Referenced on page 95.

[244] Oleg A. Starykh and Leon Balents. Dimerized Phase and Transitions in a Spatially Anisotropic Square Lattice Antiferromagnet. *Phys. Rev. Lett.*, 93:127202, Sep 2004. Referenced on page 98.

[245] Anurag Anshu, Srinivasan Arunachalam, Tomotaka Kuwahara, and Mehdi Soleimanifar. Sample-efficient learning of interacting quantum systems. *Nature Physics*, 17(8):931–935, 2021. Referenced on pages 99 and 100.

[246] M.S. Leifer and D. Poulin. Quantum Graphical Models and Belief Propagation. *Annals of Physics*, 323(8):1899–1946, 2008. Referenced on page 99.

[247] Eyal Bairey, Itai Arad, and Netanel H. Lindner. Learning a Local Hamiltonian from Local Measurements. *Phys. Rev. Lett.*, 122:020504, Jan 2019. Referenced on page 101.

[248] C. Di Franco, M. Paternostro, and M. S. Kim. Hamiltonian Tomography in an Access-Limited Setting without State Initialization. *Phys. Rev. Lett.*, 102:187203, May 2009. Referenced on page 101.

[249] Jun Zhang and Mohan Sarovar. Quantum Hamiltonian Identification from Measurement Time Traces. *Phys. Rev. Lett.*, 113:080401, Aug 2014. Referenced on page 101.

[250] Xiao-Liang Qi and Daniel Ranard. Determining a local Hamiltonian from a single eigenstate. *Quantum*, 3:159, July 2019. Referenced on page 101.

[251] Chenfeng Cao, Shi-Yao Hou, Ningping Cao, and Bei Zeng. Supervised learning in Hamiltonian reconstruction from local measurements on eigenstates. *Journal of Physics: Condensed Matter*, 33(6):064002, feb 2020. Referenced on page 101.

[252] Fabio Mezzacapo. Ground-state phase diagram of the quantum $J_1 - J_2$ model on the square lattice. *Phys. Rev. B*, 86:045115, Jul 2012. Referenced on pages 106 and 265.

[253] Wen-Jun Hu, Federico Becca, Alberto Parola, and Sandro Sorella. Direct evidence for a gapless Z_2 spin liquid by frustrating Néel antiferromagnetism. *Phys. Rev. B*, 88:060402, Aug 2013. Referenced on pages 106 and 265.

[254] Ling Wang, Didier Poilblanc, Zheng-Cheng Gu, Xiao-Gang Wen, and Frank Verstraete. Constructing a Gapless Spin-Liquid State for the Spin-1/2 $J_1 - J_2$ Heisenberg Model on a Square Lattice. *Phys. Rev. Lett.*, 111:037202, Jul 2013. Referenced on pages 106 and 265.

[255] Shou-Shu Gong, Wei Zhu, D. N. Sheng, Olexei I. Motrunich, and Matthew P. A. Fisher. Plaquette Ordered Phase and Quantum Phase Diagram in the Spin-$\frac{1}{2}$ J_1-J_2 Square Heisenberg Model. *Phys. Rev. Lett.*, 113:027201, Jul 2014. Referenced on pages 106 and 265.

[256] Hong-Chen Jiang, Hong Yao, and Leon Balents. Spin liquid ground state of the spin-$\frac{1}{2}$ square J_1-J_2 Heisenberg model. *Phys. Rev. B*, 86:024424, Jul 2012. Referenced on pages 106 and 265.

[257] R. Haghshenas and D. N. Sheng. $U(1)$-symmetric infinite projected entangled-pair states study of the spin-1/2 square J_1-J_2 Heisenberg model. *Phys. Rev. B*, 97:174408, May 2018. Referenced on pages 106 and 265.

[258] P.W. Anderson. Resonating valence bonds: A new kind of insulator? *Materials Research Bulletin*, 8(2):153–160, 1973. Referenced on pages 106 and 199.

[259] Steven A. Kivelson, Daniel S. Rokhsar, and James P. Sethna. Topology of the resonating valence-bond state: Solitons and high-T_c superconductivity. *Phys. Rev. B*, 35:8865–8868, Jun 1987. Referenced on page 106.

[260] V. Kalmeyer and R. B. Laughlin. Equivalence of the resonating-valence-bond and fractional quantum Hall states. *Phys. Rev. Lett.*, 59:2095–2098, Nov 1987. Referenced on page 106.

[261] Naoto Nagaosa and Patrick A. Lee. Normal-state properties of the uniform resonating-valence-bond state. *Phys. Rev. Lett.*, 64:2450–2453, May 1990. Referenced on page 106.

[262] G. Baskaran, Z. Zou, and P.W. Anderson. The resonating valence bond state and high-Tc superconductivity — a mean field theory. *Solid State Communications*, 88(11):853–856, 1993. Special Issue A Celebratory Issue to Commemorate 30 Years of Solid State Communications. Referenced on page 106.

[263] S. R. White, R. M. Noack, and D. J. Scalapino. Resonating Valence Bond Theory of Coupled Heisenberg Chains. *Phys. Rev. Lett.*, 73:886–889, Aug 1994. Referenced on pages 106 and 163.

[264] Cornelius F. Coll. Excitation spectrum of the one-dimensional Hubbard model. *Phys. Rev. B*, 9:2150–2158, Mar 1974. Referenced on page 111.

[265] F. Grusdt, M. Kánasz-Nagy, A. Bohrdt, C. S. Chiu, G. Ji, M. Greiner, D. Greif, and E. Demler. Parton Theory of Magnetic Polarons: Mesonic Resonances and Signatures in Dynamics. *Phys. Rev. X*, 8:011046, Mar 2018. Referenced on pages 114, 132, 151, 152, 153, 166, 224, and 232.

[266] Igor Dzyaloshinskii. Some consequences of the Luttinger theorem: The Luttinger surfaces in non-Fermi liquids and Mott insulators. *Phys. Rev. B*, 68:085113, Aug 2003. Referenced on page 120.

[267] I M Vishik. Photoemission perspective on pseudogap, superconducting fluctuations, and charge order in cuprates: a review of recent progress. *Reports on Progress in Physics*, 81(6):062501, 2018. Referenced on page 123.

[268] T. R. Thurston, R. J. Birgeneau, M. A. Kastner, N. W. Preyer, G. Shirane, Y. Fujii, K. Yamada, Y. Endoh, K. Kakurai, M. Matsuda, Y. Hidaka, and T. Murakami. Neutron scattering study of the magnetic excitations in metallic and superconducting $La_{2-x}Sr_xCuO_{4-y}$. *Phys. Rev. B*, 40:4585–4595, Sep 1989. Referenced on page 124.

[269] M. Platé, J. D. F. Mottershead, I. S. Elfimov, D. C. Peets, Ruixing Liang, D. A. Bonn, W. N. Hardy, S. Chiuzbaian, M. Falub, M. Shi, L. Patthey, and A. Damascelli. Fermi Surface and Quasiparticle Excitations of Overdoped $Tl_2Ba_2CuO_{6+\delta}$. *Phys. Rev. Lett.*, 95:077001, Aug 2005. Referenced on pages 125, 126, and 127.

[270] Kouji Segawa and Yoichi Ando. Intrinsic Hall response of the CuO_2 planes in a chain-plane composite system of $YBa_2Cu_3O_y$. *Phys. Rev. B*, 69:104521, Mar 2004. Referenced on page 127.

[271] Andreas Eberlein, Walter Metzner, Subir Sachdev, and Hiroyuki Yamase. Fermi Surface Reconstruction and Drop in the Hall Number due to Spiral Antiferromagnetism in High-T_c Cuprates. *Phys. Rev. Lett.*, 117:187001, Oct 2016. Referenced on page 130.

[272] Boris I. Shraiman and Eric D. Siggia. Mobile Vacancies in a Quantum Heisenberg Antiferromagnet. *Phys. Rev. Lett.*, 61:467–470, Jul 1988. Referenced on pages 132, 151, 203, and 208.

[273] Subir Sachdev. Hole motion in a quantum Néel state. *Phys. Rev. B*, 39:12232–12247, Jun 1989. Referenced on pages 132 and 151.

[274] C. L. Kane, P. A. Lee, and N. Read. Motion of a single hole in a quantum antiferromagnet. *Phys. Rev. B*, 39:6880–6897, Apr 1989. Referenced on pages 132 and 151.

[275] V. J. Emery. Theory of high-T_c superconductivity in oxides. *Phys. Rev. Lett.*, 58:2794–2797, Jun 1987. Referenced on pages 132 and 151.

[276] J. R. Schrieffer, X.-G. Wen, and S.-C. Zhang. Spin-bag mechanism of high-temperature superconductivity. *Phys. Rev. Lett.*, 60:944–947, Mar 1988. Referenced on pages 132, 151, and 154.

[277] P. Béran, D. Poilblanc, and R. B. Laughlin. Evidence for composite nature of quasiparticles in the 2D t-J model. *Nuclear Physics B*, 473(3):707–720, 1996. Referenced on pages 132 and 151.

[278] Annabelle Bohrdt, Eugene Demler, Frank Pollmann, Michael Knap, and Fabian Grusdt. Parton theory of angle-resolved photoemission spectroscopy spectra in antiferromagnetic Mott insulators. *Phys. Rev. B*, 102:035139, Jul 2020. Referenced on pages 132, 151, and 166.

[279] Pit Bermes, Annabelle Bohrdt, and Fabian Grusdt. Magnetic polarons beyond linear spin-wave theory: Mesons dressed by magnons. *Phys. Rev. B*, 109:205104, May 2024. Referenced on pages 132 and 151.

[280] Masaki Oshikawa. Topological Approach to Luttinger's Theorem and the Fermi Surface of a Kondo Lattice. *Phys. Rev. Lett.*, 84:3370–3373, Apr 2000. Referenced on pages 133 and 151.

[281] A. Yu. Kitaev. Fault-tolerant quantum computation by anyons. *Annals of Physics*, 303(1):2–30, 2003. Referenced on pages 134 and 149.

[282] Subir Sachdev, Max A. Metlitski, Yang Qi, and Cenke Xu. Fluctuating spin density waves in metals. *Phys. Rev. B*, 80:155129, Oct 2009. Referenced on page 142.

[283] Subir Sachdev, Erez Berg, Shubhayu Chatterjee, and Yoni Schattner. Spin density wave order, topological order, and Fermi surface reconstruction. *Phys. Rev. B*, 94:115147, Sep 2016. Referenced on page 142.

[284] Shubhayu Chatterjee, Subir Sachdev, and Mathias S. Scheurer. Intertwining Topological Order and Broken Symmetry in a Theory of Fluctuating Spin-Density Waves. *Phys. Rev. Lett.*, 119:227002, Nov 2017. Referenced on page 142.

[285] Subir Sachdev. Topological order, emergent gauge fields, and Fermi surface reconstruction. *Reports on Progress in Physics*, 82(1):014001, 2019. Referenced on page 142.

[286] Pietro M. Bonetti and Walter Metzner. SU(2) gauge theory of the pseudogap phase in the two-dimensional Hubbard model. *Phys. Rev. B*, 106:205152, Nov 2022. Referenced on page 142.

[287] Ying Zhang, Eugene Demler, and Subir Sachdev. Competing orders in a magnetic field: Spin and charge order in the cuprate superconductors. *Phys. Rev. B*, 66:094501, Sep 2002. Referenced on pages 143 and 148.

[288] J. Zaanen, O. Y. Osman, H. V. Kruis, Z. Nussinov, and J. Tworzydlo. The geometric order of stripes and Luttinger liquids. *Philosophical Magazine B*, 81(10):1485–1531, 10 2001. Referenced on pages 143, 146, 147, 148, 153, and 233.

[289] Henk Eskes, Osman Yousif Osman, Rob Grimberg, Wim van Saarloos, and Jan Zaanen. Charged domain walls as quantum strings on a lattice. *Phys. Rev. B*, 58:6963–6981, Sep 1998. Referenced on pages 144 and 148.

[290] Frank Krüger and Stefan Scheidl. Nonuniversal Ordering of Spin and Charge in Stripe Phases. *Phys. Rev. Lett.*, 89:095701, Aug 2002. Referenced on pages 145 and 148.

[291] F. D. M. Haldane. Nonlinear Field Theory of Large-Spin Heisenberg Antiferromagnets: Semiclassically Quantized Solitons of the One-Dimensional Easy-Axis Néel State. *Phys. Rev. Lett.*, 50:1153–1156, Apr 1983. Referenced on page 145.

[292] R. Peierls. On Ising's model of ferromagnetism. *Mathematical Proceedings of the Cambridge Philosophical Society*, 32(3):477–481, 1936. Referenced on page 145.

[293] Franz J Wegner. Duality in generalized Ising models and phase transitions without local order parameters. *Journal of Mathematical Physics*, 12(10):2259–2272, 1971. Referenced on pages 145 and 146.

[294] Simon M. Linsel, Annabelle Bohrdt, Lukas Homeier, Lode Pollet, and Fabian Grusdt. Percolation as a confinement order parameter in $\mathbb{Z}_2$ lattice gauge theories. *arXiv:2401.08770*, 2024. Referenced on page 146.

[295] Y. Li, V. Balédent, N. Barišić, Y. Cho, B. Fauqué, Y. Sidis, G. Yu, X. Zhao, P. Bourges, and M. Greven. Unusual magnetic order in the pseudogap region of the superconductor HgBa2CuO4+δ. *Nature*, 455(7211):372–375, 2008. Referenced on pages 147 and 155.

[296] Xiao-Gang Wen. Quantum field theory of many-body systems: From the origin of sound to an origin of light and electrons. *Oxford university press*, 2004. Referenced on page 150.

[297] Michael A. Levin and Xiao-Gang Wen. String-net condensation: A physical mechanism for topological phases. *Phys. Rev. B*, 71:045110, Jan 2005. Referenced on page 150.

[298] Simon Trebst, Philipp Werner, Matthias Troyer, Kirill Shtengel, and Chetan Nayak. Breakdown of a Topological Phase: Quantum Phase Transition in a Loop Gas Model with Tension. *Phys. Rev. Lett.*, 98:070602, Feb 2007. Referenced on page 150.

[299] Fengcheng Wu, Youjin Deng, and Nikolay Prokof'ev. Phase diagram of the toric code model in a parallel magnetic field. *Phys. Rev. B*, 85:195104, May 2012. Referenced on page 150.

[300] N E Hussey. Phenomenology of the normal state in-plane transport properties of high-Tc cuprates. *Journal of Physics: Condensed Matter*, 20(12):123201, 2008. Referenced on page 153.

[301] Subir Sachdev and Jinwu Ye. Universal quantum-critical dynamics of two-dimensional antiferromagnets. *Phys. Rev. Lett.*, 69:2411–2414, Oct 1992. Referenced on page 153.

[302] Fabian Grusdt, Annabelle Bohrdt, and Eugene Demler. Microscopic spinon-chargon theory of magnetic polarons in the $t-J$ model. *Phys. Rev. B*, 99:224422, Jun 2019. Referenced on pages 153, 166, 209, 232, 236, and 237.

[303] B. Michon, C. Girod, S. Badoux, J. Kačmarčík, Q. Ma, M. Dragomir, H. A. Dabkowska, B. D. Gaulin, J. S. Zhou, S. Pyon, T. Takayama, H. Takagi, S. Verret, N. Doiron-Leyraud, C. Marcenat, L. Taillefer, and T. Klein. Thermodynamic signatures of quantum criticality in cuprate superconductors. *Nature*, 567(7747):218–222, 2019. Referenced on page 153.

[304] Riccardo Arpaia, Leonardo Martinelli, Marco Moretti Sala, Sergio Caprara, Abhishek Nag, Nicholas B. Brookes, Pietro Camisa, Qizhi Li, Qiang Gao, Xingjiang Zhou, Mirian Garcia-Fernandez, Ke-Jin Zhou, Enrico Schierle, Thilo Bauch, Ying Ying Peng, Carlo Di Castro, Marco Grilli, Floriana Lombardi, Lucio Braicovich, and Giacomo Ghiringhelli. Signature of quantum criticality in cuprates by charge density fluctuations. *Nature Communications*, 14(1):7198, 2023. Referenced on page 153.

[305] Philipp Gegenwart, Qimiao Si, and Frank Steglich. Quantum criticality in heavy-fermion metals. *Nature Physics*, 4(3):186–197, 2008. Referenced on page 154.

[306] G. R. Stewart. Superconductivity in iron compounds. *Rev. Mod. Phys.*, 83:1589–1652, Dec 2011. Referenced on page 154.

[307] Denis Jerome and Claude Bourbonnais. Quasi one-dimensional organic conductors: from Fröhlich conductivity and Peierls insulating state to magnetically-mediated superconductivity, a retrospective. *Comptes Rendus. Physique*, 25:17–178, 2024. Referenced on page 154.

[308] Silke Paschen, Thomas Lühmann, Steffen Wirth, Philipp Gegenwart, Octavio Trovarelli, Christoph Geibel, Frank Steglich, Piers Coleman, and Qimiao Si. Hall-effect evolution across a heavy-fermion quantum critical point. *Nature*, 432(7019):881–885, 2004. Referenced on page 154.

[309] P. Monthoux, D. Pines, and G. G. Lonzarich. Superconductivity without phonons. *Nature*, 450(7173):1177–1183, 2007. Referenced on page 154.

[310] Louis Taillefer. Scattering and Pairing in Cuprate Superconductors. *Annual Review of Condensed Matter Physics*, 1(Volume 1, 2010):51–70, 2010. Referenced on page 154.

[311] Cyril Proust and Louis Taillefer. The Remarkable Underlying Ground States of Cuprate Superconductors. *Annual Review of Condensed Matter Physics*, 10(Volume 10, 2019):409–429, 2019. Referenced on page 154.

[312] K. Miyake, S. Schmitt-Rink, and C. M. Varma. Spin-fluctuation-mediated even-parity pairing in heavy-fermion superconductors. *Phys. Rev. B*, 34:6554–6556, Nov 1986. Referenced on page 154.

[313] D. J. Scalapino, E. Loh, and J. E. Hirsch. *d*-wave pairing near a spin-density-wave instability. *Phys. Rev. B*, 34:8190–8192, Dec 1986. Referenced on page 154.

[314] W. P. Su. Spin polarons in the two-dimensional Hubbard model: A numerical study. *Phys. Rev. B*, 37:9904–9906, Jun 1988. Referenced on page 154.

[315] Lukas Homeier, Hannah Lange, Eugene Demler, Annabelle Bohrdt, and Fabian Grusdt. Feshbach hypothesis of high-Tc superconductivity in cuprates, 2023. L. Homeier *et al.*, in prep. Referenced on pages 154, 170, and 172.

[316] M. R. Norman, D. Pines, and C. Kallin. The pseudogap: friend or foe of high Tc ? *Advances in Physics*, 54(8):715–733, 12 2005. Referenced on pages 154 and 174.

[317] Tom Timusk and Bryan Statt. The pseudogap in high-temperature superconductors: an experimental survey. *Reports on Progress in Physics*, 62(1):61, 1999. Referenced on page 154.

[318] B. Fauqué, Y. Sidis, V. Hinkov, S. Pailhès, C. T. Lin, X. Chaud, and P. Bourges. Magnetic Order in the Pseudogap Phase of High-T_C Superconductors. *Phys. Rev. Lett.*, 96:197001, May 2006. Referenced on page 155.

[319] Jing Xia, Elizabeth Schemm, G. Deutscher, S. A. Kivelson, D. A. Bonn, W. N. Hardy, R. Liang, W. Siemons, G. Koster, M. M. Fejer, and A. Kapitulnik. Polar Kerr-Effect Measurements of the High-Temperature $YBa_2Cu_3O_{6+x}$ Superconductor: Evidence for Broken Symmetry near the Pseudogap Temperature. *Phys. Rev. Lett.*, 100:127002, Mar 2008. Referenced on page 155.

[320] F. Laliberté, J. Chang, N. Doiron-Leyraud, E. Hassinger, R. Daou, M. Rondeau, B. J. Ramshaw, R. Liang, D. A. Bonn, W. N. Hardy, S. Pyon, T. Takayama, H. Takagi, I. Sheikin, L. Malone, C. Proust, K. Behnia, and Louis Taillefer. Fermi-surface reconstruction by stripe order in cuprate superconductors. *Nature Communications*, 2(1):432, 2011. Referenced on page 155.

[321] Jun Hou, Peng-Tao Yang, Zi-Yi Liu, Jing-Yuan Li, Peng-Fei Shan, Liang Ma, Gang Wang, Ning-Ning Wang, Hai-Zhong Guo, Jian-Ping Sun, Yoshiya Uwatoko, Meng Wang, Guang-Ming Zhang, Bo-Sen Wang, and Jin-Guang Cheng. Emergence of High-Temperature Superconducting Phase in Pressurized La3Ni2O7 Crystals. *Chinese Physics Letters*, 40(11):117302, 2023. Referenced on page 157.

[322] Victor Pardo and Warren E. Pickett. Metal-insulator transition in layered nickelates $La_3Ni_2O_{7-\delta}$ ($\delta = 0.0, 0.5, 1$). *Phys. Rev. B*, 83:245128, Jun 2011. Referenced on page 158.

[323] Zhihui Luo, Xunwu Hu, Meng Wang, Wéi Wú, and Dao-Xin Yao. Bilayer Two-Orbital Model of $La_3Ni_2O_7$ under Pressure. *Phys. Rev. Lett.*, 131:126001, Sep 2023. Referenced on pages 158, 161, 169, and 170.

[324] Yang Zhang, Ling-Fang Lin, Adriana Moreo, and Elbio Dagotto. Electronic structure, dimer physics, orbital-selective behavior, and magnetic tendencies in the bilayer nickelate superconductor $La_3Ni_2O_7$ under pressure. *Phys. Rev. B*, 108:L180510, Nov 2023. Referenced on page 158.

[325] Hirofumi Sakakibara, Naoya Kitamine, Masayuki Ochi, and Kazuhiko Kuroki. Possible High T_c Superconductivity in $La_3Ni_2O_7$ under High Pressure through Manifestation of a Nearly Half-Filled Bilayer Hubbard Model. *Phys. Rev. Lett.*, 132:106002, Mar 2024. Referenced on page 158.

[326] Yuhao Gu, Congcong Le, Zhesen Yang, Xianxin Wu, and Jiangping Hu. Effective model and pairing tendency in bilayer Ni-based superconductor $La_3Ni_2O_7$, 2023. Referenced on page 158.

[327] Viktor Christiansson, Francesco Petocchi, and Philipp Werner. Correlated Electronic Structure of $La_3Ni_2O_7$ under Pressure. *Phys. Rev. Lett.*, 131:206501, Nov 2023. Referenced on page 158.

[328] Yingying Cao and Yi-feng Yang. Flat bands promoted by Hund's rule coupling in the candidate double-layer high-temperature superconductor $La_3Ni_2O_7$ under high pressure. *Phys. Rev. B*, 109:L081105, Feb 2024. Referenced on pages 158 and 163.

[329] Yi-feng Yang, Guang-Ming Zhang, and Fu-Chun Zhang. Interlayer valence bonds and two-component theory for high-T_c superconductivity of $La_3Ni_2O_7$ under pressure. *Phys. Rev. B*, 108:L201108, Nov 2023. Referenced on page 158.

[330] Zhe Liu, Mengwu Huo, Jie Li, Qing Li, Yuecong Liu, Yaomin Dai, Xiaoxiang Zhou, Jiahao Hao, Yi Lu, Meng Wang, and Hai-Hu Wen. Electronic correlations and energy gap in the bilayer nickelate $La_3Ni_2O_7$, 2023. Referenced on page 158.

[331] Hannah Lange, Lukas Homeier, Eugene Demler, Ulrich Schollwöck, Annabelle Bohrdt, and Fabian Grusdt. Pairing dome from an emergent Feshbach resonance in a strongly repulsive bilayer model. *Phys. Rev. B*, 110:L081113, Aug 2024. Referenced on pages 160, 170, 175, 180, 181, and 186.

[332] Hannah Lange, Lukas Homeier, Eugene Demler, Ulrich Schollwöck, Fabian Grusdt, and Annabelle Bohrdt. Feshbach resonance in a strongly repulsive ladder of mixed dimensionality: A possible scenario for bilayer nickelate superconductors. *Phys. Rev. B*, 109:045127, Jan 2024. Referenced on pages 160, 170, 175, 180, 181, 183, and 186.

[333] Matthias Troyer, Hirokazu Tsunetsugu, and Diethelm Würtz. Thermodynamics and spin gap of the Heisenberg ladder calculated by the look-ahead Lanczos algorithm. *Phys. Rev. B*, 50:13515–13527, Nov 1994. Referenced on page 163.

[334] M. Greven, R. J. Birgeneau, and U. J. Wiese. Monte Carlo Study of Correlations in Quantum Spin Ladders. *Phys. Rev. Lett.*, 77:1865–1868, Aug 1996. Referenced on page 163.

[335] J Carrasquilla and M Rigol. Superfluid to normal phase transition in strongly correlated bosons in two dimensions. *Journal of Physics: Conference Series*, 414(1):012028, feb 2013. Referenced on page 169.

[336] Sumit Haldar, Sk Saniur Rahaman, and Manoranjan Kumar. Study of the Berezinskii–Kosterlitz–Thouless transition: an unsupervised machine learning approach. *Journal of Physics: Condensed Matter*, 36(41):415804, 2024. Referenced on page 169.

[337] Hui Yang, Hanbit Oh, and Ya-Hui Zhang. Strong pairing from doping-induced Feshbach resonance and second Fermi liquid through doping a bilayer spin-one Mott insulator: application to $La_3Ni_2O_7$, 2023. Referenced on pages 169 and 170.

[338] Da-Chuan Lu, Miao Li, Zhao-Yi Zeng, Wanda Hou, Juven Wang, Fan Yang, and Yi-Zhuang You. Superconductivity from Doping Symmetric Mass Generation Insulators: Application to $La_3Ni_2O_7$ under Pressure, 2023. Referenced on page 169.

[339] J.W. Loram, K.A. Mirza, J.M. Wade, J.R. Cooper, and W.Y. Liang. The electronic specific heat of cuprate superconductors. *Physica C: Superconductivity*, 235-240:134–137, 1994. Referenced on page 169.

[340] Pieter van Wyk, Hiroyuki Tajima, Ryo Hanai, and Yoji Ohashi. Specific heat and effects of pairing fluctuations in the BCS-BEC-crossover regime of an ultracold Fermi gas. *Phys. Rev. A*, 93:013621, Jan 2016. Referenced on page 169.

[341] Yu E Lozovik and VI Yudson. A new mechanism for superconductivity: pairing between spatially separated electrons and holes. *Zh. Eksp. Teor. Fiz*, 71:738, 1976. Referenced on page 171.

[342] E. Hanamura and H. Haug. Condensation effects of excitons. *Physics Reports*, 33(4):209–284, 1977. Referenced on page 171.

[343] Zefang Wang, Daniel A. Rhodes, Kenji Watanabe, Takashi Taniguchi, James C. Hone, Jie Shan, and Kin Fai Mak. Evidence of high-temperature exciton condensation in two-dimensional atomic double layers. *Nature*, 574(7776):76–80, 2019. Referenced on page 171.

[344] Xiaomeng Liu, J. I. A. Li, Kenji Watanabe, Takashi Taniguchi, James Hone, Bertrand I. Halperin, Philip Kim, and Cory R. Dean. Crossover between strongly coupled and weakly coupled exciton superfluids. *Science*, 375(6577):205–209, 2022. Referenced on page 171.

[345] Netanel H. Lindner and Assa Auerbach. Conductivity of hard core bosons: A paradigm of a bad metal. *Phys. Rev. B*, 81:054512, Feb 2010. Referenced on page 171.

[346] Zhiming Pan, Chen Lu, Fan Yang, and Congjun Wu. Effect of Rare-earth Element Substitution in Superconducting $R_3Ni_2O_7$ Under Pressure, 2023. Referenced on page 172.

[347] Mingxin Zhang, Cuiying Pei, Xian Du, Weixiong Hu, Yantao Cao, Qi Wang, Juefei Wu, Yidian Li, Huanyu Liu, Chenhaoping Wen, Yi Zhao, Changhua Li, Weizheng Cao, Shihao Zhu, Qing Zhang, Na Yu, Peihong Cheng, Lili Zhang, Zhiwei Li, Jinkui Zhao, Yulin Chen, Hanjie Guo, Congjun Wu, Fan Yang, Shichao Yan, Lexian Yang, and Yanpeng Qi. Superconductivity in trilayer nickelate La4Ni3O10 under pressure, 2024. Referenced on page 172.

[348] Yinghao Zhu, Di Peng, Enkang Zhang, Bingying Pan, Xu Chen, Lixing Chen, Huifen Ren, Feiyang Liu, Yiqing Hao, Nana Li, Zhenfang Xing, Fujun Lan, Jiyuan Han, Junjie Wang, Donghan Jia, Hongliang Wo, Yiqing Gu, Yimeng Gu, Li Ji, Wenbin Wang, Huiyang Gou, Yao Shen, Tianping Ying, Xiaolong Chen, Wenge Yang, Huibo Cao, Changlin Zheng, Qiaoshi Zeng, Jian-gang Guo, and Jun Zhao. Superconductivity in pressurized trilayer La4Ni3O10 single crystals. *Nature*, 631(8021):531–536, 2024. Referenced on page 172.

[349] Hirofumi Sakakibara, Masayuki Ochi, Hibiki Nagata, Yuta Ueki, Hiroya Sakurai, Ryo Matsumoto, Kensei Terashima, Keisuke Hirose, Hiroto Ohta, Masaki Kato, Yoshihiko Takano, and Kazuhiko Kuroki. Theoretical analysis on the possibility of superconductivity in the

trilayer Ruddlesden-Popper nickelate $La_4Ni_3O_{10}$ under pressure and its experimental examination: Comparison with $La_3Ni_2O_7$. *Phys. Rev. B*, 109:144511, Apr 2024. Referenced on page 172.

[350] Zihao Huo, Peng Zhang, Zihan Zhang, Defang Duan, and Tian Cui. Electronic Correlations and Hund's Rule Coupling in Trilayer Nickelate La4Ni3O10, 2024. Referenced on page 172.

[351] Harrison LaBollita, Jesse Kapeghian, Michael R. Norman, and Antia S. Botana. Electronic structure and magnetic tendencies of trilayer $La_4Ni_3O_{10}$ under pressure: Structural transition, molecular orbitals, and layer differentiation. *Phys. Rev. B*, 109:195151, May 2024. Referenced on page 172.

[352] A. F. Ho, M. A. Cazalilla, and T. Giamarchi. Quantum simulation of the Hubbard model: The attractive route. *Phys. Rev. A*, 79:033620, Mar 2009. Referenced on pages 175 and 191.

[353] Thomas Hartke, Botond Oreg, Carter Turnbaugh, Ningyuan Jia, and Martin Zwierlein. Direct observation of nonlocal fermion pairing in an attractive Fermi-Hubbard gas. *Science*, 381(6653):82–86, 2023. Referenced on pages 175 and 191.

[354] Alexander Impertro, Simon Karch, Julian F. Wienand, SeungJung Huh, Christian Schweizer, Immanuel Bloch, and Monika Aidelsburger. Local readout and control of current and kinetic energy operators in optical lattices, 2023. Referenced on pages 175 and 184.

[355] Thomas Chalopin, Petar Bojović, Dominik Bourgund, Si Wang, Titus Franz, Immanuel Bloch, and Timon Hilker. Optical superlattice for engineering Hubbard couplings in quantum simulation, 2024. Referenced on pages 180 and 184.

[356] Thierry Giamarchi. *Quantum physics in one dimension*, volume 121. Clarendon press, 2003. Referenced on page 183.

[357] Simon Murmann, Andrea Bergschneider, Vincent M. Klinkhamer, Gerhard Zürn, Thomas Lompe, and Selim Jochim. Two Fermions in a Double Well: Exploring a Fundamental Building Block of the Hubbard Model. *Phys. Rev. Lett.*, 114:080402, Feb 2015. Referenced on pages 184 and 189.

[358] Bing Yang, Hui Sun, Chun-Jiong Huang, Han-Yi Wang, Youjin Deng, Han-Ning Dai, Zhen-Sheng Yuan, and Jian-Wei Pan. Cooling and entangling ultracold atoms in optical lattices. *Science*, 369(6503):550–553, Sep 2020. Referenced on page 184.

[359] Philipp M. Preiss, Ruichao Ma, M. Eric Tai, Jonathan Simon, and Markus Greiner. Quantum gas microscopy with spin, atom-number, and multilayer readout. *Phys. Rev. A*, 91:041602, Apr 2015. Referenced on page 185.

[360] Marcell Gall, Nicola Wurz, Jens Samland, Chun Fai Chan, and Michael Köhl. Competing magnetic orders in a bilayer Hubbard model with ultracold atoms. *Nature*, 589(7840):40–43, 2021. Referenced on page 185.

[361] Joannis Koepsell, Sarah Hirthe, Dominik Bourgund, Pimonpan Sompet, Jayadev Vijayan, Guillaume Salomon, Christian Gross, and Immanuel Bloch. Robust Bilayer Charge Pumping for Spin- and Density-Resolved Quantum Gas Microscopy. *Phys. Rev. Lett.*, 125:010403, Jul 2020. Referenced on pages 185 and 205.

[362] Christie S. Chiu, Geoffrey Ji, Anton Mazurenko, Daniel Greif, and Markus Greiner. Quantum State Engineering of a Hubbard System with Ultracold Fermions. *Phys. Rev. Lett.*, 120:243201, Jun 2018. Referenced on page 185.

[363] Stefan Trotzky, Yu-Ao Chen, Ute Schnorrberger, Patrick Cheinet, and Immanuel Bloch. Controlling and Detecting Spin Correlations of Ultracold Atoms in Optical Lattices. *Phys. Rev. Lett.*, 105:265303, Dec 2010. Referenced on page 189.

[364] A. Bohrdt, D. Greif, E. Demler, M. Knap, and F. Grusdt. Angle-resolved photoemission spectroscopy with quantum gas microscopes. *Phys. Rev. B*, 97:125117, Mar 2018. Referenced on page 198.

[365] Luca Capriotti, Adolfo E. Trumper, and Sandro Sorella. Long-Range Néel Order in the Triangular Heisenberg Model. *Phys. Rev. Lett.*, 82:3899–3902, May 1999. Referenced on page 199.

[366] Jan O. Haerter and B. Sriram Shastry. Kinetic Antiferromagnetism in the Triangular Lattice. *Phys. Rev. Lett.*, 95:087202, Aug 2005. Referenced on pages 199, 203, and 210.

[367] J. Merino, B. J. Powell, and Ross H. McKenzie. Ferromagnetism, paramagnetism, and a Curie-Weiss metal in an electron-doped Hubbard model on a triangular lattice. *Phys. Rev. B*, 73:235107, Jun 2006. Referenced on page 199.

[368] C. N. Sposetti, B. Bravo, A. E. Trumper, C. J. Gazza, and L. O. Manuel. Classical Antiferromagnetism in Kinetically Frustrated Electronic Models. *Phys. Rev. Lett.*, 112:187204, May 2014. Referenced on pages 199, 203, and 210.

[369] C. D. Batista and G. Ortiz. Quantum Phase Diagram of the $t - J_z$ Chain Model. *Phys. Rev. Lett.*, 85:4755–4758, Nov 2000. Referenced on page 199.

[370] Ivan Morera, Annabelle Bohrdt, Wen Wei Ho, and Eugene Demler. Attraction from frustration in ladder systems, May 2021. Referenced on page 199.

[371] Zheng Zhu, D. N. Sheng, and Ashvin Vishwanath. Doped Mott insulators in the triangular-lattice Hubbard model. *Phys. Rev. B*, 105:205110, May 2022. Referenced on page 199.

[372] Shuai A. Chen, Qianqian Chen, and Zheng Zhu. Proposal for asymmetric photoemission and tunneling spectroscopies in quantum simulators of the triangular-lattice Fermi-Hubbard model. *Phys. Rev. B*, 106:085138, Aug 2022. Referenced on pages 199, 209, and 212.

[373] Jasper van de Kraats, Kristian K. Nielsen, and Georg M. Bruun. Holes and magnetic polarons in a triangular lattice antiferromagnet. *Phys. Rev. B*, 106:235143, Dec 2022. Referenced on pages 199 and 207.

[374] Wilhelm Kadow, Laurens Vanderstraeten, and Michael Knap. Hole spectral function of a chiral spin liquid in the triangular lattice Hubbard model. *Phys. Rev. B*, 106:094417, Sep 2022. Referenced on page 199.

[375] J. Struck, C. Ölschläger, R. Le Targat, P. Soltan-Panahi, A. Eckardt, M. Lewenstein, P. Windpassinger, and K. Sengstock. Quantum Simulation of Frustrated Classical Magnetism in Triangular Optical Lattices. *Science*, 333(6045):996–999, 2011. Referenced on page 199.

[376] Gyu-Boong Jo, Jennie Guzman, Claire K. Thomas, Pavan Hosur, Ashvin Vishwanath, and Dan M. Stamper-Kurn. Ultracold Atoms in a Tunable Optical Kagome Lattice. *Phys. Rev. Lett.*, 108:045305, Jan 2012. Referenced on page 199.

[377] Ryuta Yamamoto, Hideki Ozawa, David C. Nak, Ippei Nakamura, and Takeshi Fukuhara. Single-site-resolved imaging of ultracold atoms in a triangular optical lattice. *New Journal of Physics*, 22(12):123028, dec 2020. Referenced on page 199.

[378] Jin Yang, Liyu Liu, Jirayu Mongkolkiattichai, and Peter Schauss. Site-Resolved Imaging of Ultracold Fermions in a Triangular-Lattice Quantum Gas Microscope. *PRX Quantum*, 2:020344, Jun 2021. Referenced on page 199.

[379] Muqing Xu, Lev Haldar Kendrick, Anant Kale, Youqi Gang, Geoffrey Ji, Richard T. Scalettar, Martin Lebrat, and Markus Greiner. Doping a frustrated Fermi-Hubbard magnet, 2022. Referenced on page 199.

[380] Shuai A. Chen, Qianqian Chen, and Zheng Zhu. Proposal for asymmetric photoemission and tunneling spectroscopies in quantum simulators of the triangular-lattice Fermi-Hubbard model. *Phys. Rev. B*, 106:085138, Aug 2022. Referenced on page 201.

[381] Yosuke Nagaoka. Ferromagnetism in a Narrow, Almost Half-Filled s Band. *Phys. Rev.*, 147:392–405, Jul 1966. Referenced on page 202.

[382] Federico Becca and Sandro Sorella. Nagaoka Ferromagnetism in the Two-Dimensional Infinite- U Hubbard Model. *Phys. Rev. Lett.*, 86:3396–3399, Apr 2001. Referenced on page 202.

[383] Steven R. White and Ian Affleck. Density matrix renormalization group analysis of the Nagaoka polaron in the two-dimensional $t - J$ model. *Phys. Rev. B*, 64:024411, Jun 2001. Referenced on pages 202 and 210.

[384] Shang-Shun Zhang, Wei Zhu, and Cristian D. Batista. Pairing from strong repulsion in triangular lattice Hubbard model. *Phys. Rev. B*, 97:140507, Apr 2018. Referenced on page 203.

[385] W. F. Brinkman and T. M. Rice. Single-Particle Excitations in Magnetic Insulators. *Phys. Rev. B*, 2:1324–1338, Sep 1970. Referenced on pages 203 and 208.

[386] Olga Petrova and Roderich Moessner. Coulomb potential $V(r) = 1/r$ problem on the Bethe lattice. *Phys. Rev. E*, 93:012115, Jan 2016. Referenced on page 208.

[387] L. Ciorciaro, T. Smolenski, I. Morera, N. Kiper, S. Hiestand, M. Kroner, Y. Zhang, K. Watanabe, T. Taniguchi, E. Demler, and A. Imamoglu. Kinetic magnetism in triangular moirématerials. *Nature*, 623(7987):509–513, 2023. Referenced on pages 214 and 218.

[388] Chenhao Jin, Emma C. Regan, Aiming Yan, M. Iqbal Bakti Utama, Danqing Wang, Sihan Zhao, Ying Qin, Sijie Yang, Zhiren Zheng, Shenyang Shi, Kenji Watanabe, Takashi Taniguchi, Sefaattin Tongay, Alex Zettl, and Feng Wang. Observation of moiréexcitons in WSe2/WS2 heterostructure superlattices. *Nature*, 567(7746):76–80, 2019. Referenced on page 216.

[389] Mit H. Naik, Emma C. Regan, Zuocheng Zhang, Yang-Hao Chan, Zhenglu Li, Danqing Wang, Yoseob Yoon, Chin Shen Ong, Wenyu Zhao, Sihan Zhao, M. Iqbal Bakti Utama, Beini Gao, Xin Wei, Mohammed Sayyad, Kentaro Yumigeta, Kenji Watanabe, Takashi Taniguchi, Sefaattin Tongay, Felipe H. da Jornada, Feng Wang, and Steven G. Louie. Intralayer charge-transfer moiréexcitons in van der Waals superlattices. *Nature*, 609(7925):52–57, 2022. Referenced on page 216.

[390] Borislav Polovnikov, Johannes Scherzer, Subhradeep Misra, Xin Huang, Christian Mohl, Zhijie Li, Jonas Göser, Jonathan Förste, Ismail Bilgin, Kenji Watanabe, Takashi Taniguchi, Alexander Högele, and Anvar S. Baimuratov. Field-Induced Hybridization of Moiré Excitons in $MoSe_2/WS_2$ Heterobilayers. *Phys. Rev. Lett.*, 132:076902, Feb 2024. Referenced on page 216.

[391] M. A. Ruderman and C. Kittel. Indirect Exchange Coupling of Nuclear Magnetic Moments by Conduction Electrons. *Phys. Rev.*, 96:99–102, Oct 1954. Referenced on page 221.

[392] Thoralf Hanisch, Burkhard Kleine, Afra Ritzl, and Erwin Müller-Hartmann. Ferromagnetism in the Hubbard model: instability of the Nagaoka state on the triangular, honeycomb and kagome lattices. *Annalen der Physik*, 507(4):303–328, 1995. Referenced on page 224.

[393] Fabian Grusdt, Eugene Demler, and Annabelle Bohrdt. Pairing of holes by confining strings in antiferromagnets, 2022. Referenced on page 224.

[394] Ian Affleck and J. Brad Marston. Large-n limit of the Heisenberg-Hubbard model: Implications for high-T_c superconductors. *Phys. Rev. B*, 37:3774–3777, Mar 1988. Referenced on page 225.

[395] Carsten Honerkamp and Walter Hofstetter. Ultracold Fermions and the SU(N) Hubbard Model. *Phys. Rev. Lett.*, 92:170403, Apr 2004. Referenced on page 225.

[396] F. F. Assaad. Phase diagram of the half-filled two-dimensional SU(N) Hubbard-Heisenberg model: A quantum Monte Carlo study. *Phys. Rev. B*, 71:075103, Feb 2005. Referenced on page 225.

[397] Michael Hermele, Victor Gurarie, and Ana Maria Rey. Mott Insulators of Ultracold Fermionic Alkaline Earth Atoms: Underconstrained Magnetism and Chiral Spin Liquid. *Phys. Rev. Lett.*, 103:135301, Sep 2009. Referenced on page 225.

[398] Andrii Sotnikov and Walter Hofstetter. Magnetic ordering of three-component ultracold fermionic mixtures in optical lattices. *Phys. Rev. A*, 89:063601, Jun 2014. Referenced on pages 225 and 226.

[399] Andrii Sotnikov. Critical entropies and magnetic-phase-diagram analysis of ultracold three-component fermionic mixtures in optical lattices. *Phys. Rev. A*, 92:023633, Aug 2015. Referenced on pages 225 and 226.

[400] Hiromasa Yanatori and Akihisa Koga. Finite-temperature phase transitions in the SU(N) Hubbard model. *Phys. Rev. B*, 94:041110, Jul 2016. Referenced on page 225.

[401] Mohsen Hafez-Torbati and Walter Hofstetter. Artificial SU(3) spin-orbit coupling and exotic Mott insulators. *Phys. Rev. B*, 98:245131, Dec 2018. Referenced on page 225.

[402] Mohsen Hafez-Torbati and Walter Hofstetter. Competing charge and magnetic order in fermionic multicomponent systems. *Phys. Rev. B*, 100:035133, Jul 2019. Referenced on page 225.

[403] Eduardo Ibarra-García-Padilla, Sohail Dasgupta, Hao-Tian Wei, Shintaro Taie, Yoshiro Takahashi, Richard T. Scalettar, and Kaden R. A. Hazzard. Universal thermodynamics of an SU(N) Fermi-Hubbard model. *Phys. Rev. A*, 104:043316, Oct 2021. Referenced on page 225.

[404] Kliment I Kugel and Daniel I Khomskii. Crystal-structure and magnetic properties of substances with orbital degeneracy. *Zh. Eksp. Teor. Fiz*, 64:1429–1439, 1973. Referenced on page 225.

[405] Y. Q. Li, Michael Ma, D. N. Shi, and F. C. Zhang. SU(4) Theory for Spin Systems with Orbital Degeneracy. *Phys. Rev. Lett.*, 81:3527–3530, Oct 1998. Referenced on page 225.

[406] Y. Tokura and N. Nagaosa. Orbital Physics in Transition-Metal Oxides. *Science*, 288(5465):462–468, 2000. Referenced on page 225.

[407] S. Doniach. The Kondo lattice and weak antiferromagnetism. *Physica B+C*, 91:231–234, 1977. Referenced on page 225.

[408] Piers Coleman. $\frac{1}{N}$ expansion for the Kondo lattice. *Phys. Rev. B*, 28:5255–5262, Nov 1983. Referenced on page 225.

[409] Alexander Cyril Hewson. *The Kondo Problem to Heavy Fermions*. Cambridge Studies in Magnetism. Cambridge University Press, 1993. Referenced on page 225.

[410] M. O. Goerbig. Electronic properties of graphene in a strong magnetic field. *Rev. Mod. Phys.*, 83:1193–1243, Nov 2011. Referenced on page 225.

[411] Xiao Yan Xu, K. T. Law, and Patrick A. Lee. Kekulé valence bond order in an extended Hubbard model on the honeycomb lattice with possible applications to twisted bilayer graphene. *Phys. Rev. B*, 98:121406, Sep 2018. Referenced on page 225.

[412] Yuan Da Liao, Jian Kang, Clara N. Breiø, Xiao Yan Xu, Han-Qing Wu, Brian M. Andersen, Rafael M. Fernandes, and Zi Yang Meng. Correlation-Induced Insulating Topological Phases at Charge Neutrality in Twisted Bilayer Graphene. *Phys. Rev. X*, 11:011014, Jan 2021. Referenced on page 225.

[413] W. M. H. Natori, R. Nutakki, R. G. Pereira, and E. C. Andrade. SU(4) Heisenberg model on the honeycomb lattice with exchange-frustrated perturbations: Implications for twistronics and Mott insulators. *Phys. Rev. B*, 100:205131, Nov 2019. Referenced on page 225.

[414] E. V. Gorelik and N. Blümer. Mott transitions in ternary flavor mixtures of ultracold fermions on optical lattices. *Phys. Rev. A*, 80:051602, Nov 2009. Referenced on page 226.

[415] Bela Bauer, Philippe Corboz, Andreas M. Läuchli, Laura Messio, Karlo Penc, Matthias Troyer, and Frédéric Mila. Three-sublattice order in the SU(3) Heisenberg model on the square and triangular lattice. *Phys. Rev. B*, 85:125116, Mar 2012. Referenced on pages 226, 227, and 228.

[416] Congjun Wu, Jiang Hu, and Shou Zhang. Exact SO(5) Symmetry in the Spin-3/2 Fermionic System. *Phys. Rev. Lett.*, 91:186402, Oct 2003. Referenced on page 226.

[417] M A Cazalilla, A F Ho, and M Ueda. Ultracold gases of ytterbium: ferromagnetism and Mott states in an SU(6) Fermi system. *New Journal of Physics*, 11(10):103033, oct 2009. Referenced on page 226.

[418] Miguel A Cazalilla and Ana Maria Rey. Ultracold Fermi gases with emergent SU(N) symmetry. *Reports on Progress in Physics*, 77(12):124401, nov 2014. Referenced on page 226.

[419] Simon Stellmer, Florian Schreck, and Thomas C. Killian. *DEGENERATE QUANTUM GASES OF STRONTIUM*, chapter Chapter 1, pages 1–80. Referenced on page 226.

[420] Martin Miranda, Ryotaro Inoue, Yuki Okuyama, Akimasa Nakamoto, and Mikio Kozuma. Site-resolved imaging of ytterbium atoms in a two-dimensional optical lattice. *Phys. Rev. A*, 91:063414, Jun 2015. Referenced on page 226.

[421] Martin Miranda, Ryotaro Inoue, Naoki Tambo, and Mikio Kozuma. Site-resolved imaging of a bosonic Mott insulator using ytterbium atoms. *Phys. Rev. A*, 96:043626, Oct 2017. Referenced on page 226.

[422] Daichi Okuno, Yoshiki Amano, Katsunari Enomoto, Nobuyuki Takei, and Yoshiro Takahashi. Schemes for nondestructive quantum gas microscopy of single atoms in an optical lattice. *New Journal of Physics*, 22(1):013041, jan 2020. Referenced on page 226.

[423] B. Ammon, M. Troyer, and Hirokazu Tsunetsugu. Effect of the three-site hopping term on the t-J model. *Phys. Rev. B*, 52:629–636, Jul 1995. Referenced on page 229.

[424] S. A. Trugman. Interaction of holes in a Hubbard antiferromagnet and high-temperature superconductivity. *Phys. Rev. B*, 37:1597–1603, Feb 1988. Referenced on page 233.

[425] A Bohrdt, F Grusdt, and M Knap. Dynamical formation of a magnetic polaron in a two-dimensional quantum antiferromagnet. *New Journal of Physics*, 22(12):123023, dec 2020. Referenced on page 238.

[426] Claudius Hubig, Annabelle Bohrdt, Michael Knap, Fabian Grusdt, and J. Ignacio Cirac. Evaluation of time-dependent correlators after a local quench in iPEPS: hole motion in the t-J model. *SciPost Phys.*, 8:021, 2020. Referenced on page 238.

[427] K. Knakkergaard Nielsen, T. Pohl, and G. M. Bruun. Nonequilibrium Hole Dynamics in Antiferromagnets: Damped Strings and Polarons. *Phys. Rev. Lett.*, 129:246601, Dec 2022. Referenced on page 238.

[428] Eduardo Ibarra-García-Padilla, Sohail Dasgupta, Hao-Tian Wei, Shintaro Taie, Yoshiro Takahashi, Richard T. Scalettar, and Kaden R. A. Hazzard. Universal thermodynamics of an SU(N) Fermi-Hubbard model. *Phys. Rev. A*, 104:043316, Oct 2021. Referenced on pages 241 and 242.

[429] Sagar Vijay, Jeongwan Haah, and Liang Fu. Fracton topological order, generalized lattice gauge theory, and duality. *Phys. Rev. B*, 94:235157, Dec 2016. Referenced on page 244.

[430] Han Ma, Ethan Lake, Xie Chen, and Michael Hermele. Fracton topological order via coupled layers. *Phys. Rev. B*, 95:245126, Jun 2017. Referenced on page 244.

[431] J Voit. One-dimensional Fermi liquids. *Reports on Progress in Physics*, 58(9):977, sep 1995. Referenced on page 244.

[432] Giuseppe Carleo, Ignacio Cirac, Kyle Cranmer, Laurent Daudet, Maria Schuld, Naftali Tishby, Leslie Vogt-Maranto, and Lenka Zdeborová. Machine learning and the physical sciences. *Rev. Mod. Phys.*, 91:045002, Dec 2019. Referenced on page 247.

[433] Juan Carrasquilla and Giacomo Torlai. How To Use Neural Networks To Investigate Quantum Many-Body Physics. *PRX Quantum*, 2:040201, Nov 2021. Referenced on page 247.

[434] Steven Johnston, Ehsan Khatami, and Richard Scalettar. A perspective on machine learning and data science for strongly correlated electron problems. *Carbon Trends*, 9:100231, 2022. Referenced on page 247.

[435] Anna Dawid, Julian Arnold, Borja Requena, Alexander Gresch, Marcin Płodzień, Kaelan Donatella, Kim A. Nicoli, Paolo Stornati, Rouven Koch, Miriam Büttner, Robert Okuła, Gorka Muñoz-Gil, Rodrigo A. Vargas-Hernández, Alba Cervera-Lierta, Juan Carrasquilla, Vedran Dunjko, Marylou Gabrié, Patrick Huembeli, Evert van Nieuwenburg, Filippo Vicentini, Lei Wang, Sebastian J. Wetzel, Giuseppe Carleo, Eliška Greplová, Roman Krems, Florian Marquardt, Michał Tomza, Maciej Lewenstein, and Alexandre Dauphin. Modern applications of machine learning in quantum sciences, 2022. Referenced on page 247.

[436] Cole Miles, Annabelle Bohrdt, Ruihan Wu, Christie Chiu, Muqing Xu, Geoffrey Ji, Markus Greiner, Kilian Q. Weinberger, Eugene Demler, and Eun-Ah Kim. Correlator convolutional neural networks as an interpretable architecture for image-like quantum matter data. *Nature Communications*, 12(1):3905, 2021. Referenced on pages 247, 248, 250, 252, and 253.

[437] Cole Miles, Rhine Samajdar, Sepehr Ebadi, Tout T. Wang, Hannes Pichler, Subir Sachdev, Mikhail D. Lukin, Markus Greiner, Kilian Q. Weinberger, and Eun-Ah Kim. Machine learning discovery of new phases in programmable quantum simulator snapshots. *Phys. Rev. Res.*, 5:013026, Jan 2023. Referenced on pages 247 and 248.

[438] Alexander Impertro, Julian F. Wienand, Sophie Häfele, Hendrik von Raven, Scott Hubele, Till Klostermann, Cesar R. Cabrera, Immanuel Bloch, and Monika Aidelsburger. An unsupervised deep learning algorithm for single-site reconstruction in quantum gas microscopes, 2022. Referenced on page 248.

[439] Junwei Liu, Yang Qi, Zi Yang Meng, and Liang Fu. Self-learning Monte Carlo method. *Phys. Rev. B*, 95:041101, Jan 2017. Referenced on page 248.

[440] Li Huang and Lei Wang. Accelerated Monte Carlo simulations with restricted Boltzmann machines. *Phys. Rev. B*, 95:035105, Jan 2017. Referenced on page 248.

[441] E. M. Inack, G. E. Santoro, L. Dell'Anna, and S. Pilati. Projective quantum Monte Carlo simulations guided by unrestricted neural network states. *Phys. Rev. B*, 98:235145, Dec 2018. Referenced on page 248.

[442] B. McNaughton, M. V. Milošević, A. Perali, and S. Pilati. Boosting Monte Carlo simulations of spin glasses using autoregressive neural networks. *Phys. Rev. E*, 101:053312, May 2020. Referenced on page 248.

[443] Giuseppe Carleo and Matthias Troyer. Solving the quantum many-body problem with artificial neural networks. *Science*, 355(6325):602–606, 2017. Referenced on page 248.

[444] Roger G. Melko, Giuseppe Carleo, Juan Carrasquilla, and J. Ignacio Cirac. Restricted Boltzmann machines in quantum physics. *Nature Physics*, 15(9):887–892, 2019. Referenced on page 248.

[445] Zhih-Ahn Jia, Biao Yi, Rui Zhai, Yu-Chun Wu, Guang-Can Guo, and Guo-Ping Guo. Quantum Neural Network States: A Brief Review of Methods and Applications. *Advanced Quantum Technologies*, 2(7-8):1800077, 2019. Referenced on page 248.

[446] Evert P. L. van Nieuwenburg, Ye-Hua Liu, and Sebastian D. Huber. Learning phase transitions by confusion. *Nature Physics*, 13(5):435–439, 2017. Referenced on pages 248, 249, 250, and 252.

[447] Yi-Ting Hsu, Xiao Li, Dong-Ling Deng, and S. Das Sarma. Machine Learning Many-Body Localization: Search for the Elusive Nonergodic Metal. *Phys. Rev. Lett.*, 121:245701, Dec 2018. Referenced on page 248.

[448] Korbinian Kottmann, Patrick Huembeli, Maciej Lewenstein, and Antonio Acín. Unsupervised Phase Discovery with Deep Anomaly Detection. *Phys. Rev. Lett.*, 125:170603, Oct 2020. Referenced on pages 248 and 264.

[449] Daniele Contessi, Elisa Ricci, Alessio Recati, and Matteo Rizzi. Detection of Berezinskii-Kosterlitz-Thouless transition via Generative Adversarial Networks. *SciPost Phys.*, 12:107, 2022. Referenced on pages 248, 264, and 265.

[450] Juan Carrasquilla and Roger G. Melko. Machine learning phases of matter. *Nature Physics*, 13(5):431–434, 2017. Referenced on page 248.

[451] Lei Wang. Discovering phase transitions with unsupervised learning. *Phys. Rev. B*, 94:195105, Nov 2016. Referenced on page 248.

[452] Kelvin Ch'ng, Juan Carrasquilla, Roger G. Melko, and Ehsan Khatami. Machine Learning Phases of Strongly Correlated Fermions. *Phys. Rev. X*, 7:031038, Aug 2017. Referenced on page 248.

[453] Peter Broecker, Juan Carrasquilla, Roger G. Melko, and Simon Trebst. Machine learning quantum phases of matter beyond the fermion sign problem. *Scientific Reports*, 7(1):8823, 2017. Referenced on page 248.

[454] Kelvin Ch'ng, Nick Vazquez, and Ehsan Khatami. Unsupervised machine learning account of magnetic transitions in the Hubbard model. *Phys. Rev. E*, 97:013306, Jan 2018. Referenced on page 248.

[455] Jonas Greitemann, Ke Liu, and Lode Pollet. Probing hidden spin order with interpretable machine learning. *Phys. Rev. B*, 99:060404, Feb 2019. Referenced on page 248.

[456] Yi Zhang, A. Mesaros, K. Fujita, S. D. Edkins, M. H. Hamidian, K. Ch'ng, H. Eisaki, S. Uchida, J. C. Séamus Davis, Ehsan Khatami, and Eun-Ah Kim. Machine learning in electronic-quantum-matter imaging experiments. *Nature*, 570(7762):484–490, 2019. Referenced on page 248.

[457] Benno S. Rem, Niklas Käming, Matthias Tarnowski, Luca Asteria, Nick Fläschner, Christoph Becker, Klaus Sengstock, and Christof Weitenberg. Identifying quantum phase transitions using artificial neural networks on experimental data. *Nature Physics*, 15(9):917–920, 2019. Referenced on page 248.

[458] Ehsan Khatami, Elmer Guardado-Sanchez, Benjamin M. Spar, Juan Felipe Carrasquilla, Waseem S. Bakr, and Richard T. Scalettar. Visualizing strange metallic correlations in the two-dimensional Fermi-Hubbard model with artificial intelligence. *Phys. Rev. A*, 102:033326, Sep 2020. Referenced on page 248.

[459] Pedro Ponte and Roger G. Melko. Kernel methods for interpretable machine learning of order parameters. *Phys. Rev. B*, 96:205146, Nov 2017. Referenced on page 248.

[460] Ke Liu, Jonas Greitemann, and Lode Pollet. Learning multiple order parameters with interpretable machines. *Phys. Rev. B*, 99:104410, Mar 2019. Referenced on page 248.

[461] Wei Zhang, Lei Wang, and Ziqiang Wang. Interpretable machine learning study of the many-body localization transition in disordered quantum Ising spin chains. *Phys. Rev. B*, 99:054208, Feb 2019. Referenced on page 248.

[462] Philippe Suchsland and Stefan Wessel. Parameter diagnostics of phases and phase transition learning by neural networks. *Phys. Rev. B*, 97:174435, May 2018. Referenced on page 248.

[463] Yi Zhang, Paul Ginsparg, and Eun-Ah Kim. Interpreting machine learning of topological quantum phase transitions. *Phys. Rev. Res.*, 2:023283, Jun 2020. Referenced on page 248.

[464] Sebastian J. Wetzel and Manuel Scherzer. Machine learning of explicit order parameters: From the Ising model to SU(2) lattice gauge theory. *Phys. Rev. B*, 96:184410, Nov 2017. Referenced on page 248.

[465] Sebastian J. Wetzel, Roger G. Melko, Joseph Scott, Maysum Panju, and Vijay Ganesh. Discovering symmetry invariants and conserved quantities by interpreting siamese neural networks. *Phys. Rev. Res.*, 2:033499, Sep 2020. Referenced on page 248.

[466] Anna Dawid, Patrick Huembeli, Michal Tomza, Maciej Lewenstein, and Alexandre Dauphin. Phase detection with neural networks: interpreting the black box. *New Journal of Physics*, 22(11):115001, nov 2020. Referenced on page 248.

[467] Anna Dawid, Patrick Huembeli, Michał Tomza, Maciej Lewenstein, and Alexandre Dauphin. Hessian-based toolbox for reliable and interpretable machine learning in physics. *Machine Learning: Science and Technology*, 3(1):015002, nov 2021. Referenced on page 248.

[468] Julian Arnold, Frank Schäfer, Martin Žonda, and Axel U. J. Lode. Interpretable and unsupervised phase classification. *Phys. Rev. Res.*, 3:033052, Jul 2021. Referenced on page 248.

[469] Julian Arnold and Frank Schäfer. Replacing Neural Networks by Optimal Analytical Predictors for the Detection of Phase Transitions. *Phys. Rev. X*, 12:031044, Sep 2022. Referenced on page 248.

[470] M. Endres, M. Cheneau, T. Fukuhara, C. Weitenberg, P. Schauß, C. Gross, L. Mazza, M. C. Bañuls, L. Pollet, I. Bloch, and S. Kuhr. Observation of Correlated Particle-Hole Pairs and String Order in Low-Dimensional Mott Insulators. *Science*, 334(6053):200–203, 2011. Referenced on page 248.

[471] Fabio Boschini, Marta Zonno, Elia Razzoli, Ryan P. Day, Matteo Michiardi, Berend Zwartsenberg, Pascal Nigge, Michael Schneider, Eduardo H. da Silva Neto, Andreas Erb, Sergey

Zhdanovich, Arthur K. Mills, Giorgio Levy, Claudio Giannetti, David J. Jones, and Andrea Damascelli. Emergence of pseudogap from short-range spin-correlations in electron-doped cuprates. *npj Quantum Materials*, 5(1):6, 2020. Referenced on page 248.

[472] Miloje S. Makivić and Hong-Qiang Ding. Two-dimensional spin-1/2 Heisenberg antiferromagnet: A quantum Monte Carlo study. *Phys. Rev. B*, 43:3562–3574, Feb 1991. Referenced on pages 248, 251, and 252.

[473] Thereza Paiva, Richard Scalettar, Mohit Randeria, and Nandini Trivedi. Fermions in 2D Optical Lattices: Temperature and Entropy Scales for Observing Antiferromagnetism and Superfluidity. *Phys. Rev. Lett.*, 104:066406, Feb 2010. Referenced on pages 248 and 251.

[474] Chisa Hotta and Kenichi Asano. Magnetic susceptibility of quantum spin systems calculated by sine square deformation: One-dimensional, square lattice, and kagome lattice Heisenberg antiferromagnets. *Phys. Rev. B*, 98:140405, Oct 2018. Referenced on pages 248 and 251.

[475] S. R. White, D. J. Scalapino, R. L. Sugar, E. Y. Loh, J. E. Gubernatis, and R. T. Scalettar. Numerical study of the two-dimensional Hubbard model. *Phys. Rev. B*, 40:506–516, Jul 1989. Referenced on pages 249 and 251.

[476] A. Moreo. Magnetic susceptibility of the two-dimensional Hubbard model. *Phys. Rev. B*, 48:3380–3382, Aug 1993. Referenced on page 249.

[477] G. Gomez-Santos, J. D. Joannopoulos, and J. W. Negele. Monte Carlo study of the quantum spin-(1/2 Heisenberg antiferromagnet on the square lattice. *Phys. Rev. B*, 39:4435–4443, Mar 1989. Referenced on pages 249 and 252.

[478] J. Jaklič and P. Prelovšek. Thermodynamic Properties of the Planar $t - J$ Model. *Phys. Rev. Lett.*, 77:892–895, Jul 1996. Referenced on pages 249 and 252.

[479] Daniel Duffy and Adriana Moreo. Specific heat of the two-dimensional Hubbard model. *Phys. Rev. B*, 55:12918–12924, May 1997. Referenced on pages 249 and 252.

[480] Anders W. Sandvik and Juhani Kurkijärvi. Quantum Monte Carlo simulation method for spin systems. *Phys. Rev. B*, 43:5950–5961, Mar 1991. Referenced on page 251.

[481] Anders W. Sandvik. Stochastic series expansion method with operator-loop update. *Phys. Rev. B*, 59:R14157–R14160, Jun 1999. Referenced on page 251.

[482] Yves Noat, Alain Mauger, Minoru Nohara, Hiroshi Eisaki, Shigeyuki Ishida, and William Sacks. Cuprates phase diagram deduced from magnetic susceptibility: What is the 'true' pseudogap line? *Solid State Communications*, 348-349:114689, 2022. Referenced on page 251.

[483] Ashish Vaswani, Noam Shazeer, Niki Parmar, Jakob Uszkoreit, Llion Jones, Aidan N Gomez, Ł ukasz Kaiser, and Illia Polosukhin. Attention is All you Need. In I. Guyon,

U. Von Luxburg, S. Bengio, H. Wallach, R. Fergus, S. Vishwanathan, and R. Garnett, editors, *Advances in Neural Information Processing Systems*, volume 30. Curran Associates, Inc., 2017. Referenced on pages 261 and 262.

[484] Alex Sherstinsky. Fundamentals of Recurrent Neural Network (RNN) and Long Short-Term Memory (LSTM) network. *Physica D: Nonlinear Phenomena*, 404:132306, 2020. Referenced on page 261.

[485] Alexey Dosovitskiy, Lucas Beyer, Alexander Kolesnikov, Dirk Weissenborn, Xiaohua Zhai, Thomas Unterthiner, Mostafa Dehghani, Matthias Minderer, Georg Heigold, Sylvain Gelly, Jakob Uszkoreit, and Neil Houlsby. An Image is Worth 16x16 Words: Transformers for Image Recognition at Scale, 2020. Referenced on pages 261 and 262.

[486] Yuan-Hang Zhang and Massimiliano Di Ventra. Transformer Quantum State: A Multi-Purpose Model for Quantum Many-Body Problems, 2022. Referenced on page 261.

[487] Luciano Loris Viteritti, Riccardo Rende, and Federico Becca. Transformer variational wave functions for frustrated quantum spin systems, 2022. Referenced on page 261.

[488] Riccardo Rende, Federica Gerace, Alessandro Laio, and Sebastian Goldt. Optimal inference of a generalised Potts model by single-layer transformers with factored attention, 2023. Referenced on page 261.

[489] Ye-Hua Liu and Evert P. L. van Nieuwenburg. Discriminative Cooperative Networks for Detecting Phase Transitions. *Phys. Rev. Lett.*, 120:176401, Apr 2018. Referenced on page 268.

[490] Tameem Albash and Daniel A. Lidar. Adiabatic quantum computation. *Rev. Mod. Phys.*, 90:015002, Jan 2018. Referenced on pages 272 and 288.

[491] S. Kirkpatrick, C. D. Gelatt, and M. P. Vecchi. Optimization by Simulated Annealing. *Science*, 220(4598):671–680, 1983. Referenced on page 272.

[492] Tadashi Kadowaki and Hidetoshi Nishimori. Quantum annealing in the transverse Ising model. *Phys. Rev. E*, 58:5355–5363, Nov 1998. Referenced on page 272.

[493] J. Brooke, D. Bitko, T. F. Rosenbaum, and G. Aeppli. Quantum Annealing of a Disordered Magnet. *Science*, 284(5415):779–781, 1999. Referenced on page 272.

[494] Edward Farhi, Jeffrey Goldstone, Sam Gutmann, and Michael Sipser. Quantum Computation by Adiabatic Evolution, 2000. Referenced on page 272.

[495] Roman Martoňák, Giuseppe E. Santoro, and Erio Tosatti. Quantum annealing by the path-integral Monte Carlo method: The two-dimensional random Ising model. *Phys. Rev. B*, 66:094203, Sep 2002. Referenced on page 272.

[496] Tadashi Kadowaki. Study of Optimization Problems by Quantum Annealing, 2002. Referenced on page 272.

[497] Edward Farhi, Jeffrey Goldstone, and Sam Gutmann. Quantum Adiabatic Evolution Algorithms with Different Paths, 2002. Referenced on page 272.

[498] Giuseppe E. Santoro, Roman Martoňák, Erio Tosatti, and Roberto Car. Theory of Quantum Annealing of an Ising Spin Glass. *Science*, 295(5564):2427–2430, 2002. Referenced on page 272.

[499] Giuseppe E Santoro and Erio Tosatti. Optimization using quantum mechanics: quantum annealing through adiabatic evolution. *Journal of Physics A: Mathematical and General*, 39(36):R393, aug 2006. Referenced on page 272.

[500] Arnab Das and Bikas K. Chakrabarti. Colloquium: Quantum annealing and analog quantum computation. *Rev. Mod. Phys.*, 80:1061–1081, Sep 2008. Referenced on page 272.

[501] P. Ray, B. K. Chakrabarti, and Arunava Chakrabarti. Sherrington-Kirkpatrick model in a transverse field: Absence of replica symmetry breaking due to quantum fluctuations. *Phys. Rev. B*, 39:11828–11832, Jun 1989. Referenced on page 272.

[502] Vasil S. Denchev, Sergio Boixo, Sergei V. Isakov, Nan Ding, Ryan Babbush, Vadim Smelyanskiy, John Martinis, and Hartmut Neven. What is the Computational Value of Finite-Range Tunneling? *Phys. Rev. X*, 6:031015, Aug 2016. Referenced on pages 272, 273, and 274.

[503] M. Born and V. Fock. Beweis des Adiabatensatzes. *Zeitschrift für Physik*, 51(3):165–180, 1928. Referenced on page 273.

[504] Artem Rakcheev and Andreas M. Läuchli. Diabatic quantum and classical annealing of the Sherrington-Kirkpatrick model. *Phys. Rev. A*, 107:062602, Jun 2023. Referenced on pages 273 and 281.

[505] Leo Zhou, Sheng-Tao Wang, Soonwon Choi, Hannes Pichler, and Mikhail D. Lukin. Quantum Approximate Optimization Algorithm: Performance, Mechanism, and Implementation on Near-Term Devices. *Phys. Rev. X*, 10:021067, Jun 2020. Referenced on pages 273 and 281.

[506] Philipp Hauke, Helmut G Katzgraber, Wolfgang Lechner, Hidetoshi Nishimori, and William D Oliver. Perspectives of quantum annealing: methods and implementations. *Reports on Progress in Physics*, 83(5):054401, 2020. Referenced on page 273.

[507] M. W. Johnson, M. H. S. Amin, S. Gildert, T. Lanting, F. Hamze, N. Dickson, R. Harris, A. J. Berkley, J. Johansson, P. Bunyk, E. M. Chapple, C. Enderud, J. P. Hilton, K. Karimi, E. Ladizinsky, N. Ladizinsky, T. Oh, I. Perminov, C. Rich, M. C. Thom, E. Tolkacheva, C. J. S. Truncik, S. Uchaikin, J. Wang, B. Wilson, and G. Rose. Quantum annealing with manufactured spins. *Nature*, 473(7346):194–198, 2011. Referenced on page 273.

[508] N G Dickson, M W Johnson, M H Amin, R. Harris, F. Altomare, A J Berkley, P. Bunyk, J. Cai, E M Chapple, P. Chavez, F. Cioata, T. Cirip, P. deBuen, M. Drew-Brook, C. Enderud,

S. Gildert, F. Hamze, J P Hilton, E. Hoskinson, K. Karimi, E. Ladizinsky, N. Ladizinsky, T. Lanting, T. Mahon, R. Neufeld, T. Oh, I. Perminov, C. Petroff, A. Przybysz, C. Rich, P. Spear, A. Tcaciuc, M C Thom, E. Tolkacheva, S. Uchaikin, J. Wang, A B Wilson, Z. Merali, and G. Rose. Thermally assisted quantum annealing of a 16-qubit problem. *Nature Communications*, 4(1):1903, 2013. Referenced on page 273.

[509] Steven J. Weber, Gabriel O. Samach, David Hover, Simon Gustavsson, David K. Kim, Alexander Melville, Danna Rosenberg, Adam P. Sears, Fei Yan, Jonilyn L. Yoder, William D. Oliver, and Andrew J. Kerman. Coherent Coupled Qubits for Quantum Annealing. *Phys. Rev. Appl.*, 8:014004, Jul 2017. Referenced on page 273.

[510] Andrew D. King, Sei Suzuki, Jack Raymond, Alex Zucca, Trevor Lanting, Fabio Altomare, Andrew J. Berkley, Sara Ejtemaee, Emile Hoskinson, Shuiyuan Huang, Eric Ladizinsky, Allison J. R. MacDonald, Gaelen Marsden, Travis Oh, Gabriel Poulin-Lamarre, Mauricio Reis, Chris Rich, Yuki Sato, Jed D. Whittaker, Jason Yao, Richard Harris, Daniel A. Lidar, Hidetoshi Nishimori, and Mohammad H. Amin. Coherent quantum annealing in a programmable 2,000 qubit Ising chain. *Nature Physics*, 18(11):1324–1328, 2022. Referenced on page 273.

[511] Dennis Willsch, Madita Willsch, Carlos D. Gonzalez Calaza, Fengping Jin, Hans De Raedt, Marika Svensson, and Kristel Michielsen. Benchmarking Advantage and D-Wave 2000Q quantum annealers with exact cover problems. *Quantum Information Processing*, 21(4):141, 2022. Referenced on page 273.

[512] Andrew D. King, Jack Raymond, Trevor Lanting, Richard Harris, Alex Zucca, Fabio Altomare, Andrew J. Berkley, Kelly Boothby, Sara Ejtemaee, Colin Enderud, Emile Hoskinson, Shuiyuan Huang, Eric Ladizinsky, Allison J. R. MacDonald, Gaelen Marsden, Reza Molavi, Travis Oh, Gabriel Poulin-Lamarre, Mauricio Reis, Chris Rich, Yuki Sato, Nicholas Tsai, Mark Volkmann, Jed D. Whittaker, Jason Yao, Anders W. Sandvik, and Mohammad H. Amin. Quantum critical dynamics in a 5,000-qubit programmable spin glass. *Nature*, 617(7959):61–66, 2023. Referenced on page 273.

[513] A. W. Glaetzle, R. M. W. van Bijnen, P. Zoller, and W. Lechner. A coherent quantum annealer with Rydberg atoms. *Nature Communications*, 8(1):15813, 2017. Referenced on page 273.

[514] S. Ebadi, A. Keesling, M. Cain, T. T. Wang, H. Levine, D. Bluvstein, G. Semeghini, A. Omran, J.-G. Liu, R. Samajdar, X.-Z. Luo, B. Nash, X. Gao, B. Barak, E. Farhi, S. Sachdev, N. Gemelke, L. Zhou, S. Choi, H. Pichler, S.-T. Wang, M. Greiner, V. Vuletić, and M. D. Lukin. Quantum optimization of maximum independent set using Rydberg atom arrays. *Science*, 376(6598):1209–1215, 2022. Referenced on page 273.

[515] R. Islam, C. Senko, W. C. Campbell, S. Korenblit, J. Smith, A. Lee, E. E. Edwards, C.-C. J. Wang, J. K. Freericks, and C. Monroe. Emergence and Frustration of Magnetism with

Variable-Range Interactions in a Quantum Simulator. *Science*, 340(6132):583–587, 2013. Referenced on page 273.

[516] P. Richerme, C. Senko, J. Smith, A. Lee, S. Korenblit, and C. Monroe. Experimental performance of a quantum simulator: Optimizing adiabatic evolution and identifying many-body ground states. *Phys. Rev. A*, 88:012334, Jul 2013. Referenced on page 273.

[517] David Landau and Kurt Binder. *A guide to Monte Carlo simulations in statistical physics*. Cambridge university press, 2021. Referenced on page 273.

[518] Sergei V. Isakov, Guglielmo Mazzola, Vadim N. Smelyanskiy, Zhang Jiang, Sergio Boixo, Hartmut Neven, and Matthias Troyer. Understanding Quantum Tunneling through Quantum Monte Carlo Simulations. *Phys. Rev. Lett.*, 117:180402, Oct 2016. Referenced on page 274.

[519] Zhang Jiang, Vadim N. Smelyanskiy, Sergei V. Isakov, Sergio Boixo, Guglielmo Mazzola, Matthias Troyer, and Hartmut Neven. Scaling analysis and instantons for thermally assisted tunneling and quantum Monte Carlo simulations. *Phys. Rev. A*, 95:012322, Jan 2017. Referenced on page 274.

[520] Tameem Albash. Role of nonstoquastic catalysts in quantum adiabatic optimization. *Phys. Rev. A*, 99:042334, Apr 2019. Referenced on page 274.

[521] Elizabeth Crosson, Edward Farhi, Cedric Yen-Yu Lin, Han-Hsuan Lin, and Peter Shor. Different Strategies for Optimization Using the Quantum Adiabatic Algorithm, 2014. Referenced on pages 274 and 277.

[522] Layla Hormozi, Ethan W. Brown, Giuseppe Carleo, and Matthias Troyer. Nonstoquastic Hamiltonians and quantum annealing of an Ising spin glass. *Phys. Rev. B*, 95:184416, May 2017. Referenced on pages 274, 277, and 282.

[523] Yuya Seki and Hidetoshi Nishimori. Quantum annealing with antiferromagnetic fluctuations. *Phys. Rev. E*, 85:051112, May 2012. Referenced on page 274.

[524] Beatriz Seoane and Hidetoshi Nishimori. Many-body transverse interactions in the quantum annealing of the p-spin ferromagnet. *Journal of Physics A: Mathematical and Theoretical*, 45(43):435301, 2012. Referenced on page 274.

[525] Yuya Seki and Hidetoshi Nishimori. Quantum annealing with antiferromagnetic transverse interactions for the Hopfield model. *Journal of Physics A: Mathematical and Theoretical*, 48(33):335301, 2015. Referenced on page 274.

[526] Hidetoshi Nishimori and Kabuki Takada. Exponential Enhancement of the Efficiency of Quantum Annealing by Non-Stoquastic Hamiltonians. *Frontiers in ICT*, 4, February 2017. Referenced on page 274.

[527] Itay Hen and Federico M. Spedalieri. Quantum Annealing for Constrained Optimization. *Phys. Rev. Appl.*, 5:034007, Mar 2016. Referenced on page 274.

[528] Itay Hen and Marcelo S. Sarandy. Driver Hamiltonians for constrained optimization in quantum annealing. *Phys. Rev. A*, 93:062312, Jun 2016. Referenced on page 274.

[529] Dolev Bluvstein, Harry Levine, Giulia Semeghini, Tout T. Wang, Sepehr Ebadi, Marcin Kalinowski, Alexander Keesling, Nishad Maskara, Hannes Pichler, Markus Greiner, Vladan Vuletić, and Mikhail D. Lukin. A quantum processor based on coherent transport of entangled atom arrays. *Nature*, 604(7906):451–456, 2022. Referenced on page 274.

[530] Colin D Bruzewicz, John Chiaverini, Robert McConnell, and Jeremy M Sage. Trapped-ion quantum computing: Progress and challenges. *Applied Physics Reviews*, 6(2), 2019. Referenced on page 274.

[531] Subir Sachdev and Jinwu Ye. Gapless spin-fluid ground state in a random quantum Heisenberg magnet. *Phys. Rev. Lett.*, 70:3339–3342, May 1993. Referenced on page 274.

[532] A. Kitaev. A simple model of quantum holography, KITP strings seminar and Entanglement 2015 program (Feb. 12, April 7, and May 27, 2015). Referenced on page 274.

[533] Yasuhiro Sekino and L. Susskind. Fast scramblers. *Journal of High Energy Physics*, 2008(10):065, 2008. Referenced on page 275.

[534] Stephen H. Shenker and Douglas Stanford. Black holes and the butterfly effect. *Journal of High Energy Physics*, 2014(3):67, 2014. Referenced on page 275.

[535] Pavan Hosur, Xiao-Liang Qi, Daniel A. Roberts, and Beni Yoshida. Chaos in quantum channels. *Journal of High Energy Physics*, 2016(2):4, 2016. Referenced on page 275.

[536] Juan Maldacena, Stephen H. Shenker, and Douglas Stanford. A bound on chaos. *Journal of High Energy Physics*, 2016(8):106, 2016. Referenced on page 275.

[537] Bryce Kobrin, Zhenbin Yang, Gregory D. Kahanamoku-Meyer, Christopher T. Olund, Joel E. Moore, Douglas Stanford, and Norman Y. Yao. Many-Body Chaos in the Sachdev-Ye-Kitaev Model. *Phys. Rev. Lett.*, 126:030602, Jan 2021. Referenced on page 275.

[538] Debanjan Chowdhury, Antoine Georges, Olivier Parcollet, and Subir Sachdev. Sachdev-Ye-Kitaev models and beyond: Window into non-Fermi liquids. *Rev. Mod. Phys.*, 94:035004, Sep 2022. Referenced on page 275.

[539] Subir Sachdev. Bekenstein-Hawking Entropy and Strange Metals. *Phys. Rev. X*, 5:041025, Nov 2015. Referenced on page 275.

[540] G.'t Hooft. A planar diagram theory for strong interactions. *Nuclear Physics B*, 72(3):461–473, 1974. Referenced on page 275.

[541] Ippei Danshita, Masanori Hanada, and Masaki Tezuka. Creating and probing the Sachdev–Ye–Kitaev model with ultracold gases: Towards experimental studies of quantum gravity. *Progress of Theoretical and Experimental Physics*, 2017(8):083I01, August 2017. Referenced on page 275.

[542] Zhihuang Luo, Yi-Zhuang You, Jun Li, Chao-Ming Jian, Dawei Lu, Cenke Xu, Bei Zeng, and Raymond Laflamme. Quantum simulation of the non-fermi-liquid state of Sachdev-Ye-Kitaev model. *npj Quantum Information*, 5(1):53, 2019. Referenced on page 275.

[543] Daniel Jafferis, Alexander Zlokapa, Joseph D. Lykken, David K. Kolchmeyer, Samantha I. Davis, Nikolai Lauk, Hartmut Neven, and Maria Spiropulu. Traversable wormhole dynamics on a quantum processor. *Nature*, 612(7938):51–55, 2022. Referenced on page 275.

[544] Muhammad Asaduzzaman, Raghav G. Jha, and Bharath Sambasivam. Sachdev-Ye-Kitaev model on a noisy quantum computer. *Phys. Rev. D*, 109:105002, May 2024. Referenced on pages 275 and 291.

[545] P. Jordan and E. Wigner. Über das Paulische Äquivalenzverbot. *Zeitschrift für Physik*, 47(9):631–651, 1928. Referenced on page 275.

[546] Sergey B. Bravyi and Alexei Yu. Kitaev. Fermionic Quantum Computation. *Annals of Physics*, 298(1):210–226, 2002. Referenced on page 275.

[547] Masanori Hanada, Antal Jevicki, Xianlong Liu, Enrico Rinaldi, and Masaki Tezuka. A model of randomly-coupled Pauli spins. *Journal of High Energy Physics*, 2024(5):280, 2024. Referenced on pages 275, 276, and 290.

[548] Brian Swingle and Mike Winer. Bosonic model of quantum holography. *Phys. Rev. B*, 109:094206, Mar 2024. Referenced on pages 275, 276, and 285.

[549] Micha Berkooz, Prithvi Narayan, and Joan Simón. Chord diagrams, exact correlators in spin glasses and black hole bulk reconstruction. *Journal of High Energy Physics*, 2018(8):192, 2018. Referenced on pages 275 and 290.

[550] Micha Berkooz, Mikhail Isachenkov, Vladimir Narovlansky, and Genis Torrents. Towards a full solution of the large N double-scaled SYK model. *Journal of High Energy Physics*, 2019(3):79, 2019. Referenced on pages 275 and 290.

[551] C. L. Baldwin and B. Swingle. Quenched vs Annealed: Glassiness from SK to SYK. *Phys. Rev. X*, 10:031026, Aug 2020. Referenced on pages 275 and 290.

[552] Johan Hastad. Some optimal inapproximability results. *J. ACM*, 48(4):798–859, jul 2001. Referenced on page 280.

[553] Michel X. Goemans and David P. Williamson. Improved approximation algorithms for maximum cut and satisfiability problems using semidefinite programming. *J. ACM*, 42(6):1115–1145, nov 1995. Referenced on page 280.

[554] Eran Halperin, Dror Livnat, and Uri Zwick. MAX CUT in cubic graphs. *Journal of Algorithms*, 53(2):169–185, 2004. Referenced on page 280.

[555] Edward Farhi, Jeffrey Goldstone, and Sam Gutmann. A Quantum Approximate Optimization Algorithm, 2014. Referenced on page 280.

[556] Edward Farhi and Aram W Harrow. Quantum Supremacy through the Quantum Approximate Optimization Algorithm, 2019. Referenced on page 280.

[557] Phillip Weinberg and Marin Bukov. QuSpin: a Python package for dynamics and exact diagonalisation of quantum many body systems part I: spin chains. *SciPost Phys.*, 2:003, 2017. Referenced on page 282.

[558] Phillip Weinberg and Marin Bukov. QuSpin: a Python package for dynamics and exact diagonalisation of quantum many body systems. Part II: bosons, fermions and higher spins. *SciPost Phys.*, 7:020, 2019. Referenced on page 282.

[559] Shenglong Xu, Leonard Susskind, Yuan Su, and Brian Swingle. A Sparse Model of Quantum Holography, 2020. Referenced on pages 286 and 290.

[560] Antonio M. García-García, Yiyang Jia, Dario Rosa, and Jacobus J. M. Verbaarschot. Sparse Sachdev-Ye-Kitaev model, quantum chaos, and gravity duals. *Phys. Rev. D*, 103:106002, May 2021. Referenced on pages 286 and 290.

[561] Patrick Orman, Hrant Gharibyan, and John Preskill. Quantum chaos in the sparse SYK model, 2024. Referenced on pages 286 and 290.

[562] Hanteng Wang, Hsiu-Chung Yeh, and Alex Kamenev. Many-body localization enables iterative quantum optimization. *Nature Communications*, 13(1):5503, 2022. Referenced on page 287.

[563] Hao Zhang, Kelly Boothby, and Alex Kamenev. Cyclic Quantum Annealing: Searching for Deep Low-Energy States in 5000-Qubit Spin Glass, 2024. Referenced on page 287.

[564] A. Boehmer. Binary pulse compression codes. *IEEE Transactions on Information Theory*, 13(2):156–167, 1967. Referenced on page 288.

[565] M. Schroeder. Synthesis of low-peak-factor signals and binary sequences with low autocorrelation (Corresp.). *IEEE Transactions on Information Theory*, 16(1):85–89, 1970. Referenced on page 288.

[566] M. Golay. A class of finite binary sequences with alternate auto-correlation values equal to zero (Corresp.). *IEEE Transactions on Information Theory*, 18(3):449–450, 1972. Referenced on page 288.

[567] Tom Packebusch and Stephan Mertens. Low autocorrelation binary sequences. *Journal of Physics A: Mathematical and Theoretical*, 49(16):165001, mar 2016. Referenced on page 288.

[568] Irwin I. Shapiro, Gordon H. Pettengill, Michael E. Ash, Melvin L. Stone, William B. Smith, Richard P. Ingalls, and Richard A. Brockelman. Fourth Test of General Relativity: Preliminary Results. *Phys. Rev. Lett.*, 20:1265–1269, May 1968. Referenced on page 288.

[569] Werner Krauth and Marc Mézard. Aging without disorder on long time scales. *Zeitschrift für Physik B Condensed Matter*, 97(1):127–131, 1995. Referenced on page 288.

[570] J.P. Bouchaud and M. Mézard. Self induced quenched disorder: a model for the glass transition. *J. Phys. I France*, 4(8):1109–1114, 1994. Referenced on page 288.

[571] E Marinari, G Parisi, and F Ritort. Replica field theory for deterministic models: I. Binary sequences with low autocorrelation. *Journal of Physics A: Mathematical and General*, 27(23):7615–7645, December 1994. Referenced on page 288.

[572] Ruslan Shaydulin, Changhao Li, Shouvanik Chakrabarti, Matthew DeCross, Dylan Herman, Niraj Kumar, Jeffrey Larson, Danylo Lykov, Pierre Minssen, Yue Sun, Yuri Alexeev, Joan M. Dreiling, John P. Gaebler, Thomas M. Gatterman, Justin A. Gerber, Kevin Gilmore, Dan Gresh, Nathan Hewitt, Chandler V. Horst, Shaohan Hu, Jacob Johansen, Mitchell Matheny, Tanner Mengle, Michael Mills, Steven A. Moses, Brian Neyenhuis, Peter Siegfried, Romina Yalovetzky, and Marco Pistoia. Evidence of scaling advantage for the quantum approximate optimization algorithm on a classically intractable problem. *Science Advances*, 10(22):eadm6761, 2024. Referenced on page 288.

[573] Ewout van den Berg and Kristan Temme. Circuit optimization of Hamiltonian simulation by simultaneous diagonalization of Pauli clusters. *Quantum*, 4:322, September 2020. Referenced on page 291.

[574] Kaiwen Gui, Teague Tomesh, Pranav Gokhale, Yunong Shi, Frederic T. Chong, Margaret Martonosi, and Martin Suchara. Term Grouping and Travelling Salesperson for Digital Quantum Simulation, 2021. Referenced on pages 291 and 292.

[575] Aric A. Hagberg, Daniel A. Schult, and Pieter J. Swart. Exploring Network Structure, Dynamics, and Function using NetworkX. In Gaël Varoquaux, Travis Vaught, and Jarrod Millman, editors, *Proceedings of the 7th Python in Science Conference*, pages 11–15, Pasadena, CA USA, 2008. Referenced on page 291.

[576] A. Rüegg, S. D. Huber, and M. Sigrist. Z_2-slave-spin theory for strongly correlated fermions. *Phys. Rev. B*, 81:155118, Apr 2010. Referenced on page 297.

[577] Rahul Nandkishore, Max A. Metlitski, and T. Senthil. Orthogonal metals: The simplest non-Fermi liquids. *Phys. Rev. B*, 86:045128, Jul 2012. Referenced on page 297.

[578] Snir Gazit, Fakher F. Assaad, and Subir Sachdev. Fermi Surface Reconstruction without Symmetry Breaking. *Phys. Rev. X*, 10:041057, Dec 2020. Referenced on page 297.

[579] Hendrik J. Monkhorst and James D. Pack. Special points for Brillouin-zone integrations. *Phys. Rev. B*, 13:5188–5192, Jun 1976. Referenced on page 304.